



---

# **The Development of Gold Nanoparticles Labelled with Transition Metal Complexes for Imaging Applications**

---

By

**NICOLA JANE ROGERS**

A thesis submitted to the University of Birmingham for the degree of DOCTOR  
OF PHILOSOPHY

School of Chemistry  
College of Engineering and Physical Sciences  
University of Birmingham  
2014

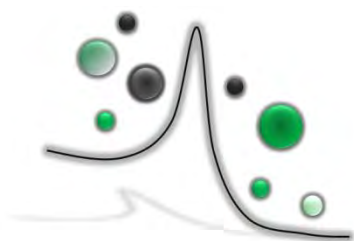
UNIVERSITY OF  
BIRMINGHAM

**University of Birmingham Research Archive**

**e-theses repository**

This unpublished thesis/dissertation is copyright of the author and/or third parties. The intellectual property rights of the author or third parties in respect of this work are as defined by The Copyright Designs and Patents Act 1988 or as modified by any successor legislation.

Any use made of information contained in this thesis/dissertation must be in accordance with that legislation and must be properly acknowledged. Further distribution or reproduction in any format is prohibited without the permission of the copyright holder.



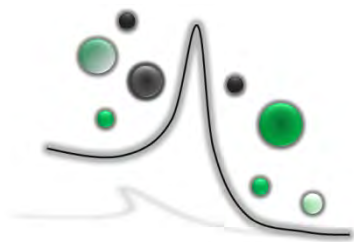
---

# Abstract

---

Aqueous dispersions of gold nanoparticles are efficiently labelled with low-spin  $d^6$  transition metal lumiphores, creating monodisperse luminescent nanoparticles with a plethora of potential imaging applications. 13 nm and 100 nm citrate-stabilised gold nanoparticles are used as inert scaffolds for the assembly of multiple transition metal lumiphores, and thiol-appended ruthenium(II) and iridium(III) polypyridyl complexes have been synthesised for surface-attachment. The direct attachment of cationic lumiphores to citrate-stabilised gold colloids with negative zeta potentials, affords nanoparticle aggregation, due to loss of electrostatic stabilisation. In order to circumvent this problem, a surfactant pre-coating step has been implemented, and the following commercial surfactants have been evaluated: Triton™ X-100, TWEEN® 20, and Zonyl® 7950. Gold nanoparticles coated with Zonyl® 7950 fluorosurfactant can be functionalised with cationic lumiphores and colloidal stability is maintained even at high nanoparticle concentrations, i.e. 9 nM. The fluorosurfactant not only ensures colloidal stability, but also enhances the emission of the ruthenium(II) and iridium(III) complexes investigated. Importantly, the complexes attached on the resultant luminescent nanoprobables do *not* exhibit luminescence quenching from the gold nanoparticles. Imaging applications of the resultant luminescent nanoparticles have been demonstrated in *in vitro* cellular uptake studies and in blood flow particle tracking within the microvasculature.

Furthermore, gold nanoparticles have been co-coated with lumiphores and both functional peptides, for targeted delivery in cells, and gadolinium(III) complexes, in order to realise imaging probes for both luminescence and MRI detection.



---

# Preface

---

Three years of doctoral training have taught me a host of skills that will stay with me for the rest of my career, from chemical techniques to a myriad of interpersonal skills. I believe that thorough scientific practice is paramount for good research, and should be thought of as one's legacy to science; however our understanding and interpretation of the world develops and changes with progression, the absolute data will never change.

This PhD experience has developed my communication skills tremendously, and I have learned to exploit opportunities beyond my own expertise whenever possible. Although my research project has focussed on the chemistry behind luminescent particle development for imaging applications, I have been very fortunate to work alongside experts in biosciences, biomedical research and chemical engineering, with significant involvement in the application developments. This has given me exposure to a wealth of different scientific fields, which I have found incredibly interesting and fulfilling.

Research by nature has its ebbs and flows, and it has taken me quite some time to recognise this; I feel that learning to accept the lows with the highs is the first step in climbing the steep learning curve of self-directed research. This transition, from directed study to independent research, can be quite daunting, and can lead to a lot of external resistance. It can be all too easy to fall into the trap of accepting theories and 'seeing' what other people 'see' without actually opening one's own eyes, but as Galileo once said:

*“for in the sciences the authority of thousands of opinions is not worth as much as one tiny spark of reason in an individual man” — Galileo Galilei, 1610*

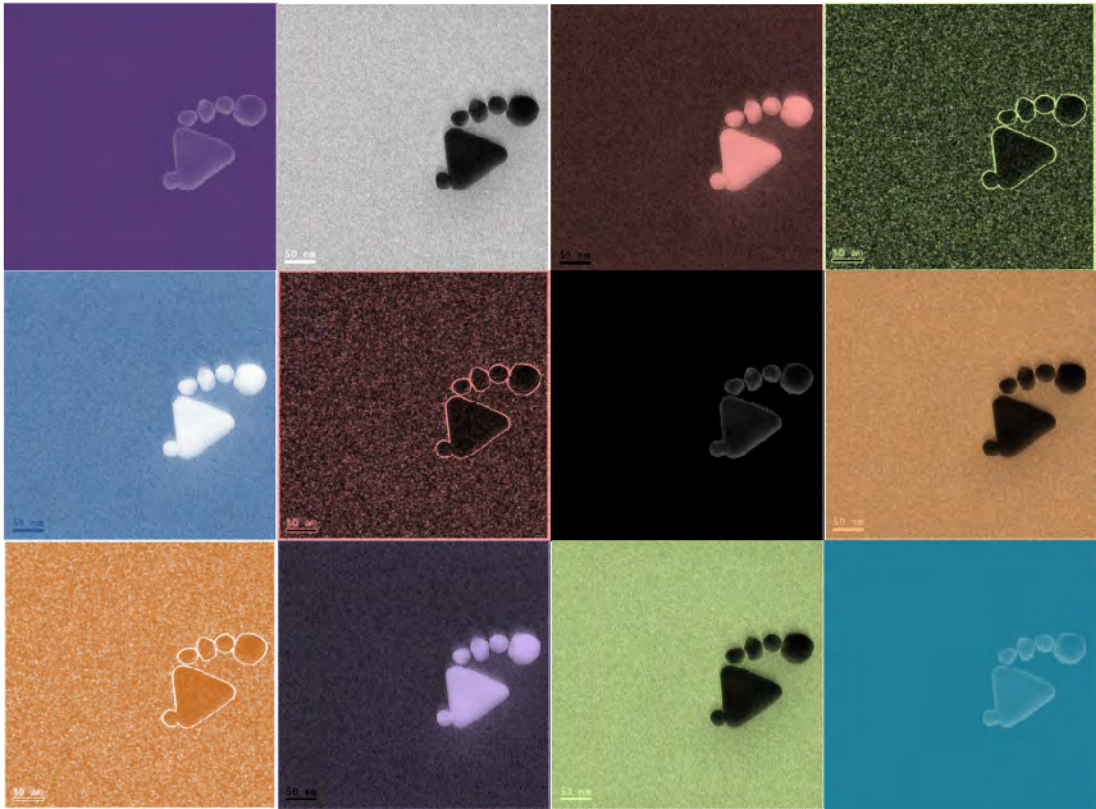
Research in any field has a creative element to it, and many artists will tell you that it is very difficult to be creative on demand. My Grandmother (Nan, aged 86) read my patent publication, and she is neither a chemist, nor a scientist, in fact she left school at 15 and committed her life to bringing up her family. However, she is one of the wisest and most lucid people I know, thus I was intrigued by her thoughts on my work.

*“Chemistry was not my forte at school. Periodic tables were not within my brushstroke but being able to reproduce by surface loading makes artistic sense, and will not alter the bulk, or should I say span, of the finished canvas.” — Nan, Phyllis Buckle, 2013*

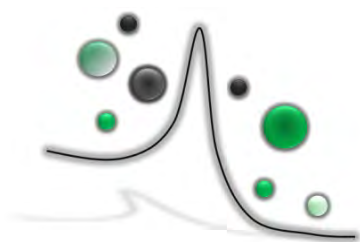
Highly specialised skills only give you the toolbox and the *in vogue* jargon to work within the confinements of a close-knit community, whereas being able to step back from the intricacies and appreciate the purpose and significance of research developments is crucial for progression; if I was not able to express what I was trying to achieve to my grandmother, then I would fear that I did not understand quite why I was doing it myself. I also believe that it is incredibly important to incorporate a great deal of candour when disseminating research to the wider community; it can be all too easy for the scientist to get carried away with hubristic experiments and lose touch with the bigger picture.

One of the greatest lessons I have learned about working closely with other people who share the passion of discovery, is that the collective achievement can far surpass the product of the individual efforts. It is my opinion that breaking down some of the political barriers in the academic environment, so that there is more openness in collaborative research, would lead to a more fruitful future for scientific research.

***Nicola Rogers 2014***



*Gold nano-footprints and silver linings; making the most of failed experiments.*



# Contents

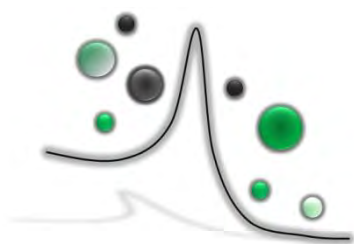
<b>1</b>	<b>Introduction</b>	<b>1</b>
-	1.1 Luminescent Nanoparticles for Imaging	2
-	1.2 Photoluminescence Imaging: A Move Towards Transition Metal Complexes	4
-	1.3 Gold Nanoparticle Imaging Probes	7
-	1.4 Thesis Outline	11
-	1.5 Acknowledgements	12
-	1.6 Chapter One References	13
<b>2</b>	<b>Surfactant-mediated Labelling of Gold Nanoparticles with a Luminescent Ruthenium(II) Complex</b>	<b>16</b>
-	2.1 Introduction	17
-	2.1.1 Methods of Gold Nanoparticle Synthesis	17
-	2.1.2 Ruthenium Polypyridyl Complexes	18
-	2.1.3 Current Strategies for Labelling Gold Nanoparticles with Transition Metal Complexes	22
-	2.1.4 Photophysical Effects Upon the Attachment of Lumiphores to Gold Nanoparticles	30
-	2.1.5 Functionalising Citrate-stabilised Gold Nanoparticles with Cationic Lumiphores	32
-	2.1.6 Chapter Outline	34
-	2.2 The Preparation of a Surface-binding Ruthenium(II) Polypyridyl Complex: <b>RuSH</b>	37
-	2.2.1 Synthesis of <b>RuSH</b>	37
-	2.2.2 Photophysical Characterisation of <b>RuSH</b>	40
-	2.3 Synthesis of 13 nm Gold Nanoparticles	43
-	2.4 Direct Attachment of <b>RuSH</b> to Citrate-stabilised 13 nm Gold Nanoparticles	47
-	2.5 Interaction of Triton™ X-100, TWEEN® 20, and Zonyl® 7950 with 13 nm Citrate-stabilised Gold Nanoparticles	49
-	2.6 Surfactant-mediated Labelling of 13 nm Citrate Nanoparticles with <b>RuSH</b> using the Surfactants Triton™ X-100, TWEEN® 20, and Zonyl® 7950	55
-	2.6.1 Further Investigations into Similar Surfactants to Zonyl® 7950, with Gold Nanoparticles	60
-	2.7 Synthesis and Characterisation of <b>Ru-T20·AuNP13</b>	62
-	2.8 Synthesis and Characterisation of <b>Ru-Z·AuNP13</b>	66
-	2.9 Photophysical Characterisation of <b>Ru-T20·AuNP13</b> and <b>Ru-Z·AuNP13</b>	74
-	2.10 Conclusion	78
-	2.11 Acknowledgements	79
-	2.12 Experimental	80
-	2.12.1 General Synthesis	80
-	2.12.2 Staining of Nanoparticles for TEM	89
-	2.12.3 X-ray Photoelectron Spectroscopy	90
-	2.13 Chapter Two References	91

<b>3</b>	<b>Cellular Imaging Applications of 13 nm and 100 nm Luminescent Ru(II)-Labelled Gold Nanoparticles</b>	<b>95</b>
-	3.1 Introduction	96
-	- 3.1.1 Chapter Outline	98
-	3.2 Seed-mediated Growth of 100 nm Gold Nanoparticles	100
-	3.3 Synthesis and Characterisation of <b>Ru-Z·AuNP100</b>	104
-	- 3.3.1 Photophysical Properties of <b>Ru-Z·AuNP100</b>	110
-	3.4 Cellular Uptake Studies of <b>Ru-Z·AuNP13</b> and <b>Ru-Z·AuNP100</b> in A549 Cells	112
-	3.5 Conclusion	120
-	3.6 Acknowledgements	121
-	3.7 Experimental	121
-	- 3.7.1 General Synthesis	121
-	- 3.7.2 Cell Studies with <b>Ru-Z·AuNP13</b> and <b>Ru-Z·AuNP100</b>	123
-	3.8 Chapter Three References	125
<b>4</b>	<b>Peptide-mediated Delivery of Luminescent Nanoparticles in Cells</b>	<b>127</b>
-	4.1 Introduction	128
-	- 4.1.1 Stabilising Gold Nanoparticles with Peptides	129
-	- 4.1.2 Cell-penetrating Peptides	130
-	- 4.1.3 Peptide-mediated Delivery of Luminescent Gold Nanoparticles in Cancerous Cells	132
-	- 4.1.4 Peptide-mediated Nuclear Targeting of Nanoparticles	136
-	- 4.1.5 Chapter Outline	138
-	4.2 Synthesis and Characterisation of Co-coated Gold Nanoparticles with Peptides and <b>RuSH</b>	140
-	- 4.2.1 Synthesis and Nanoparticle Characterisation of <b>Ru-CALNN·AuNP13</b> , <b>Ru-pHLIP·AuNP13</b> , and <b>Ru-C105Y-Z·AuNP13</b> .	144
-	- 4.2.2 Photophysical Characterisation of <b>Ru-CALNN·AuNP13</b> , <b>Ru-pHLIP·AuNP13</b> and <b>Ru-C105Y-Z·AuNP13</b> .	153
-	4.3 Applications of Peptide-mediated delivery of Luminescent Gold Nanoparticles	159
-	- 4.3.1 Cell Uptake of <b>Ru-CALNN·AuNP13</b>	159
-	- 4.3.2 pH-targeted Uptake of <b>Ru-pHLIP·AuNP13</b> in cancer cells	160
-	4.4 Conclusions and Future Work	163
-	4.5 Acknowledgements	165
-	4.6 Experimental	166
-	- 4.6.1 General Synthesis	166
-	- 4.6.2 Cell Studies with <b>Ru-CALNN·AuNP13</b>	169
-	- 4.6.3 Cell Studies with <b>Ru-pHLIP·AuNP13</b>	169
-	4.7 Chapter Four References	170

<b>5</b>	<b>Developing Iridium(III) Complexes for Labelling Gold Nanoparticles</b>	<b>173</b>
-	5.1 Introduction	174
-	- 5.1.1 Cyclometallated Iridium (III) Polypyridyl Complexes	174
-	- 5.1.2 Labelling Nanoparticles with Ir(III) Complexes	178
-	- 5.1.3 Chapter Outline	181
-	5.2 Synthesis and Characterisation of <b>IrBpySH</b> and <b>IrPhenSH</b>	185
-	5.3 Photophysical Characterisation of <b>IrBpySAc</b> and <b>IrPhenSAc</b>	188
-	5.4 Synthesis of Iridium(III)-labelled Gold Nanoparticles	197
-	- 5.4.1 Photophysical Characterisation of Ir(III)-labelled Gold Nanoparticles	201
-	5.5 Imaging Ir(III)-labelled Gold Nanoparticles in Flow Systems	206
-	5.6 Imaging Blood Flow in Biological Tissue with <b>IrBpy-Z · AuNP100</b>	208
-	- 5.6.1 Blood Flow Introduction	208
-	- 5.6.2 <i>In Vitro</i> Blood Flow Tracking	209
-	- 5.6.3 Imaging Nanoparticles in Biological Tissue	214
-	5.7 Developing Luminescent Ir(III)-labelled Gold Nanoparticles with $T_1$ MRI Contrast	217
-	5.8 Conclusion	224
-	5.9 Acknowledgements	225
-	5.10 Experimental	226
-	- 5.10.1 General Synthesis	226
-	- 5.10.2 Flow Imaging in Blood	238
-	- 5.10.3 Murine Tissue Studies	241
-	5.10.4 MRI Studies of <b>IrBpy-GdQ · AuNP13</b> Nanoparticles	242
-	5.11 Chapter Five References	243
<b>6</b>	<b>General Experimental</b>	<b>247</b>
-	6.1 Materials	248
-	6.2 General Experimental Details for Synthesis	248
-	6.3 Photophysical Characterisation Techniques	249
-	6.4 Nanoparticle Characterisation Techniques	250
-	6.5 Luminescent Microscopy	251
-	6.6 Acknowledgements	251

## Appendices

## Publications



---

# Chapter One

---

## Introduction

## 1.1 Luminescent Nanoparticles for Imaging

Luminescence imaging is a powerful tool that can achieve high sensitivity and quantitative detection using commercial optical microscopes. Developing probes for detection is a means of improving the diagnostic tools, which can be applied in a variety of very different scientific disciplines to advance fundamental research and clinical practice. Luminescence labelling offers improved resolution with optical microscopy over colorimetric staining techniques that exploit absorption/transmission and reflection of light; such techniques are often limited by scattering artifacts and relatively low contrast. Electron microscopy is another technique readily used to image biological structures, but this is a high-vacuum destructive technique and thus, sample preparation renders the imaged specimen in a state far removed from that of interest. Although electron microscopy can achieve nanometre imaging resolution, an additional disadvantage for biologically relevant applications is that it takes an incredibly long time to obtain quantitative data in respect of optical techniques: it takes >500 times as long to obtain useful data via electron microscopy than confocal optical microscopy, taking into consideration the full experimental pipeline.<sup>1</sup>

Molecular probes are useful as gross staining agents but lack the high spatial and temporal resolution required in many applications because it is difficult to image individual probes, as opposed to accumulations of stain. The design of luminescent nanoparticles can exploit the incorporation of multiple probe molecules localised on a single nanodevice, in order to ensure brightness. Nanoparticles can provide a flexible platform which can be modified to address many problems of the 21<sup>st</sup> century. Optical imaging at the nanoscale may lead to breakthroughs in biomolecular sciences, providing information on the monitoring of specific cellular processes, such as protein trafficking, and the targeting of cell organelles with high spatial resolution.<sup>2-6</sup> Optical nanoprobe for luminescence imaging present powerful tools for diagnostics in flow, such as in lab-on-a-chip devices,<sup>7</sup> or within biological systems,<sup>2,8</sup> and can

achieve high sensitivity in detection. Noble metal nanoparticles<sup>9</sup> and quantum dots<sup>10,11</sup> provide good candidates as optical nanoscale probes for detection by different imaging modalities.<sup>12</sup> The potential to target specific biochemicals, tissues or diseases, by modifying the particle surface with targeting vectors,<sup>13</sup> opens up new pathways towards diagnosis and treatment of disease, which is crucial for the progression of the medical sciences.<sup>11,14-16</sup> The emerging field of ‘theranostics’, a term used that is a portmanteau of therapeutic and diagnostic, not only seeks to image where disease occurs, but also to treat the disease, immediately upon localisation.<sup>17</sup> Nanotheranostics is applicable for the evergrowing field of ‘personalised medicine’, in which therapy can be adapted to a patient’s specific biomolecules using genetic information.<sup>18</sup> Personalised medicine may be the future for biomedicine, especially for cancer therapies, where effective treatment is far from a one-size-fits-all solution.

Luminescent tracer particles can also be used in rheological applications. The miniaturisation of technology has made microfluidic flow devices a popular area of research due to the advantages they offer: green, continuous chemistry with improved yields<sup>19</sup> and, in the case of the production of nanoparticles, improved monodispersities.<sup>20</sup> Luminescent tracer particles have been produced which faithfully follow flow in microchannels and can be imaged by techniques such as particle tracking velocimetry (PTV) as well as micro particle imaging velocimetry ( $\mu$ -PIV), to give spatial and temporal data respectively regarding the flow dynamics within a device.<sup>7</sup> Hence the ability to design nanoscale probes, which can give temporal and spatial information in one package, is desirable to assess the efficiency of new micro-devices.<sup>21,22</sup>

## 1.2 Photoluminescence Imaging: A Move Towards Transition Metal Complexes

Photoluminescence is the emission of light from matter following absorption of photons at a different wavelength. The last decade has seen the emergence of transition metal complexes as attractive candidates for luminescent imaging probes,<sup>23</sup> but until recently such stains have relied heavily on organic dyes, typically fused aromatic ring structures.<sup>24</sup> Organic fluorophores offer a good point-of-entry as molecular probes because they can offer substantial absorption cross-sections and high photoluminescence quantum yields. In addition, fluorescent proteins have revolutionised biological imaging, particularly green fluorescent protein (GFP). Such proteins can be expressed in a number of genetically modified cell lines, and even in animals, advancing the design of biosensors to study protein interactions.<sup>25</sup> Organic fluorophores can offer brightness and are relatively cheap to purchase, hence their ubiquitous usage for luminescence measurements in many different fields of research. However, the energy difference between excitation and emission peak maxima is relatively small (tens of nm) because the electronic transitions associated with the excitation and emission are to and from the same excited state and the ground state. A substantial energy difference between excitation and emission peak maxima (hundreds of nm) is desirable for three reasons: firstly, to prevent self-quenching (i.e. the re-absorption of emitted light by another proximate lumiphore of the same type); secondly to reduce the risk of detecting scattering excitation light from the excitation source, or attenuating a lot of the emission signal with filters; thirdly to distinguish the emission of the target probe from background autofluorescence (which is the fluorescence from endogenous fluorophores, e.g. DNA, that have small Stokes shifts). Organic fluorophores also have very short lifetimes (*ca.* 1 ns), which eliminates the possibility of image time-gating to remove autofluorescence signal,<sup>26</sup> and also a tendency to photobleach over time. Photobleaching is usually irreversible with

fluorophores because the dye accumulates permanent chemical damage due to the reactivity of the excited singlet state. This limits the time period over which experiments can be done.

Lanthanide chelates are also exploited for biological imaging as they have high photostability, large energy differences (>100 nm) between the excitation and emission peak maxima, and extremely long lifetimes (into the millisecond range) which can be used in time-resolved imaging techniques<sup>27</sup> and time-gated luminescence microscopy.<sup>28</sup> The highly shielded  $f$  orbitals lead to atomic-like spectral characteristics of the  $f-f$  transitions, which ensure unambiguous identification and sharp spectra. Distinct narrow spectral lines are imperative for multiplex labelling and detection, in which different probes are used to label different targets within the same sample. Clean detection channels at different wavelengths are necessary to identify each label exclusively, without signal cross-over. The relative intensities of each transition can also report on the local environment, and in some cases (e.g.  $\text{Nd}^{3+}$ ) lanthanides emit in the near-infra red (NIR) region, which is desirable for tissue penetration. In principle the trivalent lanthanides ions are ideal lumiphores for imaging because the emission is sharp and distinct, and delay-gated measurements can be implemented to remove autofluorescence in biological samples.<sup>29-31</sup> However, lanthanide ions are very toxic due to their similarity in behaviour and size to biologically ubiquitous metal ions such as  $\text{Ca}^{2+}$ , and formation of stable complexes is paramount for biological applications to avoid transmetallation.<sup>32</sup> An additional problem is the almost zero efficiency of the direct excitation of the lanthanide ion itself ( $\epsilon \sim 1-10 \text{ M}^{-1} \text{ cm}^{-1}$ ), due to the Laporte forbidden  $f-f$  (and often spin-forbidden) transitions.<sup>33</sup> This is usually circumvented by the use of organic antenna ligands, which present much greater absorption cross-sections as well as being able to transfer the absorbed energy from light, usually *via* a triplet state, to the lanthanide ion, thus populating the luminescent state indirectly. The net result of the cascade of energy through a series of concomitant energy levels ensures that the difference between the excitation and

emission wavelengths of antenna-sensitised lanthanide complexes is large (up to 400 nm). This is highly beneficial for the facile separation of excitation and emission light but can have one significant drawback; the excitation wavelength has to be pushed to a short wavelength with respect to the emission, i.e. most europium complexes require sensitisers which are excited in the UV range of electromagnetic spectrum.<sup>34,35</sup> This is disadvantageous because UV radiation is damaging to biological tissue, and in addition, short-wavelength radiation (<330 nm) and is incompatible with the glass optics of most conventional microscopes. Also, the multiple energy transfer steps involved in the luminescence of lanthanide complexes, some with efficiencies far below unity, can result in photoluminescence quantum yields that are inadequate for imaging.<sup>23</sup> Regardless of these difficulties, lanthanide imaging agents are being developed to address and overcome some of these issues, so that they can be used for biomedical analysis and cellular imaging.<sup>29</sup>

Transition metal complexes including the  $d^6$  metal centres Re(II),<sup>36</sup> Ru(II),<sup>37</sup> Os(II),<sup>38</sup> and Ir(III),<sup>39</sup> coordinated to high ligand-field polypyridyl ligands, are attractive imaging probe candidates for several reasons: these low-spin  $d^6$  complexes are closed-shell and kinetically inert because the exchange of ligands is very slow,<sup>23</sup> which is crucial to ensure low toxicity with heavy metal ions. Typically such complexes have attractive intrinsic photophysical properties in the visible region on the electromagnetic spectrum.<sup>23,24,40</sup> The lifetimes of the luminescent states are usually long (>100 ns) because de-excitation pathways arise from formally forbidden triplet electronic transitions, allowing time-gated emission techniques and luminescence lifetime imaging<sup>40,41</sup> to be employed. Transition metal lumiphores also exhibit large differences between the excitation and peak emission wavelengths because the singlet excited state (often a metal-to-ligand charge-transfer (MLCT) band) rapidly decays into the triplet state *via* spin-orbit coupling induced inter-system crossing.<sup>37</sup> Transition metal lumiphores thus luminescence from a lower energy state than the initially excited state. It is

also possible to tune the emission properties of transition metal complexes using a wide range of ligands because the emissive states emanate, at least in part, from ligand-centred transitions, and are thus sensitive to the electronic structure of the ligands.<sup>37</sup> An important criterion for the rational design of emissive  $d^6$  transition metal complexes is the position of the  $d-d$  metal-centred (MC) state; MC transitions are formally forbidden and thus have extremely long radiative lifetimes with high susceptibility to environmental quenching, and therefore have negligible luminescence quantum yields.<sup>38</sup> For this reason, Fe(II) tris(2,2'-bipyridine) is not emissive, even at 77K, because the  $^3\text{MC}$  state quenches the emission.<sup>38</sup> In addition, the  $d-d$  states of  $d^6$  transition metals are reactive with respect to decomposition by ligand displacement, and thus large crystal field splitting and hence high energy MC states are also required to prevent photochemical instability.<sup>38</sup>

### 1.3 Gold Nanoparticle Imaging Probes

Molecular lumiphores are useful labelling agents but the move towards the design of luminescent nanoparticles affords brightness by integrating multiple labels onto a single nanodevice. It is important to note that although attaching multiple lumiphores to a single reporter group may indeed produce highly luminescent imaging probes, the local high-concentrations of lumiphore complexes at the particle surface could induce self-quenching, and this lumiphore-lumiphore interactions are incredibly important when considering functionalised nanoparticles, even at low nanoparticle concentrations.<sup>42,43</sup>

The optical properties of metal nanoparticles have been of interest for centuries<sup>44</sup> and scientific research on colloidal metals dates back, at least, to the work of Michael Faraday.<sup>45</sup> Metal nanoparticles have become popular over the last few decades with the advent of nanotechnology and the desire to develop devices on scales beyond the molecule. The unique electronic band structures of these mesoscopic constructs result in their physical properties

lying somewhere between the macroscopic bulk properties of a solid and the atomic scale, whilst the large surface:bulk ratio of atoms permits many analogies between the chemical and physical properties of nanoparticles and 2D solid surfaces. The key to the popularity of gold nanoparticles lies in their ease of synthesis, as compared with traditional wet synthetic chemistry strategies; wet colloidal synthesis offers an elegant means by which to access thermodynamically stable edifices on this scale in a controlled manner.<sup>46</sup> Gold nanoparticles are regularly used in biology and medicine<sup>2,16,47</sup> due to their easily tuneable size, water-solubility, low toxicity and high surface area for drug and/or probe loading. Furthermore, the significant molecular weight of gold ensures high contrast for electron and x-ray based measurements.

Gold nanoparticles exhibit strong interactions with visible light because the conduction electrons on the metal surface undergo a collective and quantised oscillation when they are excited at a specific wavelength. This affords a highly absorptive surface plasmon resonance (SPR) peak in the UV-Vis absorption spectrum. The SPR scattering frequency and intensity are sensitive to particle size, shape and surface environment, and can be quantified by Mie theory<sup>48</sup> for spherical particles of arbitrary size.<sup>49</sup> The SPR scattering property can be exploited in optical imaging of particles<sup>44,50</sup> by both reflection microscopy techniques<sup>51,52</sup> and by dark field microscopy.<sup>53,54</sup> However, such techniques produce scattering artifacts in biological tissue, and therefore luminescence-based imaging techniques are advantageous. Over the last ten years there have been reports in the literature of gold nanoparticles exhibiting *intrinsic luminescence* properties,<sup>55</sup> although this phenomenon is much less well understood than the absorption properties of metal nanoparticles. The luminescence is attributed to the electron and hole interband recombinations within the metals. The luminescent particles reported tend to be small (sub-5 nm) and the quantum yields are low (*ca.*  $10^{-5}$ ). Nevertheless, some glutathione-capped particles have been reported to exhibit

quantum yields in the  $10^{-2}$  order of magnitude.<sup>56</sup> Although much progress in the development of these intrinsically luminescent nanoparticles has been made over the last ten years, the mechanisms of emission are not fully understood, and the emissive properties are very sensitive to particle size, surface functionalisation<sup>57</sup> and surface roughness.<sup>56</sup> This makes the design of multimodal imaging probes very difficult with such unpredictable luminescent properties, and the quantum yields are usually too low for imaging. However, recently the group of Vo-Dinh have synthesised gold ‘nanostars’,<sup>58</sup> which exhibit plasmon-enhanced two-photon luminescence, and have been used for imaging *in vitro* and *in vivo*.<sup>59,60</sup>

The development of luminescent nanoparticles by the functionalisation of nanoscale gold scaffolds with multiple luminescent reporter groups, as shown in the schematic of Figure 1.1, is therefore a more attractive approach for developing bright optical imaging probes. This strategy also allows the optical tagging of multimodal nanovehicles that can lead to theranostic devices.<sup>17</sup>

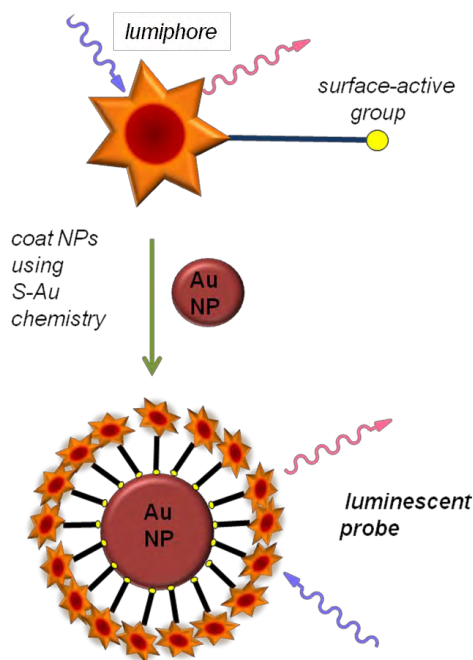


**Figure 1.1** Schematic of luminescent nanoparticle synthesis; functionalising gold nanoparticles with tailor-made surface-active lumiphores.

To consider such nanoparticles as platforms for imaging in biological environments, it is important to understand how complex nanomaterials will behave in complex environments. Several biomedical studies of gold nanoparticle uptake in tissues and tumours have been reported, both *in vivo*<sup>61,62</sup> and *in vitro*<sup>4,16,63,64</sup> mostly by destructive techniques such as electron microscopy and inductively coupled plasma mass spectrometry (ICPMS), or by imaging techniques that utilise the scattering optics of the particles alone (dark field microscopy or confocal reflection microscopy). However, luminescent probes can be assembled covalently on the surface of gold nanoparticles,<sup>65-67</sup> which provide a distinct optical signature independent of the particle properties and can be imaged both *in vitro* and *in vivo* in live tissue samples using conventional microscopy, and can also be imaged temporally in dynamic systems such as microfluidic devices. Quantum dots (i.e. semi-conductor nanocrystals which exhibit highly tuneable intrinsic luminescence following excitation and radiative relaxation across the size-dependent band gap) are often used as nanoscale luminescent probes due to their superior brightness,<sup>68-70</sup> but their luminescence properties are size dependent, they often suffer high toxicity, the surface modification is non-trivial, and the quantum dots tend to ‘blink’ upon irradiation. These limitations hinder their development as biological probes. Quantum dots also tend to be small (< 5nm), which usually leads to rapid renal clearance from circulation *in vivo*,<sup>71</sup> and they are thought to accumulate in organs over time.<sup>8</sup> Therefore, gold nanoparticles offer many advantages over quantum dots. Upconversion nanoparticles are another class of luminescent nanoprobe, which exploit non-linear optics that convert two or more low-energy photons into a higher-energy output photon, by doping nanocrystals with lanthanides. Such particles are of interest as they can be excited in the optically transparent NIR window for biological tissue.<sup>72</sup> However, upconversion particles are often difficult to synthesise, requiring high temperatures for prolonged periods of time and under hazardous reaction conditions. Furthermore, it is quite difficult to control the size and optical properties of the crystals formed, and the synthesis of sub-10 nm particles is challenging. In contrast, the

principle of using the gold nanoparticle as a scaffold for multifunctionalisation with luminescent tracers unearths a myriad of design options for the resultant nanodevice using straightforward synthetic techniques, whilst allowing control of both the particle size and luminescent properties in simple stages. Therefore the surface-functionalisation of gold nanoparticles is a flourishing area of research,<sup>65,66</sup> with applications not only in imaging probes,<sup>51,52,73,74</sup> but also nanomedicine<sup>47,75,76</sup> and catalysis.<sup>77,78</sup>

## 1.4 Thesis Outline

This thesis details the development of a novel labelling strategy to functionalise aqueous dispersions of 13 nm and 100 nm gold nanoparticles with luminescent transition metal complexes. Chapter Two focuses on the attachment of a previously developed surface-active ruthenium complex<sup>79</sup> to 13 nm gold nanoparticles. A surfactant-mediated coating process of the nanoparticles has been studied and optimised for imaging, and the resultant luminescent nanoparticles have been characterised.<sup>74</sup> Due to the success of this strategy, the luminescent nanoparticles are developed further in Chapter Three, following the synthesis of larger, 100 nm gold nanoparticles, and their subsequent functionalisation with the ruthenium(II) lumiphore. The cellular imaging applications of these 13 nm and 100 nm luminescent particles have also been explored in Chapter Three, in collaboration with Dr Nikolas Hodges, and Dr Robert Harris (School of Biosciences, University of Birmingham), with the help of Mr Sunil Claire (EPSRC Doctoral Training Centre in Physical Science for Imaging in the Biomedical Sciences – ‘PSIBS’, The University of Birmingham).

Further expansion of the nanoparticle work for biological imaging probes has been executed by the design and realisation of nanoparticles for targeted delivery. The attachment of targeting peptide probes to the luminescent nanoparticles has been investigated in Chapter Four, in an attempt to achieve actively targeted delivery of particles within living cells.

In Chapter Five, Ruthenium(II)-based luminescent probes have been replaced by cyclometallated iridium(III) complexes to produce brighter nanoparticles for imaging flow dynamics in microchannels. Successful tracer particles for particle tracking velocimetry (PTV) techniques have been investigated as tracers in blood flows, in collaboration with Professor Gerard Nash, Professor Stuart Egginton and Dr Hannah Jeffery (School of Clinical and Experimental Medicine, University of Birmingham), and with support from Dr David Lewis (School of Chemistry, University of Birmingham). Preliminary *in vivo* investigations have been performed to explore the possibility of imaging luminescent nanoparticles in biological tissue, following intravenous injection. In addition to these studies, the synthesis of bimodal imaging particles has been explored by attaching MRI-active gadolinium complexes with luminescent complexes to gold nanoparticles, with the help of Ms Lindsey van Gemeren (PSIBS, University of Birmingham), and her supervisors: Professor Michael Hannon (School of Chemistry), Professor Zoe Pikramenou, Professor David Adams, and Dr Nigel Davies (School of Clinical and Experimental Medicine, University of Birmingham).

## **1.5 Acknowledgements**

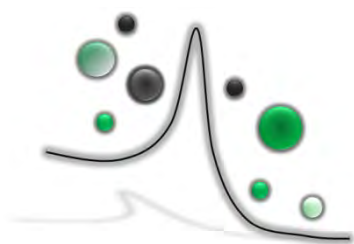
Thank you to my supervisor Professor Zoe Pikramenou for giving me the opportunity to work at the interface of the physical and biological sciences. Thank you to Dr Graham Worth, and to all the doctoral and postdoctoral researchers of the Pikramenou group, both past and present, for their support and guidance.

## 1.6 Chapter One References

- (1) Silvestri, L.; Bria, A.; Sacconi, L.; Iannello, G.; Pavone, F. S. *Opt. Express* **2012**, *20*, 20582.
- (2) Boisselier, E.; Astruc, D. *Chem. Soc. Rev.* **2009**, *38*, 1759.
- (3) Erathodiyil, N.; Ying, J. Y. *Acc. Chem. Res.* **2011**, *44*, 925.
- (4) Saha, K.; Bajaj, A.; Duncan, B.; Rotello, V. M. *Small* **2011**, *7*, 1903.
- (5) Bouzigues, C.; Gacoin, T.; Alexandrou, A. *ACS Nano* **2011**, *5*, 8488.
- (6) Shi, D.; Bedford, N. M.; Cho, H.-S. *Small* **2011**, *7*, 2549.
- (7) Lindken, R.; Rossi, M.; Grosse, S.; Westerweel, J. *Lab Chip* **2009**, *9*, 2551.
- (8) Douma, K.; Prinzen, L.; Slaaf, D. W.; Reutelingsperger, C. P. M.; Biessen, E. A. L.; Hackeng, T. M.; Post, M. J.; van Zandvoort, M. A. M. *J. Small* **2009**, *5*, 544.
- (9) Jain, P. K.; Huang, X.; El-Sayed, I. H.; El-Sayed, M. A. *Acc. Chem. Res.* **2008**, *41*, 1578.
- (10) Shimizu, K. T.; Neuhauser, R. G.; Leatherdale, C. A.; Empedocles, S. A.; Woo, W. K.; Bawendi, M. G. *Phys. Rev. B* **2001**, *63*, 205316.
- (11) Popović, Z.; Liu, W.; Chauhan, V. P.; Lee, J.; Wong, C.; Greytak, A. B.; Insin, N.; Nocera, D. G.; Fukumura, D.; Jain, R. K.; Bawendi, M. G. *Angew. Chem. Int. Ed.* **2010**, *49*, 8649.
- (12) Ali, Z.; Abbasi, A. Z.; Zhang, F.; Arosio, P.; Lascialfari, A.; Casula, M. F.; Wenk, A.; Kreyling, W.; Plapper, R.; Seidel, M.; Niessner, R.; Knöll, J.; Seubert, A.; Parak, W. J. *Anal. Chem.* **2011**, *83*, 2877.
- (13) Gu, F. X.; Karnik, R.; Wang, A. Z.; Alexis, F.; Levy-Nissenbaum, E.; Hong, S.; Langer, R. S.; Farokhzad, O. C. *Nano Today* **2007**, *2*, 14.
- (14) Kotov, N. A.; Winter, J. O.; Clements, I. P.; Jan, E.; Timko, B. P.; Campidelli, S.; Pathak, S.; Mazzatenta, A.; Lieber, C. M.; Prato, M.; Bellamkonda, R. V.; Silva, G. A.; Kam, N. W. S.; Patolsky, F.; Ballerini, L. *Adv. Mater.* **2009**, *21*, 3970.
- (15) Chithrani, B. D.; Ghazani, A. A.; Chan, W. C. W. *Nano Lett.* **2006**, *6*, 662.
- (16) Giljohann, D. A.; Seferos, D. S.; Daniel, W. L.; Massich, M. D.; Patel, P. C.; Mirkin, C. A. *Angew. Chem. Int. Ed.* **2010**, *49*, 3280.
- (17) Lammers, T.; Aime, S.; Hennink, W. E.; Storm, G.; Kiessling, F. *Acc. Chem. Res.* **2011**, *44*, 1029.
- (18) Kim, T. H.; Lee, S.; Chen, X. *Expert Rev. Mol. Diagn.* **2013**, *13*, 257.
- (19) Oelgemoeller, M. *Chem. Eng. Technol.* **2012**, *35*, 1144.
- (20) Wagner, J.; Köhler, J. M. *Nano Lett.* **2005**, *5*, 685.
- (21) Lewis, D. J.; Dore, V. D.; Goodwin, M. J.; Savage, A. C.; Nash, G. B.; Angeli, P.; Pikramenou, Z. *Meas. Sci. Technol.* **2012**, *23*, 084004.
- (22) Lewis, D. J.; Dore, V.; Rogers, N. J.; Mole, T. K.; Nash, G. B.; Angeli, P.; Pikramenou, Z. *Langmuir* **2013**, *29*, 14701.
- (23) Fernandez-Moreira, V.; Thorp-Greenwood, F. L.; Coogan, M. P. *Chem. Commun.* **2010**, *46*, 186.
- (24) Lo, K. K.-W.; Choi, A. W.-T.; Law, W. H.-T. *Dalton Trans.* **2012**, *41*, 6021.

- (25) Tsien, R. Y. *Angew. Chem., Int. Ed.* **2009**, *48*, 5612.
- (26) Jin, D.; Piper, J. A. *Anal. Chem.* **2011**, *83*, 2294.
- (27) Bünzli, J.-C. G.; Eliseeva, S. V. *Chem. Sci.* **2013**, *4*, 1939.
- (28) Connally, R. E.; Piper, J. A. *Ann. N. Y. Acad. Sci.* **2008**, *1130*, 106.
- (29) Bünzli, J.-C. G. *Chem. Rev.* **2010**, *110*, 2729.
- (30) Eliseeva, S. V.; Bünzli, J.-C. G. *Chem. Soc. Rev.* **2010**, *39*, 189.
- (31) Faulkner, S.; Pope, S. J. A.; Burton-Pye, B. P. *Appl. Spectrosc. Rev.* **2005**, *40*, 1.
- (32) Idée, J.-M.; Port, M.; Raynal, I.; Schaefer, M.; Le Greneur, S.; Corot, C. *Fundam. Clin. Pharmacol.* **2006**, *20*, 563.
- (33) Montgomery, C. P.; Murray, B. S.; New, E. J.; Pal, R.; Parker, D. *Acc. Chem. Res.* **2009**, *42*, 925.
- (34) Lewis, D. J.; Day, T. M.; MacPherson, J. V.; Pikramenou, Z. *Chem. Commun.* **2006**, 1433.
- (35) Lewis, D. J.; Moretta, F.; Holloway, A. T.; Pikramenou, Z. *Dalton Trans.* **2012**, *41*, 13138.
- (36) Stufkens, D. J.; Vlček Jr, A. *Coord. Chem. Rev.* **1998**, *177*, 127.
- (37) Juris, A.; Balzani, V.; Barigelletti, F.; Campagna, S.; Belser, P.; Von Zelewsky, A. *Coord. Chem. Rev.* **1988**, *84*, 85.
- (38) Demas, J. N.; DeGraff, B. A. *Anal. Chem.* **1991**, *63*, 829A.
- (39) Lowry, M. S.; Hudson, W. R.; Pascal, R. A.; Bernhard, S. *J. Am. Chem. Soc.* **2004**, *126*, 14129.
- (40) Baggaley, E.; Weinstein, J. A.; Williams, J. A. G. *Coord. Chem. Rev.* **2012**, *256*, 1762.
- (41) Kuil, J.; Steunenbergh, P.; Chin, P. T. K.; Oldenburg, J.; Jalink, K.; Velders, A. H.; van Leeuwen, F. W. B. *ChemBioChem* **2011**, *12*, 1897.
- (42) Pramod, P.; Sudeep, P. K.; Thomas, K. G.; Kamat, P. V. *J. Phys. Chem. B* **2006**, *110*, 20737.
- (43) Martí, A. A.; Colón, J. L. *Inorg. Chem.* **2010**, *49*, 7298.
- (44) Huang, X.; Jain, P. K.; El-Sayed, I. H.; El-Sayed, M. A. *Nanomed.* **2007**, *2*, 681.
- (45) Faraday, M. *Phil. Trans. R. Soc. London* **1857**, *147*, 145.
- (46) Shenhar, R.; Rotello, V. M. *Acc. Chem. Res.* **2003**, *36*, 549.
- (47) Weintraub, K. *Nature* **2013**, *495*, S14.
- (48) Mie, G. *Ann. Phys. (Berlin)* **1908**, *25*, 377.
- (49) Kelly, K. L.; Coronado, E.; Zhao, L. L.; Schatz, G. C. *J. Phys. Chem. B* **2003**, *107*, 668.
- (50) El-Sayed, I. H.; Huang, X.; El-Sayed, M. A. *Nano Lett.* **2005**, *5*, 829.
- (51) Davies, A.; Lewis, D. J.; Watson, S. P.; Thomas, S. G.; Pikramenou, Z. *Proc. Nat. Acad. Sci. U.S.A.* **2012**, *109*, 1862.
- (52) Rogers, N. J.; Claire, S.; Harris, R. M.; Farabi, S.; Zikeli, G.; Styles, I. B.; Hodges, N. J.; Pikramenou, Z. *Chem. Commun.* **2014**, *50*, 617.

- (53) Cai, H.; Yao, P. *Nanoscale* **2013**, *5*, 2892.
- (54) Orendorff, C. J.; Sau, T. K.; Murphy, C. J. *Small* **2006**, *2*, 636.
- (55) Eustis, S.; El-Sayed, M. A. *Chem. Soc. Rev.* **2006**, *35*, 209.
- (56) Zheng, J.; Zhou, C.; Yu, M.; Liu, J. *Nanoscale* **2012**, *4*, 4073.
- (57) Feng, J.-J.; Huang, H.; Zhou, D.-L.; Cai, L.-Y.; Tu, Q.-Q.; Wang, A.-J. *J. Mat. Chem. C* **2013**, *1*, 4720.
- (58) Yuan, H.; Khoury, C. G.; Hwang, H.; Wilson, C. M.; Grant, G. A.; Vo-Dinh, T. *Nanotechnology* **2012**, *23*, 075102.
- (59) Yuan, H.; Khoury, C. G.; Wilson, C. M.; Grant, G. A.; Bennett, A. J.; Vo-Dinh, T. *Nanomedicine: NBM* **2012**, *8*, 1355.
- (60) Yuan, H.; Fales, A. M.; Vo-Dinh, T. *J. Am. Chem. Soc.* **2012**, *134*, 11358.
- (61) Choi, C. H. J.; Zuckerman, J. E.; Webster, P.; Davis, M. E. *Proc. Natl. Acad. Sci. U. S. A.* **2011**, *108*, 6656.
- (62) Thakor, A. S.; Jokerst, J.; Zavaleta, C.; Massoud, T. F.; Gambhir, S. S. *Nano Lett.* **2011**, *11*, 4029.
- (63) Chou, L. Y. T.; Ming, K.; Chan, W. C. W. *Chem. Soc. Rev.* **2011**, *40*, 233.
- (64) Liu, X.; Huang, N.; Li, H.; Jin, Q.; Ji, J. *Langmuir* **2013**, *29*, 9138.
- (65) Thomas, K. G.; Kamat, P. V. *Acc. Chem. Res.* **2003**, *36*, 888.
- (66) Wilton-Ely, J. D. E. T. *J. Chem. Soc., Dalton Trans.* **2008**, 25.
- (67) Knight, E. R.; Leung, N. H.; Thompson, A. L.; Hogarth, G.; Wilton-Ely, J. D. E. T. *Inorg. Chem.* **2009**, *48*, 3866.
- (68) Hong, G. S.; Robinson, J. T.; Zhang, Y. J.; Diao, S.; Antaris, A. L.; Wang, Q. B.; Dai, H. J. *Angew. Chem., Int. Ed.* **2012**, *51*, 9818.
- (69) Michalet, X.; Pinaud, F. F.; Bentolila, L. A.; Tsay, J. M.; Doose, S.; Li, J. J.; Sundaresan, G.; Wu, A. M.; Gambhir, S. S.; Weiss, S. *Science* **2005**, *307*, 538.
- (70) Han, H.-S.; Martin, J. D.; Lee, J.; Harris, D. K.; Fukumura, D.; Jain, R. K.; Bawendi, M. *Angew. Chem., Int. Ed.* **2013**, *52*, 1414.
- (71) Koo, H.; Huh, M. S.; Sun, I.-C.; Yuk, S. H.; Choi, K.; Kim, K.; Kwon, I. C. *Acc. Chem. Res.* **2011**, *44*, 1018.
- (72) Wang, F.; Banerjee, D.; Liu, Y.; Chen, X.; Liu, X. *Analyst* **2010**, *135*, 1839.
- (73) Lewis, D. J.; Bruce, C.; Bohic, S.; Cloetens, P.; Hammond, S. P.; Arbon, D.; Blair-Reid, S.; Pikramenou, Z.; Kysela, B. *Nanomed.* **2010**, *5*, 1547.
- (74) Rogers, N. J.; Pikramenou, Z.; Birmingham, Ed. 2013; Vol. WO/2013/004989
- (75) You, J.-O.; Guo, P.; Auguste, D. T. *Angew. Chem., Int. Ed.* **2013**, *52*, 4141.
- (76) Ghosh, P.; Han, G.; De, M.; Kim, C. K.; Rotello, V. M. *Adv. Drug Deliv. Rev.* **2008**, *60*, 1307.
- (77) Liu, J.; Wang, F.; Qi, S.; Gu, Z.; Wu, G. *New J. Chem.* **2013**, *37*, 769.
- (78) Liu, Y.; Zhang, Y.; Ding, H.; Xu, S.; Li, M.; Kong, F.; Luo, Y.; Li, G. *J. Mater. Chem. A* **2013**, *1*, 3362.
- (79) Farabi, S., PhD Thesis, University of Birmingham, 2012.



---

# Chapter Two

---

Surfactant-mediated

Labelling of Gold

Nanoparticles with a

Luminescent

Ruthenium(II) Complex

## 2.1 Introduction

It is desirable to synthesise luminescent nanoparticles for imaging purposes; this chapter explores different procedures for attaching a tailor-made luminescent ruthenium polypyridyl complex to gold nanoparticles, in order to produce a brightly luminescent nanodevice. However, the attachment of a cationic transition metal complex to citrate-stabilised gold nanoparticles with a negative zeta potential has proved to be a challenge, and this chapter explores the development of a method to circumvent the difficulties faced, which has recently been published as a patent application.<sup>1</sup>

### 2.1.1 Methods of Gold Nanoparticle Synthesis

Top-down lithographic methods can be employed to produce well-defined sizes and often non-spherical shapes of noble metal nanoparticles without aggregation, either by photolithography or electron lithography, but commercial instrumentation is expensive and both techniques can only produce 2D structures in one step.<sup>2</sup> There are many bottom-up synthetic methods for the production of metal nanoparticles in the literature, from nanosphere lithography<sup>3</sup> to wet chemical synthesis, whereby the latter usually proceeds by the reduction of the metal ion from its salt in the presence of a suitable stabilising agent. A popular technique employed to produce aqueous gold nanoparticles is the *citrate reduction* of  $\text{HAuCl}_4$ , introduced by Turkevitch in 1951,<sup>4,5</sup> in which the gold nanoparticles are surrounded by an electrical double layer of citrate ions, chloride ions, and their associated cations; the Coulombic repulsions between capping layers override van der Waals attraction between metal centres, stabilising the nanoparticles from aggregation. Although the citrate reduction has been used for over fifty years, it is only within the last ten years that studies have been undertaken to infer more detail about the synthetic mechanism.<sup>6,7</sup> The reduction of the gold(III) salt using trisodium citrate is highly reproducible and the diameter of the particles produced can be controlled by the gold-to-citrate ratio; this effect was later investigated and

quantified by Frens,<sup>8</sup> where definite size control of the gold cores in the range 10 – 150 nm was reported. Perrault *et al.*<sup>9</sup> and Ziegler *et al.*<sup>10</sup> have recently extended this range to up to diameters of 300 nm, by the innovative use of seed-mediated synthesis in combination with various mild reducing agents, with monodisperse products as a result.

Electrostatically stabilised colloids can aggregate relatively easily,<sup>11</sup> and therefore the development of thiol-stabilised gold nanoparticle synthesis<sup>12</sup> has had a considerable impact on the bottom-up field because these nanoparticles are protected by steric repulsion. Using the paradigm of Whitesides' modification of gold surfaces by  $\omega$ -alkanethiol self-assembled monolayers,<sup>13,14</sup> Brust, Schiffrin and co-workers have translated these principles into the synthesis of nanoparticles.<sup>12</sup> The now universally utilised *Brust synthesis* involves transfer of a gold(III) salt (usually HAuCl<sub>4</sub>) to an organic phase, containing dodecanethiol and the reducing agent sodium borohydride. The phase transfer of the gold salt is mediated by a quaternary amine phase transfer catalyst. Thus, the gold(III) salt is reduced to gold(0) in the organic phase and nanoparticles are formed, which can be handled like a chemical compound. These nanoparticles tend to be < 5 nm in diameter and soluble in organic solvents; re-dispersion of the particles into various solvents can also be achieved, and the chemistry of the nanoparticles mimics that of the capping ligands exposed to the bulk solvent. The sterically stabilised particles produced by the Brust synthesis are often referred to as 'monolayer-protected clusters' (MPCs).<sup>15</sup>

### 2.1.2 Ruthenium Polypyridyl Complexes

Ru(II) polypyridyl complexes are arguably the most studied inorganic chromophores, and lend themselves to luminescent labelling for biological applications due to their intrinsic photophysical properties, including relatively long lifetimes (hundreds of ns) compared with biological background fluorescence, large differences in the excitation and emission

wavelengths, and good photostability. Ru(II) polypyridyl complexes can be excited and are emissive in the visible region of the electromagnetic spectrum. Therefore, the excitation and emission wavelengths involved are compatible with biological systems and glass microscopy optics, making this inorganic complex and its derivatives ideal for cellular imaging. As microscopy techniques continue to develop and push the boundaries of temporal and spatial resolution, there is an increasing demand for luminescent imaging labels that are resistant to photobleaching. Therefore, much work has been carried out recently with ruthenium complexes in the field of biological probes, including the development of protein labelling,<sup>16,17</sup> DNA-sensory work with intercalating ruthenium complexes,<sup>18,19</sup> and cellular staining agents.<sup>20,21</sup>

Taking the archetypal complex  $[\text{Ru}(\text{bpy})_3]^{2+}$ ,  $\text{Ru}^{2+}$  is a low-spin  $d^6$  metal ion, and the 2,2'-bipyridine ligands (bpy) are  $\sigma$ -donors through the orbitals localised on the nitrogen atoms, and have  $\pi$ -donating and  $\pi^*$ -accepting orbitals on the aromatic rings.<sup>22</sup> Low-spin  $d^6$  metal systems have low rates of ligand exchange and are thus relatively stable and unreactive, which is incredibly important when considering an imaging agent.<sup>22</sup> A simplification of the  $[\text{Ru}(\text{bpy})_3]^{2+}$  coordination geometry to octahedral symmetry, i.e. in the  $O_h$  point group (although it is in fact in the  $D_3$  point group), gives the molecular orbital diagram and energy states in **Figure 2.1**.

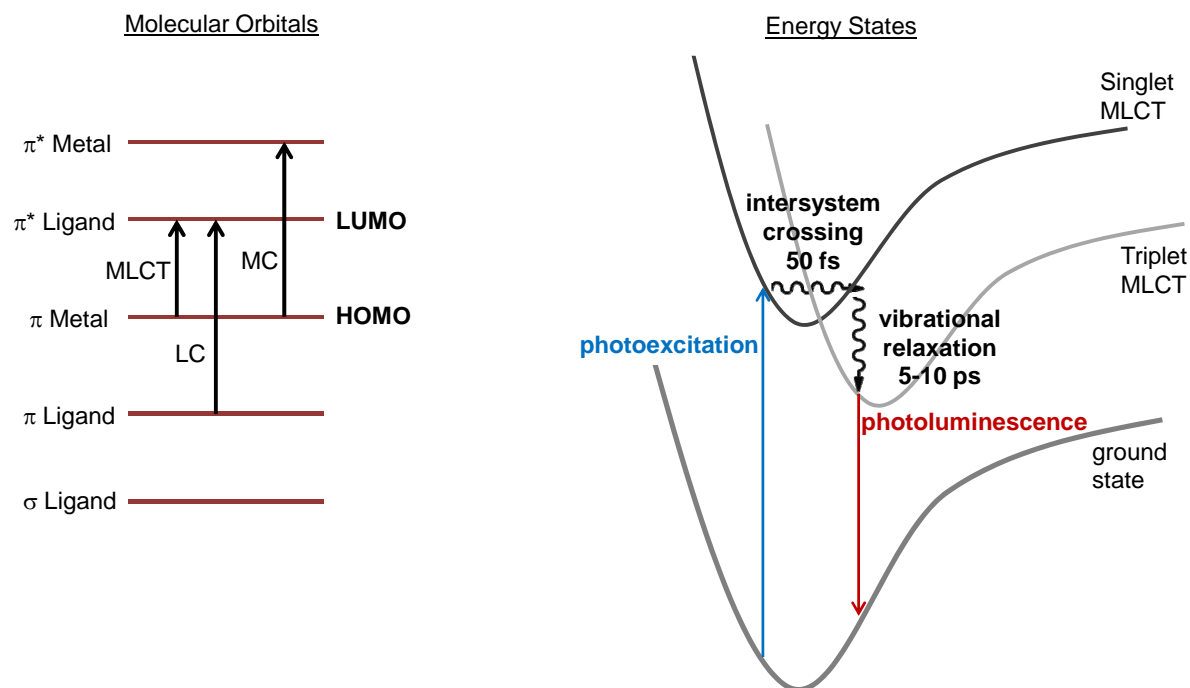


**Figure 2.1** Molecular orbital diagram (left) and energy state diagram (right) of  $\text{Ru}(\text{bpy})_3^{2+}$ , assuming  $O_h$  symmetry.

The  $[\text{Ru}(\text{bpy})_3]^{2+}$  complex absorbs light across the electromagnetic spectrum, from the blue to the UV regions, due to excitation of the singlet metal-to-ligand charge transfer (MLCT) band, or higher energy metal centred (MC) and ligand centred (LC) bands. The complex is highly absorptive, with molar absorption extinction coefficients in the order of  $10^4 \text{ mol}^{-1} \text{ dm}^3 \text{ cm}^{-1}$ .<sup>22</sup>

Excitation of  $[\text{Ru}(\text{bpy})_3]^{2+}$  in any of its absorption bands gives rise to photoluminescence from the triplet MLCT state. The relativistic heavy-atom effect (due to the presence of the ruthenium centre) allows efficient inter-system (ISC) crossing to occur, which facilitates the luminescence from the triplet MLCT state. However, despite the spin-orbit coupling induced by the heavy ruthenium centre (and thus the likelihood of the states actually being strong admixtures of singlet and triplet character), the electronic states are formally assigned as *singlet* or *triplet*.<sup>22,23</sup> Ultrafast LASER spectroscopy techniques have been employed to establish that upon excitation into the intense singlet MLCT band, ISC to the corresponding triplet MLCT band occurs within *ca.* 50 fs,<sup>24</sup> followed by vibrational relaxation on the 5–

10 ps time scale.<sup>25,26</sup> The energy position, lifetime and intensity of the photoluminescence are sensitive to solvent, due to the charge-transfer nature of the transition.

The luminescent excited state of  $[\text{Ru}(\text{bpy})_3]^{2+}$  can interact strongly with molecular oxygen, due to its long lifetime and its triplet character, resulting in luminescence quenching; the luminescence signal decreases as the non-radiative decay rate,  $k_{nr}$ , increases. The relationship between the rates of decay from the excited state, and both the observed lifetime of the luminescent state,  $\tau_{obs}$ , and the quantum yield of luminescence,  $\Phi$ , are shown below in Equations 2.1 and 2.2, where  $k_r$  is the radiative rate of decay from the excited state. ( $k_x$  are first order rate constants for generic unimolecular processes that induce the disappearance of the luminescent excited state.)

$$\tau_{obs} = \frac{1}{k_r + k_{nr}} \quad \text{Equation 2.1}$$

$$\Phi = \frac{k_r}{k_r + k_{nr}} \quad \text{Equation 2.2}$$

Ground-state molecular oxygen ( $\text{O}_2$  ( $^3\Sigma_g^-$ )) can give rise to a collision-dependent decrease in the luminescence of the triplet MLCT state, by both energy transfer and electron transfer.<sup>27</sup> This effect may be regarded as an unwanted interaction for luminescence imaging, but it can be exploited for diagnosis of oxygen concentration and/or photodynamic therapy, by production of highly reactive and toxic singlet oxygen (i.e.  $\text{O}_2$  ( $^1\Delta_g$ ) or  $\text{O}_2$  ( $^1\Sigma_g$ )) via energy transfer or superoxide radicals ( $\text{O}_2^{\bullet-}$ ) via electron transfer.<sup>27,28</sup>

### 2.1.3 Current Strategies for Labelling Gold Nanoparticles with Transition Metal Complexes

Several different strategies have been reported in the literature for the assembly of luminescent probe molecules onto gold nanoparticles,<sup>29,30</sup> as summarised in Figure 2.2., most of which use small (<10 nm) nanoparticles synthesised by the Brust-type two phase synthesis (Section 2.1.1).

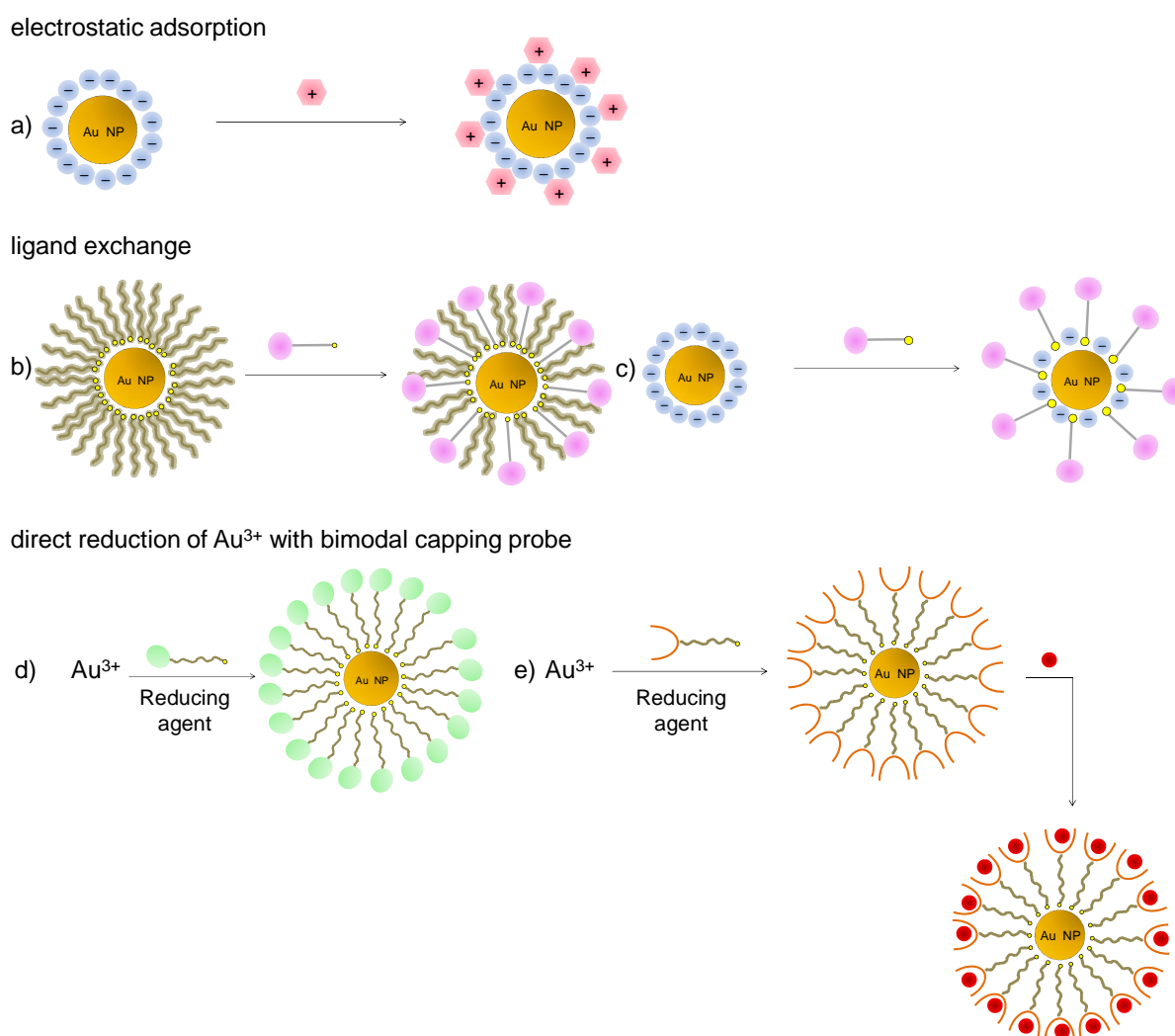


**Figure 2.2** Schematic of the different strategies available for attaching lumiphores onto gold nanoparticles. a) electrostatic attachment of probe molecules to charged nanoparticle surfaces, b) ligand displacement of alkylthiol ligands from MPCs with thiolated probe molecules, c) ligand displacement of citrate anions with thiolated probe molecules, d) direct reduction of Au(III) in the presence of thiolated probe molecules, e) direct reduction of Au(III) in the presence of thiolated coordination ligands, followed by the coordination of a metal to form surface-attached metal complexes on the nanoparticle.

The simplest way to construct lumiphore-labelled gold nanoparticles is to use electrostatic interactions between negatively-charged nanoparticle surfaces and cationic complexes (Figure 2.2a). In 2002 Huang and Murray<sup>31</sup> reported pH-dependent electrostatic binding of  $[\text{Ru}(\text{bpy})_3]^{2+}$  as its chloride salt to *ca.* 2 nm tiopronin-capped gold nanoparticles, which are negatively charged at a pH of 4.7 (Figure 2.3).

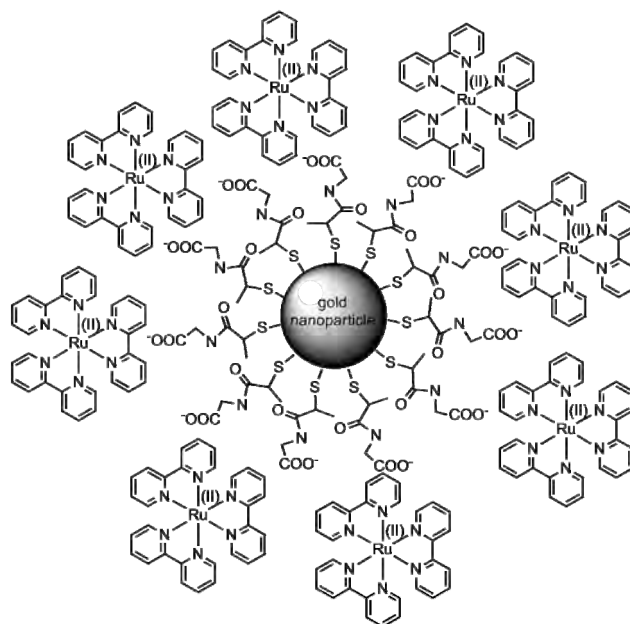


**Figure 2.3** Electrostatic binding of  $[\text{Ru}(\text{bpy})_3]^{2+}$  to tiopronin-capped gold nanoparticles, as reported by Huang and Murray.<sup>31</sup>

Upon adsorption to the negatively charged gold nanoparticles, steady-state photoluminescence studies of the  $[\text{Ru}(\text{bpy})_3]^{2+}$  complex showed a reduction in the emission intensity, and Huang and Murray report the triplet MLCT state to be quenched. Notably, substantial quenching was also reported in a control experiment with *cationic* *N,N*-trimethyl(undecylmercapto) ammonium protected nanoparticles, with which the  $[\text{Ru}(\text{bpy})_3]^{2+}$  cannot electrostatically bind. It was therefore concluded that both static *and* collisional quenching occurs in these physisorbed structures. Size-dependent nanoparticle quenching of  $[\text{Ru}(\text{bpy})_3]^{2+}$  has further been studied by the group, with particles in the 1–4 nm size range.<sup>32</sup>

There are disadvantages with electrostatic binding for probe attachment: the binding is likely to suffer from high salt concentrations due to electrostatic displacements, and electrostatic binding can reduce the colloidal stability of the nanoparticles, removing the integrity of an imaging probe. A strong covalent bond between the particle and the luminescent probe is desirable to ensure that dye leaching off the nanoparticle does not occur.

The covalent attachment of a probe molecule to gold nanoparticles can be achieved easily using well-established S-Au chemistry; tailor-made bifunctional metal complexes can be designed to incorporate a lumiphore centre with a thiolated moiety that is available for binding to gold, thus anchoring the complex on the nanoparticle surface. Brust-type thiolated gold nanoparticles (MPCs) can be functionalised post-synthesis by place-exchange reactions (Figure 2.2b), in which the thiol capping ligands are exchanged by thiolated probe molecules.<sup>33-35</sup> The ligand exchange process has been investigated extensively by Murray, and is reported to be an associative mechanism, with a rate and equilibrium stoichiometry dependent on the reaction feed ratio, and the relative steric bulk chain length.<sup>15,36,37</sup> In systems where the terminal groups of the thiols are quite different, often a large excess of the functionalising thiol moiety is necessary to drive the ligand exchange to achieve, for instance, a 1:1 binary self-assembled monolayer.<sup>38</sup> There are many examples in the literature whereby lumiphores have been attached to gold nanoparticles by place-exchange. In 2006, Pramod *et al.*<sup>39</sup> successfully attached thiol-derivatised  $\text{Ru}(\text{bpy})_3^{2+}$  complexes to gold nanoparticles by place-exchange, as shown in Figure 2.4.

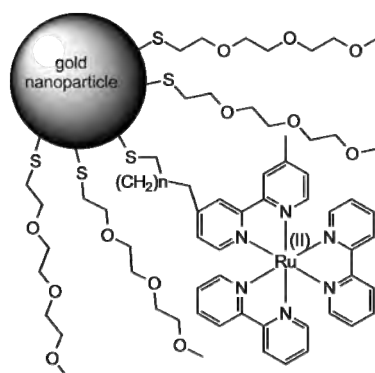


**Figure 2.4**  $Ru(bpy)_3^{2+}$  functionalised triethylene glycol-stabilised gold nanoparticles.  $n=1$  and  $n=5$ .<sup>39</sup>

The monothiol derivative of triethylene glycol was used as the initial capping agent to stabilise the gold nanoparticles, because the attachment of the Ru(II) complex to octanethiolate-protected gold nanoparticles was unsuccessful. This was thought to be due to the incompatibility of the polar dicationic Ru(II) complex and the nonpolar nature of alkanethiolated particles. The same group *has*, however, successfully attached a similar Ru(II) complex to photochemically produced dodecanethiol-capped gold nanorods by place-exchange.<sup>40</sup> Mixed monolayers were yielded in the exchange reactions of both complexes. Transient absorption spectroscopy studies of the nanohybrid systems illustrated photoinduced charge-transfer between the anchored  $[Ru(bpy)_3]^{2+}$  chromophores, rendering  $[Ru(bpy)_3]^+$  and  $[Ru(bpy)_3]^{3+}$  products that persisted for several nanoseconds before undergoing charge recombination. Charge-transfer was only observed at high Ru(II) complex concentrations on the nanoparticles and blank experiments using saturated solutions of the unattached Ru(II) complexes did not produce redox products. This confirms the necessity of the nanoparticle scaffold to anchor the Ru(II) complexes close enough together for this process.<sup>39</sup> It is noteworthy that these functionalised nanoparticles were only soluble in organic solvents, and thus not suitable for biological imaging.

Gunnaugsson and co-workers<sup>41</sup> recently attached ruthenium polypyridyl complexes (shown in Figure 2.5) to *ca.* 3 nm gold nanoparticles coated in tetraoctyl ammonium bromide, by ligand-exchange, and resuspended them in aqueous buffer. Three different complexes were synthesised using the same surface-active ligand, by varying the auxiliary ligands of the complex, to compare the DNA intercalating interactions of the resulting nanoparticles.

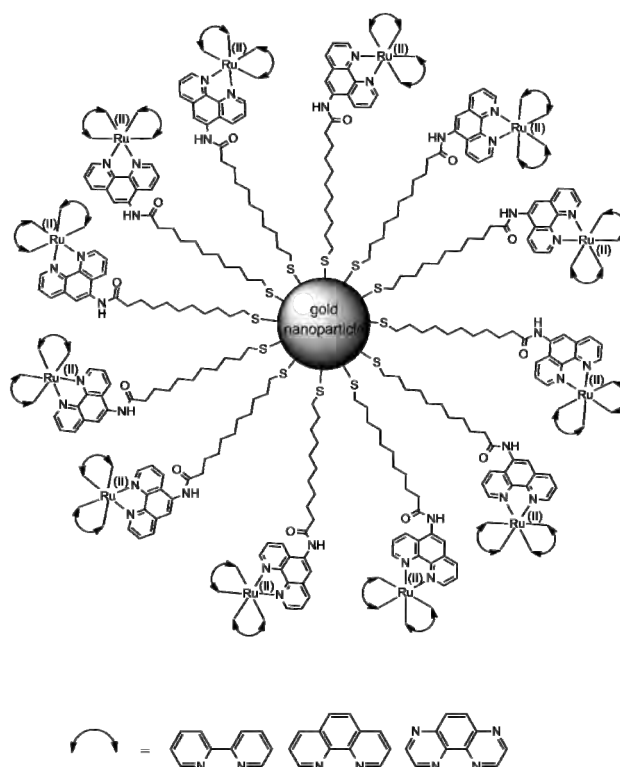


**Figure 2.5** *Ru(II)* complexes attached to tetraoctylammoniumbromide-stabilised gold nanoparticles, as reported by Gunnaugsson and co-workers.<sup>41</sup>

The resulting particles were found to be readily uptaken by HeLa cells (human cervical cancer cells), and evidence of DNA-binding *in vitro* was reported for nanoparticles coated in all three ruthenium complexes by examination of circular dichroism experiments and co-localisation of nanoparticle emission with fluorescently-labelled DNA in cell microscopy studies.

Pope and co-workers<sup>42</sup> have reported another example of place-exchange, in which they have attached a luminescent thioester-functionalised rhenium complex to poly(ethylene glycol)-coated gold nanoparticles. Unreacted rhenium was removed by extraction of the aqueous

particles with dichloromethane, and the complex attachment was confirmed by Energy Dispersive X-Ray (EDX) spectroscopy and steady-state photoluminescence. Time-resolved lifetime studies of the particles showed retention of the triplet MLCT emission lifetime upon surface attachment to the nanoparticles, in contradiction to preceding literature.

The functionalisation of *citrate*-stabilised metal nanoparticles can also be achieved by ligand-exchange, (Figure 2.2c) as the citrate anions are readily replaced by thiols.<sup>43-45</sup> However, this strategy is often problematic for cationic transition metal complexes, and is discussed in Section 2.1.4.

A different methodology sometimes used to synthesise functionalised gold nanoparticles is by the direct reduction of Au(III) by NaBH<sub>4</sub> in the presence of either a transition metal complex containing a gold-anchoring group (Figure 2.2d), or an anchoring ligand which is coordinately active (Figure 2.2e) and can complex to a metal in a second step.<sup>46</sup> This method has been explored by Mayer, in the formation of 3–4 nm gold and silver nanoparticles with fully conjugated ruthenium complexes, to facilitate potential electron transfer between ruthenium centres and silver nanoparticle cores.<sup>47</sup> Unlike most other work, Mayer's group has anchored the ruthenium complexes to the metal nanoparticles with pyridyl nitrogen atoms and thiophenyl sulphur atoms, as shown in Figure 2.6.<sup>48</sup>

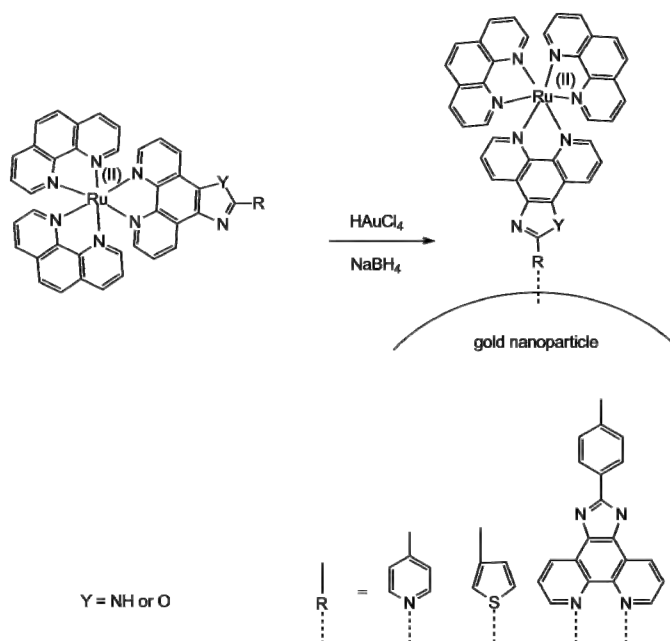


**Figure 2.6** Functionalisation of gold nanoparticles with fully conjugated Ru(II) complexes, by direct reduction of Au(III) in the presence of the stabilisation complex.<sup>47</sup>

The complex, the solvent system, and the ratio of Au(III)/Ru(II) chosen in each synthesis were all found to influence the stability, the size and the shape of the resultant nanoparticles. A 33 % decrease in the steady-state luminescence was reported on the stable particles, in respect of the free complex. This is attributed to the quenching by the gold nanoparticles. Direct reduction of Au(III) salts in the presence of ruthenium(II) bipyridyl dithiocarbamate complexes has also been reported by Beer *et al.*,<sup>49</sup> as shown in Figure 2.7. The resultant Ru(II)-coated nanoparticles were 3–4 nm in diameter, and luminescence quenching was also reported; almost complete quenching of the photoluminescence was observed upon formation of the functionalised nanoparticles.

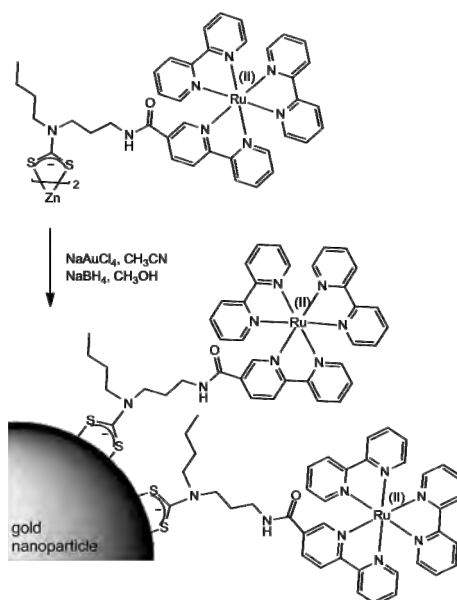


**Figure 2.7** Functionalisation of gold nanoparticles by direct reduction of Au(III) in the presence of ruthenium (II) bipyridyl dithiocarbamate complexes, as reported by Beer and co-workers<sup>49</sup>

It was also reported that displacement of the dithiocarbamate complex with dodecanthiol was not possible, even with stirring over five days, thus verifying the robustness of the system.

A similar strategy of direct reduction was also employed in 2011 by Yu *et al.*<sup>50</sup> (Figure 2.8) to produce *ca.* 7 nm ruthenium(II) labelled gold nanoparticles with electrochemiluminescence activity, using an amine group to bind to the gold.

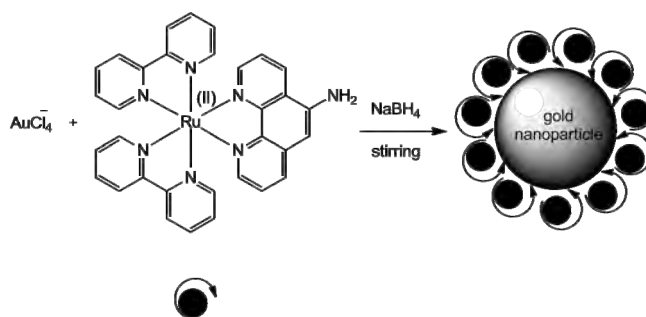


**Figure 2.8** Schematic for the one-pot synthesis of ruthenium functionalised gold nanoparticles by Yu *et al.*<sup>50</sup>

Photoluminescence was also observed on the resultant nanoparticles, although the luminescence intensity of the ruthenium complex reduced fifteen-fold upon attachment to the

gold nanoparticles, in respect of the free complex, due to luminescence quenching by the nanoparticle core.

When employing this one-pot direct reduction synthetic strategy to functionalise metal nanoparticles, the probe group has to be designed with two integral functions; not only must the probe be designed to optimise its luminescence, the stabilising properties must also be maximised so that it can provide a capping agent for the particles. The complex is introduced *in situ* during particle formation and caps the particle as it forms, and therefore has to be tuned to the size of the particle desired as well as its secondary function. Therefore, the particle size and coating cannot be varied independently from one another with ease, and the coating density or bimodal coating of the surface is difficult to control. This technique tends to yield small, relatively polydisperse nanoparticles, which are not ideal for biomedical theranostic devices.

Examples of gold nanoparticles functionalised with non-luminescent transition metal complexes, for alternative applications to imaging, have been synthesised by place-exchange with thiolated ferrocene complexes for redox sensing<sup>51</sup> and by direct reduction of Au(III) in the presence of thiolated carbonyl ligands, followed by coordination with Ru(II) for catalytic applications<sup>52,53</sup> and by direct reduction in the presence of soft-donor appended complexes for materials synthesis by Wilton-Ely and co-workers.<sup>54,55</sup>

#### **2.1.4 Photophysical Effects Upon the Attachment of Lumiphores to Gold Nanoparticles**

Upon attaching luminescent dye molecules to gold nanoparticles, the localised SPR of the gold nanoparticles can have a dramatic influence on the luminescence of the dye due to the strong electromagnetic field generated at the particle surface.<sup>2</sup> Upon excitation of the SPR, the

electromagnetic near-field is enhanced in the vicinity of the particle, which in turn interacts with the excited states of nearby lumiphores. Both enhancement and deactivation of the excited luminescent state can manifest from the proximity of the gold core, and to date, there are numerous reports on the effects of nanoparticles on the photophysics of organic dyes.<sup>29,56-</sup>

<sup>59</sup> Luminescence deactivation of the excited state can occur by energy transfer to the gold nanoparticles in a similar manner to Förster resonance energy transfer (FRET) between lumiphores, due to their high absorption extinction coefficients across the whole of the UV-Vis spectrum. Conversely, quenching can occur by electron transfer from the excited state to the continuum of energy levels in the metallic core. Both of these effects increase the non-radiative rates of decay from the excited state. However, the luminescence properties can equally be enhanced by the SPR; the light intensity enhancement by the near-field amplification at the resonant frequency of the SPR can either increase the excitation of the lumiphore by amplifying the field of the absorption light, if the excitation wavelength overlaps with the SPR, or increase the radiative rate and thus the quantum yield of the lumiphore by amplifying the electromagnetic field of the emission radiation, if the emission wavelengths overlap with SPR.<sup>2</sup> In addition to these particle-lumiphore interactions, any electronic molecule-molecule interactions are likely to occur due to the high local concentrations of the lumiphores on the nanoparticle surface. At increased distances up to *ca.* 10 nm the nanoparticle is not able to interact electronically with the excited state, but the enhanced electromagnetic field is still strong enough to increase the radiative rate and enhance the luminescence up to 100-fold.<sup>2,59</sup>

In general, it is proposed that lumiphores in very close proximity to the surface (<5 nm) interact strongly with the electronics of the particle, and tend to have quenched emission. The quenching of ruthenium(II) complexes upon attachment to gold nanoparticles has been reported in several studies, as discussed above, and is summarised in Table 2.1.

**Table 2.1** Summary of literature on luminescent ruthenium(II) complexes on gold nanoparticles

author/ publication	year	labelling strategy	size	quenching upon binding to gold nanoparticles
Murray <sup>31</sup>	2002	electrostatic binding	~ 2 nm	70% reduction in the emission intensity
Beer and Thiebaut <sup>49</sup>	2006	direct reduction	~3 nm	emission band almost completely quenched
Thomas and Kamat <sup>39</sup>	2006	ligand exchange	5 nm	20% of signal had a much reduced lifetime component
Mayer <sup>48</sup>	2006	direct reduction	2–30 nm	33% reduction in the emission intensity
Cui <sup>50</sup>	2011	direct reduction	7 nm	luminescence intensity reduced fifteen-fold
Gunnlaugsson <sup>41</sup>	2011	ligand exchange	~4 nm	significant quenching
Dietzek <sup>60</sup>	2012	ligand exchange	30 and 60 nm	luminescence not measured

### 2.1.5 Functionalising Citrate-stabilised Gold Nanoparticles with Cationic Lumiphores

For the purpose of optical tracking of individual reporter groups, larger nanoparticle centres are desired, which can be synthesised by the citrate-reduction method.<sup>5,9,10</sup> The citrate-stabilised particles are particularly attractive for biomedical applications because the sols are aqueous and preparations afford repeatable sizes with good monodispersity. The functionalisation of *citrate*-stabilised gold nanoparticles can also be achieved by ligand exchange (Figure 2.2c), and in previous studies within the Pikramenou research group *neutral* luminescent europium complexes have been successfully attached to citrate gold nanoparticles to make luminescent imaging probes.<sup>43,45,61</sup> The pre-eminence of the neutral complex designs for enabling attachment and steric stability of the particles in these studies,

without losing stability of the particles in the partially-coated states, was integral to the probe formation. Dietzek *et al.* coated 60 nm citrate-stabilised nanoparticles in anionic Ru(II) isothiocyanato complexes and maintained the nanoparticle integrity.<sup>60</sup> Similarly, Toma and co-workers<sup>62</sup> have previously coated citrate gold nanoparticles with pentacyanoferrate complexes without losing particle stability, but the transition metal complexes in this study were tri-anionic. However, if cationic complexes are added to citrate gold nanoparticles, the surface-functionalisation can initiate particle aggregation because the surface charge neutralisation upon functionalisation sacrifices electrostatic stability.<sup>63,64</sup> This can make their functionalisation difficult as electrostatic stability is often lost in the coating procedure, and thus there are few reports in the literature of such systems.

To circumvent the problem of nanoparticle aggregation upon functionalisation, Chen and co-workers<sup>65</sup> proposed a two-step functionalisation strategy of citrate nanoparticles to coat with both neutral and positively charged thiols, by first functionalising the surface with liponic acid, in order to slow down the removal of the negative charge during displacement with the modifying thiol. A similar approach has been reported using the commercial polysorbate surfactant TWEEN®.<sup>66,67</sup> It is proposed that the initial coating of citrate-stabilised gold nanoparticles with TWEEN® allows the subsequent coating of the particles with thiols because the weakly adsorbed oligo(ethylene glycol) moieties of the TWEEN® surfactant protects the gold nanoparticle surfaces sterically from aggregation. However, they can be displaced easily by thiolated species, and once completely displaced are stabilised by the coating thiols. TWEEN® surfactants have since been used to mediate peptide nucleic acid conjugated gold nanoparticles<sup>68</sup> and to coat nanoparticles and subsequently detect Cr<sup>3+</sup> chelation to citrate anions on the particle surface by surface-enhanced Raman spectroscopy (SERS), whilst resisting aggregation.<sup>69</sup> Poly(ethylene glycol) units are frequently added to gold nanoparticles in the literature to increase their stability, especially within biological

media.<sup>70-72</sup> Fluorosurfactant-capped nanoparticles have also been reported to exhibit high stability in the presence of salt for selective colorimetric detection of homocysteine via induced aggregation.<sup>73,74</sup>

### 2.1.6 Chapter Outline

In this chapter, the interaction of three commercially available surfactants (Triton™ X-100, TWEEN® 20 and Zonyl® 7950) with 13 nm citrate-stabilised gold nanoparticles is reported. The structures of these three commercial surfactants are presented in Figure 2.9 below.

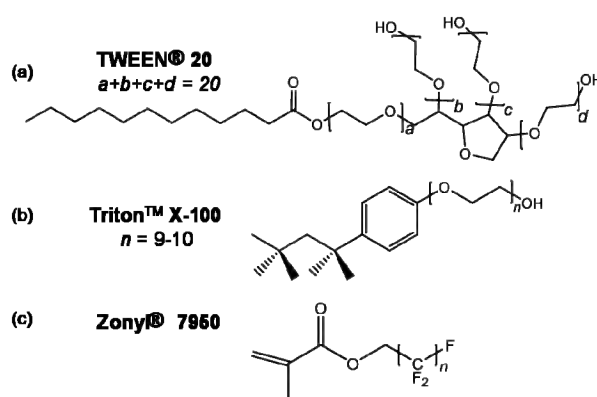


**Figure 2.9** Structures of the following surfactants: (a) TWEEN® 20; (b) Triton™ X-100; and (c) Zonyl® 7950.

TWEEN® 20 and Triton™ X-100 are supplied as viscous liquids and used without purification. Zonyl® 7950 is supplied as a formulation in isopropanol, and has been analysed by GC-MS,  $^1\text{H}$  and  $^{13}\text{C}\{^1\text{H}\}$  PENDANT NMR, to approximate that  $1 \text{ mg mL}^{-1}$  of the Zonyl® 7950 formulation is *ca.* 1 mM fluorosurfactant (see Chapter Two experimental, Section 2.12.1). 13 nm gold nanoparticles have been coated with these surfactants, and the surface-interactions with the particles have been characterised. A schematic of the particles is shown in Figure 2.10.

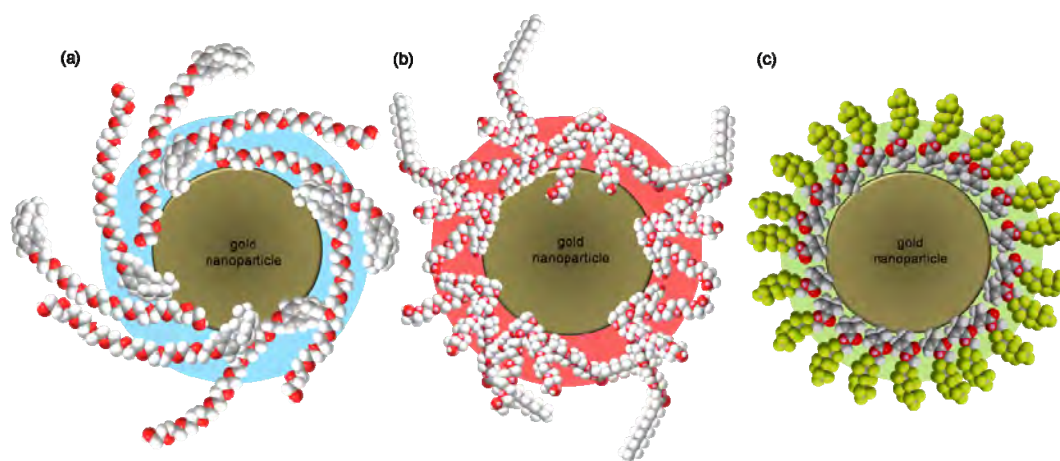


**Figure 2.10** Schematics of 13 nm gold nanoparticles coated in (a) Triton™ X-100, (b) TWEEN® 20, and (c) Zonyl® 7950.

The expediency of each surfactant to facilitate the luminescent labelling of the particles with a dicationic surface-active ruthenium polypyridyl complex, **RuSH**, without losing colloidal stability, is evaluated and discussed herein. The structure of **RuSH**, which is made *in situ* from the oxidatively stable **RuSAc** thioester analogue complex, is shown in Figure 2.11, and a schematic of the isolated nanoparticles coated in TWEEN® 20 and **RuSH**, i.e. **Ru-T20•AuNP13**, and coated in Zonyl® 7950 and **RuSH**, i.e. **Ru-Z•AuNP13**, is presented in Figure 2.12.

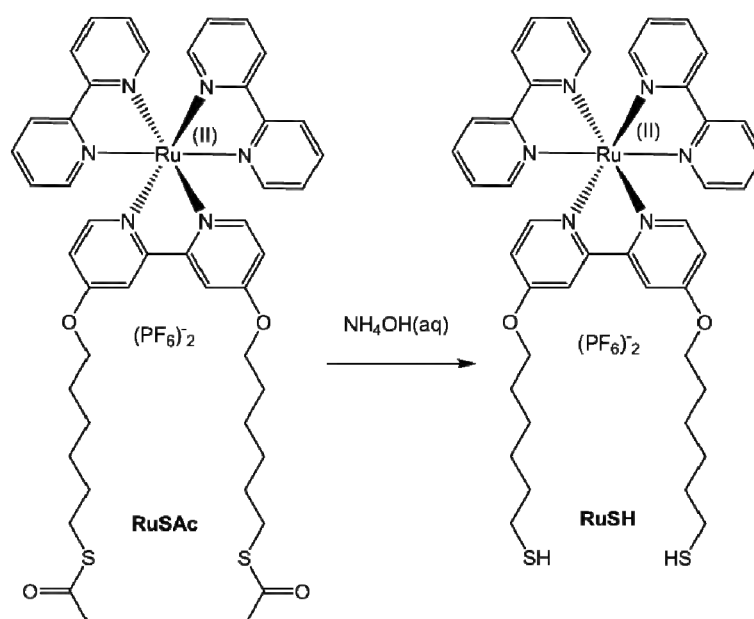


**Figure 2.11** Structures of **RuSAc** and **RuSH** complexes discussed in this chapter.

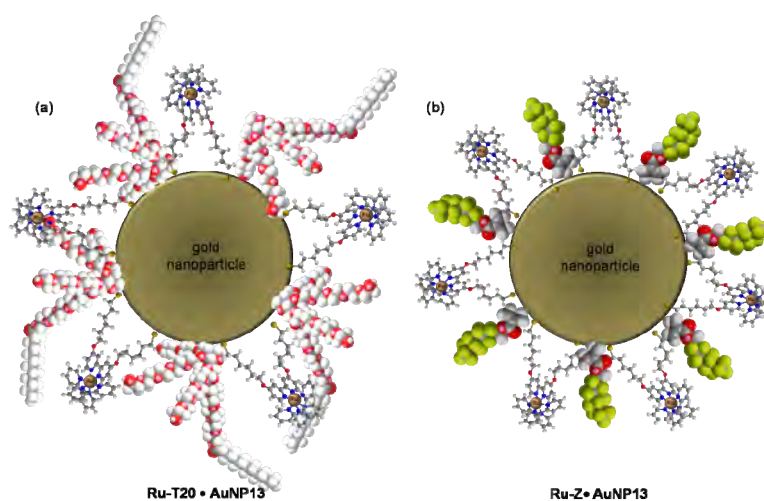


**Figure 2.12** Schematic of (a) **Ru-T20•AuNP13** and (b) **Ru-Z•AuNP13** nanoparticles, as discussed in this chapter.

## 2.2 The Preparation of a Surface-binding Ruthenium(II) Polypyridyl Complex: RuSH

### 2.2.1 Synthesis of RuSH

The tailor-made ruthenium complex **RuSH** was first prepared in the Pikramenou research group by Dr Shiva Farabi,<sup>75,76</sup> based on the parent archetypal ruthenium tris(bipyridine) lumiphore. **RuSH** incorporates two surface-binding thiols groups attached to the functionalised bipyridine ligand, separated by a hexyl spacer to prevent previously reported luminescence quenching of the chromophore by the gold surface.<sup>77</sup> In brief, the ancilliary ligand was synthesised by the Williamson reaction of 6-bromohexene with 4,4'-dihydroxy-2,2'-bipyridine, and complexed to Ru(bpy)<sub>2</sub>Cl<sub>2</sub> by refluxing in ethanol. The complex was purified by precipitation as the hexafluorophosphate salt in ethanol, and the terminal olefin groups were finally converted into thioesters by free-radical mediated nucleophilic addition of thioacetic acid, to give **RuSAc**.<sup>76</sup> This protected thiol analogue was isolated and fully characterised, and the active thiol groups were unmasked by thioester hydrolysis with aqueous ammonia to produce **RuSH**, as shown in Figure 2.13, immediately prior to addition to gold nanoparticles.<sup>1,76</sup>

The **BpyHex** ligand formation was confirmed by electrospray mass spectrometry, with a peak observed for the protonated ligand at  $m/z$  353.2, i.e. [M+H]<sup>+</sup>, and for the sodium adduct at  $m/z$  375.2, i.e. [M+Na]<sup>+</sup>. <sup>1</sup>H NMR reveals all the expected protons for **BpyHex**, integrating to the correct expected signal intensities, and the loss of the broad H-bonded O-H frequency (centred at 2760 cm<sup>-1</sup> for 4,4'-dihydroxy-2,2'-bipyridine) in the powder Fourier transform infrared spectroscopy (FT-IR) absorption spectrum of **BpyHex** corroborates the ether formation. <sup>1</sup>H and <sup>13</sup>C NMR assignments were made by analysis of 2D COSY and HSQC spectra (Appendix 9) and agree with previously reported data,<sup>75</sup> as published by the author.<sup>76</sup>

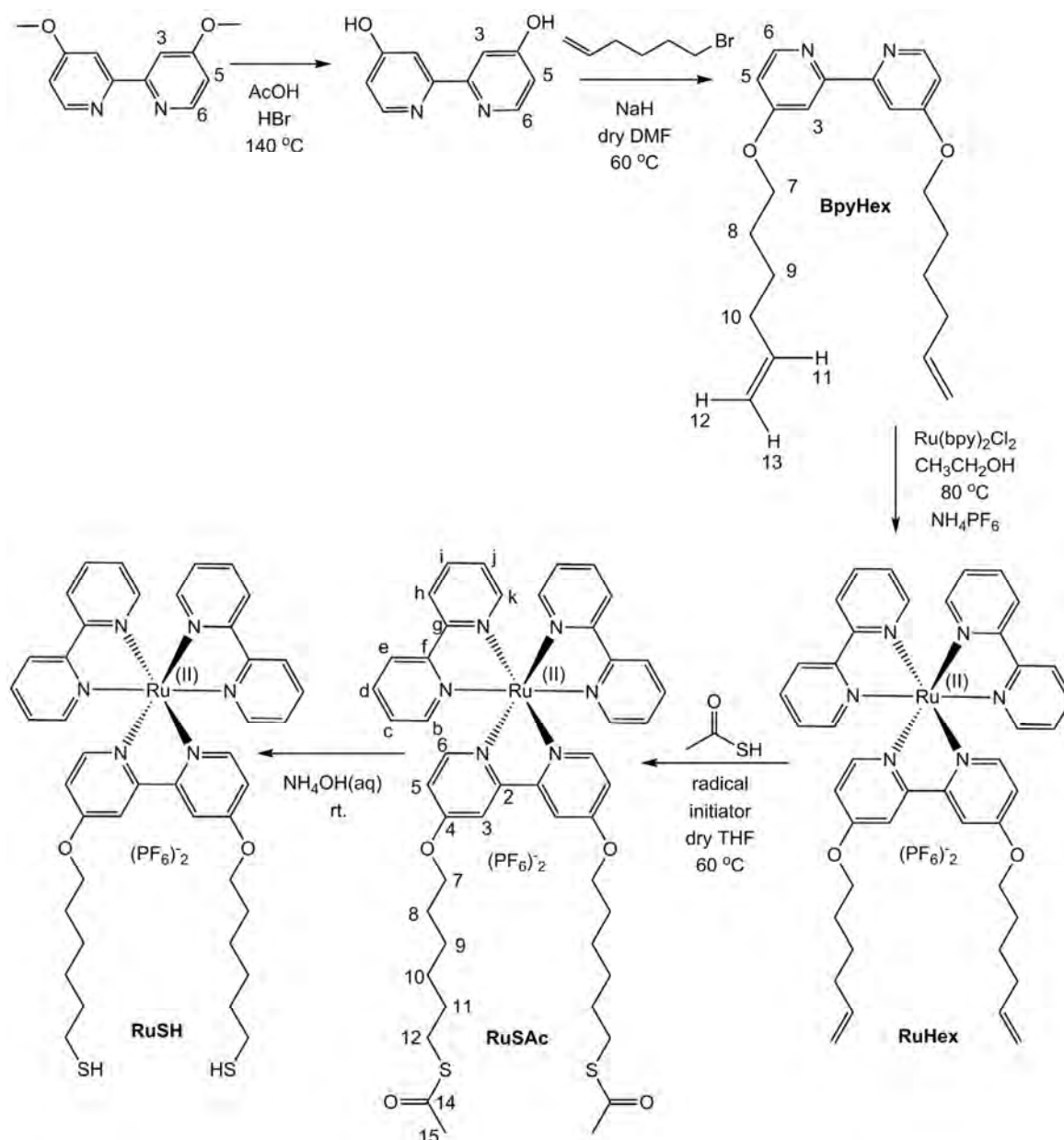


**Figure 2.13** Synthesis of the surface-binding Ru(II) complex **RuSH**.

Successful complexation of the **BpyHex** ligand to give **RuHex** is evident from electrospray mass spectrometry, with peaks observed for the cationic species following loss of counter ions, at  $m/z$  911.1, corresponding to  $[M-PF_6]^+$ , and at  $m/z$  383.2, corresponding to  $[M-2PF_6]^{2+}$ . The **BpyHex** ligand protons exhibit significant chemical shifts upon complexation to Ru<sup>2+</sup>: H<sub>6</sub> shifts upfield from 8.45 ppm in the free **BpyHex** ligand to 7.41 ppm in **RuHex**, as this proton experiences electron shielding due to the proximity of the Ru(II) *d*-electrons. H<sub>3</sub> and H<sub>5</sub>, however, shift downfield slightly, from 7.94 ppm and 6.82 ppm in the

free ligand, to 7.97 ppm and 6.90 ppm respectively in the complex: these protons face away from the metal centre and experience a slight overall deshielding effect upon complexation, due to the donation of electrons from the ligand towards the metal centre.  $^1\text{H}$  and  $^{13}\text{C}$  NMR assignments were made by analysis of 2D COSY and HSQC spectra (Appendix 9) and agree with previously reported data,<sup>75</sup> as published by the author.<sup>76</sup> The purity of the **RuHex** compound can only be estimated as *ca.* 95% by inspection of the NMR data, and was carried forward to the next step of the synthesis.

Successful thioesterification of the **RuHex** complex was confirmed by  $^1\text{H}$  and  $^{13}\text{C}\{^1\text{H}\}$ PENDANT NMR spectroscopy and mass spectrometry. Electrospray mass spectrometry of **RuSAc** revealed peaks at  $m/z$  1063.2, corresponding to the loss of one counterion, i.e.  $[\text{M}-\text{PF}_6]^+$ , and at  $m/z$  459.1 for  $[\text{M}-2\text{PF}_6]^{2+}$ , due to the loss of two counterions. It was possible to obtain CHN elemental analysis of **RuSAc** within 0.2% of the theoretical percentage mass of each element, confirming the purity of this final isolated product, and the carbonyl bond of each thioester is evident from the peak observed at  $1683\text{ cm}^{-1}$  in the FT-IR absorption spectrum. Notably, this is absent from the FT-IR absorption spectrum of **RuHex**. The successful thioesterification reaction was confirmed unequivocally by  $^1\text{H}$  NMR spectra, with loss of the olefin protons at *ca.* 5.8 ppm and 5.0 ppm, and the appearance of the triplet at 2.85 ppm ( $\text{H}_{12}$ ) and the terminal methyl group of each thioester at 2.27 ppm.  $^1\text{H}$  and  $^{13}\text{C}$  NMR assignments were made by analysis of 2D COSY and HSQC spectra (Appendix 9) and agree with previously reported data,<sup>75</sup> as published by the author.<sup>76</sup> The thiol groups were finally unmasked *in situ* by thioester hydrolysis with aqueous ammonia directly prior to addition to the nanoparticles, to give **RuSH**, which was confirmed by MALDI mass spectrometry using a gentisic acid matrix, with a peak at  $m/z$  829.7, corresponding to  $[\text{M}-2\text{PF}_6]^{1+}$ , i.e. the *monocationic* molecular parent ion (similar 1+

molecular parent ions are observed in MALDI for  $[\text{Ru}(\text{bpy})_3](\text{PF}_6)_2$  at  $m/z$  570.01, corresponding to  $[\text{Ru}(\text{bpy})_3]^{1+}$  using a sinapinic acid matrix)<sup>78</sup>.

## 2.2.2 Photophysical Characterisation of RuSH

The solution-based photophysical properties of **RuSAc** have been studied in the Pikramenou research group previously in  $\text{CH}_3\text{CN}$ ,<sup>75</sup> and the UV-Vis absorption spectrum in Figure 2.14 agrees with this work.<sup>75</sup> However, upon attachment to citrate-stabilised gold nanoparticles, the complex is exposed to an *aqueous* system, and thus the photophysical properties of the free complex in a 1% (v/v)  $\text{CH}_3\text{CN}$  in water solution, have also been measured (Figure 2.14).

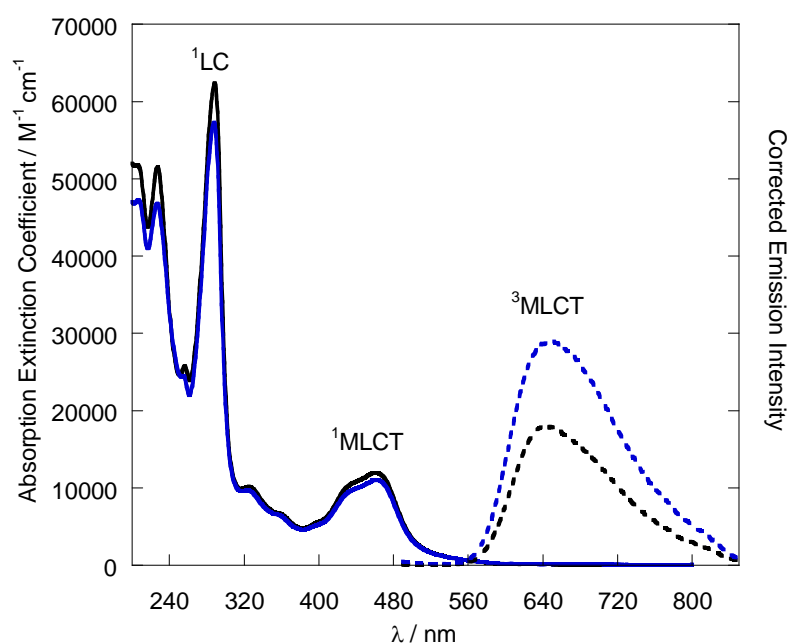


**Figure 2.14** UV-Vis absorption spectra of aerated 15  $\mu\text{M}$  **RuSAc** in  $\text{CH}_3\text{CN}$  (black solid line) and in 1%  $\text{CH}_3\text{CN}$ , water (blue solid line), and steady-state luminescence emission spectra in  $\text{CH}_3\text{CN}$  (black dashed line) and in 1%  $\text{CH}_3\text{CN}$ , water (blue dashed line),  $\lambda_{\text{exc}} = 450\text{nm}$ . Spectra corrected for instrument response.

The **RuSAc** complex is insoluble in water as the hexafluorophosphate salt, and thus 1%  $\text{CH}_3\text{CN}$  is required for solubility. Both absorption spectra exhibit the same bands at the same energies; the singlet MLCT state is observable at 410–480 nm and the sharp LC state ( $\pi$ – $\pi^*$ )

is present at 289 nm. Weak absorptions are also seen between 300–380 nm, and are thought to be MC ( $d-d$ ) transitions.<sup>22</sup> The spectra in Figure 2.14 are very similar to that of  $[\text{Ru}(\text{bpy})_3](\text{PF}_6)_2$ <sup>79,80</sup> however, the singlet MLCT state experiences a *ca.* 10 nm bathochromic shift in the absorption  $\lambda_{\text{max}}$  upon the ether functionalisation of one of the bipyridine ligands in the 4,4' positions, in **RuSAC**, with respect to  $[\text{Ru}(\text{bpy})_3](\text{PF}_6)_2$ .<sup>79,80</sup> This shift is expected due to the electron donating effect of the oxygen lone pairs to the pyridine  $\pi$ -ring. Electron-rich  $\pi$ -systems increase the energy of the  $\pi_{\text{M}}$  orbitals by increasing the formal crystal field splitting, and although the  $\pi_{\text{L}}^*$  orbitals will also increase in energy, there will still be  $\pi_{\text{L}}^*$  orbitals at the original energy position from the remaining unsubstituted bpy ligands. Thus, the energy gap of the MLCT transition decreases from  $[\text{Ru}(\text{bpy})_3](\text{PF}_6)_2$  to **RuSAC**. The excitation spectra of **RuSAC** in solutions of both  $\text{CH}_3\text{CN}$  and water (1%  $\text{CH}_3\text{CN}$ ) are shown below in Figure 2.15.

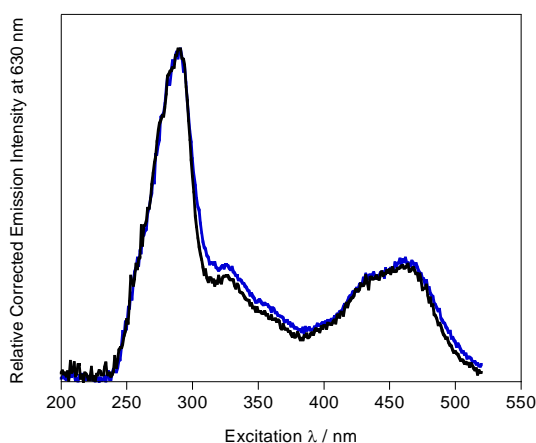


**Figure 2.15** Excitation Spectra of **RuSAC** in  $\text{CH}_3\text{CN}$  (black) and water (1%  $\text{CH}_3\text{CN}$ ) (blue),  $\lambda_{\text{em}} = 630$  nm. Spectra corrected for instrument response.

The complex emits from the triplet MLCT state (at  $\lambda_{\text{em}} = 630$  nm) following excitation into any of the singlet excited states between 250–500 nm, i.e. the LC, MC and the MLCT states, as can be seen in Figure 2.15. The excitation spectra in both aqueous and  $\text{CH}_3\text{CN}$  solvent systems resemble the photoabsorption spectra in Figure 2.14.

The steady-state luminescence spectra (Figure 2.13) display solvent dependency; aerated solutions are more emissive in 1% CH<sub>3</sub>CN/water than CH<sub>3</sub>CN solutions, per unit concentration, and exhibit a 5 nm red shift in  $\lambda_{\text{max}}$  positions. Similarly, a 10 nm red-shift is observed when the parent complex Ru(bpy)<sub>3</sub>Cl<sub>2</sub> is dissolved in water, with respect to CH<sub>3</sub>CN; the chloride salt was used for comparison due to availability. The photophysical properties are summarised in Table 2.2.

**Table 2.2** Summary of the photophysical properties of **RuSAc** and the parent complex Ru(bpy)<sub>3</sub>Cl<sub>2</sub> for comparison in aqueous and CH<sub>3</sub>CN solutions.

	$\Phi$ / % <sup>a</sup>	$\tau$ / ns <sup>b</sup>	$\lambda_{\text{max}}$ / nm <sup>c</sup>
Ru(bpy) <sub>3</sub> Cl <sub>2</sub> in H <sub>2</sub> O	2.8 <sup>d</sup> [5.5] <sup>e</sup>	405 [700]	625
Ru(bpy) <sub>3</sub> Cl <sub>2</sub> in CH <sub>3</sub> CN	1.6 <sup>f</sup> [7.8] <sup>e</sup>	155 [870]	615
<b>RuSAc</b> in 1% CH <sub>3</sub> CN/H <sub>2</sub> O	2.0±0.5 [2.5±0.5]	260 [325]	650
<b>RuSAc</b> in CH <sub>3</sub> CN	1.0±0.5 [7.0±1.0]	130 [775]	645

<sup>a</sup> aerated  $\Phi$ s measured using an integrating sphere, deaerated values in square brackets. (systems degassed with nitrogen for 20 min).

<sup>b</sup> lifetimes measured in aerated solutions, deaerated measurements shown in square brackets. Errors estimated as  $\pm 6$  %.

<sup>c</sup> error estimated as  $\pm 3$  nm.

<sup>d</sup> data taken from Nakamaru.<sup>81</sup>

<sup>e</sup> data taken from Harriman.<sup>82</sup>

<sup>f</sup> data taken from Balzani and co-workers.<sup>83</sup>

The red-shift in the emission is expected because charge-transfer bands are sensitive to solvent polarity. Spectroscopic studies provide significant evidence that the MLCT states are localised on one bipyridine unit, and therefore possess appreciable intramolecular charge separation.<sup>22</sup> This charge localisation is stabilised by polar solvent systems and thus state red-shifts.

Both the ruthenium(II) complexes (**RuSAc** and  $\text{Ru}(\text{bpy})_3\text{Cl}_2$ ) in Table 2.2 display oxygen sensitivity, in both solvent systems studied, although much greater quenching of the luminescence is observed in solutions of  $\text{CH}_3\text{CN}$ , than in aqueous systems: a *ca.* 80% decrease in the observed lifetime is observed for both **RuSAc** and  $\text{Ru}(\text{bpy})_3\text{Cl}_2$  in aerated  $\text{CH}_3\text{CN}$  solutions, with respect to deaerated systems, whereas a 20% decrease for **RuSAc** and a 40% decrease for  $\text{Ru}(\text{bpy})_3\text{Cl}_2$  are observed in an aqueous environment. Similar trends are observed in the luminescence  $\Phi$ s of each system. The  $\Phi$  of triplet MLCT luminescence (measured at  $\lambda_{\text{exc}} = 450 \text{ nm}$ ) of **RuSAc** is  $1.0 \pm 0.5\%$  in  $\text{CH}_3\text{CN}$ , whereas it increases to  $2.0 \pm 0.5\%$  in 1%  $\text{CH}_3\text{CN}/\text{water}$  (See Table 2.2). The  $\Phi$  of **RuSAc** in water is marginally lower than that of  $\text{Ru}(\text{bpy})_3\text{Cl}_2$  in all of the studied systems, which may be due to the reduction in symmetry following functionalisation of one of the ligands, which opens up more non-radiative vibrational decay paths.

### 2.3 Synthesis of 13 nm Gold Nanoparticles

13 nm sodium citrate gold nanoparticles were chosen due to their highly reproducible preparation and narrow size distribution, i.e.  $13 \pm 1.7 \text{ nm}$ , by analysis of 100 nanoparticles by TEM.<sup>5</sup> This nanoparticle preparation, initially developed by Turkevitch in 1951,<sup>4</sup> and later refined by Frens,<sup>8</sup> is the most commonly employed to synthesis aqueous sols of gold nanoparticles in the 10-20 nm size-range, with root-mean-square deviations in the size distribution of 12.5%,<sup>4</sup> and has been utilised several times in the Pikramenou research group over the last decade for nanoparticle studies, owing to the facile and repeatable preparation.<sup>1,45,61,76,84</sup>

13 nm citrate-stabilised gold nanoparticles were synthesised according to Grabar *et al.*<sup>5</sup> by reduction of the  $\text{Au}^{3+}$  salt,  $\text{HAuCl}_4$ , in water, with trisodium citrate. The trisodium citrate salt

not only reduces the gold(III) ions, it also caps the resulting nanoparticles, along with the spectator chloride ions, and presumably oxidation products of the citrate anions. These capping ions stabilise the nanoparticles electrostatically, with respect to aggregation (discussed in Section 2.1.1)<sup>6,7</sup> as shown in the schematic below, Figure 2.16.

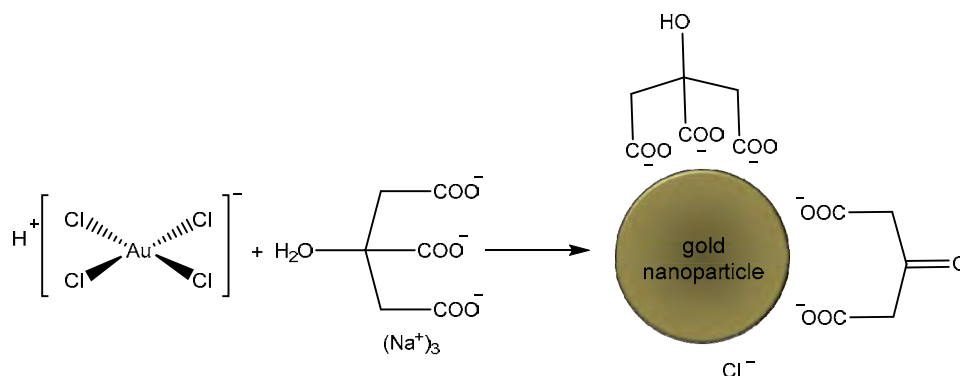


**Figure 2.16** *Synthesis of 13 nm citrate-stabilised gold nanoparticles.*

The resulting 9 nM aqueous colloid (concentration estimated from the size of the nanoparticles and the concentration of  $\text{Au}^{3+}$  ions used, assuming all ions form nanoparticles.<sup>43</sup> See Appendix 1.1) was characterised by UV-Vis absorption spectroscopy, dynamic light scattering (DLS), electrophoretic light scattering (to measure the zeta potential) and transmission electron microscopy (TEM), which are presented in Figure 2.17.

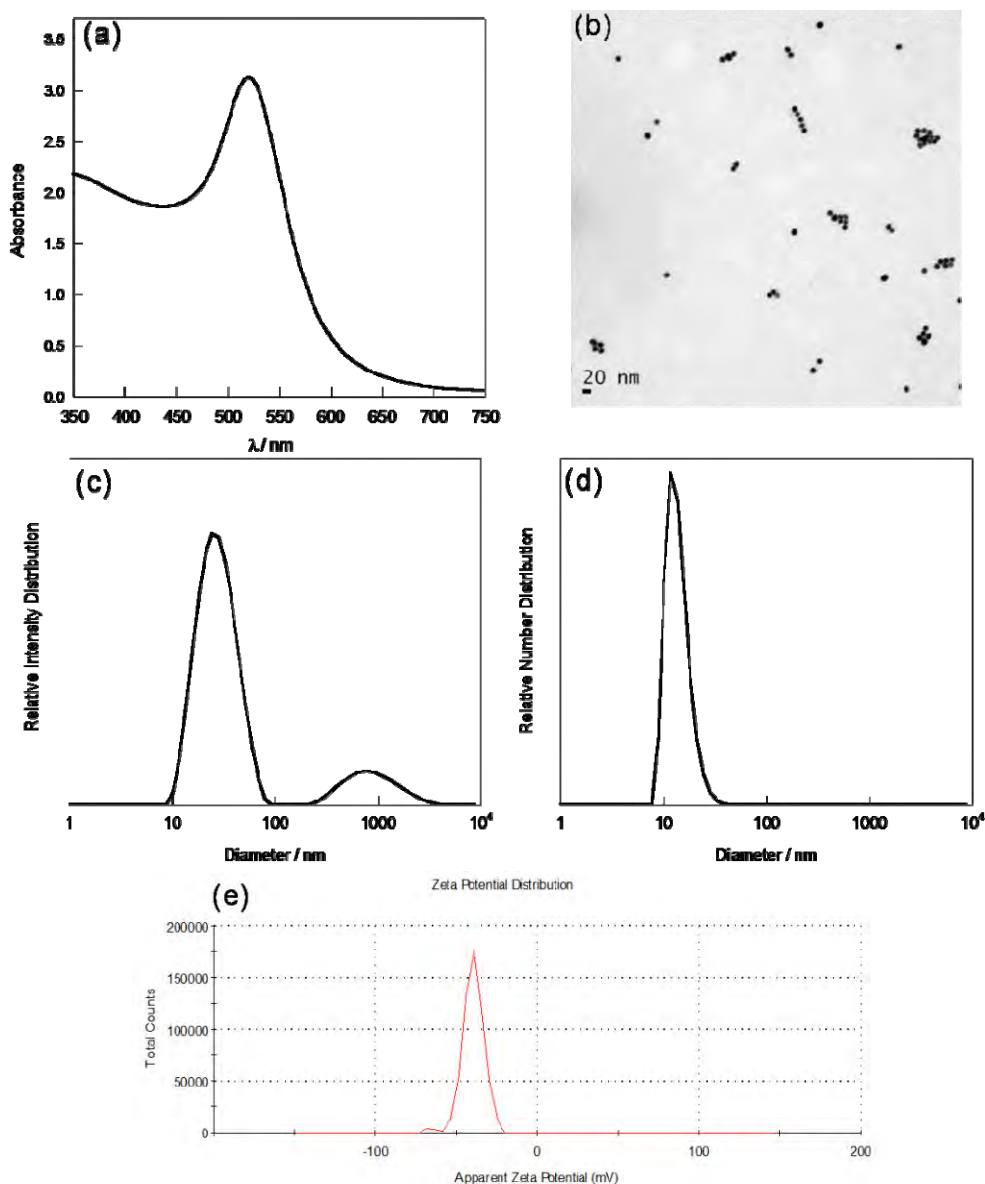


**Figure 2.17** (a) UV-Vis absorption spectrum (measured at 9 nM particle concentration), (b) TEM image, (c) DLS intensity distribution, (d) DLS number distribution, and (e) zeta potential distribution (measured at 2 nM particle concentration), of 13 nm citrate-stabilised gold nanoparticles.

The UV-Vis absorption spectrum of the 9 nM citrate-coated gold nanoparticles exhibits a highly absorptive SPR peak at 520 nm (as discussed in Section 1.3), with  $\log \epsilon = 8.5$ . Sizing of the nanoparticles by DLS gives an average *number* distribution (*vide infra*) hydrodynamic diameter of  $13 \pm 4$  nm, and an average *intensity* distribution (*vide infra*) diameter of  $29 \pm 12$  nm (86%) and  $998 \pm 624$  nm (14%). Dynamic light scattering measures the rate at which LASER scattering from the bulk colloidal suspension fluctuates due to constructive and destructive

interferences of the scattered light, off particles diffusing in Brownian motion.<sup>85</sup> The calculated hydrodynamic radius is the radius of a theoretical sphere that has the same diffusion coefficient as the measured species, and it can be affected significantly by the surface structure of the nanoparticles; surface-bound molecules will affect the diffusion speed of the nanoparticles. Hydrodynamic radii distributions are calculated from the rate of scattering fluctuations, with respect to the intensity of the scattered light, i.e. the probability of light being scattered from a sphere of a given size, and this gives the *intensity* distribution. This does not scale with the number of particles, because larger particles scatter a lot more than smaller particles. The fundamental *intensity* distribution can, however, be converted to a *number* distribution, using Mie theory,<sup>85,86</sup> to weight the probability in terms of particle concentration, although this dramatically scales up the errors in the measurements, and assumes that all particles are spherical and homogenous.

The scattering intensity contribution arising from a micrometer scale aggregates (14% of the intensity distribution) in the citrate gold nanoparticle sample (Figure 2.17c) implies that there are measurable aggregates present in this macroscopic sample. However, once converted to a number distribution, to account for the fact that the intensity of light scattered by a particle is a function of its diameter to the sixth power, it is clear that these are present in negligible concentration, i.e.  $\ll 1\%$ . The nanoparticles have a zeta potential of  $-40 \pm 5$  mV, measured in water at a 2 nM nanoparticle concentration, which is significant enough to stabilise the nanoparticles with respect to aggregation. The zeta potential is the electrokinetic potential between the dispersion medium and the stationary layer of fluid associated to the particle, which is measured by analysing the electrophoretic mobility of the particles by LASER Doppler spectroscopy. Electrostatically stabilised sols require large zeta potentials (either positive or negative) to prevent fusion of the gold cores by means of repulsive forces.

## 2.4 Direct Attachment of RuSH to Citrate-stabilised 13 nm Gold Nanoparticles

Direct addition of the cationic **RuSH** complex to 13 nm citrate gold nanoparticles was attempted and monitored by UV-Vis absorption spectroscopy, as shown in Figure 2.18. Unlike previous work in the group, in which neutral lanthanide complexes are successfully added directly to citrate gold nanoparticles,<sup>43,61</sup> full surface coverage of the gold nanoparticles was unsuccessful with the **RuSH** complex. Surface-coverage of *ca.* 1,400 europium(III) complexes per nanoparticle has been achieved in the group with a pentetic acid chelating group, appended with two similar hexyl-thioester groups for surface attachment to gold, which is thought to have a similar complex footprint as **RuSH**.<sup>61</sup>

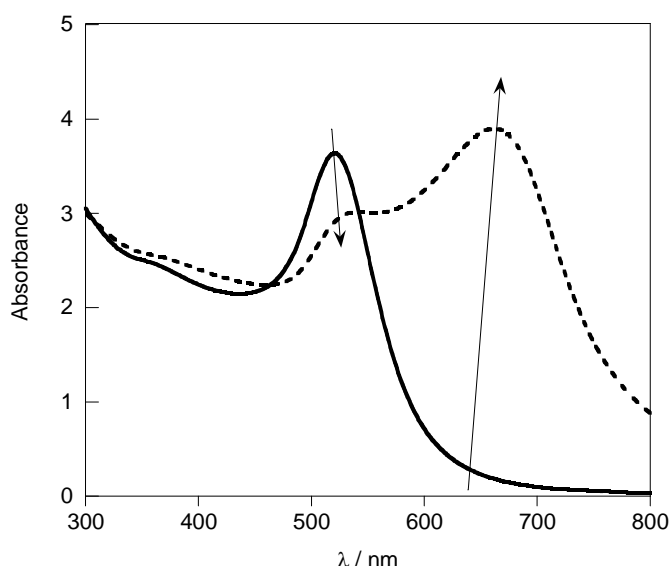


**Figure 2.18** UV-Vis absorption spectra of citrate gold nanoparticles (1 mL, 9 nM) (bold), and with the addition of **RuSH** complex (1  $\mu$ L, 3 mM), to give a final complex concentration of 3  $\mu$ M (dashed line).

Addition of only *ca.* 400 complexes of **RuSH** (1  $\mu$ L, 3 mM) per particle to citrate-stabilised 13 nm gold nanoparticles (1 mL, 9 nM), calculated from the concentration of lumiphores of nanoparticles in the solution, gives rise to the sudden formation of a new SPR band in the UV-Vis spectrum, between 600–800 nm, and a reduction in the absorbance at 520 nm. This new band formation suggests that plasmon coupling between agglomerating nanoparticles is

occurring,<sup>87</sup> and thus indicates that flocculation of the nanoparticles is occurring in solution, following the addition of the cationic **RuSH** complex. When colloidal particles aggregate additional resonances occur in the UV-Vis absorption spectrum, at wavelengths longer than the individual particles. This gives rise to a red-shift and a broadening of the convoluted SPR.<sup>66,87</sup> Similar effects have been observed with the addition of ruthenium tris(bipyridine) to citrate gold nanoparticles of varying sizes.<sup>11</sup> This signal growth, between 600–800 nm in the UV-Vis absorption spectrum, is also observed at much reduced concentrations, as shown in Figure 2.19, and the flocculation can be observed to some extent by TEM, although nanoparticle distributions which dry on a surface are not overly representative of agglomeration structures in the sol. All colloidal suspensions eventually turned steel-blue and sedimented out of suspension following the addition of **RuSH**.

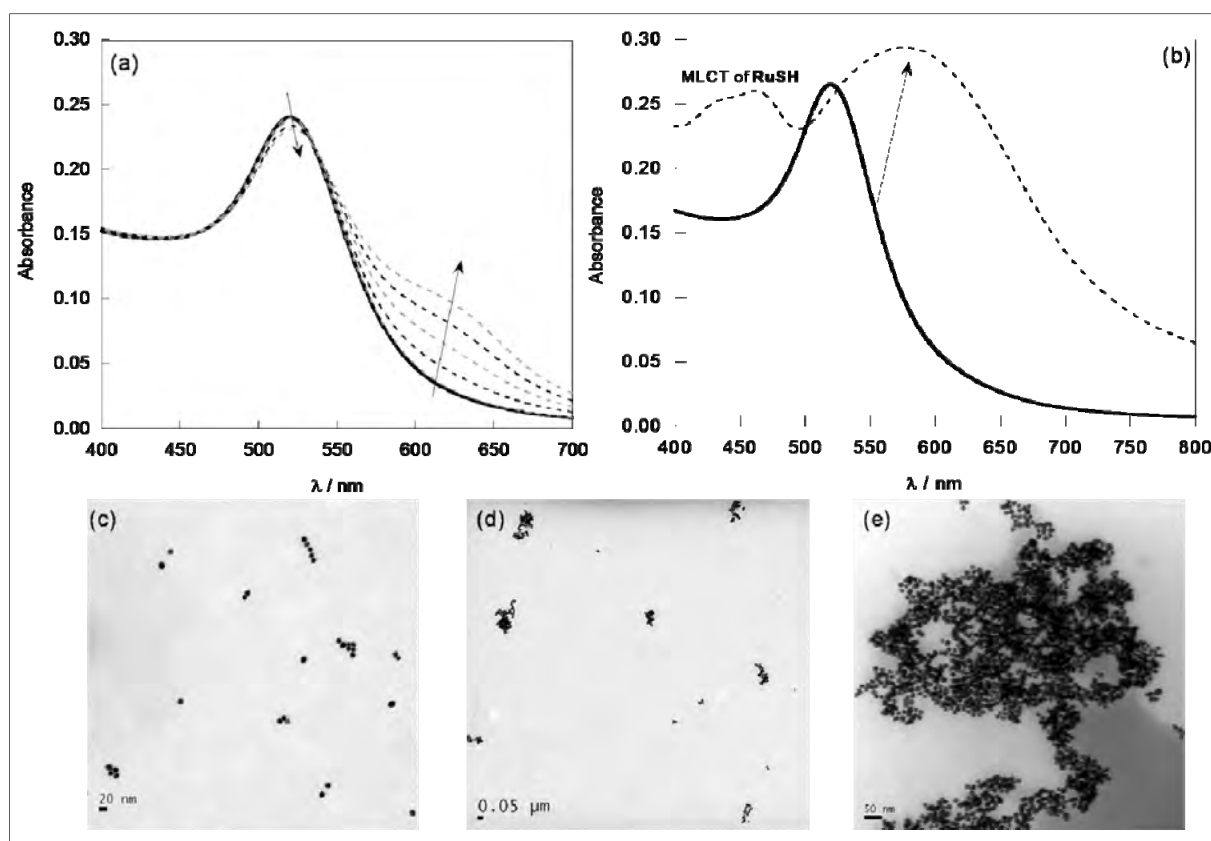


**Figure 2.19** UV-Vis absorption spectra of (a) 0.7 nM 13 nm citrate-stabilised gold nanoparticles (bold solid line) and with the addition of 6–100 nM **RuSH** complex (dashed lines), and (b) 0.7 nM nanoparticles (bold solid line) and upon addition of 9 μM **RuSH** complex. Transmission electron micrographs of (c) citrate-stabilised gold nanoparticles, (d) final titre of (a), i.e. 0.7 nM nanoparticles + 100 nM **RuSH**, and (e) final titre of (b), i.e. 0.7 nM nanoparticles + 9 μM **RuSH**.

The citrate nanoparticles are stabilised by the electrostatic repulsion between the citrate/chloride shells absorbed to each gold nanoparticle centre. Once the **RuSH** complex binds to the surface of these nanoparticles, its 2+ charge will attract the negative shells of neighbouring partially-coated nanoparticles, leading to flocculation and subsequent aggregation of the particles in solution. Addition of nanomolar concentrations to 0.7 nM nanoparticles (*ca.* 5–150 complexes per nanoparticle) gives rise to bimodal SPR formation again, as observed in Figure 2.19a, and the TEM shown in Figure 2.19d clearly shows clusters of nanoparticles, which despite drying artifacts that can occur on the grid, look different to the control study of bare citrate nanoparticles in Figure 2.19c. Addition of micromolar concentrations of **RuSH** to 0.7 nM nanoparticles, i.e. 13,000 complexes per nanoparticle, gives rise to a broad single SPR peak at *ca.* 600 nm, and large aggregates are observed in the TEM (Figure 2.19e).

## 2.5 Interactions of Triton™ X 100, TWEEN® 20, and Zonyl® 7950 with 13 nm Citrate-stabilised Gold Nanoparticles

It was not possible to directly attach cationic **RuSH** complexes to citrate-stabilised gold nanoparticles, and therefore a surfactant-mediated coating strategy was investigated, in an attempt to circumvent the aggregation problem. A surfactant pre-coating step has been introduced to the functionalization process, as previously employed by Aslan *et al.*, to coat citrate-stabilised nanoparticles with alkylthiols.<sup>66</sup> The surfactant is added to displace the negative citrate shell around the particles and stabilise the particles sterically, before addition of the cationic complex. In this study we have evaluated three commercially available surfactants: Triton™ X-100, TWEEN® 20, and Zonyl® 7950, as pre-coating moieties to allow subsequent attachment of **RuSH** without aggregation of the nanoparticles. Triton™ X-100 bears a hydrophilic polyethylene oxide chain with an aromatic hydrophobic

group (Figure 2.9b), and similarly TWEEN® 20, which is a derivative of sorbitan monolaurate, has four hydrophilic polyethylene oxide chains and a single hydrophobic aliphatic chain (Figure 2.9a). Zonyl® 7950 is a fluorosurfactant, with a hydrophilic methyl-methacrylate head-group, and a hydrophobic perfluorinated alkyl chain (Figure 2.9c). The surface-coating of 13 nm citrate gold nanoparticles with each surfactant is summarised in Figure 2.20 below:

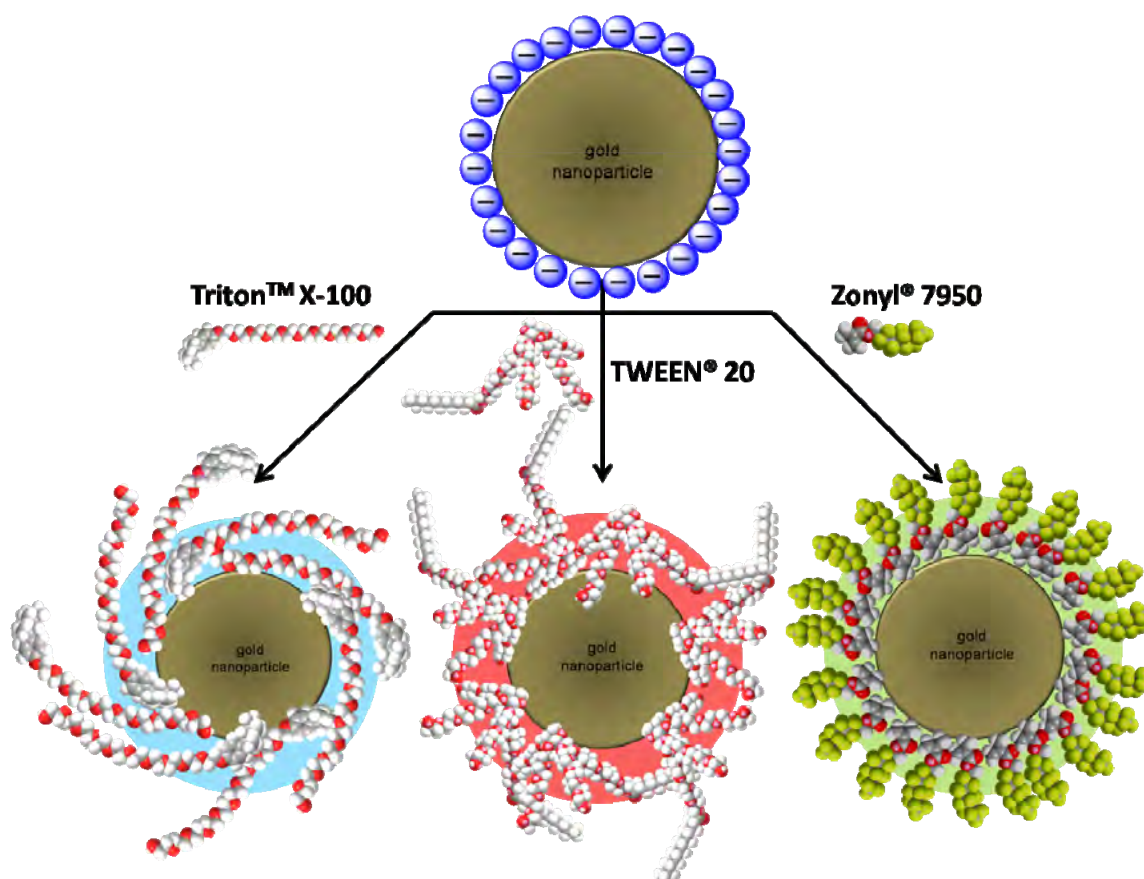


**Figure 2.20** Surface-functionalisation of gold nanoparticles with three commercial surfactants: Triton™ X-100; TWEEN® 20 and Zonyl® 7950.

Each surfactant was titrated into the 13 nm citrate gold nanoparticles, and surface binding to the surface of the gold nanoparticles is apparent for all three by the shift in the SPR peak in the UV-Vis absorption spectra; the absorption of the surfactant molecules to the gold surface changes the surface dielectric constant of the particles,<sup>43,88</sup> resulting in the observed shifts in the SPR (Figure 2.21).

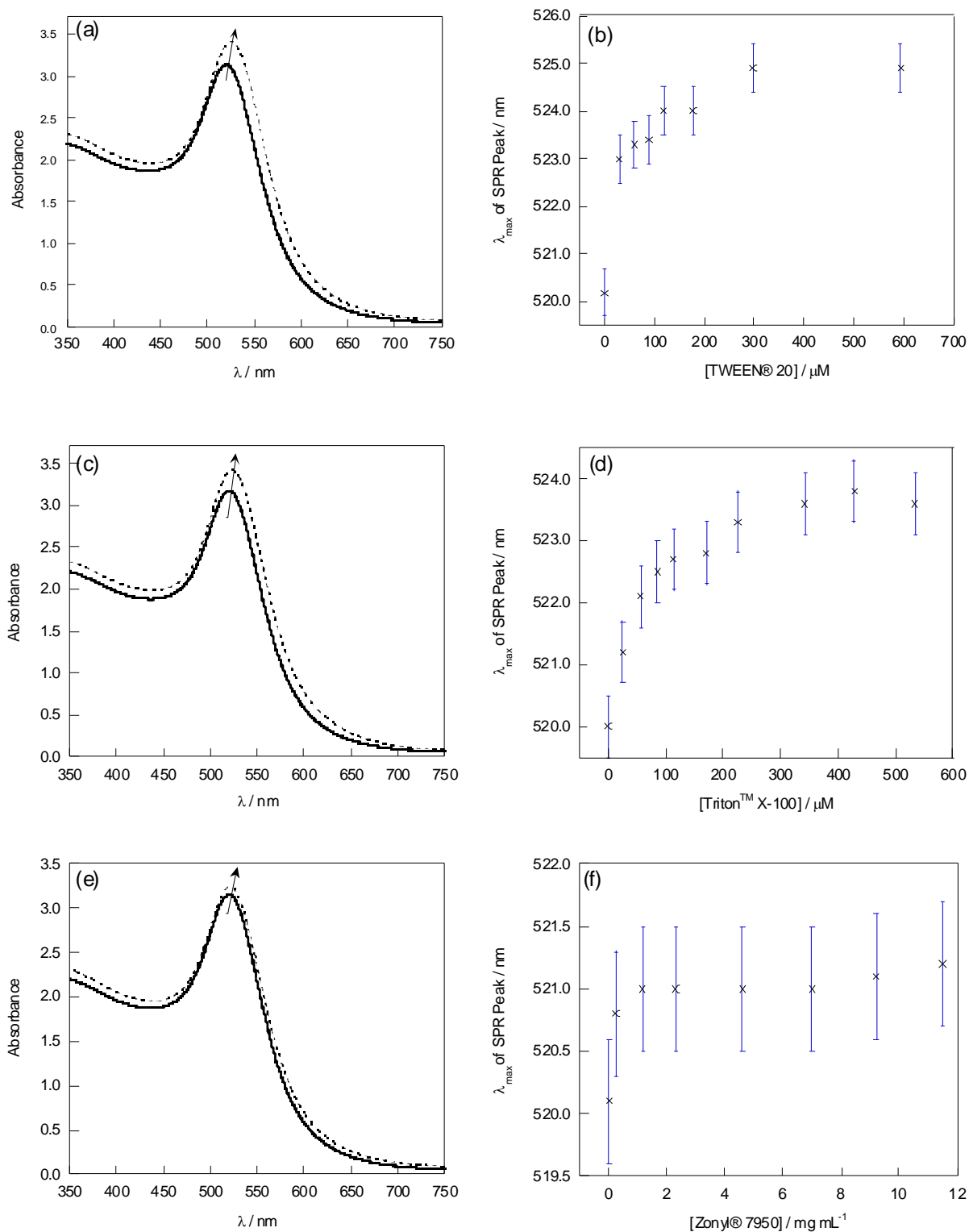


**Figure 2.21** UV-Vis absorption spectra of 13 nm gold nanoparticles (9 nM) (bold solid line) + (a) TWEEN® 20 (2 mM) (dashed line), + (c) Triton™ X-100 (0.6 mM) (dashed line) and + (e) Zonyl® 7950 (12 mg mL<sup>-1</sup>) (dashed line).  $\lambda_{\max}$  of SPR peak vs. [surfactant] titrations shown in (b), (d) and (f).

Upon the titration of the TWEEN® 20 surfactant into 9 nM citrate gold nanoparticles, a 5 nm bathochromic shift in the SPR is observed (Figure 2.21a–b). Similarly the Triton™ X-100 surfactant gives rise to a 4 nm red-shift (Figure 2.21c–d), whereas the Zonyl® 7950 surfactant only gives rise to a 1 nm bathochromic shift in the SPR of the nanoparticles (Figure 2.21e–f). The SPR peak wavelength of the gold nanoparticles shifts as the dielectric constant of the local surrounding medium changes, due to binding at the nanoparticle surface.<sup>66</sup> Saturation is observed in the  $\lambda_{\max}$  vs. surfactant concentration binding plots, upon addition of each surfactant to 9 nM gold sols, at *ca.* 400  $\mu\text{M}$  for both Triton™ X-100 and TWEEN® 20, and at *ca.* 1  $\text{mg mL}^{-1}$  (*ca.* 1 nM) for the Zonyl® 7950 fluorosurfactant. No induced aggregation is observed by UV-Vis absorption spectroscopy or by DLS upon addition of excess of each of the tested surfactants, as shown in Figures 2.21 and 2.22.

The zeta potentials and hydrodynamic diameters of the surfactant-coated nanoparticles were also studied to analyse the surface binding of each surfactant. Excess surfactant (beyond the saturation point observed by the SPR shift in the UV-Vis absorption spectra, Figure 2.20) was added to the 9 nM citrate-stabilised gold nanoparticles, and the solutions were then diluted to 2 nM and the DLS and zeta potential measurements were recorded, as displayed in Figure 2.22 and Table 2.3.

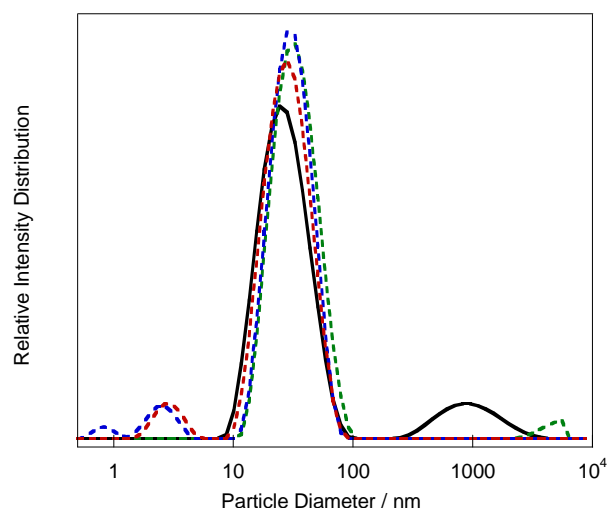


**Figure 2.22** DLS intensity distribution graph of citrate gold nanoparticles (black solid line), and particles coated in TWEEN® 20 (blue dashed line), Triton™ X-100 (red dashed line) and Zonyl® 7950 (green dashed line), all measured at 2 nM particle concentration, with 2.5 mg mL<sup>-1</sup> surfactant, in deionised water.

The addition of excess TWEEN® 20 and the Triton™ X-100 surfactant (10 mg mL<sup>-1</sup> surfactant, 9 nM gold nanoparticles) both give rise to a peak at low diameter in the DLS, by comparison with the bare citrate gold nanoparticles, which is likely to be due to micelle formation of the excess of each of the surfactants in water. This is not observed at the concentrations used with Zonyl® 7950. In all cases, upon addition of the surfactant, the most intense peak in the scattering intensity distribution is at *ca.* 30 nm, with a marginal increase (5–30%) in the peak intensity from the uncoated citrate-stabilised gold nanoparticles. This indicates that the surface interaction of each surfactant adds steric bulk to the hydrodynamic diameter of the particle, slowing down its diffusion in solution slightly.

**Table 2.3** DLS and zeta potential data for 13 nm gold nanoparticles coated in surfactants

Particle Coating:	Citrate <sup>a</sup>	TWEEN®20 <sup>a</sup>	Triton™ X-100 <sup>a</sup>	Zonyl® 7950 <sup>a</sup>
<b>DLS: Intensity</b>	29±12 (86)	32±13 (94)	31±13 (95)	
<b>Distribution / nm (%)</b>	998±624 (14)	2.0±0.4 (6)	2.0±0.7 (5)	38±18 (100)
<b>DLS: Number</b>				
<b>Distribution / nm (%)</b>	13±4(100)	- <sup>b</sup>	- <sup>b</sup>	17±5 (100)
<b>Zeta Potential / mV</b>	-40±5	-17±4	-7±2	-72±4

<sup>a</sup> colloidal dispersions of 2 nM gold nanoparticles, and 2.5 mg mL<sup>-1</sup> surfactant, in deionised water.

<sup>b</sup> number distributions not given as all contribution from micelle peak.

All errors are quoted as ±1 standard deviation.

The zeta potential of the citrate particles is  $-40\pm 5$  mV, and upon addition of the neutral non-ionic surfactants TWEEN® 20 and Triton™ X-100, the zeta potential reduces in magnitude to  $-17\pm 5$  mV and  $-7\pm 4$  mV respectively, as the negatively charged citrate ions are displaced by neutral surfactant in each case. Physisorption of both the neutral surfactant molecules TWEEN® 20 and Triton™ X-100 is evident from the change in the zeta potential and the shift on the SPR in the UV-Vis absorption, whereas aggregation is not induced by the sacrifice in surface charge, as demonstrated by the DLS data. Electrostatically stabilised sols require large zeta potentials to prevent fusion of the gold cores by means of repulsive forces, while steric stabilisation can also be employed to inhibit aggregation with neutral surface charges. In contrast, upon addition of the Zonyl® 7950 fluorosurfactant, the zeta potential increases in magnitude to a larger negative value of  $-72\pm 2$  mV. Although this surfactant is neutral, it has a perfluorinated alkyl chain with multiple polarised C–F bonds and, therefore, it is assumed from these data that the surfactant presents numerous partial negative charges to the outer surface of the hydrodynamic radii of the particles. Similar effects have been seen with silica nanoparticles.<sup>89</sup>

## 2.6 Surfactant-mediated Labelling of 13 nm Citrate Nanoparticles with RuSH, Using the Surfactants Triton™ X-100, TWEEN® 20, and Zonyl® 7950

Each surfactant-coated nanoparticle system was subsequently screened to see if the addition of **RuSH** could be achieved without aggregation of the particles, as shown below in the schematic (Figure 2.23). Nanoparticles were tested at three different particle concentrations: 9 nM, 3.5 nM and 0.7 nM, because aggregation is driven by inter-particle interactions which are more likely to occur at higher particle concentration.

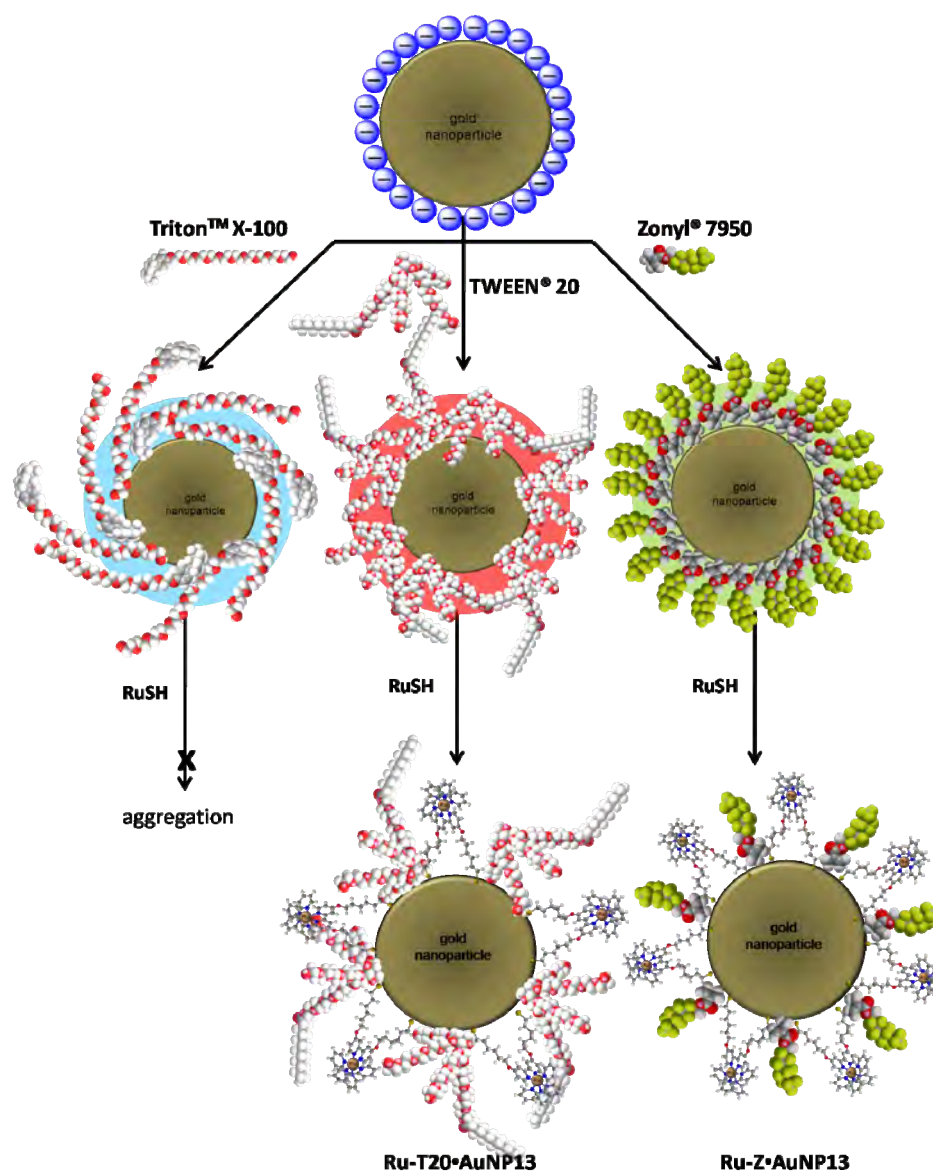


**Figure 2.23** Surface-functionalisation of gold nanoparticles with **RuSH**, mediated by a pre-coating step with three commercial surfactants: Triton™ X-100, TWEEN® 20, and Zonyl® 7950.

In each case 8,000 equivalents of **RuSH** ( i.e. 8,000 RuSH complexes per nanoparticle) were added to the nanoparticles (9 nM, 3.5 nM and 0.7 nM) following the addition of varying concentrations of each surfactant TRITON™ X-100 (0.1–20 mM), TWEEN® 20 (0.04–8 mM) and Zonyl® 7950 (0.05–10 mM), as shown below in Figure 2.24. In each case, the surfactant was added to the nanoparticles, and stirred for 20 min, and then the **RuSH** was subsequently added. The photographs (Figure 2.24) were taken 30 min after the final solutions were obtained.

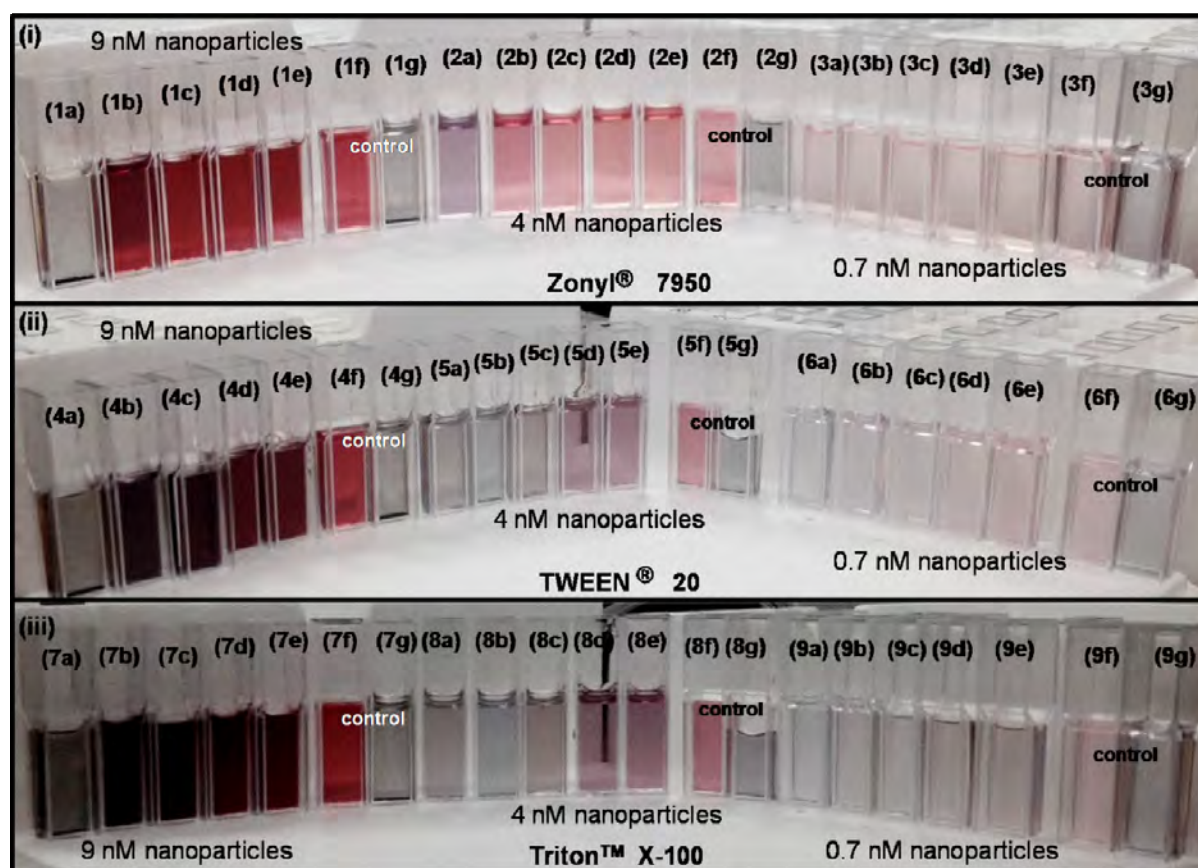


**Figure 2.24** Screening surfactant-coated nanoparticles for attachment in **RuSH**. Nanoparticles (1,4,7 = 9 nM, 2,5,8 = 3.5 nM, 3,6,9 = 0.7 nM) coated in (i) Zonyl® 7950, (ii) TWEEN® 20, and (iii) Triton™ X-100, at concentrations of (a)  $0.05 \text{ mg mL}^{-1}$ , (b)  $0.5 \text{ mg mL}^{-1}$ , (c)  $1 \text{ mg mL}^{-1}$ , (d)  $5 \text{ mg mL}^{-1}$ , and (e)  $10 \text{ mg mL}^{-1}$ , (f)  $0 \text{ mg mL}^{-1}$ , and (g)  $0 \text{ mg mL}^{-1}$ . (a–e, g) contain 8,000 equivalents of **RuSH**, (f) is an uncoated control.

Triton X-100 is not able to prevent the **RuSH** complex from aggregating the gold nanoparticles at any concentration combination of nanoparticles and surfactant tested, as can be seen in Figure 2.24(iii); at all three concentrations of nanoparticles tested (i.e. 9 nM,

3.5 nM and 0.7 nM), the nanoparticles immediately turned dark in colour (7a–7e, compared with the control uncoated nanoparticles in 7f, 8a–8e compared with 8f, and 9a–9e compared with 9f), as new resonances formed in the UV-Vis absorption spectra due to aggregation. The UV-Vis absorption spectra presented in Figure 2.25 shows the series of 0.7 nM nanoparticles tested.

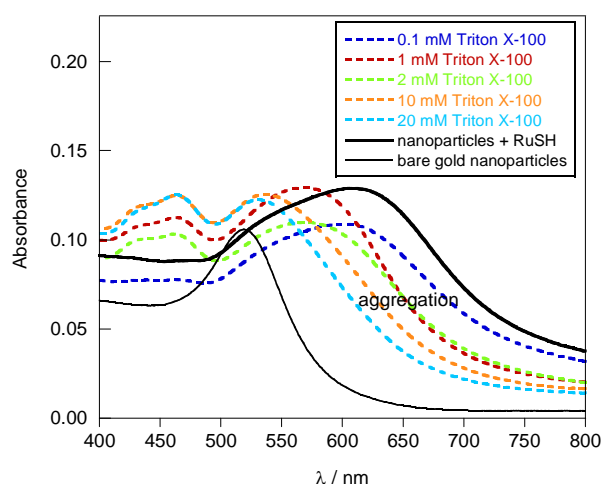


**Figure 2.25** UV-Vis absorption spectra of gold nanoparticles (0.7 nM)(solid black line), and gold nanoparticles (0.7 nM) + Triton™ X-100 surfactant (0.1–20 mM) + **RuSH** (5.5 μM)(dashed coloured lines). Gold nanoparticles (0.7 nM) with no surfactant and **RuSH** (5.5 μM)(black bold solid line). UV-Vis absorption spectra recorded 30 min after **RuSH** addition.

At all concentrations of surfactant added, a large increase in the absorbance between 600–800 nm was observed, as aggregation was occurring, and within 12 hrs the particles aggregated, and sedimented out of suspension. Therefore this surfactant was deemed unsuitable for mediating attachment of the **RuSH** to citrate gold nanoparticles.

Unlike the Triton™ X-100 surfactant the TWEEN® 20 is able to offer some stability to the nanoparticles upon addition of **RuSH**. At 9 nM and 3.5 nM concentrations of nanoparticles, the TWEEN® 20 did not prevent flocculation in solution with addition of **RuSH**, and after 30 min the solutions were all very dark (either blue or purple) in colour (Figure 2.24(ii)). The UV-Vis absorption spectra at 3.5 nM is presented in Figure 2.26.

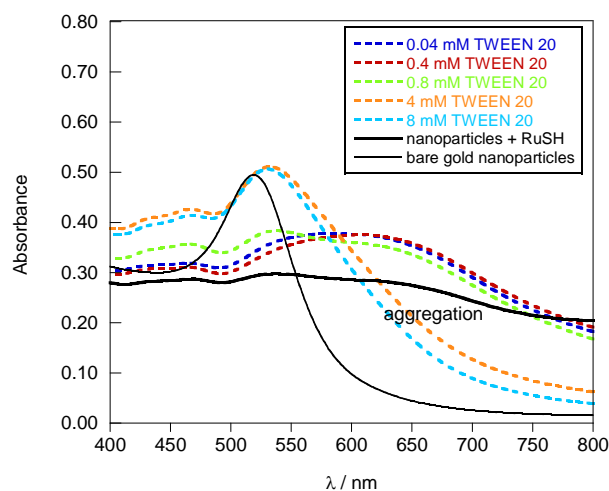


**Figure 2.26** UV-Vis absorption spectra of gold nanoparticles (3.5 nM)(solid black line), and gold nanoparticles (3.5 nM) + TWEEN® 20 surfactant (0.04–8 mM) + **RuSH** (25 μM)(dashed coloured lines). Gold nanoparticles (3.5 nM) with no surfactant and **RuSH** (25 μM)(black bold solid line). UV-Vis absorption spectra recorded 30 min after **RuSH** addition.

Aggregation was apparent with the 3.5 nM nanoparticles at all the concentrations of surfactant tested, but a significant reduction in the absorbance between 600–800 nm was observed with 4–8 mM TWEEN® 20 present, although the  $\lambda_{\max}$  of the SPR with 8 mM surfactant was still red-shifted with respect to the particles without **RuSH** (at 525 nm), at 533 nm. However, at the lower nanoparticle of 0.7 nM, the addition of millimolar TWEEN® 20 seemed to significantly reduce the aggregation of the nanoparticles, as shown in Figure 2.27, and the SPR has a  $\lambda_{\max}$  at 525 nm in 8 mM surfactant. After 12 hours, the solutions with 4 mM and 8 mM TWEEN® 20 remained suspended in solution.

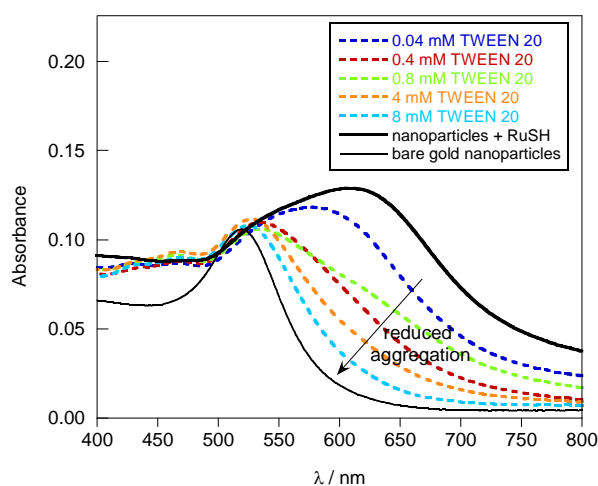


**Figure 2.27** UV-Vis absorption spectra of gold nanoparticles (0.7 nM)(solid black line), and gold nanoparticles (0.7 nM) + TWEEN® 20 surfactant (0.04–8 mM) + **RuSH** (5.5  $\mu\text{M}$ )(dashed coloured lines). Gold nanoparticles (0.7 nM) with no surfactant and **RuSH** (5.5  $\mu\text{M}$ )(black bold solid line).UV-Vis absorption spectra recorded 30 min after **RuSH** addition.

In contrast to the Triton™ X-100 and TWEEN® 20 surfactants, the Zonyl® 7950 is able to stabilise the 9 nM gold nanoparticles with respect to aggregation, with addition of the **RuSH** complex, as shown below in Figure 2.28, and in Figure 2.24(i). Addition of  $\geq 0.1$  mM fluorosurfactant allowed addition of **RuSH** without signs of aggregation, and the SPR has a  $\lambda_{\text{max}}$  at 521–522 nm in all cases.

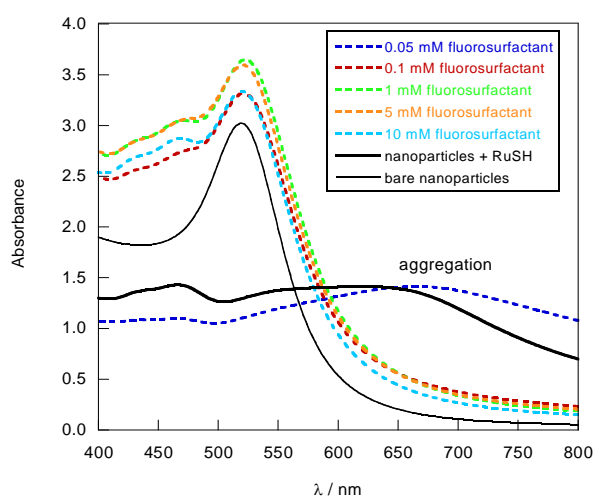


**Figure 2.28** UV-Vis absorption spectra of gold nanoparticles (9 nM)(solid black line), and gold nanoparticles (9 nM) + Zonyl® 7950 surfactant (0.1–10 mM) + **RuSH** (70  $\mu\text{M}$ )(dashed coloured lines). Gold nanoparticles (9 nM) with no surfactant and **RuSH** (70  $\mu\text{M}$ )(black bold solid line).UV-Vis absorption spectra recorded 30 min after **RuSH** addition.

Following these screening tests, nanoparticles have been coated with luminescent **RuSH** complexes with the aim of producing luminescent nanoprobes for imaging, using both TWEEN® 20 and Zonyl® 7950 as stabilising surfactants. Nanoparticles were synthesised at 0.7 nM concentrations with TWEEN® 20, as they not that stable, whereas particles coated with Zonyl® 7950 could be made at 9 nM and remained stable for several weeks.

### 2.6.1 Further Investigations into Similar Surfactants to Zonyl® 7950, with Gold Nanoparticles

The striking superiority of the commercial surfactant Zonyl® 7950 in stabilising the particles and mediating the attachment of the luminescent **RuSH** complex has been examined further by testing structurally similar molecules to try to ascertain the crux of its efficacy. As Zonyl® 7950 consists of a methyl methacrylate head group and a perfluorinated alkyl chain (Figure 2.9), a control poly(ethylene glycol) methyl ether methacrylate moiety (MMA-PEG) was studied to infer information about the head group, and 1*H*,1*H*,2*H*-perfluoro-1-decene (perfluorodecene) was studied to assess the role of the tail group (Figure 2.29).

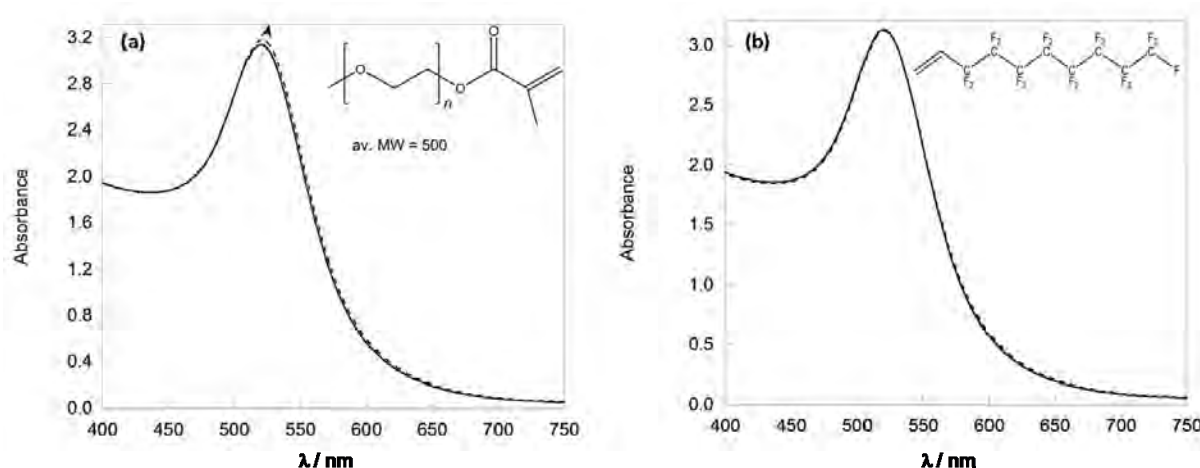


**Figure 2.29** UV-Vis absorption spectra of 13 nm citrate gold nanoparticles (9 nM) (solid line) and with addition of (a) MMA-PEG (3 mM) (dashed line) and (b) perfluorodecene (5 mM) (dashed line).

Addition of 3 mM MMA-PEG surfactant to 9 nM citrate gold nanoparticles gives rise to a 1 nm red-shift in the SPR, as can be seen in Figure 2.29a, and the zeta potential neutralised to  $0.0 \pm 0.2$  mV (at 2 nM particles, 0.7 mM MMA-PEG), compared with  $-40 \pm 5$  mV for uncoated citrate gold nanoparticles (2 nM), and thus it is evident that the MMA-PEG does bind to the gold particles. In contrast, addition of up to 5 mM perfluorodecene (using a stock solution of 20% *v/v* perfluorodecene dissolved in isopropanol as it is immiscible with water) to the nanoparticles (9 nM) gives rise to no measurable shift in the SPR of the UV-Vis absorption spectrum (Figure 2.29b), and the zeta potential remains constant, at  $-39 \pm 6$  mV (at 2 nM particles, 1 mM perfluorodecene). Thus, there is no evidence of the perfluorinated aliphatic chain binding to the gold nanoparticles. Immediate aggregation was observed at 0.7 nM, 3 nM, and 9 nM concentrations of the nanoparticles, each with excess of either perfluorodecene (70 mM) or MMA-PEG (40 mM) present, upon the addition of 8000 equivalents of **RuSH**. These two controls demonstrate that it is likely that it is the methacrylate head group of the Zonyl® 7950 surfactant that binds to the gold nanoparticles, or at least facilitates the binding of the fluorosurfactant to the surface due to its polarity. In addition, the perfluorinated chains are necessary to ensure a significant negative zeta potential at the surface of the particles to allow addition of the **RuSH** complex; the poly(ethylene glycol) moiety cannot replace the perfluorinated chains and stabilise the sol upon addition of the **RuSH** complex and the fluorinated chain does not bind to the gold particles alone.

## 2.7 Synthesis and Characterisation of Ru-T20-AuNP13

To synthesise **RuSH**-coated gold nanoparticles using TWEEN® 20 as a mediating surfactant, 0.7 nM citrate gold nanoparticles (zeta potential =  $-41\pm 5$  mV, measured at 0.7 nM in deionised water) were coated with 1 mM TWEEN® 20 (zeta potential =  $-15\pm 3$  mV, measured at 0.7 nM in deionised water), and then the **RuSH** complex (synthesised *in situ* from the oxidatively stable thioester analogue **RuSAc**) was titrated into the resulting sol, up to 9  $\mu\text{M}$ , as shown below in Figure 2.30.

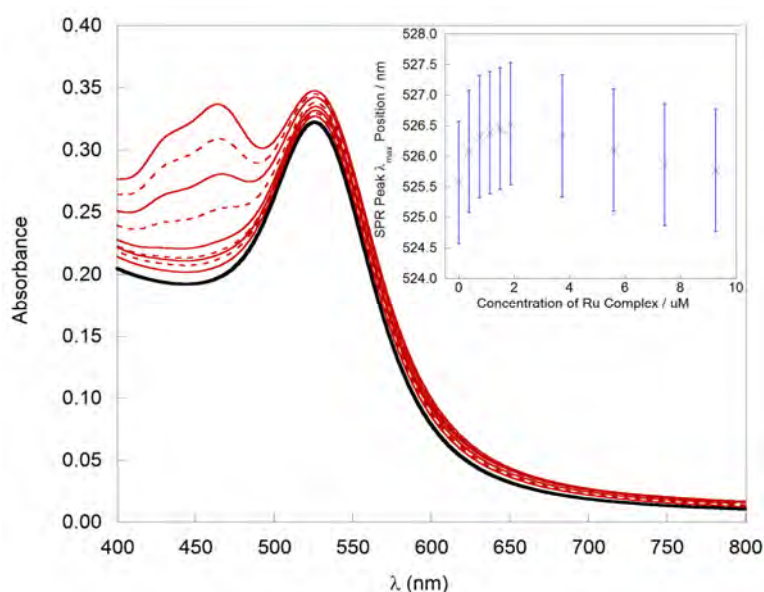


**Figure 2.30** UV-Vis absorption spectra 0.7 nM 13 nm gold nanoparticles + 1 mM TWEEN® 20 solution (black) and titration of 1–9  $\mu\text{M}$  **RuSH** into the surfactant-nanoparticle mixture (red). Inset: SPR  $\lambda_{\text{max}}$  vs.  $[\text{RuSH}]$  plot.

Upon titration of **RuSH** into the TWEEN® 20 surfactant-coated gold nanoparticles (Figure 2.30), it was difficult to follow a shift in the  $\lambda_{\text{max}}$  value of the SPR band due to its convolution with the rising singlet MLCT band of the Ru(II) complex at 410–500 nm; initially a 1 nm red-shift is observed, but with  $[\text{RuSH}] > 2 \mu\text{M}$ , convolution of the SPR absorbance with the **RuSH** absorbance gives rise to a slight blue-shift in the peak position. However, a lack of SPR peak broadening indicates the lack of nanoparticle aggregation. The zeta potential of the final sol, in its non-isolated form was  $-31\pm 5$  mV, measured at 0.7 nM in deionised water). It

was not possible to isolate the **RuSH/TWEEN® 20**-coated nanoparticles by centrifugation, as the particles flocculated and aggregated. However, it was possible to isolate a sol that did not sediment out of suspension, from free complex and surfactant in the solution, by means of size-exclusion chromatography using Sephadex® G-25, as has been performed previously with coated 13 nm gold nanoparticles.<sup>43,90</sup> The coated nanoparticles elute with water at the solvent front, through the void volume of the column, in a single pink band. The isolated nanoparticles dilute in the column, and the final particles, at a concentration of 0.3 nM, have a zeta potential of  $-24 \text{ mV} \pm 3 \text{ mV}$ . The zeta potential decreases in magnitude upon addition of the neutral surfactant, as discussed earlier, and then increases to a more negative potential of  $-31 \pm 5 \text{ mV}$  (non-isolated at 0.7 nM) and  $-24 \pm 3 \text{ mV}$  (isolated at 0.3 nM) upon the addition of the **RuSH** complex. These data suggest that the **RuSH** complex displaces some of the neutral TWEEN® 20 surfactant, and the counter ions of the **RuSH** complex are at the extremity of the hydrodynamic radius, thus giving a more negative surface charge felt in the electric field compared with the TWEEN® 20 coated nanoparticles without complex. However the zeta potential is not substantial enough to stabilise the particles well by means of electrostatics, and following isolation by size-exclusion chromatography, the SPR of the particles drastically red-shifts to 535 nm (Figure 2.31), and the DLS mean intensity distribution value increases significantly from  $31 \pm 13 \text{ nm}$  (94%), ( $3503 \pm 1256 \text{ nm}$  (6%)) (uncoated citrate gold nanoparticles) to  $47 \pm 22 \text{ nm}$  (93%), ( $4 \pm 1 \text{ nm}$  (7%, micelles)) (non-isolated **RuSH/T20**-coated gold nanoparticles) and to  $195 \pm 97 \text{ nm}$  (99%), ( $28 \pm 6 \text{ nm}$  (1%)) (isolated **Ru-T20•AuNP13**) following size-exclusion chromatography. The DLS mean number distribution value of the isolated **Ru-T20•AuNP13** particles is  $26 \pm 19 \text{ nm}$ , compared with  $16 \pm 5 \text{ nm}$  for uncoated citrate gold nanoparticles (Figure 2.31). These data indicate that the particles flocculate together in solution.

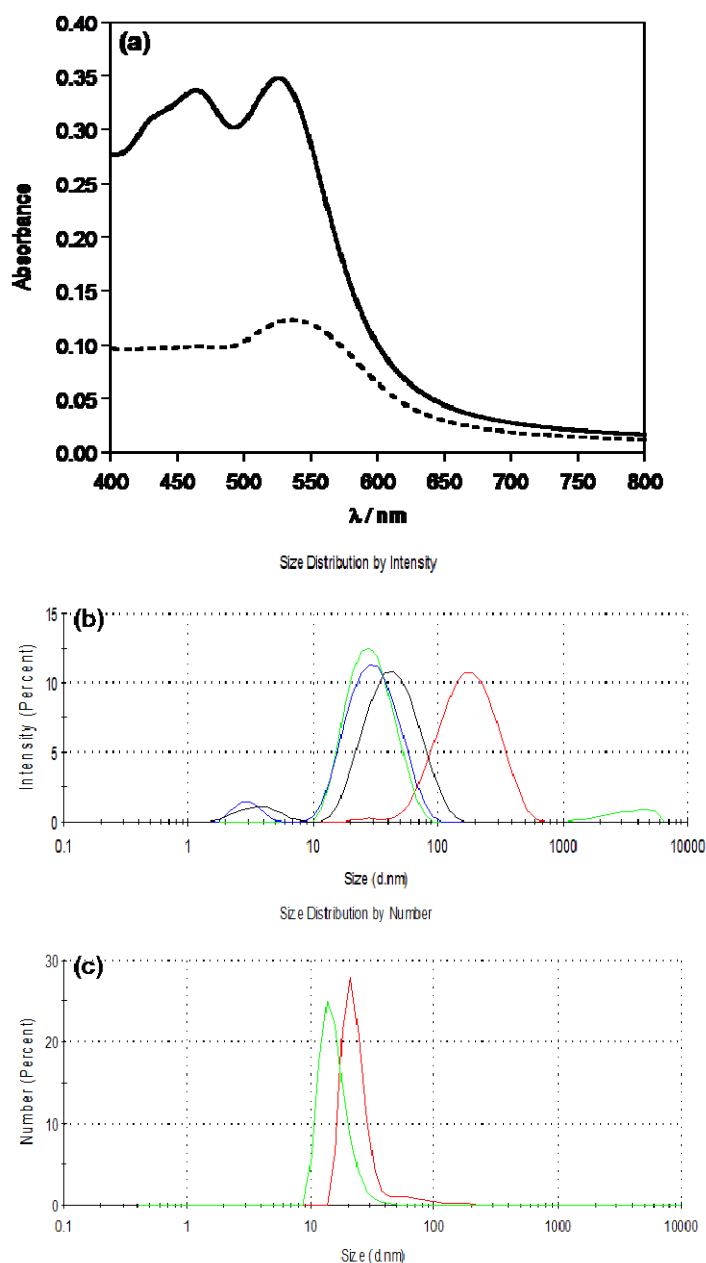


**Figure 2.31** (a) UV-Vis absorption spectra of 13 nm gold nanoparticles (0.7 nM) + TWEEN® 20 (1 mM + RuSH (9  $\mu$ M) (solid line), and the isolated Ru-T20•AuNP13 particles following size-exclusion chromatography (dashed line). (b) DLS intensity distributions and (c) DLS number distributions of 13 nm citrate gold nanoparticles (green), gold nanoparticles (0.7 nM) mixed with TWEEN® 20 (1 mM) surfactant (blue), nanoparticles (0.7 nM) + TWEEN® 20 (1 mM + RuSH (9  $\mu$ M) (black) and isolated Ru-T20•AuNP13 (red). Number distributions for non-isolated particles with TWEEN® 20 surfactant are not shown, because they are dominated by the micellar peaks at 2 nm diameter.

Despite this, the TEM image (Figure 2.32) shows the nanoparticles as discrete 13 nm particles, rather than agglomerated gold centres, and a colloidal dispersion of the flocs is maintained as opposed to their sedimentation out of suspension.

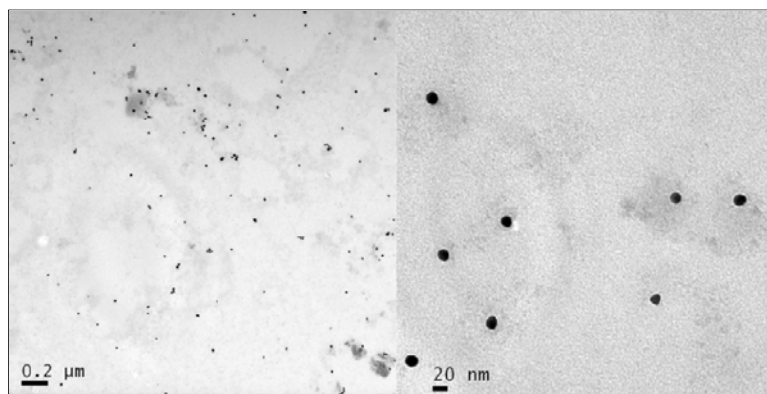


**Figure 2.32** TEM images of isolated **Ru-T20•AuNP13** particles air-dried onto grids.

The isolated **Ru-T20•AuNP13** sol was analysed by inductively-coupled plasma optical emission spectroscopy (ICP-OES) against calibration standards to find the Au:Ru ratio to be 72:1 (atoms), which equates to *ca.* 1400 Ru complexes per nanoparticle, assuming each 13 nm particle contains  $10^5$  gold atoms (see Appendix 2.1).<sup>76</sup> This gives the **RuSH** complex a molecular footprint of  $0.6 \text{ nm} \times 0.6 \text{ nm}$  when bound to the nanoparticle surface, which is reasonable for the given complex. This footprint is the surface-area per complex, but it is important to remember that there are co-coating moieties, i.e. surfactant molecules, also within this area. It must also be noted, that this calculation makes several assumptions: firstly that *all* the nanoparticles in the solution are 13 nm in diameter, whereas they actually vary by at least 10%, secondly that all the Ru(II) complexes detected in the isolated nanoparticle samples are bound to the nanoparticle in a single monolayer, with no multi-layers formed through disulphide bond formation, and thirdly it uses the spherical cluster approximation<sup>91</sup> to estimate the number of atoms per nanoparticle (this does not take into account the fact that hard spheres cannot pack to fill space exactly). Therefore, these accumulated errors render the calculated surface coverages throughout this thesis as crude approximations, and the absolute values are not overly meaningful. However, the order of magnitude of the values is useful to assess whether the isolated samples have sensible concentrations of complex bound to the surface, and the relative numbers between different nanoparticles are informative.

## 2.8 Synthesis and Characterisation of Ru-Z•AuNP13

13 nm gold nanoparticles were labelled with **RuSH** (synthesised *in situ* from the oxidatively stable thioester analogue **RuSAc**) using Zonyl® 7950 as a pre-coating surfactant to prevent the aggregation of the nanoparticles upon attachment of cationic lumiphores. Following the preliminary screening (Section 2.6), gold nanoparticles coated with Zonyl® 7950 appear to be very resistant to aggregation upon addition of **RuSH**, and nanoparticle concentrations of 9 nM can be labelled. Citrate gold nanoparticles (9 nM) (zeta potential =  $-40 \text{ mV} \pm 5 \text{ mV}$ , at 2 nM) were coated with fluorosurfactant ( $1.2 \text{ mg mL}^{-1}$ , *ca.* 1 mM), and then the **RuSH** complex was titrated into the resulting sol, up to  $70 \mu\text{M}$ , as shown in Figure 2.33.

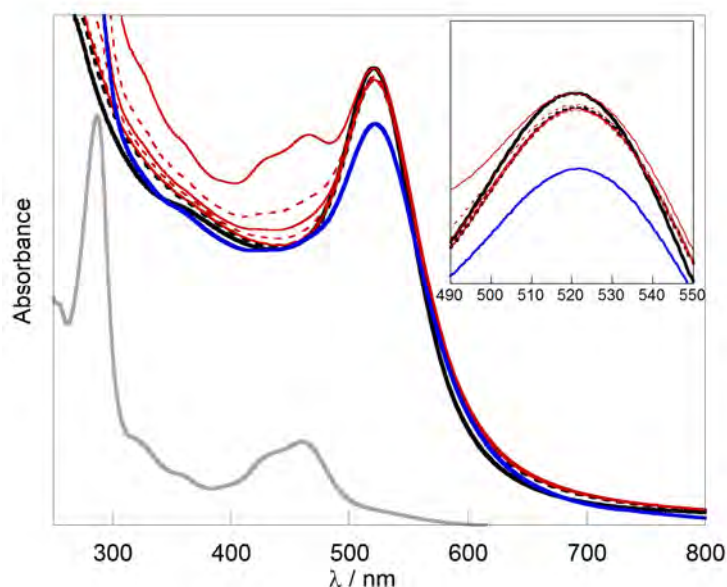


**Figure 2.33** UV-Vis absorption spectra of 13 nm citrate gold nanoparticles (9 nM) (black bold line), + Zonyl® 7950 (1 mM) (black dashed), + 1–70  $\mu\text{M}$  **RuSH** (red), and isolated **Ru-Z•AuNP13** (blue). Supernatant following the first centrifugation shown in grey.

Upon addition of the Zonyl ® 7950 surfactant, the SPR red-shifted by 1 nm, to 521 nm, as previously observed in Section 2.5 (Figure 2.21), but following the titration of **RuSH** into the surfactant-coated gold nanoparticles, no shift in the SPR peak  $\lambda_{\text{max}}$  is observed, which indicates that the dielectric constant at the surface does not change significantly. However, the retention of the SPR peak indicates the lack of nanoparticle aggregation. The particles cannot

be isolated by size-exclusion chromatography as the fluorosurfactant transports the unbound **RuSH** complex through the void volume of the stationary phase with the functionalised nanoparticles, presumably due to the formation of micelles, and thus separation of the particles from unbound material does not occur (See Appendix 3). The particles were isolated by three repeats of centrifugation, decantation of the supernatant, and resuspension in deionised water, at 12,000 g for 15 min, to render 9 nM **Ru-Z•AuNP13** (zeta potential =  $-48 \pm 2$  mV), with an SPR peak  $\lambda_{\max} = 522$  nm. Excess **RuSH** complex is clearly removed from the isolated **Ru-Z•AuNP13** nanoparticles, as can be seen in the UV-Vis absorption spectrum of the first supernatant removed in the centrifugation process to isolate **Ru-Z•AuNP13** (Figure 2.33, grey line). Isolation of the particles by centrifugation, as opposed to size-exclusion chromatography is advantageous as the final volume of the colloidal suspension can be controlled to vary the particle concentration, and high concentration particles can be obtained; column chromatography always leads to dilution of the particles upon isolation from the free species in solution. As a control Zonyl® 7950-coated gold nanoparticles were synthesised under identical conditions, without the **RuSH** complex, and purified by centrifugation to give **Z•AuNP13** (zeta potential =  $-61 \pm 4$  mV, at 2 nM), also with an SPR peak with  $\lambda_{\max} = 522$  nm. The difference in the surface charge with the presence of the **RuSH** complex is evident; the zeta potential is less negative as the **RuSH** complex displaces some of the electronegative fluorosurfactant. However, fluorosurfactant still remains, most likely packed between the **RuSH** complexes, maintaining the electrostatic stability of the resulting **Ru-Z•AuNP13** nanoparticles.

The uncoated 13 nm citrate gold nanoparticles, isolated **Z•AuNP13** and isolated **Ru-Z•AuNP13** have been characterised by DLS to examine the hydrodynamic diameters of the gold nanoparticles coated with the different surface environments, as shown in Figure 2.34.

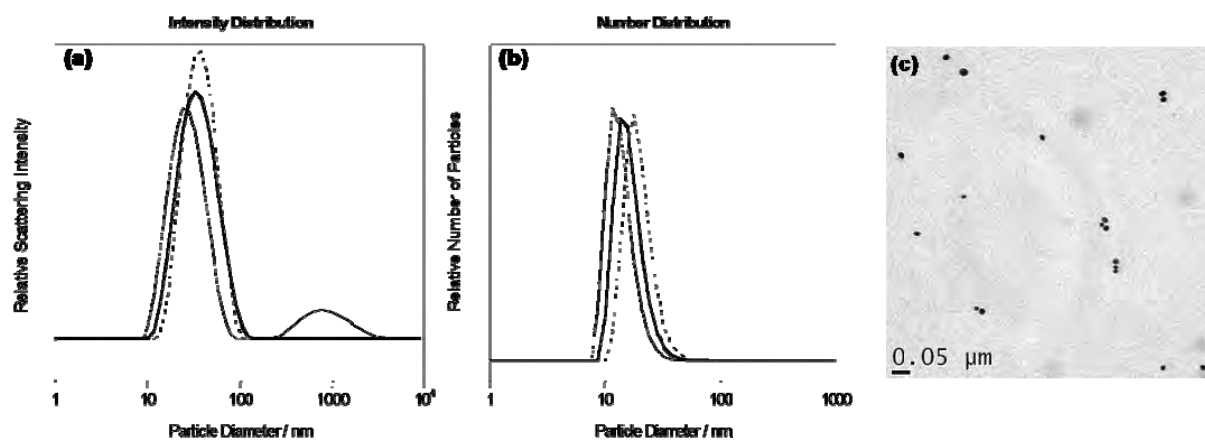


**Figure 2.34** (a) DLS intensity distributions and (b) DLS number distributions, of 2 nM citrate gold nanoparticles (solid line), 2 nM **Z•AuNP13** (dashed line) and 2 nM **Ru- Z•AuNP13** nanoparticles (bold solid line). (c) TEM image of **Ru- Z•AuNP13** particles.

The measurements were all performed on 2 nM suspensions of particles, and a peak at *ca.* 35 nm was observed in each case in the mean intensity distribution, with citrate nanoparticles having a mean intensity diameter of  $29 \pm 12$  nm (86%), (see section 2.3, Figure 2.17), the **Z•AuNP13** of  $39 \pm 15$  nm (100%) and **Ru-Z•AuNP13** of  $38 \pm 18$  nm (100%). These equate to average number distributions of  $14 \pm 4$  nm,  $20 \pm 6$  nm, and  $17 \pm 5$  nm for citrate gold nanoparticles, **Z•AuNP13**, and **Ru-Z•AuNP13** respectively. A 30% increase in the mean intensity distribution hydrodynamic diameter is observed when the fluorinated surfactant binds to the surface of the gold nanoparticles, as discussed in Section 2.5 (Figure 2.22), but no further increase in diameter is observed upon addition of **RuSH**. Thus, there is no evidence of nanoparticle aggregation, which is consistent with the large negative zeta potential of  $-48 \pm 2$  mV. The TEM image of **Ru-Z•AuNP13** confirms the uniformity of the nanoparticles (Figure 2.34c).

In order to reveal more information about the surface environment surrounding the gold nanoparticles in **Ru-Z•AuNP13**, **Z•AuNP13**, and bare citrate-coated gold nanoparticles, heavy metal staining techniques were employed, using phosphotungstic acid (PTA), as can be seen in Figure 2.35. The gold nanoparticle cores are easily visualised by electron microscopy

(as can be seen in Figure 2.35c), as the gold nucleations are electron dense and absorb electrons strongly, whereas any surface-coating made up of predominantly low-*Z* atoms will be transparent to the electron beam. Heavy metal staining of organic matter is often employed to incorporate electron-opaque heavy atoms into the matrix to enhance contrast in electron microscopy. Samples can be stained either ‘positively’, i.e. the heavy metal stain is incorporated into the material of interest, or ‘negatively’, in which the background is stained, leaving the material of interest as transparent sections on the grid against the dark electron-dense background.<sup>92,93</sup> When using PTA as a heavy metal stain, it is the phosphotungstate *anions* that provide the contrast, which is important when considering the interaction upon positive staining. Negatively stained images (Figures 2.35a, 2.35c, and 2.35e) are not easy to analyse because achieving homogenous staining of the background without artifacts is difficult. However, coronas of low contrast do appear to surround the **Ru-Z•AuNP13** (Figure 2.35a), indicating that there is a surface coating present. Similar features can be seen in Figure 2.35c for **Z•AuNP13**, although in this instance it is less clear. However, this does not appear to be visible for the bare citrate-coated gold nanoparticles.

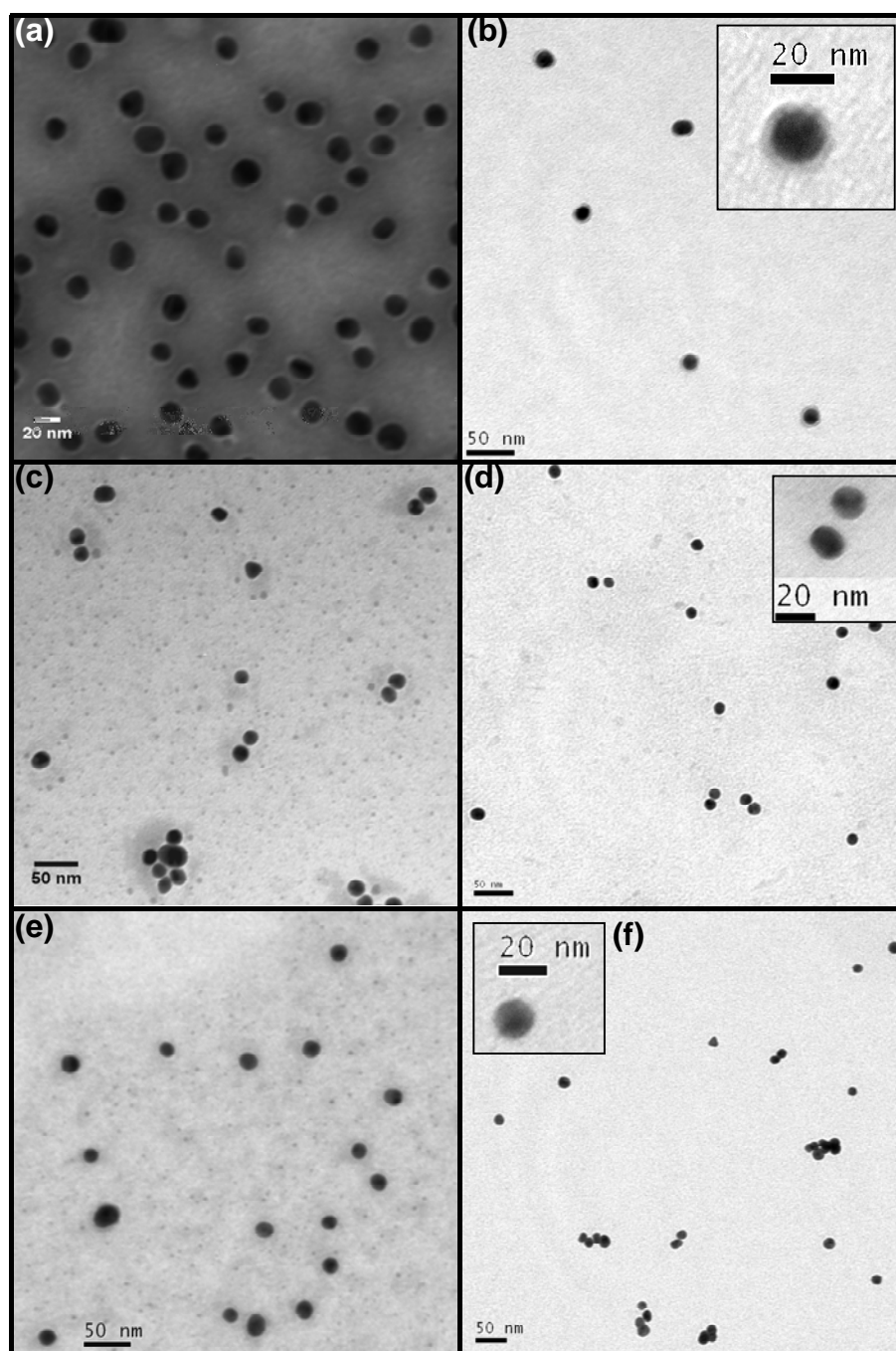


**Figure 2.35** Stained TEM images of (a–b) **Ru-Z•AuNP13**, (c–d) **Z•AuNP13**, and (e–f) citrate gold nanoparticles. Samples in (a), (c), and (e) are negatively stained with phosphotungstic acid, and samples in (b), (d), and (f) are positively stained with phoshotungstic acid.

The nanoparticles positively stained with PTA look no different to unstained samples for the bare citrate-coated nanoparticles (Figure 2.35f) and the **Z•AuNP13** (Figure 2.35d), whereas a grey corona is visible surrounding the gold nanoparticle cores in **Ru-Z•AuNP13**, Figure (Figure 2.35b). This is unsurprising because phototungstate ions tend to replace anions in

biological materials,<sup>94</sup> and can thus exchange with the **RuSH** counter ions in **Ru-Z•AuNP13**, to give the surface-coating electron contrast, whereas this does not occur in **Z•AuNP13**.

**Ru-Z•AuNP13** were analysed by X-ray photoelectron spectroscopy (XPS), along with citrate gold nanoparticles and **Z•AuNP13** in order to elucidate more information about the binding environments at the gold surface in each case (Figure 2.36), and peak fitting was performed by Dr Marc Walker, University of Warwick.

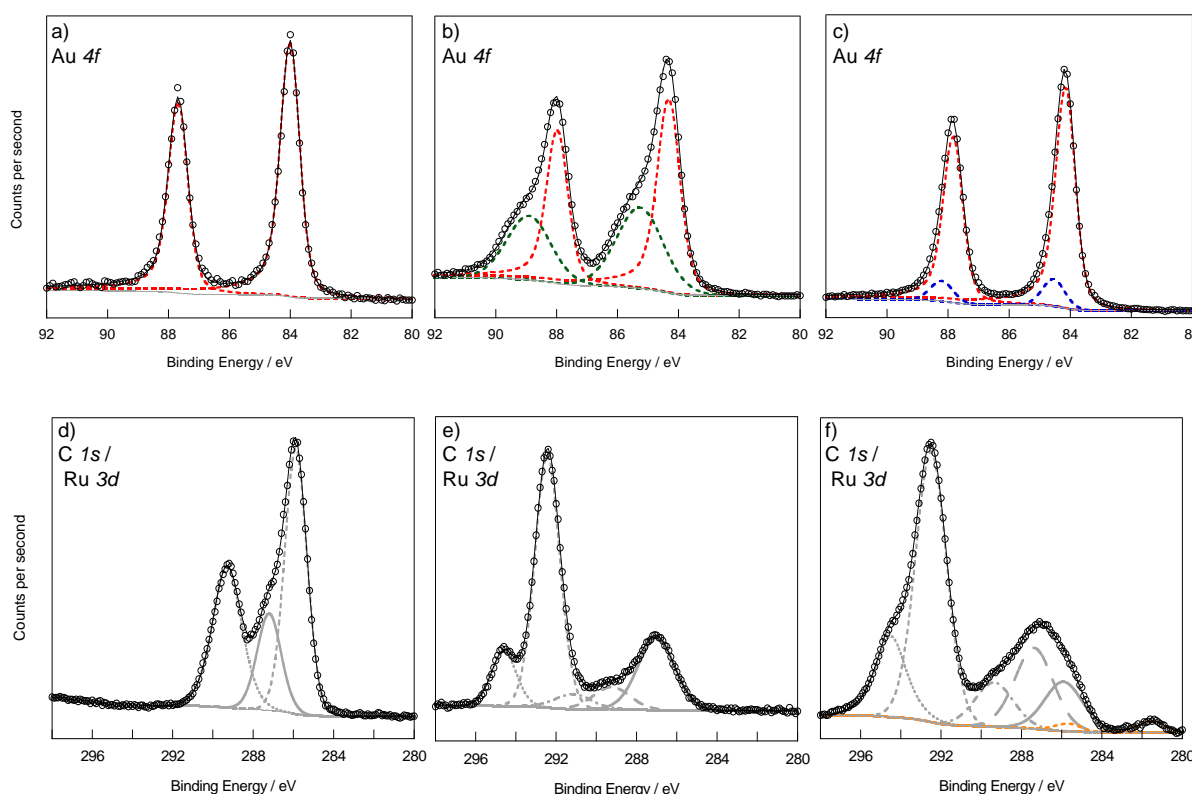


**Figure 2.36** XPS data of citrate gold nanoparticles (a and d), **Z•AuNP13** (b and e) and **Ru-Z•AuNP13** (c and f) with the raw data (open circles) the summation fitting envelope (solid black line) and deconvoluted fitting peaks (dashed lines) Fitting curves for Au 4f peaks for Au<sup>0</sup> shown in red,<sup>95</sup> and for shifted Au 4f environments shown in green and blue. Fitting curves for C 1s peaks shown in grey, and for Ru 3d peaks shown in orange.

A single Au 4f core level component, with 4f<sub>7/2</sub> and 4f<sub>5/2</sub> binding energies at 84.00 eV and 87.68 eV respectively, is observed for the citrate gold nanoparticles (Figure 2.36a), corresponding to the sole presence of Au(0),<sup>95</sup> whereas a striking difference is observed upon the addition of the Zonyl® 7950 surfactant to the nanoparticles (Figure 2.36b); two

different  $4f$  core level components are evident upon XPS analysis of **Z•AuNP13**, with the Au(0) peaks at 84.31 eV ( $4f_{7/2}$ ) and 87.97 eV ( $4f_{5/2}$ ) (63 %) and a second state (37 %) shifted to an increased binding energy by +0.95 eV, at 85.27 eV ( $4f_{7/2}$ ) and 88.91 eV ( $4f_{5/2}$ ). This is indicative of oxidised Au(I) present at the surface, due to the binding of the fluorosurfactant to the gold nanoparticles.<sup>96</sup> Whether this is attributed to the methacrylate head group of the fluorosurfactant, or the perfluorinated chain is unclear from these data, as both O and F are very electronegative species which could interact with surface gold atoms. The displacement of the citrate anions by the Zonyl® 7950 surfactant is also evident in the C  $1s$  region (Figures 2.35d and 2.35e). In Figure 2.36d there are three distinct carbon states, at 285.88 eV, 287.21 eV, and 289.29 eV which are likely to be the C–H, and different CO environments, respectively,<sup>95</sup> present in the citrate or oxidised citrate product capping the particles.<sup>6,7</sup> However, these peaks are absent upon addition of the fluorosurfactant, following the displacement of the citrate ions, and the isolated **Z•AuNP13** particles have C  $1s$  peaks with much higher binding energies, i.e. at 292.43 eV and 294.60 eV (Figure 2.36e), due to the C–F carbon  $1s$  states,<sup>95</sup> and a strong F  $1s$  peak, with a binding energy of 689.41 eV (see survey scan, Appendix 4). Interestingly, the Au  $4f_{7/2}$  and  $4f_{5/2}$  binding energies of the isolated **Ru-Z•AuNP13** nanoparticles (Figure 2.36c) differ *significantly* to the particles coated in the surfactant alone (Figure 2.36b), evidencing the ability of the **RuSH** complex to competitively bind to the gold by well-known S–Au chemistry, and displace the Zonyl® 7950 at the gold surface. The Au  $4f_{7/2}$  and  $4f_{5/2}$  peaks do not too fit well with the single Au(0) component (peaks at 84.15 eV ( $4f_{7/2}$ ) and 87.82 eV ( $4f_{7/2}$ )), rather with a second Au state (9 %) at higher binding energy, shifted by +0.39 eV peaks at 84.54 eV ( $4f_{7/2}$ ) and 88.21 eV ( $4f_{7/2}$ ). However, the Au(I) peaks that were present in the Au  $4f$  region (shifted by +0.95 eV from Au(0) for **Z•AuNP13** are no longer present for **Ru-Z•AuNP13**. A Au  $4f_{7/2}$  binding energy of 84.54 eV is consistent with gold-thiol binding at the surface.<sup>97</sup> The overall Au  $4f$  region is similar to that observed for previously reported glutathione-capped nanoclusters (< 2nm)<sup>98</sup> and

dodecanethiol-capped 1–4 nm gold nanoparticles.<sup>99</sup> Although, by inspection of the Au *4f* region of the XPS data, the fluorosurfactant does not appear to be bound to the surface of the gold nanoparticles in **Ru-Z•AuNP13**, it is still present as can be seen in the C *1s* (Figure 2.36f) and the F *1s* (Appendix 4) region; the C–F C *1s* peaks remain at 294.50 eV and 292.49 eV (Figure 5f) and the F *1s* peak is present at 689.34 eV (Appendix 4). This is commensurate with the large negative zeta potential that is observed for **Ru-Z•AuNP13**. Evidence of the **RuSH** complex can be seen with a new C *1s* peak at 285.91 eV, and Ru *3d*<sub>5/2</sub> and *3d*<sub>3/2</sub> peaks are evident at 281.42 eV and 285.59 eV respectively (Figure 2.36f), which are consistent with XPS data reported by Agnès *et al.* for Ru(bpy)<sub>3</sub><sup>2+</sup> complexes grafted onto diamond.<sup>100</sup>

**Ru-Z•AuNP13** were analysed by ICP-OES to give the atomic Au:Ru ratio of 63:1. This ratio equates to *ca.* 1600 Ru complexes per nanoparticle (see Appendix 2.2), which is very similar to the ratio with the TWEEN® 20 surfactant (1400 complexes per nanoparticle). A corresponding molecular footprint of 0.6 nm × 0.6 nm is calculated for the **RuSH** complex, when bound to the **Ru-Z•AuNP13** nanoparticles, which is the same as that observed for **Ru-T20•AuNP13** (Section 2.7). Therefore the different surfactants used do not significantly alter the packing density of the ruthenium(II) complex on the gold nanoparticle surface.

## 2.9 Photophysical Characterisation of Ru-T20•AuNP13 and Ru-Z•AuNP13

The photophysical properties of the isolated **Ru-T20•AuNP13** and **Ru-Z•AuNP13** dispersions were characterised, as presented in Figure 2.37.

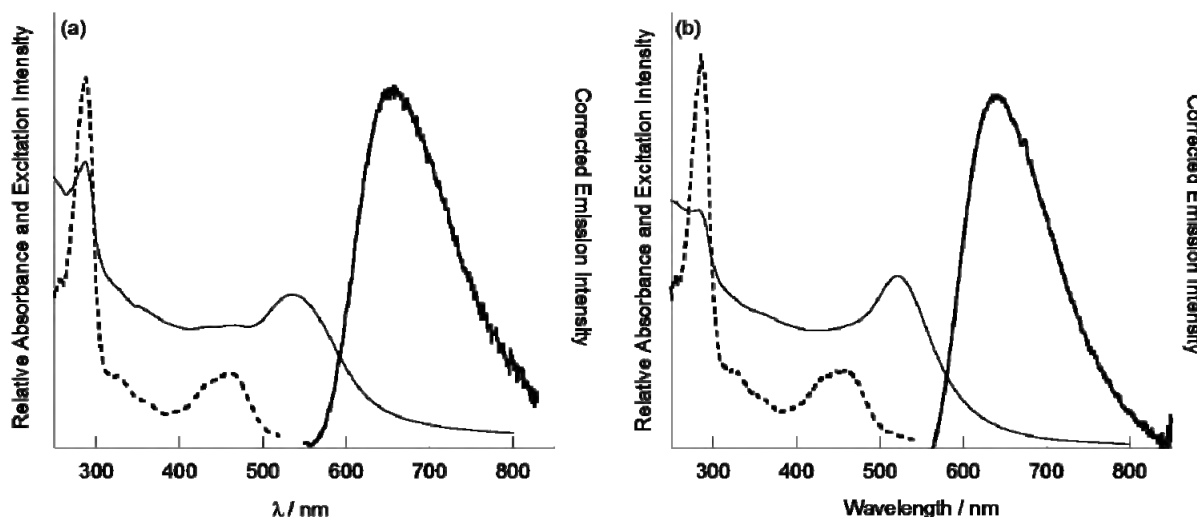


**Figure 2.37** UV-Vis absorption spectrum (solid line), excitation spectrum,  $\lambda_{em} = 630$  nm (dashed line) and steady-state emission spectrum,  $\lambda_{exc} = 450$  nm (bold solid line) of (a) **Ru-T20•AuNP13** (0.3 nM) and **Ru-Z•AuNP13** (1 nM). All spectra corrected for instrument response.

Upon excitation at 450 nm, both **Ru-T20•AuNP13** and **Ru-Z•AuNP13** exhibit broad red emission with  $\lambda_{max} = 655$  nm and 640 nm, respectively. The UV-Vis spectra are dominated by the SPR of the colloid in each case, and the excitation spectra of both **Ru-T20•AuNP13** and **Ru-Z•AuNP13**, measured at  $\lambda_{em} = 630$  nm, resemble the UV-Vis absorption spectrum and excitation spectrum of the free **RuSAc** (Section 2.2.2, Figures 2.14 and 2.15). The  $\lambda_{max}$  of the **Ru-T20•AuNP13** luminescence is red-shifted by 5 nm, with respect to the free **RuSAc** complex emission in 1 % CH<sub>3</sub>CN, water (emission peak  $\lambda_{max}$  value at 650 nm), whereas that of **Ru-Z•AuNP13** is blue-shifted by 10 nm. The photophysical data of the colloids are summarised below in Table 2.4.

**Table 2.4** Summary of the photophysical properties of gold nanoparticles coated with the **RuSH** complex, with control solution studies.

	$\Phi$ / % <sup>a</sup>	$\tau$ / ns <sup>b</sup>	$\lambda_{\max}$ / nm <sup>c</sup>
<b>Ru-T20•AuNP13</b>	- <sup>d</sup>	305±10% [375±10%]	655
<b>Ru-Z•AuNP13</b>	4±1 <sup>e</sup>	340±10% [690±10%]	640
<b>RuSAc</b> in 1% CH <sub>3</sub> CN/H <sub>2</sub> O	2.0±0.5	260 [325]	650
9 $\mu$ M <b>RuSAc</b> , 1 mM TWEEN® 20 in 1% CH <sub>3</sub> CN/H <sub>2</sub> O	2.5±0.5	340 [405]	660
9 $\mu$ M <b>RuSAc</b> , 1 mM Zonyl® 7950 in 1% CH <sub>3</sub> CN/H <sub>2</sub> O	3.0±0.5	405 [610]	635

<sup>a</sup> aerated  $\Phi$ s measured using an integrating sphere.

<sup>b</sup> lifetimes measured in aerated solutions, deaerated measurements shown in square brackets. Errors estimated as  $\pm 6\%$  by comparison on 3-5 different samples, unless otherwise stated.

<sup>c</sup> error estimated as  $\pm 3$  nm.

<sup>d</sup>  $\Phi$  measurement not possible due to low signal intensity at such low lumiphore concentrations.

<sup>e</sup>  $\Phi$  measured of nanoparticles measured using a solution of uncoated citrate gold nanoparticles as a reference solution with the integrating sphere. A calibrated neutral density filter was also employed due to low signal.

For comparison, the steady-state luminescence was measured for the free **RuSAc** complex (9  $\mu$ M) in 1 % CH<sub>3</sub>CN, water with 1 mM TWEEN® 20 surfactant, and the  $\lambda_{\max}$  value of the emission peak is at 660 nm. This 10 nm red-shift in the emission peak suggests that the TWEEN® 20 surfactant stabilises the charge-separated MLCT excited state, and this appears to occur on the **Ru-T20•AuNP13** nanoparticle surface as well, although to a lesser extent, presumably because the complex is surrounded with less surfactant. In contrast, the  $\lambda_{\max}$ =635 nm when **RuSAc** complex (9  $\mu$ M) in 1 % CH<sub>3</sub>CN, water with 1 mM Zonyl® 7950 surfactant, *i.e.* blue-shifted by 15nm, which suggests that the fluorosurfactant presents a non-polar environment to the Ru(II) complex, commensurate with its perfluorinated alkyl chains, destabilising the MLCT state. This same effect is also seen on the **Ru-Z•AuNP13** nanoparticles, again to lesser extent, similar to TWEEN® 20.

The observed luminescence lifetime of the isolated **Ru-T20•AuNP13** colloid, with excitation at 445 nm and emission collected at 630 nm, is 305 ns  $\pm$ 10 % (aerated) and 375 ns  $\pm$ 10 % (deaerated), which is slightly increased (by *ca.* 15%) from that of the free complex in 1 % CH<sub>3</sub>CN, water (260 ns  $\pm$ 6 % (aerated), 325 ns  $\pm$ 6 % (deaerated)). Time-resolved luminescence was also studied for the free **RuSAc** complex (9  $\mu$ M) in 1 % CH<sub>3</sub>CN, water with 1 mM TWEEN® 20 surfactant, and luminescence lifetimes of 340 ns  $\pm$ 6 % (aerated) and 405 ns  $\pm$ 6 % (deaerated) were observed. These lifetimes are *ca.* 10% longer than **Ru-T20•AuNP13**, which is probably due to the **RuSH** interacting with less surfactant when bound on the nanoparticle surface in **Ru-T20•AuNP13**, than in a solution of 100 equivalents surfactant. However, the increase is barely significant given the errors in the lifetimes. An increase in the lifetime of the luminescence excited state of the ruthenium(II) complex in the presence of TWEEN® 20 surfactant, accompanied by an increase in the  $\Phi$  (the free complex in an aqueous environment has a  $\Phi$  of 2.0 $\pm$ 0.5%, whereas the control solution of **RuSH** complex (9  $\mu$ M) in 1 % CH<sub>3</sub>CN, water with 1 mM TWEEN® 20 surfactant, has a  $\Phi$  = 2.5 $\pm$ 0.5%), is indicative of a reduction in the non-radiative decay rate from the excited state. This appears to be due to the surfactant rather than the gold nanoparticle on **Ru-T20•AuNP13**. (If an increase in the *radiative* rate of decay from the excited state was being observed, then an increase in  $\Phi$  would be accompanied by a *decrease* in the lifetime of the excited state). Unfortunately, it was not possible to measure the  $\Phi$  of the ruthenium(II) complex on the **Ru-T20•AuNP13** particles due to the low signal intensity at such low concentrations.

Luminescence lifetimes ( $\lambda_{em} = 445$  nm,  $\lambda_{em} = 630$  nm) of 340 ns  $\pm$ 10 % (aerated) and 690 ns  $\pm$ 10 % (deaerated) were observed for isolated **Ru-Z•AuNP13**, which are increased by 30% (aerated) and 115% (degassed) with respect to the free **RuSAc** complex in water, and similar to that of the complex mixed with fluorosurfactant in solution. In contrast to the

**Ru-T20•AuNP13** particles, however, **Ru-Z•AuNP13** appear to be far more sensitive to molecular oxygen. An increase in the observed luminescence lifetimes is again attributed to the surfactant reducing the non-radiative decay rates of the Ru(II) complex excited state, which is confirmed by an increase in the  $\Phi$  in solution to  $3.0\pm 0.5\%$  upon addition of fluorosurfactant (from  $2.0\pm 0.5\%$  **RuSAc**, aqueous environment). The presence of the surfactant may increase the rigidity of the lumiphore, thus reducing the access to vibrational states of the ground state to decay the excited state non-radiatively. The  $\Phi$  of the **Ru-Z•AuNP13** nanoparticles was measured as  $4\pm 1\%$ , using uncoated gold nanoparticles as the reference material, so that the absorbance of the Ru(II) complex only is taken into account when measuring the  $\Phi$ . This value is similar to that of the Ru(II) complex / fluorosurfactant mixture in solution, which is consistent with the lifetime data, and again demonstrates that luminescence quenching is not being induced by attachment of **RuSH** to the gold nanoparticles.

As a control study, to further verify that the frequently reported quenching of lumiphores by gold nanoparticles,<sup>31,39,41,48-50</sup> was not being observed, citrate gold nanoparticles were titrated into a mixture of the **RuSH** complex in 1 % CH<sub>3</sub>CN, water with 0.04 mM Zonyl® 7950, and the steady-state luminescence spectra were recorded, corrected for instrument response and integrated. The integrated luminescence peak areas were plotted against [gold nanoparticles] to analyse the signal intensity upon addition of the nanoparticles, as shown in Figure 2.38. The concentrations for this experiment were kept low to eliminate internal filtering effects of the nanoparticles from significantly affecting the results.

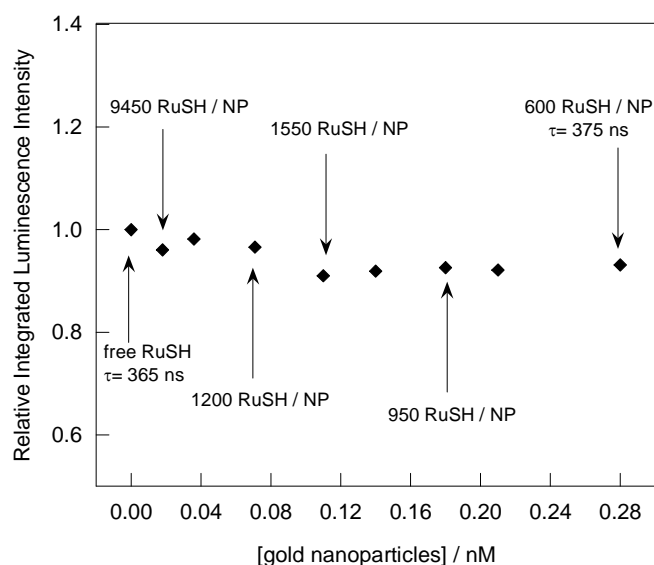


**Figure 2.38** The change in luminescence intensity of **RuSH** (0.15 mM) with Zonyl® 7950 (0.04 mM) in 1% CH<sub>3</sub>CN, water, upon the addition of 13 nm citrate-stabilised gold nanoparticles.  $\lambda_{exc} = 450$  nm. Spectra were corrected for instrument response.

As can be seen, the luminescence intensity remained constant ( $\pm 10\%$ ) across the whole titration, and even when there was an excess of gold nanoparticles in the solution (assuming binding saturation occurs at 1600 **RuSH** per nanoparticle, from the ICP-OES data) the emission intensity remained constant. The luminescent lifetime was measured at the beginning (365 ns  $\pm 10\%$ ) and end of the titration (375 ns  $\pm 10\%$ ), at 630 nm, and also remained constant within error. Thus it is evident that we do *not* observe quenching effects upon the addition of gold nanoparticles to the complex/fluorosurfactant mixture.

## 2.10 Conclusion

In conclusion, the interaction of three commercially available surfactants, Triton™ X-100, TWEEN® 20 and Zonyl® 7950 with citrate-stabilised gold nanoparticles has been reported, and it has been determined that TWEEN® 20 can be used to produce low concentration flocculated particles in solution, coated in the **RuSH** complex, whereas Zonyl® 7950 can effectively facilitate the luminescent labelling of the particles at high nanomolar

concentrations with a dicationic surface-active ruthenium polypyridyl complex in a pre-coating process. Although the TWEEN® 20 is able to mediate **RuSH** attachment to gold nanoparticles to some degree, the resulting colloid has limited applications for imaging due to its low concentration and formation of flocs. Whilst the cellular uptake of aggregates of particles is possible,<sup>70</sup> this renders the dose and uptake mechanism of the particles difficult to control. The Zonyl® 7950 not only mediates the functionalisation by means of stable particle formation, but also increases the  $\Phi$  and thus the brightness of the **RuSH** complex. Although there are many references in the literature to the undesired quenching effects of lumiphores by gold nanoparticles,<sup>31,39,41,48-50,57</sup> this is *not* observed with the tailor-made surface-active ruthenium polypyridyl complex **RuSH**. The lack of quenching is attributed to the design of **RuSH**, in which the lumiphore centre is distanced from the gold surface by a hexyl spacer-group.

By employing the Zonyl® 7950 fluorosurfactant in the nanoparticle coating process, **RuSH** complex can be used to label gold nanoparticles efficiently with multiple lumiphore tags to produce bright luminescent nanoprobes with good colloidal stability at 9 nM concentrations. These nanoprobes have great potential as imaging probes, and furthermore, new applications may be envisaged in the development of new nanomaterials in which the properties are manipulated by the surface-grafted transition metal complex.

## 2.11 Acknowledgements

Thank you to Dr Shiva Farabi for her guidance with the synthesis of the ruthenium(II) compound, and thank you to Mr Paul Stanley (Centre for Electron Microscopy, University of Birmingham) for his advice with the TEM sample staining. Thank you also to Dr Marc

Walker (School of Physics, University of Warwick) for his assistance with the execution of the XPS data, and for his extensive help with the XPS data fitting.

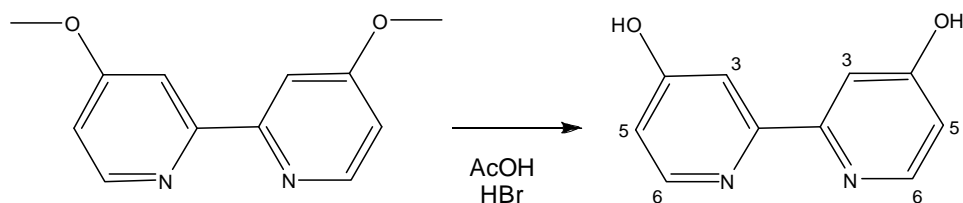
## 2.12 Experimental

### 2.12.1 General Synthesis

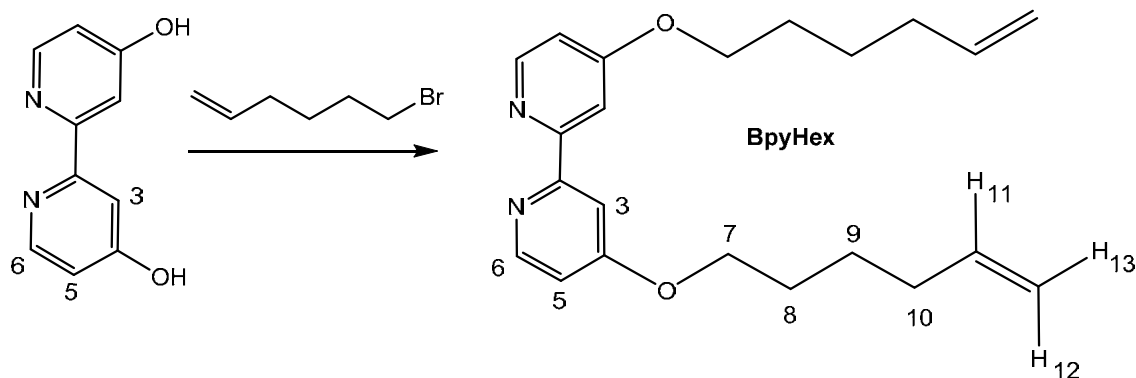
All precursors to these reactions were purchased from Sigma-Aldrich. The TWEEN® 20, Triton™ X-100, Zonyl® 7950, poly(ethylene glycol) methyl ether methacrylate (av. MW = 500), and 1*H*,1*H*,2*H*-perfluoro-1-decene were purchased from Sigma-Aldrich and used without further purification.

Zonyl® 7950, which is a commercial surfactant product containing a mixture of species within the formula, was characterised by GC-MS and NMR. <sup>1</sup>H NMR (300 MHz, *d*<sub>6</sub>-DMSO): δ<sub>H</sub> = 3.77 (septuplet, 6H, H–C of isopropanol), 3.63 (s (b), 2H, CH<sub>2</sub> of fluorosurfactant), 2.94 (s (b), 2H, CH<sub>2</sub> of fluorosurfactant), 2.68–2.54 (m, 1.5H), 2.51 (s, 0.5H), 2.45–2.17 (m, 2H), 1.01 (d (<sup>3</sup>J<sub>HH</sub> = 6.3 Hz), 36H, CH<sub>3</sub>– of isopropanol). <sup>13</sup>C{<sup>1</sup>H} PENDANT (150 MHz, *d*<sub>6</sub>-DMSO): δ<sub>C</sub> = 175 (C=O of fluorosurfactant), 117/114/110/107 (CF<sub>2</sub>s of fluorosurfactant), 62 (CH of isopropanol), 56/49 (CH<sub>2</sub> of fluorosurfactant), 24 (CH<sub>3</sub> of isopropanol). GC-MS reveals two peaks in the total ion current chromatogram, which correspond to *m/z* 452 and *m/z* 552, with relative intensity integrals of 14.5 and 11.5 respectively. Thus, an average molecular weight of *m/z* 500 is approximated. <sup>1</sup>H NMR reveals that the surfactant is formulated with isopropanol, and by integration of the resonance due to the six methyl protons per isopropanol molecule, relative to one of the fluorosurfactant CH<sub>2</sub> proton resonances, the ratio of fluorosurfactant: isopropanol is estimated as 6:1. Thus, 1 mole of fluorosurfactant = fluorosurfactant molecule+6 isopropanols, with a total molecular mass of 500 + (6×60) ≈ 900. Therefore, 1 mg mL<sup>-1</sup> = (1/900)/10<sup>-3</sup> = 1 mM.

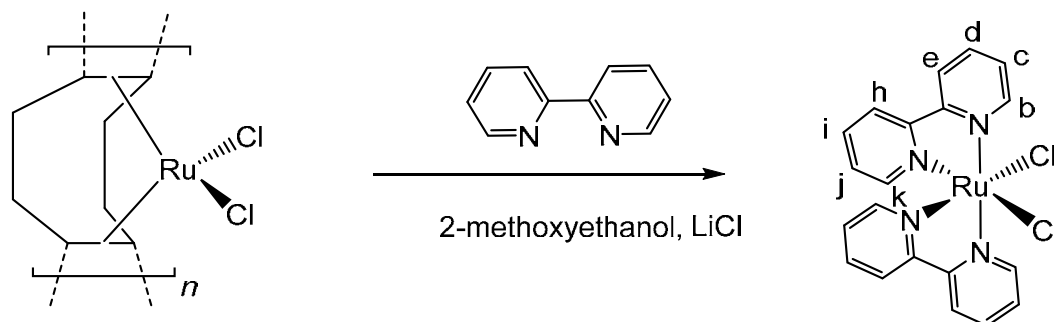
## Synthesis of 4,4'-dihydroxy-2,2'-bipyridine



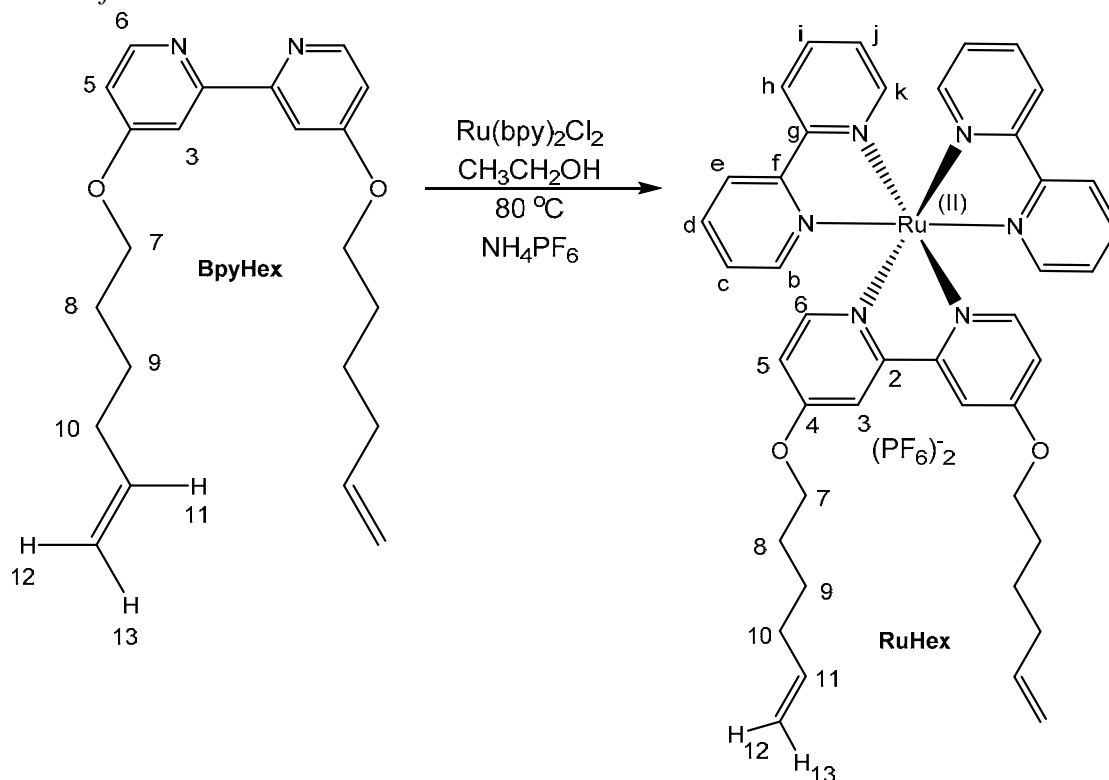
4,4'-dihydroxy-2,2'-bipyridine was synthesized according to the method of Gorman and coworkers.<sup>101</sup> To a solution of 4,4'-dimethoxy-2,2'-bipyridine (3.055g, 14.13 mmol) in glacial acetic acid (180 mL) was added HBr (aq) (25 mL, 48 wt % in water, 146 mmol). The mixture was refluxed overnight at 140 °C under N<sub>2</sub> (g). The mixture was allowed to cool and the solvent was removed *in vacuo* to render a white solid. The residue was dissolved in water (100 mL) and neutralised to pH 7 by adding aqueous ammonium hydroxide, and a white precipitate formed. The white solid (2.425 g, 12.89 mmol, 91 % yield) was filtered and dried, and used in the next step without further purification. <sup>1</sup>H NMR (300 MHz, NaOD/D<sub>2</sub>O): δ<sub>H</sub> = 7.74 (s, 1H, OH), 7.38 (d, 2H, <sup>3</sup>J<sub>H5</sub> = 5.9 Hz, H<sub>6</sub>), 6.34 (d, 2H, <sup>4</sup>J<sub>H5</sub> = 2.4 Hz, H<sub>3</sub>), 5.85 (dd, 2H, <sup>3</sup>J<sub>H6</sub> = 5.9 Hz, <sup>4</sup>J<sub>H3</sub> = 2.4 Hz, H<sub>5</sub>). EI-MS(+): *m/z* 188.1 [M]<sup>+</sup>. IR ν<sub>max</sub> (cm<sup>-1</sup>): 3209 (C–H), 3059 (C–H), 2760 b (O–H, H-bonded), 1594 (C–C<sub>ring</sub>/C–N<sub>ring</sub>), 1523, 1475, 1393, 1218. Data agree with previously reported studies<sup>75,101</sup> and thus no further characterisation was performed.

Synthesis of **BpyHex**

Method adopted from Dr Shiva Farabi.<sup>75</sup> To a solution of 4,4'-dihydroxybipyridine (2.03 g, 10.8 mmol) in anhydrous DMF was added NaH (5.00 g, 125 mmol, 60 % w/w in mineral oil), and the white suspension was stirred at 60 °C under nitrogen for 1 hr. 6-bromohex-1-ene (8.06 g, 49.4 mmol) was added dropwise, and the reaction mixture was heated at 60 °C for 20 h to render a pale yellow/brown solution. The reaction was cooled to room temperature and the NaH was quenched by adding ice-cold ethanol (150 mL). The solvent was removed *in vacuo* and the pale brown residue was extracted with CH<sub>2</sub>Cl<sub>2</sub>/H<sub>2</sub>O and dried over MgSO<sub>4</sub>. The CH<sub>2</sub>Cl<sub>2</sub> was removed *in vacuo* and the crude product was purified by recrystallisation from ethanol to yield **BpyHex** (2.32 g, 6.58 mmol, 61 % yield) as a crystalline white solid. <sup>1</sup>H NMR (400 MHz, CDCl<sub>3</sub>): δ<sub>H</sub> = 8.45 (d, 2H, <sup>3</sup>J<sub>H5</sub> = 5.7 Hz, H<sub>6</sub>), 7.94 (d, 2H, <sup>4</sup>J<sub>H5</sub> = 2.5 Hz, H<sub>3</sub>), 6.82 (dd, 2H, <sup>3</sup>J<sub>H6</sub> = 5.7 Hz, <sup>4</sup>J<sub>H3</sub> = 2.6 Hz, H<sub>5</sub>), 5.91–5.74 (m, 2H, <sup>3</sup>J<sub>H12</sub> = 17.1 Hz, <sup>3</sup>J<sub>H13</sub> = 10.3 Hz, <sup>3</sup>J<sub>H10</sub> = 6.6 Hz, H<sub>11</sub>), 5.09–5.00 (m, 2H, <sup>3</sup>J<sub>H11</sub> = 17.1 Hz, <sup>2</sup>J<sub>H13</sub> = 2.0 Hz, <sup>4</sup>J<sub>H10</sub> = 1.5 Hz, H<sub>12</sub>), 5.00–4.94 (m, 2H, <sup>3</sup>J<sub>H11</sub> = 10.3 Hz, <sup>2</sup>J<sub>H12</sub> = 2.0 Hz, <sup>4</sup>J<sub>H10</sub> = 1.3 Hz, H<sub>13</sub>), 4.14 (t, 4H, <sup>3</sup>J<sub>H8</sub> = 6.5 Hz, H<sub>7</sub>), 2.20–2.07 (m, 4H, H<sub>10</sub>), 1.90–1.78 (m, 4H, H<sub>8</sub>), 1.65–1.53 (m, 4H, H<sub>9</sub>). <sup>13</sup>C NMR (100 MHz, CDCl<sub>3</sub>): δ<sub>C</sub> = 166.1 (C<sub>2</sub>), 157.9 (C<sub>4</sub>), 150.1 (C<sub>6</sub>), 138.3 (C<sub>11</sub>), 114.9 (C<sub>12</sub>), 111.3 (C<sub>5</sub>), 106.7 (C<sub>3</sub>), 67.8 (C<sub>7</sub>), 33.3 (C<sub>10</sub>), 28.4 (C<sub>8</sub>), 25.2 (C<sub>9</sub>). TOF ES-MS(+) *m/z*: 375.2 [M+Na]<sup>+</sup>, 353.2 [M+H]<sup>+</sup>. IR ν<sub>max</sub> (cm<sup>-1</sup>): 3070 (C–H), 3008 (C–H), 2952 (C–H), 2920 (C–H), 1577 (C–C<sub>ring</sub>/C–N<sub>ring</sub>), 1558, 1456, 1297, 1245, 1003.

Synthesis of  $Ru(bpy)_2Cl_2$ 

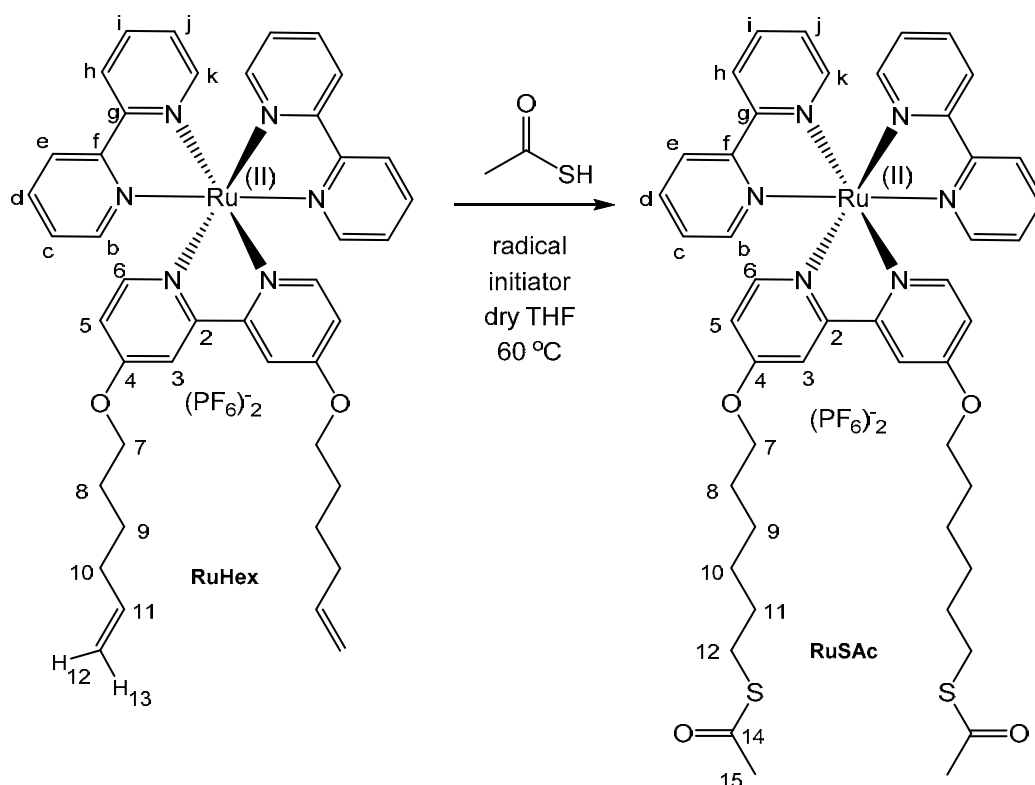
Method adopted from Dr Shiva Farabi<sup>75</sup> 2-methoxyethanol (200 mL) was purged with nitrogen for 15 min and  $Ru(COD)Cl_2$  (dichloro(1,5-cyclooctadiene)ruthenium (II) polymer) (501.0 mg, 1.79 mmol) and LiCl (593.5 mg, 14.0 mmol) were added. The suspension was stirred at reflux for 30 min under nitrogen. 2,2'-bipyridine (547.8 mg, 3.51 mmol, 1.96 eq) was dissolved in 2-methoxyethanol (50 ml) and added dropwise to the refluxing mixture, over 15 min. The solution was left to reflux overnight to give a dark purple solution. This was cooled to room temperature under nitrogen, and the solvent was removed *in vacuo* to render a dark oil. This oil was added to cold, fast-stirring acetone (100 ml) in an ice-bath and left to stir for 1 hr, and then placed in the fridge overnight to precipitate. The black solid was filtered, and washed with water and diethyl ether to give  $[Ru(bpy)_2Cl_2] \cdot 2H_2O$  (385.8 mg, 0.741 mmol, 41% yield) as a dark green solid, which streaks purple upon scratching.  $^1H$  NMR (300 MHz, DMSO):  $\delta_H = 9.97$  (d, 2H,  $^3J_{Hc} = 4.7$  Hz,  $H_b$ ), 8.64 / 8.49 (d, 2H,  $^3J_{Hd/Hi} = 7.8$  Hz,  $H_e/H_h$ ), 8.07 (m, 2H,  $H_d$ ), 7.77 (m, 2H,  $H_c$ ), 7.68 (m, 2H,  $H_i$ ), 7.51 (d, 2H,  $^3J_{Hj} = 4.6$  Hz,  $H_k$ ), 7.10 (m, 2H,  $H_j$ ).  $^{13}C$  NMR (100 MHz, DMSO):  $\delta_C = 160.1/158.1$  ( $C_f/C_g$ ), 153.1 ( $C_b$ ), 151.9 ( $C_k$ ), 134.5 ( $C_d$ ), 133.2 ( $C_i$ ), 125.3/125.2 ( $C_j/C_j$ ), 122.8/122.4 ( $C_e/C_h$ ). TOF ES-MS(+):  $m/z$  523.0  $[M+K]^+$ , 507.0  $[M+Na]^+$ , 481.1  $[Ru(bpy)_2(OCH_3)Cl+H]^+$ , 449.0  $[M-Cl]^+$ . TOF LD-MS(+):  $m/z$  484.2  $[M]^+$ , 449.4  $[M-Cl]^+$ , 413.5  $[M-2Cl]^+$ , 328.7  $[M-bpy]^+$ , 293.2  $[Ru(bpy)Cl]^+$ . UV-VIS (DCM)  $\lambda_{max}$  [nm]: 555, 378, 300. IR  $\nu_{max}$  ( $cm^{-1}$ ): 3100 (C-H), 3069 (C-H), 3029 (C-H), 1613(C-C<sub>ring</sub>/C-N<sub>ring</sub>), 1601(C-C<sub>ring</sub>/C-N<sub>ring</sub>), 1460, 1442, 1418, 1308, 1265.

Synthesis of **RuHex**<sup>76</sup>

$\text{Ru}(\text{bpy})_2\text{Cl}_2 \cdot 2\text{H}_2\text{O}$  (107.7 mg, 0.207 mmol) and **BpyHex** (119.1 mg, 0.338 mmol) were heated to reflux in ethanol (10 mL) for 17 hr under nitrogen to give a deep red solution. This was cooled to room temperature and was concentrated to 3 mL *in vacuo*. A saturated aqueous solution of  $\text{NH}_4\text{PF}_6$  (3.5 mL) was added, followed by  $\text{H}_2\text{O}$  (7 mL), and a red precipitate was formed. The flask was put in the fridge for 30 min, and the red solid was filtered under suction, washed with water and diethyl ether to yield **RuHex** (131.6 mg, 0.125 mmol, 60 % yield) as a red solid.  $^1\text{H}$  NMR (400 MHz,  $\text{CD}_3\text{CN}$ ):  $\delta_{\text{H}} = 8.47$  (2×d, 4H,  $^3J_{\text{Hd}/\text{Hi}} = 8.3$  Hz,  $\text{H}_c/\text{H}_h$ ), 8.06–7.99 (m, 4H,  $\text{H}_d/\text{H}_i$ ), 7.97 (d, 2H,  $^4J_{\text{H5}} = 2.5\text{f}$  Hz,  $\text{H}_3$ ), 7.81/7.71 (2×d, 4H,  $^3J_{\text{Hc}/\text{Hj}} = 5.5$  Hz,  $\text{H}_b/\text{H}_k$ ), 7.43–7.39/7.38–7.33 (2×m, 4H,  $\text{H}_c/\text{H}_j$ ), 7.41 (d, 2H,  $^3J_{\text{H5}} = 6.5$  Hz,  $\text{H}_6$ ), 6.90 (dd, 2H,  $^3J_{\text{H6}} = 6.5$  Hz,  $^4J_{\text{H3}} = 2.5$  Hz,  $\text{H}_5$ ), 5.86 (m, 2H,  $^3J_{\text{H12}} = 17.1$  Hz,  $^3J_{\text{H13}} = 10.3$  Hz,  $^3J_{\text{H10}} = 6.6$  Hz,  $\text{H}_{11}$ ), 5.05 (m, 2H,  $^3J_{\text{H11}} = 17.1$  Hz,  $\text{H}_{12}$ ), 4.97 (m, 2H,  $^3J_{11} = 10.3$  Hz,  $\text{H}_{13}$ ), 4.19 (t, 4H,  $^3J_{\text{H8}} = 6.5$  Hz,  $\text{H}_7$ ), 2.17–2.09 (m, 4H,  $\text{H}_{10}$ ), 1.85–1.77 (m, 4H,  $\text{H}_8$ ), 1.61–1.51 (m, 4H,  $\text{H}_9$ ).  $^{13}\text{C}$  NMR (100 MHz,  $\text{CD}_3\text{CN}$ ):  $\delta_{\text{C}} = 153.0$  ( $\text{C}_6$ ), 152.7/152.5 ( $\text{C}_b/\text{C}_k$ ), 139.5 ( $\text{C}_{11}$ ), 138.3 ( $\text{C}_d/\text{C}_i$ ), 128.3 ( $\text{C}_c/\text{C}_j$ ), 125.0 ( $\text{C}_e/\text{C}_h$ ), 115.3 ( $\text{C}_{12}$ ), 115.0 ( $\text{C}_5$ ), 112.3 ( $\text{C}_3$ ),

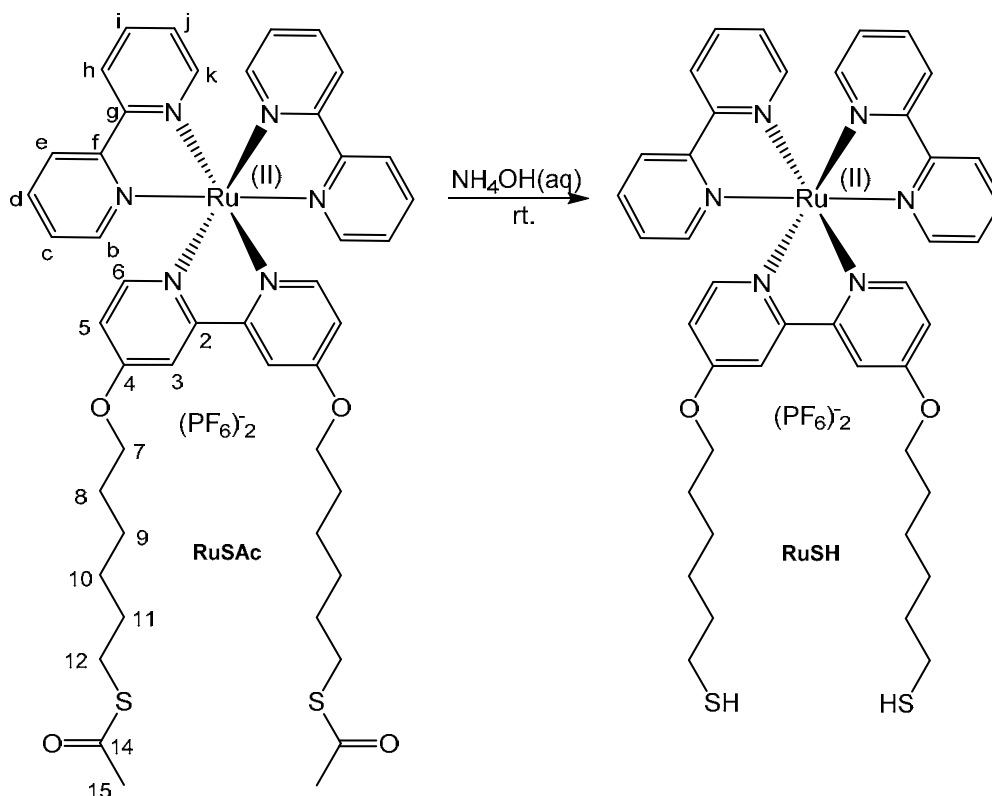
70.5 ( $C_7$ ), 33.8 ( $C_{10}$ ), 28.7 ( $C_8$ ), 25.7 ( $C_9$ ). TOF ES-MS(+):  $m/z$  911.1  $[M-PF_6]^+$ , 383.2  $[M-2PF_6]^{2+}$ . IR  $\nu_{max}$  ( $cm^{-1}$ ): 2935 (C-H), 2867 (C-H), 1612 (C-C<sub>ring</sub>/C-N<sub>ring</sub>), 1491, 1465, 1445, 1337, 1314, 1219.

### Synthesis of **RuSAc**<sup>76</sup>



A solution of thioacetic acid (100 mg, 1.31 mmol) and ABCN (1,1'-azobiscyclohexane carbonitrile) (120 mg, 0.49 mmol) in dry THF (2 mL) was heated at 60 °C and degassed under nitrogen for 30 min. **RuHex** (105.9 mg, 0.100 mmol) was dissolved in THF (4 mL), and added dropwise to the solution. The double bond disappearance was monitored by proton NMR. The reaction was stirred at 60 °C followed by addition of one portion of ABCN (120 mg, 0.49 mmol) and thioacetic acid (100 mg, 1.31 mmol) after 15 hr, and another portion of ABCN (120 mg, 0.49 mmol) and thioacetic acid (100 mg, 1.31 mmol) after 24 hr. After a total of 40 hr stirring the reaction was pushed to completion and the ABCN was quenched with saturated  $NaHCO_3$  solution (10 mL). The THF was removed *in vacuo*, and the residue was extracted in  $CH_2Cl_2/H_2O$ , washed with brine, and dried over  $MgSO_4$ . The  $CH_2Cl_2$

was removed *in vacuo* and the solid was filtered under suction, and washed with a copious amount of hexane and diethyl ether to yield **RuSAc** (52.9 mg, 0.044 mmol, 43.8 % yield) as a red solid.  $^1\text{H}$  NMR (400 MHz,  $\text{CD}_3\text{CN}$ ):  $\delta_{\text{H}} = 8.47$  (2×d, 4H,  $^3J_{\text{Hd/Hi}} = 8.1$  Hz,  $\text{H}_e/\text{H}_h$ ), 8.06–7.99 (m, 4H,  $\text{H}_d/\text{H}_i$ ), 7.97 (d, 2H,  $^4J_{\text{H5}} = 2.5$  Hz,  $\text{H}_3$ ), 7.81/7.71 (2×d, 4H,  $^3J_{\text{Hc/Hj}} = 5.5$  Hz,  $\text{H}_b/\text{H}_k$ ), 7.43–7.39/7.37–7.33 (2×m, 4H,  $\text{H}_c/\text{H}_j$ ), 7.41 (d, 2H,  $^3J_{\text{H5}} = 6.5$  Hz,  $\text{H}_6$ ), 6.90 (dd, 2H,  $^3J_{\text{H6}} = 6.5$  Hz,  $^4J_{\text{H3}} = 2.5$  Hz,  $\text{H}_5$ ), 4.18 (t, 4H,  $^3J_{\text{H8}} = 6.5$  Hz,  $\text{H}_7$ ), 2.85 (t, 4H,  $^3J_{\text{H11}} = 7.3$  Hz,  $\text{H}_{12}$ ), 2.27 (s, 6H,  $\text{H}_{15}$ ), 1.84–1.76 (m, 4H,  $\text{H}_8$ ), 1.61–1.53 (m, 4H,  $\text{H}_{11}$ ), 1.52–1.38 (m, 8H,  $\text{H}_9/\text{H}_{10}$ ).  $^{13}\text{C}$  NMR (100 MHz,  $\text{CDCl}_3$ ):  $\delta_{\text{C}} = 153.0$  ( $\text{C}_6$ ), 152.7/152.5 ( $\text{C}_b/\text{C}_k$ ), 138.3 ( $\text{C}_d/\text{C}_i$ ), 128.5 ( $\text{C}_c/\text{C}_j$ ), 125.1 ( $\text{C}_e/\text{C}_h$ ), 115.1 ( $\text{C}_5$ ), 112.3 ( $\text{C}_3$ ), 70.6 ( $\text{C}_7$ ), 30.8 ( $\text{C}_{15}$ ), 30.2 ( $\text{C}_{11}$ ), 29.4 ( $\text{C}_{12}$ ), 29.1 ( $\text{C}_8$ ), 28.9/25.8 ( $\text{C}_9/\text{C}_{10}$ ). TOF ES-MS(+):  $m/z$  1063.2  $[\text{M}-\text{PF}_6]^+$ , 459.1  $[\text{M}-2\text{PF}_6]^{2+}$ . Anal. Calc. for  $\text{C}_{46}\text{H}_{52}\text{F}_{12}\text{N}_6\text{O}_4\text{P}_2\text{RuS}_2$  : C 45.73, H 4.34, N 6.96. Found: C 45.66, H 4.17, N 7.03. IR  $\nu_{\text{max}}$  ( $\text{cm}^{-1}$ ): 2930 (C–H), 2857 (C–H), 1683 (C=O), 1611 (C– $\text{C}_{\text{ring}}/\text{C}-\text{N}_{\text{ring}}$ ), 1556, 1492, 1464, 1444, 1396, 1339, 1278, 1222, 1120. UV-VIS ( $\text{CH}_3\text{CN}$ )  $\lambda_{\text{max}}$  [nm] (log  $\epsilon$ ): 462 (4.1), 436 (sh), 289 (4.8). Emission ( $\text{CH}_3\text{CN}$ ,  $\lambda_{\text{exc}} = 450$  nm)  $\lambda_{\text{max}}$  [nm] = 645.

*Synthesis of RuSH:*

NH<sub>4</sub>OH (aq) solution (50  $\mu$ l, 30 % wt) was added to **RuSAC** (100  $\mu$ l, 1.52 mM in CH<sub>3</sub>CN, 152 nmol) and stirred for 10 min in a sealed vial to give **RuSH** *in situ*, directly prior to titration into the colloid. TOF LD-MS(+):  $m/z$  829.7 [M-2PF<sub>6</sub>]<sup>+</sup>.

*Synthesis of 13 nm citrate gold nanoparticles*

Synthesis according to Grabar *et al.* (preparation 1).<sup>5</sup> All glassware was washed with aqua regia (HCl:HNO<sub>3</sub>, 3:1), rinsed with deionised water and dried in an oven overnight. HAuCl<sub>4</sub>.3H<sub>2</sub>O (49.85 % Au) (0.0988 g, 0.2501 mmol) was dissolved in deionised water (250 mL), and the solution was heated to reflux, with vigorous stirring. A solution of trisodium citrate (0.2858 g, 0.9718 mmol) in deionised water (25 mL water, 38.87 mM) was added rapidly to the vortex. The yellow solution slowly darkened to a deep burgundy colour, and was kept at reflux for 10 min. The solution was cooled to room temperature, with stirring for a further 15 mins to yield 13 nm gold nanoparticles. Colloids were kept at room temperature and in the dark. UV-VIS (H<sub>2</sub>O)  $\lambda_{\max}$  [nm]: 520 (SPR), 260. Diameter = 13 $\pm$ 1 nm (DLS

number distribution), =  $29 \pm 12$  nm (86 %),  $998 \pm 624$  nm (14 %) (DLS intensity distribution). Zeta potential =  $-40 \pm 5$  mV (2 nM in deionised water).

#### *Synthesis of Ru-T20•AuNP13:*

13 nm citrate gold nanoparticles (80  $\mu$ L) were diluted in deionised water (920  $\mu$ L), and TWEEN® 20 (10  $\mu$ L, 125 mM) was added to give a final nanoparticle concentration of 0.7 nM, and a final surfactant concentration of 1.2 mM. The solution was stirred for 20 min and the  $\lambda_{\max}$  of the SPR was monitored by UV-Vis absorption spectroscopy. **RuSH** complex (2.5  $\mu$ L, 3.5 mM, (made *in situ*,  $\text{NH}_4\text{OH}(\text{aq})$  30 % w/w:  $\text{CH}_3\text{CN}$  (1:1) solution)) was added into the nanoparticle/surfactant solution, whilst monitoring the coating process by UV-Vis absorption spectroscopy. The particles were isolated by size-exclusion chromatography on Sephadex® G-25, eluting with water, to give a final nanoparticle concentration of 0.3 nM (estimated by UV-Vis absorption spectroscopy). UV-Vis ( $\text{H}_2\text{O}$ )  $\lambda_{\max}$  [nm] = 525 (SPR). Diameter =  $26 \pm 19$  nm (DLS number distribution), =  $195 \pm 91$  nm (99%),  $28 \pm 6$  nm (1%), (DLS intensity distribution), zeta potential =  $-24 \pm 3$  mV (isolated, 0.3 nM in deionised water diluent). Emission ( $\text{H}_2\text{O}$ ,  $\lambda_{\text{exc}} = 450$  nm)  $\lambda_{\max}$  [nm] = 655. Lifetime ( $\text{H}_2\text{O}$ ,  $\lambda_{\text{exc}} = 445$  nm,  $\lambda_{\text{em}} = 630$  nm) = 305 ns (aerated), = 375 ns (degassed). ICP-OES Au:Ru atomic ratio = 72:1.

#### *Synthesis of Ru-Z•AuNP13:*

Zonyl® 7950 ( $\text{CH}_2\text{-C}(\text{CH}_3)\text{COOC}_2\text{H}_4(\text{CF}_2)_n\text{F}$ , MW *ca.* 500, 1  $\mu$ L, 1.15 g  $\text{mL}^{-1}$ ) was added to 13 nm citrate gold nanoparticles (1 mL, 9 nM nanoparticles, zeta potential at 2 nM in deionised water =  $-40 \pm 5$  mV, diameter =  $13 \pm 4$  nm (DLS number distribution), =  $29 \pm 12$  nm (86 %),  $998 \pm 624$  nm (14 %) (DLS intensity distribution)) to give fluorosurfactant coated nanoparticles (9 nM nanoparticles), with a final fluorosurfactant concentration of *ca.* 1 mM. (Isolated **Z•AuNP13**, by three rounds of centrifugation, decantation of the supernatant and resuspension of the pellet have a zeta potential of  $-61 \pm 4$  mV (2 nM in deionised water) and

diameter of  $20 \pm 2$  nm (DLS number distribution), and of  $32 \pm 15$  nm (DLS intensity distribution)). A solution of **RuSH** (20  $\mu$ L, 3.5 mM, (made *in situ*,  $\text{NH}_4\text{OH}(\text{aq})$  30 % *w/w*: $\text{CH}_3\text{CN}$  (1:1) solution)) was added to the fluorosurfactant / nanoparticle mixture (not isolated), and was stirred for 20 min. The particles were centrifuged at 12,000 g for 15 min, and the supernatant was decanted from each pellet to remove unbound material. The nanoparticles were resuspended in deionised water, and this was repeated twice to give **Ru-Z•AuNP13**. UV-Vis ( $\text{H}_2\text{O}$ )  $\lambda_{\text{max}}$  [nm] = 522 (SPR). Diameter =  $18 \pm 5$  nm (DLS number distribution), =  $30 \pm 10$  nm (27%),  $166 \pm 86$  nm (27%), (DLS intensity distribution), zeta potential =  $-48 \pm 2$  mV (isolated, 2 nM in deionised water diluent). Emission ( $\text{H}_2\text{O}$ ,  $\lambda_{\text{exc}} = 450$  nm)  $\lambda_{\text{max}}$  [nm] = 640. Lifetime ( $\text{H}_2\text{O}$ ,  $\lambda_{\text{exc}} = 445$  nm,  $\lambda_{\text{em}} = 630$  nm) = 340 ns (aerated), = 690 ns (degassed).  $\Phi$  ( $\text{H}_2\text{O}$ ,  $\lambda_{\text{exc}} = 355$  nm) = 4% (aerated). ICP-OES Au:Ru atomic ratio = 63:1.

### 2.12.2 Staining of Nanoparticles for TEM

#### *Negative staining of nanoparticles with PTA*

For negative staining, nanoparticles (50  $\mu$ L, 9 nM, aqueous) were added to a 200-mesh formvar-coated copper TEM grid. After 20 min the solution was wicked off the grid with filter paper, taking care not to remove all the liquid, and aqueous PTA solution (50  $\mu$ L, 1% *w/v* solution, solid PTA purchased from Sigma Aldrich) was added to the grid. The solution was wicked off the grid with filter paper, leaving a very thin layer of stain on the grid to air-dry.

#### *Positive staining of nanoparticles with PTA*

Nanoparticle samples were positively stained by centrifuging the nanoparticles (1 mL, 9 nM, aqueous) at 12000 g for 15 min, decanting the supernatant, and redispersing in aqueous PTA solution (total volume of 1 mL, 1% *w/v* solution). After 24 hr the colloidal dispersion was centrifuged at 12000 g for 15 min, the supernatant was decanted, and the particles were

redispersed in deionised water (total volume 1 mL). The nanoparticle solution (50  $\mu\text{L}$ , 9 nM) was added to a TEM grid, and after 20 min the solution was wicked off the grid with filter paper. The grid was washed with water and left to air-dry.

### 2.12.3 X-ray Photoelectron Spectroscopy

Gold nanoparticles (100  $\mu\text{L}$ , 9 nM) were air-dried on 1 cm  $\times$  1 cm silicon wafers. The x-ray photoemission spectroscopy (XPS) data were collected at the Science City Photoemission Facility, School of Physics, University of Warwick, with the help of Dr Marc Walker. More details of which are available at <http://go.warwick.ac.uk/XPS>. The samples investigated in this study were mounted on Omicron sample plates using electrically conductive carbon tape and loaded in to the fast-entry chamber. Once a pressure of less than  $1 \times 10^{-7}$  had been achieved (approx. 1 hour), the samples were transferred to a 12-stage storage carousel, located between the preparation and main analysis chambers, for storage at pressures of less than  $2 \times 10^{-10}$  mbar.

XPS measurements were conducted in the main analysis chamber (base pressure  $2 \times 10^{-11}$  mbar), with the sample being illuminated using an XM1000 monochromatic Al  $k_{\alpha}$  x-ray source (Omicron Nanotechnology). The measurements were conducted at room temperature and at a take-off angle of  $90^{\circ}$ . The photoelectrons were detected using a Sphera electron analyser (Omicron Nanotechnology), with the core levels recorded using a pass energy of 10 eV (resolution approx. 0.47 eV). The data were analysed by Dr Marc Walker, using the CasaXPS package, using Shirley backgrounds, mixed Gaussian-Lorentzian (Voigt) lineshapes and asymmetry parameters where appropriate. All binding energies were calibrated to the C 1s peak at 284.6 eV.<sup>102</sup>

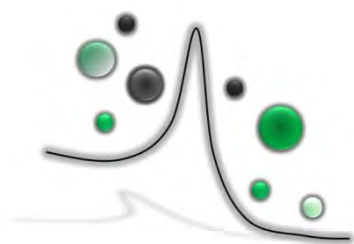
## 2.13 Chapter Two References

- (1) Rogers, N. J.; Pikramenou, Z. *Patent* **2013**, WO/2013/004989.
- (2) Eustis, S.; El-Sayed, M. A. *Chem. Soc. Rev.* **2006**, *35*, 209.
- (3) Haynes, C. L.; Van Duyne, R. P. *J. Phys. Chem. B* **2001**, *105*, 5599.
- (4) Turkevitch, J.; Stephenson, P. C.; Hillier, J. *Discuss. Faraday Soc.* **1951**, *11*, 55.
- (5) Grabar, K. C.; Freeman, R. G.; Hommer, M. B.; Natan, M. J. *Anal. Chem.* **1995**, *67*, 735.
- (6) Polte, J.; Ahner, T. T.; Delissen, F.; Sokolov, S.; Emmerling, F.; Thünemann, A. F.; Kraehnert, R. *J. Am. Chem. Soc.* **2010**, *132*, 1296.
- (7) Ojea-Jiménez, I.; Campanera, J. M. *J. Phys. Chem. C* **2012**, *116*, 23682.
- (8) Frens, G. *Nature Phys. Sci.* **1973**, *241*, 20.
- (9) Perrault, S. D.; Chan, W. C. W. *J. Am. Chem. Soc.* **2010**, *132*, 11824.
- (10) Ziegler, C.; Eychmueller, A. *J. Phys. Chem. C* **2011**, *115*, 4502.
- (11) Xu, X.-H. N.; Huang, S.; Brownlow, W.; Salaita, K.; Jeffers, R. B. *J. Phys. Chem. B* **2004**, *108*, 15543.
- (12) Brust, M.; Walker, M.; Bethell, D.; Schiffrin, D. J.; Whyman, R. *Chem. Commun.* **1994**, 801.
- (13) Bain, C. D.; Troughton, E. B.; Tao, Y. T.; Evall, J.; Whitesides, G. M.; Nuzzo, R. G. *J. Am. Chem. Soc.* **1989**, *111*, 321.
- (14) Love, J. C.; Estroff, L. A.; Kriebel, J. K.; Nuzzo, R. G.; Whitesides, G. M. *Chem. Rev.* **2005**, *105*, 1103.
- (15) Templeton, A. C.; Wuelfing, M. P.; Murray, R. W. *Acc. Chem. Res.* **2000**, *33*, 27.
- (16) Baggaley, E.; Weinstein, J. A.; Williams, J. A. G. *Coord. Chem. Rev.* **2012**, *256*, 1762.
- (17) Lo, K. K.-W.; Choi, A. W.-T.; Law, W. H.-T. *Dalton Trans.* **2012**, *41*, 6021.
- (18) Komor, A. C.; Barton, J. K. *Chem. Commun.* **2013**, *49*, 3617.
- (19) Frasconi, M.; Liu, Z.; Lei, J.; Wu, Y.; Strelakova, E.; Malin, D.; Ambrogio, M. W.; Chen, X.; Botros, Y. Y.; Cryns, V. L.; Sauvage, J.-P.; Stoddart, J. F. *J. Am. Chem. Soc.* **2013**, *135*, 11603.
- (20) Fernandez-Moreira, V.; Thorp-Greenwood, F. L.; Coogan, M. P. *Chem. Commun.* **2010**, *46*, 186.
- (21) Thorp-Greenwood, F. L.; Balasingham, R. G.; Coogan, M. P. *J. Organomet. Chem.* **2012**, *714*.
- (22) Juris, A.; Balzani, V.; Barigelletti, F.; Campagna, S.; Belser, P.; Von Zelewsky, A. *Coord. Chem. Rev.* **1988**, *84*, 85.
- (23) Hipps, K. W.; Crosby, G. A. *J. Am. Chem. Soc.* **1975**, *97*, 7042.
- (24) Damrauer, N. H.; Cerullo, G.; Yeh, A.; Boussie, T. R.; Shank, C. V.; McCusker, J. K. *Science* **1997**, *275*, 54.
- (25) Henry, W.; Coates, C. G.; Brady, C.; Ronayne, K. L.; Matousek, P.; Towrie, M.; Botchway, S. W.; Parker, A. W.; Vos, J. G.; Browne, W. R.; McGarvey, J. J. *J. Phys. Chem. A* **2008**, *112*, 4537.
- (26) Wallin, S.; Davidsson, J.; Modin, J.; Hammarström, L. *J. Phys. Chem. A* **2005**, *109*, 4697.
- (27) Ruggi, A.; van Leeuwen, F. W. B.; Velders, A. H. *Coord. Chem. Rev.* **2011**, *255*, 2542.

- (28) Zhong, W.; Urayama, P.; Mycek, M.-A. *J. Phys. D: Appl. Phys.* **2003**, *36*, 1689.
- (29) Thomas, K. G.; Kamat, P. V. *Acc. Chem. Res.* **2003**, *36*, 888.
- (30) Wilton-Ely, J. D. E. T. *J. Chem. Soc., Dalton Trans.* **2008**, 25.
- (31) Huang, T.; Murray, R. W. *Langmuir* **2002**, *18*, 7077.
- (32) Cheng, P. P. H.; Silvester, D.; Wang, G.; Kalyuzhny, G.; Douglas, A.; Murray, R. W. *J. Phys. Chem. B* **2006**, *110*, 4637.
- (33) Song, Y.; Murray, R. W. *J. Am. Chem. Soc.* **2002**, *124*, 7096.
- (34) Woehrle, G. H.; Brown, L. O.; Hutchison, J. E. *J. Am. Chem. Soc.* **2005**, *127*, 2172.
- (35) Brust, M.; Fink, J.; Bethell, D.; Schiffrin, D. J.; Kiely, C. *J. Chem. Soc., Chem. Commun.* **1995**, 1655.
- (36) Hostetler, M. J.; Green, S. J.; Stokes, J. J.; Murray, R. W. *J. Am. Chem. Soc.* **1996**, *118*, 4212.
- (37) Hostetler, M. J.; Templeton, A. C.; Murray, R. W. *Langmuir* **1999**, *15*, 3782.
- (38) Kassam, A.; Bremner, G.; Clark, B.; Ulibarri, G.; Lennox, R. B. *J. Am. Chem. Soc.* **2006**, *128*, 3476.
- (39) Pramod, P.; Sudeep, P. K.; Thomas, K. G.; Kamat, P. V. *J. Phys. Chem. B* **2006**, *110*, 20737.
- (40) Jebb, M.; Sudeep, P. K.; Pramod, P.; Thomas, K. G.; Kamat, P. V. *J. Phys. Chem. B* **2007**, *111*, 6839.
- (41) Elmes, R. B. P.; Orange, K. N.; Cloonan, S. M.; Williams, D. C.; Gunnlaugsson, T. *J. Am. Chem. Soc.* **2011**, *133*, 15862.
- (42) Hallett, A. J.; Christian, P.; Jones, J. E.; Pope, S. J. A. *Chem. Commun.* **2009**, 4278.
- (43) Lewis, D. J.; Day, T. M.; MacPherson, J. V.; Pikramenou, Z. *Chem. Commun.* **2006**, 1433.
- (44) Fendler, J. H. *Chem. Mater.* **2001**, *13*, 3196.
- (45) Lewis, D. J.; Bruce, C.; Bohic, S.; Cloetens, P.; Hammond, S. P.; Arbon, D.; Blair-Reid, S.; Pikramenou, Z.; Kysela, B. *Nanomed.* **2010**, *5*, 1547.
- (46) Mayer, C. R.; Dumas, E.; Michel, A.; Sécheresse, F. *Chem. Commun.* **2006**, 4183.
- (47) Mayer, C. R.; Dumas, E.; Sécheresse, F. *Chem. Commun.* **2005**, 345.
- (48) Mayer, C. R.; Dumas, E.; Miomandre, F.; Meallet-Renault, R.; Warmount, F.; Vigneron, J.; Pansu, R.; Etcheberry, A.; Sécheresse, F. *New J. Chem.* **2006**, *30*, 1628.
- (49) Vickers, M. S.; Cookson, J.; Beer, P. D.; Bishop, P. T.; Thiebaut, B. *J. Mater. Chem.* **2006**, *16*, 209.
- (50) Yu, Y.; Zhou, M.; Cui, H. *J. Mater. Chem.* **2011**, *21*, 12622.
- (51) Labande, A.; Ruiz, J.; Astruc, D. *J. Am. Chem. Soc.* **2002**, *124*, 1782.
- (52) Bartz, M.; Küther, J.; Seshadri, R.; Tremel, W. *Angew. Chem., Int. Ed.* **1998**, *37*, 2466.
- (53) Wang, S.; Sim, W.-S. *Langmuir* **2006**, *22*, 7861.
- (54) Knight, E. R.; Leung, N. H.; Thompson, A. L.; Hogarth, G.; Wilton-Ely, J. D. E. T. *Inorg. Chem.* **2009**, *48*, 3866.
- (55) Naeem, S.; Ribes, A.; White, A. J. P.; Haque, M. N.; Holt, K. B.; Wilton-Ely, J. D. E. T. *Inorg. Chem.* **2013**, *52*, 4700.

- (56) Battistini, G.; Cozzi, P. G.; Jalkanen, J.-P.; Montalti, M.; Prodi, L.; Zaccheroni, N.; Zerbetto, F. *ACS Nano* **2007**, *2*, 77.
- (57) Cannone, F.; Chirico, G.; Bizzarri, A. R.; Cannistraro, S. *J. Phys. Chem. B* **2006**, *110*, 16491.
- (58) Dulkeith, E.; Morteani, A. C.; Niedereichholz, T.; Klar, T. A.; Feldmann, J.; Levi, S. A.; van Veggel, F. C. J. M.; Reinhoudt, D. N.; Möller, M.; Gittins, D. I. *Phys. Rev. Lett.* **2002**, *89*, 203002.
- (59) Kang, K. A.; Wang, J.; Jasinki, J. B.; Achilefu, S. *J. Nanobiotechnol.* **2011**, *9*, 16.
- (60) Zedler, L.; Theil, F.; Csaki, A.; Fritzsche, W.; Rau, S.; Schmitt, M.; Popp, J.; Dietzek, B. *R. Soc. Chem. Adv.* **2012**, *2*, 4463.
- (61) Davies, A.; Lewis, D. J.; Watson, S. P.; Thomas, S. G.; Pikramenou, Z. *Proc. Nat. Acad. Sci. U.S.A.* **2012**, *109*, 1862.
- (62) Nunes, F. S.; Bonifacio, L. D. S.; Araki, K.; Toma, H. E. *Inorg. Chem.* **2006**, *45*, 94.
- (63) Li, M.-J.; Liu, X.; Nie, M.-J.; Wu, Z.-Z.; Yi, C.-Q.; Chen, G.-N.; Yam, V. W.-W. *Organometallics* **2012**, *31*, 4459.
- (64) Craig, G. E.; Brown, S. D.; Lamprou, D. A.; Graham, D.; Wheate, N. J. *Inorg. Chem.* **2012**, *51*, 3490.
- (65) Lin, S.-Y.; Tsai, Y.-T.; Chen, C.-C.; Lin, C.-M.; Chen, C.-h. *J. Phys. Chem. B* **2004**, *108*, 2134.
- (66) Aslan, K.; Perez-Luna, V. H. *Langmuir* **2002**, *18*, 6059.
- (67) Zhao, Y.; Wang, Z.; Zhang, W.; Jiang, X. *Nanoscale* **2010**, *2*, 2114.
- (68) Duy, J.; Connell, L.; Eck, W.; Collins, S.; Smith, R. *J. Nanopart. Res.* **2010**, *12*, 2363.
- (69) Ye, Y.; Liu, H.; Yang, L.; Liu, J. *Nanoscale* **2012**, *4*, 6442.
- (70) Nativo, P.; Prior, I. A.; Brust, M. *ACS Nano* **2008**, *2*, 1639.
- (71) Tiwari, P.; Vig, K.; Dennis, V.; Singh, S. *Nanomaterials* **2011**, *1*, 31.
- (72) Yuan, H.; Fales, A. M.; Vo-Dinh, T. *J. Am. Chem. Soc.* **2012**, *134*, 11358.
- (73) Lu, C.; Zu, Y.; Yam, V. W.-W. *Anal. Chem.* **2007**, *79*, 666.
- (74) Huang, C.-C.; Tseng, W.-L. *Anal. Chem.* **2008**, *80*, 6345.
- (75) Farabi, S., PhD Thesis, University of Birmingham, 2012.
- (76) Rogers, N. J.; Claire, S.; Harris, R. M.; Farabi, S.; Zikeli, G.; Styles, I. B.; Hodges, N. J.; Pikramenou, Z. *Chem. Commun.* **2014**, *50*, 617.
- (77) Bertoncello, P.; Kefalas, E. T.; Pikramenou, Z.; Unwin, P. R.; Forster, R. J. *J. Phys. Chem. B* **2006**, *110*, 10063.
- (78) Ham, J. E.; Durham, B. *J. Am. Soc. Mass Spectrom.* **2003**, *14*, 393.
- (79) Durham, B.; Caspar, J. V.; Nagle, J. K.; Meyer, T. J. *J. Am. Chem. Soc.* **1982**, *104*, 4803.
- (80) Calvert, J. M.; Caspar, J. V.; Binstead, R. A.; Westmoreland, T. D.; Meyer, T. J. *J. Am. Chem. Soc.* **1982**, *104*, 6620.
- (81) Nakamaru, K. *Bull. Chem. Soc. Jpn.* **1982**, *55*, 2697.
- (82) Harriman, A. *J. Chem. Soc., Chem. Commun.* **1977**, 777.

- (83) Vögtle, F.; Plevoets, M.; Nieger, M.; Azzellini, G. C.; Credi, A.; De Cola, L.; De Marchis, V.; Venturi, M.; Balzani, V. *J. Am. Chem. Soc.* **1999**, *121*, 6290.
- (84) Savage, A. C.; Pikramenou, Z. *Chem. Commun.* **2011**, *47*, 6431.
- (85) Goldberg, W. I. *Am. J. Phys.* **1999**, *67*, 1152.
- (86) Mie, G. *Ann. Phys. (Berlin)* **1908**, *25*, 377.
- (87) Quinten, M.; Kreibitz, U. *Surf. Sci.* **1986**, *172*, 557.
- (88) Feng, J.-J.; Huang, H.; Zhou, D.-L.; Cai, L.-Y.; Tu, Q.-Q.; Wang, A.-J. *J. Mat. Chem. C* **2013**, *1*, 4720.
- (89) Lewis, D. J.; Dore, V.; Rogers, N. J.; Mole, T. K.; Nash, G. B.; Angeli, P.; Pikramenou, Z. *Langmuir* **2013**, *29*, 14701.
- (90) Lévy, R.; Thanh, N. T. K.; Doty, R. C.; Hussain, I.; Nichols, R. J.; Schiffrin, D. J.; Brust, M.; Fernig, D. G. *J. Am. Chem. Soc.* **2004**, *126*, 10076.
- (91) Johnston, R. L. *Atomic and Molecular Clusters*; Taylor and Francis: London, 2002.
- (92) Jackson, C. L.; Chanzy, H. D.; Booy, F. P.; Drake, B. J.; Tomalia, D. A.; Bauer, B. J.; Amis, E. J. *Macromolecules* **1998**, *31*, 6259.
- (93) Li, K.; Zhang, Z.-P.; Luo, M.; Yu, X.; Han, Y.; Wei, H.-P.; Cui, Z.-Q.; Zhang, X.-E. *Nanoscale* **2012**, *4*, 188.
- (94) Watson, M. L. *J. Biophys. Biochem. Cytol.* **1958**, *4*, 475.
- (95) Moulder, J.; Stickle, W. F.; Sobol, P. E. *Handbook of X-ray Photoelectron Spectroscopy*; Perkin Elmer Corporation, 1992.
- (96) Abis, L.; Armelao, L.; Belli Dell'Amico, D.; Calderazzo, F.; Garbassi, F.; Merigo, A.; Quadrelli, E. A. *J. Chem. Soc., Dalton Trans.* **2001**, 2704.
- (97) McNeillie, A.; Brown, D. H.; Smith, W. E.; Gibson, M.; Watson, L. *J. Chem. Soc., Dalton Trans.* **1980**, 767.
- (98) Chen, C.-T.; Chen, W.-J.; Liu, C.-Z.; Chang, L.-Y.; Chen, Y.-C. *Chem. Commun.* **2009**, 7515.
- (99) Zhang, P.; Sham, T. K. *Phys. Rev. Lett.* **2003**, *90*, 245502.
- (100) Agnes, C.; Arnault, J.-C.; Omnes, F.; Jusselme, B.; Billon, M.; Bidan, G.; Mailley, P. *Phys. Chem. Chem. Phys.* **2009**, *11*, 11647.
- (101) Hong, Y.-R.; Gorman, C. B. *J. Org. Chem.* **2003**, *68*, 9019.
- (102) Lide, D. R. *CRC Handbook of Chemistry and Physics, 94th Edition*; Taylor and Francis, London, 2013-2014.



---

# Chapter Three

---

Cellular Imaging

Applications of 13 nm  
and 100 nm Luminescent

Ru(II)-labelled Gold

Nanoparticles

### 3.1 Introduction

Optical imaging at the nanoscale can lead to breakthroughs in the biomolecular sciences, providing information on the monitoring of specific cellular processes, such as protein trafficking and the targeting of cell organelles, with high spatial resolution.<sup>1-5</sup> Specifically, luminescence imaging has many advantages over colorimetric optical imaging, including higher resolution and sensitivity, and several advantages over electron imaging, such as significantly faster acquisition times and live cell imaging. This is discussed in Chapter One. Noble metal nanoparticles and quantum dots provide good candidates as optical nanoscale probes for detection by different imaging modalities, and have the potential to target specific biomolecules, tissues or diseases with modifications of their outer shell properties.<sup>6-9</sup>

Gold nanoparticles offer an inert scaffold onto which one can assemble a variety of functional probes, using very simple S–Au self-assembly, and their high surface area: volume ratio is extremely attractive for this.<sup>3</sup> In general, gold nanoparticles are deemed to be relatively biocompatible, compared with many inorganic nanoparticles,<sup>1,10</sup> and thus lend themselves to a host of biomedical applications, including imaging,<sup>10,11</sup> chemical sensing<sup>12</sup> and theranostic nanomedicine.<sup>13</sup> In parallel with the interest in biomedical applications, a growing number of questions are being raised concerning the effects of nanoparticles on human health and the environment, and thus the toxicology of nanoparticles is becoming more important with the advances and exposure to nanotechnology.<sup>14,15</sup> Therefore it is incredibly important to investigate the complex processes that govern the cellular uptake and fate of given nanomaterials, and thus there are several studies of gold nanoparticle uptake in tissues and tumours, both *in vivo*<sup>16,17</sup> and *in vitro*.<sup>3,18,19</sup>

The cellular uptake of nanoparticles is affected by both particle size and surface functionality,<sup>3,20,21</sup> and the importance of the size of nanoparticles and quantum dots has been highlighted for their uptake in tumour tissues,<sup>22,23</sup> as well as in cell lines.<sup>24,25</sup>

Chan and co-workers have investigated the effect of the size of citrate-stabilised gold nanoparticles on cellular uptake in a HeLa (human cervical cancer) cell line in the 14–74 nm size range.<sup>24</sup> Cells were incubated with particles, washed, and the gold uptake was analysed by inductively-coupled plasma atomic absorption spectroscopy (ICP–AES), at various time points. It was found that the uptake (number of nanoparticles per cell) was greatest for 50 nm gold nanoparticles, and that the uptake of all sizes saturated after *ca.* 6 hr. The mechanism was speculated to be via endocytosis, in which the particles are engulfed by the cell and localised in a vesicle of extracellular fluid, see schematic in Figure 3.1, below.<sup>26</sup>

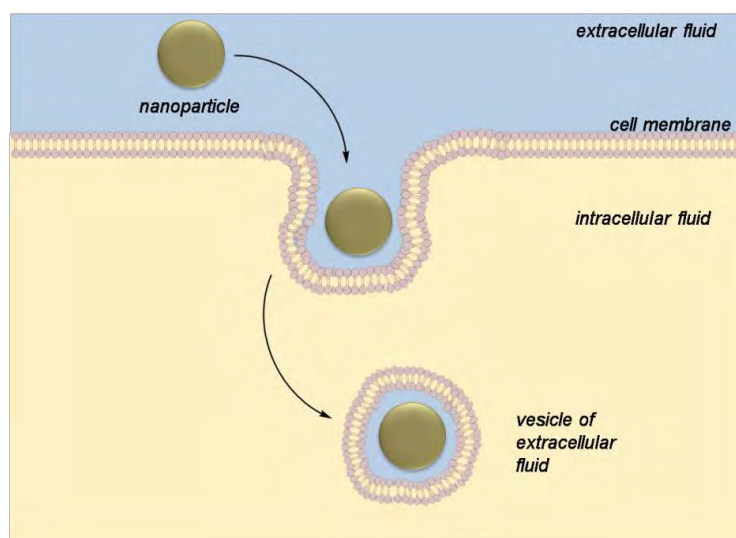


**Figure 3.1** Schematic representation of the cellular endocytic uptake mechanism of nanoparticles.

The group has also investigated the size-dependence of uptake of transferrin-coated gold nanoparticles made from citrate-stabilised precursors (transferrin is an iron-binding protein found in the blood).<sup>27</sup> Mammalian cells (fibroblasts, HeLa cells and SNP19 human brain

tumour cells) were incubated with 14–100 nm transferrin-coated gold nanoparticles, and again the 50 nm particles were found to enter all mammalian cells tested faster than the 14 nm and 100 nm particles. The group postulate that the 50 nm particles are the optimum size for the cell membrane to wrap around the particle and enclose it in a vesicle in the cells tested.<sup>27</sup> Many further investigations into the cellular uptake of functionalised gold nanoparticles made from citrate-stabilised precursors, have been performed within the literature; unsurprisingly the surface-functionalisation of the nanoparticles can drastically alter both the uptake and the cellular response,<sup>21,28</sup> and many such studies have been reviewed by Mirkin,<sup>29</sup> and more recently by Khlebstov.<sup>30</sup>

### 3.1.1 Chapter Outline

In this chapter, luminescent gold nanoparticles coated with the **RuSH** complex, as developed in Chapter Two, (using the optimized coating method mediated with the fluorinated surfactant, Zonyl® 7950), are used to investigate the cellular uptake in A549 human lung cancer cells. The advantage of coating gold nanoparticles with a luminescent complex, rather than using other luminescent nanoprobes such as quantum dots, is that the size of the gold nanoparticle can be tuned independently of its luminescent properties. In order to investigate whether the size of the gold nanoparticle core has an effect on the photophysical properties of the labelling ruthenium(II) complex, the studies of 13 nm luminescent gold nanoparticles in Chapter Two, i.e. **Ru-Z•AuNP13**, have been developed further by growing larger nanoparticles. 100 nm gold nanoparticles have been coated with **RuSH**, and the properties of the resultant **Ru-Z•AuNP00** are compared to **Ru-Z•AuNP13**. Larger particles open up the prospect of *single* nanoparticle detection by optical techniques, as each individual particle should exhibit a stronger luminescence intensity, per particle, due to the greater number of surface-grafted lumiphores.

In order to assess the potential of such nanoparticles in biological imaging applications, the uptake of both **Ru-Z•AuNP13** and **Ru-Z•AuNP100** in A549 cells has been studied by confocal luminescence microscopy and electron microscopy to determine cellular localisation. In addition to this, gross cellular labelling has been studied by flow cytometry, and toxicology studies have been performed. The findings in this chapter have been recently published by the author.<sup>31</sup>

The synthesis of **RuSH**, which is made *in situ* from **RuSAC**, is described in Chapter Two (Section 2.2), and the structures of the **RuSAC** and **RuSH** complexes are shown in Figure 3.2, and schematics of **Ru-Z•AuNP13** and **Ru-Z•AuNP100** are presented in 3.3.

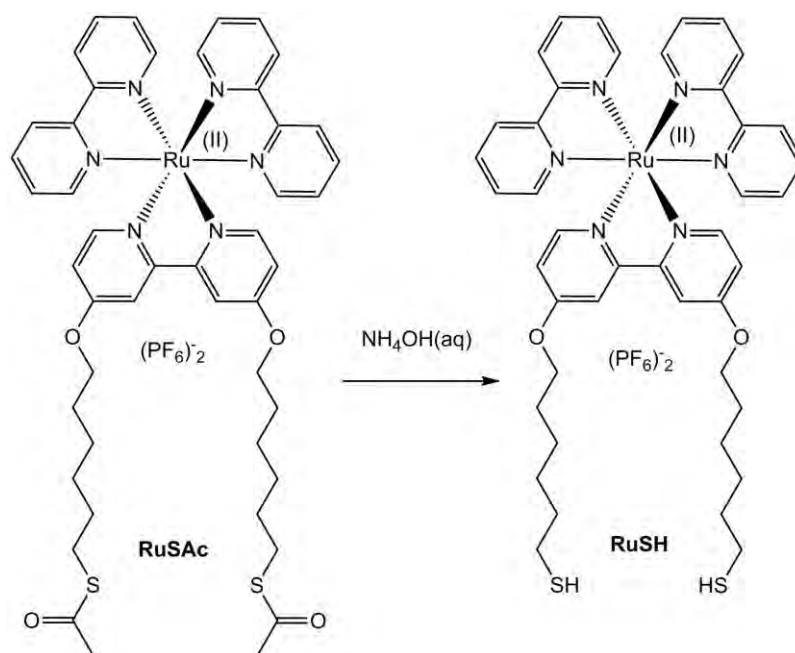


**Figure 3.2** Structures of **RuSAC** and **RuSH** complexes discussed in this chapter.

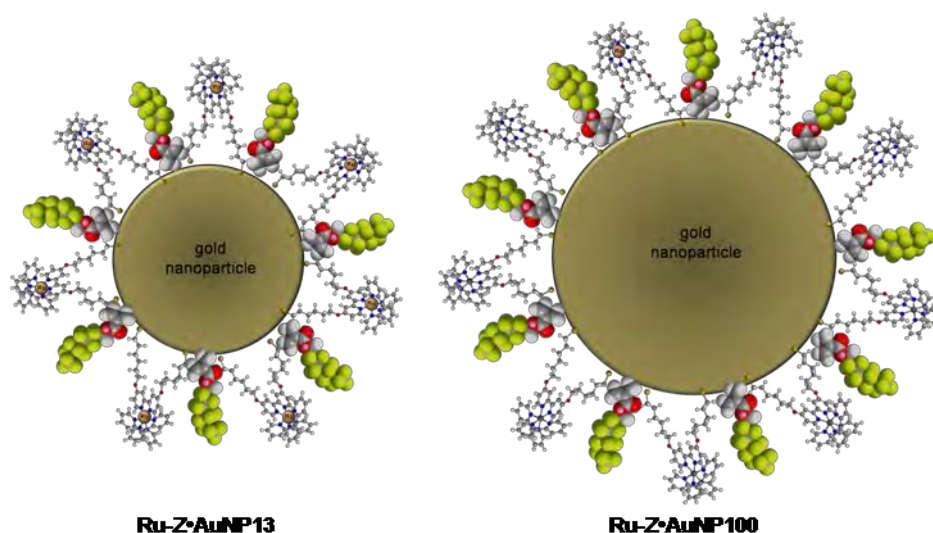


**Figure 3.3** Schematics of *Ru-Z•AuNP13* and *Ru-Z•AuNP100* discussed in this chapter.

### 3.2 Seed-mediated Growth of 100 nm Gold Nanoparticles

There are several reports in the literature of synthetic routes towards large ( $> 20$  nm) gold nanoparticles, including one-pot reactions<sup>32</sup> and seed-mediated processes.<sup>33-36</sup> In general, the former produce low concentration, highly polydisperse gold nanoparticles, with little shape control, whereas seed-mediated growth offers more control over shape and size.<sup>36</sup> Cetyl trimethylammonium bromide (CTAB)-stabilised nanoparticles have been grown from seeds by Liz-Marzán and co-workers,<sup>33</sup> with a post-synthetic cleanup step to obtain spherical particles only. Another popular synthesis, proposed by Perrault *et al.*<sup>34</sup> uses hydroquinone as a reducing agent to produce nanoparticles in the 50–200 nm range, but these particles are still relatively polydisperse, and the benzoquinone oxidation product is toxic. Natan's group have also used hydroxylamine as a reducing agent,<sup>36</sup> but again shape-control is problematic. In this chapter, 100 nm aqueous gold nanoparticles have been synthesised in a seeded-growth method, using a synthesis adapted from a recent publication by Ziegler and Eychmüller;<sup>37</sup> this simple synthetic process requires no post-synthesis cleanup steps, and uses nontoxic, biocompatible reducing agents which can easily be replaced by thiol-appended groups to

allow surface functionalisation. The nanoparticles were prepared in a three step growth process,<sup>31</sup> starting with 13 nm citrate-stabilised gold nanoparticles, which were synthesised according to the standard citrate reduction, described in Chapter Two, Section 2.3.<sup>38</sup> In brief,  $\text{HAuCl}_4$  is added to nanoparticle seeds, and a mixture of sodium citrate and ascorbic acid is slowly added to reduce the gold(III) ions to gold(0), whilst nucleating on the nanoparticle seeds, as shown below in Figure 3.4.

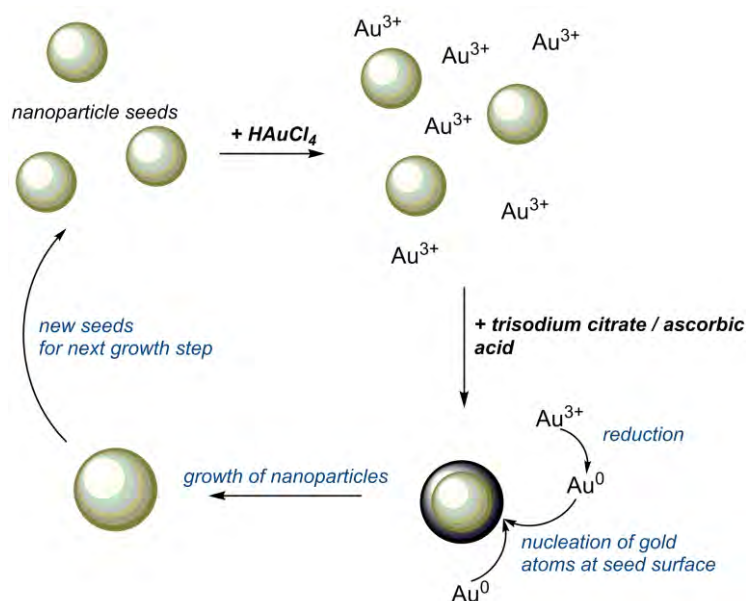


**Figure 3.4** Schematic of the seeded-growth synthesis used to produce 100 nm gold nanoparticles.

In each growth step, the nanoparticles tend to double in size, approximately; the 13 nm seeds grow to *ca.* 25 nm in step one, which then grow to *ca.* 50 nm in step two, and finally grow to *ca.* 100 nm in the third growth step. Size is estimated by inspection of the TEM data. UV-Vis absorption spectra and TEM images were recorded at each stage of the growth process to elucidate information about the particle sizes at each step, as shown below in Figure 3.5.

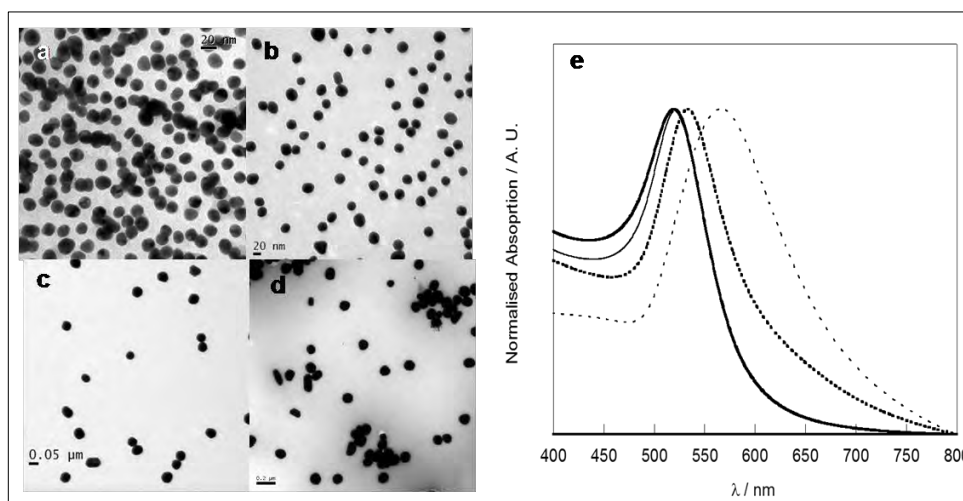


**Figure 3.5** TEM images of air-dried nanoparticles, following the nanoparticle growth process, of a) 13 nm seeds, b) 25 nm particles following the first growth step, c) 50 nm particles following the second growth step, and d) 100 nm particles following the third (final) growth step. e) Normalised UV-Vis absorption spectra of the 13 nm seeds (bold solid line), 25 nm particles (solid line), 50 nm particles (bold dashed line), and 100 nm particles (dashed line).

The SPR of the nanoparticles shifts to the red as the particles increase in size at each growth step (Figure 3.5e); the 13 nm seeds have an SPR  $\lambda_{\max} = 520$  nm (as described in Chapter Two, Section 2.3), whereas the 25 nm particles have SPR  $\lambda_{\max} = 522$  nm (Figure 3.5e). The SPR  $\lambda_{\max}$  of the 50 nm and 100 nm particles are observed at 533 nm and 566 nm respectively (Figure 3.5e). This is because the SPR is the collective oscillation of electrons in the nanoparticle, which is smaller than the mean free path of an electron in bulk gold, and thus the resonant electronic motion is determined by the size of the particle; as the diameter increases in size the resonant frequency decreases.<sup>39</sup> All particles displayed good particle stability (for > 1 month), and although the 50 nm and 100 nm particles settle out of solution within 24 hr (due to their mass), redispersion is quickly achieved by a short (*ca.* 30 s) sonication.

The resulting 40 pM 100 nm gold aqueous sol (for concentration calculation see Appendix 1.2) was characterised by UV-Vis absorption spectroscopy, DLS, electrophoretic light scattering (zeta potential), as shown below in Figure 3.6, and by TEM (Figure 3.5e).

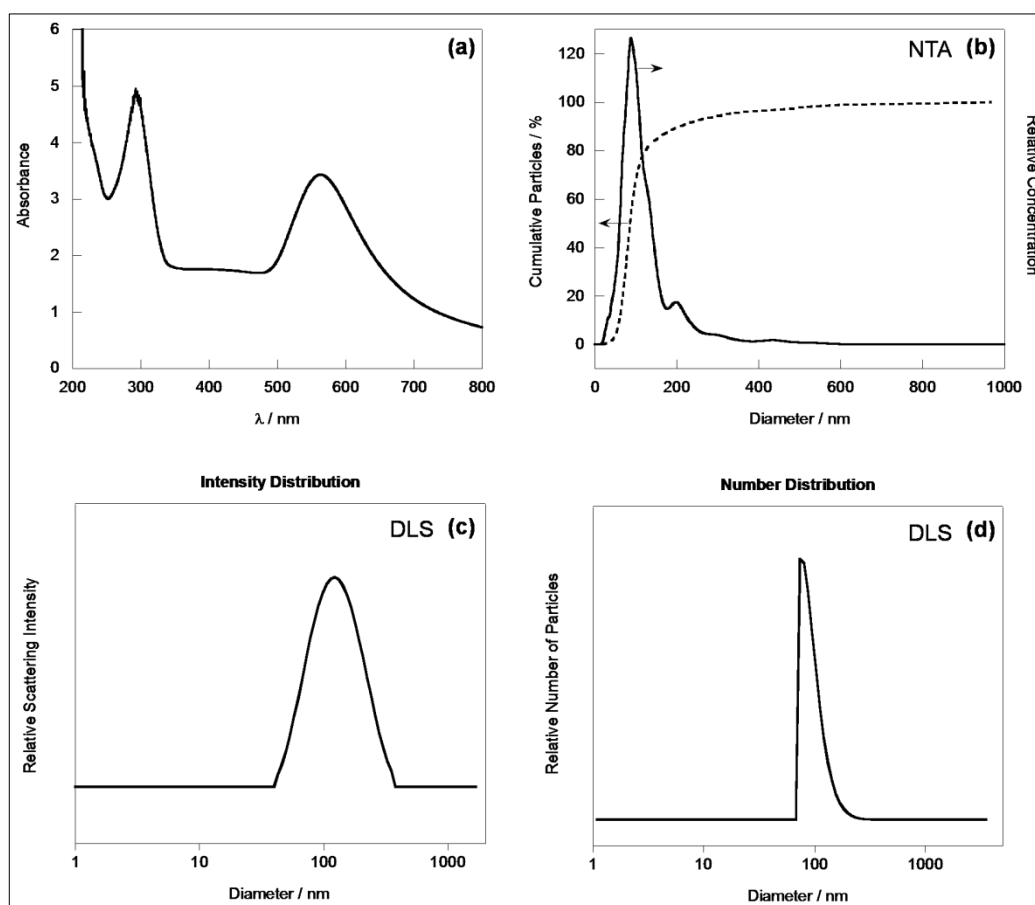


**Figure 3.6** (a) UV-Vis absorption spectrum of 40 pM 100 nm gold nanoparticles. (b) Sizing of the 100 nm gold nanoparticles by nanoparticle tracking analysis. (c) DLS Intensity distribution and (d) DLS number distribution of 100 nm gold nanoparticles, measured at 10 pM concentration.

The UV-Vis absorption spectrum has a highly absorptive SPR peak with  $\log \epsilon = 10.9$  at 566 nm, in terms of nanoparticle concentration, and the absorption band at 295 nm is due to the absorption of the ascorbic acid (Figure 3.6a); this disappears upon centrifugation, decantation of the supernatant and resuspension of the particles in deionised water. Sizing of the nanoparticles by DLS gives an average number distribution hydrodynamic diameter of  $98 \pm 27$  nm (Figure 3.6d), and an average intensity distribution diameter of  $136 \pm 62$  nm (Figure 3.6c). The nanoparticles were also large enough to detect by NanoSight nanoparticle tracking analysis (NTA), and track as single nanoparticles by laser scattering on a microscope ( $\lambda = 405$  nm) using tracking software (Figure 3.6b); the mean diameter = 119 nm, and the mode = 79 nm, with a standard deviation of 102 nm. The NTA, DLS and TEM data all corroborate

each other, in terms of sizing the ‘100 nm’ gold nanoparticles synthesised. Electrophoretic light scattering measurements reveal that the 100 nm gold nanoparticles have a zeta potential of  $-33 \pm 3$  mV, measured at 4 pM concentration in deionised water. This is marginally less than that of the 13 nm citrate gold nanoparticles (Chapter Two, Section 2.3), which have a zeta potential of  $-40 \pm 5$  mV, measured in water at a 2 nM nanoparticle concentration.

### 3.3 Synthesis and Characterisation of Ru-Z•AuNP100

As was observed with the direct addition of **RuSH** to 13 nm citrate-stabilised gold nanoparticles in Chapter Two (Section 2.4), addition of **RuSH** (synthesised *in situ* from **RuSAc**) to the 100 nm gold nanoparticles gives rise to the immediate aggregation of the nanoparticles, evident from a colour change from a purple to a grey colour, and subsequent sedimentation of solid out of suspension. Unlike 100 nm nanoparticles that are not aggregated, the sedimentation formed of these aggregates does not redisperse into solution upon sonication. In a similar fashion to the 13 nm gold nanoparticle studies in Chapter Two (Section 2.4, Figures 2.18 and 2.19), the titration of 5–20  $\mu$ M **RuSH** complex into 40 pM 100 nm gold nanoparticles gives rise to SPR reduction at 566 nm and to the growth of a new plasmonic band at  $>700$  nm, due to plasmon coupling between aggregating nanoparticles<sup>40</sup>, as shown below in Figure 3.7.

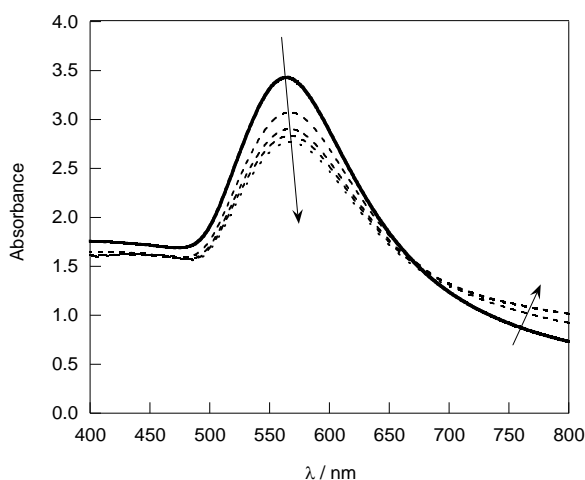


**Figure 3.7** UV-Vis absorption spectra of 100 nm gold nanoparticles (1 mL, 40 pM) (bold), and with the addition of **RuSH** complex (5–20  $\mu$ M)(dashed).

In order to circumvent nanoparticle aggregation upon functionalization with the **RuSH** lumiphore, the pre-coating fluorosurfactant, Zonyl® 7950 was employed, as shown below in Figure 3.8<sup>31,41</sup> in a similar fashion to **Ru-Z•AuNP13**, reported in Chapter Two, Section 2.8; 100 nm gold nanoparticles were initially coated with Zonyl® 7950, **RuSH** was subsequently added, and the coated 100 nm particles were isolated by centrifugation, followed by decantation of the supernatant and resuspension of the pellet in deionised water.

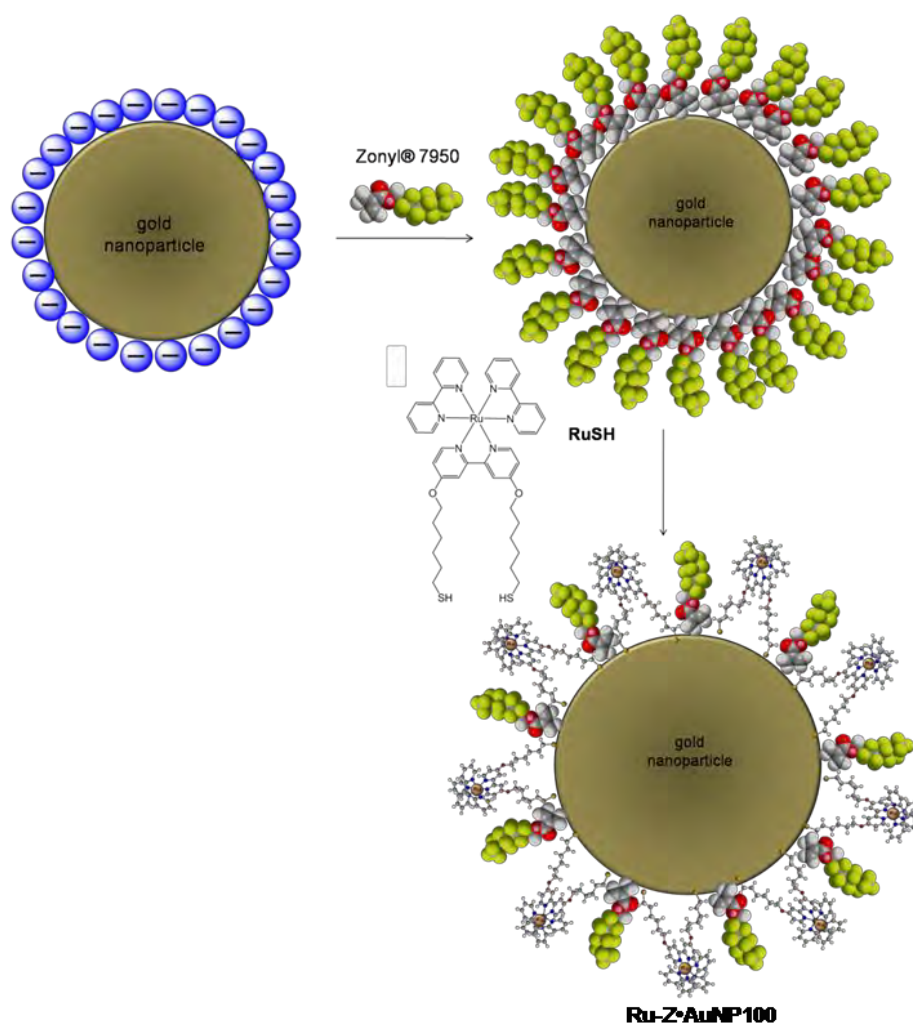


**Figure 3.8** Synthesis of **Ru-Z•AuNP100**, with the initial coating of the 100 nm gold nanoparticles with Zonyl® 7950 fluorosurfactant, followed by the addition of **RuSH** complex.

The addition of Zonyl® 7950 to the 100 nm gold nanoparticles gives rise to 1 nm red-shift in the SPR (indicated by the black arrow, Figure 3.9), and no further shift in the SPR is observed upon subsequent titration of **RuSH** complex (indicated by the red arrow, Figure 3.9), as shown below in Figure 3.9. This is identical to the changes in UV-Vis absorption observed during the preparation of **Ru-Z•AuNP13**, discussed in Chapter Two (Section 2.8).

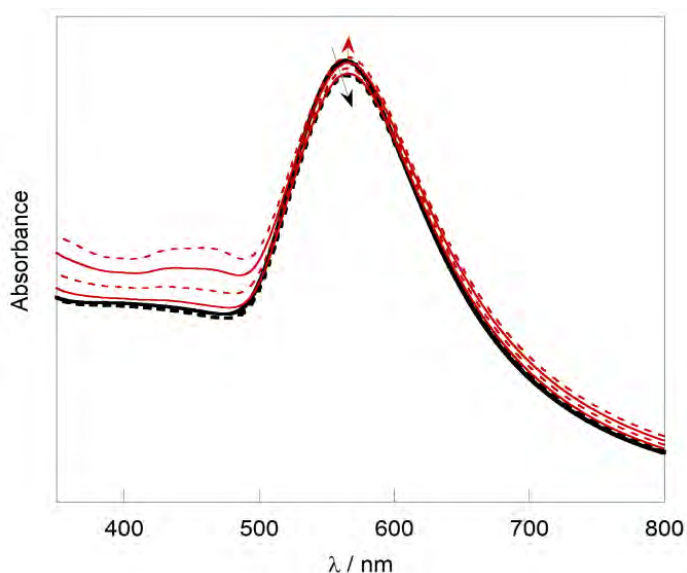


**Figure 3.9** UV-Vis absorption spectra of 100 nm gold nanoparticles (40 pM) (black solid line), + Zonyl® 7950 (1 mM) (black dashed), + 5–60  $\mu$ M **RuSH** (red).

Isolated **Ru-Z•AuNP100** have a SPR absorption with  $\lambda_{\text{max}} = 567$  nm (see Section 3.3.1, Figure 3.11) and have been characterised by DLS (Figure 3.10a,b), NanoSight NTA (Figure 3.10c), and TEM (Figure 3.10d), to analyse the size of the coated nanoparticles.

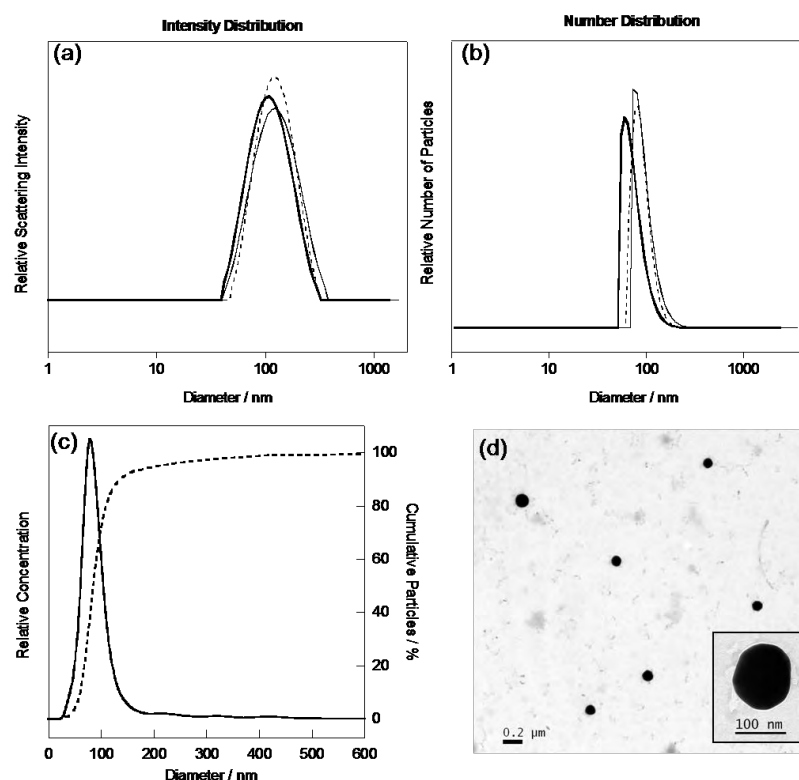


**Figure 3.10** (a) DLS intensity distributions and (b) DLS number distributions, of 4 pM 100 nm gold nanoparticles (solid line), 4 pM **Z•AuNP100** (dashed line) and 4 pM **Ru-Z•AuNP100** nanoparticles (bold solid line). (c) NanoSight NTA **Ru-Z•AuNP100**. (d) TEM image of **Ru-Z•AuNP100** particles.

As a control Zonyl® 7950-coated gold nanoparticles were synthesised under identical conditions, without the **RuSH** complex, and purified by centrifugation to give **Z•AuNP100**, also with an SPR peak with  $\lambda_{\max} = 567$  nm. DLS measurements of uncoated 100 nm gold nanoparticles, **Z•AuNP100** and **Ru-Z•AuNP100**, all reveal a single peak in the scattering intensity distribution at *ca.* 130 nm and a single peak in the number distribution at *ca.* 90 nm, showing an absence of aggregates in all cases. The uncoated 100 nm nanoparticles having a mean intensity diameter of  $136 \pm 62$  nm (100%), (Section 3.2), the **Z•AuNP100** of  $131 \pm 51$  nm (100%) and **Ru-Z•AuNP100** of  $122 \pm 51$  nm (100%). These equate to average number distributions of  $98 \pm 27$  nm,  $92 \pm 21$  nm, and  $76 \pm 22$  nm for uncoated nanoparticles, **Z•AuNP100**, and **Ru-Z•AuNP100** respectively. Sizing by NTA gives a mean particle size of 100 nm for **Ru-Z•AuNP100**, with a modal value of 79 nm (Figure 3.10c), and TEM reveals the **Ru-Z•AuNP100** nanoparticles as quite monodisperse spherical nanoparticles with a gold

core diameter of *ca.*100 nm. All sizing data in Figure 3.10 confirm the uniformity of the **Ru-Z•AuNP100** nanoparticles.

Electrophoretic light scattering measurements of the uncoated nanoparticles, **Z•AuNP100**, and **Ru-Z•AuNP100** were performed at 4 pM concentrations to analyse the change in the zeta potentials of the nanoparticles upon functionalization (see Table 3.1). In a similar fashion to the 13 nm gold nanoparticles described in Chapter Two (Section 2.8), upon addition of fluorosurfactant, the zeta potential of the isolated **Z•AuNP100** increases in magnitude to a larger negative voltage of  $-47\pm 3$  mV (4 pM in deionised water), with respect to that of  $-33\pm 3$  mV (4 pM in deionised water) for the uncoated 100 nm gold nanoparticles. (This compares to an increase from  $-40\pm 5$  mV to  $-61\pm 4$  mV for uncoated 13 nm nanoparticles and **Z•AuNP13** respectively.) This is attributed to the partial negative charges of the fluoropolymer C–F bonds on the peralkyl chains, presented to the outer surface of the hydrodynamic radii of the particles, as discussed in Section 2.5 (Chapter Two). Addition of the **RuSH** complex to the 100 nm nanoparticles also changes their surface charge, as previously observed in the preparation of **Ru-Z•AuNP13** (Section 2.8); isolated **Ru-Z•AuNP100** nanoparticles have a zeta potential of  $-35\pm 3$  mV (4 pM in deionised water), which is less negative than that of **Z•AuNP100** ( $47\pm 3$  mV) as the **RuSH** complex displaces some of the electronegative fluorosurfactant. The zeta potential data are summarised below in Table 3.1.

**Table 3.1** Summary of zeta potential data for **Ru-Z•AuNP100** and related particles for comparison

Nanoparticles	Zeta Potential / mV <sup>a</sup>
uncoated 13 nm gold nanoparticles	-40±5
<b>Z•AuNP13</b>	-61±4
<b>Ru-Z•AuNP13</b>	-48±2
uncoated 100 nm gold nanoparticles	-33±3
<b>Z•AuNP100</b>	-47±3
<b>Ru-Z•AuNP100</b>	-35±3

<sup>a</sup> measured at 4 pM in deionised water. Errors quoted as ± 1SD.

The zeta potential data for the 100 nm nanoparticles are all *ca.* 20% lower than their 13 nm nanoparticle equivalents, which is expected from the electrophoretic mobility measurements; the surface area:volume ratio decreases by a factor of *ca.* 7 as the particle radius increases by the same factor, and thus the mobility of the nanoparticles in an electric field will reduce.

The surface-coating of **RuSH** complexes to the gold nanoparticles in **Ru-Z•AuNP100** is estimated as 108,000 complexes per nanoparticle, by inspection of the singlet MLCT band in the UV-Vis absorption spectrum of the first supernatant from the isolation process, due to the insufficiently low ruthenium(II) signal at the nanoparticle concentrations prepared for ICP-OES analysis (See Appendix 2.3).<sup>31</sup> 108,000 complexes per nanoparticle is equivalent to a molecular footprint of 0.5 nm × 0.5 nm, which is similar to that observed for the **Ru-Z•AuNP13** particles (i.e. 1400 RuSH complexes per nanoparticle, 0.6 nm × 0.5 nm footprint, Section 2.8, Appendix 2.2).

### 3.3.1 Photophysical Properties of Ru-Z•AuNP100

The isolated **Ru-Z•AuNP100** particles are luminescent upon excitation at 450 nm, with broad red emission spanning the range 550–800 nm, and  $\lambda_{\text{max}} = 640$  nm. The UV-Vis absorption spectrum, excitation spectrum, measured at  $\lambda_{\text{em}} = 630$  nm, and the steady-state luminescence spectrum,  $\lambda_{\text{exc}} = 450$  nm, are presented below in Figure 3.11.

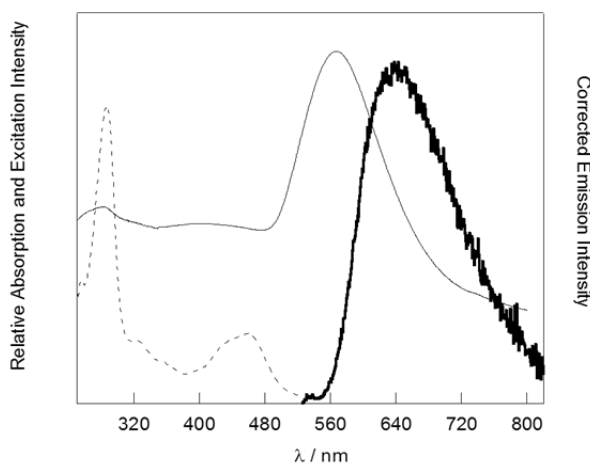


**Figure 3.11** UV-Vis absorption spectra (solid line), excitation spectra,  $\lambda_{\text{em}} = 630$  nm (dashed line), and luminescence spectra,  $\lambda_{\text{exc}} = 450$  nm (bold solid line) of 10 pM **RuS•AuNP100**. Spectra corrected for instrument response.

The UV-Vis absorption spectrum is dominated by the SPR of the gold nanoparticles, with  $\lambda_{\text{max}} = 567$  nm. The excitation spectrum resembles the UV-Vis absorption spectrum and excitation spectrum of the free **RuSAc** (Section 2.2.2, Figures 2.14 and 2.15), as is also observed for **Ru-Z•AuNP13** (Chapter Two, Section 2.9), and the time-resolved luminescence studies reveal that the observed luminescence lifetime of **Ru-Z•AuNP100** = 360 ns  $\pm$ 10% (aerated) and 630 ns  $\pm$ 10% (degassed), with excitation at 445 nm and emission collected at 630 nm. The luminescent properties of the ruthenium(II)-coated gold nanoparticles are virtually identical, and thus the size of the nanoparticle core appears to have no effect upon the lumiphore properties: both **Ru-Z•AuNP13** and **Ru-Z•AuNP100** have luminescence with  $\lambda_{\text{max}} = 640$  nm, and equivalent aerated and degassed lifetimes, within error. (The observed luminescence lifetime of **Ru-Z•AuNP13** = 340 ns  $\pm$ 10 % (aerated) and 690 ns  $\pm$ 10 %

(deareted), discussed in Chapter Two, Section 2.9). This corroborates the fact that the nanoparticle surface plasmon does not interact with the luminescence of the **RuSH** complex, because if it did the effect would be size-dependent. Hence, we do not observe the oft cited luminescence quenching<sup>42-47</sup> with the **RuSH** complex in either **Ru-Z•AuNP13** or **Ru-Z•AuNP100**.

**Ru-Z•AuNP100** were imaged in Brownian motion within a 100  $\mu\text{m}$  deep, 1 mm wide microchannel (ibidi), by epiluminescence microscopy, as shown in Figure 3.12.

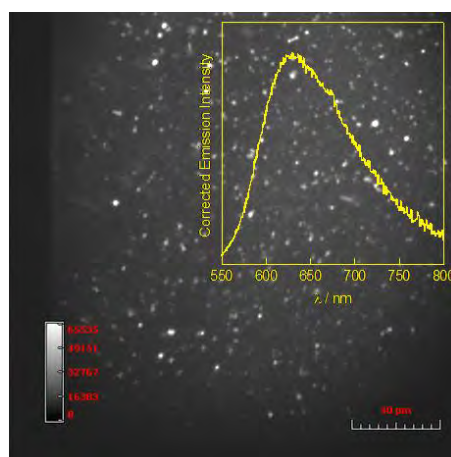


**Figure 3.12** Luminescence image and spectrum (inset) of **RuS•AuNP100** imaged in Brownian motion within a 100  $\mu\text{m}$  deep, 1 mm wide ibidi microchannel, by epiluminescence microscopy.  $\lambda_{exc} = 450 \text{ nm}$ ,  $\lambda_{em} > 510 \text{ nm}$ . The emission spectrum (inset) is taken from the field of view in the image.

**Ru-Z•AuNP100** nanoparticles are visualised as bright spots in the epiluminescence image (Figure 3.12), in which the particles are excited at 450 nm, and the signal is detected using a dichroic mirror at  $>510 \text{ nm}$ . A luminescence spectrum was collected by feeding the luminescence signal from the image field-of-view to the spectrometer, confirming the characteristic profile of the **Ru-Z•AuNP100** nanoparticles (inset). Successful detection of the nanoparticles by luminescence microscopy allows imaging applications to be explored in the following section for cellular interactions with the nanoparticles.

### 3.4 Cellular Uptake Studies of Ru-Z•AuNP13 and Ru-Z•AuNP100 in A549 Cells

To investigate their potential as cell imaging agents, A549 human lung cancer cells were incubated with **Ru-Z•AuNP13** and **Ru-Z•AuNP100** by Dr Robert Harris and Mr Sunil Claire, in collaboration with Dr Nikolas Hodges. Cells were incubated for 24 hr, and fixed cells were stained with Hoechst 33258, a nuclear stain which fluoresces intensely upon binding to the A-T rich regions of dsDNA. Confocal luminescence images of the cells are shown below in Figures 3.13 and 3.14.

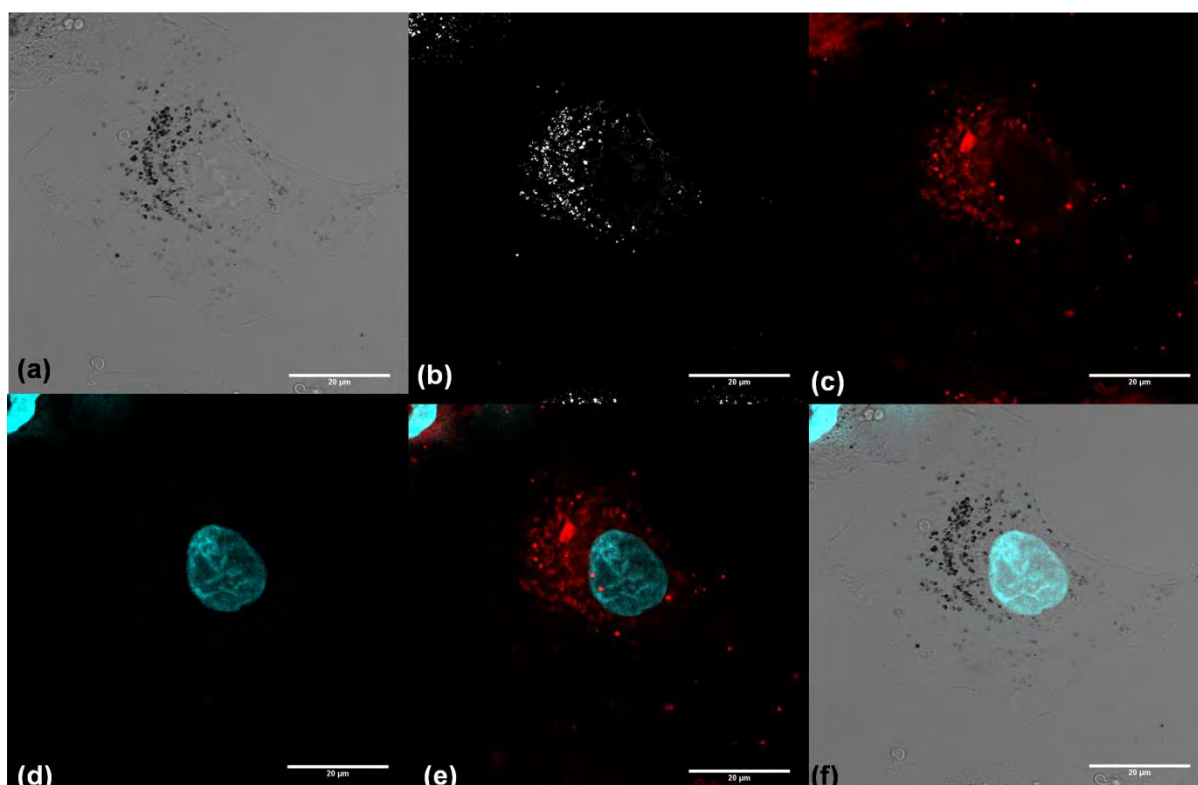


**Figure 3.13** Confocal images of **RuS•AuNP13** in A549 cells following incubation for 24 hr. (a) white light transmission image, (b) reflection image  $\lambda_{exc} = 633 \text{ nm}$ ,  $\lambda_{em} = 623\text{--}643 \text{ nm}$ , (c) ruthenium luminescence, red channel,  $\lambda_{exc} = 453 \text{ nm}$ ,  $\lambda_{em} = 555\text{--}800 \text{ nm}$ , (d) nuclear Hoechst staining, blue channel,  $\lambda_{exc} = 405 \text{ nm}$ ,  $\lambda_{em} = 410\text{--}455 \text{ nm}$ , (e) overlay of blue and red channel, (f) overlay of blue channel and reflection transmission image. White scale bar represents  $20 \mu\text{m}$ .

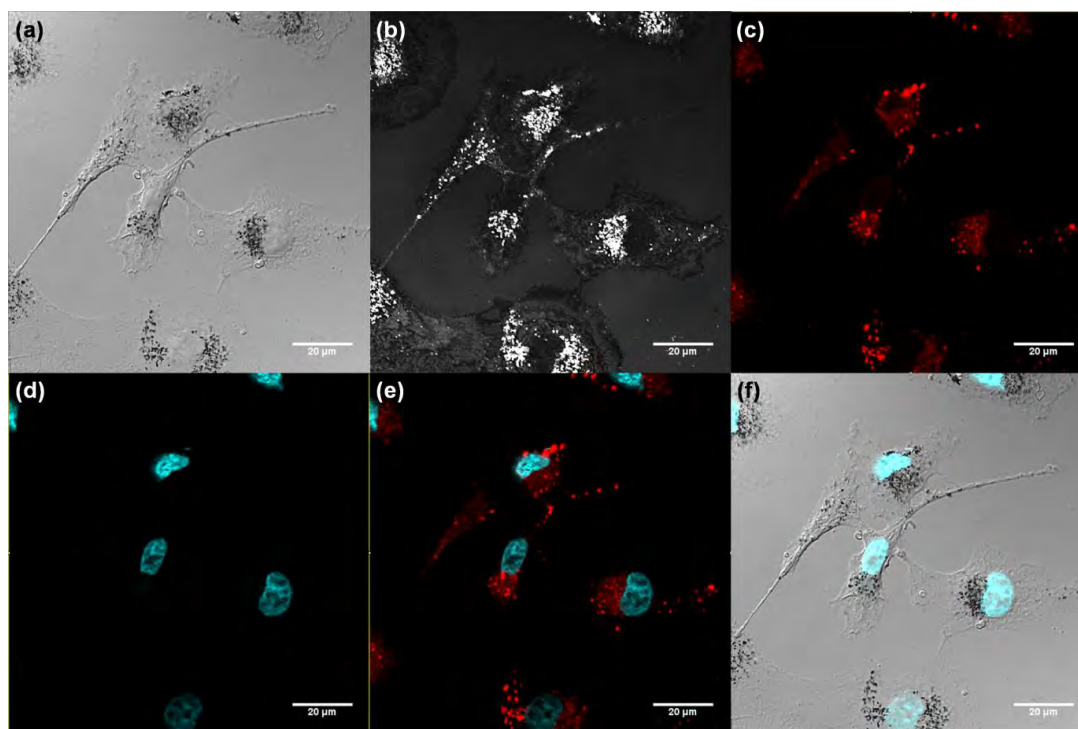


**Figure 3.14** Images of **RuS•AuNP100** nanoparticles in A549 cells monitored by confocal luminescence and reflection microscopy. (a) white light transmission image, (b) reflection image  $\lambda_{exc} = 488 \text{ nm}$ ,  $\lambda_{em} = 478\text{--}498 \text{ nm}$ , (c) **Ru-Z•AuNP100** luminescence, red channel,  $\lambda_{exc} = 453 \text{ nm}$ ,  $\lambda_{em} = 555\text{--}800 \text{ nm}$ , (d) nuclear Hoechst staining, blue channel,  $\lambda_{exc} = 405 \text{ nm}$ ,  $\lambda_{em} = 410\text{--}455 \text{ nm}$ , (e) overlay of blue and red channels, and (f) overlay of blue channel and transmission image. White scale bar is  $20 \mu\text{m}$ .

Gold nanoparticles appear as bright spots in the confocal reflection images (Figures 3.13b and 3.14b) due to the high elastic scattering cross-section of the gold nanoparticles in comparison with that of biological tissue,<sup>48</sup> and dark spots in the transmission images due to the absorption of white light. The **RuSH** luminescence signal is visualised in the red channel (Figures 3.13c and 3.14c), in which the Ru(II)-coated nanoparticles are excited by a 453 nm laser, and emission is gated between 555–800 nm. Co-localisation of the red (**RuSH** emission) and reflection (gold scattering) signals in both Figures 3.13 and 3.14 confirms the stability of the nanoprobe after the 24 hr incubation. Cellular uptake by A549 cells was observed for both **Ru-Z•AuNP13** and **Ru-Z•AuNP100** nanoparticles, and the luminescent nanoparticles were bright enough to image effectively by confocal luminescence microscopy, with each image taking *ca.* 60 s to acquire. Un-treated Hoechst-stained control cells were also

imaged by confocal microscopy; no bright spots were visible in the reflection channel, and luminescence was absent in the red channel (see Appendix 7).

The **Ru-Z•AuNP100** nanoparticles are large enough to image as *single* nanoparticles in the cells, and to investigate this further, a convolution of the point-spread function from the confocal luminescence measurements was convolved with a simple model of a nanoparticle sphere by Mr Sunil Claire and Dr Iain Styles. Due to the effects of light diffraction, the model predicts that individual **Ru-Z•AuNP100** nanoparticles should appear as 300 nm particles, which is consistent with the actual measurements obtained.<sup>31</sup>

To monitor the uptake and accumulation of nanoparticles in cells over time, a pulse-chase experiment with **Ru-Z•AuNP13** was performed by Dr Robert Harris.<sup>31</sup> In this experiment, A549 cells are incubated with **Ru-Z•AuNP13** for 24 hr, and then washed to remove any extracellular nanoparticles. The cells are then further cultured for 3 days, post-treatment, and imaged each day. Pulse-chase images as shown below in Figure 3.15.

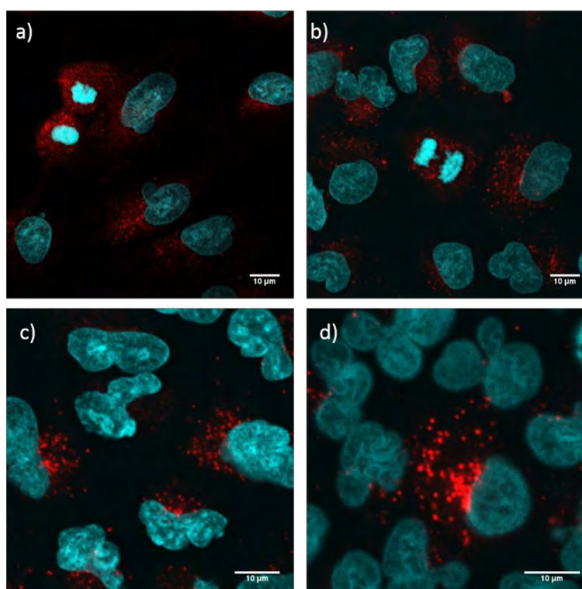


**Figure 3.15** Pulse-chase confocal images of the distribution of **Ru-Z•AuNP13** in A549 cells, following incubation for 24 hr (pulse), (a) immediately after the 24 hr treatment, and (b) 1 day, (c) 2 days, and (d) 3 days post-treatment. Nuclear Hoechst staining, blue channel,  $\lambda_{exc} = 405$  nm,  $\lambda_{em} = 410\text{--}455$  nm, and ruthenium luminescence, red channel,  $\lambda_{exc} = 453$  nm,  $\lambda_{em} = 555\text{--}800$  nm. Scale bar = 10  $\mu$ m.

Interestingly, even 3 days post-treatment in the chase experiment, which is estimated to represent *ca.* three cell divisions (based on the number of nuclei per field of view), many of the cells contained **Ru-Z•AuNP13** nanoparticles, demonstrating the long half-life and poor clearance of these particles.<sup>31</sup> Importantly, cell division proceeds seemingly unperturbed by the **Ru-Z•AuNP13**, and no toxic effect is obvious by inspection of the micrographs.

Analysis of the confocal luminescence images of A549 cells incubated with **Ru-Z•AuNP100** reveal that sometimes the nanoparticles localise within the nucleus. Co-localisation of the red channel and the blue (nuclear stain) channel in the confocal luminescence images shown below in Figure 3.16 indicate nuclear localisation of the **Ru-Z•AuNP100** nanoparticles.

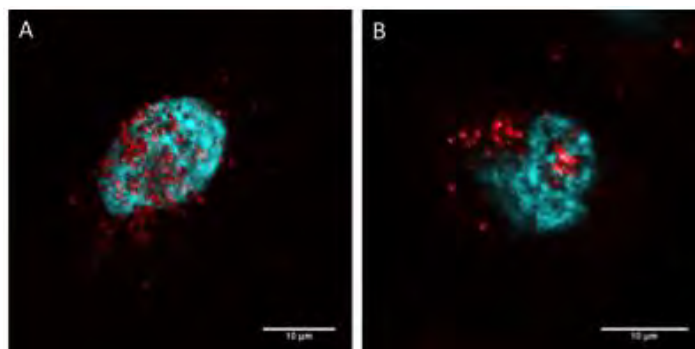


**Figure 3.16** Confocal luminescence images of nuclear localisation of **Ru-Z•AuNP100** in A549 cells which has been stained with Hoechst. Nuclear Hoechst staining, blue channel,  $\lambda_{exc} = 405 \text{ nm}$ ,  $\lambda_{em} = 410\text{--}455 \text{ nm}$ , and **Ru-Z•AuNP100** luminescence, red channel,  $\lambda_{exc} = 453 \text{ nm}$ ,  $\lambda_{em} = 555\text{--}800 \text{ nm}$ . Scale bar =  $10 \mu\text{m}$ .

In contrast, little evidence of nuclear uptake of **Ru-Z•AuNP13** is observed, although it cannot be excluded, as it is believed that accumulations of **Ru-Z•AuNP13** are required for their visualisation.<sup>31</sup> However, it is possible that the larger nanoparticles are selectively found in the nucleus due to their size; the crossing of the nuclear envelope (a double phospholipid bilayer membrane, embedded with proteins), may only occur when the cells divide, and the nuclear envelope breaks down. Subsequently, when the new nuclear envelopes form for the daughter cells, it is possible that **Ru-Z•AuNP100** get trapped in the nucleus, whereas **Ru-Z•AuNP13** are expelled out of the nucleus through the pores in the envelope.

Electron microscopy was also performed on *ca.* 100 nm slices of treated A549 cells to examine the intracellular localisation of the functionalized nanoparticles within the cells, following the uptake in more detail (Figures 3.17 and 3.18).

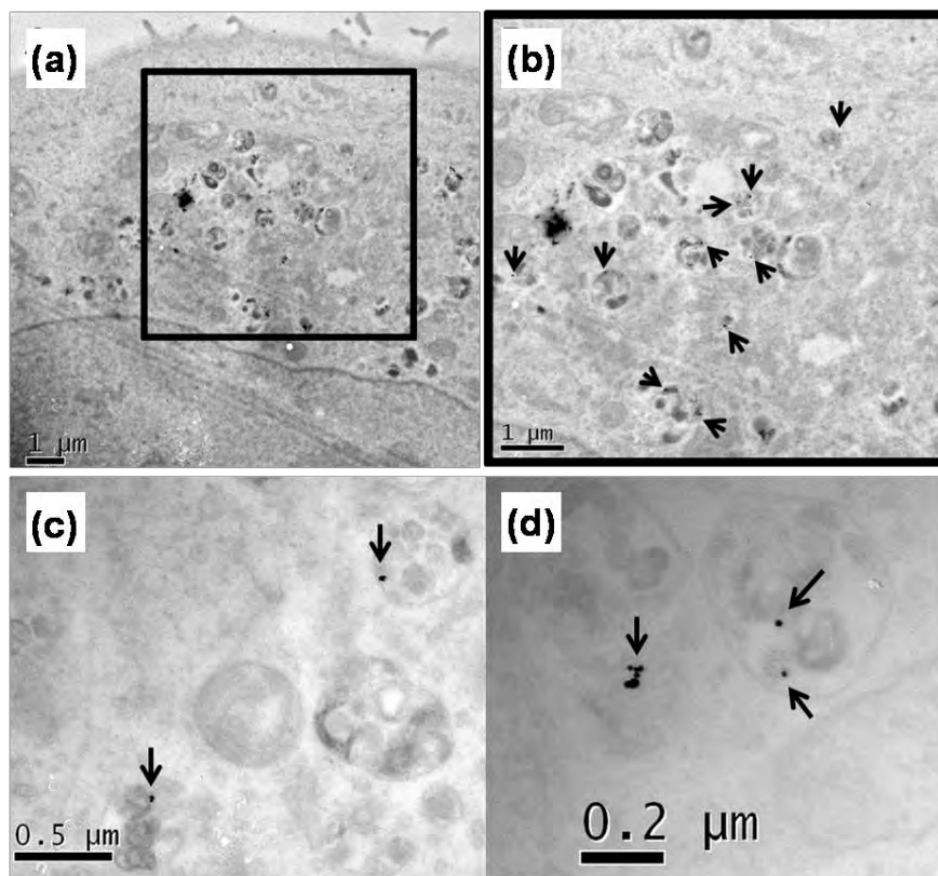


**Figure 3.17** TEM images of a cell section, from an A549 cell that has been incubated with **Ru-Z•AuNP13** for 24 hr (a), and zoomed images (b–d).

The **Ru-Z•AuNP13** (Figure 3.17) and **Ru-Z•AuNP100** (Figure 3.18) appear as dark spheres against the cell section, and are found throughout the cell. **Ru-Z•AuNP13** tend to be localised in vesicles, as can be seen in Figure 3.17c and 3.17d, which is indicative that the nanoparticles are taken up by endocytosis,<sup>26</sup> and no **Ru-Z•AuNP13** nanoparticles were observed in the nucleus in the samples imaged.

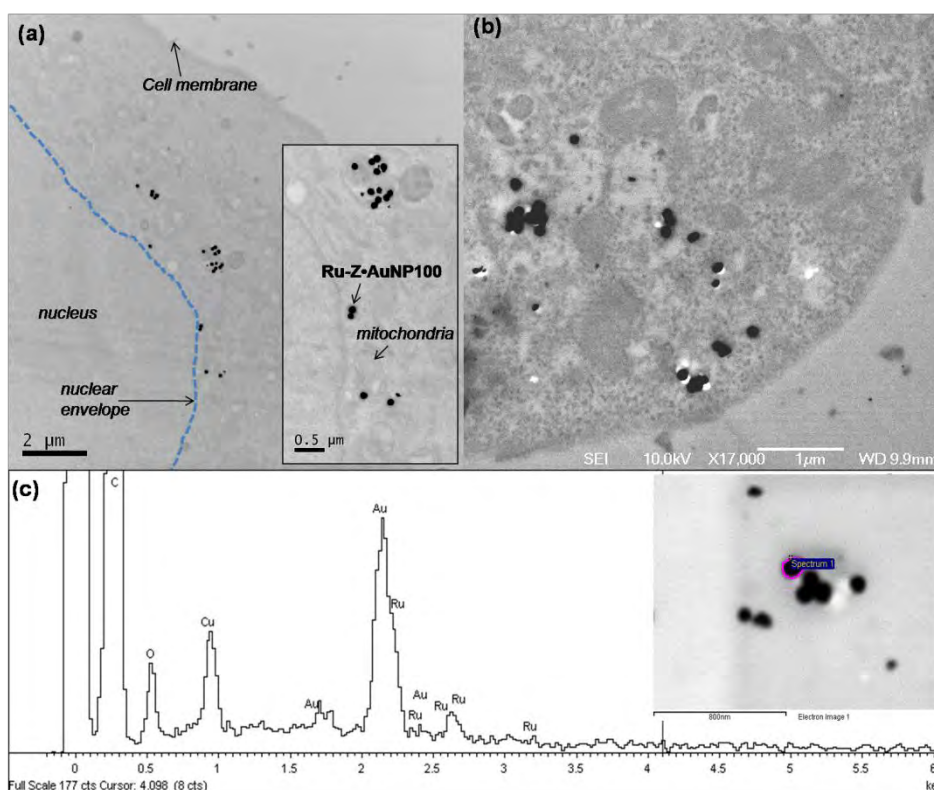


**Figure 3.18** Electron microscopy of a cell section, from an A549 cell that has been incubated with **Ru-Z•AuNP100** for 24 hr. (a) TEM image, (b) SEM image and (c) EDX spectra of region of interest (inset), taken from the field of view imaged in (b).

**Ru-Z•AuNP100** were observed throughout the A549 cells, within the cytoplasm, within vesicles (Figure 3.18a and 3.18b) and occasionally within the cell nucleus.<sup>31</sup> Energy-dispersive X-ray spectroscopy (EDX), which provides chemical atomic characterisation, was performed on a single **Ru•AuNP100** in the cell shown in Figure 3.17b, to confirm that the observed high contrast dark spots were indeed gold nanoparticles (see spectra in Figure 3.18c). The electron microscopy performed corroborates the luminescence imaging performed, and confirms that the nanoparticles are indeed internalised by A549 cancer cells, rather than just adhering to the surface of the cells.

In order to test whether nanoparticle uptake could be observed by fluorescence-activated cell sorting flow cytometry (FACS), A549 cells dosed with **Ru-Z•AuNP100** for 24 hr were

washed (to remove excess nanoparticles) and analysed by FACS (schematic of FACS shown in Figure 3.19, data shown in Figure 3.20).

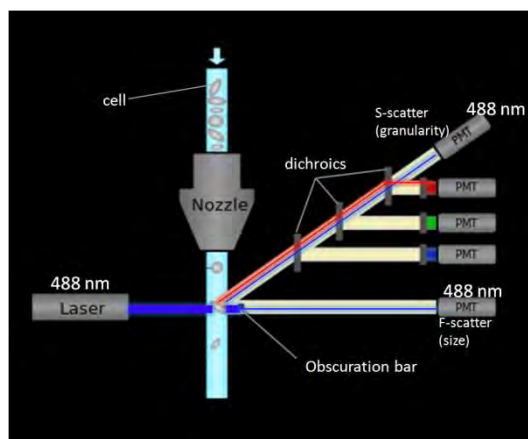


**Figure 3.19** Schematic of a FACS flow cytometry set-up.

During FACS analysis, cells are focussed into a stream of liquid, and each suspended cell passes through a laser beam (in this instance a 488 nm laser), and the scattering intensity and fluorescence (luminescence) intensity is recorded at various emission wavelengths, selected by band-pass filter, as shown in Figure 3.18. These data are recorded per cell, and usually several thousand cells are analysed to obtain statistical data. Comparison of the FACS data for A549 cells dosed with **Ru-Z•AuNP100** with control cells (incubated without nanoparticles) reveals that there is no difference in the forward scatter of cells, a measure of cell size between control and treated cells. However, the median red luminescence increased 19-fold in the dosed cells, with respect to the control, indicating the presence of fluorescent red nanoparticles within the cell, as can be seen below in Figure 3.20.

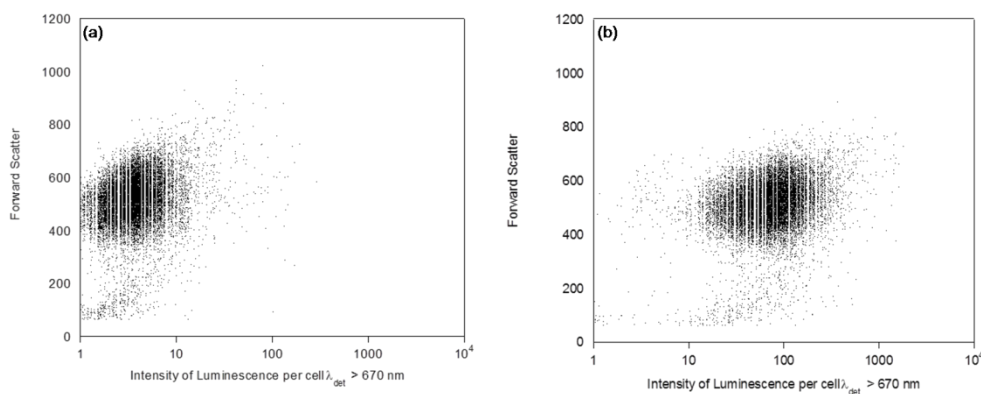


**Figure 3.20** Cellular uptake of nanoparticles by FACS flow cytometry. (a) un-dosed control A549 cells, and (b) A549 cells incubated with **Ru-Z•AuNP100** for 24 hr.  $\lambda_{exc} = 488$  nm,  $\lambda_{det} = 488$  nm for forward scatter (y-axis, a measure of cell size), and  $\lambda_{det} > 670$  nm for luminescence signal (x-axis). One dot represents data for one cell. 50,000 cells were analysed in each experiment.

These data are promising as they demonstrate that the macroscopic cell luminescence can be detected by FACS, and thus the nanoparticles can be used as cell labels. In addition to this, more detailed uptake studies and time courses could be performed in the future by this technique, in a fraction of the time that is required for quantitative microscopic cell imaging. The ability to analyse several thousand cells in minutes means that statistically significant data can be obtained with ease and without subjective bias.

Toxicity assays have been performed by Mr Sunil Claire using both an MTT colorimetric assay, which assess mitochondrial function, and an adenylate kinase release assay, to determine cell viability by detecting cell membrane integrity. Both assays show that no statistically significant toxicity of either **Ru-Z•AuNP13** or **Ru-Z•AuNP100** is observed at concentrations up to five times the concentrations used for the imaging studies, over a 24 hr period.<sup>31</sup> Although these 24 hr studies cannot determine that there is an absence of cytotoxicity, because it is possible for toxic responses to take longer than 1 day to present themselves, these assays show that no toxicity is observed on the time-scale of the microscopy experiments.

### 3.5 Conclusion

Gold nanoparticles have been synthesised successfully at 100 nm in diameter, and functionalised with the luminescent complex, **RuSH**, using Zonyl® 7950 fluorosurfactant to prevent aggregation. The resulting **Ru-Z•AuNP100** nanoparticles have  $10^5$  lumiphores per nanoparticle, and exhibit bright red luminescence with similar photophysical properties to the **Ru-Z•AuNP13** nanoparticles. Importantly, no luminescence quenching is observed when the **RuSH** complex is grafted to 100 nm gold nanoparticles. Cellular uptake studies of both **Ru-Z•AuNP13** and **Ru-Z•AuNP100** nanoparticles have been performed, and both sizes of particle can be imaged in cell by conventional and widely-available optical microscopy methods, with sensible acquisition times. Electron microscopy has been employed to verify the cellular internalisation of the nanoparticles observed by luminescence microscopy. The possibility to visualise uptake by optical techniques is hugely advantageous over electron-based methods, both in terms of preparation and imaging time, as well as being able to image live cells. Gross cell labelling is also possible by flow cytometry techniques, which opens up many opportunities for more detailed uptake studies to be performed on a statistically significant scale.

The **Ru-Z•AuNP13** and **Ru-Z•AuNP100** nanoprobos do not present any significant toxicity in cells, and no dissociation of the **RuSH** complex from the nanoparticle surface is observed following 24 hr incubation in a biological environment. In addition, the brightness of the particles allows the imaging of single **Ru-Z•AuNP100** nanoparticles associated with DNA material of the nucleus. Therefore, these particles have great potential for cellular imaging probes, which can be developed further by attaching other cargo to the labelled gold nanoparticles, using simple S–Au chemistry.

## 3.6 Acknowledgements

Thank you to Mr Sunil Claire (PSIBS), Dr Robert Harris and Dr Nikolas Hodges (School of Biosciences, University of Birmingham) for the cell work detailed in this Chapter, and thank you to Dr Iain Styles (School of Computer Sciences, University of Birmingham) for advice with the confocal image processing. Thank you to Ms Theresa Morris for the TEM preparation of the cell sections, and for help with the SEM and EDX analysis of the nanoparticles in A549 cells. Acknowledgement must also go to my BNatSci project student, Mr Gerald Zikeli, for all his help in the laboratory with the gold nanoparticle growth synthesis.

## 3.7 Experimental

### 3.7.1 General Synthesis

**RuSH** (3.5 mM (aq) 30 % w/w:CH<sub>3</sub>CN (1:1)) was synthesised *in situ* from its **RuSAc** precursor, as described in Chapter Two, Section 2.12.1. Zonyl® 7950 was purchased from Sigma Aldrich and 13 nm gold nanoparticles were synthesised by the citrate reduction method,<sup>38</sup> as described in Section 2.12.1.

#### *Synthesis of 100 nm gold nanoparticles:*

This method was adapted from that published by *Ziegler and Eychmüller*.<sup>37</sup>

The following stock solutions were prepared for the seeded-growth synthesis: ascorbic acid (aq) (502 mg, 2.85 mmol, 1% w/v); trisodium citrate dehydrate (aq) (500 mg, 1.70 mmol, 1% w/v); HAuCl<sub>4</sub>·3H<sub>2</sub>O (aq) (100 mg, 0.25 mmol, 0.2% w/v); citrate gold nanoparticle seeds (9 nM) used as prepared in Section 2.12.1.

13 nm citrate gold nanoparticles (6 mL, 9 nM colloid in water) were diluted in deionised water to 40 mL, and all further steps were performed under stirring. The Au<sup>3+</sup> stock solution (4 mL, 0.2% w/v) was diluted to 20 mL in deionised water, then added dropwise over 15 min to the seeds. Ascorbic acid stock solution (1 mL, 1% w/v) was combined with trisodium citrate stock solution (0.5 mL, 1% w/v) and diluted to 20 mL in deionised water. This solution was added dropwise over 15 minutes to give a dark red solution. The mixture was refluxed for 30 min at 100 °C. An aliquot of the reaction mixture (9 mL) was left to cool, and was diluted to 40 mL. Au<sup>3+</sup> stock solution (4 mL, 0.2% w/v), diluted to 20 mL, and was added dropwise to the diluted aliquot over 15 min. Ascorbic acid stock solution (1 mL, 1% w/v) and trisodium citrate stock solution (0.5 mL, 1% w/v) were diluted to 20 mL, and added dropwise over 15 min. The mixture was refluxed at 100 °C for 30 min to render a red/purple solution, and an aliquot of the reaction mixture (40 mL) was left to cool. Au<sup>3+</sup> stock solution (16 mL, 0.2% w/v) was diluted to 20 mL and added dropwise to the aliquot over 15 min. Ascorbic acid stock (4 mL, 1% w/v) with trisodium citrate stock (2 mL, 1% w/v), diluted to 20 mL, was added dropwise to the mixture over 15 min to give a dark brown colloid. The mixture was refluxed for 30 min at 100 °C, and allowed to cool to yield 100 nm gold nanoparticles as an orange/light brown colloid in water (40 pM), with a purple colour due to the SPR absorption, visible when held up to the light. UV-VIS (H<sub>2</sub>O)  $\lambda_{\text{max}}$  [nm] = 567 (SPR). Zeta Potential (4 pM in deionised water diluent) =  $-33 \pm 3$  mV.

*Synthesis of Ru-Z•AuNP100:*

Zonyl® 7950 (CH<sub>2</sub>-C(CH<sub>3</sub>)COOC<sub>2</sub>H<sub>4</sub>(CF<sub>2</sub>)<sub>n</sub>F, MW *ca.* 500, 1  $\mu$ l, 1.15 g mL<sup>-1</sup>) was added to 100 nm citrate gold nanoparticles (1 mL, 40 pM nanoparticles, zeta potential at 4 pM in deionised water =  $-33 \pm 3$  mV, diameter =  $98 \pm 21$  nm (DLS number distribution), =  $136 \pm 62$  nm (DLS intensity distribution)) to give fluorosurfactant coated nanoparticles (40 pM nanoparticles), with a final fluorosurfactant concentration of *ca.* 1mM (isolated Z•AuNP100,

by three rounds of centrifugation, decantation of the supernatant and resuspension of the pellet have a zeta potential of  $-47\pm 3$  mV (4 pM in deionised water) and diameter of  $92\pm 21$  nm (DLS number distribution), and of  $131\pm 51$  nm (DLS intensity distribution)). A solution of **RuSH** (20  $\mu$ l, 3.5 mM, (made *in situ*,  $\text{NH}_4\text{OH}(\text{aq})$  (30 % *w/w*): $\text{CH}_3\text{CN}$  (1:1) solution)) was added to the fluorosurfactant / nanoparticle mixture (not isolated), and was stirred for 20 min. The particles were centrifuged at 12,000 g for 90 s, and the supernatant was decanted from each pellet to remove unbound material. The nanoparticles were resuspended in deionised water, and this was repeated twice to give **Ru-Z•AuNP100**. UV-Vis ( $\text{H}_2\text{O}$ )  $\lambda_{\text{max}}$  [nm] = 567 (SPR). Diameter  $76\pm 22$  nm (DLS number distribution), =  $122\pm 51$  nm (DLS intensity distribution), = 100 nm (mean diameter by NanoSight NTA). Zeta potential =  $-35\pm 3$  mV (isolated, 4 pM in deionised water diluent). Emission ( $\text{H}_2\text{O}$ ,  $\lambda_{\text{exc}}$  = 450 nm)  $\lambda_{\text{max}}$  [nm] = 640. Lifetime ( $\text{H}_2\text{O}$ ,  $\lambda_{\text{exc}}$  = 445 nm,  $\lambda_{\text{em}}$  = 630 nm) = 360 ns (aerated), = 630 ns (degassed).

### 3.7.2 Cell Studies with Ru-Z•AuNP13 and Ru-Z•AuNP100

Cell culture was performed by Mr Sunil Claire and Dr Robert Harris in the School of Biosciences, University of Birmingham, and Confocal luminescence microscopy was carried out by both Mr Sunil Claire and the author. Toxicology data was obtained by Mr Sunil Claire, and flow cytometry was performed by Dr Nikolas Hodges.<sup>31</sup>

#### *Preparation of Cells for Electron Microscopy*

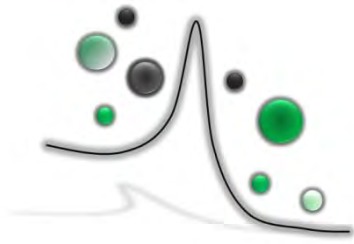
Cells were grown on coverslips and incubated with nanoparticles as described in the protocol for luminescence microscopy,<sup>31</sup> by Sunil Claire. Following incubation cells were washed twice in PBS and fixed in 2.5% glutaraldehyde for 24 hours. Samples were subsequently prepared at the Centre for Electron Microscopy, University of Birmingham: Samples were placed in 1% osmium tetroxide solution and gradually dehydrated with alcohol and propylene

oxide. The cells were embedded in resin and ultrathin sections (50–150 nm) were obtained and mounted onto formvar-coated 200 mesh copper electron microscope grids. Samples were stained with uranyl acetate to improve cell contrast.

### 3.8 Chapter Three References

- (1) Boisselier, E.; Astruc, D. *Chem. Soc. Rev.* **2009**, *38*, 1759.
- (2) Erathodiyil, N.; Ying, J. Y. *Acc. Chem. Res.* **2011**, *44*, 925.
- (3) Saha, K.; Bajaj, A.; Duncan, B.; Rotello, V. M. *Small* **2011**, *7*, 1903.
- (4) Bouzigues, C.; Gacoin, T.; Alexandrou, A. *ACS Nano* **2011**, *5*, 8488.
- (5) Shi, D.; Bedford, N. M.; Cho, H.-S. *Small* **2011**, *7*, 2549.
- (6) Kotov, N. A.; Winter, J. O.; Clements, I. P.; Jan, E.; Timko, B. P.; Campidelli, S.; Pathak, S.; Mazzatenta, A.; Lieber, C. M.; Prato, M.; Bellamkonda, R. V.; Silva, G. A.; Kam, N. W. S.; Patolsky, F.; Ballerini, L. *Adv. Mater.* **2009**, *21*, 3970.
- (7) Chithrani, B. D.; Ghazani, A. A.; Chan, W. C. W. *Nano Lett.* **2006**, *6*, 662.
- (8) Gilijohann, D. A.; Seferos, D. S.; Daniel, W. L.; Massich, M. D.; Patel, P. C.; Mirkin, C. A. *Angew. Chem. Int. Ed.* **2010**, *49*, 3280.
- (9) Popović, Z.; Liu, W.; Chauhan, V. P.; Lee, J.; Wong, C.; Greytak, A. B.; Insin, N.; Nocera, D. G.; Fukumura, D.; Jain, R. K.; Bawendi, M. G. *Angew. Chem. Int. Ed.* **2010**, *49*, 8649.
- (10) Murphy, C. J.; Gole, A. M.; Stone, J. W.; Sisco, P. N.; Alkilany, A. M.; Goldsmith, E. C.; Baxter, S. C. *Acc. Chem. Res.* **2008**, *41*, 1721.
- (11) Tantra, R.; Knight, A. *Nanotoxicology* **2011**, *5*, 381.
- (12) Saha, K.; Agasti, S. S.; Kim, C.; Li, X.; Rotello, V. M. *Chem. Rev.* **2012**, *112*, 2739.
- (13) Lammers, T.; Aime, S.; Hennink, W. E.; Storm, G.; Kiessling, F. *Acc. Chem. Res.* **2011**, *44*, 1029.
- (14) Cattaneo, A. G.; Gornati, R.; Sabbioni, E.; Chiriva-Internati, M.; Cobos, E.; Jenkins, M. R.; Bernardini, G. *J. Appl. Toxicol.* **2010**, *30*, 730.
- (15) Zhao, F.; Zhao, Y.; Liu, Y.; Chang, X. L.; Chen, C. Y.; Zhao, Y. L. *Small* **2011**, *7*, 1322.
- (16) Choi, C. H. J.; Zuckerman, J. E.; Webster, P.; Davis, M. E. *Proc. Natl. Acad. Sci. U. S. A.* **2011**, *108*, 6656.
- (17) Thakor, A. S.; Jokerst, J.; Zavaleta, C.; Massoud, T. F.; Gambhir, S. S. *Nano Lett.* **2011**, *11*, 4029.
- (18) Gilijohann, D. A.; Seferos, D. S.; Daniel, W. L.; Massich, M. D.; Patel, P. C.; Mirkin, C. A. *Angew. Chem., Int. Ed.* **2010**, *49*, 3280.
- (19) Chou, L. Y. T.; Ming, K.; Chan, W. C. W. *Chem. Soc. Rev.* **2011**, *40*, 233.
- (20) Yeh, Y.-C.; Creran, B.; Rotello, V. M. *Nanoscale* **2012**, *4*, 1871.
- (21) Nativo, P.; Prior, I. A.; Brust, M. *ACS Nano* **2008**, *2*, 1639.
- (22) Popović, Z.; Liu, W.; Chauhan, V. P.; Lee, J.; Wong, C.; Greytak, A. B.; Insin, N.; Nocera, D. G.; Fukumura, D.; Jain, R. K.; Bawendi, M. G. *Angew. Chem., Int. Ed.* **2010**, *49*, 8649.
- (23) Huang, K. Y.; Ma, H. L.; Liu, J.; Huo, S. D.; Kumar, A.; Wei, T.; Zhang, X.; Jin, S. B.; Gan, Y. L.; Wang, P. C.; He, S. T.; Zhang, X. N.; Liang, X. J. *ACS Nano* **2012**, *6*, 4483.
- (24) Chithrani, B. D.; Ghazani, A. A.; Chan, W. C. W. *Nano Lett.* **2006**, *6*, 662.

- (25) Bartczak, D.; Muskens, O. L.; Nitti, S.; Sanchez-Elsner, T.; Millar, T. M.; Kanaras, A. G. *Small* **2012**, *8*, 122.
- (26) Möbius, W.; Van Donselaar, E.; Ohno-Iwashita, Y.; Shimada, Y.; Heijnen, H. F. G.; Slot, J. W.; Geuze, H. *J. Traffic* **2003**, *4*, 222.
- (27) Chithrani, B. D.; Chan, W. C. W. *Nano Lett.* **2007**, *7*, 1542.
- (28) Tkachenko, A. G.; Xie, H.; Coleman, D.; Glomm, W.; Ryan, J.; Anderson, M. F.; Franzen, S.; Feldheim, D. L. *J. Am. Chem. Soc.* **2003**, *125*, 4700.
- (29) Giljohann, D. A.; Seferos, D. S.; Daniel, W. L.; Massich, M. D.; Patel, P. C.; Mirkin, C. A. *Angew. Chem. Int. Ed.* **2010**, *49*, 3280.
- (30) Dykman, L. A.; Khlebtsov, N. G. *Chem. Rev.* **2014**, *114*, 1258.
- (31) Rogers, N. J.; Claire, S.; Harris, R. M.; Farabi, S.; Zikeli, G.; Styles, I. B.; Hodges, N. J.; Pikramenou, Z. *Chem. Commun.* **2014**, *50*, 617.
- (32) Frens, G. *Nature Phys. Sci.* **1973**, *241*, 20.
- (33) Rodríguez-Fernández, J.; Pérez-Juste, J.; García de Abajo, F. J.; Liz-Marzán, L. M. *Langmuir* **2006**, *22*, 7007.
- (34) Perrault, S. D.; Chan, W. C. W. *J. Am. Chem. Soc.* **2010**, *132*, 11824.
- (35) Jana, N. R.; Gearheart, L.; Murphy, C. J. *Chem. Mater.* **2001**, *13*, 2313.
- (36) Brown, K. R.; Walter, D. G.; Natan, M. J. *Chem. Mater.* **1999**, *12*, 306.
- (37) Ziegler, C.; Eychmueller, A. *J. Phys. Chem. C* **2011**, *115*, 4502.
- (38) Grabar, K. C.; Freeman, R. G.; Hommer, M. B.; Natan, M. J. *Anal. Chem.* **1995**, *67*, 735.
- (39) Mie, G. *Ann. Phys. (Berlin)* **1908**, *25*, 377.
- (40) Quinten, M.; Kreibitz, U. *Surf. Sci.* **1986**, *172*, 557.
- (41) Rogers, N. J.; Pikramenou, Z. *Patent* **2013**, WO/2013/004989.
- (42) Huang, T.; Murray, R. W. *Langmuir* **2002**, *18*, 7077.
- (43) Vickers, M. S.; Cookson, J.; Beer, P. D.; Bishop, P. T.; Thiebaut, B. *J. Mater. Chem.* **2006**, *16*, 209.
- (44) Pramod, P.; Sudeep, P. K.; Thomas, K. G.; Kamat, P. V. *J. Phys. Chem. B* **2006**, *110*, 20737.
- (45) Mayer, C. R.; Dumas, E.; Miomandre, F.; Meallet-Renault, R.; Warmount, F.; Vigneron, J.; Pansu, R.; Etcheberry, A.; Sécheresse, F. *New J. Chem.* **2006**, *30*, 1628.
- (46) Yu, Y.; Zhou, M.; Cui, H. *J. Mater. Chem.* **2011**, *21*, 12622.
- (47) Elmes, R. B. P.; Orange, K. N.; Cloonan, S. M.; Williams, D. C.; Gunnlaugsson, T. *J. Am. Chem. Soc.* **2011**, *133*, 15862.
- (48) Davies, A.; Lewis, D. J.; Watson, S. P.; Thomas, S. G.; Pikramenou, Z. *PNAS* **2012**, *109*, 1852.



---

# Chapter Four

---

Peptide-mediated

Delivery of

Luminescent

Nanoparticles in Cells

## 4.1 Introduction

This chapter discusses the preparation of different peptide sequences attached to gold nanoparticles in order to target the delivery of nanomaterials in biological systems. The amino acid abbreviations and structures used in this chapter are presented in Appendix 8. Peptide-coated nanoparticles are of interest in the field of biomedicine for the delivery of nanodevices into living organisms.<sup>1-4</sup> Nanomedicine is an ever growing area of research, but the progress in theranostic nanomaterials depends heavily on the development of targeted delivery.<sup>5</sup> Nanoparticles offer a scaffold on which to assemble targeting, labelling and therapeutic probes, thereby producing a multifunctional nanovehicle, as presented in the schematic of Figure 4.1. The targeting probe needs to deliver the cargo with high specificity to reduce the undesirable side-effects of unwanted therapeutic activity on healthy tissue.<sup>6</sup>

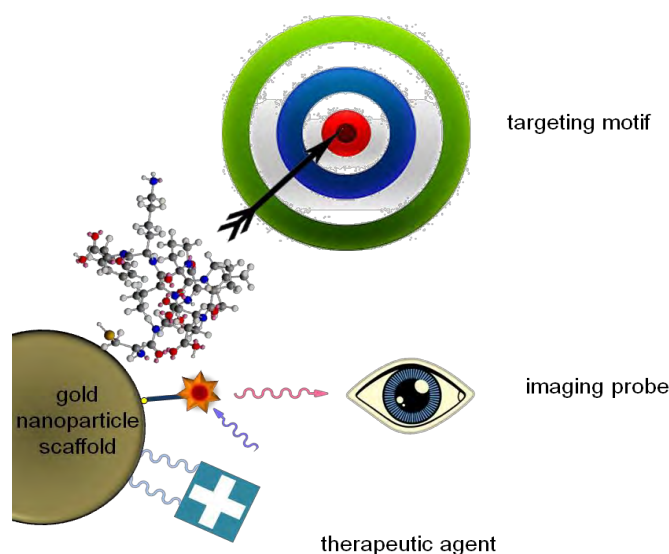


**Figure 4.1** Schematic of theranostic nanomaterials assembled by attachment of multiple probes onto a gold nanoparticle scaffold.

Understanding the effects of nanomaterials on cellular functions can provide useful insight into potential therapeutic applications. For example, gold nanoparticles have proved to be effective anti-cancer drug delivery systems<sup>7,8</sup> and photothermal cancer treatment agents.<sup>9-14</sup> Nanoparticle-mediated photothermal therapy exploits the unique absorptive properties of gold

nanoparticles; the particles absorb electromagnetic radiation at wavelengths resonant with the SPR, and can convert this energy into heat with almost 100 % efficiency on a picosecond timescale.<sup>15</sup> The localised heat produced can induce cellular damage and destroy diseased tissue, and is thus considered to be a potential anti-cancer therapeutic. The potential to target specific disease biomarkers, by modifying the particle surface with targeting vectors,<sup>16</sup> opens up new pathways towards diagnosis and treatment of disease using such therapeutic methods.

#### 4.1.1 Stabilising Gold Nanoparticles with Peptides

In 2004 Lévy and co-workers designed a short pentapeptide sequence, CALNN, to stabilise aqueous gold nanoparticles. The CALNN sequence (shown in Figure 4.2) incorporates a cysteine residue at the *N*-terminus, which provides a thiol functional group for attachment to gold nanoparticles. The alanine (A) and leucine (L) amino acids are relatively hydrophobic and promote the self-assembly of the peptide close to the particle surface to minimise their exposure to water. The two asparagine (N) amino acids are hydrophilic, which aids the solubility of the nanoparticles at the peptide terminus facing the solvent.<sup>17</sup>

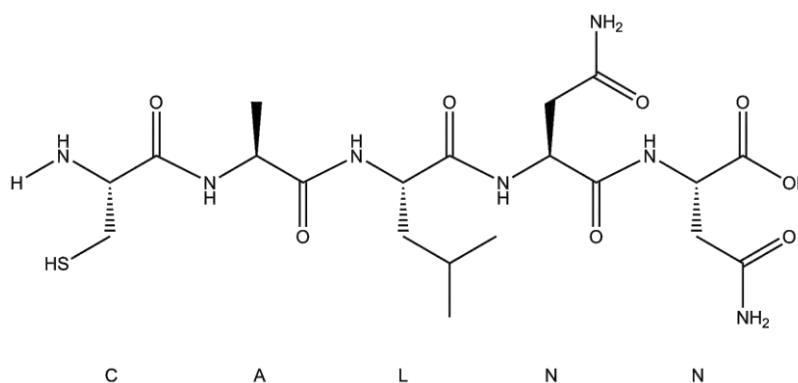


**Figure 4.2** *CALNN peptide sequence.*

The resulting CALNN-coated gold nanoparticles are very stable in aqueous buffer, can be freeze-dried, stored as powders and redispersed. Gold nanoparticles functionalised with CALNN, and

longer derivatives of the peptide, have since been used in the delivery of gold nanoparticles into HeLa cells (human ovarian cancer cell-line).<sup>18,19</sup>

#### 4.1.2 Cell-penetrating Peptides

The cell membrane (plasma membrane) is comprised of a phospholipid bilayer, which is abundant in negatively charged heparan sulphate proteins on the extracellular face.<sup>20</sup> The effective transport of hydrophilic molecules (such as proteins, peptides, drugs and dyes) into cells is very difficult due to the impermeable barrier of the membrane to such moieties, and thus there has been a growth of interest in the development of cell-penetrating peptides (CPP) due to their potential as transport vectors for attached cargo. The mechanism of cargo delivery can either be via penetration of the membrane or by endocytic processes, and is found to be greatly affected by the size and nature of the cargo.<sup>21-24</sup>

In the field of synthetic peptides, there are several properties of amino acids which can be exploited to induce transport across the cell membrane. Hydrophobicity helps to translocate cargo but often leads to solubility problems in water,<sup>23</sup> and therefore there are two main strategies employed in CPP design: The first mechanism for cell penetration is to use electrostatic recognition, by producing peptides which contain multiple positively charged amino acid groups; amino acids such as lysine, histidine, ornithine and arginine, which are all cationic at physiological pH, interact strongly with the negatively-charged cell membrane.<sup>20,23-25</sup> The most popular naturally occurring peptides that have been found to penetrate the cell membrane through screening assays are: the Tat peptide, which is the 48–60 amino-acid chain peptide (GRKKRRQRRRPPQ) taken from the Tat protein found in the HIV-1 virus;<sup>25</sup> and penetratin, from the *Drosophila* (fruit fly).<sup>26</sup> Both of these peptides are rich in arginine residues, which are particularly favourable because they can form bidentate

hydrogen bonds with the cell membrane through the guanidinium head group on the side-chain (as shown in Figure 4.3), and are particularly potent in facilitating cell delivery.<sup>13,25,27</sup> Amongst the polyarginines, sequences of seven or nine arginine residues have been the most widely used.<sup>20</sup> The second mechanism for cell penetration is to utilise amphiphilic peptides which can interact with the lipid bilayer of the cell membrane. Primary amphiphilic peptides can be used by the sequential assembly of hydrophobic and hydrophilic domains within the sequence, or the secondary structure can play a role in cell delivery; amphiphilic alpha-helical structures expose the hydrophilic amino acids to one side of the helix, and the hydrophobic residues to the other, making the peptide ideal for binding to a lipid bilayer, such as the model amphiphilic peptide (MAP).<sup>28</sup>

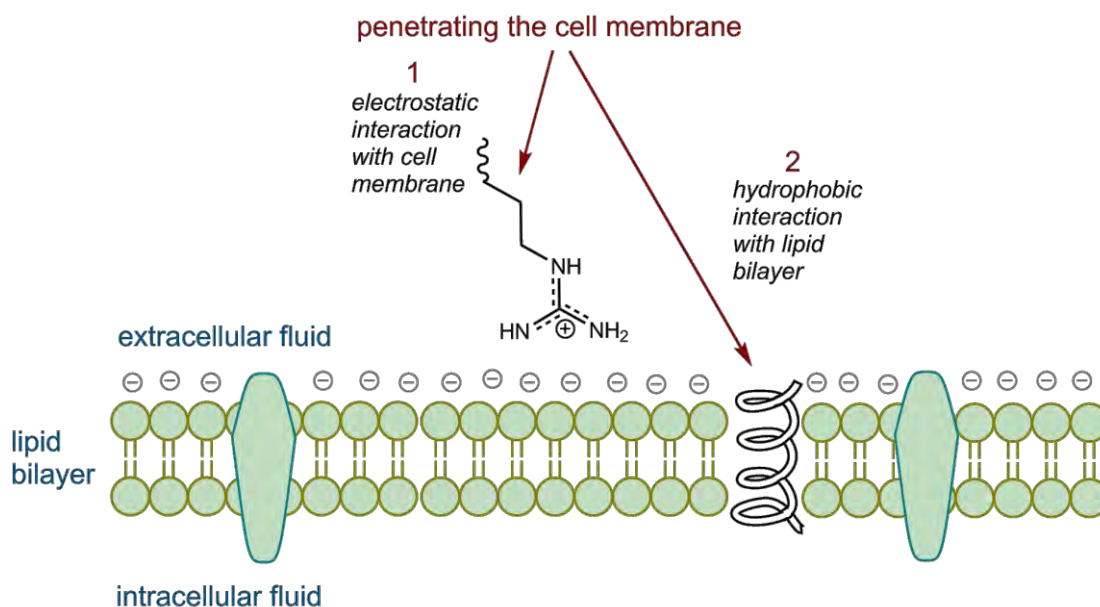


**Figure 4.3** Schematic of strategies to cross the cell membrane. 1- electrostatic interaction of the guanidinium head group of an arginine residue with the negatively charged cell membrane. 2- insertion of an amphiphilic peptide structure into the amphiphilic cell membrane due to hydrophobicity.

Similar structure occurs naturally in membrane proteins such as ion channels. However, these amphiphilic peptides can irreversibly destabilise the cell membrane and induce cytotoxicity.<sup>23</sup>

So far, a simplistic picture of nanoparticles coated with targeting peptides has been assumed, in which the nanoparticles present the targeting peptides to the bulk solvent, and thus can interact accordingly. This tenet holds true in simple solvent systems, such as water or buffer. However, the picture is far more complex in biological matrices and it is important to consider these additional effects upon the surface-chemistry of the nanoparticles when trying to achieve targeting. As with many foreign bodies, nanoparticles can be surrounded by a dynamic layer of proteins and other biomolecules following contact with biological media, which is often referred to as a protein ‘corona’.<sup>29</sup> This *in situ* protein layer is complex and variable, and can mask targeting motifs on the surface. The corona can also create a recognition signature on the surface of the particle, and direct its internalisation route both *in vitro* and *in vivo*, thus directing the nanoparticle off its intended target.<sup>30,31</sup> Therefore, peptide-mediated specific delivery of nanoparticles is far from trivial in biological systems.

### **4.1.3 Peptide-mediated Delivery of Luminescent Gold Nanoparticles in Cancerous Cells**

The cellular uptake of nanoparticles has been found to depend on both particle size and the surface functionality,<sup>32-35</sup> and many types of nanomaterials are thought to enter cells by endocytic pathways, which compartmentalise the particles in vesicles of extra-cellular fluid within the cell. However, it is usually desirable to deliver nanomaterial into the intracellular fluid (cytosol), so that the surface-functionalisation is exposed to the intra-cellular environment, which can be achieved by coating the particles in CPP. Capping gold nanoparticles with Tat and penetratin peptides has been found to enhance the cellular uptake and, in some instances, deliver many particles into the cytosol.<sup>13,18,36,37</sup> Similarly, polyarginine-capped 20 nm gold nanoparticles have been reported to increase uptake in Jurkat (human T lymphocyte) cells, up to five-fold.<sup>38</sup> Polyarginines have also been conjugated to

quantum dots to aid their cellular uptake,<sup>27,39</sup> and work by Lagerholm *et al.* shows that their cellular uptake increases by two orders of magnitude in a variety of mammalian cell lines.<sup>39</sup>

Despite the developments in nanoparticle delivery with CPP, such peptides are inherently non-specific in their translocation properties,<sup>40</sup> whereas targeted delivery is desirable for most *in vivo* applications of cellular delivery. Intrinsically, nanoparticles can be very useful for targeted delivery to tumour tissue, using their *size* as a passive targeting technique; upon injection *in vivo*, particles < 5nm tend to be removed from the blood rapidly by renal clearance *via* the kidneys, and microsized particles are mechanically filtrated from the blood and cleared by the liver and the spleen, whereas nanoparticles in the 10–500 nm size range can have long circulation half-lives.<sup>6</sup> In addition to this, the vasculature of tumorous tissue tends to be fenestrated and the lymphatic system poor, due to the speed at which the tissue grows, and therefore tumours are more permeable to nanoparticles than normal tissue. This is referred to as the enhanced permeation and retention (EPR) effect, and can be exploited as a *passive* targeting strategy for drug delivery to tumour tissue, although the effect is not substantial.<sup>5,41,42</sup>

The *active* targeting of cancerous cells for drug delivery can be achieved by exploiting the disparity in local pH between cancerous and non-cancerous tissue. Cancer cells tend to suffer oxygen deprivation (hypoxia) because they rapidly outgrow their blood supply. The cells adapt to the hypoxic environment and metabolise glucose through alternative pathways. This increases the acidity of the extracellular environment, mainly due to the production of lactic acid, and the slightly reduced pH in the extracellular environment of cancerous cells can therefore be employed as an effective cancer biomarker;<sup>43,44</sup> normal non-cancerous human tissue has an average pH of 7.5, and human tumour tissue of 7.0.<sup>45</sup> Acid-activated peptide delivery of nanoparticles is an established strategy for targeted distribution; surface-bound

peptides which can shield their cell-penetrating function, and then unmask this upon pH change, can potentially target cancerous cells. A recent example of such strategy by Jin *et al.*,<sup>46</sup> employs a modified Tat peptide to deliver micelles, in which all the amines in the lysine side-chains were converted to succinyl amides, to inhibit the Tat peptide's non-specific interactions with cell membranes. Upon interaction with acidic tumour tissue, the amides can hydrolyse to amines, and restore the function of the Tat peptide (see Figure 4.4) to allow translocation across the membranes of the tumorous cells and delivery of the attached micelles (*ca.* 100 nm in diameter).<sup>46</sup>

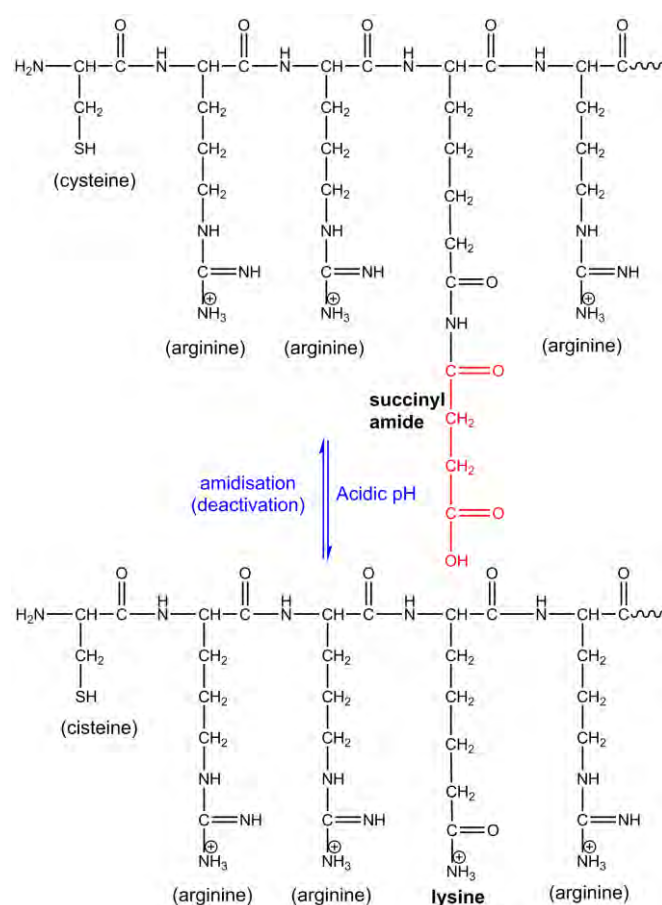


**Figure 4.4** Schematic, adapted from Shen *et al.*, showing CRRKR portion of Tat sequence.<sup>46</sup>

Another acid-activated peptide, which has been developed by Engelman and co-workers, is the pH low insertion peptide (pHLIP), which is derived from a sequence in bacteriorhodopsin.<sup>47-50</sup> In the isolated pHLIP form (AAEQNPIYWARYADWLFTTPLL<sub>5</sub>LDLALLVDADEGTCG), the carboxylic acid side

chains of the aspartic acid residues (D) can be either deprotonated (at  $\text{pH} > 7$ ) or protonated (at  $\text{pH} < 7$ ). At  $\text{pH} > 7$ , the peptide is hydrophilic, water-soluble and weakly coordinates to the cell membrane, with no ordered secondary structure. However, at  $\text{pH} < 7$ , the protonated peptide is hydrophobic, which induces its partitioning from aqueous solution by insertion into cell membrane via the formation of a transmembrane  $\alpha$ -helix structure (See Figure 4.5).<sup>51,52</sup> The peptide also has a cysteine residue near the C-terminus, which can attach to cargo through the thiol group for cellular insertion.

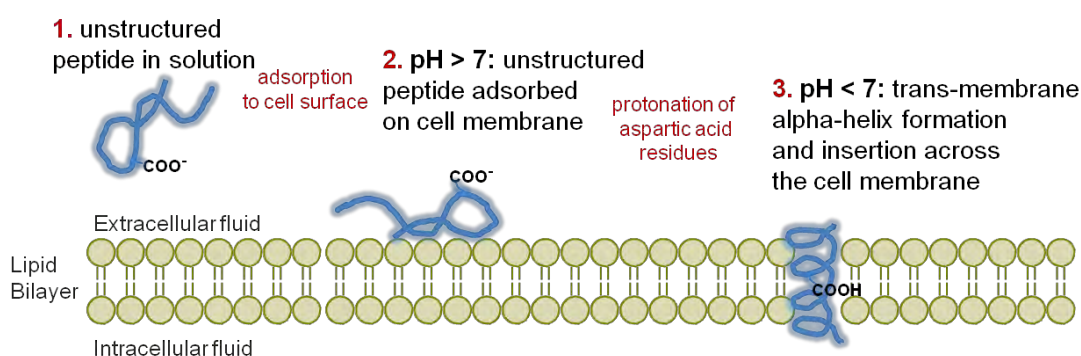


**Figure 4.5** Schematic of the insertion mechanism of pHLIP across the cell membrane. Adapted from reference.<sup>53</sup>

The delivery of 13 nm gold nanoparticles using pHLIP (by attaching the gold to the peptide via the cysteine using S–Au chemistry) has been reported recently by Pikramenou and co-workers, for pH-controlled delivery into platelets.<sup>3</sup> The nanoparticles were also labelled with a luminescent europium(III) probe for optical tracking of the pH-active probes. However, the europium(III) complex has to be excited in the UV region of the electromagnetic spectrum (*ca.* 340 nm), which is often not possible with glass optics and conventional microscopes, and is also undesirable for biological tissue. Similarly, the pH-sensitive uptake of pHLIP-coated 1 nm nanogold by HeLa cells (human ovarian cancer cells) and *in vivo* in a murine model has been reported by the Engelman group.<sup>54</sup> Cellular uptake was analysed in a destructive fashion by fixing cells and then treating them with silver enhancement solution, in order to visualise

the gold nanoparticles, and an enhancement by a factor of 1.6 was observed for cells incubated with particles at acidic pH (6.5). The gold content of organ tissue following the *in vivo* studies was analysed by inductively-coupled plasma mass spectrometry (ICP-MS) of digested tissue, and enhanced gold concentrations were found in the tumorous tissue due to the peptide. More recently, Zhang and Tan<sup>55</sup> have pushed the application of pHLIP-mediated delivery of nanoparticles further towards pH-targeted drug delivery systems, for the delivery of 140 nm mesoporous silica nanoparticles (with 3 nm pores), and loaded with Doxorubicin (a chemotherapy drug) to tumorous tissue.

#### 4.1.4 Peptide-mediated Nuclear Targeting of Nanoparticles

The cell *nucleus* is a desirable target for many applications because the genetic information and transcription machinery all reside within the nuclear envelope. Therefore, nuclear targeting opens up a route to both diagnosis of disease phenotype and gene therapy.<sup>56</sup> Targeting the nucleus of a cell is not trivial because the probe must firstly enter the cell, secondly escape the endosomal or lysosomal pathways to be exposed to intracellular fluid, thirdly possess a nuclear localising signal to interact with the nuclear pore, and finally physically be able to cross the nuclear envelope (a double phospholipid bilayer membrane, embedded with proteins).<sup>57</sup> The nuclear uptake of gold nanoparticles has been shown by attachment of peptides to gold nanoparticles and nanorods, namely well-known nuclear localisation signal (NLS) peptides, by El-Sayed and co-workers.<sup>57,58</sup> However, Brust and co-workers have studied nanoparticle uptake in cancer cells and found that gold nanoparticles capped in a mixture of NLS peptides with Tat and penetratin (CPPs) did cross the nuclear membrane, whereas particles coated with each single peptide did not.<sup>18</sup> Similarly Feldheim and co-workers<sup>59,60</sup> attached similar NLS peptide-conjugated BSA (bovine serum albumen) to gold nanoparticles, but nuclear uptake was only observed if the particles were injected into the cytosol; they were not translocated to the nucleus following cell incubation from outside of

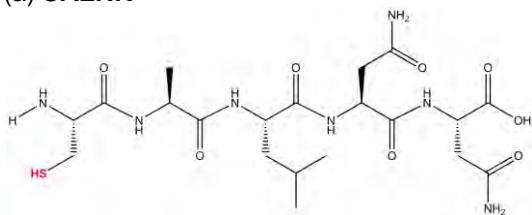
the cell membrane because the particles became trapped in endosomal compartments following endocytic uptake.

A new synthetic peptide, C105Y (CSIPPEVKFNKPFVYLI) has been found to enhance gene expression by conjugating the peptide to polylysine-condensed DNA complexes, forming DNA nanoparticles of *ca.* 25 nm.<sup>61-63</sup> Since these empirical discoveries of enhanced expression with the C105Y peptide, Rhee and Davis have interrogated the mechanism by which the peptide itself enters the cell.<sup>63</sup> Uptake and nuclear localisation within 10 min of incubation was observed for both fluorescently-labelled C105Y and PFVYLI peptides, but nuclear localisation was not observed for labelled SIPPEVKFNK sequences. Therefore it is believed that C105Y peptide enters the cell through the PFVYLI sequence. The internalisation process was observed at both 37 °C and 4 °C, which suggests that the uptake occurs in an energy-independent fashion (i.e. a non endocytic process), as endocytic pathways are completely inhibited at 4 °C; endocytosis is an energy-requiring process, unlike passive transport, and thus the process is retarded at low temperatures. In addition, control experiments with D-C105Y peptides (all amino acids of D isomers rather than L isomers) showed cellular internalisation, but no transport to the nucleus. This suggests that the cellular uptake is not receptor-mediated, as no specific spatial orientation is required, but that nuclear targeting *is* because the process is stereoselective.

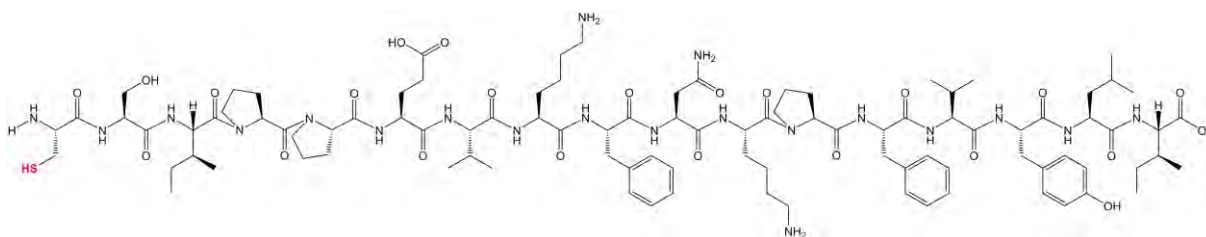
The mechanism by which C105Y appears to target the cell nucleus lends itself to attachment to gold nanoparticles as the *N*-terminal cysteine residue (C) can be used to attach to the nanoparticle, leaving the active PFVYLI sequence exposed at the *C*-terminus for targeting.<sup>63</sup> In addition, the non-endocytic uptake and successful translocation of 25 nm DNA nanoparticles with C105Y<sup>61-63</sup> suggest that the peptide may prevent gold nanoparticles from becoming trapped in endosomes within the cell.



(a) CALNN



(b) C105Y (CSIPPEVKFNKPFVYLI)



(c) pHLIP (AAEQNPIYWARYADWLFTTPLL LLDLALLVDADEGTCG)

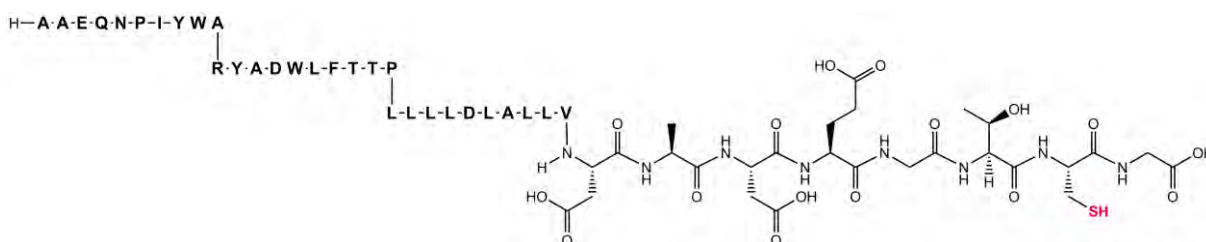


**Figure 4.7** Structures of the peptide sequences discussed in this chapter, each consisting of L-amino acids. Cysteine 'SH' groups are the expected sites at which each peptide will strongly bind to gold nanoparticles via S–Au chemistry (highlighted in red).

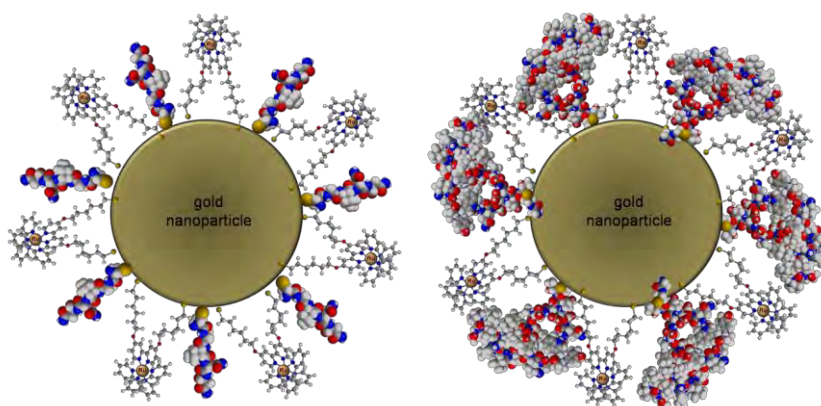


**Figure 4.8** Schematics of *Ru-CALNN•AuNP13* (left) and *Ru-pHLIP•AuNP13* (right).

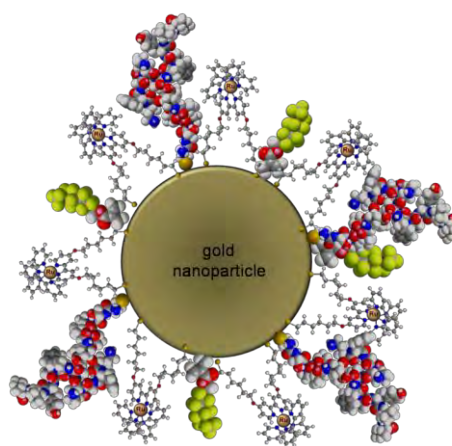


**Figure 4.9** Schematic of *Ru-C105Y-Z•AuNP13*.

As a preliminary study, CALNN was chosen for its known stabilising effects imparted to gold nanoparticles (as discussed in Section 4.1), pHLIP was chosen for targeting cancer cells using pH-activated uptake, and C105Y for its nuclear targeting properties. Following the study of surfactant-mediated coating of nanoparticles with **RuSH**,<sup>64,65</sup> outlined in Chapter Two, each peptide was examined to see if it could function in the same fashion as the surfactant moieties, displacing the citrate anions and preventing aggregation upon addition of the cationic **RuSH** complex.

## 4.2 Synthesis and Characterisation of Co-coated Gold Nanoparticles with Peptides and RuSH

**RuSH** and citrate-stabilised 13 nm gold nanoparticles were synthesised as reported in Chapter Two (Sections 2.2 and 2.3), and the three peptides were purchased from Alta Biosciences. The C105Y and CALNN peptides are both soluble in water, whereas the pHLIP sequence is not, and thus had to be dissolved in 10 % DMSO / phosphate buffer, as previously carried out by Davies *et al.*<sup>3</sup> All three peptides contain a single cysteine amino acid which has a free thiol group available for binding to gold (Figure 4.7).

The surface coating of 13 nm citrate gold nanoparticles (9 nM) with CALNN, C105Y and pHLIP is monitored by UV-Vis absorption spectroscopy of the SPR (Figure 4.10).

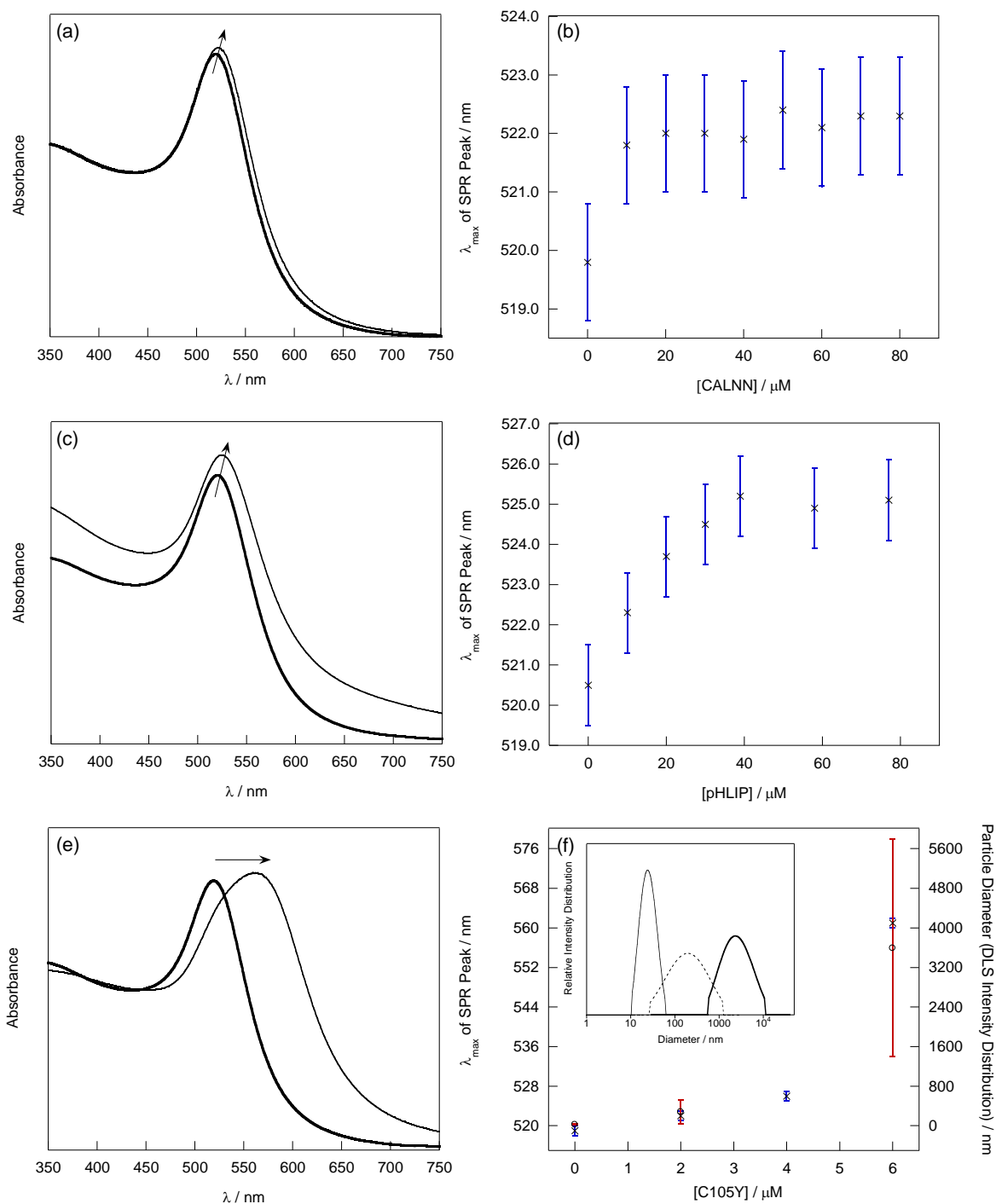


**Figure 4.10** UV-Vis absorption spectra of 9 nM citrate gold nanoparticles (bold solid line) (a,c,e) and upon the addition of (a) 80  $\mu\text{M}$  CALNN (solid line), (b) 80  $\mu\text{M}$  pHLIP (solid line), and (c) 6  $\mu\text{M}$  C105Y (solid line). SPR  $\lambda_{max}$  vs. [peptide] plotted for titrations of (b) 10–80  $\mu\text{M}$  CALNN (d) 10–80  $\mu\text{M}$  pHLIP, and (f) 2–6  $\mu\text{M}$  C105Y, into 9 nM citrate gold nanoparticles (x). DLS intensity distributions vs. [peptide] also plotted in (f) as (o), with DLS intensity distribution of 2  $\mu\text{M}$  (solid), 4  $\mu\text{M}$  (dashed) and 6  $\mu\text{M}$  (bold) C105Y shown in the inset. UV-Vis absorption error bars represent the precision of the spectrometer, and DLS error bars represent the calculated errors of the intensity distributions,  $\pm 1$  SD.

Absorption of peptide to the gold nanoparticle surface changes the surface dielectric constant, and results in a shift in the SPR  $\lambda_{\max}$  because the quantum-confined electrons oscillate at a slightly different frequency with this electronic change. Similar effects are seen with adsorption of surfactant molecules to gold nanoparticles in Chapter Two, Section 2.5. Titration of CALNN (0–80  $\mu\text{M}$ ) into 13 nm gold nanoparticles (9 nM) gives rise to a 2 nm bathochromic shift to 522 nm in the SPR band (Figure 4.10a/b), as reported by Brust and co-workers (with the addition of 0.7 mM CALNN to 7 nM 13 nm citrate gold nanoparticles),<sup>17</sup> and saturation occurs at *ca.* 20  $\mu\text{M}$  CALNN, i.e. *ca.* 2000 peptides per nanoparticle. The addition of pHLIP to the nanoparticles gives rise to a greater, 5 nm red-shift in the SPR  $\lambda_{\max}$ , to 525 nm (Figure 4.10c/d), similar to that reported by Pikramenou and co-workers,<sup>3</sup> although in this Chapter the pHLIP peptide used has a cysteine thiol group at the *C*-terminus (Figure 4.7), whereas in the study by Davies *et al.*, a cysteine-thiopyridyl derivative was used.<sup>3</sup> Saturation is observed at *ca.* 50  $\mu\text{M}$  pHLIP (5500 peptides per nanoparticle), which indicates that pHLIP does not bind as strongly to the nanoparticles as CALNN. This is not surprising because the cysteine residue at the *N*-terminus of CALNN is far more exposed for binding to the gold surface than the cysteine in pHLIP, which is the penultimate amino-acid to the *C*-terminus of a 38-amino acid chain.

Unlike CALNN and pHLIP, addition of C105Y to citrate-stabilised gold nanoparticles induces a large red-shift and a broadening of the SPR upon titration into 13 nm citrate gold nanoparticles (Figure 4.10e/f), which is indicative of aggregation.<sup>66</sup> DLS was performed during the titration (Figure 4.10f), and demonstrates that even upon addition of only 2  $\mu\text{M}$  C105Y (200 peptides per nanoparticle) an increase in the average intensity distribution diameter is observed, from 26 $\pm$ 10 nm to 280 $\pm$ 240 nm (i.e. an increase in the average number distribution from 14 $\pm$ 3 nm to 35 $\pm$ 9 nm). The diameter increases further to 3590 $\pm$ 2200 nm (i.e. 730 $\pm$ 190 nm, average number distribution) with 600 peptides per particle (Figure 4.10f inset).

This is unsurprising, because at pH 7 the C105Y peptide is monocationic due to protonation of the lysine sidechain ( $pK_a = 10.67$ ),<sup>67</sup> whereas CALNN carries an overall neutral charge and pHLIP possesses a 5<sup>-</sup> charge. The positive charge of the C105Y peptide induces aggregation of the negatively charged citrate nanoparticles, as was observed with ruthenium(II) complexes in Chapter Two, and thus C105Y•AuNP13 could not be isolated.

Nanoparticles coated in both CALNN and pHLIP were isolated by size-exclusion chromatography using Sephadex® G-25, eluting with water, analogous to the method used by Brust<sup>17</sup> and Pikramenou.<sup>3</sup> The coated nanoparticles elute first in a single band through the void volume of the column, isolating **CALNN•AuNP13** and **pHLIP•AuNP13** as aqueous sols; the excess free complex and peptide interact with the stationary phase and elute much more slowly. The zeta potential of the nanoparticles changes with the coating of each peptide; displacement of citrate anions by the neutral CALNN peptide gives rise to a reduction in the magnitude of the negative potential between the dispersion medium and the stationary layer of fluid associated with the particle, from  $-40 \pm 5$  mV (uncoated citrate 13 nm gold nanoparticles) to  $-22 \pm 4$  mV for isolated **CALNN•AuNP13** (both measured at 2 nM). Similarly, displacement of the citrate anions with the negatively charged pHLIP peptide also reduces the negative zeta potential (from  $-40 \pm 5$  mV) to  $-19 \pm 4$  mV for isolated **pHLIP•AuNP13** (measured at 2 nM), in agreement with previously reported data.<sup>3</sup> The bulky 38-amino acid peptide is likely to be less charge dense than the corresponding anions displaced at the surface, and thus a reduction in the zeta potential magnitude is expected, even though pHLIP bears a 5<sup>-</sup> charge.

For the purpose of imaging, the targeted delivery of nanoparticles in cells, luminescent gold nanoparticles are prepared by coating 13 nm citrate gold nanoparticles with each peptide and **RuSH**, as described below.

### 4.2.1 Synthesis and Nanoparticle Characterisation of Ru-CALNN•AuNP13, Ru-pHLIP•AuNP13 and Ru-C105Y-Z•AuNP13.

The co-coating of 13 nm gold nanoparticles with the luminescent ruthenium(II) complex **RuSH** and either CALNN or pHLIP (shown in Figure 4.11) is achieved in an analogous fashion to the method reported by Pikramenou and co-workers,<sup>3</sup> in which gold nanoparticles are co-coated with pHLIP and a europium(III) complex.

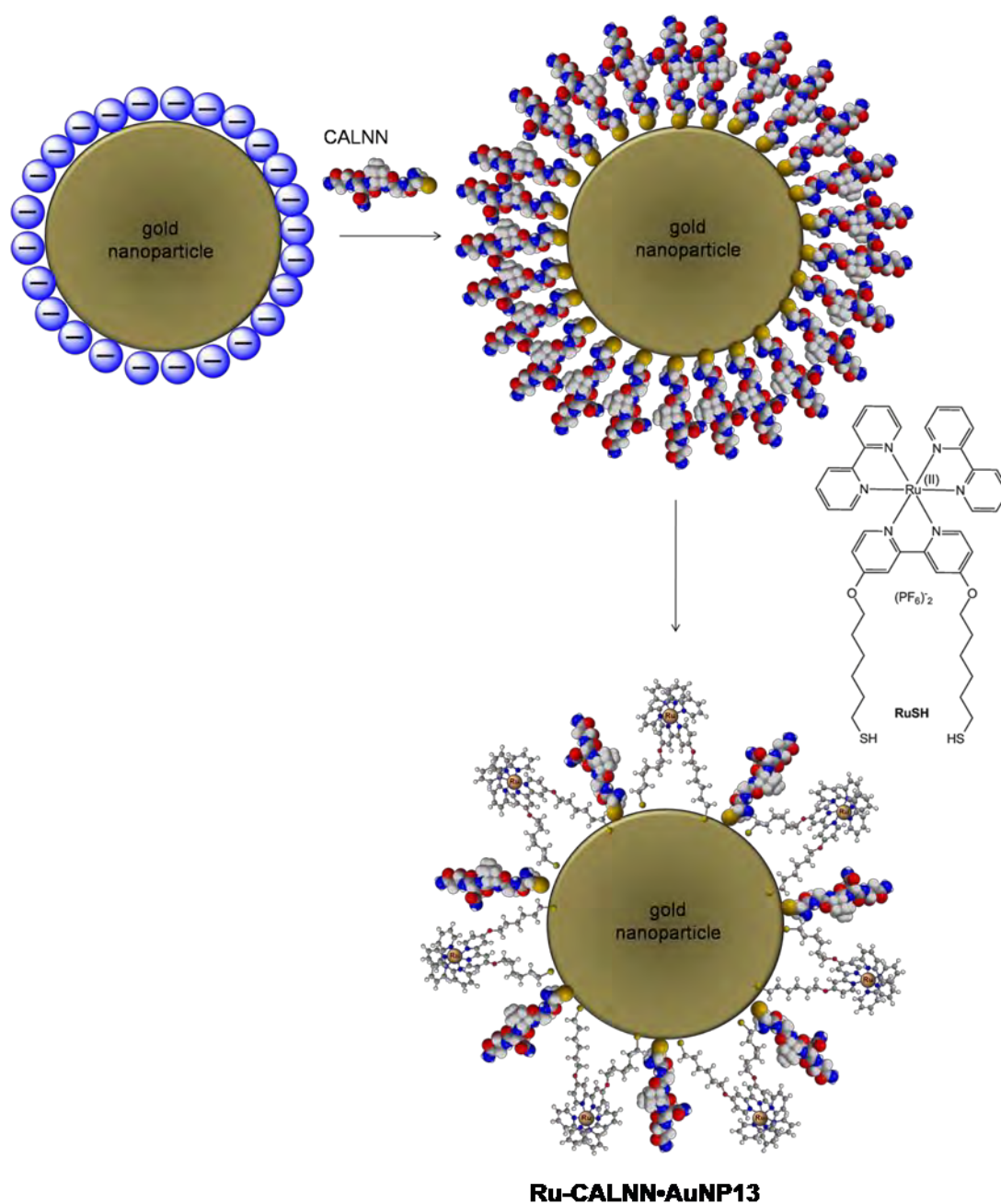


**Figure 4.11** Schematic of co-coating procedure for peptide/**RuSH** gold nanoparticles, with CALNN.

The initial coating of the gold nanoparticles with peptide can stabilise the particles to some extent, with respect to aggregation, and subsequently the **RuSH** cationic complex can be added. This strategy is not possible, however, with the C105Y peptide, as it also induces aggregation of the nanoparticles due to its overall positive charge at pH 7. Therefore, a surfactant-mediated coating process was implemented to circumvent this problem.

13 nm citrate gold nanoparticles (9 nM) are initially coated in peptide by adding either CALNN or pHLIP to a final concentration of 80  $\mu\text{M}$ . Subsequently, **RuSH** is added to the solution, and the SPR of the nanoparticles is monitored by UV-Vis absorption spectroscopy, as shown in Figures 4.12 and 4.13.

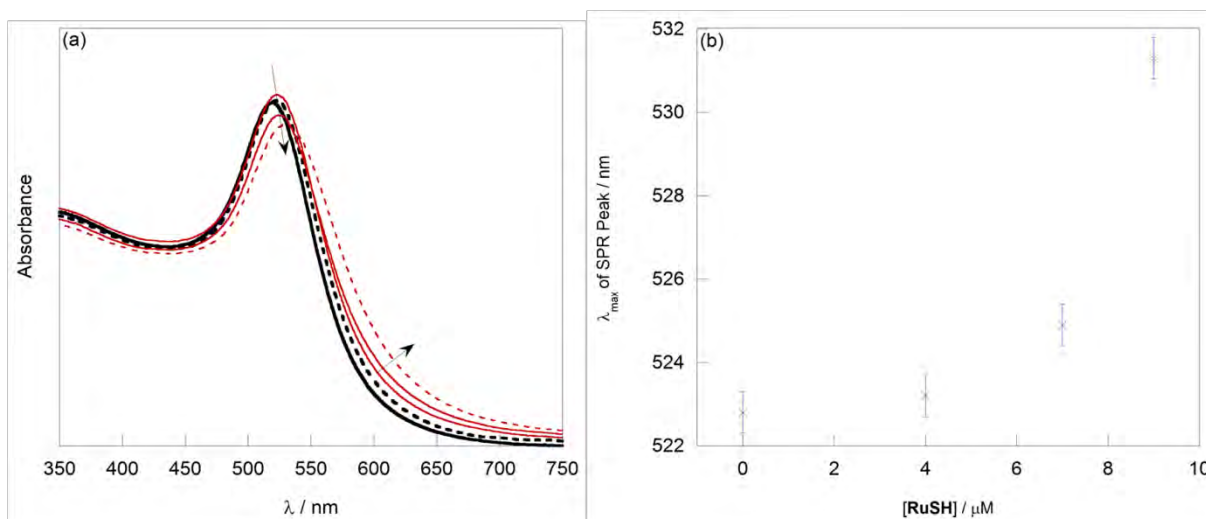


**Figure 4.12** UV-Vis absorption spectra of 1 mL (9 nM) 13 nm citrate gold nanoparticles (black solid line), with the addition of 80  $\mu\text{M}$  CALNN (black dashed line), followed by the titration of 4–7  $\mu\text{M}$  (red full line). Final addition of 9  $\mu\text{M}$  **RuSH** (red dashed) showed aggregation.

CALNN provides some stabilisation with respect to aggregation (Figure 4.12), by comparison with the addition of 4  $\mu\text{M}$  **RuSH** directly to uncoated 13 nm citrate gold nanoparticles, which gives rise to an immediate aggregation of the particles, as discussed in Chapter Two (Section 2.4). However, it was only possible to add 7  $\mu\text{M}$  (ca. 800 complexes per nanoparticles) **RuSH** before a significant increase in the SPR in the 550–750 nm range was apparent<sup>66</sup> (red dashed line, Figure 4.12a), accompanied by a shift in the SPR peak to 531 nm (Figure 4.12b).

In a similar fashion to CALNN, the pHLIP sequence appears to stabilise the particles enough to add **RuSH** complex without aggregation being induced, although to a much greater extent with this longer peptide (Figure 4.13). There is no evidence of aggregation upon addition of **RuSH** into the 9 nM gold nanoparticles/80  $\mu$ M pHLIP solution by inspection of the SPR, which shifts an additional 5 nm upon addition of **RuSH** to the 80  $\mu$ M pHLIP/9 nM gold nanoparticle mixture, saturating at *ca.* 50  $\mu$ M **RuSH** (Figure 4.13b).

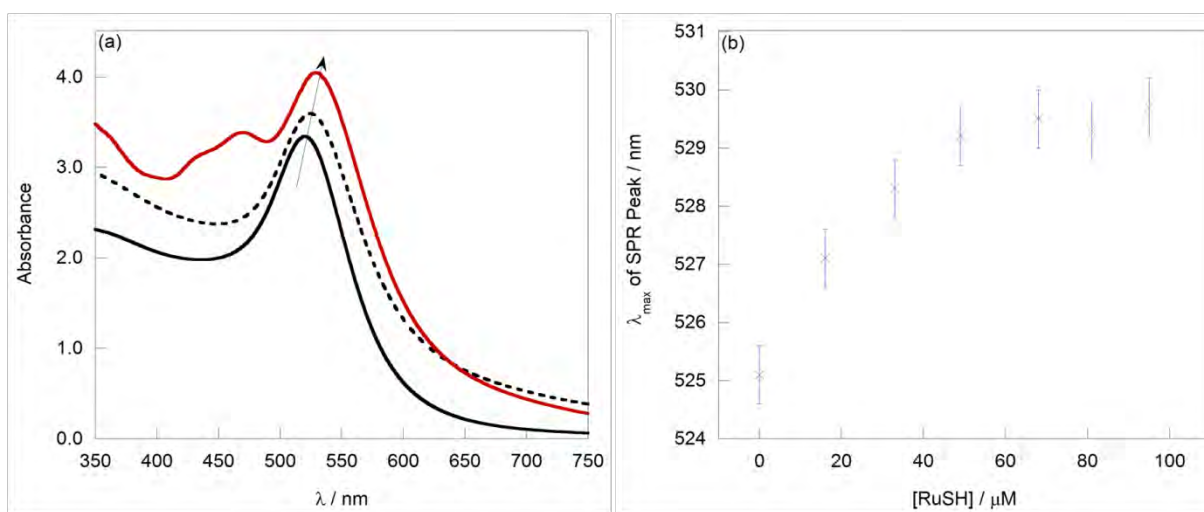


**Figure 4.13** (a) UV-Vis absorption spectra of 9 nM 13 nm gold nanoparticles (black solid), with the addition of 80  $\mu$ M pHLIP (black dashed) and 80  $\mu$ M **RuSH** complex. (b) Titration of 20–95  $\mu$ M **RuSH** into the 9 nM gold nanoparticles/80  $\mu$ M pHLIP solution, monitoring the shift in the SPR.

Both **Ru-CALNN•AuNP13** and **Ru-pHLIP•AuNP13** were isolated from excess free complex and peptide by size-exclusion chromatography using Sephadex® G-25, in the same fashion as **CALNN•AuNP13** and **pHLIP•AuNP13**, and characterised by UV-Vis absorption spectroscopy, as shown below (Figure 4.14).

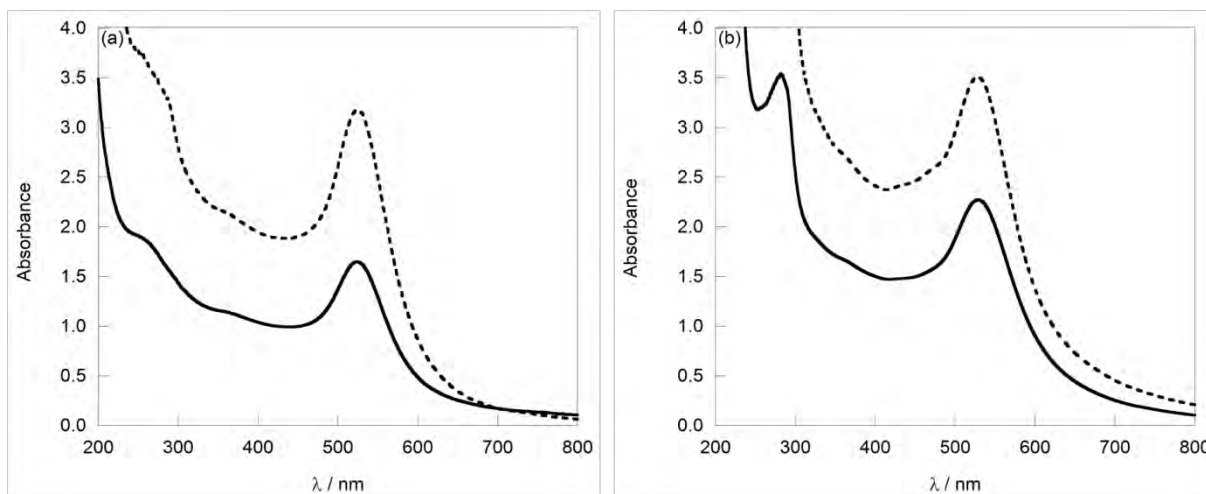


**Figure 4.14** (a) peptide = CALNN, (b) peptide = pHLIP. UV-Vis absorption spectra of non-isolated mixtures of gold nanoparticles (9 nM) / peptide (80  $\mu$ M) / RuSH (7  $\mu$ M (a) or 80  $\mu$ M (b)) (dashed line), and isolated **Ru-CALNN•AuNP13** (a) / **Ru-pHLIP•AuNP13** (b) (solid line) following size-exclusion chromatography.

Following isolation by size-exclusion, the  $\lambda_{\max}$  of the SPR for the isolated **Ru-CALNN•AuNP13** persisted at 525 nm, suggesting that the surface environment was not altered significantly during the isolation process, and dilution in the column by a factor of 1.8 was observed. The  $\lambda_{\max}$  of the isolated **Ru-pHLIP•AuNP13** also remained the same as the pre-columned solution, at 530 nm, and dilution by a factor of 1.5 was observed.

DLS (Figure 4.15) and electrophoretic light scattering have been used to analyse the coating process of the nanoparticles with peptide and RuSH; the particle properties of **Ru-CALNN•AuNP13** and **Ru-pHLIP•AuNP13** are summarised below in Table 4.1. Following the addition of peptide (either CALNN or pHLIP), the subsequent addition of RuSH is substantiated by changes in the SPR (Figures 4.12 and 4.13), the hydrodynamic radii (Figure 4.15, Table 4.1) and the zeta potential of the particles (Table 4.1); in both instances the average number distribution of **Ru-CALNN•AuNP13** and **Ru-pHLIP•AuNP13** increases slightly with respect to their **CALNN•AuNP13** and **pHLIP•AuNP13** analogues, and the zeta potentials decrease in value. In addition, the SPR  $\lambda_{\max}$  values red-shift, which indicates that

the surface dielectric constant has changes<sup>68</sup> upon functionalisation with the ruthenium(II) complex.

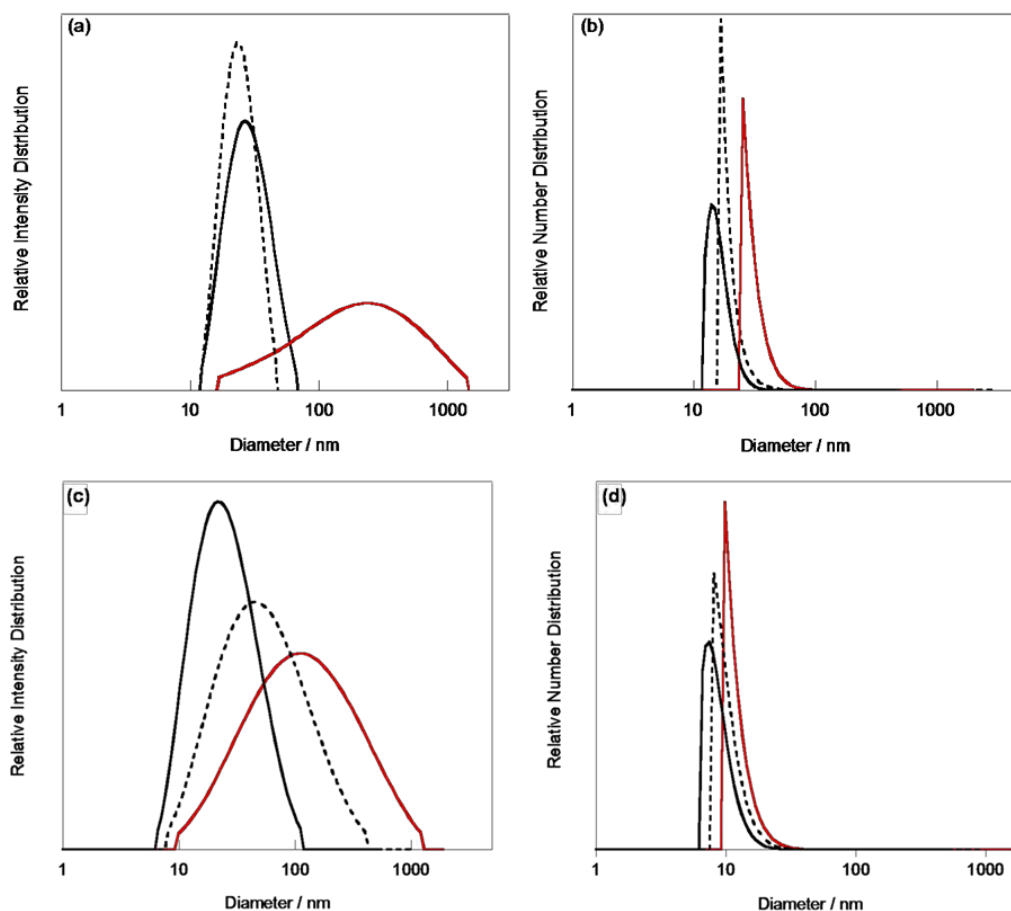


**Figure 4.15** DLS intensity distribution (a) and number distribution (b) of 2 nM citrate gold nanoparticles (bold solid black line), **CALNN•AuNP13** (dashed black line) and **Ru-CALNN•AuNP13** (solid red line). DLS intensity distribution (c) and number distribution (d) of 2 nM citrate gold nanoparticles (black), **pHLIP•AuNP13** (blue) and **Ru-pHLIP•AuNP13** (red).

**Table 4.1** Summary of nanoparticle characterisation data for nanoparticles coated with **CALNN**, **pHLIP** and **RuSH** complex

sample	diameter (DLS average number distribution) / nm	zeta potential (measured at 2 nM in water) / mV
<b>CALNN•AuNP13</b>	16±4	-19±4
<b>Ru-CALNN•AuNP13</b>	20±5	-34±2
<b>pHLIP•AuNP13</b>	11±3	-22±4
<b>Ru-pHLIP•AuNP13</b>	13±3	-24±2

All errors are quoted as ±1 standard deviation.

Isolated **Ru-pHLIP•AuNP13** were analysed by inductively-coupled plasma optical emission spectroscopy (ICP-OES) and an atomic Au:Ru ratio = 48:1 was observed, corresponding to 2000 complexes per nanoparticle and a molecular footprint of  $0.5 \text{ nm} \times 0.5 \text{ nm}$  (see Appendix 2.4). This is a higher loading than could be achieved with CALNN (only 700 **RuSH** complexes per particle could be added) and is similar to the loading of 1600 complexes per particle for the **Ru-Z•AuNP13** nanoparticles and 1400 complexes per particle for the **Ru-T20•AuNP13** particles discussed in Chapter Two (both corresponding to a molecular footprint =  $0.6 \text{ nm} \times 0.6 \text{ nm}$ ). Isolated **Ru-pHLIP•AuNP13** were also imaged by TEM, as shown below in Figure 4.16, showing the particles as discrete nanoparticles with gold core diameters of 13 nm.

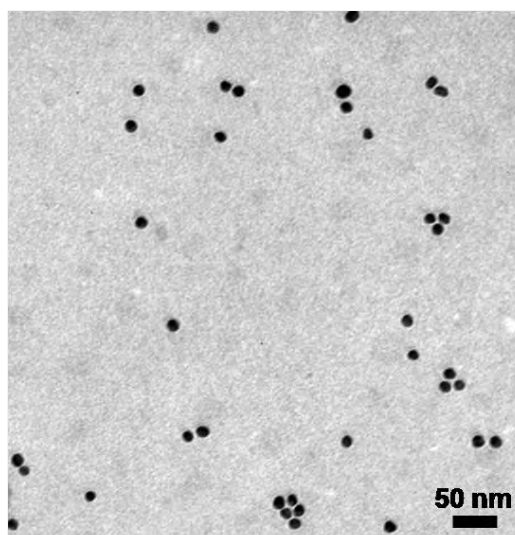


**Figure 4.16** *Transmission electron micrograph of Ru-pHLIP•AuNP13.*

In contrast to CALNN and pHLIP, co-coating 13 nm citrate gold nanoparticles with C105Y and **RuSH** proved impossible because both the peptide and the **RuSH** complex induce particle aggregation upon addition to the nanoparticles. Therefore, the strategy employed in Chapter Two, using the fluorosurfactant Zonyl® 7950 (**Z**) to stabilise the particles prior to coating, has been employed to circumvent this problem, as presented in the following schematic, Figure 4.17.

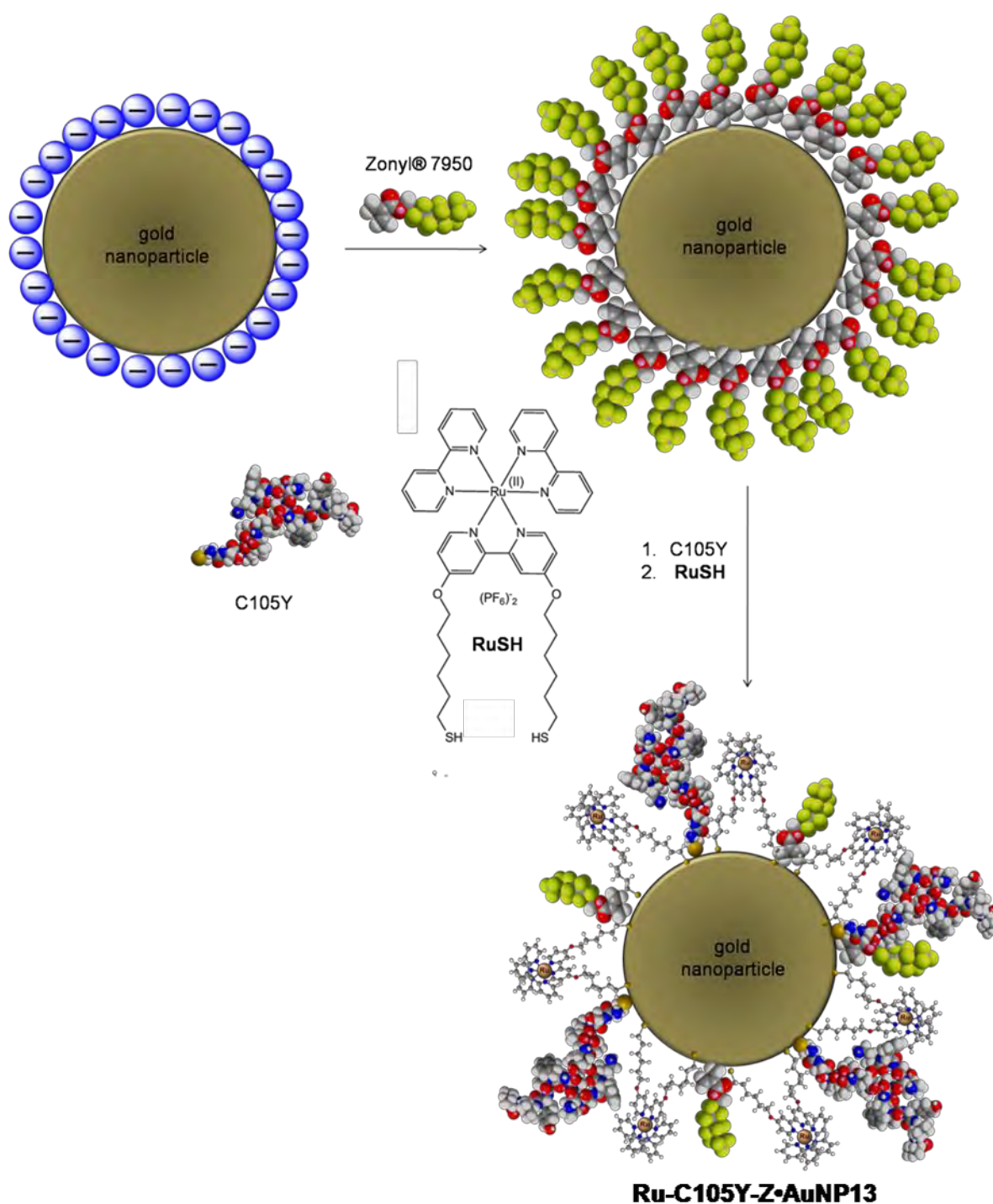


**Figure 4.17** Schematic of surfactant-mediated co-coating procedure for peptide/**RuSH** gold nanoparticles, with C105Y.

The citrate nanoparticles (9 nM) are initially coated in fluorosurfactant (*ca.* 1 mM), and then C105Y is added (80  $\mu$ M, 9000 peptides per nanoparticles), followed by an equimolar amount of **RuSH** (80  $\mu$ M), with respect to peptide. This process is followed by UV-Vis absorption spectroscopy, as shown in Figure 4.18.

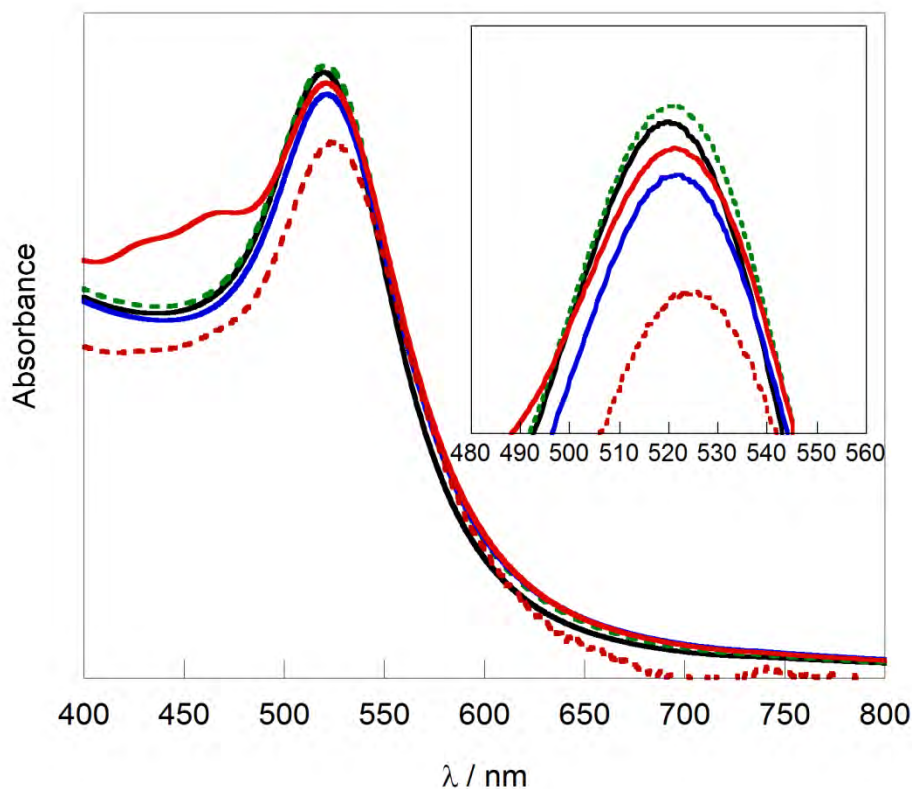


**Figure 4.18** UV-Vis absorption spectra of 13 nm uncoated citrate gold nanoparticles (black), with the addition of 1 mM Zonyl® 7950 fluorosurfactant (green dashed), upon the subsequent addition of C105Y peptide (80  $\mu\text{M}$ ) (blue) and addition of **RuSH** complex (80  $\mu\text{M}$ ) to this mixture (red solid line). Red dashed line shows the isolated **Ru-C105Y-Z•AuNP13** (9 nM) following isolation by centrifugation.

Upon addition of Zonyl® 7950 to the citrate nanoparticles, a 1 nm red-shift in the SPR is observed, to 521 nm, as observed previously in Chapter Two, Section 2.5 (Figure 2.21), and the subsequent addition of C105Y and **RuSH** does not shift the SPR peak (Figure 4.18). The particles cannot be isolated by size-exclusion chromatography as the fluorosurfactant transports the unbound **RuSH** complex through the void volume of the stationary phase with the functionalised nanoparticles, and thus separation of the particles from unbound material does not occur (see Chapter Two, Section 2.8, and Appendix 3). Particles were therefore isolated by centrifugation, decantation of the supernatant and resuspension of the pellet in deionised water. Isolated **Ru-C105Y-Z•AuNP13** have an SPR  $\lambda_{\text{max}}$  of 525 nm, as can be seen in Figure 4.18, which is red-shifted by 4 nm from the non-isolated precursor. However, neither SPR peak broadening nor peak growth at 600–800 nm are observed, and thus

aggregation does not appear to be occurring. **Ru-C105Y-Z•AuNP13** and analogous **C105Y-Z•AuNP13** (without the **RuSH** lumiphore label, with an SPR  $\lambda_{\max}$  of 522 nm) have been characterised by DLS and electrophoretic mobility measurements to give zeta potential data, which is presented in Figure 4.19 and Table 4.2 below.

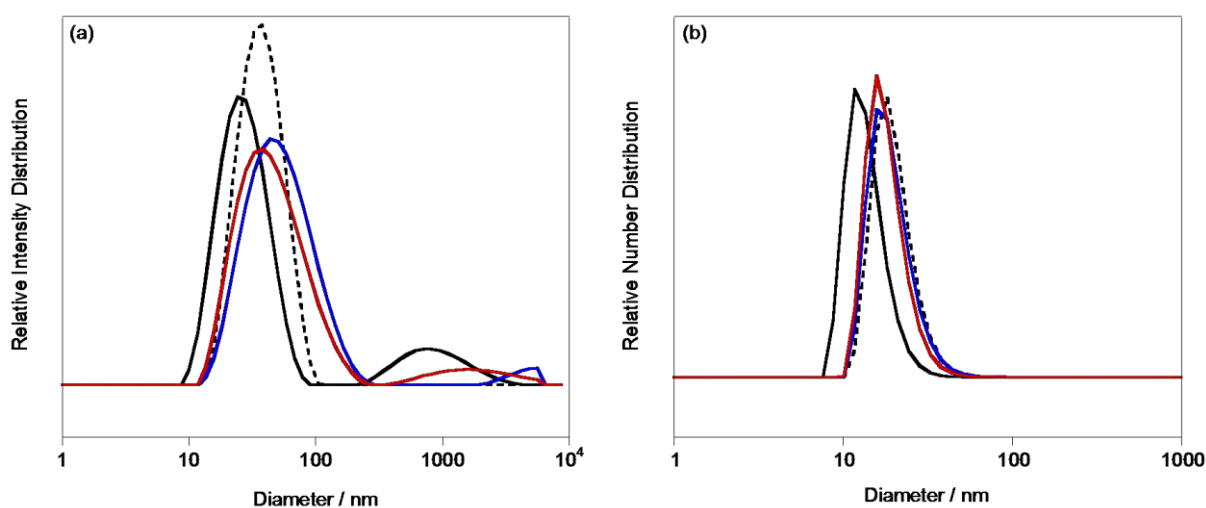


**Figure 4.19** DLS intensity distribution (a) and number distribution (b) of citrate gold nanoparticles (bold solid black line), **Z•AuNP13** (dashed black line), **C105Y-Z•AuNP13** (blue line), and **Ru-C105Y-Z•AuNP13** (red line,) measured at a concentration of 2 nM.

**Table 4.2** Summary of nanoparticle characterisation data for nanoparticles coated with C105Y, Zonyl® 7950 and **RuSH** complex.

Sample	diameter (DLS average number distribution) / nm	zeta potential (measured at 2 nM in water) / mV
<b>uncoated 13 nm citrate gold nanoparticles</b>	13±4	-40±5
<b>Z•AuNP13</b>	20±2	-61±4
<b>C105Y-Z•AuNP13</b>	19±6	-51±1
<b>Ru-C105Y-Z•AuNP13</b>	18±5	-57±4
<b>Ru-Z•AuNP13</b>	17±5	-48±2

A 30% increase in the mean intensity distribution hydrodynamic diameter is observed when Zonyl® 7950 binds to the surface of the gold nanoparticles, as discussed in Chapter Two Section 2.8, but no further increase in diameter is observed upon addition of either C105Y, **RuSH**, or both C105Y and **RuSH** together. Thus, there is no evidence of nanoparticle aggregation, which is consistent with the large negative zeta potentials of  $-51\pm 1$  mV for **C105Y-Z•AuNP13** and  $-57\pm 4$  mV for **Ru-C105Y-Z•AuNP13**. All the particles coated in Zonyl® 7950 exhibit larger negative zeta potential values than the uncoated citrate nanoparticles ( $|\text{zeta potential}| > 40$  mV), due to the electronegative C–F bonds of the fluorosurfactant, and thus the particles are quite stable in solution.

#### **4.2.2 Photophysical Characterisation of Ru-CALNN•AuNP13, Ru-pHLIP•AuNP13 and Ru-C105Y-Z•AuNP13.**

The photophysical properties of **Ru-CALNN•AuNP13**, **Ru-pHLIP•AuNP13** and **Ru-C105Y-Z•AuNP13** were investigated to determine whether the co-coating peptide has an influence upon the photophysical properties of the ruthenium(II) complex appended to the particles. The UV-Vis absorption spectra of all three types of co-coated nanoparticles, **Ru-CALNN•AuNP13** (Figure 4.20, solid line), **Ru-pHLIP•AuNP13** (Figure 4.21, solid line) and **Ru-C105Y-Z•AuNP13** (Figure 4.22, solid line) are dominated by the SPR of the gold nanoparticles, and the excitation spectra of the red emission,  $\lambda_{\text{em}} = 630$  nm, exhibit the typical LC and MLCT singlet states of the free **RuSAC** complex (see Chapter Two, Section 2.2.2) in each case (dashed line, Figures 4.20, 4.21(a) and 4.22).

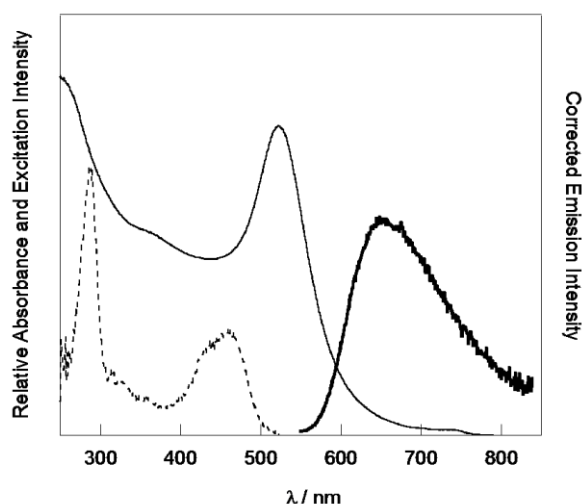


**Figure 4.20** UV-Vis absorption spectrum (solid line), excitation spectrum,  $\lambda_{em} = 630$  nm (dashed line) and steady-state emission spectrum,  $\lambda_{exc} = 450$  nm (bold solid line) of 4nm **Ru-CALNN•AuNP13**. Emission and excitation spectra are corrected for instrument response.

The steady-state luminescence spectrum of **Ru-CALNN•AuNP13** (bold line, Figure 4.20) presents a broad emission peak, with  $\lambda_{max}$  at 650 nm, following excitation at 450 nm into the singlet MLCT state, with an observed luminescence lifetime of 230 ns  $\pm$ 10% (aerated) and 300 ns  $\pm$ 10% (degassed), measured at a  $\lambda_{em} = 630$  nm. The emission properties of the ruthenium(II) complex bound in **Ru-CALNN•AuNP13** are very similar to those of the free **RuSAC** complex in 1% CH<sub>3</sub>CN, water, which also has a  $\lambda_{max}$ =650 nm, and lifetimes of 260 ns  $\pm$  6% (aerated) and 325 ns  $\pm$  6% (degassed). Within the error of the experiment, there is no evidence that the luminescence of the ruthenium(II) complex is quenched upon binding to the nanoparticles, and the surrounding CALNN peptide does not alter the photophysical properties of the complex with respect to the free complex in water. Similarly, the quenching by oxygen suggests that the complex is exposed to solvent, which is perhaps not surprising as CALNN is a short sequence and cannot shield the complex to the extent that this luminescence quenching pathway, which relies on bimolecular collision, is removed.

In contrast, when **Ru-pHLIP•AuNP13** particles are excited at 450 nm (bold line, Figure 4.21) they exhibit broad red emission at  $\lambda_{max} = 635$  nm, and enhanced luminescence lifetimes of

550 ns  $\pm 10\%$  (aerated) and 590 ns  $\pm 10\%$  (degassed) are observed by time-resolved luminescence spectroscopy.

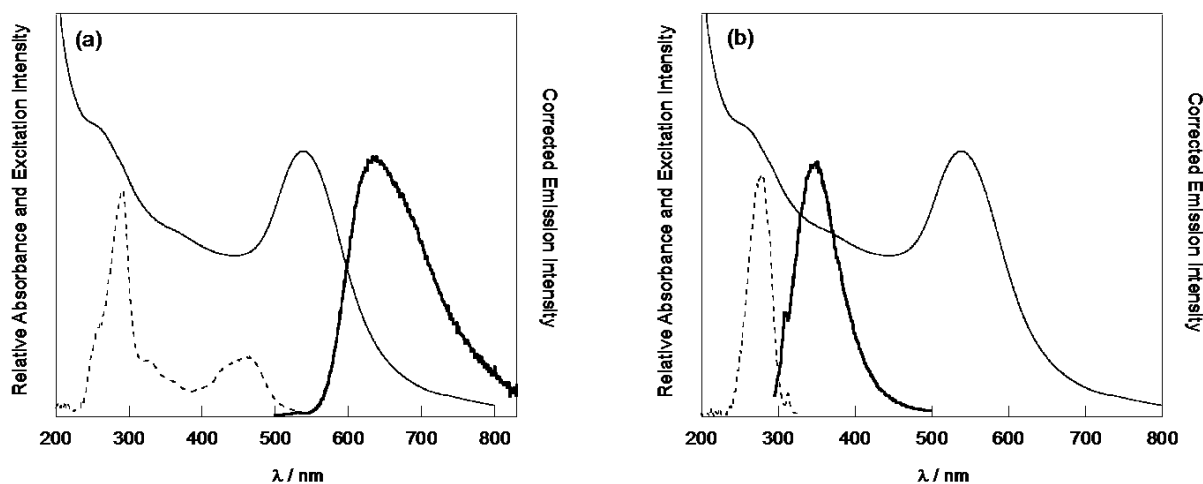


**Figure 4.21** (a) UV-Vis absorption spectrum (solid line), excitation spectrum,  $\lambda_{em} = 630$  nm (dashed line) and steady-state emission spectrum,  $\lambda_{exc} = 450$  nm (bold solid line), (b) (a) UV-Vis absorption spectrum (solid line), excitation spectrum,  $\lambda_{em} = 350$  nm (dashed line) and steady-state emission spectrum,  $\lambda_{exc} = 280$  nm (bold solid line) of 1 nm **Ru-pHLIP•AuNP13**. Emission and excitation spectra are corrected for instrument response.

The  $\lambda_{max}$  value is blue-shifted by 15 nm from the free **RuSac** complex in water, the aerated lifetime is increased *ca.* two-fold, and the luminescence is far less oxygen-sensitive than both the free complex in water and **Ru-CALNN•AuNP13**. These results suggest that the pHLIP sequence shields the ruthenium(II) complex from the bulk solvent, as well as from quenching by  $^3O_2$ , by creating a steric barrier to collisional quenching mechanisms. The blue-shift in the emission peak demonstrates that pHLIP exposes the ruthenium(II) complex to a less polar environment than the aqueous solvent, and subsequently destabilises the emissive charge transfer state. This behaviour is not observed with the short CALNN pentapeptide, whereas the 38-amino acid peptide can protect the ruthenium(II) complex from solvent and molecular oxygen to a much greater extent. In addition to the ruthenium(II) complex emission from **Ru-pHLIP•AuNP13**, pHLIP contains two tryptophan (W) residues, which can be detected by fluorescence, following excitation at 280 nm (Figure 4.17 (b)). Steady-state emission was

observed at  $\lambda_{\text{max}} = 346$  nm, consistent with the tryptophan emission observed by Engelman and co-workers in the free peptide.<sup>69</sup>

The steady-state luminescence spectrum of **Ru-C105Y-Z•AuNP13**, as presented in Figure 4.22 (bold line), exhibits broad emission in the red region of the electromagnetic spectrum, with  $\lambda_{\text{max}} = 640$  nm, following excitation into the singlet MLCT state at  $\lambda_{\text{exc}} = 450$  nm.

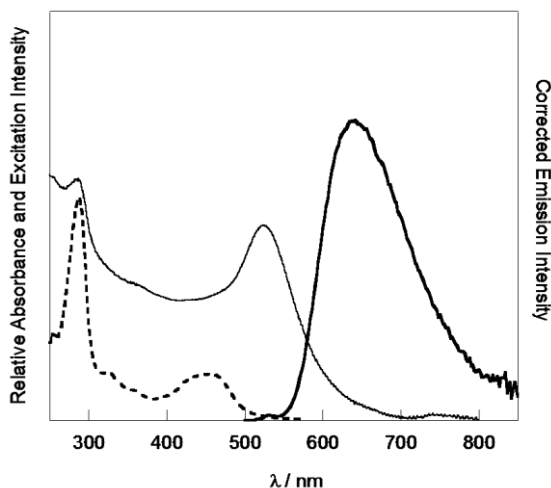


**Figure 4.22** UV-Vis absorption spectrum (solid line), excitation spectrum,  $\lambda_{\text{em}} = 630$  nm (dashed line) and steady-state emission spectrum,  $\lambda_{\text{exc}} = 450$  nm (bold solid line) of 1 nM **Ru-C105Y-Z•AuNP13**. Excitation and emission spectra are corrected for instrument response.

Similar to the **Ru-pHLIP•AuNP13** particles, the emission of the ruthenium(II) complex on **Ru-C105Y-Z•AuNP13** is blue-shifted with respect to the free complex in water, although in this instance to a lesser degree, by 10 nm. The observed luminescence lifetime of the triplet MLCT state of the ruthenium(II) complex in **Ru-C105Y-Z•AuNP13** is 380 ns  $\pm 10\%$  (aerated) and 720 ns  $\pm 10\%$  (degassed). The photophysical properties of **Ru-C105Y-Z•AuNP13** are similar to those of **Ru-Z•AuNP13**, discussed in Chapter Two, in which red emission with  $\lambda_{\text{max}} = 640$  nm is also observed, with luminescence lifetimes of 340  $\pm 10\%$  ns (aerated) and 690  $\pm 10\%$  ns (degassed). It is therefore clear that the presence of the fluorosurfactant influences the photophysical properties on the ruthenium(II) complex, and this has been explored extensively in Chapter Two. However, the presence of the C105Y peptide appears to enhance the luminescence lifetime of the ruthenium(II) complex

marginally with respect to **Ru-Z•AuNP13**. As is observed with the **Ru-Z•AuNP13** particles, the ruthenium(II) complex still remains quite oxygen sensitive on **Ru-C105Y-Z•AuNP13** particles, unlike on **Ru-pHLIP•AuNP13**.

Due to the effect of pHLIP on the photophysical properties of the ruthenium(II) complex upon co-coating of gold nanoparticles, the interaction of the peptide with the complex was studied separately in solution. Titration of 1–120  $\mu\text{M}$  pHLIP into 20  $\mu\text{M}$  **RuSAc** in 1 %  $\text{CH}_3\text{CN}$  / water gives rise to a luminescence enhancement, with a steady-state integrated emission increase by a factor of 4. In addition to this, a 20 nm blue-shift in the  $\lambda_{\text{max}}$  from 648 nm (complex in water) to 628 nm is observed and the aerated lifetime increases by a factor of 3 (Figure 4.19). The induced enhancement of both the steady-state emission *and* the observed lifetime of **RuSAc** by pHLIP indicates that the non-radiate rate of decay of the triplet MLCT excited state of **RuSAc** is reduced upon interaction with pHLIP. This suggests that the peptide protects the complex from molecular oxygen quenching. The blue-shift in the triplet MLCT emission band is indicative of the **RuSAc** complex being exposed to a less polar environment with respect to water, which destabilises the charge-separated excited state. It is likely that the interaction between the complex and pHLIP is electrostatically driven, as **RuSAc** is 2+ and pHLIP is 5-, and displacement of small counter ions by the long peptide sequence is entropically favourable.

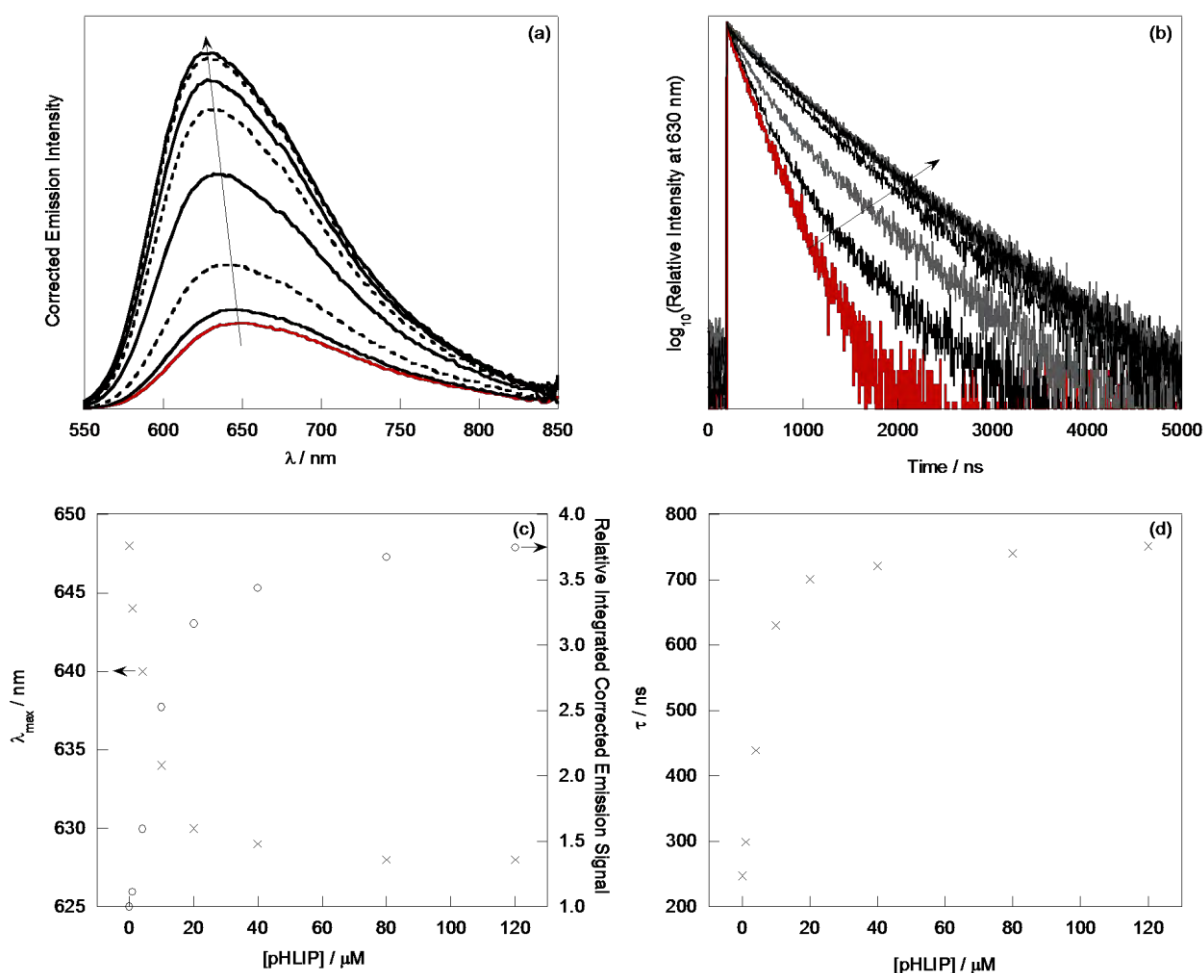


**Figure 4.23** (a) Steady-state emission,  $\lambda_{exc} = 450$  nm, and (b) time-resolved luminescence,  $\lambda_{exc} = 445$  nm,  $\lambda_{em} = 630$  nm, of  $20 \mu\text{M}$  **RuSAC** in 1 %  $\text{CH}_3\text{CN}$  / water (red) following the titration of 1–120  $\mu\text{M}$  pHLIP (black and grey). (c) Plot of steady-state emission  $\lambda_{max}$  and relative integrated corrected emission intensity vs. [pHLIP]. (d) Plot of luminescence lifetime of **RuSAC** vs. [pHLIP]. Emission spectra are corrected for instrument response.

The observed aerated luminescence lifetime (550 ns) and steady-state emission ( $\lambda_{max} = 635$  nm) of the **Ru-pHLIP•AuNP13** particles lies between the extremes of the data shown in Figure 4.23 which is expected on a nanoparticle surface where all moieties are bound to the gold nanoparticle *via* S–Au bonds, and thus the pHLIP is less free to interact with the ruthenium(II) complex.

In summary, the CALNN peptide is able to stabilise the attachment of **RuSH** to aqueous gold nanoparticles to some extent, and the photophysical properties of the ruthenium(II) complex are unaffected by attachment to **Ru-CALNN•AuNP13**. In contrast, the co-coating of gold

nanoparticles with **RuSH** and pHLIP enhances the luminescence of the ruthenium(II) complex, hence, **Ru-pHLIP•AuNP13** have great potential as optical imaging probes that can target delivery to cancer cells, which is explored in section 4.3. In order to co-coat 13 nm gold nanoparticles with C105Y and **RuSH**, the particles had to be coated initially in the fluorosurfactant Zonyl® 7950, to prevent aggregation, and the resulting particles again exhibited enhanced luminescence properties with respect to the free **RuSAc** complex in water.

### 4.3 Applications of Peptide-mediated Delivery of Luminescent Gold Nanoparticles

#### 4.3.1 Cell Uptake of Ru-CALNN•AuNP13

Preliminary imaging of A549 human lung cancer cells incubated with **Ru-CALNN•AuNP13** particles was attempted but the particles were not bright enough to image by confocal luminescence microscopy, as shown in Figure 4.24. Cell culture and incubation was performed by Mr Sunil Claire, and microscopy was carried out by the author.

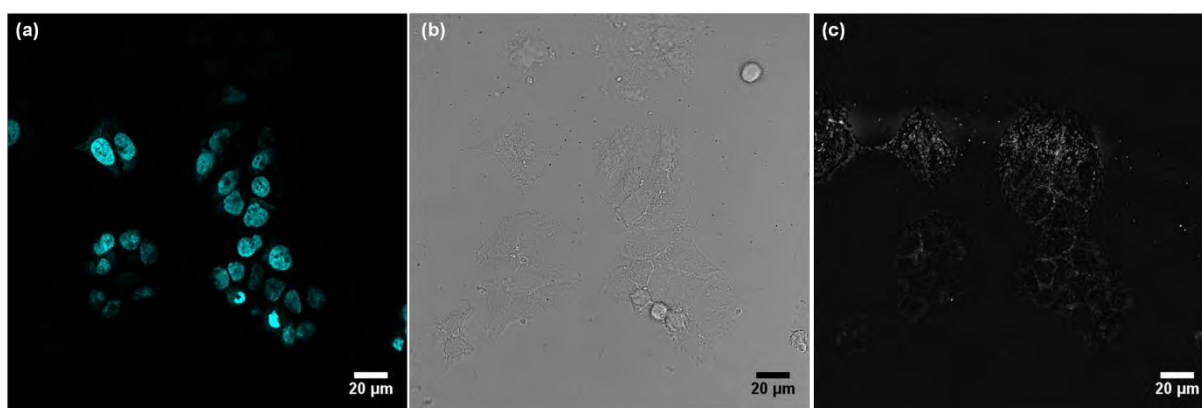


**Figure 4.24** A549 cancer cells dosed with **Ru-CALNN•AuNP13** and imaged by confocal microscopy. (a) overlay of blue channel ( $\lambda_{exc} = 405 \text{ nm}$ ,  $\lambda_{em} = 410\text{--}545 \text{ nm}$ ) and red channel ( $\lambda_{exc} = 453 \text{ nm} / 476 \text{ nm}$ ,  $\lambda_{em} = 555\text{--}800 \text{ nm}$ ), (b) transmission channel, (c) reflection channel ( $\lambda_{exc} = 488 \text{ nm}$ ,  $\lambda_{em} = 478\text{--}498 \text{ nm}$ ).

Figure 4.24(a) shows no detectable ruthenium emission in the red channel, but the nuclei of the cells are visible in the blue channel as the cells were stained with Hoechst 33258 (nuclear stain). Aggregates of nanoparticles appear as black spots on the coverslip in the transmission image (Figure 4.24(b)), and white points of reflection in Figure 4.24(c), but are not bright enough to image from the ruthenium red luminescence channel. This is unsurprising as there are <800 complexes per nanoparticle. It is therefore concluded that although CALNN can facilitate low-labelling of the resulting nanoparticles with the ruthenium(II) optical probe, **Ru-CALNN•AuNP13** particles are not suitable for imaging by confocal luminescence.

### 4.3.2 pH-targeted Uptake of Ru-pHLIP•AuNP13 in Cancer Cells

The selective uptake of nanoparticles by cancer cells, using their slightly reduced pH as a biomarker, is attempted in an *in vitro* model using **Ru-pHLIP•AuNP13**, by incubation of cancer cells with the particles at pH 6.4 and pH 7.5. To verify that the nanoparticles are stable at these pHs, particles were incubated at 0.6 nM in Tyrode's buffer at pH 6.4 and 7.5 for 24 hr at 37 °C, to emulate the incubation conditions with the A549 cells. The nanoparticles were then analysed by DLS and UV-Vis absorption spectroscopy, as shown in Figure 4.25.

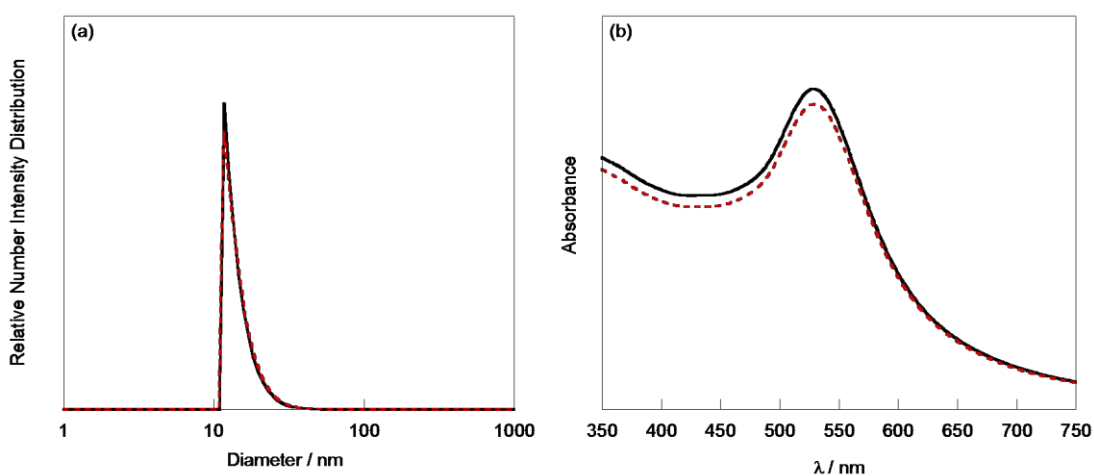


**Figure 4.25** (a) DLS Number distribution and (b) UV-Vis absorption Spectroscopy of 0.6 nM **Ru-pHLIP•AuNP13** incubated for 1 hr in Tyrode's buffer, at pH 6.4 (red) and pH 7.4 (black).

The particles maintained their SPR peak at 530 nm at both pHs, and DLS number distributions of  $15\pm 4$  nm were observed in both cases, thus verifying that the particles are stable at both pHs used within the cell studies.

A549 human cervical cancer cells were incubated with 0.6 nM **Ru-pHLIP•AuNP13** at pH 6.5 and pH 7.4 for 3 hr, by Dr Robert Harris and Dr Nikolas Hodges in the School of Biosciences, and imaged by confocal microscopy, as shown in Figure 4.26. Incubation of the cells in extracellular environments at pH 6.5 is used to model cancerous tissue, as has been employed previously,<sup>48,53,70</sup> and extracellular changes to pH will not alter the intracellular pH as this is regulated by cells within 10–15 min.<sup>71</sup>

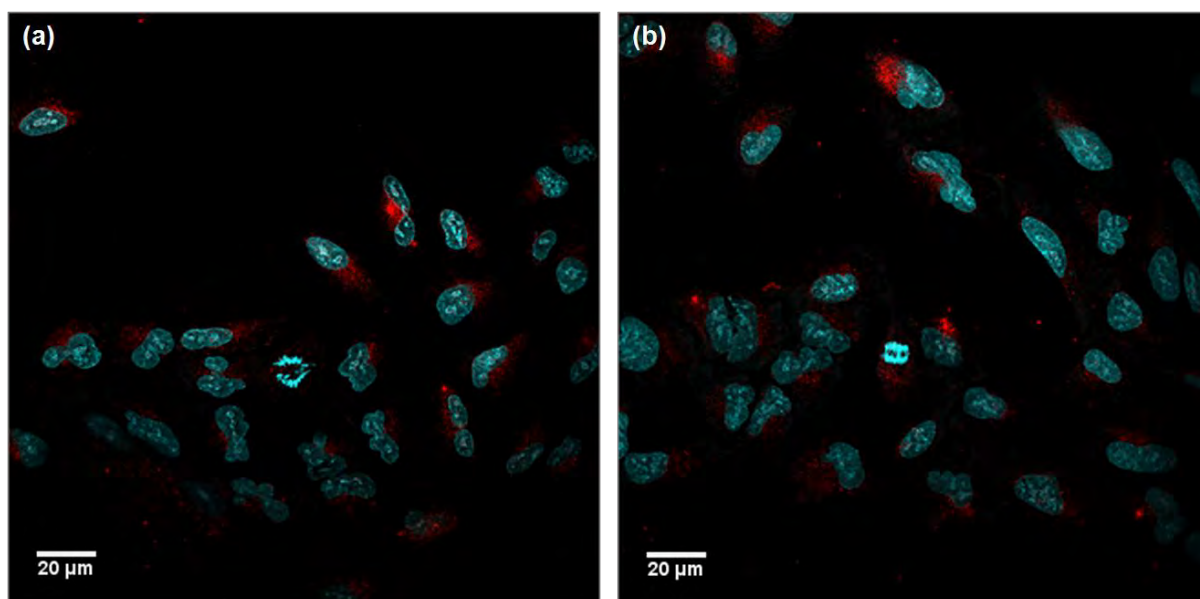


**Figure 4.26** Fixed A549 cells dosed with **Ru-pHLIP•AuNP13** in serum-free media at (a) pH 6.5 (b) pH 7.4. A549 cells. Cells dosed and imaged by Dr Robert Harris. Images are overlays of blue channel ( $\lambda_{exc} = 405$  nm,  $\lambda_{em} = 410\text{--}545$  nm) and red channel ( $\lambda_{exc} = 453$  nm / 476 nm,  $\lambda_{em} = 555\text{--}800$  nm).

As can be seen in Figure 4.26, the **Ru-pHLIP•AuNP13** nanoparticles are bright enough to be visualised by confocal luminescence microscopy, unlike **Ru-CALNN•AuNP13**. The red emission from **Ru-pHLIP•AuNP13** was observed at both pHs in the red channels of Figures 4.26(a) and 4.26(b). Cellular uptake of the nanoparticles was observed at both pHs, following

a 3 hr incubation time, but quantitative analysis of the nanoparticle uptake was difficult to assess by confocal microscopy, with only 20–30 cells in the field of view.

In order to achieve statistical analysis of **Ru-pHLIP•AuNP13** uptake in cells at pH 6.5 and pH 7.4, HL-60 cells (human leukaemia white blood cells) were incubated with particles in Tyrode's buffer for 30 min, and analysed by flow cytometry, using fluorescence-activated cell sorting (FACS). A shorter incubation time (30 min, rather than 3 was chosen to reduce the amount of particle uptake by endocytosis, and HL-60 cells were used for ease as the cells grow in suspension (unlike the adherent A459 cell line), which is more suitable for flow cytometry studies. The graph presented in Figure 4.27 shows the intensity of signal at  $\lambda > 620$  nm detected per cell, integrated over all cells detected in the flow cytometer, for control cells (undosed HL-60 cells) and cells dosed with of **Ru-pHLIP•AuNP13** at pH 7.5 and 6.4.

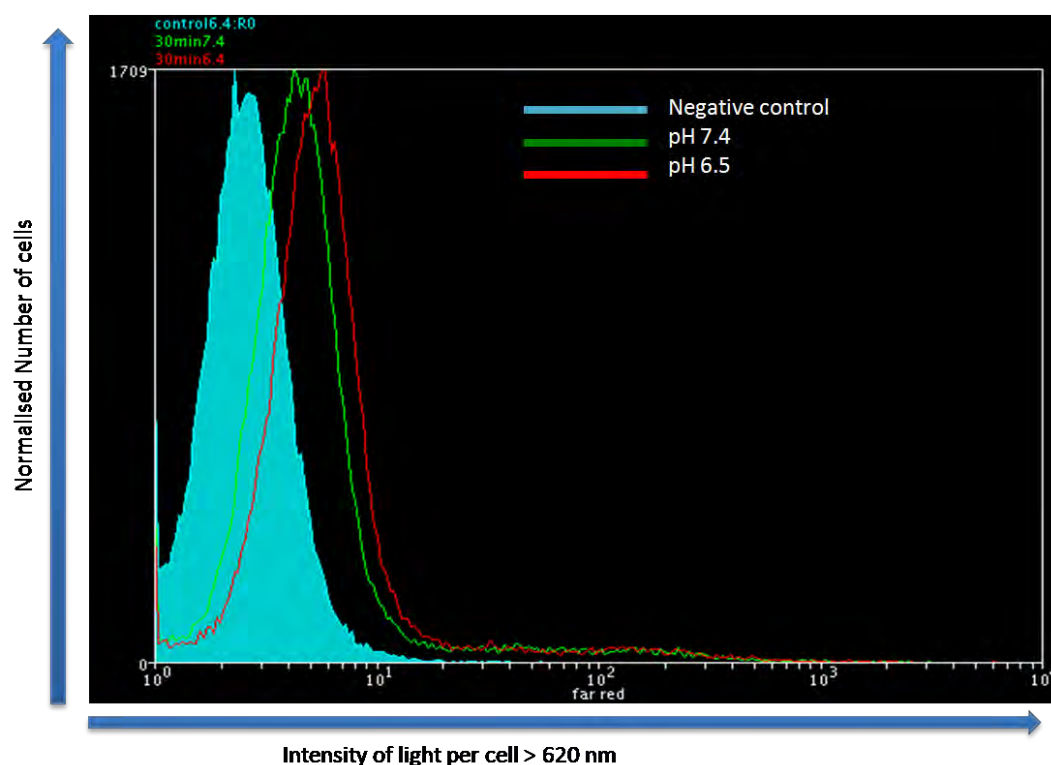


**Figure 4.27** Flow Cytometry of HL-60 cells incubated with **Ru-pHLIP•AuNP13** in Tyrode's buffer for 30 min, at pH 6.5 (red) and pH 7.4 (green). Negative control (HL-60 cells incubated with no nanoparticles) shown in blue. Analysis of 50,000 cells was performed at each condition.

At pH 6.5 there was a 50% increase in uptake of **Ru-pHLIP•AuNP13** particles as compared with the cells incubated with particles at pH 7.4, observed by the shift in the frequency value for the distribution of red signal per cell. This is similar to the uptake enhancement that was observed for pHLIP-conjugated 1 nm gold nanoparticles by Engelman and co-workers,<sup>54</sup> in which a 60% increase was observed. These preliminary cell studies confirm that pH-activated delivery of **Ru-pHLIP•AuNP13** is possible in cancer cells, and the result is indeed promising for future applications of these nanoparticles.

There are two main advantages of the **Ru-pHLIP•AuNP13** system over the pHLIP-conjugated 1 nm gold nanoparticles studied by Engelman and co-workers:<sup>54</sup> Firstly, the particles are larger, i.e. 13 nm, and are thus more likely to be able to exploit passive EPR mechanisms to further enhance the selective targeting to tumorous tissue *in vivo*. Secondly, **Ru-pHLIP•AuNP13** can be imaged by luminescence techniques, as opposed to staining cells with a silver solution post-fixing and subsequently imaging in bright-field mode. Luminescence detection offers high sensitivity, is less prone to artifacts, and can also be used to image live cells. In addition, unlike the nanoparticles studied previously in the group by Davies *et al.*,<sup>3</sup> which are visualised by epilluminescence microscopy using UV excitation of the europium(III) luminescent probe, **Ru-pHLIP•AuNP13** can be detected using *conventional* confocal luminescence microscopy and FACS techniques, because the ruthenium(II) lumiphore can be excited in the visible range of the electromagnetic spectrum, between 400–500 nm, and the luminescence is bright enough to detect.

#### 4.4 Conclusions and Future Work

13 nm gold nanoparticles have been successfully co-coated with a red luminescent ruthenium (II) polypyridyl complex, **RuSH**, and three different peptides; CALNN, pHLIP and C105Y. CALNN and pHLIP stabilised the 13 nm enough to add the cationic **RuSH** complex without

aggregation of the particles, although only 800 complexes per particle could be added to CALNN-coated particles before aggregation became apparent by inspection of the SPR by UV-Vis absorption spectroscopy. The long (36-amino acid) negatively charged sequence, pHLIP, was able to withstand aggregation by addition of 9,000 equivalents of **RuSH**, and isolated particles were loaded with 2000 complexes per particle. The monocationic peptide sequence C105Y aggregated the nanoparticles, and thus co-coating of particles with this peptide and **RuSH** was achieved using surfactant-mediated coating with Zonyl® 7950 fluorosurfactant. The photophysical properties of the ruthenium(II) complex were found to vary when bound to nanoparticles with different co-coating moieties; The ruthenium(II) complex bound to nanoparticles in **Ru-CALNN•AuNP13** behaved in a similar fashion to the free **RuSAc** complex in water (1% CH<sub>3</sub>CN), whereas a blue shift in the emission and enhanced luminescence lifetimes were observed in both **Ru-pHLIP•AuNP13** and **Ru-C105Y-Z•AuNP13** samples.

Preliminary cell studies with **Ru-pHLIP•AuNP13** show successful pH-targeted uptake in cancer cells; an uptake increase of 50% at pH 6.5 vs. pH 7.5 is observed, which demonstrates that these particles have the potential to improve nanoparticle delivery to tumor cells *in vivo*. Future *in vitro* studies of **Ru-pHLIP•AuNP13** uptake in cancer cells vs. non-cancerous cells would lead to further insight into how such particles can be applied as targeted nanovectors, and eventually *in vivo* studies would demonstrate the capabilities of such particles in the body. It would also be of interest to look at the uptake and localisation of **Ru-C105Y-Z•AuNP13** nanoparticles in cells, to see if the C105Y peptide maintains its nuclear targeting properties once bound to this complex nanovehicle.

## **4.5 Acknowledgements**

Thank you to Mr Sunil Claire, Dr Robert Harris, and Dr Nikolas Hodges for the cell studies performed in this Chapter. Thank you also to Dr Alison Savage, Ms Kimberley Wright and Ms Amy Davies for their useful advice regarding the peptide work.

## 4.6 Experimental

### 4.6.1 General Synthesis

**RuSH** (3.5 mM (aq) 30 % w/w:CH<sub>3</sub>CN (1:1)) was synthesised *in situ* from its **RuSAc** precursor, as described in Chapter Two, Section 2.12.1, directly prior to titration into the colloid. CALNN, C105Y and pHLIP, were purchased from Alta Biosciences with purities of >95 % for CALNN, >90 % for C105Y and >80 % for pHLIP (HPLC assay) and used without further purification. Zonyl® 7950 was purchased from Sigma Aldrich. 13 nm gold nanoparticles were synthesised by the citrate reduction method,<sup>72</sup> as described in Section 2.12.1.

#### *Synthesis of CALNN•AuNP13*

An aqueous solution of CALNN (20–80 µL, 1 mM) was titrated into 13 nm citrate gold nanoparticles, to a final peptide concentration of 80 µM, and the  $\lambda_{\max}$  of the SPR was monitored by UV-Vis absorption spectroscopy to ensure saturation of the binding sites. The particles were isolated by size-exclusion chromatography on Sephadex® G-25. Dilution in the column was examined by UV-Vis absorption spectroscopy and the final nanoparticle concentration was estimated to be 5 nM. UV-Vis (H<sub>2</sub>O)  $\lambda_{\max}$  [nm] = 522 (SPR). Diameter = 16 ± 4 nm (DLS number distribution), = 30 ± 12 nm (DLS intensity distribution). Zeta potential = -22 ± 4 mV (isolated, 2 nM in deionised water).

#### *Synthesis of Ru-CALNN•AuNP13*

An aqueous solution of CALNN (20–80 µL, 1 mM) was titrated into 13 nm citrate gold nanoparticles (1 mL, 9 nM), to a final peptide concentration of 80 µM, and the  $\lambda_{\max}$  of the SPR was monitored by UV-Vis absorption, as described for the preparation of CALNN•AuNP13. Following this, a solution of **RuSH** (0.5–2.0 µL, 3.5 mM (aq) 30 %

$w/w:CH_3CN$  (1:1)) was titrated in, again following the  $\lambda_{max}$  of the SPR to a final **RuSH** concentration of 7  $\mu M$ . The particles were isolated by size-exclusion chromatography on Sephadex® G-25, and dilution in the column was examined by UV-Vis absorption spectroscopy. The final nanoparticle concentration was estimated to be 5 nM. UV-Vis ( $H_2O$ )  $\lambda_{max}$  [nm] = 525 (SPR). Diameter =  $20 \pm 5$  nm (DLS number distribution), =  $269 \pm 269$  nm (DLS intensity distribution). Zeta potential =  $-34 \pm 2$  mV (isolated, 2 nM in deionised water). Emission ( $H_2O$ ,  $\lambda_{exc} = 450$  nm)  $\lambda_{max}$  [nm] = 650.

#### *Synthesis of pHLIP•AuNP13*

Adapted from procedure by Davies *et al.*<sup>333</sup> A solution of pHLIP (5–40  $\mu L$ , 2 mM in 10% DMSO, phosphate buffer saline) was titrated into 13 nm citrate gold nanoparticles (1 mL, 9 nM), to a final peptide concentration of 80  $\mu M$ , and the  $\lambda_{max}$  of the SPR was monitored by UV-Vis absorption spectroscopy. The particles were isolated by size-exclusion chromatography on Sephadex® G-25, and to give a final nanoparticle concentration of 6 nM (estimated by UV-Vis spectroscopy). UV-Vis ( $H_2O$ )  $\lambda_{max}$  [nm] = 525 (SPR). Diameter =  $11 \pm 3$  nm (DLS number distribution), =  $72 \text{ nm} \pm 66 \text{ nm}$  (DLS intensity distribution). Zeta potential =  $-19 \pm 4$  mV (isolated, 2 nM in deionised water).

#### *Synthesis of Ru-pHLIP•AuNP13*

A solution of pHLIP (5–40  $\mu L$ , 2 mM in 10% DMSO, phosphate buffer saline) was titrated into 13 nm citrate gold nanoparticles (1 mL, 9 nM), to a final peptide concentration was 80  $\mu M$ , in a similar fashion to the preparation of **pHLIP•AuNP13**. A solution of **RuSH** (5–25  $\mu L$ , 3.5 mM (aq) 30 %  $w/w:CH_3CN$  (1:1)) was titrated in, again following the  $\lambda_{max}$  of the SPR, to a final concentration was 80  $\mu M$ . The particles were isolated by size-exclusion chromatography on Sephadex® G-25, and dilution in the column was examined by UV-Vis absorption spectroscopy; the final nanoparticle concentration was estimated to be 6 nM. UV-

Vis (H<sub>2</sub>O)  $\lambda_{\max}$  [nm] = 530 (SPR). Diameter =  $13 \pm 4$  nm (DLS number distribution), =  $186 \pm 202$  nm (DLS intensity distribution). Zeta potential =  $-24 \pm 2$  mV (isolated, 2 nM in deionised water). Emission (H<sub>2</sub>O,  $\lambda_{\text{exc}} = 450$  nm)  $\lambda_{\max}$  [nm] = 635. ICP-OES Au:Ru atomic ratio = 48:1.

#### *Synthesis of C105Y-Z•AuNP13*

Zonyl® 7950 (CH<sub>2</sub>-C(CH<sub>3</sub>)COOC<sub>2</sub>H<sub>4</sub>(CF<sub>2</sub>)<sub>n</sub>F, MW *ca.* 500, 1  $\mu$ l, 1.15 g mL<sup>-1</sup>) was added to 13 nm citrate gold nanoparticles (1 mL, 9 nM), to give fluorosurfactant coated nanoparticles (9 nM nanoparticles), with a final fluorosurfactant concentration of *ca.* 1mM. Subsequently, a solution of C105Y (80  $\mu$ L, 1 mM, aqueous) was added, and the  $\lambda_{\max}$  of the SPR was monitored by UV-Vis absorption spectroscopy. The particles were isolated by centrifugation at 12,000 g for 15 min, followed by removal of the supernatant and re-dispersion in deionised water (1mL). This was repeated twice. UV-Vis (H<sub>2</sub>O)  $\lambda_{\max}$  [nm] = 523 (SPR). Diameter =  $19 \pm 6$  nm (DLS number distribution), =  $59 \text{ nm} \pm 36 \text{ nm}$  (97%),  $4240 \text{ nm} \pm 1000 \text{ nm}$  (3%) (DLS intensity distribution). Zeta potential =  $-51 \pm 1$  mV (isolated, 2 nM in deionised water).

#### *Synthesis of Ru-C105Y-Z•AuNP13*

Zonyl® 7950 (CH<sub>2</sub>-C(CH<sub>3</sub>)COOC<sub>2</sub>H<sub>4</sub>(CF<sub>2</sub>)<sub>n</sub>F, MW *ca.* 500, 1  $\mu$ l, 1.15 g mL<sup>-1</sup>) was added to 13 nm citrate gold nanoparticles (1 mL, 9 nM), to give fluorosurfactant coated nanoparticles (9 nM nanoparticles), with a final fluorosurfactant concentration of *ca.* 1mL. Subsequently a solution of C105Y (80  $\mu$ L, 1 mM, aqueous) was added, similar to the preparation of **C105Y-Z•AuNP13**. A solution of **RuSH** (20  $\mu$ l, 3.5 mM (aq) 30 % w/w:CH<sub>3</sub>CN (1:1)) was added and the  $\lambda_{\max}$  of the SPR was monitored by UV-Vis absorption spectroscopy. The particles were isolated by centrifugation at 12,000 g for 15 min, followed by removal of the supernatant and re-dispersion in deionised water (1mL). This was repeated twice. UV-Vis

(H<sub>2</sub>O)  $\lambda_{\max}$  [nm] = 524 (SPR). Diameter =  $18 \pm 5$  nm (DLS number distribution),  $52 \text{ nm} \pm 33$  nm (93%),  $2000 \text{ nm} \pm 1260$  nm (7%) (DLS intensity distribution). Zeta potential =  $-57 \pm 4$  mV (isolated, 2 nM in deionised water).

#### 4.6.2 Cell Studies with Ru-CALNN•AuNP13

A549 tissue culture was performed by Mr Sunil Claire. Cells were incubated with 0.5 nM **Ru-CALNN•AuNP13** for 24 hr in Dulbecco's modified Eagle Medium as previously described.<sup>65</sup> Cofocal microscopy was performed by the author.

#### 4.6.3 Cell Studies with Ru-pHLIP•AuNP13

A549 tissue culture and microscopy was performed by Dr Robert Harris, School of Biosciences. Cells were incubated with 0.6 nM **Ru-pHLIP•AuNP13** for 3 hr in serum-free media, using phosphoric acid to adjust the pH, and stained with Hoechst 33258 (3  $\mu$ l, 2.5  $\mu$ g mL<sup>-1</sup>). Cell media was removed and the cells washed twice in PBS followed by fixation with methanol for 5 min followed by two further washes with PBS. Coverslips were removed and mounted on a droplet of Hydromount media (national diagnostics) on glass slides, sealed with clear nail varnish and stored for 24 hours at 4°C before imaging.

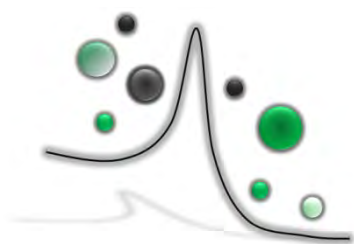
Flow cytometry studies and HL-60 cell work was performed by Dr Nikolas Hodges, School of Biosciences. Cells were incubated with **Ru-pHLIP•AuNP13** (0.6 nM in Tyrode's buffer) for 30 min, and washed in PBS by centrifugation, resuspended in PBS and transferred to flow cytometry tubes for analysis (FACScalibur, BD Biosciences, USA). Forward scatter, side scatter and red luminescence ( $\lambda_{\text{exc}}=488$  nm with light collected through a 620 nm band pass filter) of 50,000 cells were collected and Weasel freeware software was used for data analysis.

## 4.7 Chapter Four References

- (1) Rio-Echevarria, I. M.; Tavano, R.; Causin, V.; Papini, E.; Mancin, F.; Moretto, A. *J. Am. Chem. Soc.* **2010**, *133*, 8.
- (2) Savage, A. C.; Pikramenou, Z. *Chem. Commun.* **2011**, *47*, 6431.
- (3) Davies, A.; Lewis, D. J.; Watson, S. P.; Thomas, S. G.; Pikramenou, Z. *Proc. Nat. Acad. Sci. U.S.A.* **2012**, *109*, 1862.
- (4) Feng, J.-J.; Huang, H.; Zhou, D.-L.; Cai, L.-Y.; Tu, Q.-Q.; Wang, A.-J. *J. Mat. Chem. C* **2013**, *1*, 4720.
- (5) Sun, J.; Luo, C.; Wang, Y.; He, Z. *Nanoscale* **2013**, *5*, 845.
- (6) Koo, H.; Huh, M. S.; Sun, I.-C.; Yuk, S. H.; Choi, K.; Kim, K.; Kwon, I. C. *Acc. Chem. Res.* **2011**, *44*, 1018.
- (7) Brown, S. D.; Nativo, P.; Smith, J.-A.; Stirling, D.; Edwards, P. R.; Venugopal, B.; Flint, D. J.; Plumb, J. A.; Graham, D.; Wheate, N. J. *J. Am. Chem. Soc.* **2010**, *132*, 4678.
- (8) Ghosh, P.; Han, G.; De, M.; Kim, C. K.; Rotello, V. M. *Adv. Drug Deliv. Rev.* **2008**, *60*, 1307.
- (9) Hirsch, L. R.; Stafford, R. J.; Bankson, J. A.; Sershen, S. R.; Rivera, B.; Price, R. E.; Hazle, J. D.; Halas, N. J.; West, J. L. *Proc. Nat. Acad. Sci. U.S.A.* **2003**, *100*, 13549.
- (10) Boisselier, E.; Astruc, D. *Chem. Soc. Rev.* **2009**, *38*, 1759.
- (11) Gobin, A. M.; Lee, M. H.; Halas, N. J.; James, W. D.; Drezek, R. A.; West, J. L. *Nano Lett.* **2007**, *7*, 1929.
- (12) You, J.-O.; Guo, P.; Auguste, D. T. *Angew. Chem., Int. Ed.* **2013**, *52*, 4141.
- (13) Yuan, H.; Fales, A. M.; Vo-Dinh, T. *J. Am. Chem. Soc.* **2012**, *134*, 11358.
- (14) Yuan, H.; Khoury, C. G.; Wilson, C. M.; Grant, G. A.; Bennett, A. J.; Vo-Dinh, T. *Nanomedicine: NBM* **2012**, *8*, 1355.
- (15) Link, S.; El-Sayed, M. A. *Int. Rev. Phys. Chem.* **2000**, *19*, 409.
- (16) Gu, F. X.; Karnik, R.; Wang, A. Z.; Alexis, F.; Levy-Nissenbaum, E.; Hong, S.; Langer, R. S.; Farokhzad, O. C. *Nano Today* **2007**, *2*, 14.
- (17) Lévy, R.; Thanh, N. T. K.; Doty, R. C.; Hussain, I.; Nichols, R. J.; Schiffrin, D. J.; Brust, M.; Fernig, D. G. *J. Am. Chem. Soc.* **2004**, *126*, 10076.
- (18) Nativo, P.; Prior, I. A.; Brust, M. *ACS Nano* **2008**, *2*, 1639.
- (19) Sun, L.; Liu, D.; Wang, Z. *Langmuir* **2008**, *24*, 10293.
- (20) Futaki, S. *Adv. Drug Delivery Rev.* **2005**, *57*, 547.
- (21) Walrant, A.; Bechara, C.; Alves, I. D.; Sagan, S. *Nanomed.* **2011**, *7*, 133.
- (22) Deshayes, S.; Morris, M. C.; Divita, G.; Heitz, F. *Cell. Mol. Life Sci.* **2005**, *62*, 1839.
- (23) *Peptide and Protein Delivery*; 1 ed.; Van Der Walle, C., Ed.; Academic Press, 2011; Vol. Chapter 10.
- (24) Zorko, M.; Langel, Ü. *Adv. Drug Delivery Rev.* **2005**, *57*, 529.
- (25) Brooks, H.; Lebleu, B.; Vivès, E. *Adv. Drug Delivery Rev.* **2005**, *57*, 559.
- (26) Derossi, D.; Joliot, A. H.; Chassaing, G.; Prochiantz, A. *J. Biol. Chem.* **1994**, *269*, 10444.

- (27) Ruan, G.; Agrawal, A.; Marcus, A. I.; Nie, S. *J. Am. Chem. Soc.* **2007**, *129*, 14759.
- (28) McLean, L. R.; Hagaman, K. A.; Owen, T. J.; Krstenansky, J. L. *Biochemistry* **1991**, *30*, 31.
- (29) Aggarwal, P.; Hall, J. B.; McLeland, C. B.; Dobrovolskaia, M. A.; McNeil, S. E. *Adv. Drug Delivery Rev.* **2009**, *61*, 428.
- (30) Harrison, C. *Nat. Rev. Drug Discov.* **2013**, *12*, 264.
- (31) Lynch, I.; Dawson, K. A. *Nano Today* **2008**, *3*, 40.
- (32) Popović, Z.; Liu, W.; Chauhan, V. P.; Lee, J.; Wong, C.; Greytak, A. B.; Insin, N.; Nocera, D. G.; Fukumura, D.; Jain, R. K.; Bawendi, M. G. *Angew. Chem. Int. Ed.* **2010**, *49*, 8649.
- (33) Huang, K. Y.; Ma, H. L.; Liu, J.; Huo, S. D.; Kumar, A.; Wei, T.; Zhang, X.; Jin, S. B.; Gan, Y. L.; Wang, P. C.; He, S. T.; Zhang, X. N.; Liang, X. J. *ACS Nano* **2012**, *6*, 4483.
- (34) Chithrani, B. D.; Ghazani, A. A.; Chan, W. C. W. *Nano Lett.* **2006**, *6*, 662.
- (35) Bartzak, D.; Muskens, O. L.; Nitti, S.; Sanchez-Elsner, T.; Millar, T. M.; Kanaras, A. G. *Small* **2012**, *8*, 122.
- (36) Krpetić, Ž.; Saleemi, S.; Prior, I. A.; Sée, V.; Qureshi, R.; Brust, M. *ACS Nano* **2011**, *5*, 5195.
- (37) Oh, E.; Delehanty, J. B.; Sapsford, K. E.; Susumu, K.; Goswami, R.; Blanco-Canosa, J. B.; Dawson, P. E.; Granek, J.; Shoff, M.; Zhang, Q.; Goering, P. L.; Huston, A.; Medintz, I. L. *ACS Nano* **2011**, *5*, 6434.
- (38) Lee, J. S.; Tung, C.-H. *Adv. Funct. Mater.* **2012**, *22*, 4924.
- (39) Lagerholm, B. C.; Wang, M.; Ernst, L. A.; Ly, D. H.; Liu, H.; Bruchez, M. P.; Waggoner, A. S. *Nano Lett.* **2004**, *4*, 2019.
- (40) Huang, Y.; Jiang, Y.; Wang, H.; Wang, J.; Shin, M. C.; Byun, Y.; He, H.; Liang, Y.; Yang, V. C. *Adv. Drug Delivery Rev.* **2013**, *65*, 1299.
- (41) Petros, R. A.; DeSimone, J. M. *Nat. Rev. Drug Discovery* **2010**, *9*, 615.
- (42) Brigger, I.; Dubernet, C.; Couvreur, P. *Adv. Drug Delivery Rev.* **2012**, *64*, Supplement, 24.
- (43) Gatenby, R. A.; Gillies, R. J. *Nat. Rev. Cancer* **2008**, *8*, 56.
- (44) Gatenby, R. A.; Gillies, R. J. *Nat. Rev. Cancer* **2004**, *4*, 891.
- (45) Tannock, I. F.; Rotin, D. *Cancer Res.* **1989**, *49*, 4373.
- (46) Jin, E.; Zhang, B.; Sun, X.; Zhou, Z.; Ma, X.; Sun, Q.; Tang, J.; Shen, Y.; Van Kirk, E.; Murdoch, W. J.; Radosz, M. *J. Am. Chem. Soc.* **2012**, *135*, 933.
- (47) Reshetnyak, Y. K.; Andreev, O. A.; Lehnert, U.; Engelman, D. M. *Proc. Nat. Acad. Sci. U.S.A.* **2006**, *103*, 6460.
- (48) Reshetnyak, Y. K.; Andreev, O. A.; Segala, M.; Markin, V. S.; Engelman, D. M. *Proc. Nat. Acad. Sci. U.S.A.* **2008**, *105*, 15340.
- (49) Andreev, O. A.; Karabadzha, A. G.; Weerakkody, D.; Andreev, G. O.; Engelman, D. M.; Reshetnyak, Y. K. *Proc. Nat. Acad. Sci. U.S.A.* **2010**, *107*, 4081.
- (50) Sosunov, E. A.; Anyukhovsky, E. P.; Sosunov, A. A.; Moshnikova, A.; Wijesinghe, D.; Engelman, D. M.; Reshetnyak, Y. K.; Andreev, O. A. *Proc. Nat. Acad. Sci. U.S.A.* **2013**, *110*, 82.
- (51) Hunt, J. F.; Rath, P.; Rothschild, K. J.; Engelman, D. M. *Biochemistry* **1997**, *36*, 15177.

- (52) Weerakkody, D.; Moshnikova, A.; Thakur, M. S.; Moshnikova, V.; Daniels, J.; Engelman, D. M.; Andreev, O. A.; Reshetnyak, Y. K. *Proc. Nat. Acad. Sci. U.S.A.* **2013**, *110*, 5834.
- (53) Andreev, O. A.; Dupuy, A. D.; Segala, M.; Sandugu, S.; Serra, D. A.; Chichester, C. O.; Engelman, D. M.; Reshetnyak, Y. K. *Proc. Nat. Acad. Sci. U.S.A.* **2007**, *104*, 7893.
- (54) Yao, L.; Daniels, J.; Moshnikova, A.; Kuznetsov, S.; Ahmed, A.; Engelman, D. M.; Reshetnyak, Y. K.; Andreev, O. A. *Proc. Nat. Acad. Sci. U.S.A.* **2013**, *110*, 465.
- (55) Zhao, Z.; Meng, H.; Wang, N.; Donovan, M. J.; Fu, T.; You, M.; Chen, Z.; Zhang, X.; Tan, W. *Angew. Chem., Int. Ed.* **2013**, *52*, 7487.
- (56) Niidone, T.; Huang, L. *Gene Ther.* **2002**, *9*, 1647.
- (57) Oyelere, A. K.; Chen, P. C.; Huang, X.; El-Sayed, I. H.; El-Sayed, M. A. *Bioconjug. Chem.* **2007**, *18*, 1490.
- (58) Kang, B.; Mackey, M. A.; El-Sayed, M. A. *J. Am. Chem. Soc.* **2010**, *132*, 1517.
- (59) Tkachenko, A. G.; Xie, H.; Liu, Y.; Coleman, D.; Ryan, J.; Glomm, W. R.; Shipton, M. K.; Franzen, S.; Feldheim, D. L. *Bioconjug. Chem.* **2004**, *15*, 482.
- (60) Tkachenko, A. G.; Xie, H.; Coleman, D.; Glomm, W.; Ryan, J.; Anderson, M. F.; Franzen, S.; Feldheim, D. L. *J. Am. Chem. Soc.* **2003**, *125*, 4700.
- (61) Joslin, G.; Fallon, R. J.; Bullock, J.; Adams, S. P.; Perlmutter, D. H. *J. Biol. Chem.* **1991**, *266*, 11282.
- (62) Ziady, A.-G.; Ferkol, T.; Dawson, D. V.; Perlmutter, D. H. *J. Biol. Chem.* **1999**, *247*, 4908.
- (63) Rhee, M.; Davis, P. *J. Biol. Chem.* **2006**, *281*, 1233.
- (64) Rogers, N. J.; Pikramenou, Z. *Patent* **2013**, WO/2013/004989.
- (65) Rogers, N. J.; Claire, S.; Harris, R. M.; Farabi, S.; Zikeli, G.; Styles, I. B.; Hodges, N. J.; Pikramenou, Z. *Chem. Commun.* **2014**, *50*, 617.
- (66) Kreibig, U.; Genzel, L. *Surf. Sci.* **1985**, *156*, Part 2, 678.
- (67) Lide, D. R. *CRC Handbook of Chemistry and Physics, 94th Edition*; Taylor and Francis, London, 2013-2014.
- (68) Lewis, D. J.; Day, T. M.; MacPherson, J. V.; Pikramenou, Z. *Chem. Commun.* **2006**, 1433.
- (69) Hunt, J. F.; Rath, P.; Rothschild, K. J.; Engelman, D. M. *Biochemistry* **1997**, *36*, 15177.
- (70) An, M.; Wijesinghe, D.; Andreev, O. A.; Reshetnyak, Y. K.; Engelman, D. M. *Proc. Nat. Acad. Sci. U.S.A.* **2010**, *107*, 20246.
- (71) Madshus, I. H. *Biochem. J.* **1988**, *250*, 1.
- (72) Grabar, K. C.; Freeman, R. G.; Hommer, M. B.; Natan, M. J. *Anal. Chem.* **1995**, *67*, 735.



---

# Chapter Five

---

Developing Iridium(III)

Complexes for

Labelling Gold

Nanoparticles

## 5.1 Introduction

Transition metal complexes can be exploited in the design of luminescent nanoparticle flow tracers by taking advantage of their high photostability and large differences in excitation and emission wavelengths. Throughout this thesis so far, luminescent nanoparticles have been developed using a tailor-made surface-binding derivative of the archetypal low-spin  $d^6$  transition metal lumiphore ruthenium tris(bipyridine), i.e. **RuSH**.<sup>1,2</sup> Such nanoparticles were ideal for imaging cancer cells *in vitro*, but for flow imaging it is important to be able to ensure extremely high particle brightness so that the exposure time per image frame can be reduced as low as possible to increase the temporal resolution of the dynamic flow data. Therefore in this chapter surface-binding iridium(III) probes have been developed to label nanoparticles, because many iridium(III) complexes have superior luminescence efficiencies to ruthenium(II) complexes.

### 5.1.1 Cyclometallated Iridium(III) Polypyridyl Complexes

Cyclometallated iridium(III) complexes are an emerging choice of luminescent agent for imaging applications; they are used in organic light-emitting diode (OLED) applications,<sup>3-5</sup> dye-sensitised solar cells,<sup>6</sup> and are beginning to flourish in the field of biological probes.<sup>7-9</sup> Interest in cyclometallated iridium(III) complexes began in the 1980s, when it was discovered that bipyridine ligands ortho-metallate upon complexation with the metal ion, to form complexes such as  $[\text{Ir}(\text{Hbpy-C3,N}')(\text{bpy})_2]^{3+}$ .<sup>10,11</sup> Following this, efforts have been focussed on developing deliberately ortho-metallated complexes with analogous polypyridyl complexes such as phenylpyridine (ppy). Bis(cyclometallated) iridium(III) compounds are most commonly applied to luminescence applications, usually of the generic formula  $[\text{Ir}(\text{C}^{\wedge}\text{N})_2(\text{N}^{\wedge}\text{N})]^+$ , whereby the (C<sup>^</sup>N) ligand is the cyclometallating monoanionic ligand and

the (N<sup>^</sup>N) ligand is a neutral chelating species, datively bonding through the N atoms, such as bipyridine, as shown in Figure 5.1.

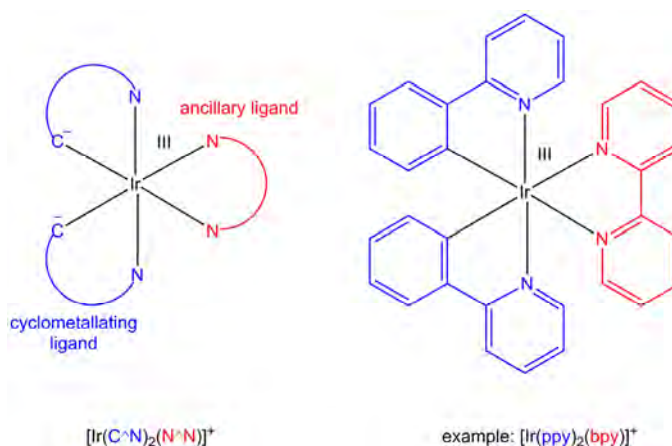


**Figure 5.1** Schematic of generic Ir(III) cyclometallated complexes, i.e.  $[\text{Ir}(\text{C}^{\ominus}\text{N})_2(\text{N}^{\oplus}\text{N})]^+$ .

The sigma-bonded carbon-metal bonds impart spectroscopic properties upon the complex which are quite distinct from their N-coordinated equivalents; the MLCT state is dramatically stabilised by the sigma-donating C<sup>-</sup>, and the MC *d-d* transitions are very high in energy due to the ‘strong’ nature of the ligands such as ppy in the spectroscopic series.<sup>10</sup> Several groups have previously studied the excited-state properties of cyclometallated iridium complexes, especially with phenylpyridyl ligands, and it is believed that the luminescent state of such complexes is the lowest-lying excited state, which is the triplet LC state.<sup>12-14</sup> However, due to the proximity of the LC and MLCT state in cyclometallated complexes such as  $[\text{Ir}(\text{ppy})_2(\text{bpy})]^+$  (Figure 5.1), strong mixing of the charge transfer state into the lowest triplet LC state is induced.<sup>14-16</sup> In general structured bands with small shifts in the  $\lambda_{\text{max}}$  upon reducing the temperature of the samples, are attributed to triplet LC transitions, whereas broad and structureless bands with large shifts in the  $\lambda_{\text{max}}$  are characteristic charge transfer transitions. In addition to this mixing, many cyclometallated iridium(III) complexes exhibit significant spin-orbit coupling between the *singlet* MLCT state and the triplet LC state, which is mediated by the relativistic effects of the proximal heavy iridium(III) ion. Spin-orbit coupling of these states gives rise to the significantly enhanced oscillator strengths of the

transitions in such iridium(III) complexes, with respect to those usually observed for triplet LC transitions, as shown in Figure 5.2.<sup>12,16</sup> Further to this, empirical observations of the intense luminescence of several iridium(III) cyclometallated complexes relative to their analogous rhenium(III) complexes, which only give measurable emission at low temperatures, are consistent with the strong spin-orbit splitting proposed.<sup>14,16,17</sup>

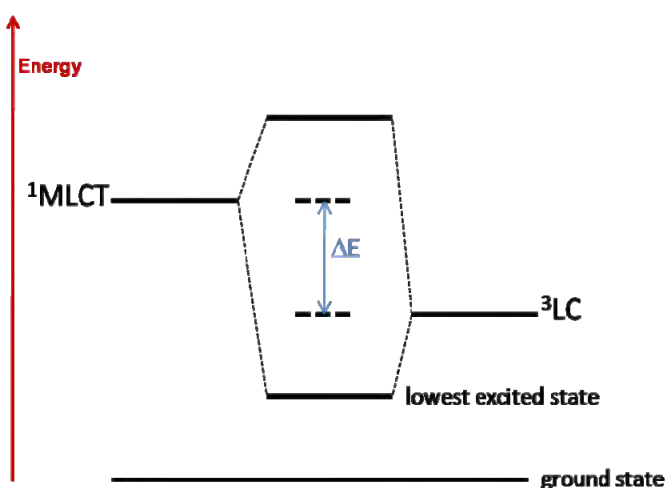


**Figure 5.2** Schematic showing the mixing of the low-lying LC and MLCT excited states in  $5d^6$  complexes, mediated by spin-orbit coupling.<sup>12</sup>

The degree of mixing between the singlet MLCT state and the triplet LC state depends upon the energy gap between the two states and the strength of the spin-orbit coupling between the two wavefunctions.<sup>15</sup> This can be studied by high resolution optical spectroscopy techniques, such as polarised single crystal absorption spectra and luminescence at cryogenic temperatures.<sup>14,16</sup> Just a small degree of singlet MLCT character has a dramatic effect upon the photophysical properties of the resultant emissive state, increasing both the oscillator strength and radiative rate of decay, thus enhancing the phosphorescence efficiency and reducing the excited state lifetime.<sup>12</sup> Therefore such complexes can display intense emission with long-lived emissive excited states, and the choice of ligand can drastically alter the excited-state characteristics. The ability to control the nature of the excited state is an advantage over the common ruthenium(II) polypyridyl complexes, which are confined to triplet MLCT states.<sup>7</sup>

Much of the biological imaging work using iridium(III) bis(cyclometallated) complexes has been pioneered by Lo and co-workers,<sup>7</sup> who have developed iridium(III) complexes with various cyclometallating (C<sup>-</sup>N) ligands, and a third biomodal ancillary (N<sup>-</sup>N) ligand for coordination. The ancillary ligand incorporates reactive groups for bioconjugation,<sup>18,19</sup> or molecular probes for various biological applications.<sup>20,21</sup> In 2010, Lo reported a series of emissive Ir(III) bis(cyclometallated) complexes coordinated to an ancillary ligand with a DNA-binding motif, as shown below in Figure 5.3.<sup>22</sup>

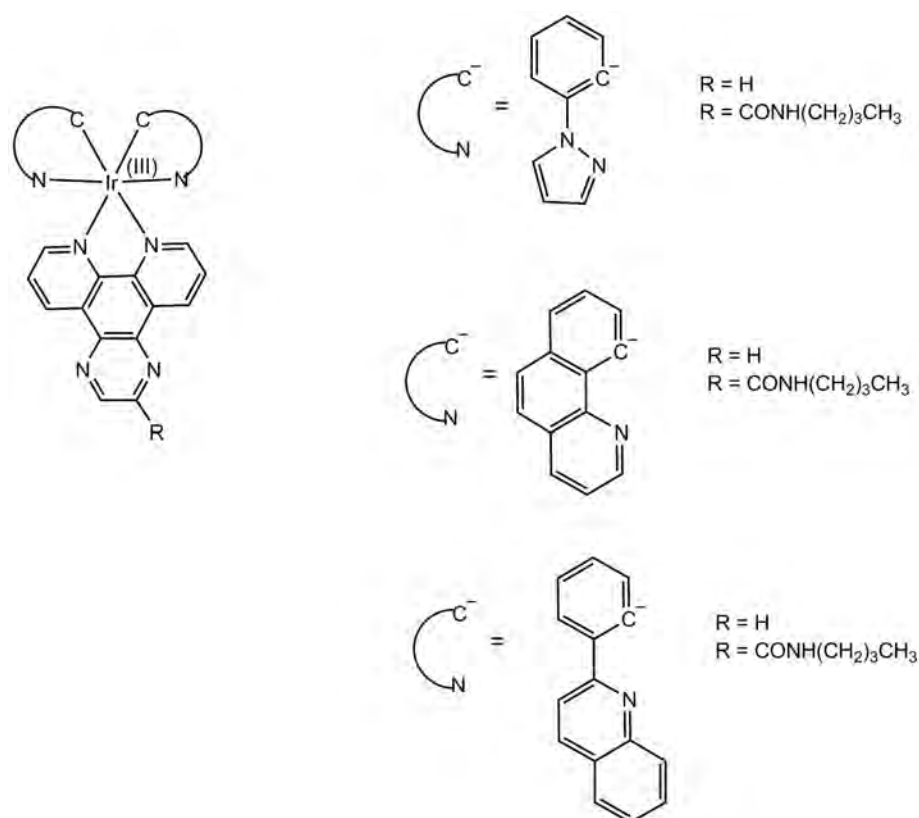


**Figure 5.3** Structures of Ir(III) complexes designed by Lo and co-workers for DNA-binding.<sup>22</sup>

Cellular uptake of all complexes shown in Figure 5.3 was demonstrated in canine kidney cells (MDCK cell line) and considerable nuclear uptake was observed in all cases. The complexes were all found to intercalate with calf thymus dsDNA in *in vitro* studies, enhancing the emission of each complex in steady-state luminescence titrations; these complexes (Figure 5.3) are the first example of Ir(III) polypyridyl that exhibit nuclear staining in cells. The group has also synthesised complexes that produce high levels of singlet oxygen (<sup>1</sup>O<sub>2</sub>) upon

photoexcitation, and such complexes demonstrate tuneable photodynamic activity.<sup>23</sup> Research has also been undertaken by Pope and co-workers to try to design water-soluble cyclometallated iridium(III) complexes so that biological applications can be achieved more easily.<sup>24,25</sup>

### 5.1.2 Labelling Nanoparticles with Ir(III) Complexes

There are a few examples of strategies to label silica nanoparticles with iridium(III) polypyridyl complexes,<sup>26-29</sup> whereas there are only two reports to date of labelling gold nanoparticles with iridium(III) complexes, both by Mayer and co-workers.<sup>30,31</sup> The group initially developed a novel bifunctional heteroleptic Ir(III) complex, as shown in Figure 5.4, which upon addition of  $\text{HAuCl}_4$  under basic conditions, both reduced the  $\text{Au}^{3+}$  to  $\text{Au}^0$  and capped the resulting particles *in situ*, to give Ir(III)-functionalised gold nanoparticles 2–3 nm in size, which were soluble in THF.<sup>30</sup>

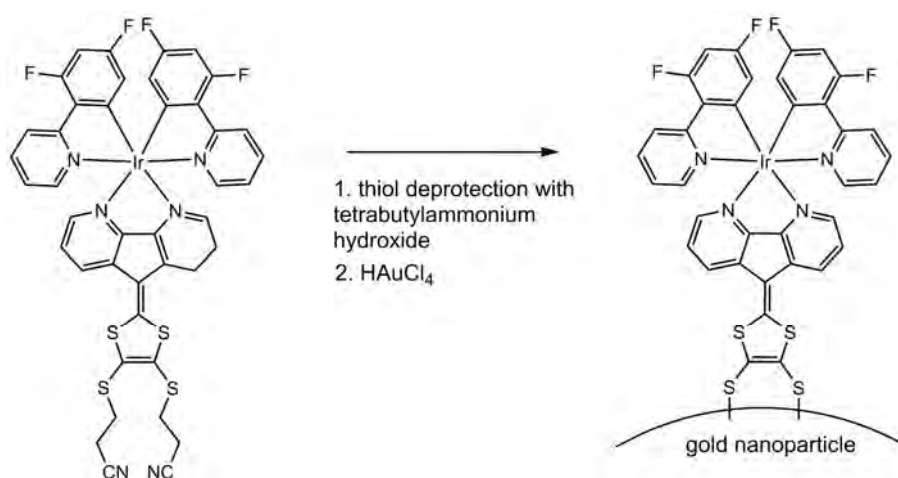


**Figure 5.4** Reduction of  $\text{HAuCl}_4$  and *in situ* capping process of resulting gold nanoparticles by the bifunctional Ir(III) complex with its 4,5-diazafluorenedithiolate ancillary ligand by Nasr et al.<sup>30</sup>

The iridium(III) complex features a 4,5-diazafluorenedithiolate ligand which acts as the efficient reducing agent for the  $\text{HAuCl}_4$ . Interestingly, however, studies of the uncomplexed ligand in a similar reaction reveal a very slow reduction process, thus demonstrating the essential role of the iridium(III) metal centre in the reduction mechanism. The free complex

displayed bright yellow luminescence with  $\lambda_{\text{max}}$  at 537 nm, and a quantum yield of 40% in degassed acetonitrile. However, no luminescence was observed from the functionalised nanoparticles, and thus it is believed that significant non-radiative quenching pathways from the emissive excited state are introduced upon grafting the complex to gold nanoparticles.<sup>30</sup> Although these particles have no potential as imaging probes, the synthesis of new nanocomposite materials presents promising candidates for catalysis.

Mayer has recently published another study using a different bis(cyclometallated) heteroleptic Ir(III) complex, as shown in Figure 5.5, which is the first report of functionalising metallic nanoparticles with luminescent iridium(III) complexes that retain their luminescence upon immobilisation at the surface.<sup>31</sup> 5–6 nm gold and silver nanoparticles were synthesised by reduction of  $\text{HAuCl}_4$  with  $\text{NaBH}_4$  in the presence of dodecylamine, and then postfunctionalisation of the nanoparticles with the Ir(III) complex was achieved via ligand-exchange. The exchange reaction was carried out at low concentrations of complex, to afford nanoparticles labelled with 2 to 15 complexes each. Low loading was performed to maintain colloidal stability and to minimise intermolecular charge transfer between grafted Ir(III) complexes.

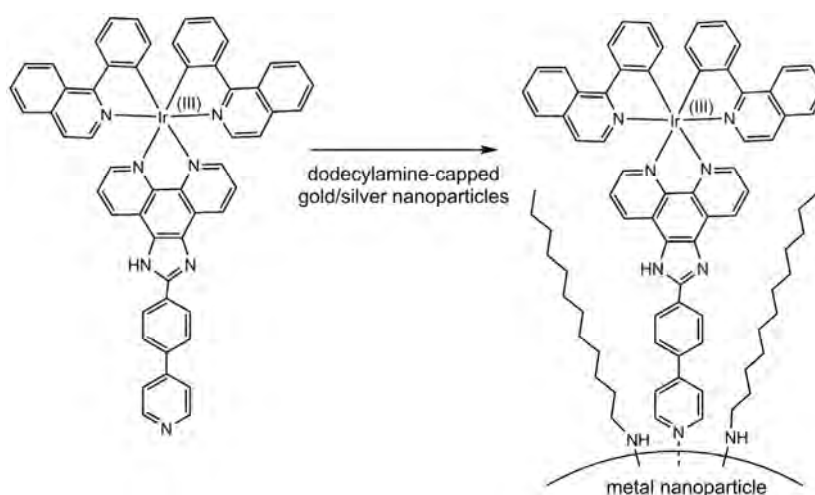


**Figure 5.5** Functionalisation of gold and silver nanoparticles with luminescent Ir(III) cyclometallated complexes, by ligand-exchange of dodecylamine-capped metal nanoparticles.<sup>31</sup>

Steady-state luminescence studies of the free complex *vs.* the same concentration of complex bound to nanoparticles revealed a reduction in signal intensity upon grafting the Ir(III) complex to both gold and silver nanoparticles, although more significant quenching was observed on the gold nanoparticles. In addition, a shortening of the observed luminescence lifetime of the complex was observed upon attachment to nanoparticles, and again a greater reduction in the lifetime was observed on the gold nanoparticles. This difference in the quenching effect of each metal has been rationalised by the greater spectral overlap of the SPR of the gold nanoparticles (at 516 nm, compared with that of the silver nanoparticles at 422 nm) and the luminescence of the iridium(III) complex ( $\lambda_{\text{max}}$  of free complex in  $\text{CH}_2\text{Cl}_2 = 633 \text{ nm}$ ). Thus it is proposed that excitation of the SPR of the nanoparticles, which enhances the electromagnetic field in the vicinity of the particle, deactivates the excited state of the Ir(III) complex by either energy transfer or electron transfer.

Flow fields on the micron scale are generated within small blood vessels, which produce unsteady flow phenomena and govern the transport rates of oxygen, nutrients, waste and drugs. The flow dynamics determine the mechanical shear forces imparted on the vessel walls, and can influence pathophysiological mechanisms within the vascular bed.<sup>32</sup> Thus, the continued study of blood flow dynamics will improve the understanding of the circulatory system function, and will also be important in the design of biomedical devices and drug-delivery platforms.<sup>33-37</sup> Not only are the flow dynamics and delivery of intravenous theranostic nanoparticles important but also their fate *in vivo* is of prime interest.<sup>38-40</sup> Furthermore, a drug platform which can be tracked, e.g. by luminescence, would be highly advantageous for studying pharmacokinetics and for targeting in nanomedicine.

Further development of the iridium(III)-labelled gold nanoparticles has been explored to extend their imaging potential to gross tissue imaging, by designing multimodal imaging

nanoprobes with both MRI-active gadolinium(III) complexes and luminescent iridium(III) complexes to nanoparticles. Gadolinium(III) chelates are highly paramagnetic, with seven unpaired electrons, and give  $T_1$ -contrast in proton MRI imaging by reducing the longitudinal relaxation time of nearby water protons, which enhances local contrast with respect to background tissue.<sup>41-43</sup> The combination of multiple imaging probes onto a single nanoprobe can offer synergetic multifunctional nanomedical devices, with the possibility of multimodal imaging;<sup>44-46</sup> every imaging technique has advantages and disadvantages, and the integration of two different imaging modality probes can optimise both the precision and the speed of diagnosis. Such particles have the potential for locating gross tissue *in vivo* by MRI, and then subsequent pathological biopsy of the microvasculature could be performed optically to give higher resolution detail regarding disease progression. This, combined with a targeting moiety, has potential as a multimodal theranostic probe.<sup>47-49</sup>

### 5.1.3 Chapter Outline

In this chapter the labelling-strategy of gold nanoparticles developed with ruthenium(II) polypyridyl complexes in Chapters Two and Three, has been extended by developing surface-active iridium(III) polypyridyl complexes with superior photophysical properties, with the aim of achieving brighter nanoparticles which can be imaged in dynamic systems. Two luminescent surface-active iridium(III) complexes, **IrBpySAc** and **IrPhenSAc**, have been synthesised and characterised. 13 nm and 100 nm citrate gold nanoparticles have been coated with **IrBpySH** and **IrPhenSH**, synthesised *in situ* from **IrBpySAc** and **IrPhenSAc** respectively, in a surfactant-mediated process using the fluorosurfactant Zonyl® 7950. The structures of **IrBpySH** and **IrPhenSH** are presented in Figure 5.6 and the labelled nanoparticles discussed in this chapter are shown in Figure 5.7.

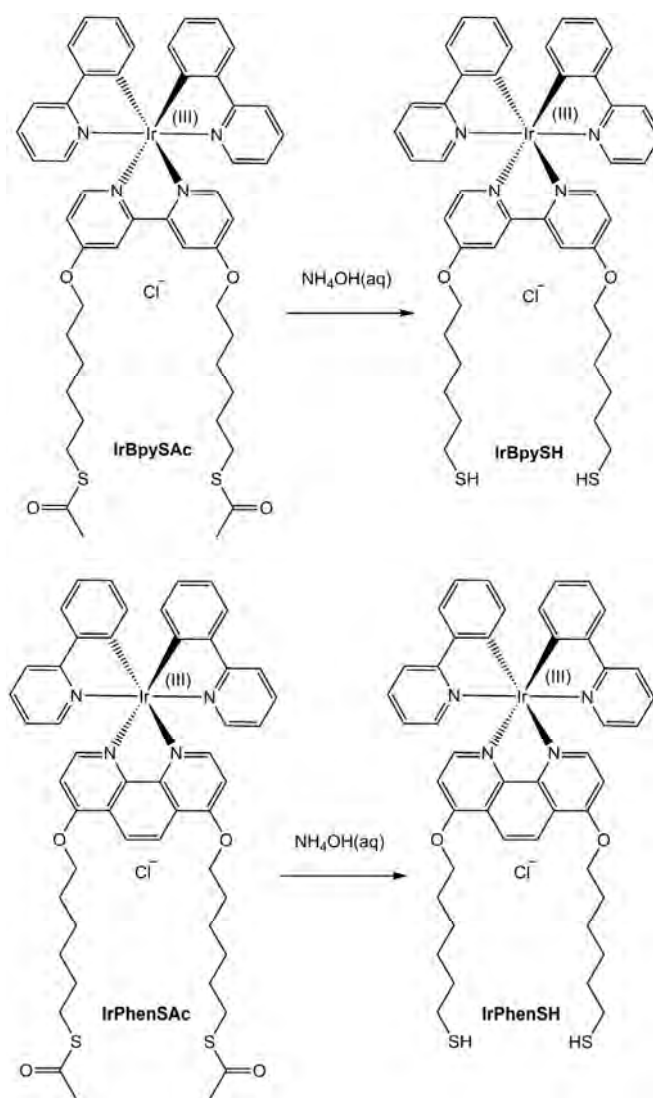


**Figure 5.6** Structures of *IrBpySAC*, *IrBpySH*, *IrPhenSAC*, and *IrPhenSH* complexes discussed in this chapter.

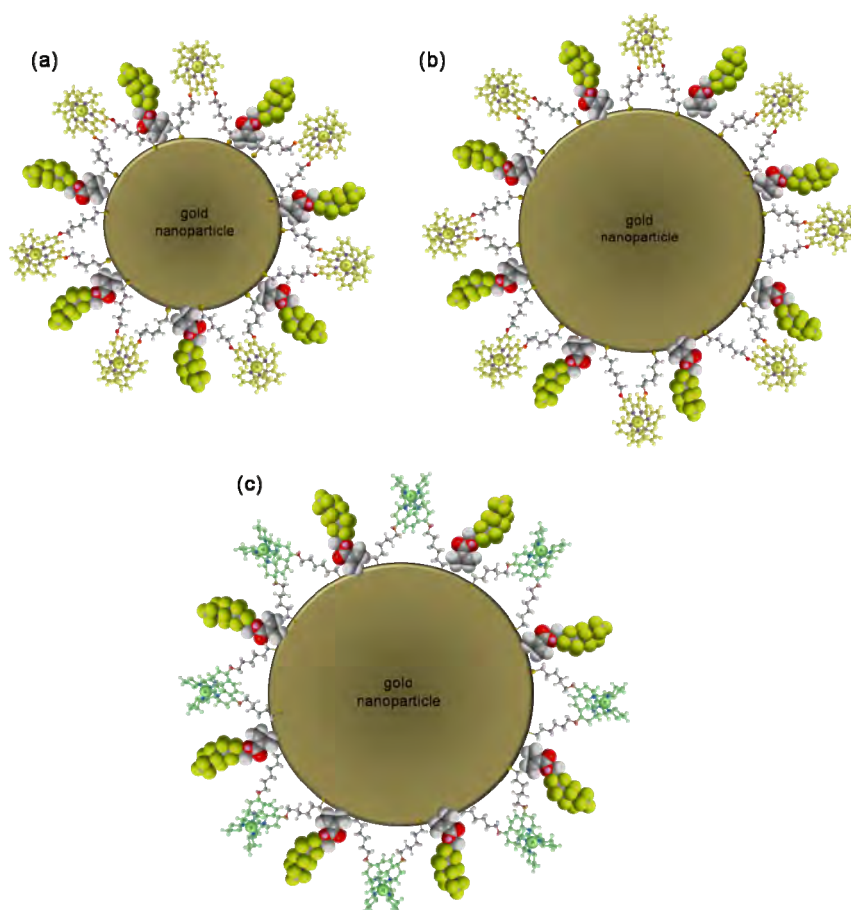


**Figure 5.7** Schematics of *IrBpy-Z•AuNP13*, (b) *IrBpy-Z•AuNP100*, and (c) *IrPhen-Z•AuNP100*.

The brightest nanoparticles, **IrBpy-Z•AuNP100**, were studied in flow, to see if they could be imaged flowing through microchannels, and thus be used as velocimetry tracers to analyse fluid mechanics. Flow studies were explored in blood in an *in vitro* channel model, and the biodistribution and detection of nanoparticles in biological tissue have been investigated in a murine model. 13 nm gold nanoparticles have also been co-coated with the gadolinium(III) pentetic acid derivative, **GdQSH** (Figure 5.8) and **IrBpySH** (Figure 5.6) to give **IrBpy-GdQ•AuNP13** (Figure 5.8), which can be detected by optical luminescence microscopy and by proton MRI using  $T_1$ -weighted contrast. **GdQ•AuNP13** nanoparticles were also synthesised for comparison (Figure 5.8).

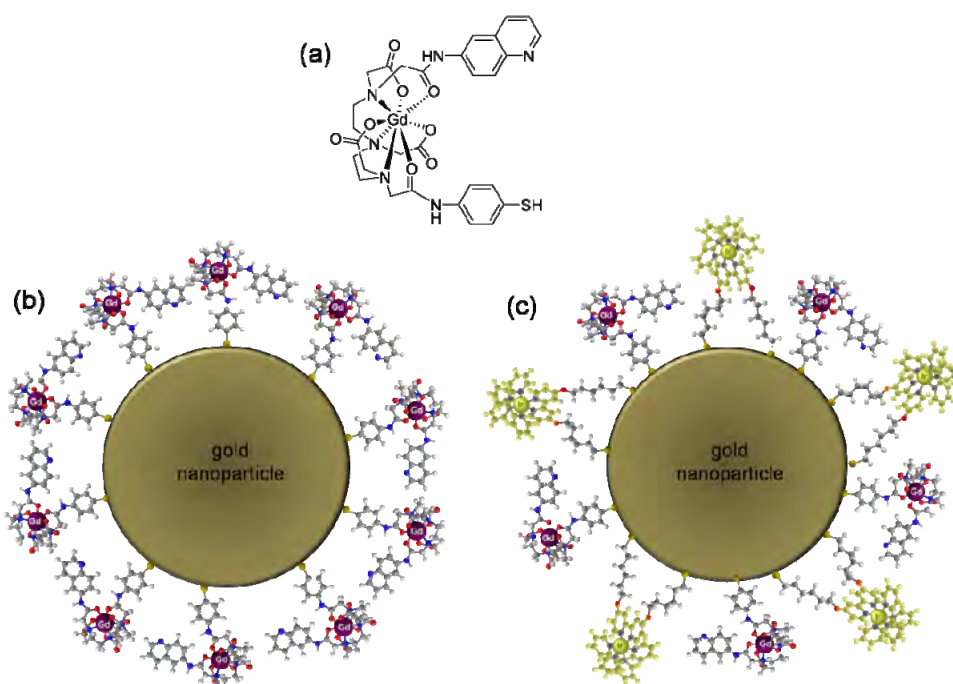


**Figure 5.8** Schematics of (a) *GdQSH* complex, (b) *GdQ•AuNP13* nanoparticles made for comparative purposes and (c) *IrBpy-GdQ•AuNP13*, as discussed in Section 5.5.

## 5.2 Synthesis and Characterisation of IrBpySH and IrPhenSH

**IrBpySH** and **IrPhenSH** were synthesised according to the schematic shown in Figure 5.9.

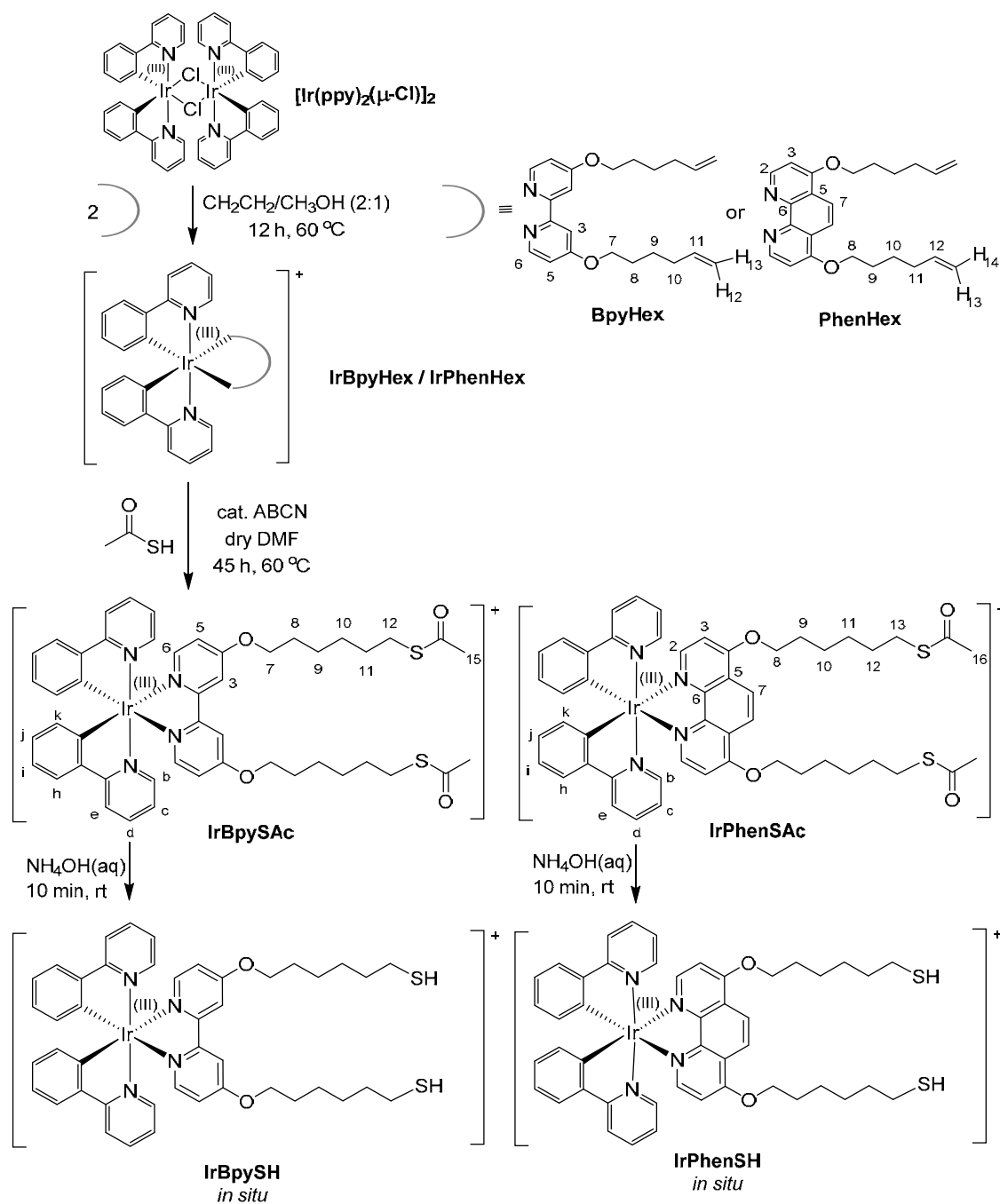


**Figure 5.9** Synthesis of the surface-binding Ir(III) complexes **IrBpySH** and **IrPhenSH**.

The bis-cyclometallated  $\mu$ -dichloro bridged complex,  $[\text{Ir}(\text{ppy})_2(\mu\text{-Cl})]_2$ , was synthesised by Nonoyama reaction<sup>50</sup> of 2-phenylpyridine with iridium(III) chloride hydrate, according to literature procedure,<sup>17</sup> forming the kinetic product, i.e. the dimer with the *N*-coordinated

heterocycles in a *trans*-relationship, as this positions the sigma-donating C<sup>-</sup> atoms trans to the Cl<sup>-</sup> bridging ligands.<sup>12</sup> The dimer was isolated, and a solution of the solid in *d*<sub>6</sub>-DMSO was characterised by NMR (<sup>1</sup>H and <sup>13</sup>C{<sup>1</sup>H} PENDANT) spectroscopy and mass spectrometry. Each proton resonance of the phenylpyridyl ligand (H<sub>b</sub>, H<sub>c</sub>, H<sub>d</sub>, H<sub>e</sub>, H<sub>h</sub>, H<sub>i</sub>, H<sub>j</sub>, H<sub>k</sub>) is split into two different environments in a 50:50 ratio in the <sup>1</sup>H NMR spectrum, due to the DMSO solvent breaking the dimer and forming [Ir(ppy)<sub>2</sub>(DMSO)Cl] monomers, and only the [Ir(ppy)<sub>2</sub>]<sup>+</sup> fragment peak is observed by mass-spectrometry, at *m/z* = 501.1. (Splitting is not seen if the dimer is dissolved in CD<sub>2</sub>Cl<sub>2</sub><sup>17</sup>).

The ancillary ligands were synthesised by the Williamson reaction of 4,4'-dihydroxy-2,2'-bipyridine or 4,7-dihydroxy-1,10-phenanthroline with bromohex-1-ene in the presence of base to give **BpyHex**<sup>1</sup> (see Chapter 2, Section 2.2.1) and **PhenHex** (synthesised by Dr Shiva Farabi<sup>51</sup>) respectively. Facile replacement of the bridging chloride ligands in the dimer with the ancillary ligand was achieved by heating [Ir(ppy)<sub>2</sub>(μ-Cl)]<sub>2</sub> with two equivalents of each ligand in the mixed solvent system CH<sub>2</sub>Cl<sub>2</sub>:CH<sub>3</sub>OH (2:1). **IrPhenHex** was isolated as a hexafluorophosphate salt by addition of 10-fold molar excess ammonium hexafluorophosphate, according to the literature procedure by Sun *et al.*,<sup>52</sup> whereas **IrBpyHex** was isolated directly as the chloride salt. Purification of the resulting complexes by column chromatography afforded **IrBpyHex** and **IrPhenHex**, which were characterised by NMR spectroscopy (both <sup>1</sup>H and <sup>13</sup>C{<sup>1</sup>H} PENDANT) and mass spectrometry. Successful complexation of both **IrBpyHex** and **IrPhenHex** is evident from their electrospray mass spectra, with peaks observed for each monocharged complex after loss of its counterion, at *m/z* 853.5 for **IrBpyHex**, corresponding to [M-Cl]<sup>+</sup>, and at *m/z* 877.4 for **IrPhenHex**, corresponding to [M-PF<sub>6</sub>]<sup>+</sup>. The <sup>1</sup>H NMR spectra of both **IrBpyHex** and **IrPhenHex** feature protons of the two phenylpyridyl ligands and the ancillary ligand (**BpyHex** or **PhenHex**) all integrating in the correct ratios with respect to one another. The protons of each ancillary

ligand exhibit quite striking chemical shifts upon complexation to Ir<sup>3+</sup>: H<sub>6</sub> shifts upfield from 8.45 ppm in the free **BpyHex** ligand to 7.59 ppm in **IrBpyHex**, whereas H<sub>3</sub> and H<sub>5</sub> shift downfield, from 7.94 ppm and 6.82 ppm in the free ligand, to 8.46 ppm and 7.28 ppm respectively in the complex. Similarly in **PhenHex**, H<sub>2</sub> shifts upfield from 8.89 ppm to 7.93 ppm, and H<sub>3</sub> and H<sub>7</sub> shift downfield from 7.28 ppm and 8.15 ppm, to 7.56 ppm and 8.36 ppm respectively, upon complexation. In each case, the CH proton adjacent to the donating nitrogen atom on the aromatic ring experiences electron shielding due to the proximity of the Ir(III) *d*-electrons, whereas the remaining protons, which face away from the metal centre, experience an overall deshielding effect upon complexation, due to the donation of electrons from the ligand towards the metal centre. The same effect is seen upon complexation with Ru<sup>2+</sup>.<sup>1,51</sup> In addition, an upfield shift in H<sub>b</sub> of the phenylpyridyl ligands, by *ca.* 2 ppm, corroborates the metathesis reaction.

The olefin groups of **IrBpyHex** and **IrPhenHex** were converted into thioester groups by the free-radical mediated nucleophilic addition reaction of thioacetic acid to give the oxidatively stable bis-thioacetyl groups, according to the previously reported reaction<sup>1,2</sup> used to form **RuSAc** in Chapter Two. **IrBpySAc** and **IrPhenSAc** were both isolated as chloride salts and characterised by <sup>1</sup>H and <sup>13</sup>C{<sup>1</sup>H}PENDANT NMR spectroscopy and mass spectrometry. Electrospray mass spectrometry of each complex revealed peaks for each monocharged complex after loss of its counterion, observed at *m/z* 1005.4 for **IrBpySAc** and at *m/z* 1029.3 for **IrPhenSAc**, and it was possible to obtain high-resolution mass spectra within 5 ppm of the theoretical mass in each case. The carbonyl bond of each thioester is evident from the peak observed at 1682 cm<sup>-1</sup> and 1684 cm<sup>-1</sup> in the FT-IR absorption spectra of **IrBpySAc** and **IrPhenSAc** respectively, which are absent in the spectra of **IrBpyHex** and **IrPhenHex**. The successful thioesterification reaction was confirmed undoubtedly by <sup>1</sup>H NMR spectra, with loss of the olefin protons at *ca.* 5.8 ppm and 5.0 ppm, and the appearance of the triplet at 2.83

ppm ( $H_{12}$  in **IrBpySAc**) and at 2.86 ppm ( $H_{13}$  in **IrPhenSAc**), as well as the appearance of the terminal methyl group of each thioester at *ca.* 2.3 ppm. In all cases, the relative peak areas by integration matched theory. The thiol groups were finally unmasked *in situ* by thioester hydrolysis with aqueous ammonia directly prior to addition to the nanoparticles, which was confirmed by MALDI mass spectrometry using a gentisic acid matrix; peaks were observed for each monocharged complex after loss of its counterion, at  $m/z$  920.2 for **IrBpySH** and at  $m/z$  944.2 for **IrPhenSH**.

### 5.3 Photophysical Characterisation of IrBpySAc and IrPhenSAc

Often, iridium(III) complexes are studied in degassed solvents or in rigid films and/or glasses at 77 K, where they tend to phosphoresce brightly because the non-radiative decay paths are minimised. Whilst such studies may be suited for OLED applications where such formulation is appropriate, when considering complexes for imaging agents in biological environments, it is important to undertake studies in conditions which are relevant to the application. The photophysical properties of **IrBpySAc** and **IrPhenSAc** were, therefore, characterised in both aerated  $CH_3CN$  and aerated 1%  $CH_3CN$ ,  $H_2O$ , to emulate the solvent conditions within an aqueous colloidal dispersion, whilst facilitating solubility, as presented in Figure 5.10.

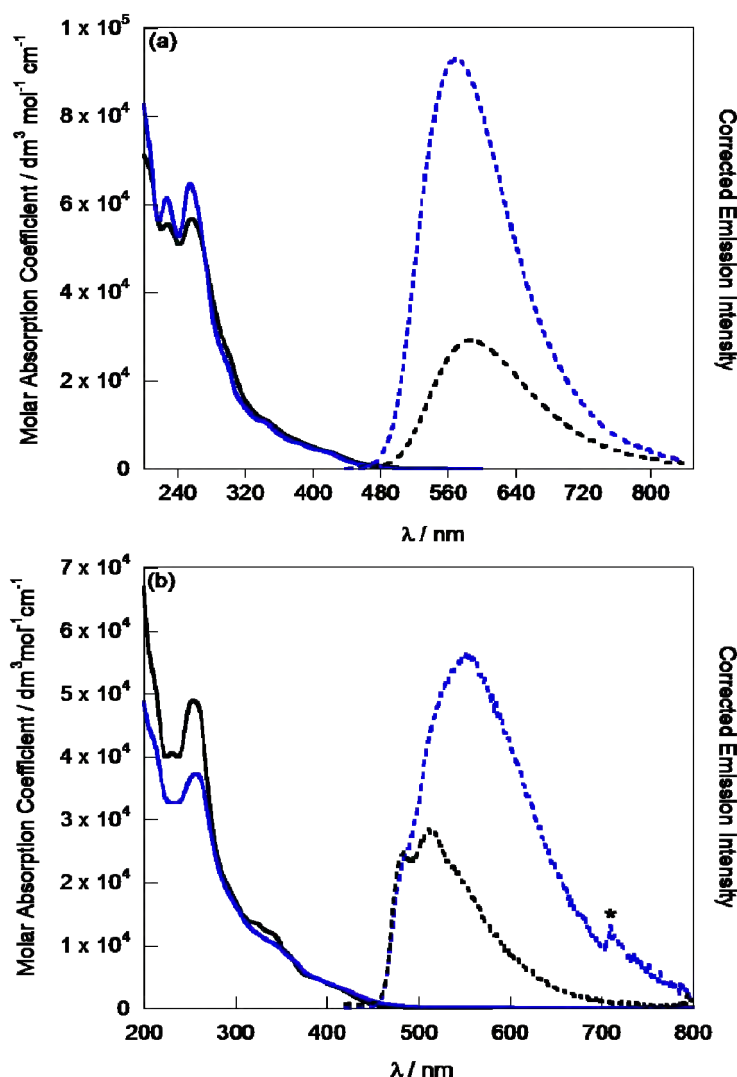


**Figure 5.10** UV-Vis absorption spectra (solid lines) of 20  $\mu\text{M}$  (a) **IrBpySAc** and (b) **IrPhenSAc** solutions in  $\text{CH}_3\text{CN}$  (black) and water, 1%  $\text{CH}_3\text{CN}$  (blue). Steady-state luminescence spectra (dashed lines),  $\lambda_{\text{exc}} = 355 \text{ nm}$ . \* = scattering peak, i.e. second harmonic of 355 nm. Spectra corrected for instrument response.

The UV-Vis absorption profiles of both **IrBpySAc** and **IrPhenSAc** exhibit intense spin-allowed singlet LC ( $\pi\text{-}\pi^*$ ) transitions of the (C<sup>^</sup>N) and (N<sup>^</sup>N) ligands in the far UV region (200–300 nm) with molar absorption coefficients in the order of  $10^4 \text{ dm}^3 \text{ mol}^{-1} \text{ cm}^{-1}$ . The spectra of both complexes exhibit maxima at 255 nm, and a peak at 230 nm in the case of **IrBpySAc**, presumably due to the singlet LC state associated with the bipyridyl-ancillary ligand. The corresponding LC absorption associated with the ancillary (N<sup>^</sup>N) ligand in **IrPhenSAc** appears to overlap with the phenylpyridyl peak, red-shifted with respect to the

bipyridyl equivalent. The absorption profiles of both complexes show weaker absorptions extending from 300 nm into the near-visible, corresponding to direct absorptions into the spin-allowed singlet MLCT excited state, with molar absorption coefficients of the order of  $10^3 \text{ dm}^3 \text{ mol}^{-1} \text{ cm}^{-1}$ . These features are similar to the UV-Vis absorption spectral features observed for the parent compounds  $[\text{Ir}(\text{ppy})_2\text{bpy}]^{+53,54}$  and  $[\text{Ir}(\text{ppy})\text{phen}]^+.$ <sup>52</sup> Excitation of both **IrBpySAc** and **IrPhenSAc** complexes at 355 nm, gives rise to a broad emission peak in the luminescence spectra from 450–800 nm. The steady-state luminescence spectrum of **IrBpySAc** in an aerated solution of  $\text{CH}_3\text{CN}$  is structureless with  $\lambda_{\text{max}}$  at 585 nm and a quantum yield of 3%, whereas the emission spectrum of **IrPhenSAc** peaks at 515 nm, with a smaller quantum yield of 1%, whilst exhibiting some vibronic structure, with a peak at 480 nm and a shoulder at 545 nm (Figure 5.10). Excitation spectra of both complexes can be found in Appendix 10.

Solutions of both **IrBpySAc** and **IrPhenSAc** exhibit significant changes in their emission profiles as the polarity of the solvent changes from  $\text{CH}_3\text{CN}$  to  $\text{H}_2\text{O}$  (with 1 %  $\text{CH}_3\text{CN}$ ), as has been observed by Pope and co-workers<sup>25</sup> and as is observed with the ruthenium(II) polypyridyl complexes described in Chapter Two, due to the charge-transfer nature of the excited states. The solution photophysical characterisations of each compound are summarised in Table 5.1, along with the corresponding data for the two parent compounds:  $[\text{Ir}(\text{ppy})_2\text{bpy}]^+$ , taken from work by Constable<sup>55</sup> and Watts;<sup>10</sup> and  $[\text{Ir}(\text{ppy})_2\text{phen}]^+$ , which was synthesised by the author as a control, and has been published in a separate study.<sup>29</sup>

**Table 5.1** Summary of the solution photophysical properties of **IrBpySAc** and **IrPhenSAc** in  $CH_3CN$  and 1%  $CH_3CN$ ,  $H_2O$ .

solvent system:	<b>IrBpySAc</b>		<b>IrPhenSAc</b>		$[Ir(ppy)_2bpy]^+$	$[Ir(ppy)_2phen]^+$
	$CH_3CN$	1% $CH_3CN$ , $H_2O$	$CH_3CN$	1% $CH_3CN$ , $H_2O$	$CH_3CN$	$CH_3CN$
$\lambda_{max} / nm^a$	585	570	515	550	585 <sup>b</sup>	595 <sup>c</sup>
$\tau_{obs} / ns^d$	60	75 (25%) 300 (75%)	40	110 (6%) 325 (80%) 745 (14%)	-	60 <sup>c</sup>
	[325]	-	[2250]	-	[340] <sup>e</sup>	[780] <sup>c</sup>
$\Phi^f$	0.03 [0.09]	0.05 -	0.01 [0.28]	0.04 -	- [0.14] <sup>b</sup>	0.02 <sup>c</sup> [0.20] <sup>c</sup>

<sup>a</sup>estimated error =  $\pm 3$  nm<sup>b</sup>data taken from Constable and co-workers<sup>55</sup><sup>c</sup>data measured by the author and published in a separate study.<sup>29</sup><sup>d</sup>lifetimes measured in aerated solutions, deaerated measurements (systems degassed with nitrogen for 20 min), shown in square brackets. Multi-component lifetimes quoted with *intensity weightings* in parenthesis. Errors estimated as  $\pm 6\%$  for measured data.<sup>e</sup>data taken from Watts and co-workers<sup>10</sup><sup>f</sup>aerated  $\Phi$  measurements, deaerated measurements (systems degassed with nitrogen for 20 min) shown in square brackets. Estimated error for  $\Phi = \pm 25\%$ .

A 35 nm bathochromic shift in the emission  $\lambda_{max}$  is observed when **IrPhenSAc**, is dissolved in an aqueous (1%  $CH_3CN$ ) solution, with respect to a 100%  $CH_3CN$  solution, similar to the smaller 15 nm red shift that is observed with  $[Ir(ppy)_2phen]^+$  (see Appendix 12).<sup>29</sup> In addition the emission peak broadens (FWHM increases by 40%) in the aqueous solution and the vibronic structure disappears. This effect is most likely due to the stabilisation of the MLCT state in the more polar environment, which increases the mixing between the MLCT and LC states, reducing the energy gap between the first excited state and ground state, whilst giving the state more MLCT character, as shown below in Figure 5.11.

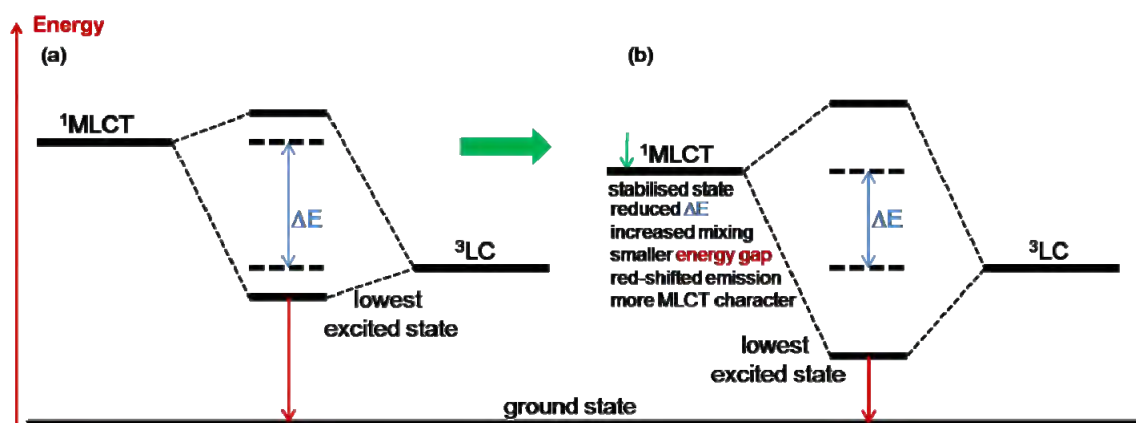


**Figure 5.11** Schematic of the energy levels of the lowest excited states of **IrPhenSAC** in (a)  $\text{CH}_3\text{CN}$  and (b)  $\text{H}_2\text{O} / 1\% \text{CH}_3\text{CN}$ .

In contrast, a 15 nm hypsochromic shift in the emission maximum is observed in the aqueous solution of **IrBpySAC**, with respect to the  $\text{CH}_3\text{CN}$  solution, which is an unusual observation for a MLCT excited state; usually increasing the polarity of the solvent system stabilises the polar charge-transfer state, lowering the energy of the transition. A similar iridium(III) bis(phenylpyridyl) chloride salt, with a 4,4'-ethoxyamino-2,2'-bipyridine ancillary ligand<sup>29</sup> has a similar blue shift in water, from 575 nm to 550 nm (see Appendix 11). Chen and co-workers<sup>53</sup> recently investigated the relaxation dynamics of  $[\text{Ir}(\text{ppy})_2\text{bpy}]^+$  using time-resolved emission spectroscopy and proposed that there are, in fact, multiple emission bands that overlap in energy, as was first shown in by King and Watts in 1987.<sup>54</sup> It is believed that emission is observed from three states; a triplet ligand-to-ligand ( $\pi \text{ppy} \rightarrow \pi^* \text{bpy}$ ) charge transfer (LLCT) band, an MLCT ( $d\pi \rightarrow \text{ppy}$ ) band, and also an MLCT ( $d\pi \rightarrow \text{bpy}$ ) band, and thus solvation effects are far from trivial.<sup>53</sup> It was not possible to tail-fit (i.e. fit the decay beyond the time point where the excitation light pulse has disappeared) the observed lifetimes of either **IrBpySAC** or **IrPhenSAC** in aqueous environments with a monoexponential decay model; such fitting rendered unacceptable reduced chi-square fitting parameters and oscillating residual data. Therefore, the exponential order was increased until the residual plot presented random noise distributed about zero, with a reduced chi-square value between 1.0-

1.3. (see Appendix 13). The reduced chi-square value estimates the predicted variation of the fitted data, divided by the actual variance of the parent dataset, which should be close to unity if the function is a good fit for the data.

Solution studies of both **IrBpySAc** and **IrPhenSAc** in CH<sub>3</sub>CN show an increase in the steady-state luminescence and a lengthening of the observed lifetime upon de-aeration of the solution, due to quenching of the triplet excited state by ground-state molecular oxygen (O<sub>2</sub>(<sup>3</sup>Σ<sub>g</sub><sup>-</sup>)), as described in Chapter Two, Section 2.1.2. Degassing the solutions removes these quenching pathways and reduces the non-radiative rate of decay. A three-fold increase in the quantum yield and a five-fold increase in the luminescence lifetime are observed upon deaeration of **IrBpySAc** in CH<sub>3</sub>CN, which equates to a six-fold decrease in the non-radiative rate of decay from the excited state, whereas a *ca.* 60-fold increase in the lifetime and a *ca.* 30-fold increase in the quantum yield (an 80-fold decrease in the non-radiative rate of decay) is observed for **IrPhenSAc**. Therefore, **IrPhenSAc** appears to be far more oxygen sensitive than **IrBpySAc**, which complements the significant LC character observed in the steady-state luminescence, as the excited-state also has more triplet character. Using the Stern-Volmer equation<sup>56</sup> below (Equation 5.1), the bimolecular quenching rate constant,  $k_q$ , can be calculated from the lifetime data measured in aerated and de-aerated solutions.

$$\frac{\tau}{\tau_0} = 1 + k_q \tau [Q] \quad \text{Equation 5.1}$$

$\tau$  = the quenched lifetime,  $\tau_0$  = the unquenched lifetime,  $k_q$  = the bimolecular quenching rate constant, and  $[Q]$  = the concentration of the quenching species, i.e. [O<sub>2</sub>]. Assuming that the [O<sub>2</sub>] = 2.4 mM in air-saturated CH<sub>3</sub>CN,<sup>57</sup>  $k_q$  is  $6 \times 10^9 \text{ dm}^3 \text{ mol}^{-1} \text{ s}^{-1}$  for **IrBpySAc**, and  $10 \times 10^9 \text{ dm}^3 \text{ mol}^{-1} \text{ s}^{-1}$  for **IrPhenSAc**, in CH<sub>3</sub>CN.

The ether functionalisation of the bipyridine ligand with the surface-active appendages in **IrBpySAc** has very little effect upon the photophysical properties of the lumiphore, with respect to the parent complex  $[\text{Ir}(\text{ppy})_2\text{bpy}]^+$ ; the  $\lambda_{\text{max}}$  value and the degassed lifetime are the same within an experimental error of  $\pm 5\%$ . The quantum yield is reduced by 35 %, which may be due to the additional appendages opening up further non-radiate vibrational relaxation pathways from the excited state, which compete with the luminescence. For comparison, ether functionalisation of the bipyridine ligand a similar iridium(III) bis(phenylpyridyl) chloride salt, with a 4,4'-ethoxyamino-2,2'-bipyridine ancillary ligand, blue-shifts the  $\lambda_{\text{max}}$  value by 10 nm, and bi-exponential degassed lifetimes of 380 ns (32%) and 1325 ns (68%) (*intensity* weightings shown in parenthesis), and a similar quantum yield of 0.16 is observed.<sup>29</sup> In this instance, 4,4'-ethoxyamino- groups appear to affect the excited state energies more so than the hexyl-ether appendages in **IrBpySAc**, which is expected due to the proximity of the electron-donating amine groups. A similar blue shift is observed by Pope<sup>25</sup> with Ir(III) bis(cyclometallated) complexes in which the cyclometallating ligands are ethyl-2-phenylquinoline-4-carboxylates, and the ancillary ligand is bipyridine-based; upon esterification in the 4,4'-positions of the ancillary bipyridine ligand, a 7 nm blue-shift is observed in the steady-state emission.<sup>25</sup>

The ether functionalisation of the phenanthroline unit in **IrPhenSAc** has a marked effect upon the excited state of the complex, with respect to  $[\text{Ir}(\text{ppy})\text{phen}]\text{Cl}$ ; the MLCT state of the complex appears to be destabilised due to the electron-donating ether-group, which in turn reduces the MLCT–LC mixing, and increases the energy gap between the ground-state and the first-excited state, as represented in Figure 5.12 below:

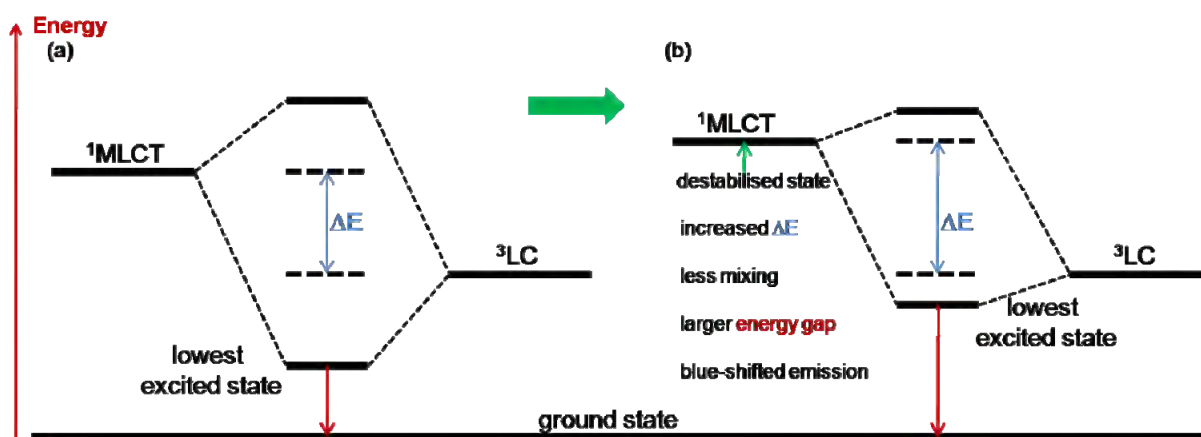


**Figure 5.12** Schematic of the energy levels of the lowest excited states of (a)  $[\text{Ir}(\text{ppy})_2\text{phen}]^+$  and (b) *IrPhenSAC* in  $\text{CH}_3\text{CN}$ .

The destabilisation of the MLCT state results in a blue-shifted  $\lambda_{\text{max}}$  emission peak and more LC character and hence the appearance of vibronic structure, due to less mixing of the two states. In addition, the degassed lifetime of **IrPhenSAC** extends into the microsecond time range, unlike that of  $[\text{Ir}(\text{ppy})_2\text{phen}]^+$ , which is again indicative of significant triplet LC character. A similar blue-shift is observed upon methylation of the phenanthroline ligand in the 4 and 7 position, in a similar  $[\text{Ir}(\text{ppy})_2(\text{N}^{\wedge}\text{N})]^+$  complex (( $\text{N}^{\wedge}\text{N}$  = 4,7-dimethyl-1,10-phenanthroline), in which a 17 nm blue-shift is observed.<sup>58</sup>

To investigate the excited-state characteristics further, the steady-state luminescence spectra of each compound were measured in  $\text{CH}_3\text{CN}$  at 77 K, as presented in Figure 5.13.

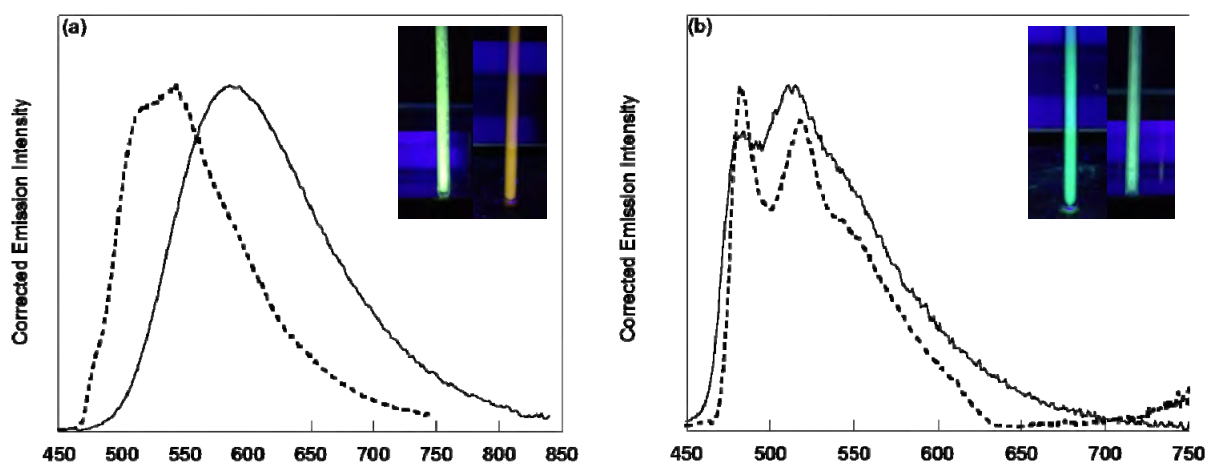


**Figure 5.13** Steady-state luminescence spectra of 20  $\mu\text{M}$  (a) **IrBpySAc** and (b) **IrPhenSAc**,  $\lambda_{\text{exc}} = 355 \text{ nm}$ , in  $\text{CH}_3\text{CN}$  at 298 K (solid) and 77 K (dashed). Insets – photograph of each complex in  $\text{CH}_3\text{CN}$  at 77 K (left) and 298 K (right),  $\lambda_{\text{exc}} = 370 \text{ nm}$ . Spectra corrected for instrument response.

The two complexes behave very differently upon reducing the temperature from 298 K to 77 K in  $\text{CH}_3\text{CN}$ ; the steady-state spectrum of **IrBpySAc** exhibits a rigidochromic blue-shift of *ca.* 50 nm, which is indicative of a charge-transfer excited state. In fluid solution at room temperature, solvent reorganisation can stabilise the polar charge-transfer excited state, whereas at 77 K this stabilisation process is impeded in the rigid matrix, and thus the emissive excited state increases in energy. In addition, at 77 K, the rigidity of the complex itself increases, which prevents access to the excited vibrational states of the ground state, and subsequently blue-shifts the emission  $\lambda_{\text{max}}$  as transitions can only occur to the low energy vibrational states of the ground electronic state. In contrast, no spectral shift is observed for **IrPhenSAc**, rather the vibronic fine structure sharpens upon cooling, which is indicative of LC character.

In summary, the luminescence excited state of the **IrBpySAc** complex appears to have MLCT character, as the broad emission peak is structureless and blue-shifts upon cooling to 77 K, whereas that of the **IrPhenSAc** complex appears to have much more LC character when dissolved in  $\text{CH}_3\text{CN}$ , indicated by the vibronic fine structure present, the weaker

luminescence quantum yield and the lack of rigidochromic effect. The emissive excited state of **IrPhenSAc** also appears to have significant triplet character, as it is incredibly oxygen sensitive; an 80-fold decrease in the quantum yield is observed upon oxygenation of acetone with air-saturated solvent, and a large bimolecular collisional quenching rate constant of  $10 \times 10^9 \text{ dm}^3 \text{ mol}^{-1} \text{ s}^{-1}$  is observed. However, in a predominantly aqueous environment, the MLCT excited state of **IrPhenSAc** appears to be stabilised in the higher polarity solvent, and thus reduces in energy and mixes into the LC state to give MLCT-characteristics, i.e. higher quantum yield, and a structureless emission peak.

#### 5.4 Synthesis of Iridium(III)-labelled Gold Nanoparticles

Gold nanoparticles were labelled with **IrBpySH** and **IrPhenSH** (synthesised *in situ* from their oxidatively stable thioester analogues **IrBpySAc** and **IrPhenSAc**) using the surfactant-mediated process developed and discussed in Chapter Two.<sup>1,2</sup> Citrate-stabilised gold nanoparticles of 13 nm and 100 nm in diameter were synthesised according to the methods described in Chapter Two (Section 2.3)<sup>1</sup> and Chapter Three (Section 3.2)<sup>1</sup> respectively, and initially coated in the stabilising agent Zonyl® 7950. Subsequently, **IrBpySH** or **IrPhenSH** was added to the colloid, as presented in the schematic below, Figure 5.14. The coated particles were isolated by centrifugation, followed by decantation of the supernatant and resuspension of the pellet in deionised water. Neither complex could be added directly to the colloids without fluorosurfactant as this afforded aggregation and sedimentation of the particles out of suspension.

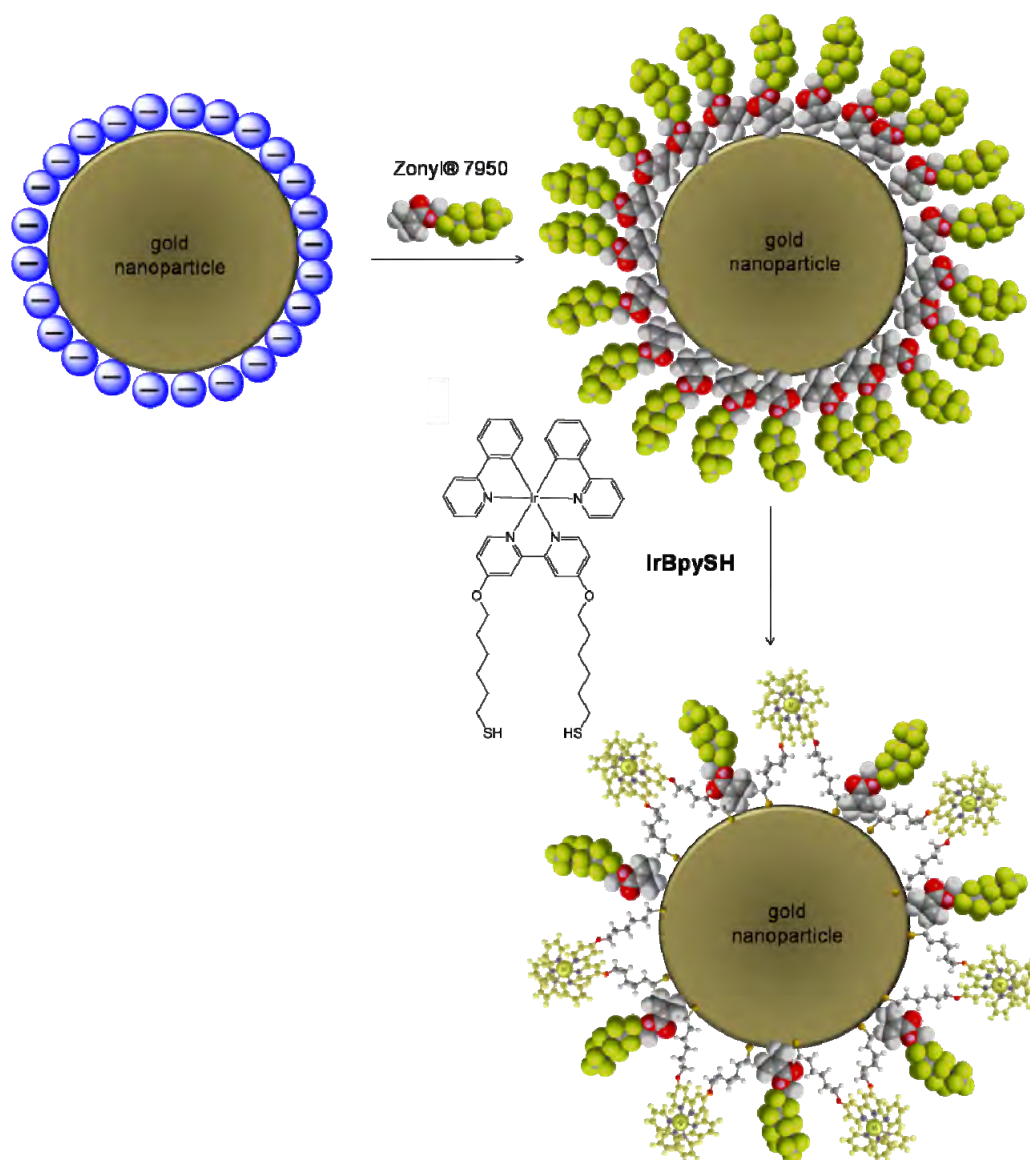


**Figure 5.14** Schematic of surfactant-mediated co-coating procedure for iridium(III)/ zonyl® 7950-coated gold nanoparticles, with **IrBpySH** as an example.

Isolated **IrBpy-Z•AuNP13**, **IrBpy-Z•AuNP100**, and **IrPhen-Z•AuNP100** have been characterised by UV-Vis absorption spectroscopy, DLS (Figure 5.15), TEM and electrophoretic mobility measurements to give zeta potential data.

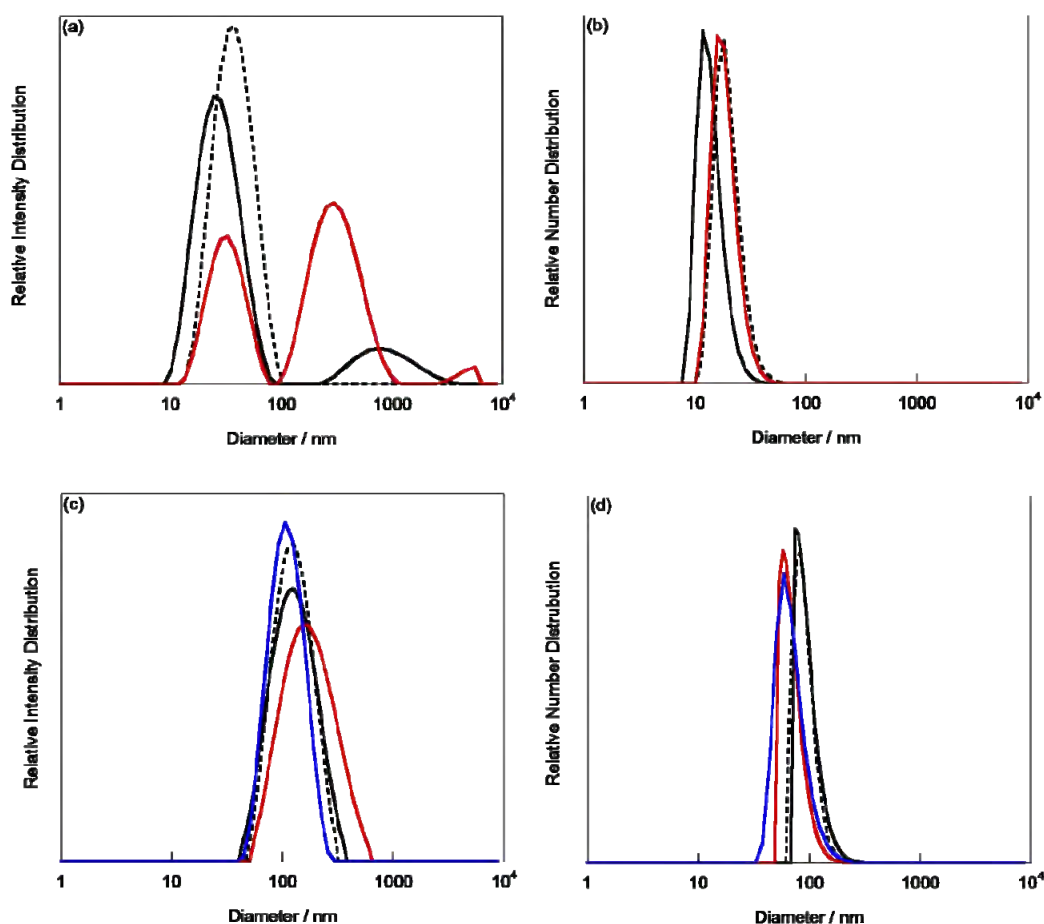


**Figure 5.15** DLS intensity distribution (a),(c) and number distribution (b),(d) of functionalised gold nanoparticles. (a) and (b): citrate 13 nm gold nanoparticles (black), isolated **Z•AuNP13** (black dashed), and **IrBpy-Z•AuNP13** (red). (c) and (d): 100 nm gold nanoparticles (black), isolated **Z•AuNP100** (black dashed), **IrBpy-Z•AuNP100** (red), and **IrPhen-Z•AuNP100** (blue).

The DLS average number distribution of **IrBpy-Z•AuNP13** is the same, within error, as the fluorosurfactant-coated 13 nm gold nanoparticles, and thus there is no evidence of aggregation occurring upon addition of **IrBpySH**. A change in the zeta potential from  $-61 \pm 4$  mV, for **Z•AuNP13**, to  $-35 \pm 3$  mV for **IrBpy-Z•AuNP13** indicates that some of the highly electronegative fluoropolymer has been displaced from the surface of the nanoparticles upon addition of the Ir(III) complex, as is presented in Table 5.2 below. A similar effect is seen when **RuSH** is added to the fluorosurfactant-coated nanoparticles, to give **Ru-Z•AuNP13** with a zeta potential of  $-48 \pm 2$  mV, in Chapter Two, Section 2.33.

**Table 5.2** Summary of nanoparticle characterisation data for nanoparticles coated with Zonyl® 7950 and **IrBpySH** or **IrPhenSH** complexes

sample	diameter (DLS average number distribution) / nm	zeta potential (measured at 2 nM in water) / mV
<b>Z•AuNP13</b>	20±2	-61±4
<b>IrBpy-Z•AuNP13</b>	19±5	-35±3
<b>Z•AuNP100</b>	92±21	-47±3
<b>IrBpy-Z•AuNP100</b>	71±19	-33±3
<b>IrPhen-Z•AuNP100</b>	70±24	-32±3

All errors are quoted as  $\pm 1$  standard deviation

Similarly, the DLS data for the 100 nm coated nanoparticles show no evidence of aggregation, and the same effect is observed with the zeta potentials; a change in the zeta potential from  $-47\pm 3$  mV to  $-33\pm 3$  mV and  $-32\pm 3$  mV is observed upon addition of **IrBpySH** and **IrPhenSH** to fluorosurfactant-coated gold nanoparticles respectively. This is very similar to the zeta potential observed for **Ru-Z•AuNP100**, discussed in Chapter Three, Section 3.3, of  $-35\pm 3$  mV. Transmission electron microscopy (TEM) was also performed on **IrBpy-Z•AuNP13** and **IrBpy-Z•AuNP100** samples, as shown in Figure 5.16, which confirms the size and uniformity of the resultant nanoparticles.

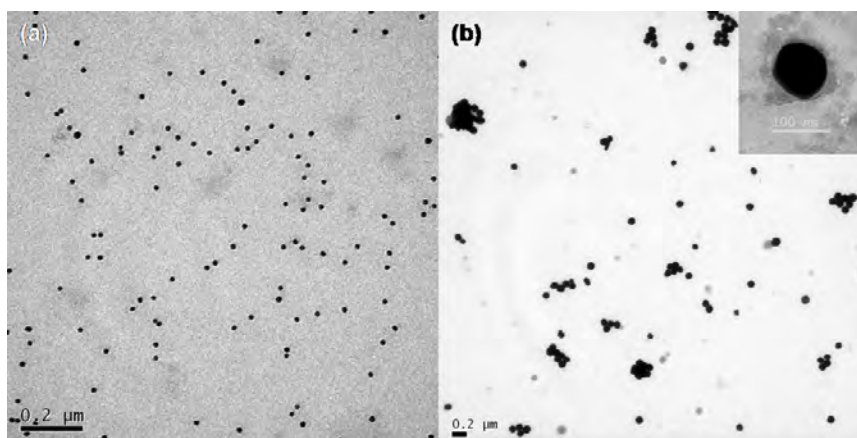


**Figure 5.16** TEM images of (a) **IrBpy-Z•AuNP13** and (b) **IrBpy-Z•AuNP100**.

**IrBpy-Z•AuNP100** nanoparticles were also sized using NanoSight nanoparticle tracking analysis, as shown below in Fig 5.17.

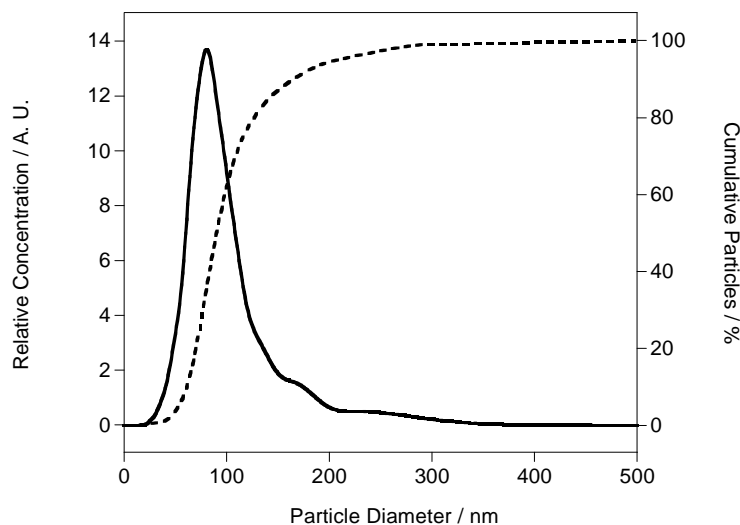


**Figure 5.17** NanoSight nanoparticle tracking analysis of **IrBpy-Z•AuNP100** at 20 °C (solid line) with cumulative frequency distribution shown (dashed).

NanoSight nanoparticle tracking analysis of **IrBpy-Z•AuNP100** revealed a mean particle diameter of 80 nm and a modal diameter of 104 nm, in agreement with the sizing by DLS and TEM.

The Ir(III)-loading of the isolated **IrBpy-Z•AuNP13** nanoparticles was measured by ICP-OES, and the atomic Au:Ir ratio of 106:1 was observed. This corresponds to 940 **IrBpySH** complexes per **IrBpy-Z•AuNP13** (see Appendix 2.5), which is slightly lower than the loading observed with **RuSH** in Chapter Two (1600 complexes per 13 nm nanoparticle).

#### 5.4.1 Photophysical Characterisation of Ir(III)-labelled Gold Nanoparticles

The photophysical properties of **IrBpy-Z•AuNP13**, **IrBpy-Z•AuNP100**, and **IrPhen-Z•AuNP100** were investigated to determine whether the surface-grafting to gold nanoparticles had an effect upon the photophysical properties of each iridium(III) lumiphore.

The UV-Vis absorption spectra of all three types of nanoparticles were dominated by the SPR of the gold nanoparticles, with the LC peak of each Ir(III) complex superimposed at *ca.* 260 nm, as shown in Figures 5.18 and 5.19 below.

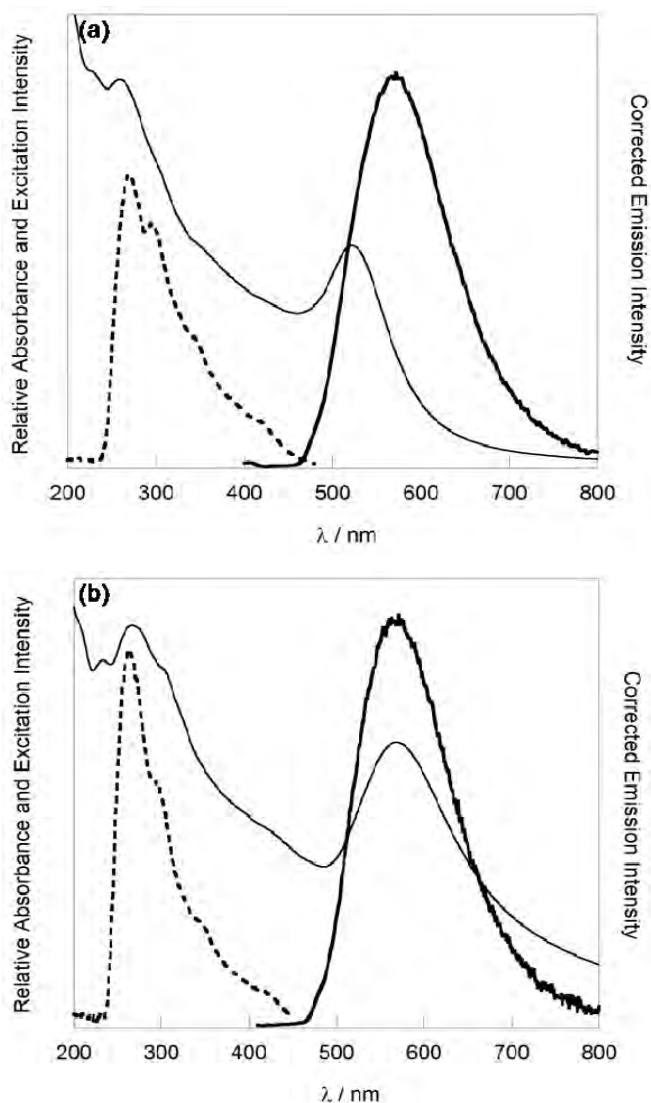


**Figure 5.18** UV-Vis absorption spectrum (solid line), excitation spectrum,  $\lambda_{em} = 550$  nm (dashed line) and steady-state emission spectrum  $\lambda_{exc} = 355$  nm, (bold solid line) of (a) 1nM **IrPhen-Z•AuNP13**, and (b) 10 mM **IrPhen-Z•AuNP100**. Spectra corrected for instrument response.

The isolated **IrBpyZ•AuNP13** and **IrBpyZ•AuNP100** particles are highly emissive upon excitation at 355 nm, both with  $\lambda_{max}$  at 570 nm, which is the same as the free **IrBpySAC** complex in water (with 1%  $\text{CH}_3\text{CN}$ ). However, the quantum yields of luminescence of the

nanoparticles were greater than the free complex in water (with 1% CH<sub>3</sub>CN), at 0.14 and 0.19 for **IrBpyZ•AuNP13** and **IrBpyZ•AuNP100** respectively, compared with only 0.05 for the complex in a predominantly aqueous environment. The excitation spectra, measured at 550 nm, for both **IrBpyZ•AuNP13** and **IrBpyZ•AuNP100** are very similar, displaying the spectral features of the UV-Vis absorption spectrum of the **IrBpySAc** complex in solution. As a control experiment, 20 μM **IrBpySAc** complex was dissolved in 1% CH<sub>3</sub>CN, water, with 1 mM Zonyl® 7950 fluorosurfactant, and the steady-state emission was measured with excitation at 355 nm. Again, a  $\lambda_{\max}$  at 570 nm was observed under these conditions, and a 140% increase in the quantum yield to 0.12 was observed, with respect to the free complex in water (1% CH<sub>3</sub>CN). This is very similar to the quantum yields measured for the coated 13 nm and 100 nm gold particles, for which the error is relatively high as the difference in the absorbance between uncoated and coated nanoparticles at 355 nm is such a small component of the absolute absorbances.

**IrPhen-Z•AuNP100** behave somewhat differently to the free complex in water; upon excitation at 355 nm the nanoparticles exhibit broad emission with evidence of some vibronic fine-structure, with shoulders at 490 nm and 530 nm, and a  $\lambda_{\max}$  at 555 nm. In 1% CH<sub>3</sub>CN, water, the emission has a  $\lambda_{\max}$  at 550 nm, with no obvious shoulders in the broad peak (Figure 5.19). The steady-state emission of 20 μM **IrPhenSAc** complex dissolved in 1% CH<sub>3</sub>CN, water, with 1 mM Zonyl® 7950 fluorosurfactant, exhibits emission with clear vibronic fine-structure and a  $\lambda_{\max}$  at 515 nm, when excited at 355 nm, which is similar to the complex dissolved in CH<sub>3</sub>CN (Section 5.2, Figures 5.10 and 5.13b), and very different to the nanoparticles co-coated with both the complex and fluorosurfactant. The quantum yield of **IrPhen-Z•AuNP100** could not be measured due to the low signal intensity at such low concentration of lumiphore; low colloidal concentrations (7 pM) are used to minimise the scattering, and thus bright signal is required for measuring quantum yields on nanoparticles.

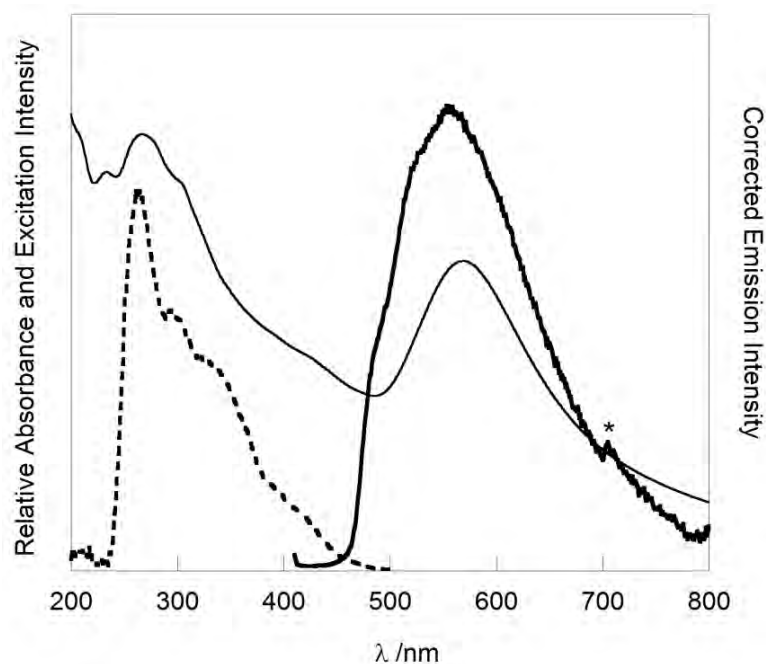


**Figure 5.19** UV-Vis absorption spectrum (solid line), excitation spectrum,  $\lambda_{em} = 550$  nm (dashed line) and steady-state emission spectrum  $\lambda_{exc} = 355$  nm, (bold solid line) of 10 pM **IrPhen-Z•AuNP100**. \* = scattering peak (second harmonic of 355 nm excitation). Spectra corrected for instrument response.

The photophysical properties of **IrBpy-Z•AuNP13**, **IrBpy-Z•AuNP100**, **IrPhen-Z•AuNP100** and the control studies of each **IrBpySAC** and **IrPhenSAC** complexes mixed with the Zonyl® 7950 fluorosurfactant in solution are summarised below in Table 5.3:

**Table 5.3** Summary of the photophysical properties of **IrBpy-Z•AuNP13**, **IrBpy-Z•AuNP100** and **IrPhen-Z•AuNP100** nanoparticles, and control studies of aqueous free complexes mixed with fluorosurfactant in solution.

	<b>IrBpy-Z•AuNP13<sup>a</sup></b>	<b>IrBpy-Z•AuNP100<sup>b</sup></b>	<b>IrPhen-Z•AuNP100<sup>b</sup></b>	<b>IrBpySAc</b> (aq) with Zonyl 7950 <sup>c</sup>	<b>IrPhenSAc</b> (aq) with Zonyl 7950 <sup>c</sup>
$\lambda_{\max}$ / nm <sup>d</sup>	570	570	555	570	515
$\tau_{\text{obs}}$ / ns <sup>e</sup>	80 (7%) 380 (93%)	90 (10%) 400 (90%)	50 (25%) 335 (75%)	140 (32%) 380 (68%)	145 (31%) 375 (69%)
	[75 (6%)] [435 (94%)]	[85 (11%)] [420 (89%)]	[300 (15%)] [1570 (85%)]	[165 (18%)] [625 (82%)]	[150(5%)] [1605 (95%)]
$\Phi^f$	0.19	0.14	- <sup>g</sup>	0.12	0.02

<sup>a</sup> nanoparticle measurements at 2 nM in aqueous solution

<sup>b</sup> nanoparticle measurements at 7 pM in aqueous solution

<sup>c</sup> 20  $\mu$ M Ir complex dissolved in 1% CH<sub>3</sub>CN, H<sub>2</sub>O, with 1.2 mM Zonyl® 7950

<sup>d</sup> error estimated as  $\pm 3$  nm

<sup>e</sup> lifetimes measured in aerated solutions, deaerated measurements (systems degassed with nitrogen for 20 min) shown in square brackets. Multi-exponential fits shown with *intensity weightings* shown in parenthesis. Errors estimated as  $\pm 6\%$  for solution data, and  $\pm 10\%$  for nanoparticle samples.

<sup>f</sup> aerated  $\Phi$  s measured using an integrating sphere, using un-coated nanoparticles as the reference. Errors estimated as  $\pm 25\%$ .

<sup>g</sup> signal intensity too weak to at pM concentrations of particles to measure  $\Phi$  with integrating sphere

The observed luminescence lifetimes of **IrBpy-Z•AuNP13** and **IrBpy-Z•AuNP100** are very similar to one another, and relatively insensitive to molecular oxygen quenching; upon degassing, neither the short component nor the long component of the biexponential lifetime changes by more than 15%, whereas this is not observed in the control experiment of **IrBpySAc** complex mixed with fluorosurfactant. In contrast, **IrPhen-Z•AuNP100** are very sensitive to molecular oxygen quenching, and a *ca.* five-fold increase in both the short and the long components of the observed lifetimes is observed. The absence of oxygen quenching is highly desirable for biological imaging applications for two reasons: firstly, blood and biological tissue have significant triplet oxygen present, and quenching would reduce the brightness of luminescent probes *in situ*; secondly, the quenching process of triplet O<sub>2</sub> with a triplet excited state usually produces singlet oxygen, which is highly reactive and has

associated toxicity.<sup>59</sup> However, the production of toxic singlet oxygen by **IrPhen-Z•AuNP100** has the potential to be applied as a means of photodynamic therapy.

There is no evidence of luminescence quenching of the **IrBpySH** complex upon attachment to gold nanoparticles, as the quantum yield does not decrease upon attachment to gold nanoparticles, whereas this is difficult to assess for the **IrPhenSH** because the quantum yield could not be measured on nanoparticles. However, the luminescence lifetime of the **IrPhenSH** complex does not shorten upon addition to the 100 nm gold nanoparticles, and thus these data support a lack of quenching by the gold nanoparticles in **IrPhen-Z•AuNP100** also. Notably, the **IrBpy-Z•AuNP100** nanoparticles are a lot brighter than **IrPhen-Z•AuNP100**, with a measurable quantum yield within the integrating sphere setup.

## 5.5 Imaging Ir(III)-labelled Gold Nanoparticles in Flow Systems

Bright luminescent nanoparticles have the potential to be used as flow tracers in microfluidic systems; the particles have to be bright enough to capture images many times per second so that velocities can be mapped with high temporal resolution and thus **IrBpy-Z•AuNP100** have been chosen as potential candidates for flow tracers; the **IrBpySH** complex offers advantageous photophysical properties for optical imaging over the **IrPhenSH** complex, as discussed in Section 5.2, and the larger nanoparticles have been chosen as they offer brighter (i.e. more lumiphore labels per probe) tracers to track by luminescence.

There are two different approaches to particle imaging, both of which give velocity profiles within a given system, but with resolution in different dimensions. Particle tracking velocimetry (PTV) is a technique used to measure the velocity of particles by means of tracking individual particles as they move through space, through several time frames of a video sequence.<sup>60</sup> The resolution of the particle position is limited by the particle size, and

thus can be measured with sub-micrometer accuracy, but the velocity measurement is calculated by averaging the change in position of the particle across several frames in time. Therefore there is *high spatial resolution* of individual particles, but the velocity is averaged over a significant period of time and temporal flow information within the time scale of the averaged tracks is lost. On the other hand, particle imaging velocimetry (PIV) extracts velocity fields with *high temporal resolution* by dividing a flow domain into windows of interrogation and using pairs of images to produce a displacement vector from a cross-correlation routine, whilst averaging out the correlation over a significant interrogation area in space.<sup>61,62</sup>

PIV is the preferred technique if studying velocity fields in systems where the flow is not continuous, so that the temporal variation in the velocity fields can be resolved. PIV requires many seeding particles within each frame to ensure high spatial resolution with sub-pixel accuracy, and relies on the seeding particles to faithfully follow the flow of the fluid. Traditional macroscopic PIV methods use glass beads or oil droplets as seeding tracers, and image their movement from their scattering of laser light, and more recently, fluorescent particles with scales between 1 and 10  $\mu\text{m}$  have been used.<sup>60</sup> However, the advent of micro-PIV ( $\mu\text{-PIV}$ )<sup>63</sup> requires smaller seeding particles to analyse microchannel flow dynamics. Nanoparticles present a unique opportunity to exploit a bottom-up approach to materials fabrication to produce tracers for PIV, and luminescence imaging significantly improves image quality over scattering measurements as scattering artifacts from channel walls and obstacles are removed and signal to noise ratio is significantly increased.<sup>63</sup>

$\mu\text{-PIV}$  studies were attempted by flowing **IrBpy-Z•AuNP100** particles through a microchannel and capturing images for processing at UCL, but it was not possible to achieve high enough seeding densities in the channel for good image correlation. In addition, the

significant Brownian motion of the 100 nm particles was difficult to filter out of the flow velocities. Therefore, 500 nm silica nanoparticles were synthesised and labelled with a similar surface-active Ir(III) complex, and these were deemed suitable for PIV measurements. This has been published as a separate study by the author.<sup>29</sup>

## 5.6 Imaging Blood Flow in Biological Tissue with IrBpy-Z•AuNP100

Particle tracking velocimetry studies have been performed with **IrBpy-Z•AuNP100** in microchannels, and for the application of measuring blood flow dynamics in microvessels in the body, the study of **IrBpy-Z•AuNP100** in blood flow has been explored.

### 5.6.1 Blood Flow Introduction

The cardiovascular system is a circulatory pressure system in which the heart pumps blood, which is a concentrated suspension of cells in plasma, around the body. Studies of transport phenomena in the microvasculature using optical techniques are extremely challenging due to the high absorption of visible light by haemoglobin, and the scattering produced by red blood cells (RBC). Goldsmith and co-workers have investigated tracer-particle flows in dispersions of ghost RBC (i.e. RBC which have had the haemoglobin removed)<sup>64,65</sup> but this type of model does not replicate the correct viscosity ratios of RBC relative to the extra-cellular fluid. More recently, work has been carried out by tracking fluorescently-labelled blood cells *in vitro*<sup>66,67</sup> and by tracking cells with confocal scanning laser microscopy (CLSM) in reflection mode *in vivo*,<sup>68</sup> but these methods limit the spatial resolution to the cell size (*ca.* 8  $\mu\text{m}$ ), which is problematic for the narrow vessels and when tracking flow-rates near to the channel walls. Studies have also been executed by co-flowing luminescent tracer microparticles (as small as 0.4  $\mu\text{m}$ ) with blood *in vitro*<sup>69</sup> and *in vivo*,<sup>70-72</sup> but nano-scale particles are required to investigate narrow microchannels and to provide flow information on a scale relevant to the transport of drugs. The flow dynamics of nanoparticles are also incredibly important when

considering the intravenous administration of the evergrowing research field of nanomedical devices.<sup>73-75</sup>

### 5.6.2 *In Vitro* Blood Flow Tracking

To determine whether **IrBpy-Z•AuNP100** particles could be used as tracers to measure flow dynamics in the microvasculature, they were initially studied *in vitro* by seeding RBC suspensions with **IrBpy-Z•AuNP100**, as shown in Figure 5.20. The RBC were spiked with *ca.* 1% RBC that had been fluorescently-labelled with a fluorescein dye, cell tracker® green 5-chloromethylfluorescein diacetate, to give CMFDA-labelled RBC. These labelled RBC could be excited between 450–500 nm, and detected between 500–600 nm ( $\lambda_{\text{max}} = 517$  nm) in order to facilitate independent tracking of the RBC for comparative purposes.

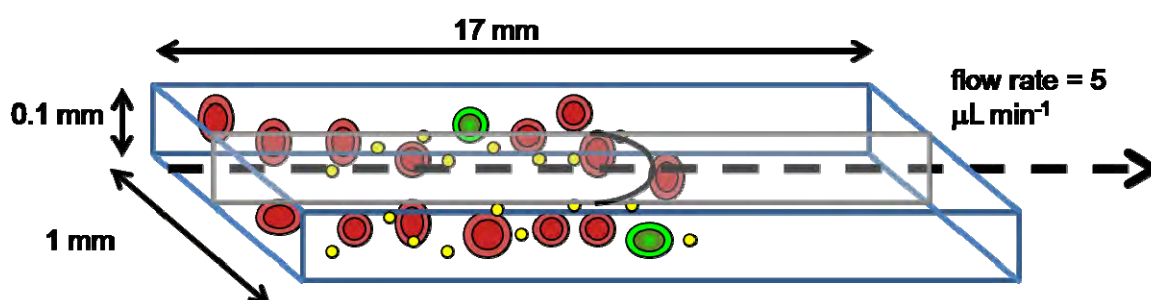


**Figure 5.20** Schematic of RBC (red) flowing through a 100 μm deep rectangular microchannel, spiked with 1% CMFDA-labelled RBC (green) and **IrBpy-Z•AuNP100** nanoparticles (yellow).

The nanoparticles and the labelled RBC were imaged by epiluminescence microscopy, in the centre of the channel. The two luminescence channels (of **IrBpy-Z•AuNP100** and CMFDA-labelled RBC) were separated by excitation wavelength: **IrBpy-Z•AuNP100** were imaged with  $\lambda_{\text{exc}} = 355$  nm,  $\lambda_{\text{em}} > 510$  nm, and the labelled RBC were imaged with  $\lambda_{\text{exc}} = 475$  nm,  $\lambda_{\text{em}} > 510$  nm. An example video sequence of the two channels is presented as a two-dimensional image in Figure 5.21, with the sequences projected onto the time axis. The blood model in this example is 10% haematocrit, i.e. the volume percentage of RBC in the system is 10%.

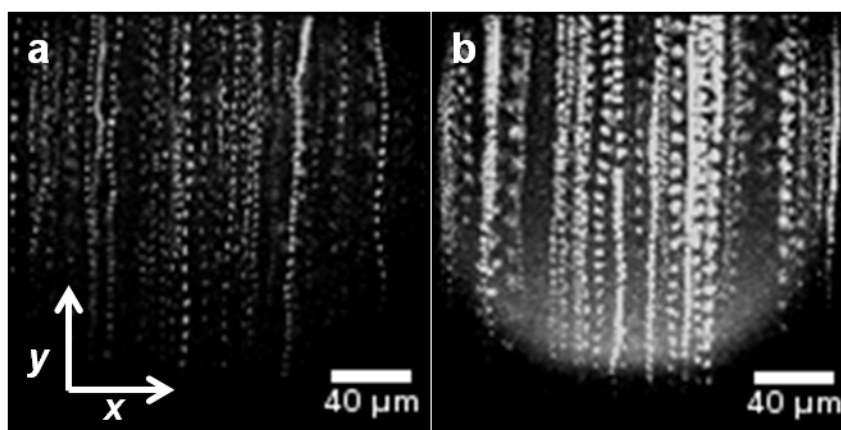


**Figure 5.21** Overlay of time frames of consecutive luminescence images of **IrBpy-Z•AuNP100** (left,  $\lambda_{exc} = 355 \text{ nm}$ ,  $\lambda_{em} \text{ nm} > 510 \text{ nm}$ ) and luminescence images of stained RBC (right,  $\lambda_{exc} = 475 \text{ nm}$ ,  $\lambda_{em} \text{ nm} > 510 \text{ nm}$ ) flowing in 10% haematocrit at 12  $\mu\text{m}$  channel depth, 5  $\mu\text{L min}^{-1}$  flow rate. Imaging at 30 fps.

There were noticeable differences between the appearances of the **IrBpy-Z•AuNP100** and the labelled RBC tracks (Figure 5.21): the former appeared as smaller spots of luminescence and showed more variance in the  $x$ -direction. This is unsurprising because it has been reported that when blood flows through vessels, the flow fields enhance substance diffusion to a greater degree than simple Brownian motion<sup>76</sup> and *in vitro* models of micron tracer particles within RBC suspensions have also shown significant radial dispersions within the flow.<sup>77</sup> It was possible to image the particles and the labelled RBC up to a depth of *ca.* 25  $\mu\text{m}$  into the 10–30% haematocrit suspensions by luminescence microscopy; beyond this, visualisation was impaired by the opacity of the suspension at the visible wavelengths used. Although these findings indicate that as blood tracers, the **IrBpy-Z•AuNP100** particles may only be suitable for the measurement of flow rates across very narrow vessels or close to the vessel wall, their performance was no worse than that of the labelled RBC, which are *ca.* 70 times larger in diameter. Moreover, it is blood flow within the *narrow* channels of the vascular tree (as small as 8  $\mu\text{m}$  diameter) which is the least understood. Video sequences of **IrBpy-Z•AuNP100** and labelled RBC were recorded at 64 fps, at varying depths into the channel, and were tracked manually to gain  $v_y$  data, Figure 5.22. For **IrBpy-Z•AuNP100** suspended in 0% haematocrit (i.e. PBS), the particles could be tracked throughout the whole channel, and the expected

parabolic flow profile was observed, with a flow maximum of *ca.*  $1100 \mu\text{m s}^{-1}$ . This is comparable to the simple model maximum flow value of  $1250 \mu\text{m s}^{-1}$  (see Appendix 14), assuming a Poiseuille flow between infinitely wide parallel plates (Figure 4.22). This not only substantiated the suitability of **IrBpy-Z•AuNP100** for determining flow rates but also facilitated calibration of the starting depth for the image sequences by fitting the data with a second-order polynomial and setting the turning-point as the centre of the channel (i.e. channel depth of  $50 \mu\text{m}$ ). Due to the large size difference between **IrBpy-Z•AuNP100** and RBC, it was hypothesised that the RBC concentration (the percentage haematocrit) might affect the ability of the nanoparticle tracers to follow the flow paths faithfully in the suspension. Indeed, blood rheology can significantly affect the flow characteristics of smaller haematopoietic cells *in vivo*; for example, the margination of platelets to the walls of blood vessels is dependent upon the rheology, which is a crucial phenomenon for clotting processes.<sup>78,79</sup> The percentage haematocrit was varied from 0–30% to assess the effect of this, as presented in Figure 5.22b. However, the percentage haematocrit did not affect the  $v_y$  of either the particles or the labelled RBC at any of the depths studied.

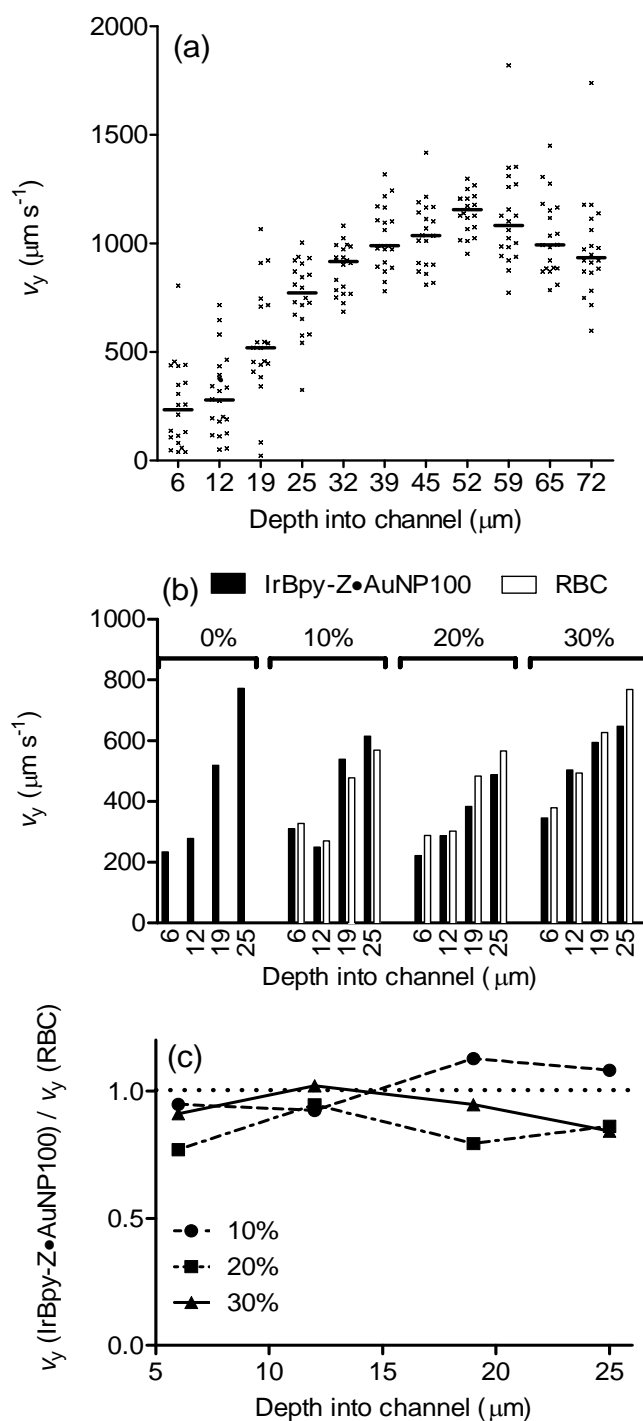


**Figure 5.22** a) Measured  $v_y$  of *IrBpy-Z•AuNP100* suspended in 0% haematocrit solution (PBS) at depths up to 72  $\mu\text{m}$  from the wall of a cuboidal channel (depth 100  $\mu\text{m}$ ) when perfused at rate 5  $\mu\text{L min}^{-1}$ , (x) data point, (—) median  $v_y$ . *IrBpy-Z•AuNP100* were visualised by their luminescence ( $\lambda_{em} > 510$  nm). b) Median  $v_y$  of *IrBpy-Z•AuNP100* (filled bars) and CMFDA-labelled RBC (open bars) suspended in RBC suspensions between 0 and 30%, at depths up to 25  $\mu\text{m}$  from the channel wall when perfused at 5  $\mu\text{L min}^{-1}$  through a cuboidal channel (depth 100  $\mu\text{m}$ ). *IrBpy-Z•AuNP100* and labelled RBC were tracked sequentially at each depth from their emission ( $\lambda_{em} > 510$  nm) by switching the excitation wavelength between  $\lambda_{exc} = 355$  nm (*IrBpy-Z•AuNP100*) and  $\lambda_{exc} = 475$  nm (labelled-RBC). c) Median  $v_y$  of *IrBpy-Z•AuNP100* and RBC, plotted in (b), expressed as relative  $v_y$  (*IrBpy-Z•AuNP100*/RBC).

Normalization of the **IrBpy-Z•AuNP100**  $v_y$  to the RBC  $v_y$  (Figure 5.22c) showed that the particles followed the flow speeds of the RBC in all cases.

The presence of fibrinogen and other macromolecules within blood often supports the assembly of RBC into tube-like aggregates, known as ‘rouleaux’, and plug-flow dynamics can arise, which tend to blunt the flow profile and alter the degree of margination of certain species within particulate flow.<sup>80</sup> RBC aggregation can be artificially manipulated *in vitro* using dextrans of different molecular weights.<sup>79</sup> Therefore, in order to investigate whether aggregation conditions may alter the velocity of the nanoparticles in flow, 30% haematocrit was prepared in 1% Dextran500 (aggregating) and 2% Dextran40 (non-aggregating viscosity control), and **IrBpy-Z•AuNP100** and RBC were tracked up to a depth of 25  $\mu\text{m}$  (Figure 5.24). RBC aggregation was verified by bright-field microscopy using a static sample, as shown in Figure 5.23 below.

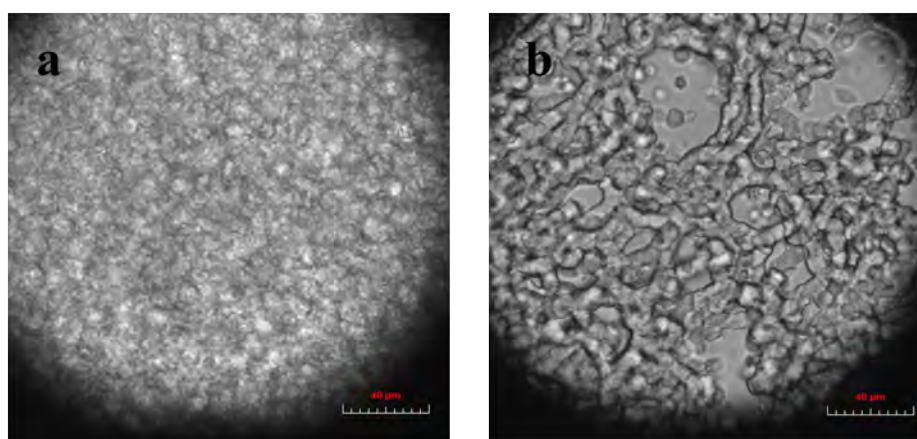


**Figure 5.23** Brightfield microscopy images of 30% haematocrit prepared in 2% Dextran40 (viscosity control) (a) and 1% Dextran500 (b), both containing **IrBpy-Z•AuNP100** at 2pM. Aggregated RBC are observed in (b).

However, under flow conditions, the aggregation did not appear to alter the  $v_y$  of either the **IrBpy-Z•AuNP100** or the RBC, as presented in Figure 5.24.

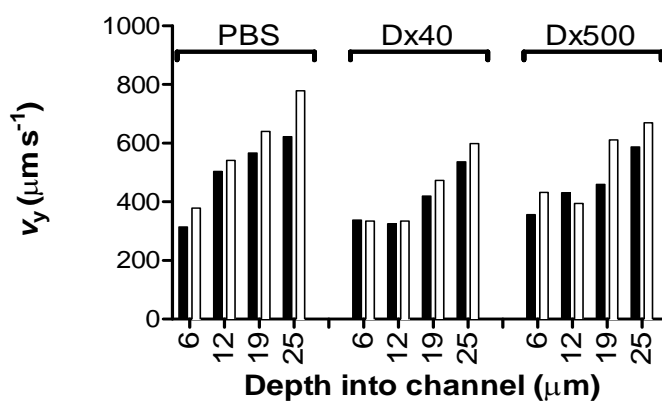


**Figure 5.24** Measured  $v_y$  of **IrBpy-Z•AuNP100** (filled bars) and CMFDA-labelled RBC (open bars) suspended in 30% haematocrit solution prepared in PBS, 2%Dextran40 (Dx40) or 1%Dextran500 (Dx500) at depths up to 25  $\mu\text{m}$  from the wall of a cuboidal channel (depth 100  $\mu\text{m}$ ) when perfused at rate 5  $\mu\text{L min}^{-1}$ .

These results are noteworthy in terms of the ability of nanoparticles to act as faithful flow tracers regardless of their position within the channel and, perhaps regardless of the architecture of the vasculature being examined. This may be significant for the study of blood vasculature *in vivo* in the early diagnosis of conditions where abnormal changes in flow are indicative of the pathological state.

Current methods to explore such pathological states are based on Doppler ultrasound, or the injection of contrast agents, and are inherently macroscopic low-resolution techniques, which are limited in their ability to study the microvasculature. **IrBpy-Z•AuNP100** nanoparticles, therefore, present a unique opportunity to explore the microvasculature, in terms of resolution and size, and when combined with their ability to track blood flow faithfully under a range of blood rheologies, they represent a highly suitable tool for imaging.

### 5.6.3 Imaging Nanoparticles in Biological Tissue

In order to investigate the suitability of the **IrBpy-Z•AuNP100** for blood flow studies *in vivo*, nanoparticle suspensions in PBS were injected into mice, and excised tissue sections of the lungs, mesentery and *extensor hallucis proprius* skeletal leg muscle were imaged using

epiluminescence microscopy following wet mounting of the tissue onto coverslips.

**IrBpy-Z•AuNP100** particles were observed in all tissues investigated, and images of particles in the mesentery tissue and skeletal muscle are shown below, in Figure 5.25.

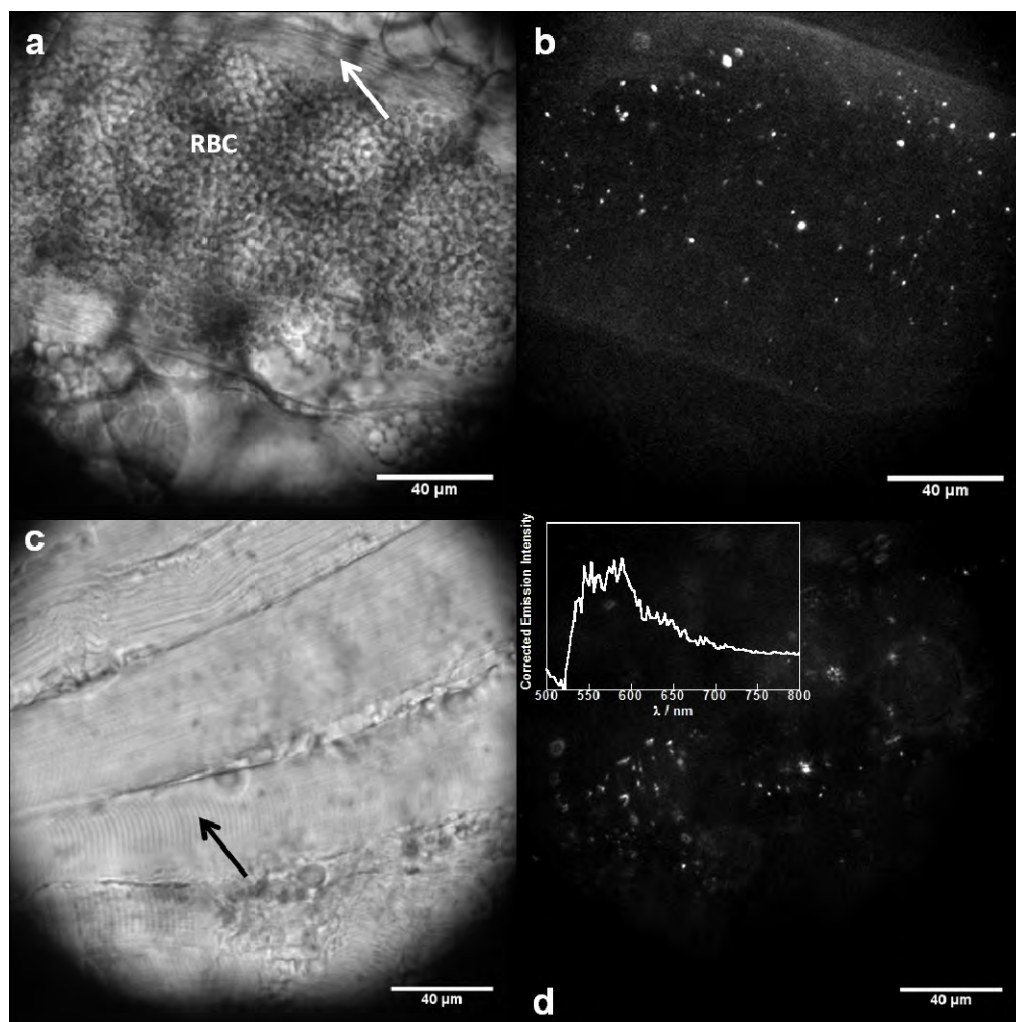


**Figure 5.25** Bright field (a and c) image and luminescence images ( $\lambda_{exc} = 405 \text{ nm}$ ,  $\lambda_{em} > 510$  (b and d) of a small blood vessel in the mesentery tissue (a and b), with the white arrow indicating the endothelial cells lining the vessel (adipocytes, i.e. fat cells, are evident as spherical objects beneath the vasculature), and in the skeletal muscle (c and d) of a mouse injected with **IrBpy-Z•AuNP100**, with the black arrow indicating the striated muscle fibres. The steady-state emission spectrum obtained from the field of view in image d is shown, corrected for instrument response (inset).

Under bright-field illumination, a *ca.* 100  $\mu\text{m}$  diameter blood vessel was located within the mesentery tissue. RBC filling the vessel and endothelial cells lining the vessel, were visible (Figure 5.25a) and spots of luminescence were clearly visible in the luminescence image (Figure 5.25b). Characteristic skeletal muscle fibres were visible in the *extensor hallucis*

*proprius* which gave it a striated appearance by bright-field microscopy (Figure 5.25c) and the point-source luminescence of the nanoparticles was observed under epiluminescence detection. Steady-state emission spectra taken for the fields of view displayed the characteristic peak expected for **IrBpy-Z•AuNP100** (Figure 5.25d inset), which together with luminescence lifetimes (measured from image with a 375 nm laser at 550 nm to be 86 ns (15%) and 320 ns (85%)), confirmed that the observed signal is from the nanoparticles, not autofluorescence. These results confirm that **IrBpy-Z•AuNP100** had reached the small capillaries within this tissue. The nanoparticles were similarly detected in the lungs (Appendix 15).

Preliminary biodistribution data of the **IrBpy-Z•AuNP100** in mice have been collected by analysing the gold content of excised organs in four different specimens by inductively-coupled plasma mass spectrometry (ICP-MS). The data are presented below in Figure 5.26.

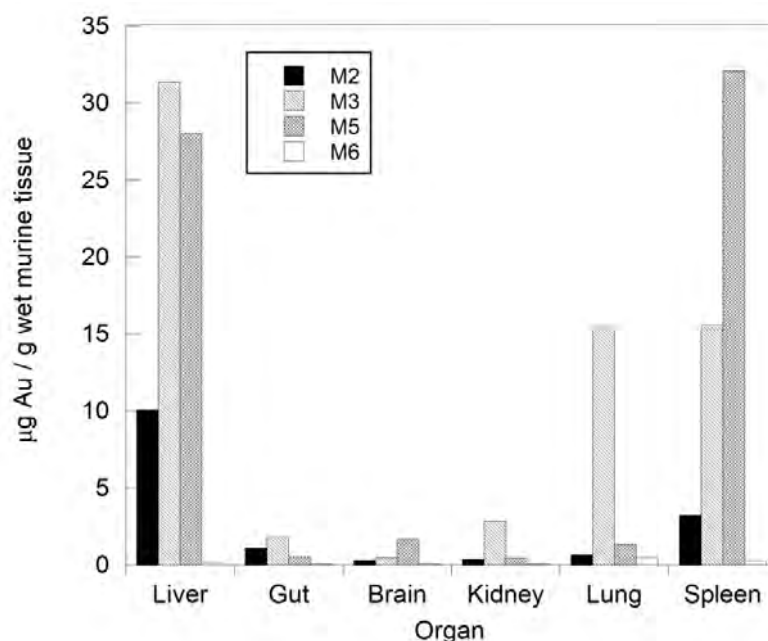


**Figure 5.26** Biodistribution of gold in four specimen mice, administered with 100 µL (80 pM)(M2) or 200 µL(M3) **IrBpy-Z•AuNP100** by intracardial injection, or with 500 µL (80 pM) **IrBpy-Z•AuNP100** by carotid artery cannulation (M5). M6 is a control, with a saline intracardial injection.

These pilot data show a zero background with negative controls (saline injection), and a dose-dependent effect with injected particle number. Carotid artery cannulation to deliver nanoparticles to the heart (in the left ventricle, thus avoiding the lung perfusion on first pass) confirmed good clearance in the liver and spleen, but not the lungs. It is of interest that clearance of nanoparticles (unlike microparticles) may be greater in the viscera (with sinusoidal, fenestrated endothelium) rather than the lung (with continuous endothelium). This may prove to be important for future targeting studies.

## 5.7 Developing Luminescent Ir(III)-labelled Gold Nanoparticles with $T_1$ MRI Contrast

Due to the success of the **IrBpySH** complex in labelling gold nanoparticles to form bright enough nanoconstructs to image in flow, an attempt has been made at designing multimodal imaging nanoprobes by incorporating the supplied **GdQSH** complex (synthesised by Dr D. J. Lewis) and **IrBpySH** onto the same nanoparticles, thus rendering an imaging agent that can be visualised optically and imaged using nuclear magnetic resonance.

Magnetic resonance can be exploited for imaging purposes by exciting nuclei which possess spin with a radio frequency pulse, within a strong magnetic field (analogous to NMR), whilst using magnetic gradients to spatially encode the signal of each voxel to produce an image. Conventional clinical MRI studies resonate the water protons within a sample, and the intensity of each voxel (i.e. the contrast of the image) can be weighted with various parameters, including proton density, longitudinal relaxation times ( $T_1$ ), and transverse relaxation times ( $T_2$ ). As discussed in the introduction to this chapter (Section 5.2.1), gadolinium(III) chelates are often used as MRI contrast agents for imaging, because the tricationic lanthanide centres are highly paramagnetic, with seven unpaired electrons. Such

paramagnetic centres give  $T_1$ -contrast in proton MRI imaging by reducing the longitudinal relaxation time of nearby water protons, which enhances local contrast with respect to background tissue.<sup>41-43</sup> In brief,  $T_1$  is the time taken for the macroscopic magnetisation vector to return to thermal equilibrium, following excitation by a  $90^\circ$  radio frequency pulse.  $T_1$  relaxation depends upon magnetic fluctuations in the transverse plane (relative to the static magnetic field), which stimulate transitions from the excited spin state back to the ground spin state, if the fluctuations occur at the correct frequency (i.e. that of the energy gap between the two states). Therefore the relative molecular motion between water protons and highly paramagnetic Gd(III) metal centres rapidly increases the  $1/T_1$  relaxation rates.

13 nm gold nanoparticles were chosen for this pilot study, rather than 100 nm particles, to maximise the surface area:volume ratio of the colloid, and thus enhance the sensitivity of the probes by maximising the area available for surface-grafted complexes. The **GdQSH** complex has two functions in the 13 nm citrate nanoparticle coating process; both to give  $T_1$  contrast in proton MRI imaging, and to stabilise the particles with respect to aggregation, in a similar fashion to the neutral surfactant molecules investigated in Chapter Two. The nanoparticles (9 nM) are initially coated in excess **GdQSH** complex, i.e. beyond the saturation in the shift of the SPR band of the nanoparticles upon adding the complex, as has been previously reported by Dr A. C. Savage.<sup>81</sup> Once the neutral **GdQSH** has displaced the citrate anions from the surface, and surrounds each nanoparticle with a bulky neutral group, **IrBpySH** can be added without aggregation of the nanoparticles occurring, as shown below in Figure 5.27. Upon titration of **GdQSH** (0–100  $\mu\text{L}$ , 1mM) into 13 nm gold nanoparticles (1 mL, 9 nM), a 6 nm red-shift in the SPR of the nanoparticles is observed, as has previously been reported in the group.<sup>81</sup>

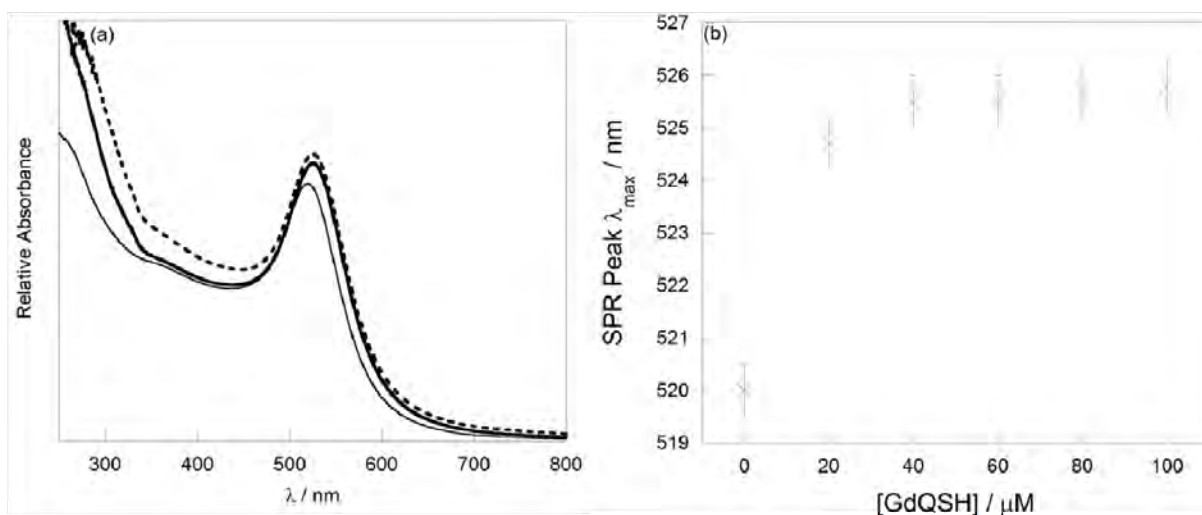


**Figure 5.27** (a) UV-Vis absorption spectra of citrate gold nanoparticles (1 mL, 9 nM) (solid line), and upon addition of **GdQSH** (100  $\mu$ L, 1 mM in  $\text{CH}_3\text{OH}$ ) (bold solid line) and subsequent addition of **IrBpySH** (6  $\mu$ L, 3.5 mM in 1:1 (30 % w/v  $\text{NH}_4\text{OH}(\text{aq})$ ): $\text{CH}_3\text{CN}$ ) (dashed line). (b) Plot of SPR  $\lambda_{\text{max}}$  vs.  $[\text{GdQSH}]$  upon titration 0–100  $\mu\text{M}$  into 9 nM 13 nm gold nanoparticles.

Excess **GdQSH**, was added to ensure that the particles were fully coated with a neutral complex and to try to maximise their stability before addition of a cationic complex. Upon addition of **IrBpySH** (made *in situ* from **IrBpySAc**), no further shift in the SPR was observed, and there was no evidence of nanoparticle aggregation by inspection of the UV-Vis absorption spectrum. Notably, if the same concentration of **IrBpySH** is added directly to 13 nm citrate-coated gold nanoparticles, the nanoparticles immediately aggregate; the solution turns steel blue and eventually the aggregates sediment out of suspension.

The resultant nanoparticles were isolated by centrifugation, decantation of the supernatant and resuspension of the pellet in deionised water to give **IrBpy-GdQ•AuNP13**. These nanoparticles were characterised by UV-Vis spectroscopy, ICP-OES, TEM and DLS, and their photophysical properties have been analysed, as presented in Figure 5.28.

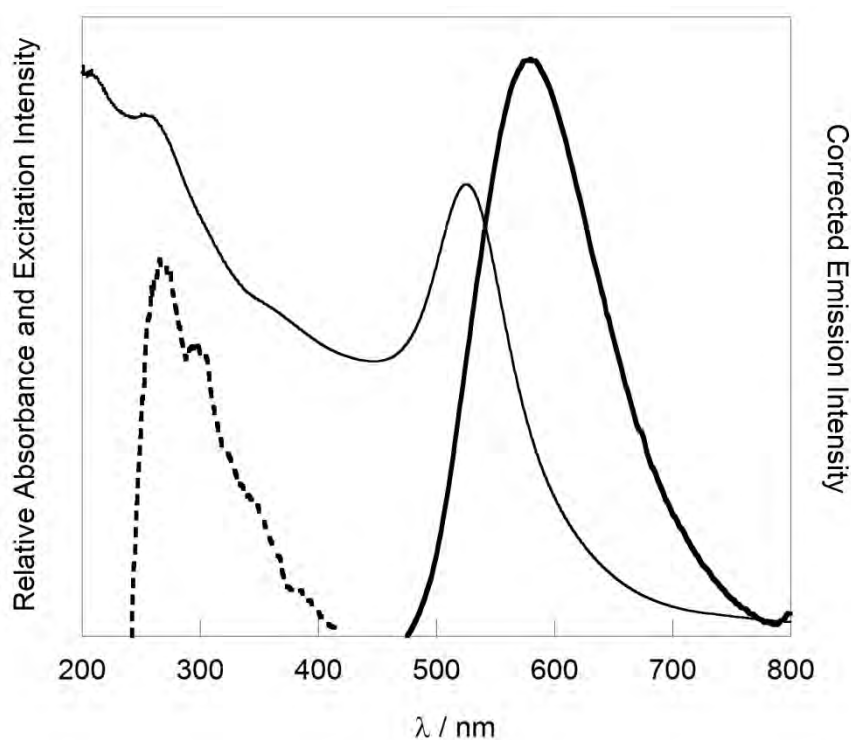


**Figure 5.28** UV-Vis absorption spectrum (solid line), excitation spectrum,  $\lambda_{em} = 550$  nm (dashed line) and steady-state emission spectrum  $\lambda_{exc} = 355$  nm, (bold solid line) of 1nM **IrBpy-GdQ•AuNP13** Spectra corrected for instrument response.

The UV-Vis absorption spectrum of the isolated **IrBpy-GdQ•AuNP13** is dominated by the SPR of the gold nanoparticles, with a  $\lambda_{max}$  maintained at 526 nm, following isolation from the excess gadolinium(III) and iridium(III) complexes. Upon excitation at 355 nm, the nanoparticles emit bright yellow luminescence, with  $\lambda_{max} = 580$  nm, and time-resolved luminescence measurements taken at  $\lambda_{em} = 550$  nm, after excitation with a 375 nm laser, reveal observed luminescence lifetimes of 90 ns (29%) and 285 ns (71%) for aerated nanoparticles, with *intensity* weightings in parenthesis. The steady-state  $\lambda_{max}$  red-shifts 10 nm in comparison to the **IrBpy-Z•AuNP13**, which indicates, as expected, that the Zonyl®7950 fluoropolymer and the **GdQSH** co-coating moieties affect the photophysical properties of the surface-bound **IrBpySH** complex. The time-resolved emission decay in aerated aqueous systems follows biexponential law for the **IrBpy-GdQ•AuNP13** nanoparticles ( $\tau = 90$  ns

(29%) and 285 ns (71%) ), with a similar short component to that of **IrBpy-Z•AuNP13** ( $\tau = 80$  ns (7%), 380 ns (93%)). The long component is, however, 25% shorter.

The nanoparticle sizing data is shown below in Figure 5.29. The nanoparticles do not appear to aggregate, as the DLS number distribution has a mean value of  $11 \pm 3$  nm, and the TEM displays individual spherical nanoparticles.

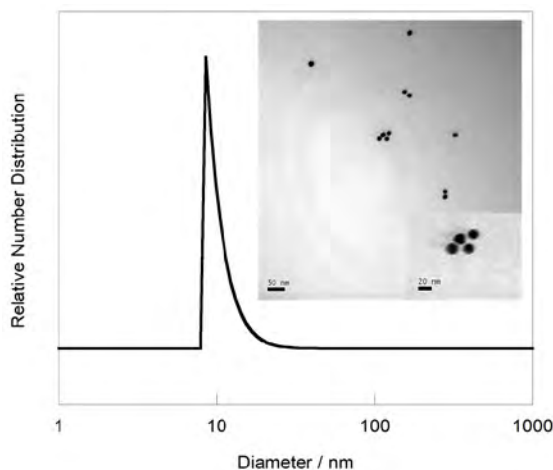


**Figure 5.29** DLS number distribution of **IrBpy-GdQ•AuNP13**. Inset: TEM image of **IrBpy-GdQ•AuNP13**.

To calculate the number of Gd(III) and Ir(III) complexes per nanoparticle, samples were analysed by ICP-OES to give atomic ratios of Au:Gd of 98:1 for **GdQ•AuNP13** particles, and of 73:1 for **IrBpy-GdQ•AuNP13** particles. Assuming that the gold nanoparticles are 13 nm in diameter, this equates to 1020 and 1370 gadolinium(III) complexes per nanoparticles for **GdQ•AuNP13** and **IrBpy-GdQ•AuNP13** respectively (see appendices 2.6 and 2.7 respectively). The atomic ratio of Au:Ir for **IrBpy-GdQ•AuNP13** particles = 300:1, which equates to 330 complexes per nanoparticle (Appendix 2.7).

To investigate the  $r_1$  relaxivity of **IrBpy-GdQ•AuNP13**, i.e. the change in rate of the longitudinal relaxation rate of solvent water protons ( $1/T_1$ ), per concentration of contrast agent,<sup>41</sup> a concentration series of the free complex, **GdQSH**, **IrBpy-GdQ•AuNP13** and a

control study of **GdQ•AuNP13** (i.e. particles made analogous to **IrBpy-GdQ•AuNP13**, but with omission of the addition of **IrBpySH**), was analysed. To increase the concentration of the samples beyond 9 nM (i.e. the concentration at which the 13 nm citrate nanoparticles are synthesised), the final volume of water that the pellet was dispersed in was altered accordingly. The samples were imaged in a 3T clinical MRI instrument by Ms Lindsey van Gemeren, and  $T_1$  relaxation times were analysed. These values are used to calculate the  $r_1$  relaxivities of the nanoparticles, using the ICP-OES data to calculate  $r_1$  relaxivities with respect to Gd(III) concentration.  $T_1$  relaxation times were collected by Ms Lindsey van Gemeren at 5 different concentrations of free complex (10–90  $\mu\text{M}$ ) or coated-nanoparticles (1–40 nM), and a linear regression of  $1/T_1$  vs. [Gd(III)] was fitted to the data to calculate the  $r_1$  relaxivities. The  $r_1$  relaxivity of the free **GdQSH** complex in water (with 10%  $\text{CH}_3\text{OH}$  for solubility) was measured as  $5.1 \text{ s}^{-1}\text{mM}^{-1}$ , which is very similar to that of Gadidiamide (sold under the name of Omniscan<sup>TM</sup>), for  $r_1 = 4.8 \text{ s}^{-1}\text{mM}^{-1}$ , measured in a 3T field.<sup>82</sup> (Gadidiamide is a similar pentetic acid gadolinium(III) chelate, in which two of the carboxyl groups are methyl amides.) A 40–60% increase in the  $r_1$  relaxivity per unit Gd(III) is observed when the complex is attached to nanoparticles, with  $r_1$  relaxivities measured as  $7.1 \text{ s}^{-1}\text{mM}^{-1}$  and  $8.4 \text{ s}^{-1}\text{mM}^{-1}$  for **GdQ•AuNP13** and **IrBpy-GdQ•AuNP13** respectively. Relaxivity increases are often observed when molecular contrast agents are attached to nanomaterials, because this dramatically alters the diffusion dynamics of the complex, which affects the ability of the gadolinium(III) centres to influence the  $T_1$  longitudinal relaxation rate of surrounding water protons.<sup>42,83</sup>

As a preliminary study, to verify whether the nanoparticles were optically tracable in cells, A549 human lung cancer cells were incubated with 1 nM **IrBpy-GdQ•AuNP13** for 24 hr, and imaged by confocal microscopy, as shown in Figure 5.30.

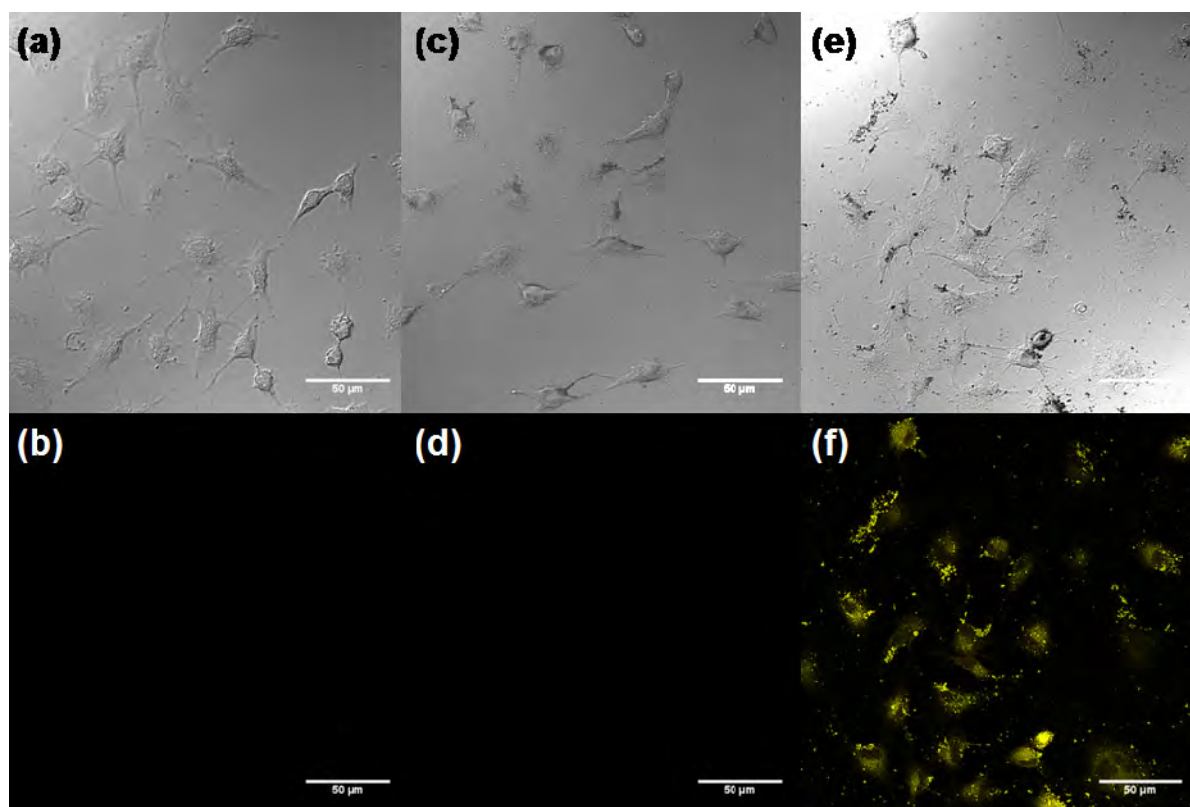


**Figure 5.30** Confocal micrographs of A549 cancer cells dosed with (a,b) no nanoparticles, (c,d) **GdQ•AuNP13**, and (e,f) **IrBpy-GdQ•AuNP13**. (a,c,e = brightfield transmission channel, b,d,f = luminescence channel:  $\lambda_{exc} = 405\text{nm}$ ,  $\lambda_{em} = 500\text{--}750\text{ nm}$ ).

The **IrBpy-GdQ•AuNP13** nanoparticles are optically bright enough to image in cells, as can be seen in the yellow channel, Figure 5.30(f). Control studies with blank A549 cells (a,b) and cell dosed with the same concentration of **GdQ•AuNP13** confirm that the luminescence in the yellow channel is due to the presence of the **IrBpySH** complex bound to the **IrBpy-GdQ•AuNP13** nanoparticles.

Solution studies of **IrBpy-GdQ•AuNP13** nanoparticles demonstrate that they are promising candidates for multimodal imaging probes, and preliminary *in vitro* studies suggest that the particles can be visualised optically in cells. *In vitro* studies of these particles are ongoing by Ms Lindsey van Gemeren, to verify whether the MRI-contrast is applicable at particle concentrations that can be achieved in living cells.

## 5.8 Conclusion

Two luminescent Ir(III) complexes have been evaluated in this Chapter, **IrBpySAc**, and **IrPhenSAc**. The photophysical properties of **IrBpySAc** were found to be more suitable for luminescent imaging applications, due to the larger quantum yield and reduced sensitivity to molecular oxygen quenching of the luminescent state, with respect to **IrPhenSAc**. Both complexes have been attached to 100 nm gold nanoparticles, using a fluorosurfactant-mediated strategy, and the resulting nanoparticles were all emissive and maintained their colloidal stability. The 100 nm particles coated in **IrPhenSAc** were emissive, but the aerated particles were not bright enough to measure a quantum yield in an integrating sphere. Similarly to the free complex, the coated particles were very sensitive to quenching by molecular oxygen. **IrBpySAc** was attached to 13 nm and 100 nm gold nanoparticles, and both sizes of labelled nanoparticles have very similar photophysical properties; the quantum yields of the particles were higher than the free complex in an aqueous environment, and the enhancement is expected to be mainly due to the presence of the Zonyl® 7950 surfactant. Importantly neither size of **IrBpySH**-labelled nanoparticle is sensitive to luminescence quenching by molecular oxygen, and no luminescence quenching of the **IrBpySH** complex was observed, upon attachment to gold nanoparticles.

**IrBpy-Z•AuNP100** nanoparticles were studied in dynamic blood flow systems to assess their ability as tracking velocimetry tracers. It was possible to measure the particles by epiluminescence microscopy to depths of 25  $\mu\text{m}$  in 30% haematocrit, and the particles appear to follow the flow velocities of the RBCs, even when RBC aggregation is induced in the system by macromolecular Dextran500. *Ex-vivo* imaging of particles in tissue from mice injected intravenously with **IrBpy-Z•AuNP100** was performed successfully, and biodistribution studies of the gold in surgically excised organs was investigated.

In addition, 13 nm gold nanoparticles have been successfully co-coated with **IrBpySH** and **GdQSH**, with the aim to develop luminescent nanoparticles with additional  $T_1$ -contrast for imaging by optical microscopy and MRI. The resultant nanoparticles are emissive, and do give  $T_1$ -weighted contrast, with a  $r_1$  relaxivity of  $8.4 \text{ s}^{-1} \text{ mM}^{-1}$  ([Gd]) in a 3T field, which is 60% enhanced with respect to the free gadolinium(III) complex in solution.

In summary, the iridium complex **IrBpySH** is a valuable luminescent label which can be attached to gold nanoparticles to produce imaging probes with much-improved quantum yields over the analogous ruthenium(II)-labelled nanoparticles in Chapter Two. This chapter demonstrates that nanoparticles coated in **IrBpySH** can be optimised for a variety of applications.

## 5.9 Acknowledgements

Thank you to Dr Shiva Farabi for the provision of the **PhenHex** ligand, to Dr David Lewis for providing the **GdQSH** complex, and to Dr Alison Savage for her advice with the Gd(III)-coated nanoparticles. Thank you to Dr Hannah Jeffery, Professor Gerard Nash (School of Clinical and Experimental Medicine, University of Birmingham) and to Dr David Lewis for their help and guidance with the collaborative blood-flow project, and thank you to Professor Stuart Egginton (School of Clinical and Experimental Medicine, University of Birmingham) for the *in vivo* work. Thank you also to Ms Lindsey van Gemeren (PSIBS) and Dr Nigel Davies (School of Clinical and Experimental Medicine, University of Birmingham) for running the relaxivity measurements, and thank you to Mr Sunil Claire (PSIBS) for the A549 cell culture.

## 5.10 Experimental

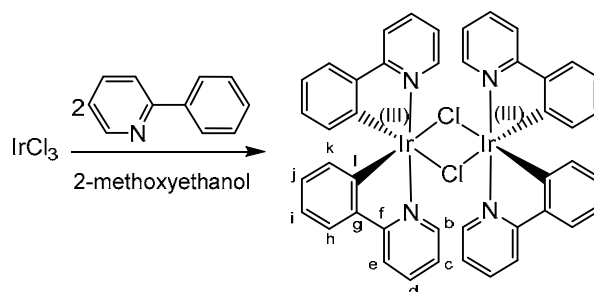
### 5.10.1 General Synthesis

Zonyl® 7950 was purchased from Sigma Aldrich and used without further purification. 13 nm gold nanoparticles were synthesised by the citrate reduction method,<sup>84</sup> as described in Section 2.12.1, and 100 nm gold nanoparticles were synthesised according to the growth method described in Section 3.7.1, adapted from the published procedure by Ziegler and Eychmüller.<sup>85</sup> The **BpyHex** ligand was synthesised according to the method described in Section 2.12.1<sup>2</sup> and the **PhenHex** ligand provided by Dr Shiva Farabi.<sup>51</sup> **GdQSH** was provided by Dr D. J. Lewis, synthesised by the reported method.<sup>86</sup>

#### *Characterisation of 4,7-bis(hex-5-en-1-yloxy)-1,10-phenanthroline (PhenHex ligand)*

The **PhenHex** ligand was synthesised by Dr Shiva Farabi<sup>51</sup> and characterised by NMR. Data agree with previously reported work and thus no further characterisation is reported. <sup>1</sup>H NMR (300 MHz, *d*<sup>6</sup>-DMSO):  $\delta_{\text{H}} = 8.89$  (d, 2H,  $^3J_{\text{H}_3} = 5.3$  Hz, H<sub>2</sub>), 8.15 (s, 2H, H<sub>7</sub>), 7.28 (d, 2H,  $^3J_{\text{H}_2} = 5.3$  Hz, H<sub>3</sub>), 5.94–5.74 (m, 2H, H<sub>12</sub>), 5.12–4.96 (m, 4H, H<sub>13</sub>/H<sub>14</sub>), 4.31 (t, 4H,  $^3J_{\text{H}_9} = 6.3$  Hz, H<sub>8</sub>), 2.22–2.12 (m, 4H, H<sub>11</sub>), 1.98–1.86 (m, 4H, H<sub>9</sub>), 1.670–1.57 (m, 4H, H<sub>10</sub>).

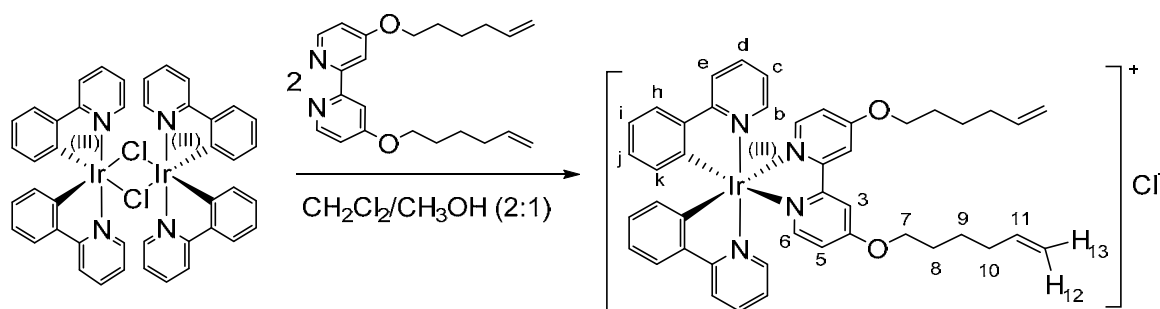
#### *Synthesis of tetrakis(2-phenylpyridine-C2,N')(μ-dichloro)diiridium ([Ir(ppy)<sub>2</sub>(μ-Cl)<sub>2</sub>])*



Synthesis was performed according to the method of Sprouse, and is detailed herein.<sup>87</sup> A solution of iridium(III) trichloride hydrate (805 mg, 2.70 mmol) and 2-phenylpyridine (1.593 g, 10.3 mmol) in 2-methoxyethanol (60 mL) was refluxed at 130 °C overnight to give a

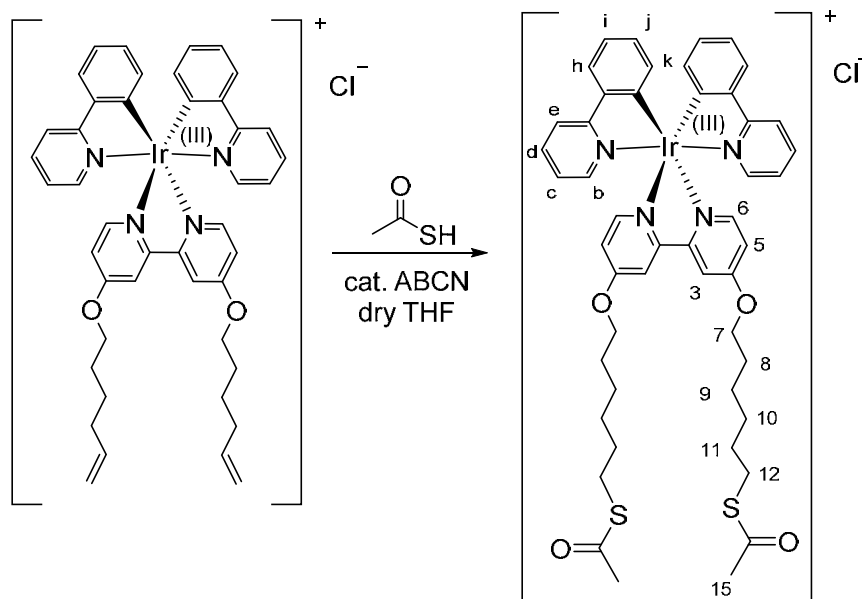
yellow/brown suspension. This was left to cool and was filtered under suction to render a yellow powder. The residue was washed with ethanol (100 mL) and dissolved in  $\text{CH}_2\text{Cl}_2$  (150 mL). The solution was filtered and hexane (20 mL) and toluene (50 mL) were added. The volume was reduced *in vacuo* to 100 mL and cooled on ice to crystallise. The product was retrieved by filtration as yellow crystalline solid (0.7369 g, 0.687 mmol, 51 % yield).  $R_f = 0.81$  ( $\text{CH}_2\text{Cl}_2:\text{CH}_3\text{OH}$  10:1).  $^1\text{H}$  NMR (300 MHz,  $d^6$ -DMSO):  $\delta_{\text{H}} = 9.81 / 9.53$  (d, 4H,  $^3J_{\text{Hc}} = 5.8$  Hz,  $\text{H}_b$ ),  $8.27 / 8.19$  (d, 4H,  $^3J_{\text{Hd}} = 7.9$  Hz,  $\text{H}_e$ ),  $8.10 / 8.01$  (m (apparent t,  $^3J_{\text{He}} \approx ^3J_{\text{Hc}} = 7.6$  Hz) 4H,  $\text{H}_d$ ),  $7.79 / 7.74$  (d, 4H,  $^3J_{\text{Hi}} = 7.9$  Hz,  $\text{H}_b$ ),  $7.57 / 7.46$  (m (apparent t,  $^3J_{\text{Hd}} \approx ^3J_{\text{Hb}} = 6.6$  Hz) 4H,  $\text{H}_c$ ),  $6.94\text{--}6.68$  (m, 8H,  $\text{H}_i$ ,  $\text{H}_j$ ),  $6.25 / 5.66$  (d, 4H,  $^3J_{\text{Hj}} = 7.3$  Hz,  $\text{H}_k$ ).  $^{13}\text{C}$  NMR (100 MHz,  $d^6$ -DMSO):  $\delta_{\text{C}} = 166.9 / 152.0 / 145.4 / 143.7 / 143.1$  (quaternary C),  $152.1 / 150.6$  ( $\text{C}_b$ ),  $139.2 / 138.1$  ( $\text{C}_d$ ),  $131.2 / 129.6$  ( $\text{C}_k$ ),  $129.9 / 128.9 / 122.2 / 121.9$  ( $\text{C}_i/\text{C}_j$ ),  $124.8 / 123.8$  ( $\text{C}_h$ ),  $123.5 / 122.8$  ( $\text{C}_c$ ),  $120.0 / 119.4$  ( $\text{C}_e$ ). TOF ES-MS(+): 501.1  $[\text{Ir}(\text{ppy})_2]^+$  IR  $\nu_{\text{max}}$  ( $\text{cm}^{-1}$ ): 3040 (C–H), 1605 (C–C<sub>ring</sub>/C–N<sub>ring</sub>), 1581(C–C<sub>ring</sub>/C–N<sub>ring</sub>), 1561, 1476, 1414, 1030, 754. UV-Vis ( $\text{CH}_3\text{CN}$ )  $\lambda_{\text{max}}$  [nm] = 259, 350 (shoulder), 390 (shoulder), 430 (shoulder). Emission ( $\text{CH}_3\text{CN}$ ,  $\lambda_{\text{exc}} = 355$  nm)  $\lambda_{\text{max}}$  [nm] = 510.

#### Synthesis of $[\text{Ir}(\text{ppy})_2\text{BpyHex}]\text{Cl}$ (**IrBpyHex** complex)



The cyclometalated iridium(III) dimer  $[\text{Ir}(\text{ppy})_2(\mu\text{-Cl})_2]$  (634 mg, 0.591 mmol) and BpyHex (310 mg, 0.876 mmol, 1.5 eq) were dissolved in  $\text{CH}_2\text{Cl}_2/\text{CH}_3\text{OH}$  (45 mL, 2:1) and refluxed overnight at 60 °C under nitrogen. Following cooling, the solvent was removed *in vacuo* to render a yellow residue. The residue was purified by chromatography on silica eluting

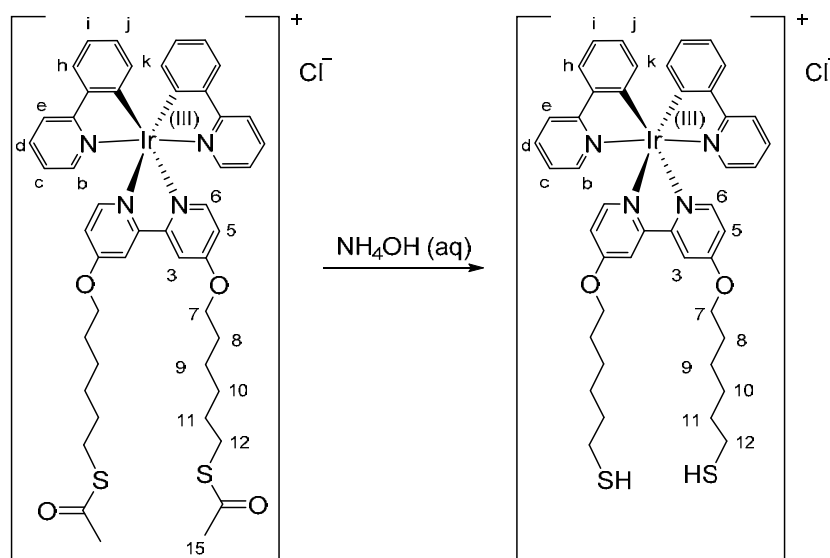
$\text{CH}_2\text{Cl}_2:\text{CH}_3\text{OH}$  10:1 ( $R_f = 0.44$ ) to give **IrBpyHex** as a yellow powder (0.602 g, 0.677 mmol, 77% yield).  $R_f = 0.44$  ( $\text{CH}_2\text{Cl}_2:\text{CH}_3\text{OH}$  10:1).  $^1\text{H}$  NMR (400 MHz,  $d_6$ -DMSO):  $\delta_{\text{H}} = 8.46$  (s, 2H,  $\text{H}_3$ ), 8.25 (d, 2H,  $^3J_{\text{Hd}} = 8.2$  Hz,  $\text{H}_e$ ), 7.98–7.88 (m, 4H,  $\text{H}_d/\text{H}_h$ ), 7.69 (d, 2H,  $^3J_{\text{Hc}} = 5.6$  Hz,  $\text{H}_b$ ), 7.59 (d, 2H,  $^3J_{\text{H5}} = 6.6$  Hz,  $\text{H}_6$ ), 7.28 (dd, 2H,  $^3J_{\text{H6}} = 6.6$  Hz,  $^4J_{\text{H3}} = 2.5$  Hz,  $\text{H}_5$ ), 7.19 (m (apparent t,  $^3J_{\text{Hd}} \approx ^3J_{\text{Hb}} = 5.7$  Hz) 2H,  $\text{H}_c$ ), 7.00 (m (apparent t,  $^3J_{\text{Hh}} \approx ^3J_{\text{Hj}} = 7.5$  Hz) 2H,  $\text{H}_i$ ), 6.88 (m (apparent t,  $^3J_{\text{Hk}} \approx ^3J_{\text{Hi}} = 7.5$  Hz) 2H,  $\text{H}_j$ ), 6.19 (d, 2H,  $^3J_{\text{Hj}} = 7.5$  Hz,  $\text{H}_k$ ), 5.90–5.76 (m, 2H,  $\text{H}_{11}$ ), 5.09–4.95 (m, 4H,  $\text{H}_{12}/\text{H}_{13}$ ), 4.24 (t, 4H,  $^3J_{\text{H8}} = 6.3$  Hz,  $\text{H}_7$ ), 2.16–2.06 (m, 4H,  $\text{H}_{10}$ ), 1.85–1.73 (m, 4H,  $\text{H}_8$ ), 1.59–1.46 (m, 4H,  $\text{H}_9$ ).  $^{13}\text{C}$  NMR (100 MHz,  $d^6$ -DMSO):  $\delta_{\text{C}} = 150.5$  ( $\text{C}_6$ ), 148.7 ( $\text{C}_b$ ), 138.5 / 138.3 ( $\text{C}_d/\text{C}_{11}$ ), 131.1 ( $\text{C}_k$ ), 130.1 ( $\text{C}_j$ ), 125.9 ( $\text{C}_h$ ), 125.0 ( $\text{C}_e$ ), 123.8 ( $\text{C}_i$ ), 121.9 ( $\text{C}_c$ ), 115.1 ( $\text{C}_{12}$ ), 114.5 ( $\text{C}_5$ ), 111.9 ( $\text{C}_3$ ), 69.1 ( $\text{C}_7$ ), 32.6 ( $\text{C}_{10}$ ), 27.6 ( $\text{C}_8$ ), 24.5 ( $\text{C}_9$ ). TOF ES-MS(+):  $m/z$  853.5  $[\text{M}-\text{Cl}]^+$ . IR  $\nu_{\text{max}}$  ( $\text{cm}^{-1}$ ): 3045 (C–H), 2940 (C–H), 1606 (C–C<sub>ring</sub> / C–N<sub>ring</sub>), 1472, 1436, 1341, 1284, 1226, 1031, 994, 756.

Synthesis of  $[Ir(ppy)_2BpySAc]Cl$  (**IrBpySAc** complex)

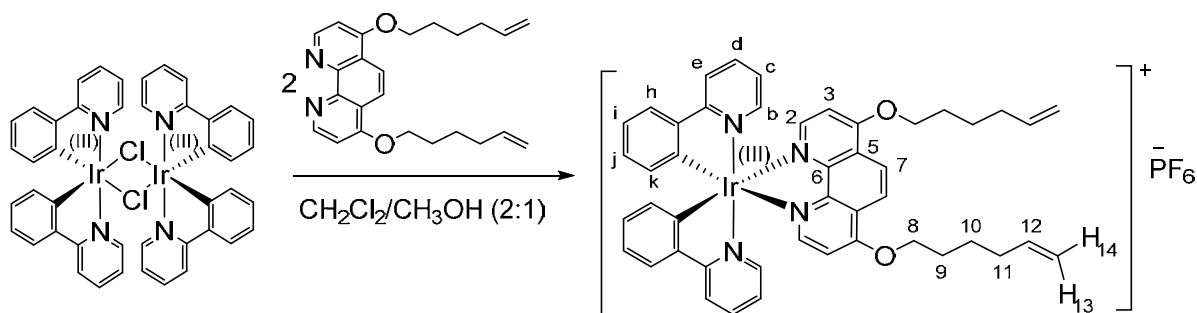
Thioacetic acid (564  $\mu$ L, 7.890 mmol) and 1,1'-azobiscyclohexane carbonitrile (ABCN, 756 mg, 3.093 mmol) in anhydrous THF (10 mL) were heated at 60  $^{\circ}$ C under  $N_2$  (g) for 30 min. **IrBpyHex** (600 mg, 0.675 mmol) in anhydrous THF (40 mL) was added dropwise to the mixture, which was then stirred at 60  $^{\circ}$ C under  $N_2$ (g). The progress of the reaction was monitored by the disappearance of the terminal olefins by  $^1H$  NMR. Thioacetic acid (100  $\mu$ L, 1.399 mmol) and ABCN (125 mg, 0.512 mmol) were added after 18 hr, another portion of thioacetic acid (120 mL, 1.679 mmol) and ABCN (150 mg, 0.614 mmol) was added after 22 hr. After a total of 45 hr, the reaction was pushed to completion and the ABCN was quenched with saturated  $NaHCO_3$  (aq) (150 mL). The solution was extracted with  $CH_2Cl_2/H_2O$ , dried over  $MgSO_4$ , and filtered. The solvent was removed *in vacuo* to render a dark brown viscous residue which was purified by column chromatography on silica, eluting  $CH_2Cl_2:CH_3OH$  10:1 to give **IrBpySAc** as a bright yellow solid (459 mg, 0.441 mmol, 65% yield).  $R_f = 0.56$  ( $CH_2Cl_2:CH_3OH$  10:1).  $^1H$  NMR (300 MHz,  $d_6$ -DMSO) :  $\delta_H = 8.44$  (d, 2H,  $^4J_{H_5} = 2.5$  Hz,  $H_3$ ), 8.25 (d, 2H,  $^3J_{H_d} = 8.1$  Hz,  $H_e$ ), 7.96–7.86 (m, 4H,  $H_d/H_h$ ), 7.68 (d, 2H,  $^3J_{H_c} = 5.1$  Hz,  $H_b$ ), 7.58 (d, 2H,  $^3J_{H_5} = 6.4$  Hz,  $H_6$ ), 7.27 (dd, 2H,  $^3J_{H_6} = 6.4$  Hz,  $^4J_{H_3} = 2.4$  Hz,  $H_5$ ), 7.18 (m (apparent t,  $^3J_{H_d} \approx ^3J_{H_b} = 5.7$  Hz) 2H,  $H_c$ ), 6.99 (m (apparent t,  $^3J_{H_j} \approx ^3J_{H_h} = 7.5$  Hz) 2H,  $H_i$ ),

6.85 (m (apparent t,  ${}^3J_{\text{HK}} \approx {}^3J_{\text{Hi}} = 7.4$  Hz) 2H,  $\text{H}_j$ ), 6.18 (d, 2H,  ${}^3J_{\text{Hj}} = 6.6$  Hz,  $\text{H}_k$ ), 4.21 (t, 4H,  ${}^3J_{\text{H8}} = 6.1$  Hz,  $\text{H}_7$ ), 2.83 (t, 4H,  ${}^3J_{\text{H11}} = 7.2$  Hz,  $\text{H}_{12}$ ), 2.30 (s, 6H,  $\text{H}_{15}$ ), 1.80–1.71 (m, 4H,  $\text{H}_{10}$ ), 1.56–1.48 (m, 4H,  $\text{H}_8$ ), 1.46–1.34 (m, 8H,  $\text{H}_9/\text{H}_{11}$ ).  ${}^{13}\text{C}$  NMR (100 MHz,  $d^6$ -DMSO):  $\delta_{\text{C}} = 166.9 / 166.8 / 156.9 / 151.1 / 143.9$  (quaternary C), 150.5 ( $\text{C}_6$ ), 148.7 ( $\text{C}_b$ ), 138.5 / 125.0 ( $\text{C}_d/\text{C}_h$ ), 131.1 ( $\text{C}_k$ ), 130.1 ( $\text{C}_j$ ), 123.8 ( $\text{C}_c$ ), 121.9 ( $\text{C}_i$ ), 119.9 ( $\text{C}_e$ ), 114.5 ( $\text{C}_5$ ), 111.9 ( $\text{C}_3$ ), 69.2 ( $\text{C}_7$ ), 30.6 ( $\text{C}_{15}$ ), 29.0 ( $\text{C}_8$ ), 28.2 ( $\text{C}_{12}$ ), 28.0 ( $\text{C}_{10}$ ), 27.7 / 24.8 ( $\text{C}_9/\text{C}_{11}$ ). TOF ES-MS(+):  $m/z$  1006.2  $[\text{M}-\text{Cl}]^+$ . HRMS (ES $^+$ ): Calc. for  $\text{C}_{48}\text{H}_{52}{}^{193}\text{IrN}_4\text{O}_4\text{S}_2$  1005.3060, found 1005.3046. Anal. calcd for  $\text{C}_{48}\text{H}_{52}\text{ClIrN}_4\text{O}_4\text{S}_2$ : C 55.4, H 5.0, N 5.4. Found: C 55.1, H 4.9, N 5.2. IR,  $\nu_{\text{max}}$  ( $\text{cm}^{-1}$ ): 3043 (C–H), 2930 (C–H), 2857 (C–H), 1682(C=O), 1605 (C–C $_{\text{ring}}$  / C–N $_{\text{ring}}$ ), 1476, 1417, 1337, 1269, 1225, 1063, 1030, 952, 757. UV-Vis ( $\text{CH}_3\text{CN}$ )  $\lambda_{\text{max}}$  [nm, (log  $\epsilon$ )] = 228 (4.7), 256 (4.8), 295 (4.5), 346 (4.0), 420 (3.6). Emission ( $\text{CH}_3\text{CN}$ ,  $\lambda_{\text{exc}} = 355$  nm)  $\lambda_{\text{max}}$  [nm] = 585. Lifetime ( $\text{CH}_3\text{CN}$ ,  $\lambda_{\text{exc}} = 375$  nm,  $\lambda_{\text{em}} = 550$  nm) = 60 ns (aerated), =325 ns (degassed).  $\Phi$  ( $\text{CH}_3\text{CN}$ ,  $\lambda_{\text{exc}} = 355$  nm) = 0.03 (aerated), = 0.09 (degassed).

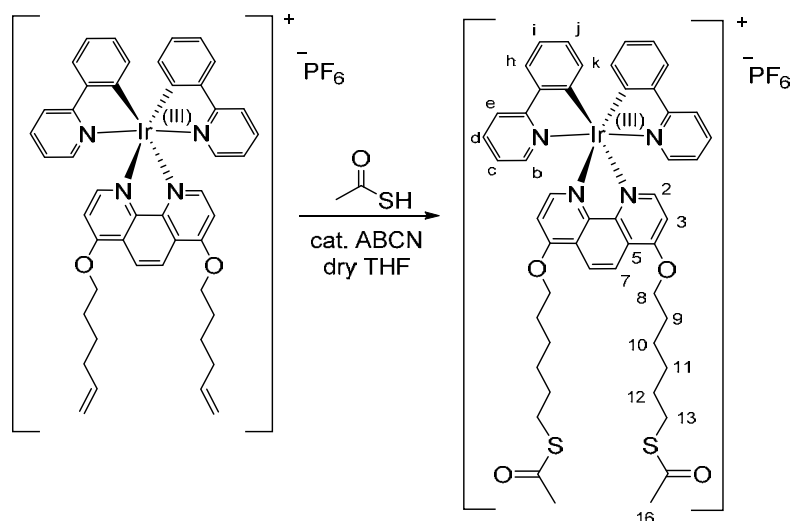
*Synthesis of  $[\text{Ir}(\text{ppy})_2\text{BpySH}]\text{Cl}$  (**IrBpySH** complex)*



To **IrBpySAc** (50  $\mu\text{L}$ , 7.0 mM in MeCN, 350 nmol) was added  $\text{NH}_4\text{OH}_{(\text{aq})}$  solution (50  $\mu\text{L}$ , 30%  $w/w$ ). The mixture was stirred for 10 min in a sealed vial to render **IrBpySH** (3.5 mM) directly prior to titration into the colloid. TOF MALDI-MS(+): 920.15  $[\text{M}-\text{Cl}]^+$ .

Synthesis of  $[Ir(ppy)_2PhenHex]PF_6$  (**IrPhenHex** complex)

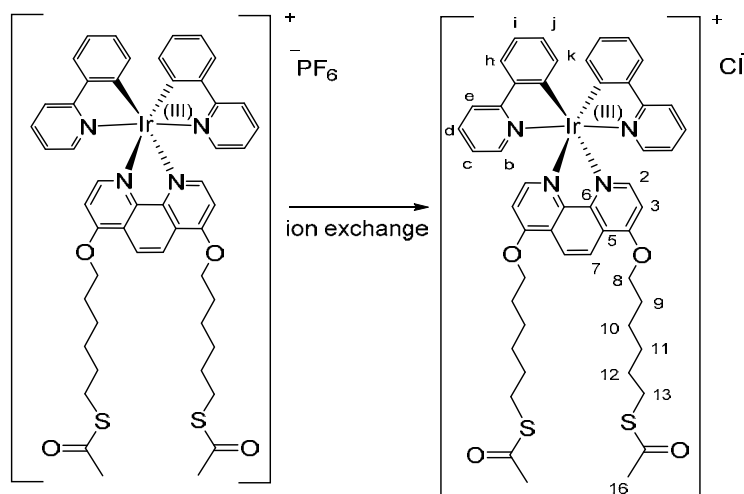
The cyclometalated iridium(III) dimer  $[Ir(ppy)_2(\mu\text{-Cl})_2]$  (290 mg, 0.271 mmol) and **PhenHex** (177 mg, 0.470 mmol, 1.7 eq) were dissolved in  $CH_2Cl_2:CH_3OH$  (45 mL, 2:1) and refluxed overnight at 60 °C under nitrogen. The reaction was cooled to room temperature and a 10-fold excess of  $NH_4PF_6$  was added. The suspension was stirred for 15 min and filtered to remove any insoluble inorganic salts. The solvent was removed *in vacuo* to render an orange solid, which was purified by chromatography on silica eluting  $CH_2Cl_2:CH_3OH$  10:1 ( $R_f = 0.36$ ) to give **IrPhenHex** as an orange powder (0.291 g, 0.285 mmol, 53% yield).  $R_f = 0.36$  ( $CH_2Cl_2:CH_3OH$  10:1).  $^1H$  NMR (400 MHz,  $d_6$ -DMSO):  $\delta_H = 8.36$  (s, 2H, H<sub>7</sub>), 8.24 (d, 2H,  $^3J_{Hd} = 8.1$  Hz, H<sub>e</sub>), 7.96–7.91 (m, 4H, H<sub>2</sub>/H<sub>b</sub>), 7.87 (t, 2H,  $^3J_{Hc} \approx ^3J_{He} \approx 7.9$  Hz, H<sub>d</sub>), 7.58–7.54 (m, 4H, H<sub>3</sub>/H<sub>b</sub>), 7.07–6.97 (m, 4H, H<sub>c</sub>/H<sub>i</sub>), 6.92 (t, 2H,  $^3J_{Hi} \approx ^3J_{Hk} \approx 7.3$  Hz, H<sub>j</sub>), 6.30 (d, 2H,  $^3J_{Hj} = 7.5$  Hz, H<sub>k</sub>), 5.91–5.79 (m, 2H, H<sub>12</sub>), 5.09–5.02 (m, 2H, H<sub>13</sub>), 5.01–4.96 (m, 2H, H<sub>14</sub>), 4.36 (t, 4H,  $^3J_{H9} = 6.4$  Hz, H<sub>8</sub>), 2.18–2.10 (m, 4H, H<sub>11</sub>), 1.95–1.86 (m, 4H, H<sub>9</sub>), 1.66–1.57 (m, 4H, H<sub>10</sub>).  $^{13}C$  NMR (100 MHz,  $d_6$ -DMSO):  $\delta_C = 167.0, 162.5, 150.6, 146.7, 144.1$  (C<sub>quaternary</sub>), 151.6 (C<sub>2</sub>), 148.9 (C<sub>b</sub>), 138.4 (C<sub>d</sub>/C<sub>12</sub>), 131.3 (C<sub>k</sub>), 130.0 (C<sub>j</sub>), 124.9 (C<sub>h</sub>), 123.7/122.0 (C<sub>c</sub>/C<sub>i</sub>), 121.0 (C<sub>7</sub>), 119.8 (C<sub>e</sub>), 115.1 (C<sub>13</sub>), 107.9 (C<sub>3</sub>), 69.8 (C<sub>8</sub>), 32.7 (C<sub>11</sub>), 27.5 (C<sub>9</sub>), 24.6 (C<sub>10</sub>). TOF ES-MS(+):  $m/z$  877.4  $[M-PF_6]^+$ . IR  $\nu_{max}$  (cm<sup>-1</sup>): 3043 (C–H), 2927 (C–H), 2858 (C–H), 1605 (C–C<sub>ring</sub> / C–N<sub>ring</sub>), 1577, 1524, 1504, 1477, 1416, 1353, 1299, 1267, 1227, 1188, 1163, 1062, 1031, 998, 914, 835, 756, 730.

Synthesis of  $[\text{Ir}(\text{ppy})_2\text{PhenSAC}]\text{PF}_6$ 

Thioacetic acid (200  $\mu\text{L}$ , 2.798 mmol) and 1,1'-azobiscyclohexane carbonitrile (ABCN, 400 mg, 1.637 mmol) in anhydrous THF (10 mL) were heated at 60  $^{\circ}\text{C}$  under  $\text{N}_2$  (g) for 30 min. IrPhenHex (197 mg, 0.193 mmol) in anhydrous THF (10 mL) was added dropwise to the mixture, which was then stirred at 60  $^{\circ}\text{C}$  under  $\text{N}_2$ (g). The progress of the reaction was monitored by the disappearance of the terminal olefins by  $^1\text{H}$  NMR. Thioacetic acid (100  $\mu\text{L}$ , 1.399 mmol) and ABCN (125 mg, 0.512 mmol) were added after 18 hr, another portion of thioacetic acid (120  $\mu\text{L}$ , 1.679 mmol) and ABCN (150 mg, 0.614 mmol) was added after 22 hr. After a total of 45 hr, the reaction was pushed to completion and the ABCN was quenched with saturated  $\text{NaHCO}_3$  (aq) (80 mL). The solid residue was stirred in excess hexane (50 mL) for 30 min and filtered and washed with more hexane (20 mL), and dried under vacuum to give  $[\text{Ir}(\text{ppy})_2\text{PhenSAC}]\text{PF}_6$  as an orange solid (158 mg, 0.135 mmol, 70% yield).  $^1\text{H}$  NMR (400 MHz,  $d_6$ -DMSO):  $\delta_{\text{H}} = 8.36$  (s, 2H,  $\text{H}_7$ ), 8.25 (d, 2H,  $^3J_{\text{Hd}} = 8.2$  Hz,  $\text{H}_e$ ), 7.96–7.91 (m, 4H,  $\text{H}_2/\text{H}_h$ ), 7.87 (t, 2H,  $^3J_{\text{Hc}} \approx ^3J_{\text{He}} \approx 7.7$  Hz,  $\text{H}_d$ ), 7.59–7.54 (m, 4H,  $\text{H}_3/\text{H}_b$ ), 7.08–6.98 (m, 4H,  $\text{H}_c/\text{H}_i$ ), 6.93 (t, 2H,  $^3J_{\text{Hi}} \approx ^3J_{\text{Hk}} \approx 7.6$  Hz,  $\text{H}_j$ ), 6.31 (d, 2H,  $^3J_{\text{Hj}} = 7.4$  Hz,  $\text{H}_k$ ), 4.34 (t, 4H,  $^3J_{\text{H9}} = 6.2$  Hz,  $\text{H}_8$ ), 2.86 (t, 4H,  $^3J_{\text{H12}} = 7.2$  Hz,  $\text{H}_{13}$ ), 2.31 (s, 6H,  $\text{H}_{16}$ ), 1.95–1.84 (m, 4H,  $\text{H}_9$ ), 1.61–1.49 (m, 4H,  $\text{H}_{10}/\text{H}_{12}$ ), 1.48–1.39 (m, 4H,  $\text{H}_{11}$ ).  $^{13}\text{C}$  NMR (100 MHz,  $d^6$ -DMSO):  $\delta_{\text{C}} = 162.0$ , 150.6, 146.7, 144.2 ( $\text{C}_{\text{quaternary}}$ ), 151.7 ( $\text{C}_2$ ), 148.9 ( $\text{C}_b$ ), 138.4 ( $\text{C}_d$ ), 131.3 ( $\text{C}_k$ ), 130.0

(C<sub>j</sub>), 124.9 (C<sub>h</sub>), 123.7/122.0 (C<sub>c</sub>/C<sub>i</sub>), 121.0 (C<sub>7</sub>), 119.8 (C<sub>e</sub>), 107.9 (C<sub>3</sub>), 69.9 (C<sub>8</sub>), 30.5 (C<sub>16</sub>), 29.0/27.9 (C<sub>11</sub>/C<sub>12</sub>), 28.2 (C<sub>13</sub>), 27.7 (C<sub>9</sub>), 24.9 (C<sub>10</sub>). TOF ES-MS(+): m/z 1030.2 [M-PF<sub>6</sub>]<sup>+</sup>. HRMS (ES<sup>+</sup>): Calcd for C<sub>50</sub>H<sub>52</sub><sup>193</sup>IrN<sub>4</sub>O<sub>4</sub>S<sub>2</sub>: 1029.3060, found: 1029.3018. Anal. calcd for C<sub>50</sub>H<sub>52</sub>F<sub>6</sub>IrN<sub>4</sub>O<sub>4</sub>PS<sub>2</sub>: C 51.1, H 4.5, N 4.8. Found: C 51.0, H 5.0, N 5.5. IR ν<sub>max</sub> (cm<sup>-1</sup>): 3041 (C-H), 2931 (C-H), 2856 (C-H), 1684 (C=O), 1605 (C-C<sub>ring</sub> / C-N<sub>ring</sub>), 1577, 1525, 1504, 1477, 1417, 1354, 1299, 1269, 1227, 1188, 1164, 1134, 1110, 1062, 1031, 989, 956, 835, 759, 730.

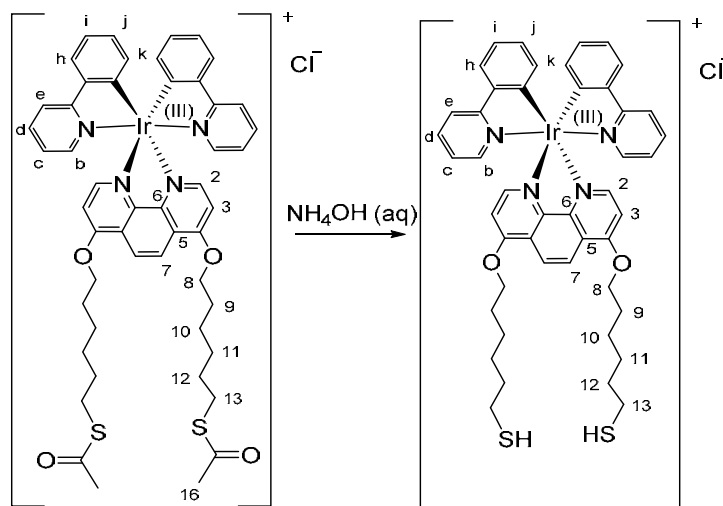
#### Synthesis of [Ir(ppy)<sub>2</sub>PhenSAc]Cl (**IrPhenSAc**)



[Ir(ppy)<sub>2</sub>PhenSAc]PF<sub>6</sub> (20 mg, 0.017 mmol) was dissolved in ethanol (1mL) and passed through a Dowex 1x8, 50–100 mesh ion exchange column, eluting with ethanol. The solvent was removed *in vacuo* to afford the chloride salt, **IrPhenSAc** (11 mg, 61 % yield). <sup>1</sup>H NMR (400 MHz, d<sub>6</sub>-DMSO): δ<sub>H</sub> = 8.36 (s, 2H, H<sub>7</sub>), 8.25 (d, 2H, <sup>3</sup>J<sub>Hd</sub> = 8.3 Hz, H<sub>e</sub>), 7.96–7.91 (m, 4H, H<sub>2</sub>/H<sub>h</sub>), 7.87 (t, 2H, <sup>3</sup>J<sub>Hc</sub> ≈ <sup>3</sup>J<sub>He</sub> ≈ 7.7 Hz, H<sub>d</sub>), 7.59–7.54 (m, 4H, H<sub>3</sub>/H<sub>b</sub>), 7.08–6.98 (m, 4H, H<sub>c</sub>/H<sub>i</sub>), 6.93 (t, 2H, <sup>3</sup>J<sub>Hi</sub> ≈ <sup>3</sup>J<sub>Hk</sub> ≈ 7.6 Hz, H<sub>j</sub>), 6.31 (d, 2H, <sup>3</sup>J<sub>Hj</sub> = 7.5 Hz, H<sub>k</sub>), 4.35 (t, 4H, <sup>3</sup>J<sub>H9</sub> = 6.2 Hz, H<sub>8</sub>), 2.86 (t, 4H, <sup>3</sup>J<sub>H12</sub> = 7.2 Hz, H<sub>13</sub>), 2.31 (s, 6H, H<sub>16</sub>), 1.95–1.84 (m, 4H, H<sub>9</sub>), 1.61–1.49 (m, 4H, H<sub>10</sub>/H<sub>12</sub>), 1.48–1.39 (m, 4H, H<sub>11</sub>). TOF ES-MS(+): m/z 1029.3 [M-Cl]<sup>+</sup>. HRMS (ES<sup>+</sup>): Calcd for C<sub>50</sub>H<sub>52</sub><sup>193</sup>IrN<sub>4</sub>O<sub>4</sub>S<sub>2</sub>: 1029.3059, found: 1029.3077. UV-VIS (CH<sub>3</sub>CN) λ<sub>max</sub> [nm(log ε)] = 254 (4.7), 322 (4.1), 343 (4.1), 390 (3.7), 420 (3.5). Emission (CH<sub>3</sub>CN, λ<sub>exc</sub>

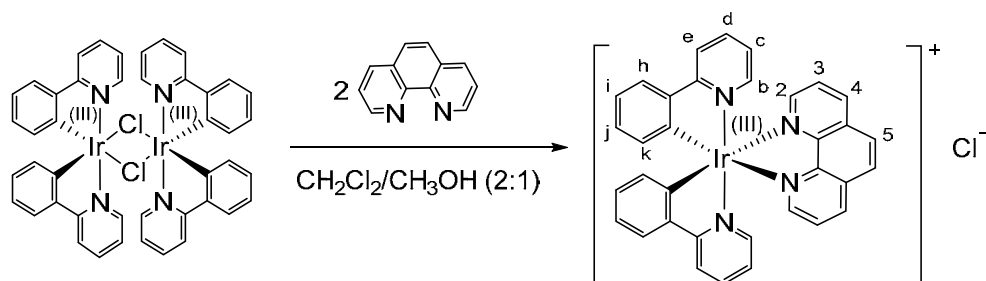
= 355 nm)  $\lambda_{\max}$  [nm] = 515. Lifetime ( $\text{CH}_3\text{CN}$ ,  $\lambda_{\text{exc}} = 375$  nm,  $\lambda_{\text{em}} = 550$  nm) = 40 ns (aerated), =2250 ns (degassed).  $\Phi$  ( $\text{CH}_3\text{CN}$ ,  $\lambda_{\text{exc}} = 355$  nm) = 0.01 (aerated), = 0.28 (degassed).

### Synthesis of *IrPhenSH*



To **IrPhenSAc** (50  $\mu\text{L}$ , 7.0 mM in  $\text{CH}_3\text{CN}$ , 350 nmol) was added  $\text{NH}_4\text{OH}_{(\text{aq})}$  solution (50  $\mu\text{L}$ , 30% *w/w*). The mixture was stirred for ten minutes in a sealed vial to render **IrPhenSH** (3.5 mM) directly prior to titration into the colloid. TOF MALDI-MS(+): 944.16  $[\text{M}-\text{Cl}]^+$

### Synthesis of $[\text{Ir}(\text{ppy})_2\text{phen}]\text{Cl}$



Method as published by author.<sup>29</sup> The cyclometalated iridium(III) dimer,  $[\text{Ir}(\text{ppy})_2(\mu\text{-Cl})]_2$  (0.103 g, 0.096 mmol, 1.0 eq) and 1, 10-phenanthroline (0.037 g, 0.187 mmol, 1.9 eq.) were suspended in a mixture of dichloromethane (8 mL) and methanol (4 mL) and heated to 60  $^\circ\text{C}$

for 7 hours. The solvent was then reduced to *ca.* 1 mL and the product was purified by column chromatography on silica gel eluting dichloromethane : methanol (20 : 1) ( $R_f = 0.14$ ) to give  $[\text{Ir}(\text{ppy})_2\text{phen}]\text{Cl}$  as an orange solid (0.086 g, 63 %).  $^1\text{H}$  NMR (300 MHz,  $\text{CDCl}_3$ )  $\delta$  ppm: 8.93 (dd, 2H,  $^3J_{\text{H}_3} = 8.2$  Hz,  $^4J_{\text{H}_2} = 1.0$  Hz,  $\text{H}_4$ ), 8.41 (s, 2H,  $\text{H}_5$ ), 8.28 (d, 2H,  $^3J_{\text{H}_d} = 8.1$  Hz,  $\text{H}_e$ ), 8.21 (dd, 2H,  $^3J_{\text{H}_3} = 5.0$  Hz,  $^4J_{\text{H}_4} = 1.0$  Hz,  $\text{H}_2$ ), 8.07 (dd, 2H,  $^3J_{\text{H}_4} = 8.2$  Hz,  $^3J_{\text{H}_2} = 5.0$  Hz,  $\text{H}_3$ ), 7.97 (d, 2H,  $^3J_{\text{H}_i} = 7.9$  Hz,  $\text{H}_h$ ), 7.92–7.85 (m, 2H,  $\text{H}_d$ ), 7.47 (d, 2H,  $^3J_{\text{H}_c} = 5.2$  Hz,  $\text{H}_b$ ), 7.16 – 6.90 (m, 6H,  $\text{H}_c/\text{H}_i/\text{H}_j$ ), 6.30 (d, 2H,  $^3J_{\text{H}_j} = 6.7$  Hz,  $\text{H}_k$ ).  $^{13}\text{C}$  NMR (100 MHz,  $\text{CDCl}_3$ )  $\delta$  ppm: 166.8/149.8/146.1/144.0/131.1 ( $\text{C}_{\text{quaternary}}$ ), 150.6 ( $\text{C}_2$ ), 149.1 ( $\text{C}_a$ ), 138.8 / 138.7 ( $\text{C}_c / \text{C}_4$ ), 131.2 ( $\text{C}_h$ ), 130.2 / 123.8 / 122.3 ( $\text{C}_b / \text{C}_f / \text{C}_g$ ), 128.3 ( $\text{C}_c$ ), 127.1 ( $\text{C}_3$ ), 125.0 ( $\text{C}_e$ ), 120.0 ( $\text{C}_d$ ). TOF ES-MS(+)  $m/z$ : 681  $[\text{M}-\text{Cl}]^+$ . HRMS ( $\text{ES}^+$ ) calc. for  $\text{C}_{34}\text{H}_{24}^{191}\text{IrN}_4$ : 679.1607. Found: 679.1635. Emission ( $\text{CH}_3\text{CN}$ ,  $\lambda_{\text{exc}} = 355$  nm)  $\lambda_{\text{max}}$  [nm] = 595. Lifetime ( $\text{CH}_3\text{CN}$ ,  $\lambda_{\text{exc}} = 375$  nm,  $\lambda_{\text{em}} = 550$  nm) = 60 ns (aerated), = 780 ns (degassed).  $\Phi$  ( $\text{CH}_3\text{CN}$ ,  $\lambda_{\text{exc}} = 355$  nm) = 0.02 (aerated), = 0.20 (degassed).

### Synthesis of **IrBpy-Z•AuNP13**

Zonyl® 7950 ( $\text{CH}_2-\text{C}(\text{CH}_3)\text{COOC}_2\text{H}_4(\text{CF}_2)_n\text{F}$ ), MW *ca.* 500, 1  $\mu\text{l}$ , 1.15  $\text{g mL}^{-1}$ ) was added to 13 nm citrate gold nanoparticles (1 mL, 9 nM nanoparticles, zeta potential at 2 nM in deionised water =  $-40 \pm 5$  mV, diameter =  $13 \pm 4$  nm (DLS number distribution), =  $29 \pm 12$  nm (86%),  $998 \pm 624$  nm (14%) (DLS intensity distribution)) to give fluorosurfactant coated nanoparticles (9 nM nanoparticles), with a final fluorosurfactant concentration of *ca.* 1 mL. (Isolated **Z•AuNP13**, by three rounds of centrifugation, decantation of the supernatant and resuspension of the pellet have a zeta potential of  $-61 \pm 4$  mV (2 nM in deionised water) and diameter of  $20 \pm 2$  nm (DLS number distribution), and of  $32 \pm 15$  nm (DLS intensity distribution)). A solution of **IrBpySH** (20  $\mu\text{l}$ , 3.5 mM, (made *in situ*,  $\text{NH}_4\text{OH}(\text{aq})$  30 %  $w/w$ : $\text{CH}_3\text{CN}$  (1:1) solution)) was added to the fluorosurfactant / nanoparticle mixture (not isolated), and was stirred for 20 min. The particles were centrifuged at 12,000 g for 15 min,

and the supernatant was decanted from each pellet to remove unbound material. The nanoparticles were resuspended in deionised water, and this was repeated twice to give **IrBpy-Z•AuNP13**. UV-Vis (H<sub>2</sub>O)  $\lambda_{\max}$  [nm] = 522 (SPR). Diameter = 19±5 nm (DLS number distribution), = 340±166 nm (60%), 33±1 nm (38%), 4567±844 nm (2%) (DLS intensity distribution), zeta potential = -35±3 mV (isolated, 2 nM in deionised water diluent). Emission (H<sub>2</sub>O,  $\lambda_{\text{exc}}$  = 355 nm)  $\lambda_{\max}$  [nm] = 570. Lifetime (H<sub>2</sub>O,  $\lambda_{\text{exc}}$  = 375 nm,  $\lambda_{\text{em}}$  = 550 nm) = 80 ns (7%), 380 ns (93%) (aerated), = 75 ns (6%), 435 ns (94%) (degassed).  $\Phi$  (H<sub>2</sub>O,  $\lambda_{\text{exc}}$  = 355 nm) = 0.19 (aerated). ICP-OES Au:Ir atomic ratio = 106:1.

#### *Synthesis of IrBpy-Z•AuNP100 and IrPhen-Z•AuNP100*

Zonyl® 7950 (CH<sub>2</sub>-C(CH<sub>3</sub>)COOC<sub>2</sub>H<sub>4</sub>(CF<sub>2</sub>)<sub>n</sub>F), MW *ca.* 500, 1  $\mu$ l, 1.15 g mL<sup>-1</sup>) was added to 100 nm citrate gold nanoparticles (1 mL, 40 pM nanoparticles, zeta potential at 4 pM in deionised water = -33 ± 3 mV, diameter = 98 ± 27 nm (DLS number distribution), = 136 ± 62 nm (DLS intensity distribution)) to give fluorosurfactant coated nanoparticles (40 pM nanoparticles), with a final fluorosurfactant concentration of *ca.* 1mL. (Isolated **Z•AuNP100**, by three rounds of centrifugation, decantation of the supernatant and resuspension of the pellet have a zeta potential of -47±3 mV (4 pM in deionised water) and diameter of 92±21 nm (DLS number distribution), 131±62 nm (DLS intensity distribution).) A solution of **IrBpySH** or **IrPhenSH** (20  $\mu$ l, 3.5 mM (made *in situ*, NH<sub>4</sub>OH(aq) 30 % w/w:CH<sub>3</sub>CN (1:1) solution)) was added to the fluorosurfactant / nanoparticle mixture (not isolated), and was stirred for 20 min. The particles were centrifuged at 12,000 g for 15 min, and the supernatant was decanted from each pellet to remove unbound material. The nanoparticles were resuspended in deionised water, and this was repeated twice to give **IrBpy-Z•AuNP100** and **IrPhen-Z•AuNP100**. **IrBpy-Z•AuNP100**: UV-Vis  $\lambda_{\max}$  [nm] = 568(SPR). Diameter = 71 ± 19 nm (DLS number distribution) = 169 ± 84 nm (DLS intensity distribution), zeta potential = -33±3 mV (isolated, 4 pM in deionised water). Emission (H<sub>2</sub>O,  $\lambda_{\text{exc}}$  = 355 nm)  $\lambda_{\max}$

[nm] = 570. Lifetime ( $\text{H}_2\text{O}$ ,  $\lambda_{\text{exc}} = 375 \text{ nm}$ ,  $\lambda_{\text{em}} = 550 \text{ nm}$ ) = 90 ns (10%), 400 ns (90%) (aerated), = 85 ns (11%), 420 ns (89%) (degassed).  $\Phi$  ( $\text{H}_2\text{O}$ ,  $\lambda_{\text{exc}} = 355 \text{ nm}$ ) = 0.14 (aerated). ICP-OES Au:Ir atomic ratio = 1974:1. **IrPhen-Z•AuNP100**: UV-Vis  $\lambda_{\text{max}}$  ( $\text{H}_2\text{O}$ )  $\lambda_{\text{max}}$  [nm] = 569 (SPR). Diameter =  $70 \pm 24 \text{ nm}$  (DLS number distribution) =  $114 \pm 40 \text{ nm}$  (DLS intensity distribution), zeta potential (isolated, 4 pM in deionised water) =  $-32 \pm 3 \text{ mV}$ . Emission ( $\text{H}_2\text{O}$ ,  $\lambda_{\text{exc}} = 355 \text{ nm}$ )  $\lambda_{\text{max}}$  [nm] = 555. Lifetime ( $\text{H}_2\text{O}$ ,  $\lambda_{\text{exc}} = 375 \text{ nm}$ ,  $\lambda_{\text{em}} = 550 \text{ nm}$ ) = 50 ns (25%), 335 ns (75%) (aerated), = 300 ns (15%), 1570 ns (85%) (degassed).

#### *Synthesis of GdQ•AuNP13*

**GdQSH** (20–100  $\mu\text{L}$ , 1 mM,  $\text{CH}_3\text{OH}$ ) was titrated into 13 nm gold nanoparticles (1 mL, 9 nM), to a final complex concentration of 100  $\mu\text{M}$ , and the SPR was monitored by UV-Vis absorption spectroscopy. The nanoparticles were isolated from unbound material by centrifugation at 12,000 g for 15 min; the supernatant was decanted from each pellet to remove unbound material and the nanoparticles were resuspended in deionised water. This was repeated twice to give **GdQ•AuNP13**. UV-Vis ( $\text{H}_2\text{O}$ )  $\lambda_{\text{max}}$  [nm] = 526 (SPR),  $T_1$  relaxivity =  $7.1 \text{ s}^{-1} \text{ mM}^{-1}$  ([Gd]), at 3T. ICP-OES Au:Gd atomic ratio = 98:1.

#### *Synthesis of IrBpy-GdQ•AuNP13*

**GdQSH** (20–100  $\mu\text{L}$ , 1 mM,  $\text{CH}_3\text{OH}$ ) was titrated into 13 nm gold nanoparticles (1 mL, 9 nM), to a final complex concentration of 100  $\mu\text{M}$ . Subsequently, **IrBpySH**, (1–6  $\mu\text{M}$ , 3.4 mM, (made *in situ*,  $\text{NH}_4\text{OH}(\text{aq})$  30 % w/w: $\text{CH}_3\text{CN}$  (1:1) solution)) was added. The SPR was monitored by UV-Vis absorption spectroscopy throughout the titration. The nanoparticles were isolated from unbound material by centrifugation at 12,000 g for 15 min; the supernatant was decanted from each pellet to remove unbound material and the nanoparticles were resuspended in deionised water. This was repeated twice to give **IrBpy-GdQ•AuNP13**. UV-Vis ( $\text{H}_2\text{O}$ )  $\lambda_{\text{max}}$  [nm] = 526 (SPR), diameter =  $11 \pm 3 \text{ nm}$  (DLS number distribution) =  $128 \pm 135$

nm (DLS intensity distribution). Emission ( $\text{H}_2\text{O}$ ,  $\lambda_{\text{exc}} = 355 \text{ nm}$ )  $\lambda_{\text{max}} [\text{nm}] = 580$ . Lifetime ( $\text{H}_2\text{O}$ ,  $\lambda_{\text{exc}} = 375 \text{ nm}$ ,  $\lambda_{\text{em}} = 550 \text{ nm}$ ) = 90 ns (29%), 285 ns (71%) (aerated).  $r_1$  relaxivity =  $7.1 \text{ s}^{-1} \text{ mM}^{-1}$  ([Gd]), at 3T. ICP-OES Au:Gd atomic ratio = 73:1, Au:Ir ratio = 300:1.

### 5.10.2 Flow Imaging in Blood

#### *Isolation of RBC and preparation of defined percentage haematocrit suspensions*

Isolation was performed by Dr Hannah Jeffery in the laboratory of Professor G. Nash. Venous blood from healthy individuals was added to citrate phosphate dextrose adenine (CPDA) solution (Sigma Aldrich) in sterile 15 mL round bottom polystyrene tubes (Sterilin, Appleton Woods, Birmingham, UK) at ratio of 9:1 following informed consent and with approval from the University of Birmingham Local Ethical Review Committee. RBC were isolated by centrifugation (2500 rpm, 10 min) and washed twice with 10 mL phosphate buffered saline (PBS) (3000 rpm, 10 min). RBC pellets from 27 mL venous blood were pooled and centrifuged (3000 rpm, 5 min) to pack cells. The supernatant was removed and the packed RBC diluted 1:1 with PBS. RBC density was determined using a Coulter Particle Count and Size Analyser (Beckman Coulter). Percentage haematocrit of the RBC suspension was also measured using the microhaematocrit method; RBC suspension was drawn into glass capillary tubes under capillary action and one end of the tube sealed by melting the glass. The capillary tube was centrifuged (15,000 g, 5 min) to separate the RBC from the liquid phase. Percentage haematocrit was calculated by dividing the length of the RBC column into the total length of the RBC suspension column. No corrections were made for small volumes of solution trapped within the tightly packed RBC. 2.5 mL suspensions of known percentage haematocrit were prepared by dilution with PBS. In order to allow tracking of the RBC, the preparations were spiked with  $2.8 \times 10^7$  CellTracker Green<sup>TM</sup>/5-Chloromethylfluorescein Diacetate (CMFDA) (Molecular probes, Life Technologies)-labelled RBC per 2.5 mL RBC suspension. The number of labelled RBC added was negligible compared to the total present

(0.27–0.79%) and was kept constant, irrespective of the percent haematocrit, in order that the frequency of labelled cells passing the field of view under flow conditions was uniform across test conditions. To investigate effects of RBC aggregation on the dynamics of nanoparticles under flow conditions, 62.5% of the fluid phase was replaced with solutions of different molecular weight dextrans: 1.6% high molecular weight 500kDa dextran (Dextran500) to induce aggregation and 3.25% low molecular weight 40kDa dextran (Dextran40) as a viscosity control.

#### *Fluorescent labelling of RBC*

Labelling was performed by Dr Hannah Jeffery.  $90 \times 10^6$  washed RBC were suspended in 15 mL CMFDA (10 $\mu$ M) diluted in non-supplemented medium M199 (Gibco, Invitrogen, Paisley, Scotland) and incubated (37 °C, 5% CO<sub>2</sub>) for 40min. Cells were pelleted by centrifugation (1500 rpm, 5 min) then resuspended in 15 mL medium M199 supplemented with 10% Foetal Calf Serum and incubated (37 °C, 5% CO<sub>2</sub>) for 40 min. Cells were pelleted by centrifugation (1500 rpm, 5 min), washed in 15 mL PBS (1500 rpm, 5 min) and resuspended in 800  $\mu$ l PBS. 250  $\mu$ l volumes were added per 2.5 mL preparation of each percent haematocrit suspension as a component of the total diluent volume.

#### *Flow Imaging*

Imaging was performed by the author, Dr David J. Lewis and Dr Hannah Jeffery. Assays were performed using a set-up described previously.<sup>88</sup> Briefly, prefabricated channel slides of rectangular cross-section ( $\mu$ -slide VI<sup>0.1</sup>(non-coated, ibidi GmbH, Martisried Germany)), channel dimensions 1 mm ( $x$ -axis)  $\times$  17 mm ( $y$ -axis, parallel to the flow)  $\times$  0.1 mm ( $z$ -axis)) 17 mm length ( $y$ -axis)  $\times$  1 mm width ( $x$ -axis), were pre-treated with 4% bovine serum albumin solution in PBS for 3 hr, rinsed with PBS and mounted on the stage of an inverted microscope (Olympus IX-71) fitted with an LUCPLFLN 40 $\times$  objective lens, numerical

aperture 0.6, field number 22 and a variable focus collar with a working distance 2.7 – 4 mm. The barrel of a 5 mL syringe was fitted into the luer port at one end of the channel to act as a sample reservoir and 1.5 mm diameter plastic tubing fitted via a luer adaptor into the port at the opposite end of the channel. A three-way tap was fitted to the other end of the tubing and connected to both a Harvard withdrawal syringe pump and a 10 mL syringe. These syringes respectively facilitated the controlled perfusion of sample during imaging at a flow rate of  $5\mu\text{L min}^{-1}$  and the removal of wash buffer (PBS) that was perfused to rinse the channel between samples. The observation plane was located in the centre of the channel with respect to the  $x$ -axis. Two image sets each containing 500 16-bit images taken with 4 x 4 binning (128 x 128 pixels) were acquired at 64 frames per second (fps) at each depth. The microscope was focussed on the channel wall for the first image sequence (the channel wall was identified by focussing on occasional nanoparticles that had become stuck on the wall) and then, the focal point was varied by increments of  $5\mu\text{m}$  through the  $z$ -axis and image sequences captured at each depth across the channel. 2 pM nanoparticles in PBS with 0% to 30% haematocrit, were perfused through the model vessel at a volumetric flow rate of  $5\mu\text{m min}^{-1}$ . To monitor the velocities of **IrBpy-Z•AuNP10** and RBC at the same depth, image sets were collected under both 355 nm excitation (**IrBpy-Z•AuNP10**) and 475 nm excitation (labelled RBC). Image sets were converted to audio video interleave (AVI) files for offline analysis of particle velocity.

#### *Calculation of particle velocity from AVIs*

AVIs were processed in the open source ImageJ64 software as 3D projections of the  $x$ -axis/ $y$ -axis/time stacks, by the author and Hannah Jeffery, and were projected onto the  $x$ -axis. Background was subtracted from the images using a sliding paraboloid with 1.0 pixel rolling ball radius. Flowing luminescent nanoparticles or stained RBC appeared as diagonal tracks within the  $y$ -axis vs time projection. The angles of 20–30 track lines were measured manually

at each depth and the velocities of the particles, with respect to the flow axis ( $v_y$ ), were calculated. To avoid bias, every line encountered on movement left to right across the  $y$ -axis vs time projection was measured.

### 5.10.3 Murine Tissue Studies

Murine studies were conducted by Professor S. Egginton, under licence PPL 30/2789, and C57/B16 mice were obtained from Charles River (UK). Mice were anaesthetised using isoflurane (3%, balance oxygen) and intracardial or tail-vein injections of 100–200  $\mu$ L sterile 80 pM nanoparticle samples suspended in PBS were performed. Animals were sacrificed at 5 min by cervical dislocation. The author, Dr Hannah Jeffery, and Dr David J. Lewis performed tests on post-mortem tissue.

#### *Microscopy*

Tissues including the mesentery, lung and *extensor hallucis proprius* skeletal muscle were excised and immersed in 4% paraformaldehyde in PBS for 15 min, washed with 3 x PBS, and mounted onto glass coverslips with Vectashield (Vector Labs) mounting medium. Tissues were imaged within 5 hours of euthanasia using an inverted microscope (Olympus IX-71) fitted with an LUCPLFLN 40X objective lens, numerical aperture 0.6, field number 22 and a variable focus collar with a working distance 2.7 – 4 mm.

#### *Biodistribution Studies*

The following organ samples were excised for digestion and ICP-MS was employed to calculate gold content: lung, spleen, gut, kidney, liver, brain. The tissue was frozen immediately post-excision, and then later defrosted for analysis. Glass vials were cleaned thoroughly with ultrapure aqua regia (HCl:HNO<sub>3</sub>, 3:1, using ultrapure grade acids) before use. The organs were weighed, and then digested in sealed vials in aqua regia (3 mL), and heated

to 100 °C for 10 hr. Samples were cooled and filtered (to remove and insoluble material) into falcon tubes, and diluted to 10 mL. The samples were then analysed for gold concentration by ICP-MS.

#### **5.10.4 MRI Studies of IrBpy-GdQ•AuNP13 Nanoparticles**

##### *T<sub>1</sub> relaxation time analysis*

Analysis was performed by Ms Lindsey van Gemeren, under the supervision of Dr Nigel Davies. Imaging was performed on a 3T Siemens MAGNETOM Verio clinical imaging machine at Birmingham Women's Hospital. *T<sub>1</sub>* mapping was executed using a 16 channel head coil with a saturation recovery pulse sequence.

##### *Preliminary in vitro studies in A549 cells*

A549 tissue culture was performed by Mr Sunil Claire in the School of Biosciences. Cells were incubated with 0.9 nM **GdQ•AuNP13** and **IrBpy-GdQ•AuNP13** for 24 hr in complete media. Cell media was removed and the cells washed twice in PBS and subsequently fixed with paraformaldehyde for 5 min, followed by two further washes with PBS. Coverslips were removed and mounted on a droplet of Hydromount media (national diagnostics) on glass slides, sealed with clear nail varnish and stored for 24 hours at 4°C before imaging. Confocal imaging was performed by the author.

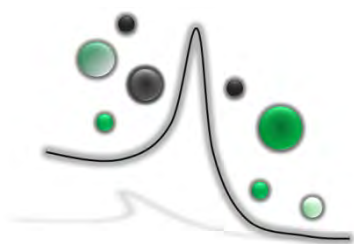
## 5.11 Chapter Five References

- (1) Rogers, N. J.; Claire, S.; Harris, R. M.; Farabi, S.; Zikeli, G.; Styles, I. B.; Hodges, N. J.; Pikramenou, Z. *Chem. Commun.* **2014**, 50, 617.
- (2) Rogers, N. J.; Pikramenou, Z. *Patent* **2013**, WO/2013/004989.
- (3) Baldo, M. A.; Thompson, M. E.; Forrest, S. R. *Nature* **2000**, 403, 750.
- (4) Baranoff, E.; Yum, J.-H.; Graetzel, M.; Nazeeruddin, M. K. *J. Organomet. Chem.* **2009**, 694, 2661.
- (5) Wu, C.; Chen, H.-F.; Wong, K.-T.; Thompson, M. E. *J. Am. Chem. Soc.* **2010**, 132, 3133.
- (6) Mayo, E. I.; Kilsa, K.; Tirrell, T.; Djurovich, P. I.; Tamayo, A.; Thompson, M. E.; Lewis, N. S.; Gray, H. B. *Photochem. Photobiol. Sci.* **2006**, 5, 871.
- (7) Lo, K. K.-W.; Li, S. P.-Y.; Zhang, K. Y. *New J. Chem.* **2011**, 35, 265.
- (8) Fernandez-Moreira, V.; Thorp-Greenwood, F. L.; Coogan, M. P. *Chem. Commun.* **2010**, 46, 186.
- (9) Baggaley, E.; Weinstein, J. A.; Williams, J. A. G. *Coord. Chem. Rev.* **2012**, 256, 1762.
- (10) Ohsawa, Y.; Sprouse, S.; King, K. A.; DeArmond, M. K.; Hanck, K. W.; Watts, R. J. *J. Phys. Chem.* **1987**, 91, 1047.
- (11) Braterman, P. S.; Heath, G. A.; MacKenzie, A. J.; Noble, B. C.; Peacock, R. D.; Yellowlees, L. J. *Inorg. Chem.* **1984**, 23, 3425.
- (12) *Organometallic Complexes for Optoelectronic Applications*; Thompson, M. E.; Djurovich, P. E.; Barlow, S.; Marder, S., Eds.; Elsevier, 2007; Vol. 12.
- (13) Lamansky, S.; Djurovich, P.; Murphy, D.; Abdel-Razzaq, F.; Kwong, R.; Tsyba, I.; Bortz, M.; Mui, B.; Bau, R.; Thompson, M. E. *Inorg. Chem.* **2001**, 40, 1704.
- (14) Colombo, M. G.; Güdel, H. U. *Inorg. Chem.* **1993**, 32, 3081.
- (15) Vanhelmont, F. W. M.; Güdel, H. U. *Inorg. Chem.* **1997**, 36, 5512.
- (16) Colombo, M. G.; Hauser, A.; Güdel, H. U. *Inorg. Chem.* **1993**, 32, 3088.
- (17) Sprouse, S.; King, K. A.; Spellane, P. J.; Watts, R. J. *J. Am. Chem. Soc.* **1984**, 106, 6647.
- (18) Hua-Wei, L.; Zhang, K. Y.; Law, W. H.-T.; Lo, K. K.-W. *Organometallics* **2010**, 29, 3474.
- (19) Lee, P.-K.; Liu, H.-W.; Yiu, S.-M.; Louie, M.-W.; Lo, K. K.-W. *Dalton Trans.* **2011**, 40, 2180.
- (20) Lo, K. K.-W.; Chan, B. T.-N.; Liu, H.-W.; Zhang, K. Y.; Li, S. P.-Y.; Tang, T. S.-M. *Chem. Commun.* **2013**, 49, 4271.
- (21) Law, W. H.-T.; Lee, L. C.-C.; Louie, M.-W.; Liu, H.-W.; Ang, T. W.-H.; Lo, K. K.-W. *Inorg. Chem.* **2013**, 52, 13029.
- (22) Zhang, K. Y.; Li, S. P.-Y.; Zhu, N.; Or, I. W.-S.; Cheung, M. S.-H.; Lam, Y.-W.; Lo, K. K.-W. *Inorg. Chem.* **2010**, 49, 2530.
- (23) Li, S. P.-Y.; Lau, C. T.-S.; Louie, M.-W.; Lam, Y.-W.; Cheng, S. H.; Lo, K. K.-W. *Biomaterials* **2013**, 34, 7519.
- (24) Jones, J. E.; Jenkins, R. L.; Hicks, R. S.; Hallett, A. J.; Pope, S. J. A. *Dalton Trans.* **2012**, 41, 10372.

- (25) Smith, R. A.; Stokes, E. C.; Langdon-Jones, E. E.; Platts, J. A.; Kariuki, B. M.; Hallett, A. J.; Pope, S. J. A. *Dalton Trans.* **2013**, 42, 10347.
- (26) Kim, O.-H.; Ha, S.-W.; Kim, J. I.; Lee, J.-K. *ACS Nano* **2010**, 4, 3397.
- (27) de Barros e Silva Botelho, M.; Fernandez-Hernandez, J. M.; de Queiroz, T. B.; Eckert, H.; De Cola, L.; de Camargo, A. S. S. *J. Mater. Chem.* **2011**, 21, 8829.
- (28) Zanarini, S.; Rampazzo, E.; Bonacchi, S.; Juris, R.; Marcaccio, M.; Montalti, M.; Paolucci, F.; Prodi, L. *J. Am. Chem. Soc.* **2009**, 131, 14208.
- (29) Lewis, D. J.; Dore, V.; Rogers, N. J.; Mole, T. K.; Nash, G. B.; Angeli, P.; Pikramenou, Z. *Langmuir* **2013**, 29, 14701.
- (30) Nasr, G.; Guerlin, A.; Dumur, F.; Baudron, S. A.; Dumas, E.; Miomandre, F.; Clavier, G.; Sliwa, M.; Mayer, C. R. *J. Am. Chem. Soc.* **2011**, 133, 6501.
- (31) Miomandre, F.; Stancheva, S.; Audibert, J.-F.; Brosseau, A.; Pansu, R. B.; Lepeltier, M.; Mayer, C. R. *J. Phys. Chem. C* **2013**, 117, 12806.
- (32) Sheikh, S.; Rainger, G. E.; Gale, Z.; Rahman, M.; Nash, G. B. *Blood* **2003**, 102, 2828.
- (33) Chauhan, V. P.; Stylianopoulos, T.; Martin, J. D.; Popovic, Z.; Chen, O.; Kamoun, W. S.; Bawendi, M. G.; Fukumura, D.; Jain, R. K. *Nat. Nanotechnol.* **2012**, 7, 383.
- (34) Parveen, S.; Misra, R.; Sahoo, S. K. *Nanomedicine: NBM* **2012**, 8, 147.
- (35) Korin, N.; Kanapathipillai, M.; Matthews, B. D.; Crescente, M.; Brill, A.; Mammoto, T.; Ghosh, K.; Jurek, S.; Bencherif, S. A.; Bhatta, D.; Coskun, A. U.; Feldman, C. L.; Wagner, D. D.; Ingber, D. E. *Science* **2012**, 337, 738.
- (36) Lavik, E.; von Recum, H. *ACS Nano* **2011**, 5, 3419.
- (37) Douma, K.; Prinzen, L.; Slaaf, D. W.; Reutelingsperger, C. P. M.; Biessen, E. A. L.; Hackeng, T. M.; Post, M. J.; van Zandvoort, M. A. M. *J. Small* **2009**, 5, 544.
- (38) Owens, D. E.; Peppas, N. A. *Int. J. Pharm.* **2006**, 307, 93.
- (39) Sonavane, G.; Tomoda, K.; Makino, K. *Colloids Surf., B* **2008**, 66, 274.
- (40) Popović, Z.; Liu, W.; Chauhan, V. P.; Lee, J.; Wong, C.; Greytak, A. B.; Insin, N.; Nocera, D. G.; Fukumura, D.; Jain, R. K.; Bawendi, M. G. *Angew. Chem. Int. Ed.* **2010**, 49, 8649.
- (41) Caravan, P.; Ellison, J. J.; McMurry, T. J.; Lauffer, R. B. *Chem. Rev.* **1999**, 99, 2293.
- (42) Moriggi, L. c.; Cannizzo, C.; Dumas, E.; Mayer, C. d. R.; Ulianov, A.; Helm, L. *J. Am. Chem. Soc.* **2009**, 131, 10828.
- (43) Raymond, K. N.; Pierre, V. C. *Bioconjug. Chem.* **2004**, 16, 3.
- (44) Kim, J.; Piao, Y.; Hyeon, T. *Chem. Soc. Rev.* **2009**, 38, 372.
- (45) Lee, D.-E.; Koo, H.; Sun, I.-C.; Ryu, J. H.; Kim, K.; Kwon, I. C. *Chem. Soc. Rev.* **2012**, 41, 2656.
- (46) Louie, A. *Chem. Rev.* **2010**, 110, 3146.
- (47) Chen, X.; Gambhir, S. S.; Cheon, J. *Acc. Chem. Res.* **2011**, 44, 841.
- (48) Kim, T. H.; Lee, S.; Chen, X. *Expert Rev. Mol. Diagn.* **2013**, 13, 257.
- (49) Lammers, T.; Aime, S.; Hennink, W. E.; Storm, G.; Kiessling, F. *Acc. Chem. Res.* **2011**, 44, 1029.

- (50) Nonoyama, M. *Bull. Chem. Soc. Jpn.* **1974**, *47*, 767.
- (51) Farabi, S., PhD Thesis, University of Birmingham, 2012.
- (52) Sun, J.; Wu, W.; Guo, H.; Zhao, J. *Eur. J. Inorg. Chem.* **2011**, 3165.
- (53) Wu, S.-H.; Ling, J.-W.; Lai, S.-H.; Huang, M.-J.; Cheng, C. H.; Chen, I. C. *J. Phys. Chem. A* **2010**, *114*, 10339.
- (54) King, K. A.; Watts, R. J. *J. Am. Chem. Soc.* **1987**, *109*, 1589.
- (55) Costa, R. D.; Ortí, E.; Bolink, H. J.; Graber, S.; Schaffner, S.; Neuburger, M.; Housecroft, C. E.; Constable, E. C. *Adv. Funct. Mater.* **2009**, *19*, 3456.
- (56) Carraway, E. R.; Demas, J. N.; DeGraff, B. A.; Bacon, J. R. *Anal. Chem.* **1991**, *63*, 337.
- (57) Franco, C.; Olmsted Iii, J. *Talanta* **1990**, *37*, 905.
- (58) Dragonetti, C.; Falciola, L.; Mussini, P.; Righetto, S.; Roberto, D.; Ugo, R.; Valore, A.; De Angelis, F.; Fantacci, S.; Sgamellotti, A.; Ramon, M.; Muccini, M. *Inorg. Chem.* **2007**, *46*, 8533.
- (59) Ruggi, A.; van Leeuwen, F. W. B.; Velders, A. H. *Coord. Chem. Rev.* **2011**, *255*, 2542.
- (60) Adrian, R. J. *Annual Review of Fluid Mechanics* **1991**, *23*, 261.
- (61) Adrian, R. J. *Annu. Rev. Fluid Mech.* **1991**, *23*, 261.
- (62) Adrian, R. J. *Exp. Fluids* **2005**, *39*, 159.
- (63) Lindken, R.; Rossi, M.; Grosse, S.; Westerweel, J. *Lab Chip* **2009**, *9*, 2551.
- (64) Goldsmith, H. L.; Marlow, J. C. *J. Colloid Interface Sci.* **1979**, *71*, 383.
- (65) Goldsmith, H. L.; Karino, T. *Ann. N. Y. Acad. Sci.* **1977**, *283*, 241.
- (66) Lima, R.; Ishikawa, T.; Imai, Y.; Takeda, M.; Wada, S.; Yamaguchi, T. *Ann. Biomed. Eng.* **2009**, *37*, 1546.
- (67) Abbitt, K. B.; Nash, G. B. *Br. J. Haematol.* **2001**, *112*, 55.
- (68) Choi, S. M.; Kim, W. H.; Cote, D.; Park, C. W.; Lee, H. *Opt. Express* **2011**, *19*, 4357.
- (69) Saadatmand, M.; Ishikawa, T.; Matsuki, N.; Abdekhodaie, M. J.; Imai, Y.; Ueno, H.; Yamaguchi, T. *J. Biomech.* **2011**, *44*, 170.
- (70) Ha, H.; Nam, K. H.; Lee, S. J. *Microvasc. Res.* **2012**, *84*, 242.
- (71) Ravnic, D. J.; Zhang, Y. Z.; Tsuda, A.; Pratt, J. P.; Huss, H. T.; Mentzer, S. J. *Microvasc. Res.* **2006**, *72*, 27.
- (72) Vennemann, P.; Kiger, K. T.; Lindken, R.; Groenendijk, B. C. W.; Stekelenburg-de Vos, S.; ten Hagen, T. L. M.; Ursem, N. T. C.; Poelmann, R. E.; Westerweel, J.; Hierck, B. P. *J. Biomech.* **2006**, *39*, 1191.
- (73) Petros, R. A.; DeSimone, J. M. *Nat. Rev. Drug Discovery* **2010**, *9*, 615.
- (74) Brigger, I.; Dubernet, C.; Couvreur, P. *Adv. Drug Delivery Rev.* **2012**, *64*, Supplement, 24.
- (75) Herrmann, I. K.; Schlegel, A.; Graf, R.; Schumacher, C. M.; Senn, N.; Hasler, M.; Gschwind, S.; Hirt, A.-M.; Gunther, D.; Clavien, P.-A.; Stark, W. J.; Beck-Schimmer, B. *Nanoscale* **2013**, *5*, 8718.
- (76) Ahuja, A. S.; Hendee, W. R.; Carson, P. L. *Phys. Med. Biol.* **1978**, *23*, 928.

- (77) Saadatmand, M.; Ishikawa, T.; Matsuki, N.; Jafar Abdekhodaie, M.; Imai, Y.; Ueno, H.; Yamaguchi, T. *J. Biomech.* **2011**, *44*, 170.
- (78) Yeh, C.; Eckstein, E. C. *Biophys. J.* **1994**, *66*, 1706.
- (79) Nash, G. B.; Watts, T.; Thornton, C.; Barigou, M. *Clin. Hemorheol. Microcirc.* **2008**, *39*, 303.
- (80) Pries, A. R.; Secomb, T. W.; Gaehtgens, P. *Cardiovasc. Res.* **1996**, *32*, 654.
- (81) Savage, A. C., PhD Thesis, University of Birmingham, 2013.
- (82) Sasaki, M.; Shibata, E.; Kanbara, Y.; Ehara, S. *Magn. Reson. Med. Sci.* **2005**, *4*, 145.
- (83) Park, J.-A.; Reddy, P. A. N.; Kim, H.-K.; Kim, I.-S.; Kim, G.-C.; Chang, Y.; Kim, T.-J. *Bioorg. Med. Chem. Lett.* **2008**, *18*, 6135.
- (84) Grabar, K. C.; Freeman, R. G.; Hommer, M. B.; Natan, M. J. *Anal. Chem.* **1995**, *67*, 735.
- (85) Ziegler, C.; Eychmueller, A. *J. Phys. Chem. C* **2011**, *115*, 4502.
- (86) Lewis, D. J., PhD Thesis, University of Birmingham, 2006.
- (87) Sprouse, S.; King, K. A.; Spellane, P. J.; Watts, R. J. *J. Am. Chem. Soc.* **1984**, *106*, 6647.
- (88) Butler, L. M.; Jeffery, H. C.; Wheat, R. L.; Rae, P. C.; Townsend, K.; Alkharsah, K. R.; Schulz, T. F.; Nash, G. B.; Blackbourn, D. J. *J. Virol.* **2011**, *85*, 7321.



---

# Chapter Six

---

## General Experimental

## 6.1 Materials

Solvents were purchased from Fisher or Sigma Aldrich and anhydrous solvents were dried over 3Å molecular sieves under N<sub>2</sub>(g) for 1 hr, or by PureSolv-EN solvent purification system. Deuterated solvents for NMR were also purchased from Sigma Aldrich. HPLC grade solvents were used in photophysical studies and water was deionised using an Elga Option 3 water purifier. All compounds were synthesised under N<sub>2</sub>(g) unless otherwise indicated, using standard Schlenk techniques.

## 6.2 General Experimental Details for Synthesis

<sup>1</sup>H and <sup>13</sup>C{<sup>1</sup>H} PENDANT NMR spectra were recorded using a Bruker AC 300, AV 300, AMX 400 or AV 400 spectrometer, and Si(CH<sub>3</sub>)<sub>4</sub> was used as the external reference. Electrospray mass spectra were recorded on a Waters Micromass LCT time of flight mass spectrometer, using a nitrogen laser, and matrix assisted laser desorption ionisation time of flight (MALDI-TOF) mass spectrometry was performed on a Bruker Diflex IV mass spectrometer, using gentisic acid (CH<sub>3</sub>CN solution with 0.1% TFA) as the matrix.

Elemental analysis was performed on either a Carlo Erba EA1110 Simultaneous CHN elemental analyser (University of Birmingham), or at the London School of Pharmacy, UCL, on an Elemental Analyser, Model 1108 (Carlo-Erba, Milan, Italy) with PC based data system, Eager 200 for Windows™ and a Sartorius Ultra Micro Balance, 4504MP8.

Fourier transform infra red (FT-IR) spectroscopy was performed on powder samples, using a Perkin Elmer Spectrum 100 FT-IR, with a universal attenuated total reflectance attachment.

### 6.3 Photophysical Characterisation Techniques

UV-Vis absorption spectroscopy measurements were performed on a Varian Cary 5000 spectrometer at a  $300 \text{ nm min}^{-1}$  acquisition rate. Samples were prepared in either 1 cm or 0.4 cm path length low volume quartz cuvettes.

Steady-state and time-resolved luminescence measurements were executed on an Edinburgh Instruments FLS920 spectrometer, with a 450 W xenon arc lamp illumination source. The detection system uses a Hamamatsu R928 photomultiplier tube (PMT), and an emission monochromator blazed at 500 nm. Samples were prepared in quartz cuvettes with four transparent faces, and appropriate long-pass filters were employed to eliminate second-order photon scattering. 77 K studies were measured in an in-house built sample holder within a nitrogen cryostat (Oxford Instruments), using the Edinburgh Instruments FLS920 spectrophotometer.

Luminescence lifetimes ( $\tau$ ) were measured with a 375 nm or a 445 nm picosecond pulse length diode laser excitation source, using the time-correlated single-photon counting module of the FLS920 spectrometer set-up, with the Hamamatsu R928 photomultiplier tube (PMT). Lifetimes were tail-fitted using the Edinburgh Instruments F900 or FAST PC software, i.e. fitted beyond the time point where the excitation light has disappeared, and thus in a region where there is no further sample signal generation. The quality of the fit results was evaluated by analysing the reduced chi-square parameter, and the residual data. The exponential order was increased until the residual plot presented random noise distributed about zero, with a reduced chi-square value between 1.0–1.3. All lifetimes were fitted using a Marquardt-Levenberg algorithm.

Quantum yield ( $\Phi$ ) measurements were performed on the spectrometer using an integrating sphere. Solution measurements were referenced to the solvent used, and nanoparticles were referenced to un-labelled gold nanoparticles. Low intensity signal (for low  $\Phi$  solutions or low concentration nanoparticle samples) were measured using a calibrated neutral density filter.

## 6.4 Nanoparticle Characterisation Techniques

Zeta potential and dynamic light scattering measurements were performed using either a Zetasizer Nano ZS, (Malvern Instruments), or a Beckmann Coulter Delsa Nano C instrument, calibrated with a zeta potential transfer standard (Malvern Instruments). DLS size distributions are calculated by analysis of the scattered light autocorrelation function with the CONTIN algorithm (i.e. an inverse Laplace transform).

Nanoparticle Tracking Analysis (NTA) was performed using a Nanosight LM-10 (Nanosight, UK) system equipped with a 488 nm laser in scattering mode, using the analysis of at least 2000 tracks.

Transmission electron microscopy (TEM) was performed using a JEOL JEM-1200EX and a JEOL JEM-2100 electron microscope fitted with a Gatan camera by drying colloid onto formvar-coated copper grids (Agar Scientific). Images were acquired using Digital Micrograph 1.8 software (Gatan, CA, USA). Scanning electron microscopy (SEM) imaging was performed at the Centre for Electron Microscopy with the help of Theresa Morris, on a Jeol JSM 7000F Microscope fitted with an Oxford Inca Energy Dispersive X-Ray Spectrometer.

Inductively coupled plasma optical emission spectroscopy was performed using a 5300DV ICP-OES system (Perkin-Elmer) at the University of Warwick. Inductively coupled plasma optical mass spectrometry (ICP-MS) measurements were performed on a 7500cx ICP-MS with an integrated auto-sampler (Agilent). Metal concentrations were determined using PlasmaCal calibration standards (QMX laboratories), with  $R^2 > 0.999$  linear calibration curves in all cases. For these experiments, colloidal suspensions were digested in ultrapure aqua regia (Sigma Aldrich) and then diluted ten-fold in deionised water.

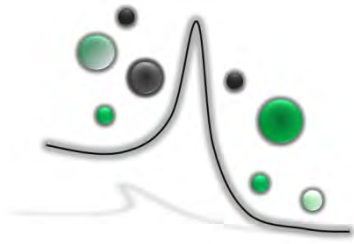
## 6.5 Luminescence Microscopy

Epiluminescence images were acquired with the Edinburgh Instruments FLSP920 Spectrometer appended to an Olympus IX71 Inverted Microscope, with a LUCPLFLN 40×0.60 NA objective. Samples were excited with a 450 W xenon arc lamp, using the double monochromator in the excitation arm to select the excitation wavelength, and images were acquired with a Hamamatsu EM CCD C9100-13 camera. Confocal laser scanning microscopy was performed using a Leica TCS SP2 confocal microscope (Leica Microsystems).

## 6.6 Acknowledgements

Thank you to Dr Shiva Farabi for all her help and training in the laboratory, and thanks to Dr David Lewis, Dr Alison Savage and Dr Stephen Hammond for their support with all the photophysical equipment. I must also acknowledge Mr Mark McCallam (Edinburgh Instruments) for his help and support with the Luminescence Spectrophotometer, and Mr Stuart Arkless for his help with all the Science City equipment at the University of Birmingham. Thank you also to Dr Neil Spencer and all the analytical staff at the University of Birmingham for their support with NMR, mass-spectrometry and elemental analysis. Acknowledgment must also go to Mr Paul Stanley and Ms Theresa Morris for all their help and ideas at the Centre for Electron Microscopy, University of Birmingham. Finally, I must

thank Dr Lijiang Song and Philip Aston at the University of Warwick for all their help with ICP-OES and ICP-MS measurements.



---

# Appendices

---

## Appendix 1: Nanoparticle Size and Concentration Calculations

### -1.1 Concentration of 13 nm Gold Nanoparticles

Mass of  $\text{HAuCl}_4$  (49 % Au by assay) = 0.09889 g

Mass of Au =  $0.49 \times 0.09889 = 0.04846$  g

Moles of Au =  $0.04846 / 197 = 2.4597 \times 10^{-4}$  moles

Concentration of Au =  $2.4597 \times 10^{-4}$  moles /  $0.275 \text{ dm}^3 = 8.944 \times 10^{-4} \text{ M}$ .

Estimated atomic radius of gold = 140 pm

Number of gold atoms per 13 nm nanoparticle =  $(6.5 \times 10^{-9})^3 / (140 \times 10^{-12})^3 = 100,000$

(assuming that the particles are perfectly spherical).

Concentration of 13 nm gold nanoparticles =  $8.944 \times 10^{-4} \text{ M} / 100,000 = \underline{\mathbf{9 \text{ nM}}}$ .

### -1.2 Concentration of the 100 nm Gold Nanoparticles

During growth step one, 6 mL of the 13 nm gold nanoparticle seeds (9 nM) are diluted in 80 mL. Assuming no new seeds are formed, the concentration of the 25 nm particles formed = 0.7 nM.

In the second growth step 9 mL of the 25 nm gold nanoparticle seeds (0.7 nM) are diluted to 80 mL. Again, assuming no new seeds are formed, the concentration of the 50 nm particles formed = 80 pM.

In the final growth step, 40 mL of the 50 nm gold nanoparticles (80 pM) are diluted to 80 mL, rendering 100 nm gold nanoparticles at **40 pM**.

## Appendix 2: Nanoparticle Lumiphore-loading Calculations

Estimated atomic radius of gold = 140 pm

Number of gold atoms per 13 nm nanoparticle =  $(6.5 \times 10^{-9})^3 / (140 \times 10^{-12})^3 = 100,000$

Number of gold atoms per 100 nm gold nanoparticle =  $(50 \times 10^{-9})^3 / (140 \times 10^{-12})^3 = 46 \times 10^6$

### -2.1 Ru-T20•AuNP13

Au:Ru measured by ICPOES = 72:1 (atoms).

Assuming 100,000 gold atoms per 13 nm gold nanoparticle:

$72/100,000 = 7.2 \times 10^{-4}$  particles per Ru(II) complex

$1/7.2 \times 10^{-4} = \underline{\underline{1390 \text{ RuSH complexes per gold nanoparticle.}}}$

Surface area of the 13 nm gold nanoparticle =  $4\pi (6.5 \times 10^{-9})^2 = 5.31 \times 10^{-16} \text{ m}^2$  Surface area per **RuSH** complex =  $5.31 \times 10^{-16} / 1390 = 3.82 \times 10^{-19} \text{ m}^2$  (**0.6 nm × 0.6 nm**).

### -2.2 Ru-Z•AuNP13

Au:Ru measured by ICPOES = 63:1 (atoms).

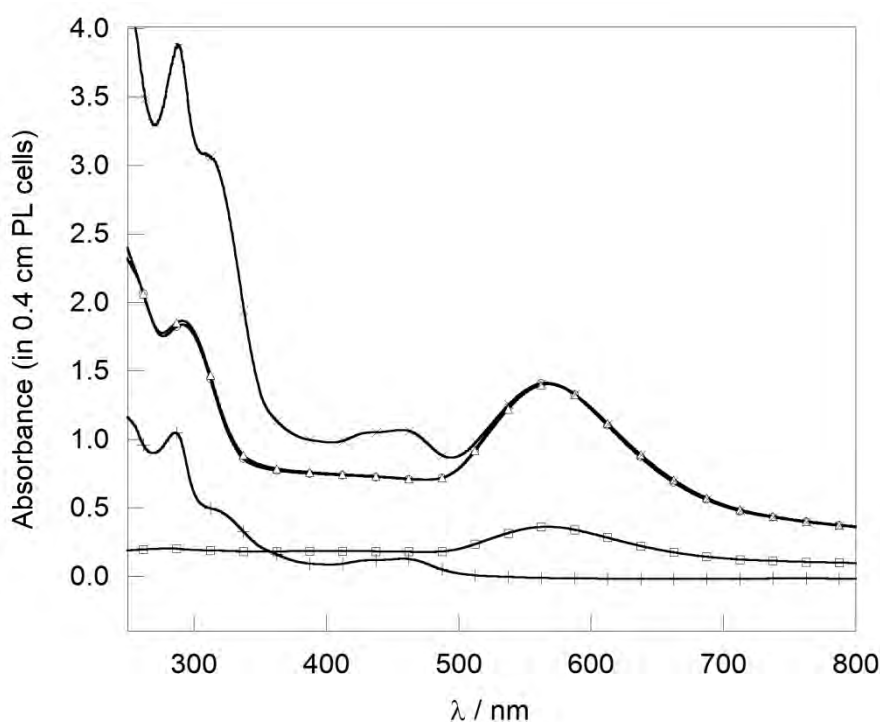
Assuming 100,000 gold atoms per 13 nm gold nanoparticle:

$63/100,000 = 6.3 \times 10^{-4}$  particles per Ru(II) complex

$1/6.3 \times 10^{-4} = \underline{\underline{1590 \text{ RuSH complexes per gold nanoparticle.}}}$

Surface area of the 13 nm gold nanoparticle =  $4\pi (6.5 \times 10^{-9})^2 = 5.31 \times 10^{-16} \text{ m}^2$  (assuming particle is spherical).

Surface area per **RuSH** complex =  $5.31 \times 10^{-16} / 1590 = 3.34 \times 10^{-19} \text{ m}^2$  (**0.6 nm × 0.6 nm**).

**-2.3 Ru-Z•AuNP100**

**Figure A1** UV-Vis absorption spectra of 100 nm gold nanoparticles in water (40 pM) (-o-), gold nanoparticles +fluorosurfactant ( $1.15 \mu\text{g mL}^{-1}$ , ca. 1 mM) (-Δ-), gold nanoparticles (40 pM) +fluorosurfactant ( $1.15 + \mu\text{g mL}^{-1}$ ) +**RuSH** (40  $\mu\text{M}$ ) (-x-), 40 pM centrifuged **Ru-ZAu100NP**(-□-), supernatant from first wash of **Ru-ZAu100NP** (-+-).

Concentration of **RuSH**, left on the nanoparticles, estimated from absorbance at 460 nm:

Abs (460) by the 40  $\mu\text{M}$  **RuSH** in the uncentrifuged sample = Abs (460) of (-x-) – abs (460) of (-o-), =  $1.06 - 0.705 = 0.355$ . Abs (460) in the supernatant of first wash = 0.317.

Concentration of **RuSH** in the supernatant =  $0.317 / 0.355 \times 40 \mu\text{M} = 35.7 \mu\text{M}$ .

Concentration of **RuSH** on the nanoparticles =  $40 - 35.7 \mu\text{M} = 4.3 \mu\text{M}$ .

This assumes that the Beer-Lambert law applies, assuming that all **RuSH** complexes on each nanoparticles have the same absorbance.

Ratio of **RuSH** complexes : 100 nm gold nanoparticles =  $4.3 \mu\text{M} / 40 \text{ pM} = \underline{\underline{107,500}}$ .

Surface area of **AuNP100** =  $4\pi (50 \times 10^{-9})^2 = 3.14 \times 10^{-14} \text{ m}^2$  (assuming particles are spherical).

Surface area per complex =  $3.14 \times 10^{-14} / 107500 = 2.92 \times 10^{-19} \text{ m}^2$ . (**0.5 nm × 0.5 nm**).

### -2.4 Ru-pHLIP•AuNP13

Au:Ru measured by ICPOES = 48:1 (atoms). Assuming 100,000 gold atoms per 13 nm gold nanoparticle:  $48/100,000 = 4.8 \times 10^{-4}$  particles per Ru(II) complex.

$1/4.8 \times 10^{-4} = \underline{\underline{2080 \text{ RuSH complexes per gold nanoparticle.}}}$

Surface area of the 13 nm gold nanoparticle =  $4\pi (6.5 \times 10^{-9})^2 = 5.31 \times 10^{-16} \text{ m}^2$  (assuming particle is spherical).

Surface area per **RuSH** complex =  $5.31 \times 10^{-16} / 2080 = 2.55 \times 10^{-19} \text{ m}^2$  (**0.5 nm × 0.5 nm**).

### -2.5 IrBpy-Z•AuNP13

Au:Ir measured by ICPOES = 106:1 (atoms). Assuming 100,000 gold atoms per 13 nm gold nanoparticle:  $106/100,000 = 1.06 \times 10^{-3}$  particles per Ir(III) complex.

$1/1.06 \times 10^{-3} = \underline{\underline{940 \text{ IrBpySH complexes per gold nanoparticle.}}}$

Surface area of the 13 nm gold nanoparticle =  $4\pi (6.5 \times 10^{-9})^2 = 5.31 \times 10^{-16} \text{ m}^2$  (assuming particle is spherical).

Surface area per **IrBpySH** complex =  $5.31 \times 10^{-16} / 940 = 5.65 \times 10^{-19} \text{ m}^2$  (**0.8 nm × 0.8 nm**).

### -2.6 IrBpy-Z•AuNP100

Au:Ir measured by ICPOES = 1974:1 (atoms). Assuming  $46 \times 10^6$  gold atoms per 100 nm gold nanoparticle:  $2000/46 \times 10^6 = 4.35 \times 10^{-5}$  particles per Ir(III) complex

$1/4.35 \times 10^{-5} = \underline{\underline{23,000 \text{ IrBpySH complexes per gold nanoparticle.}}}$

Surface area of the 100 nm gold nanoparticle =  $4\pi (50 \times 10^{-9})^2 = 3.14 \times 10^{-14} \text{ m}^2$ .

Surface area per **RuSH** complex =  $3.14 \times 10^{-14} / 23,000 = 1.37 \times 10^{-20} \text{ m}^2$  (**1 nm × 1 nm**).

**-2.7 GdQ•AuNP13**

Au:Gd measured by ICPOES = 98:1 (atoms). Assuming 100,000 gold atoms per 13 nm gold nanoparticle:  $98/100,000 = 9.8 \times 10^{-4}$  particles per Gd(III) complex

$1/9.8 \times 10^{-4} = \underline{\underline{1020 \text{ GdQSH complexes per gold nanoparticle.}}}$

Surface area of the 13 nm gold nanoparticle =  $4\pi (6.5 \times 10^{-9})^2 = 5.31 \times 10^{-16} \text{ m}^2$  (assuming particle is spherical).

Surface area per **GdQSH** complex =  $5.31 \times 10^{-16} / 1020 = 5.21 \times 10^{-19} \text{ m}^2$  (**0.7 nm × 0.7 nm**).

**-2.8 IrBpy-GdQ•AuNP13**

73:1 Gd (1300), 300:1 Ir (330)

Au:Gd measured by ICPOES = 73:1 (atoms).

Assuming 100,000 gold atoms per 13 nm gold nanoparticle:  $73/100,000 = 7.3 \times 10^{-4}$  particles per Gd(III) complex

$1/7.3 \times 10^{-4} = \underline{\underline{1370 \text{ GdQSH complexes per gold nanoparticle.}}}$

Au:Ir measured by ICPOES = 300:1 (atoms).

Assuming 100,000 gold atoms per 13 nm gold nanoparticle:

$300/100,000 = 3.0 \times 10^{-3}$  particles per Ir(III) complex

$1/3.0 \times 10^{-3} = \underline{\underline{330 \text{ IrBpySH complexes per gold nanoparticle.}}}$

### Appendix 3: Size-exclusion Chromatography Study with Zonyl® 7950

The following samples (Table A1) were loaded onto a size-exclusion column, using Sephadex® G-25, and the elution volumes and elution times were observed.

Column = 3 cm in diameter, and 8 cm in length; 60 mL in total volume

The dead space in the column (according to Sephadex®-G25 superfine high-trap column manual) =  $60 \times 1.5/5 = 18$  mL

Thus, the nanoparticles should elute in **18 mL**.

Fractioning range of Sephadex®-G25 = 1000-5000, i.e. anything in this range should interact with the beads and be retarded.

**Table A1** Elution times and volumes using Sephadex® G-25 Column Chromatography.

Sample	Elution volume / mL	Elution time / min	Sample in void volume of column?
<b>RuSAc</b> <sup>a</sup>	>210	> 20	NO – sample stuck to the sephadex
<b>RuSAc+ Zonyl® 7950</b> <sup>b</sup>	10–17	1.5–2.5	YES
<b>Z•Au13</b>	10–15	1.5–3.0	YES
<b>Ru-Z•AuNP13</b>	10–15	1.5–2.5	YES

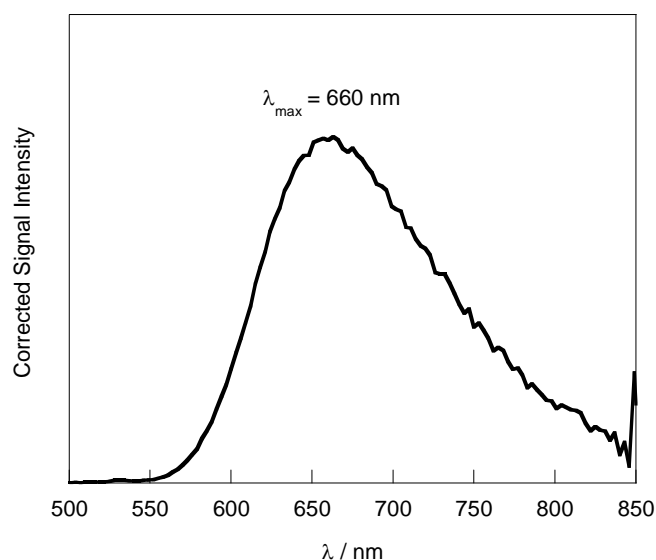
<sup>a</sup> dissolved in 1% CH<sub>3</sub>CN, H<sub>2</sub>O.  
<sup>b</sup> dissolved in 1% CH<sub>3</sub>CN, H<sub>2</sub>O, with 1 mM Zonyl® 7950.

The fluorosurfactant transports the unbound **RuSAc** complex through the void volume of the stationary phase with the functionalised nanoparticles, presumably due to the formation of micelles, and thus separation of the particles from unbound material does not occur.



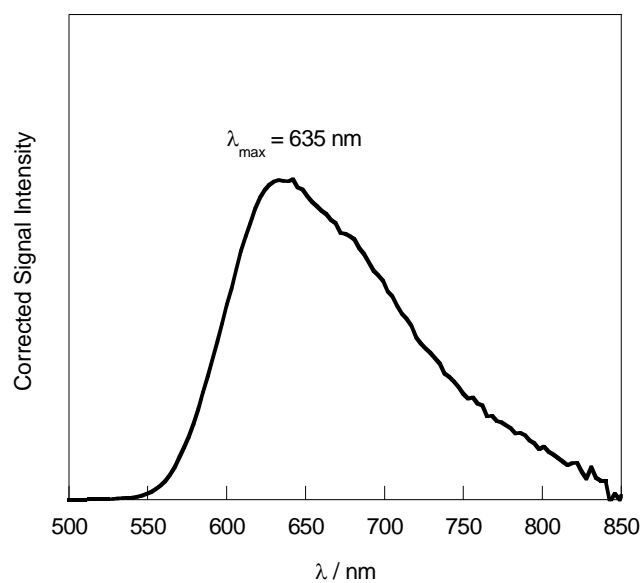
## Appendix 5: Control Steady-state Luminescence Spectra of the RuSAC Complex

### -5.1 Aqueous Emission of RuSAC, in the presence of TWEEN® 20 Surfactant



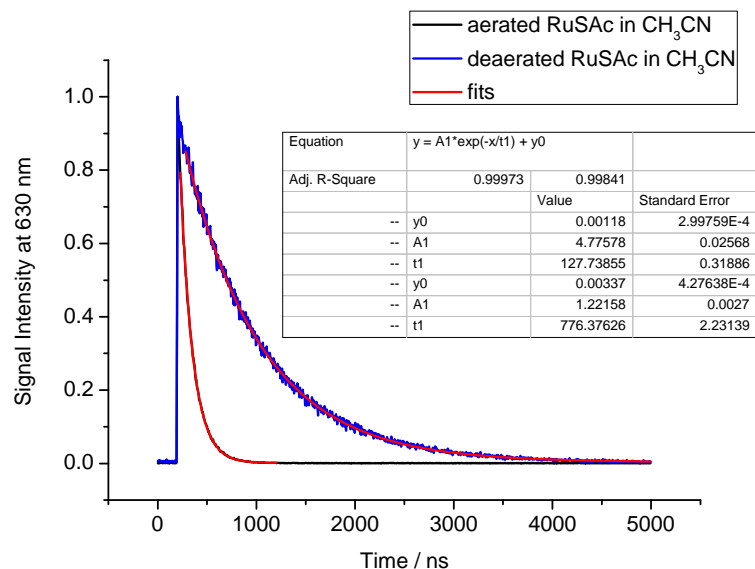
**Figure A3** Steady-state luminescence spectrum of  $9 \mu\text{M}$  RuSAC, with  $1 \text{ mM}$  TWEEN® 20 in  $1\%$   $\text{CH}_3\text{CN}/\text{H}_2\text{O}$ . Spectrum corrected for instrument response.

### -5.2 Aqueous Emission of RuSAC, in the presence of Zonyl® 7950 Surfactant

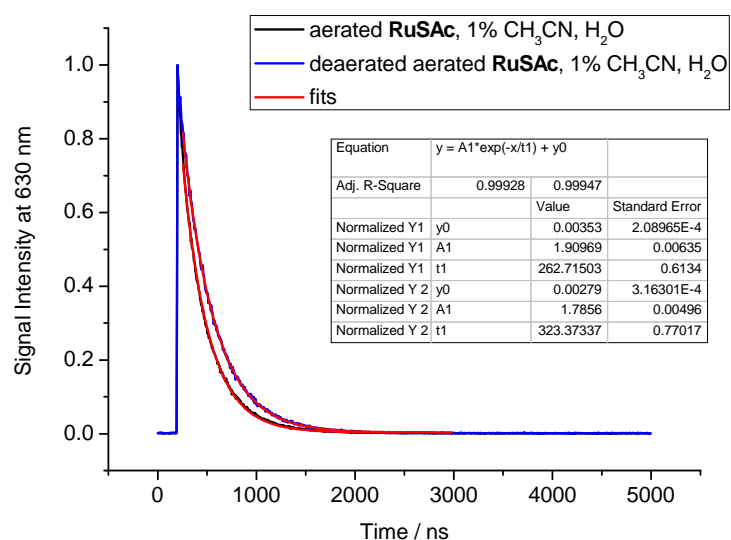


**Figure A4** Steady-state luminescence spectrum of  $9 \mu\text{M}$  RuSAC, with  $1 \text{ mM}$  Zonyl® 7950 in  $1\%$   $\text{CH}_3\text{CN}/\text{H}_2\text{O}$ . Spectrum corrected for instrument response.

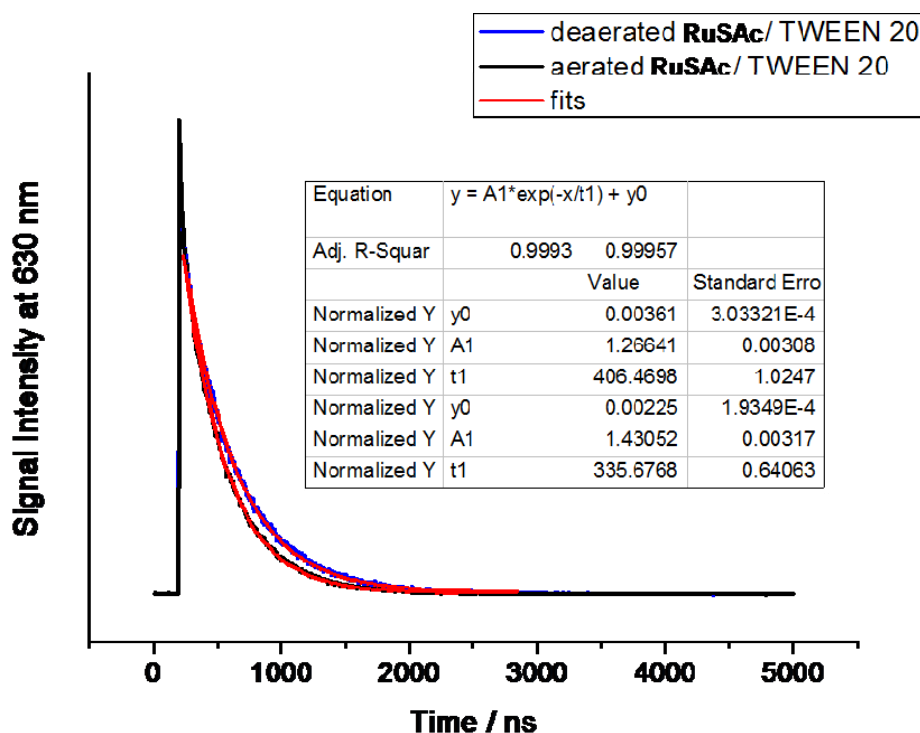
## Appendix 6: Luminescence Lifetimes of the RuSAC Complex and Ru(II)-functionalised Nanoparticles



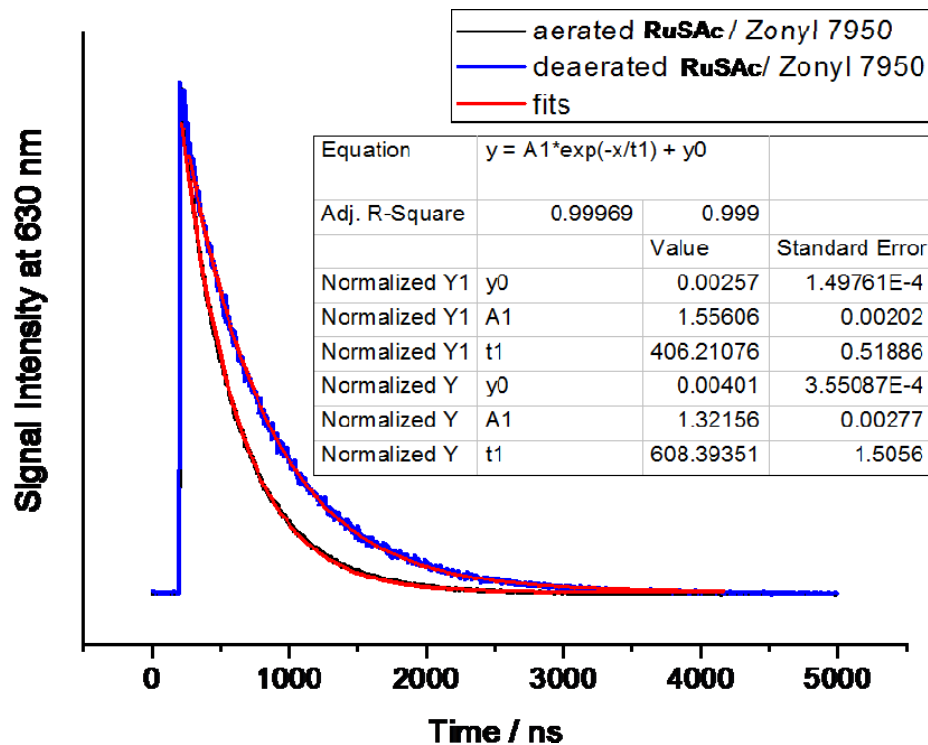
**Figure A5** Luminescence lifetime data of aerated (black) and deaerated (blue) RuSAC measured in  $\text{CH}_3\text{CN}$  solution,  $\lambda_{exc} = 445 \text{ nm}$ ,  $\lambda_{em} = 630 \text{ nm}$ . Monoexponential fits shown in red.



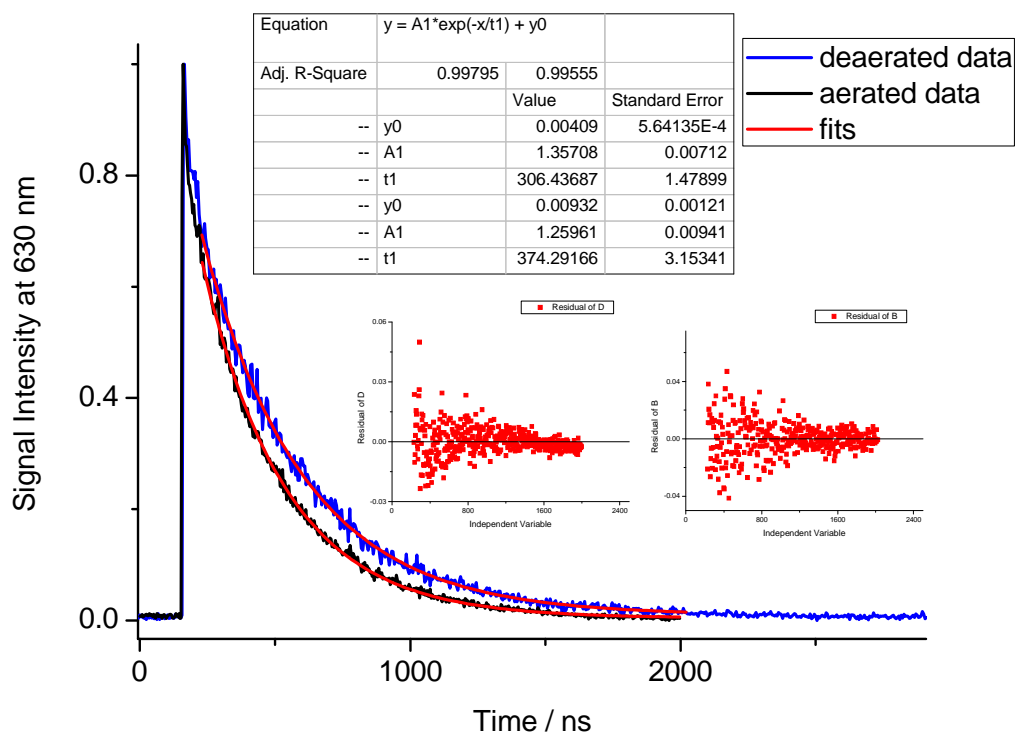
**Figure A6** Luminescence lifetime data of aerated (black) and deaerated (blue) RuSAC measured in 1%  $\text{CH}_3\text{CN}$ ,  $\text{H}_2\text{O}$  (predominantly aqueous solution),  $\lambda_{exc} = 445 \text{ nm}$ ,  $\lambda_{em} = 630 \text{ nm}$ . Monoexponential fits shown in red.



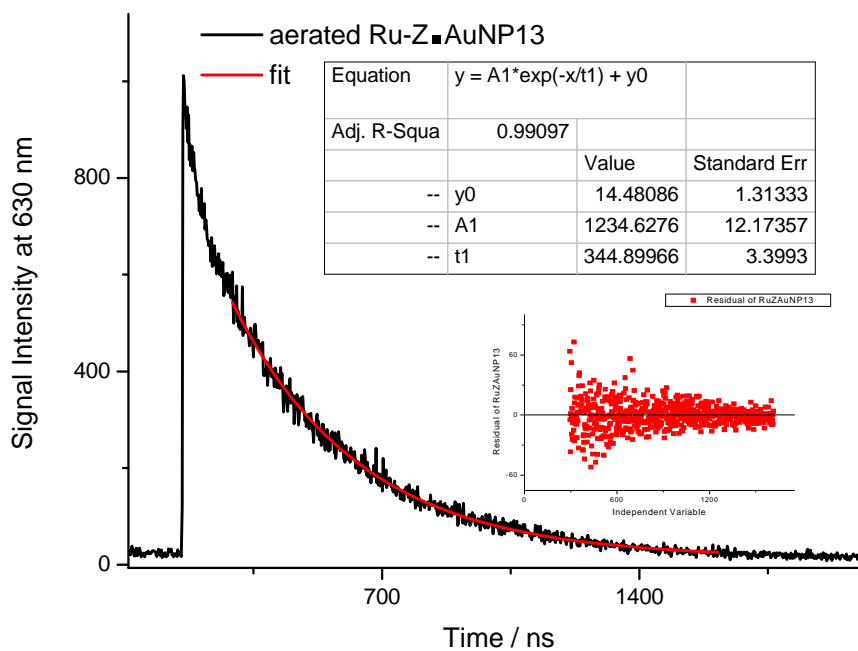
**Figure A7** Luminescence lifetime data of degassed (blue) and aerated (black) 9  $\mu\text{M}$  RuSAc, with 1 mM TWEEN® 20 in 1%  $\text{CH}_3\text{CN}/\text{H}_2\text{O}$ .  $\lambda_{\text{exc}} = 445 \text{ nm}$ ,  $\lambda_{\text{em}} = 630 \text{ nm}$ . Monoexponential fits shown in red.



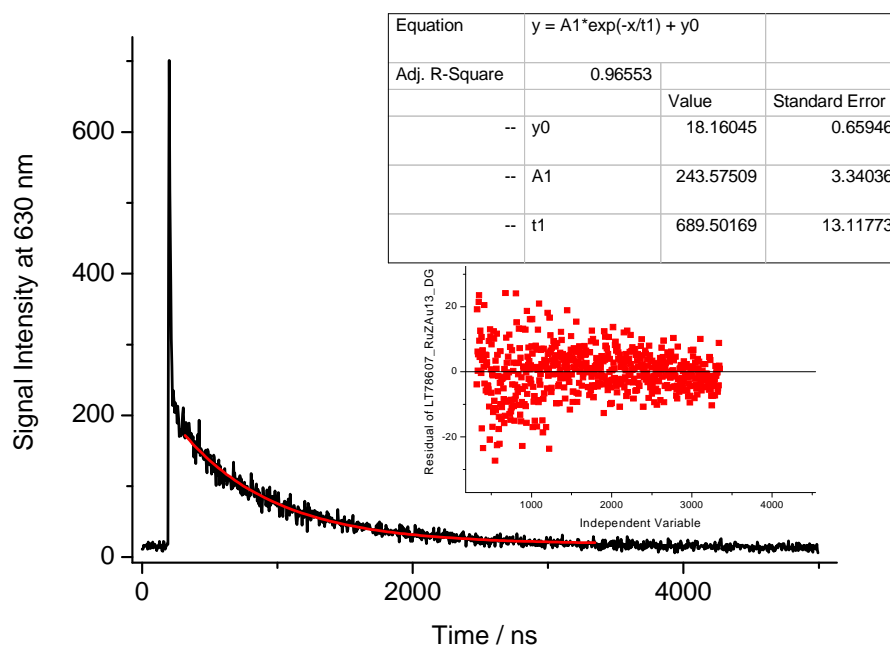
**Figure A8** Luminescence lifetime data of degassed (blue) and aerated (black) 9  $\mu\text{M}$  RuSAc, with 1 mM Zonyl® 7950 in 1%  $\text{CH}_3\text{CN}/\text{H}_2\text{O}$ .  $\lambda_{\text{exc}} = 445 \text{ nm}$ ,  $\lambda_{\text{em}} = 630 \text{ nm}$ . Monoexponential fits shown in red.



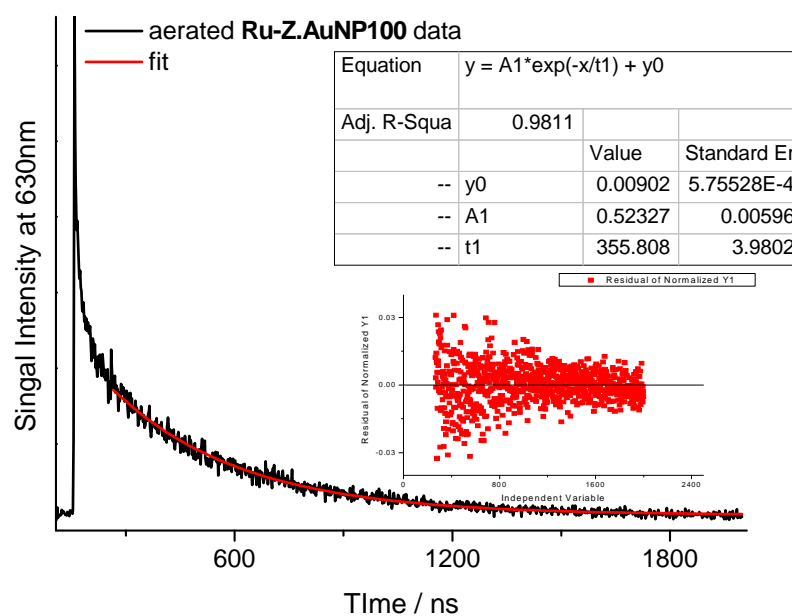
**Figure A9** Luminescence lifetime data of aerated (black) and deaerated (blue) **Ru-T20•AuNP13** (0.3 nM) in water,  $\lambda_{exc} = 445$  nm,  $\lambda_{em} = 630$  nm. Monoexponential fits shown in red. Residuals shown in insets.



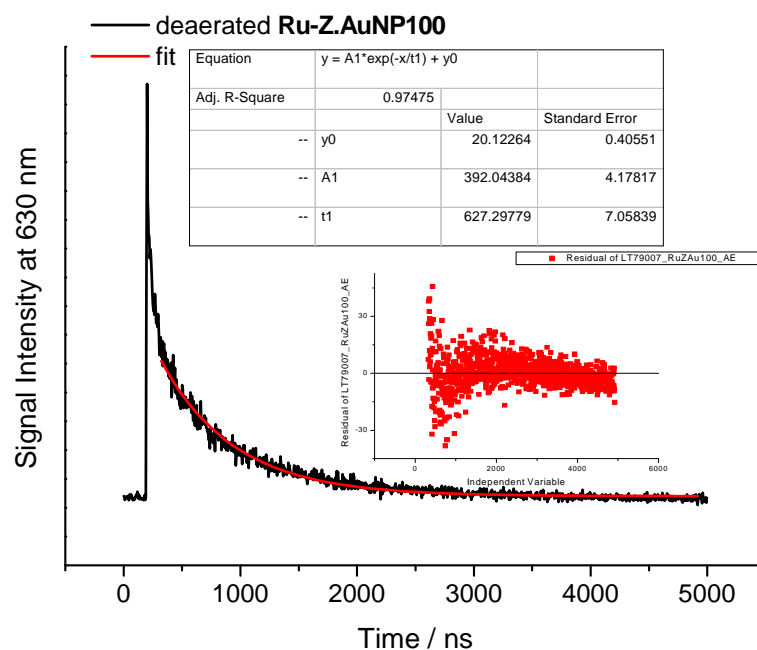
**Figure A10** Luminescence lifetime data of aerated **Ru-Z•AuNP13** (1 nM) in water,  $\lambda_{exc} = 445$  nm,  $\lambda_{em} = 630$  nm. Monoexponential fit shown in red. Residual shown in inset.



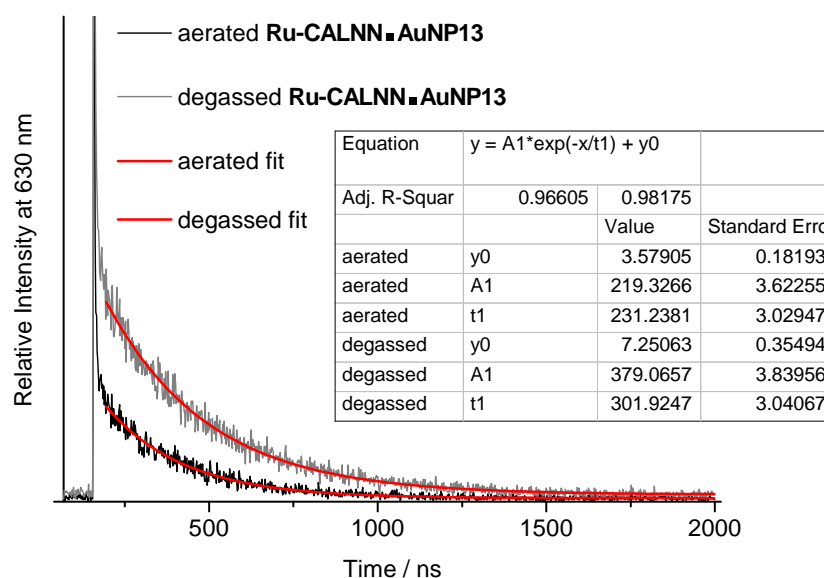
**Figure A11** Luminescence lifetime data of degassed **Ru-Z•AuNP13** (1 nM) in water,  $\lambda_{exc} = 445$  nm,  $\lambda_{em} = 630$  nm. Monoexponential fit shown in red. Residual shown in inset.



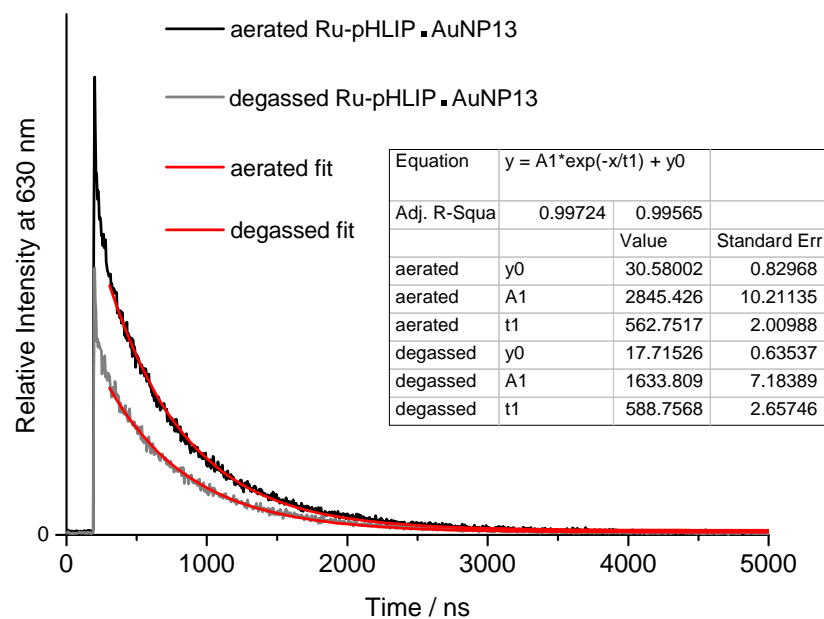
**Figure A12** Luminescence lifetime data of aerated **Ru-Z•AuNP100** (10 pM) in water,  $\lambda_{exc} = 445$  nm,  $\lambda_{em} = 630$  nm. Monoexponential fit shown in red. Residual shown in inset.



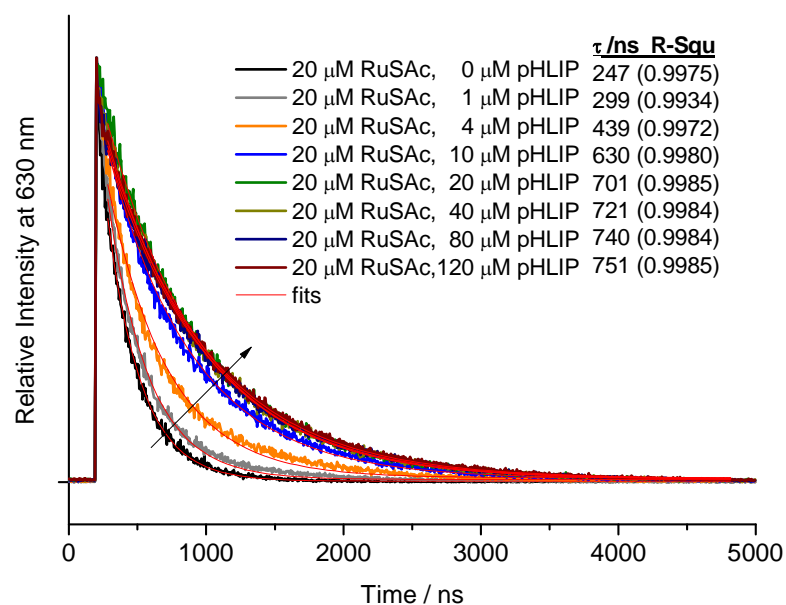
**Figure A13** Luminescence lifetime data of deaerated **Ru-Z•AuNP100** (10 pM) in water,  $\lambda_{exc} = 445$  nm,  $\lambda_{em} = 630$  nm. Monoexponential fit shown in red. Residual shown in inset.



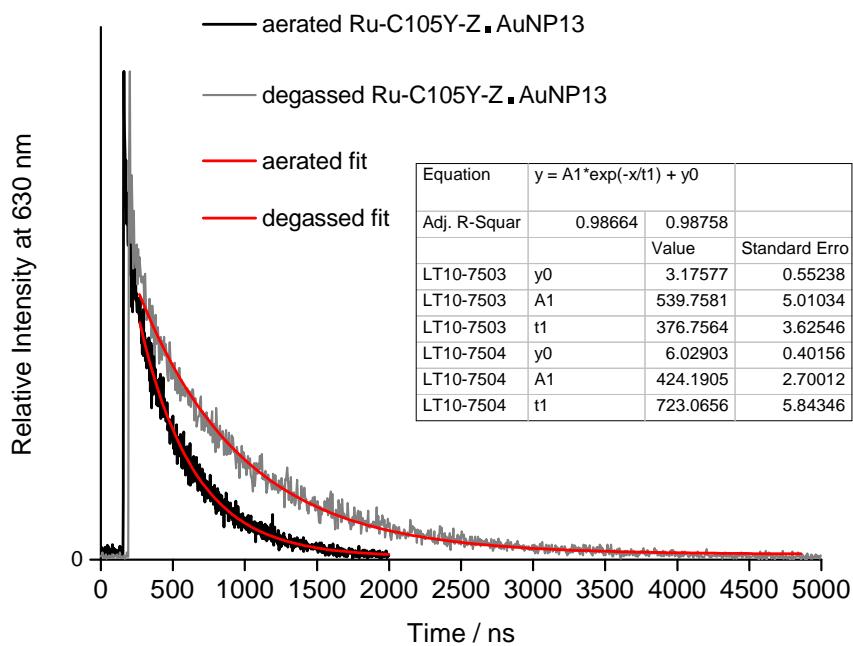
**Figure A14** Luminescence lifetime data of aerated (black) and deaerated (grey) **Ru-CALNN•AuNP13** (1 nM) in water,  $\lambda_{exc} = 445$  nm,  $\lambda_{em} = 630$  nm. Monoexponential fits shown in red.



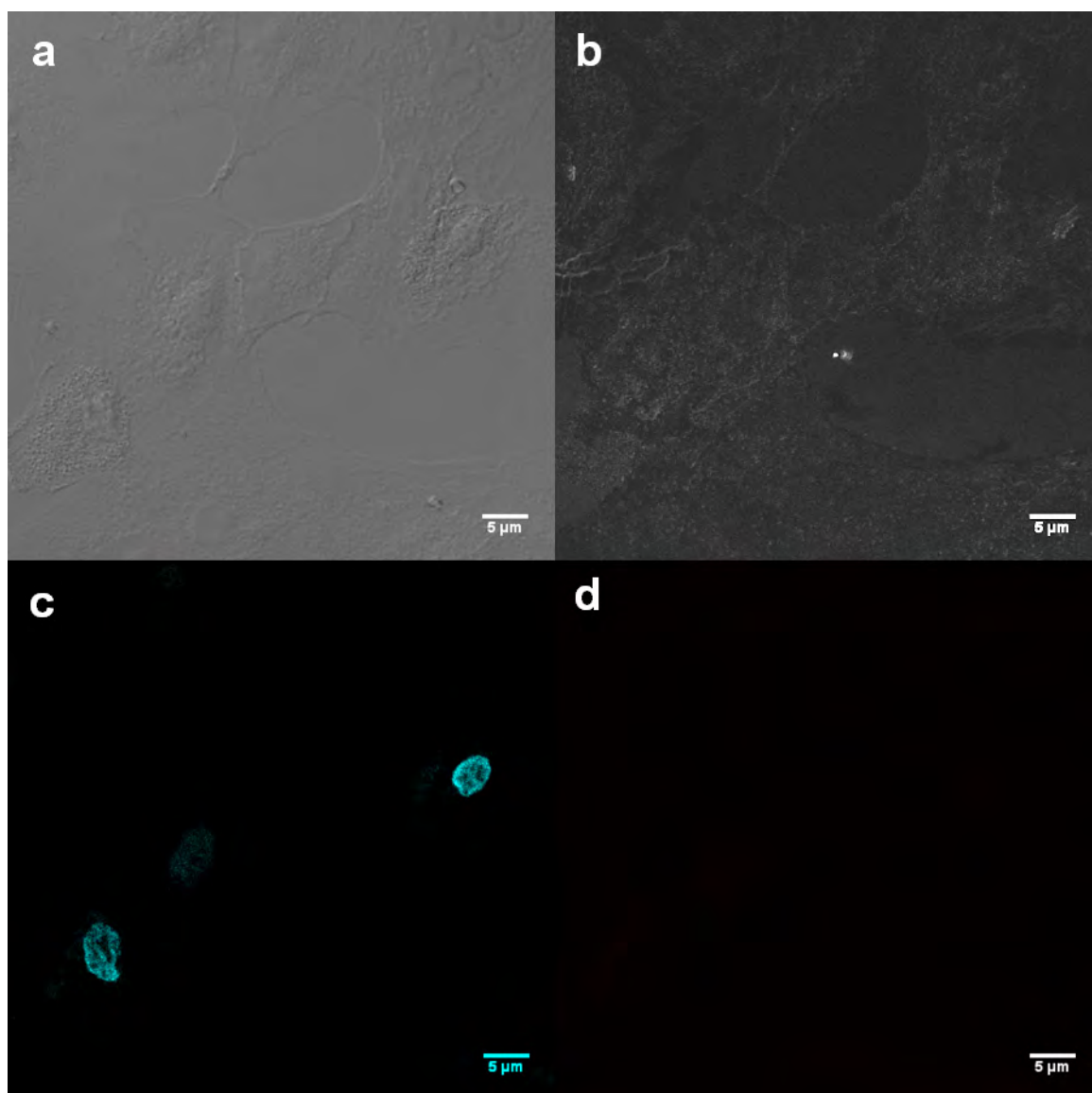
**Figure A15** Luminescence lifetime data of aerated (black) and deaerated (grey) **Ru-pHLIP•AuNP13** (1 nM) in water,  $\lambda_{exc} = 445$  nm,  $\lambda_{em} = 630$  nm. Monoexponential fits shown in red.



**Figure A16** Luminescence lifetimes of pHLIP (1–120 mM) titrated into **RuSAC** (20 mM), in 1%  $CH_3CN$ ,  $H_2O$ .  $\lambda_{exc} = 445$  nm,  $\lambda_{em} = 630$  nm. Monoexponential fits shown in red.

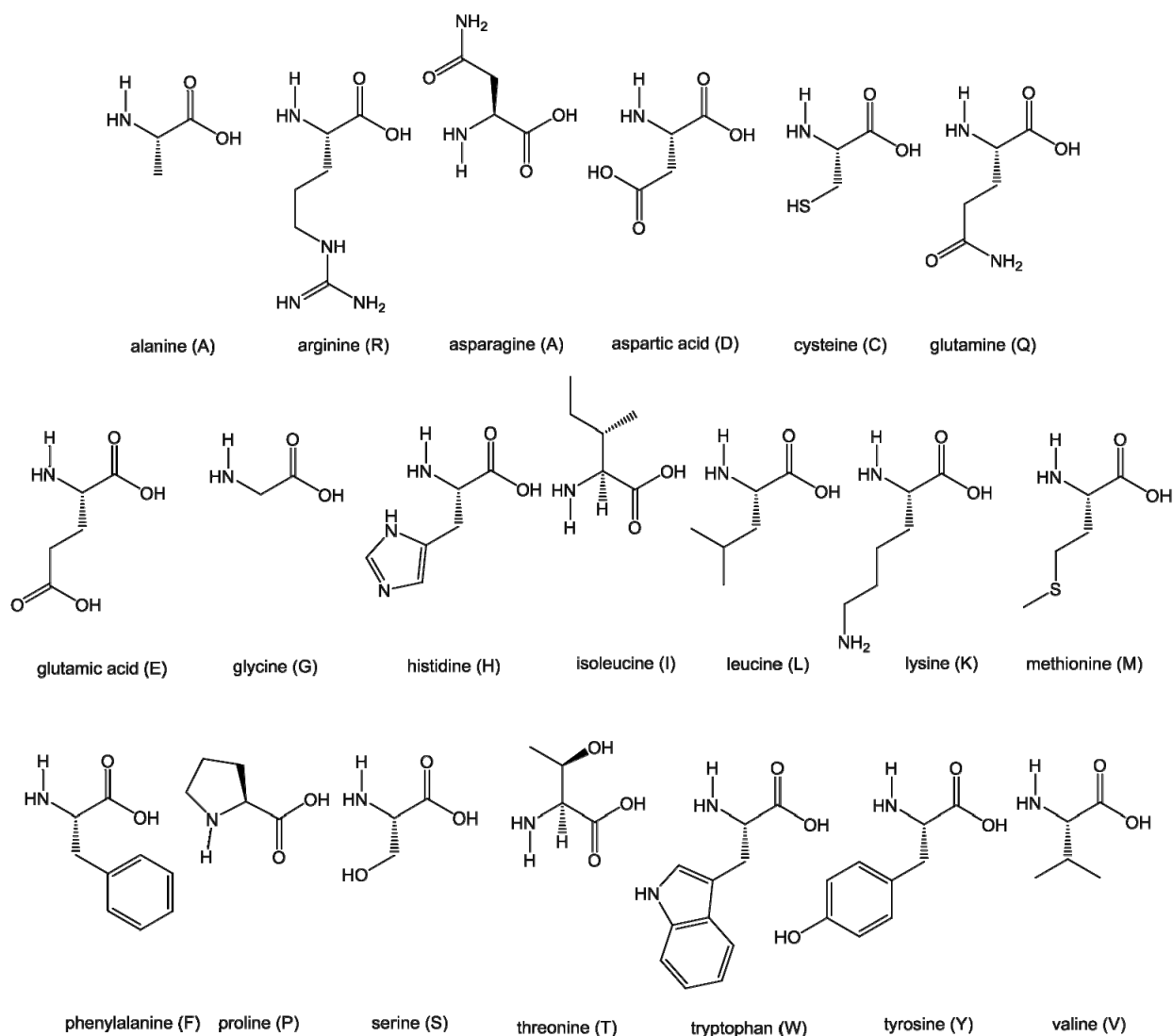


**Figure A17** Luminescence lifetime data of aerated (black) and deaerated (grey) *Ru-C105Y-Z•AuNP13* (1 nM) in water,  $\lambda_{exc} = 445$  nm,  $\lambda_{em} = 630$  nm. Monoexponential fits shown in red.

**Appendix 7: Confocal Microscopy of Undosed Control A549 Cells**

**Figure A18** Confocal Micrographs of control A549 cells incubated without nanoparticles, and stained with Hoechst 33258 in (a) the transmission micrograph ( $\lambda_{exc} = 488 \text{ nm}$ ), (b) confocal reflectance ( $\lambda_{exc} = 488 \text{ nm}$ ,  $\lambda_{em} = 478\text{--}498 \text{ nm}$ ), (c) the blue channel (nuclear stain) ( $\lambda_{exc} = 405 \text{ nm}$ ,  $\lambda_{em} = 410\text{--}455 \text{ nm}$ ) and (d) the red channel ( $\lambda_{exc} = 453 \text{ nm}$ ,  $\lambda_{em} = 550\text{--}800 \text{ nm}$ ).

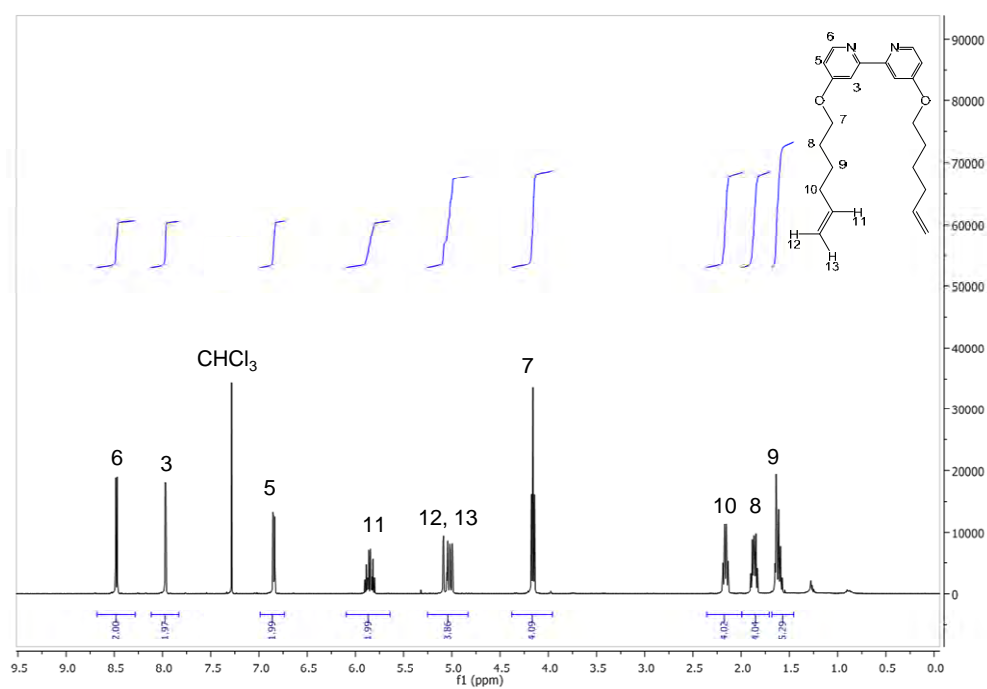
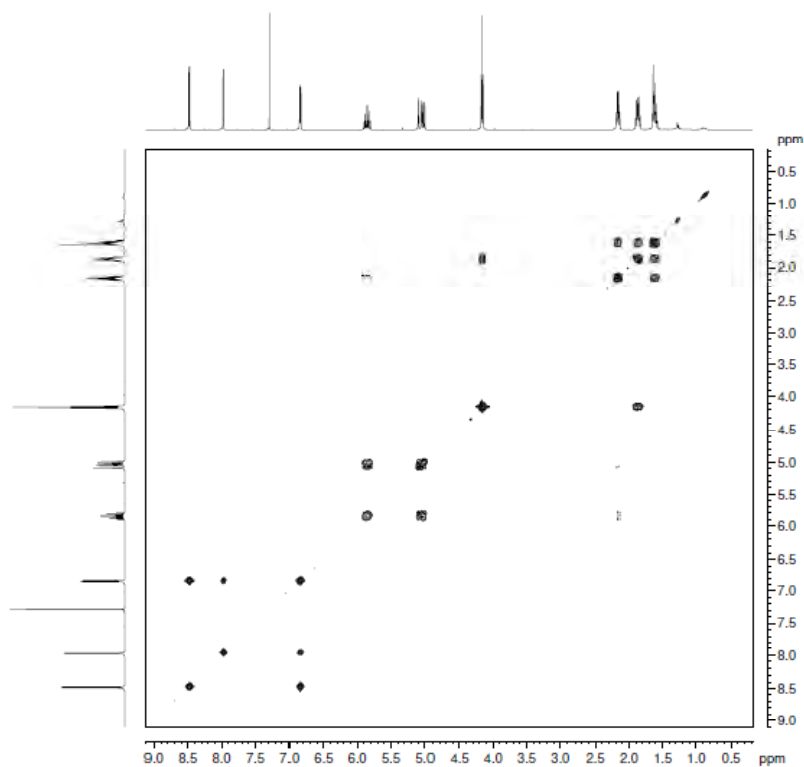
## Appendix 8: Structures and Abbreviations of Amino Acids



**Figure A19** Structures and abbreviations of amino acids discussed in chapter Four.

## Appendix 9: Data for Synthesis of Ru(II) and Ir(III) Compounds

## -9.1 NMR and FT-IR of Spectra BpyHex Ligand

Figure A20  $^1\text{H}$  NMR spectrum of *BpyHex* in  $\text{CDCl}_3$ .Figure A21  $^1\text{H}$ - $^1\text{H}$  COSY NMR spectrum of *BpyHex* ligand, in  $\text{CDCl}_3$ .

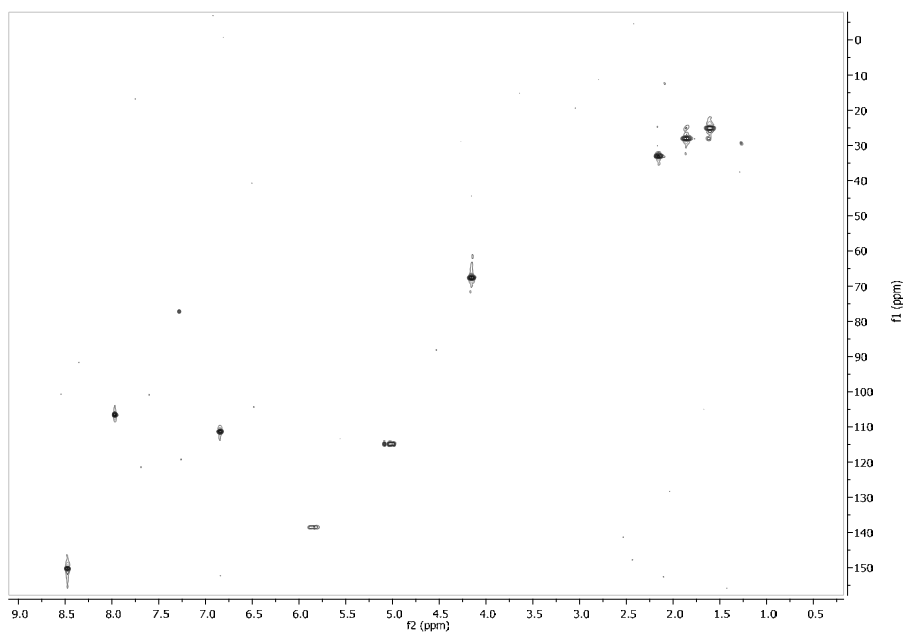


Figure A22  $^1\text{H}$ ,  $^{13}\text{C}$ -HSQC NMR spectrum of *BpyHex* ligand, in  $\text{CDCl}_3$ .

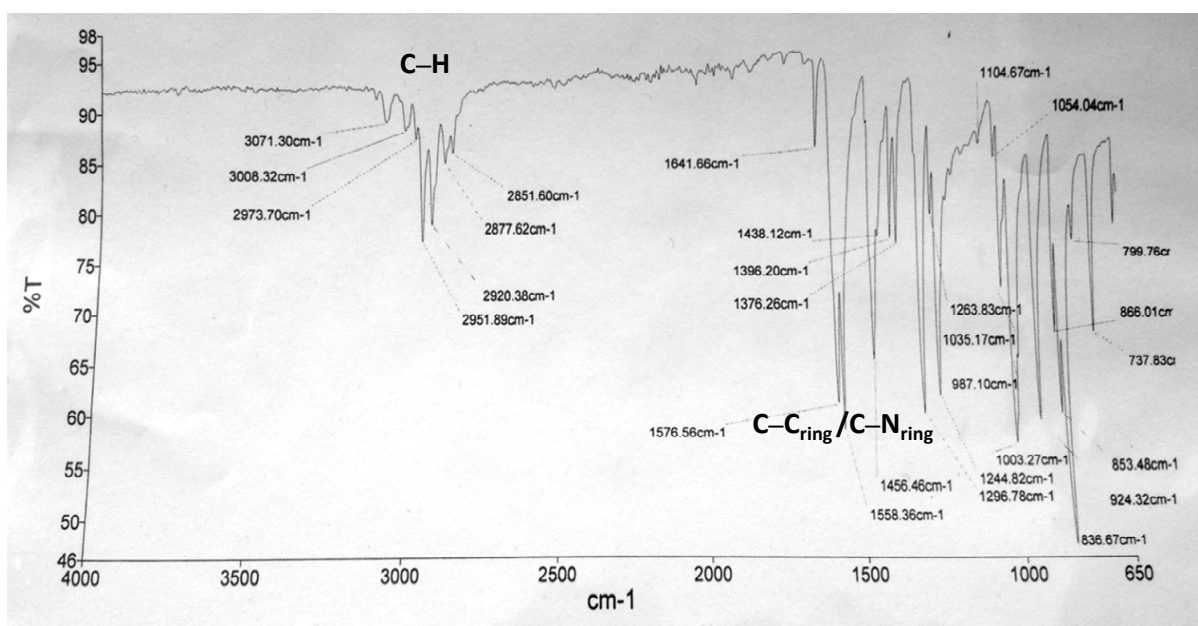
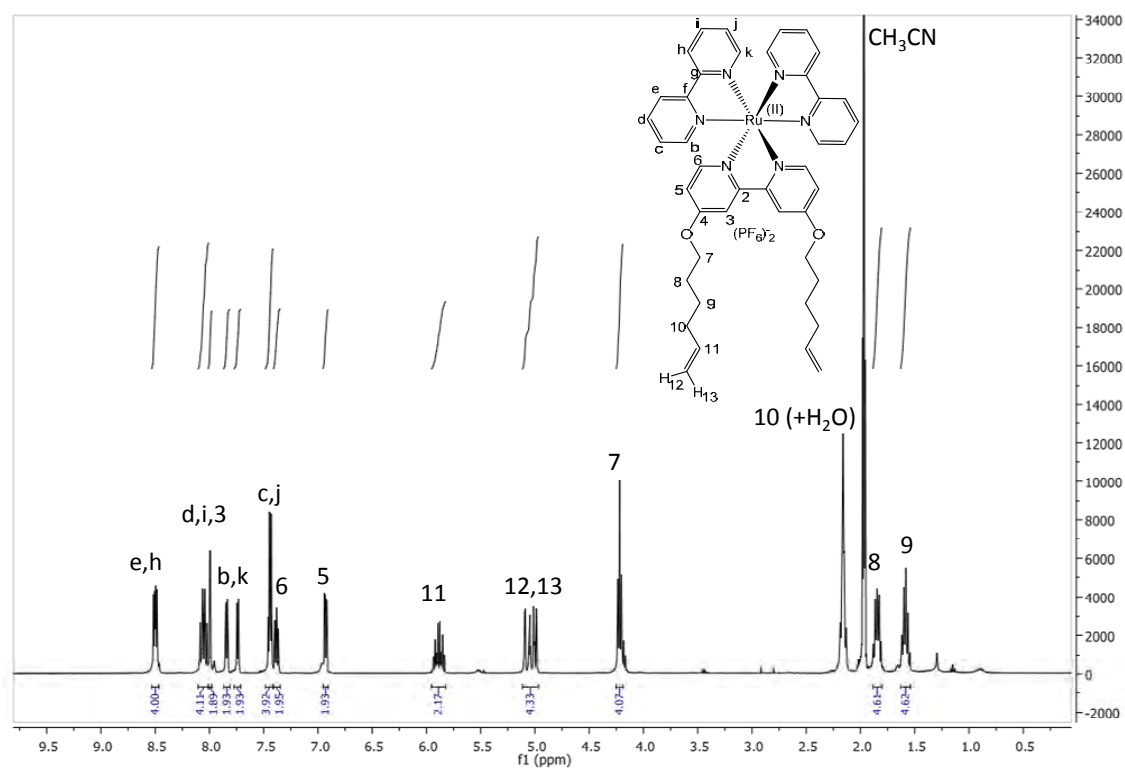
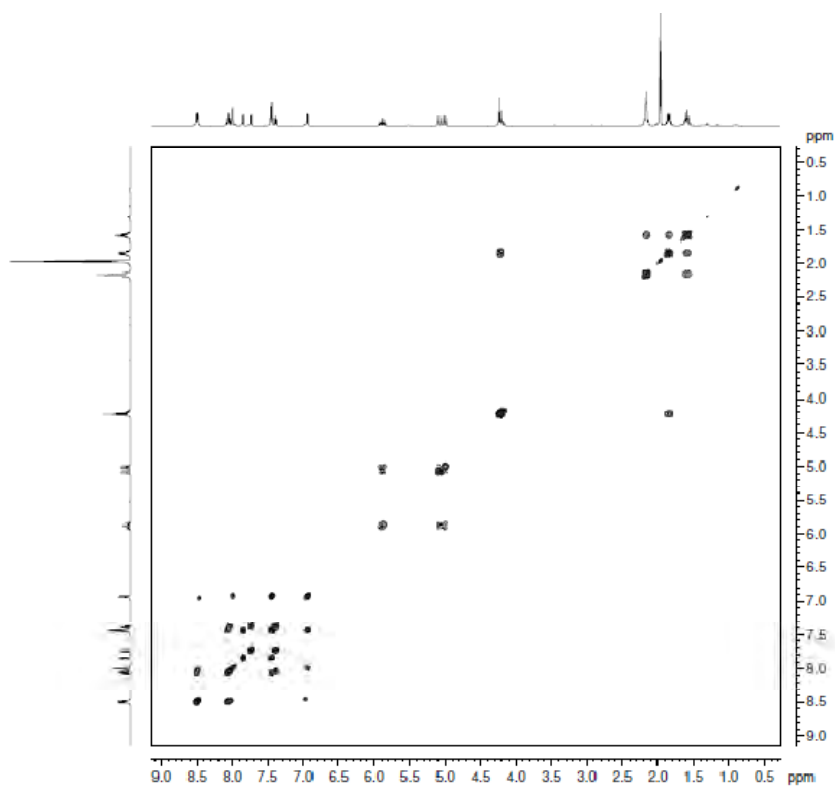


Figure A23 FT-IR spectrum of *BpyHex* solid powder.

**-9.2 NMR and FT-IR Spectra of RuHex****Figure A24**  $^1\text{H}$  NMR spectrum of **RuHex** in  $\text{CD}_3\text{CN}$ .**Figure A25**  $^1\text{H}$ - $^1\text{H}$  COSY NMR spectrum of **RuHex**, in  $\text{CD}_3\text{CN}$ .

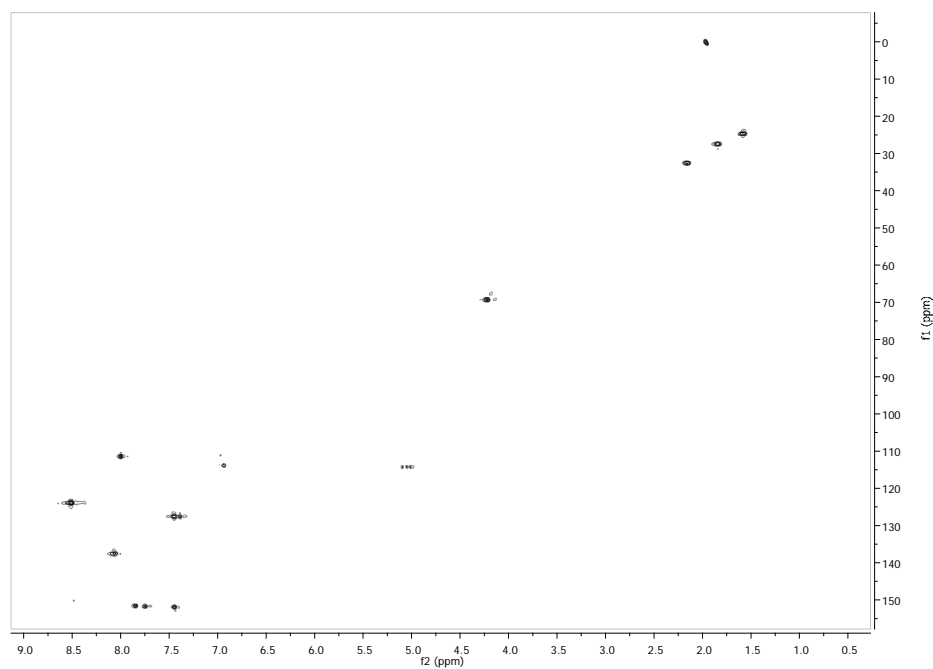


Figure A26  $^1\text{H}$ ,  $^{13}\text{C}$ -HSQC NMR spectrum of **RuHex**, in  $\text{CD}_3\text{CN}$ .

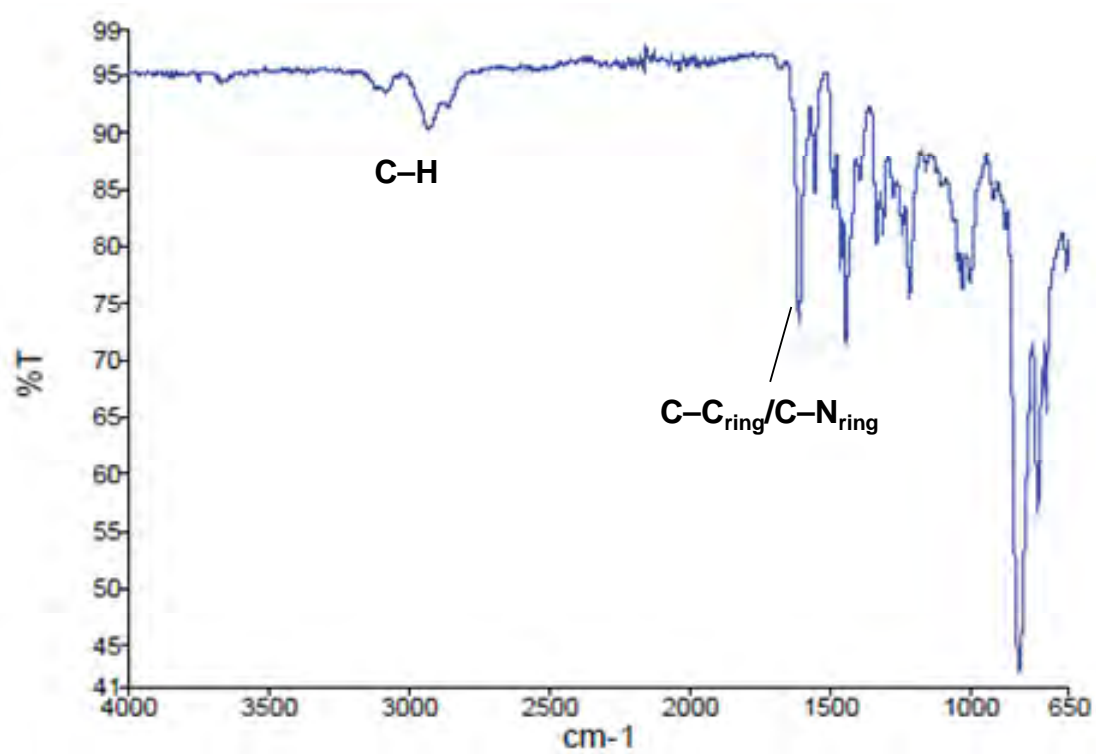
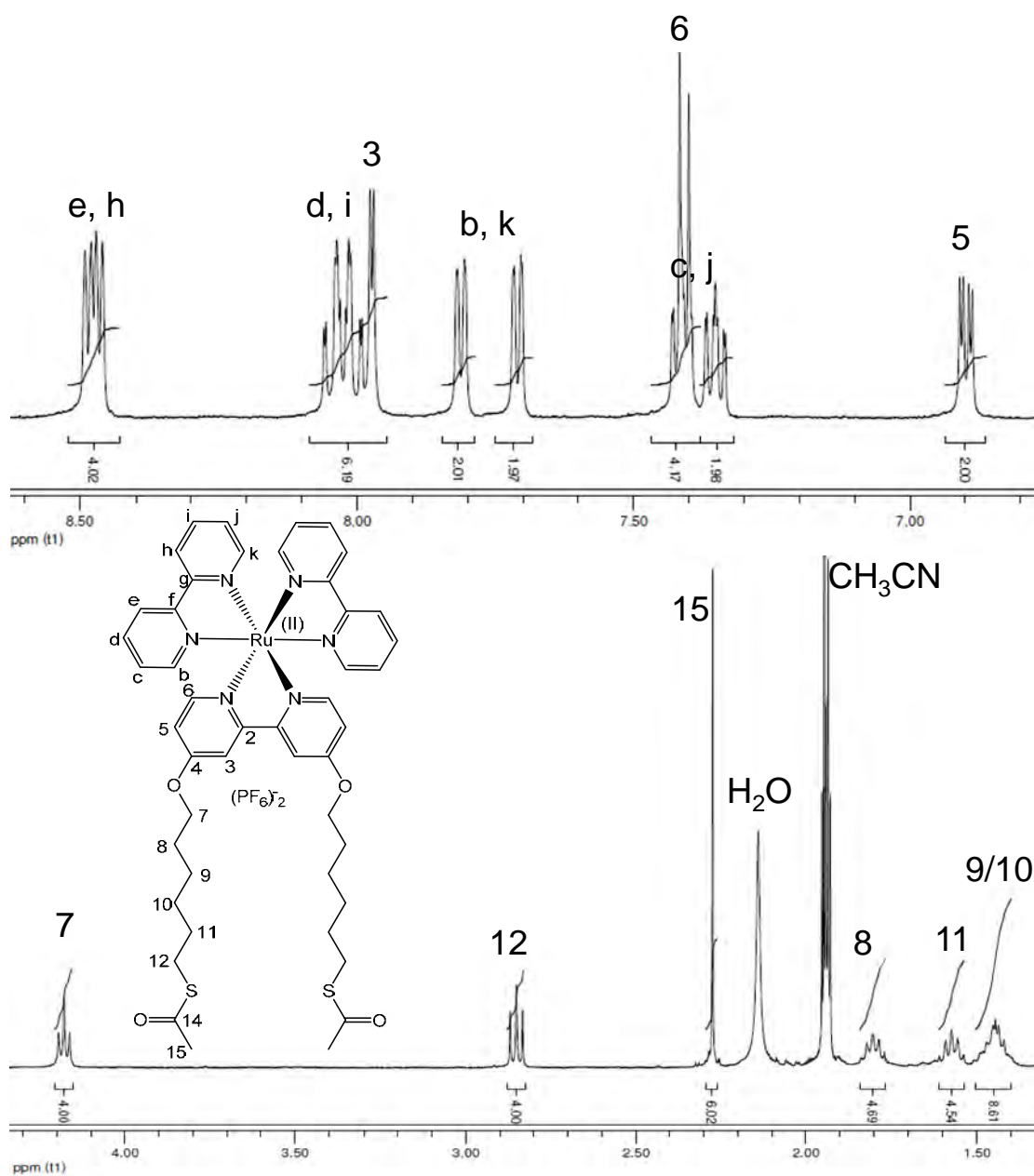
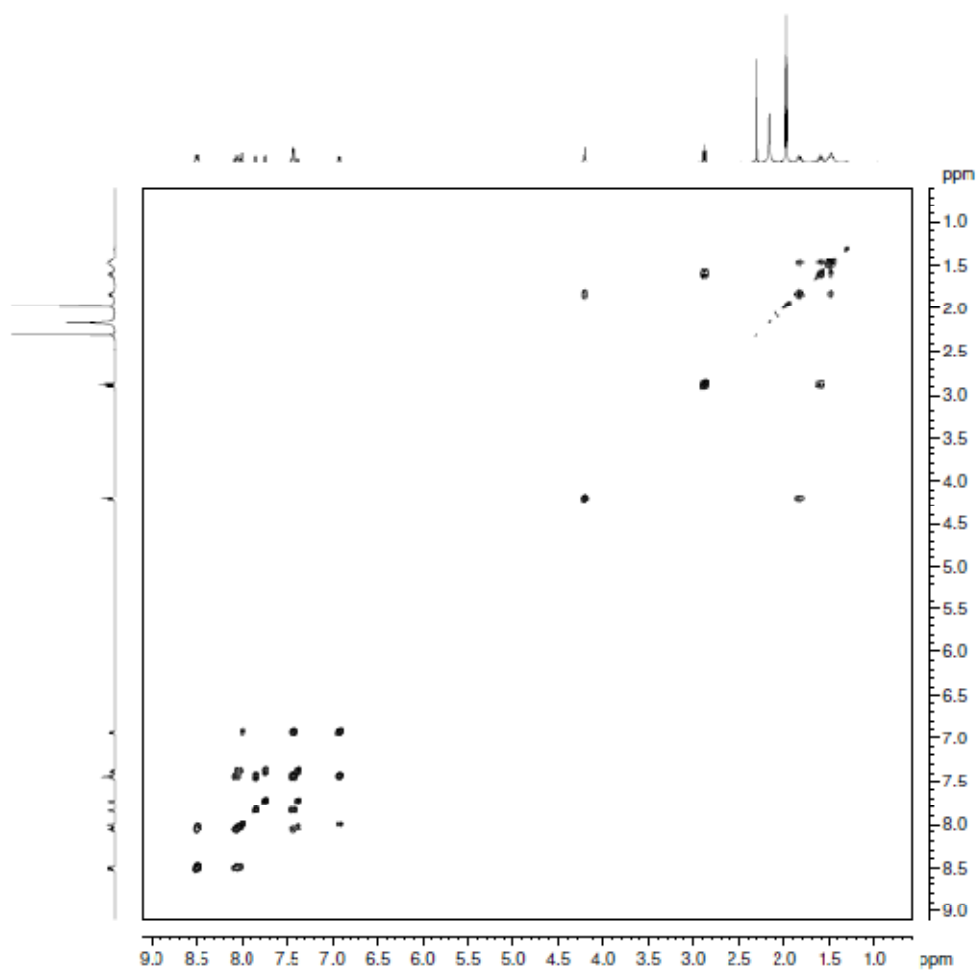
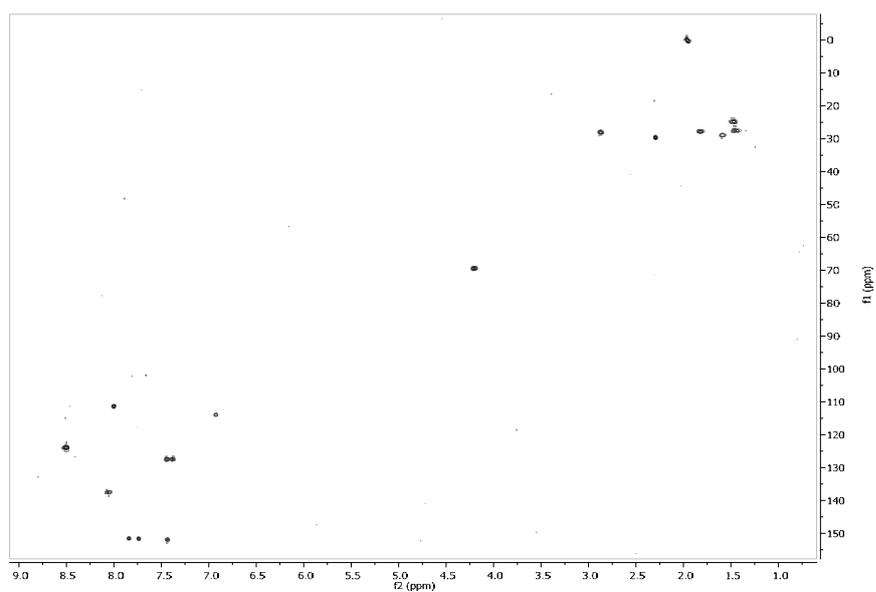


Figure A27 FT-IR spectrum of **RuHex** solid powder.

**-9.3 NMR and FT-IR Spectra of RuSAC****Figure A28**  $^1\text{H}$  NMR spectrum of RuSAC in  $\text{CD}_3\text{CN}$ .



**Figure A29**  $^1\text{H}$ - $^1\text{H}$  COSY NMR spectrum of *RuSAc*, in  $\text{CD}_3\text{CN}$ .



**Figure A30**  $^1\text{H}$ ,  $^{13}\text{C}$ -HSQC NMR spectrum of *RuSAc*, in  $\text{CD}_3\text{CN}$ .

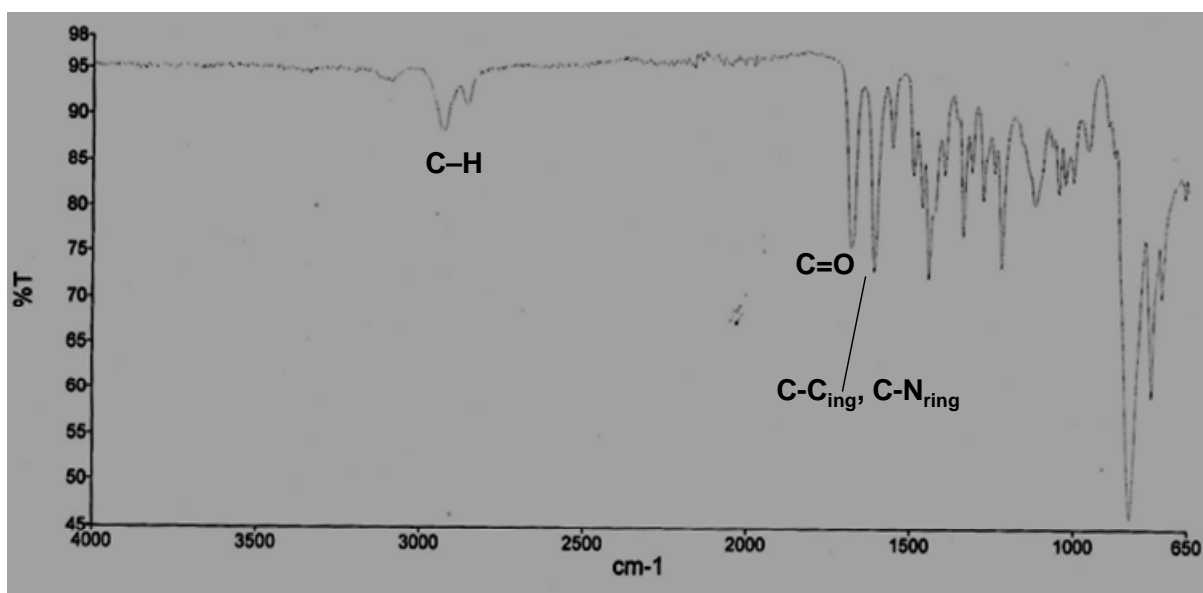


Figure A31 FT-IR spectrum of *RuSAc* solid powder.

#### -9.4 NMR and FT-IR Spectra of *IrBpyHex*

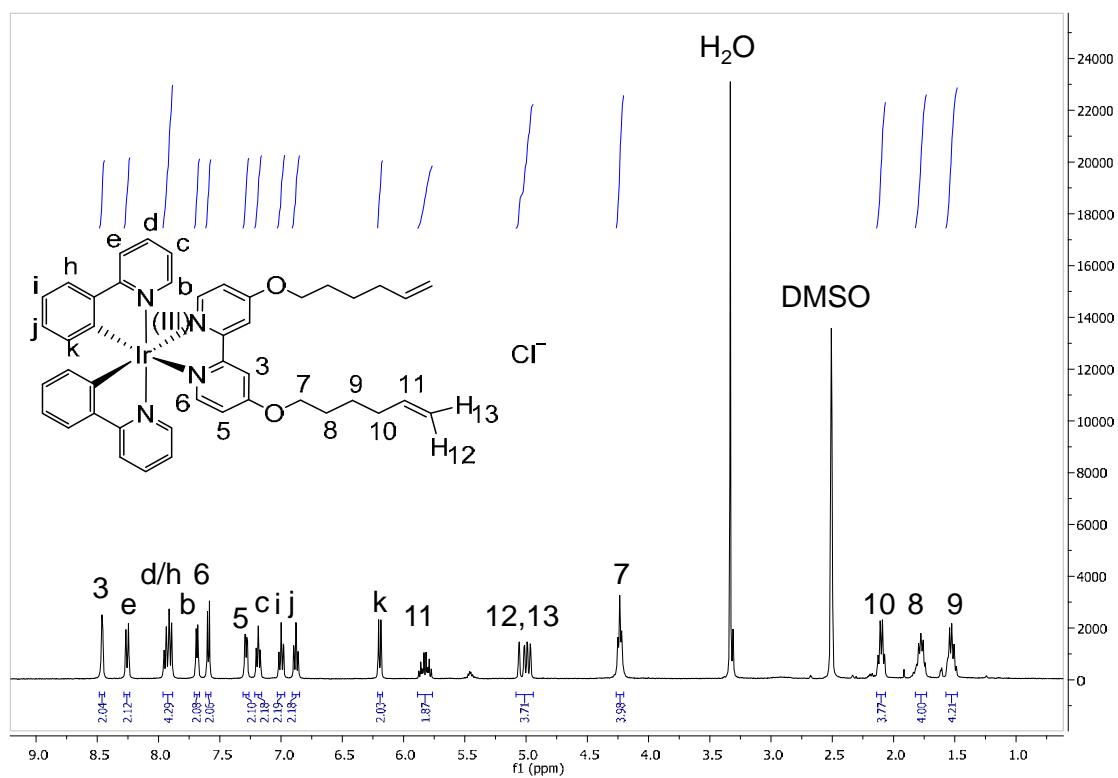
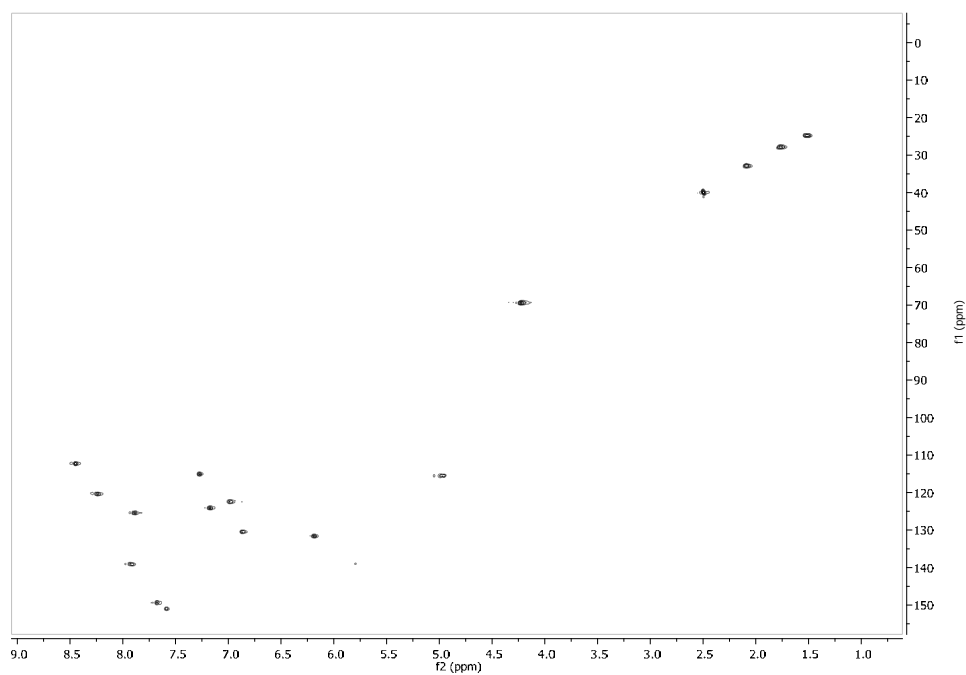
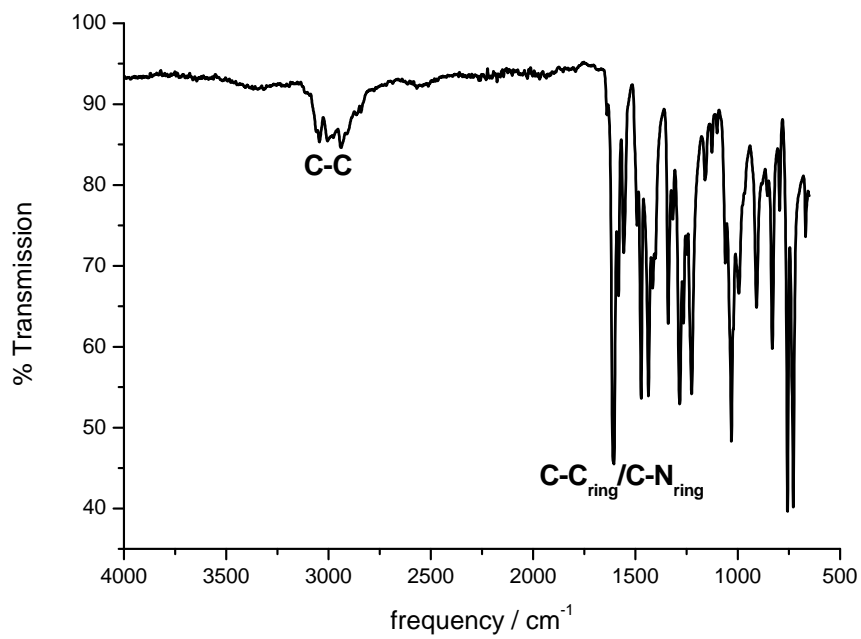


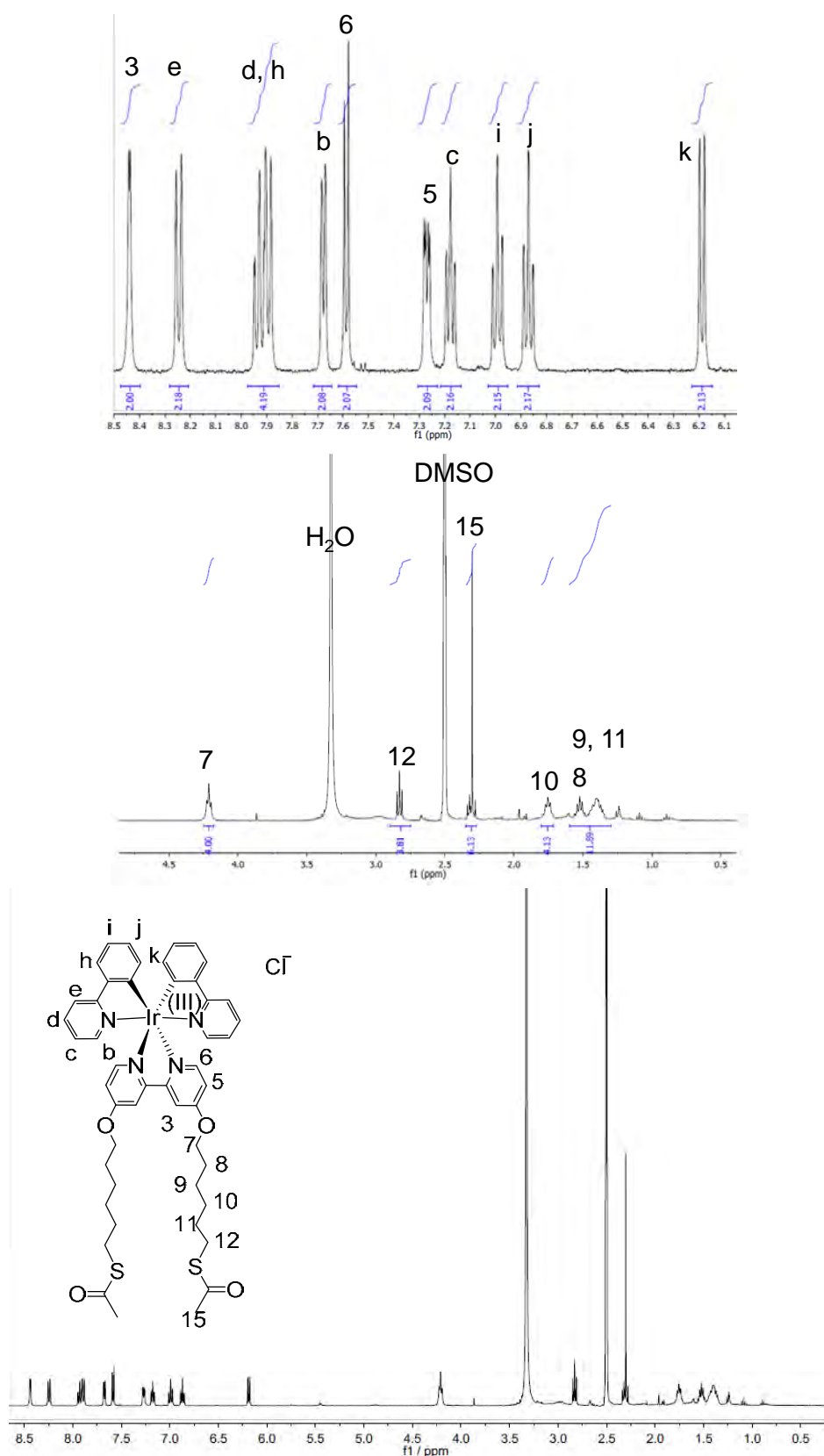
Figure A32 <sup>1</sup>H NMR spectrum of *IrBpyHex* in *d*<sub>6</sub>-DMSO.



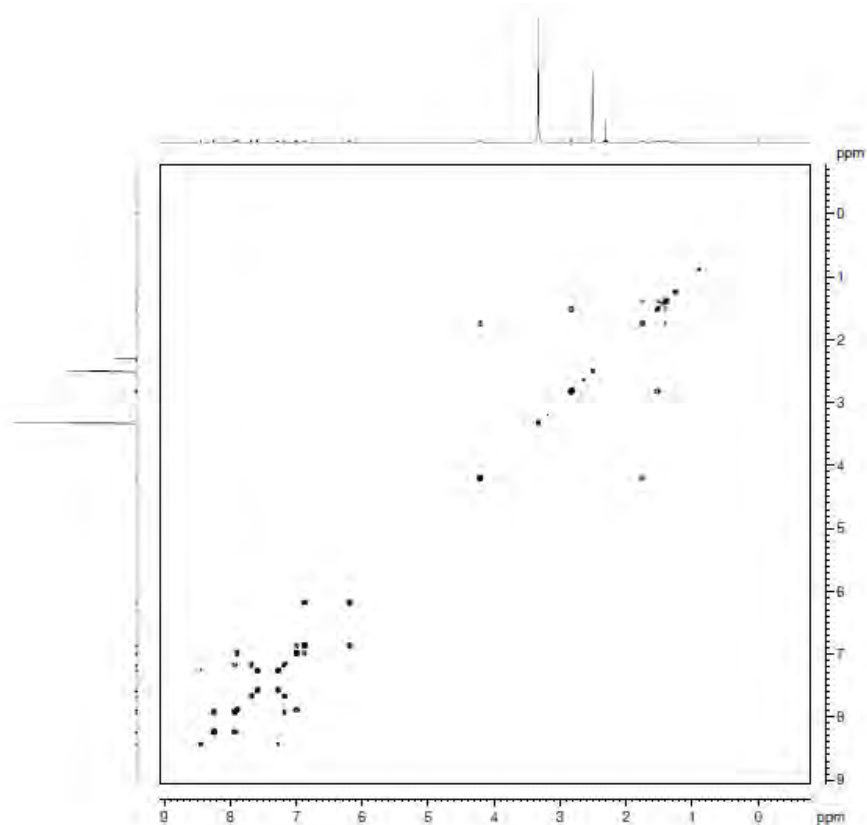
**Figure A33**  $^1\text{H}$ - $^1\text{H}$  COSY NMR spectrum of *IrBpyHex*, in  $d_6$ -DMSO.



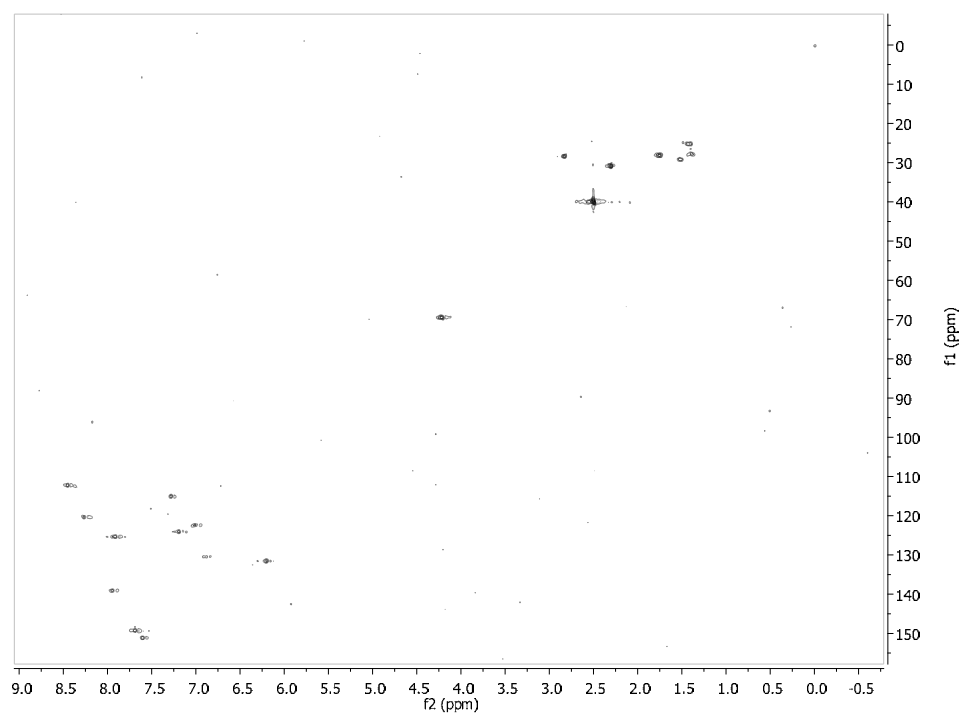
**Figure A34** FT-IR spectrum of *IrBpyHex* solid powder.

**-9.5 NMR, HRMS and FT-IR Spectra of IrBpySAC**

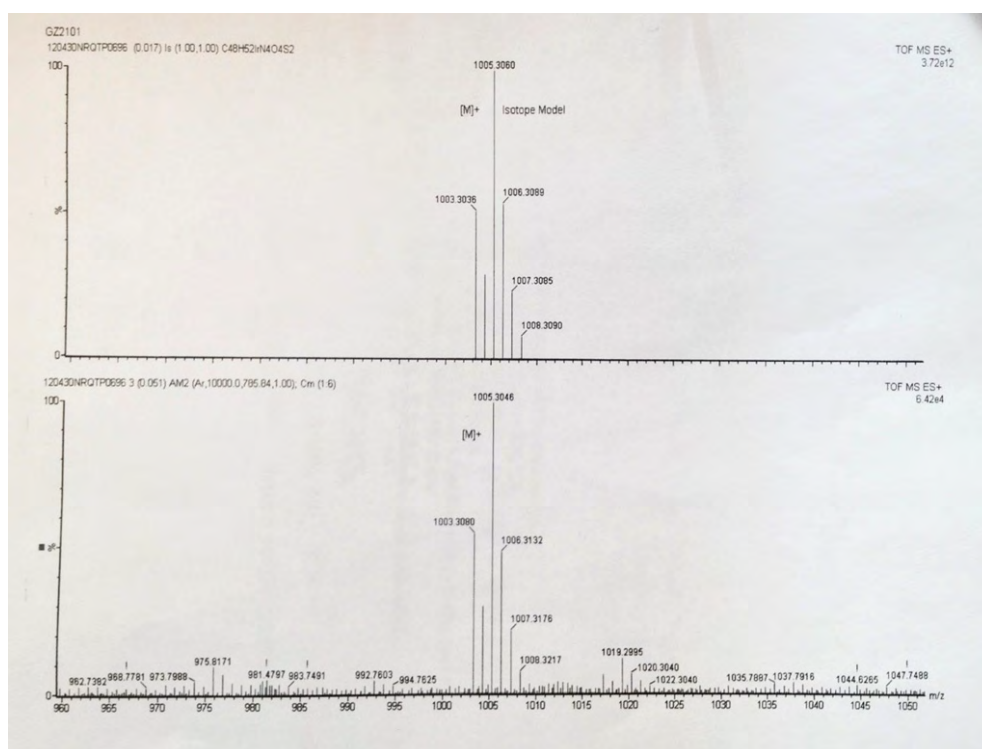
**Figure A35**  $^1\text{H}$  NMR spectrum of IrBpySAC in  $d_6$ -DMSO, zoom of aromatic region (top), zoom of aliphatic region (middle) and full spectrum (bottom).



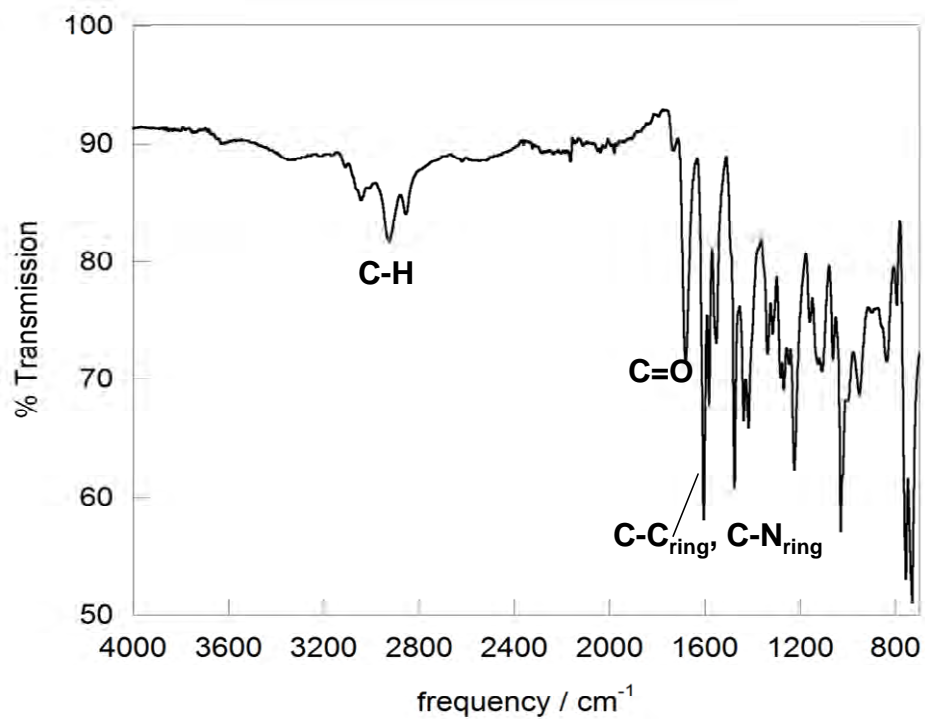
**Figure A36**  $^1\text{H}$ - $^1\text{H}$  COSY NMR spectrum of *IrBpySac*, in  $d_6$ -DMSO.



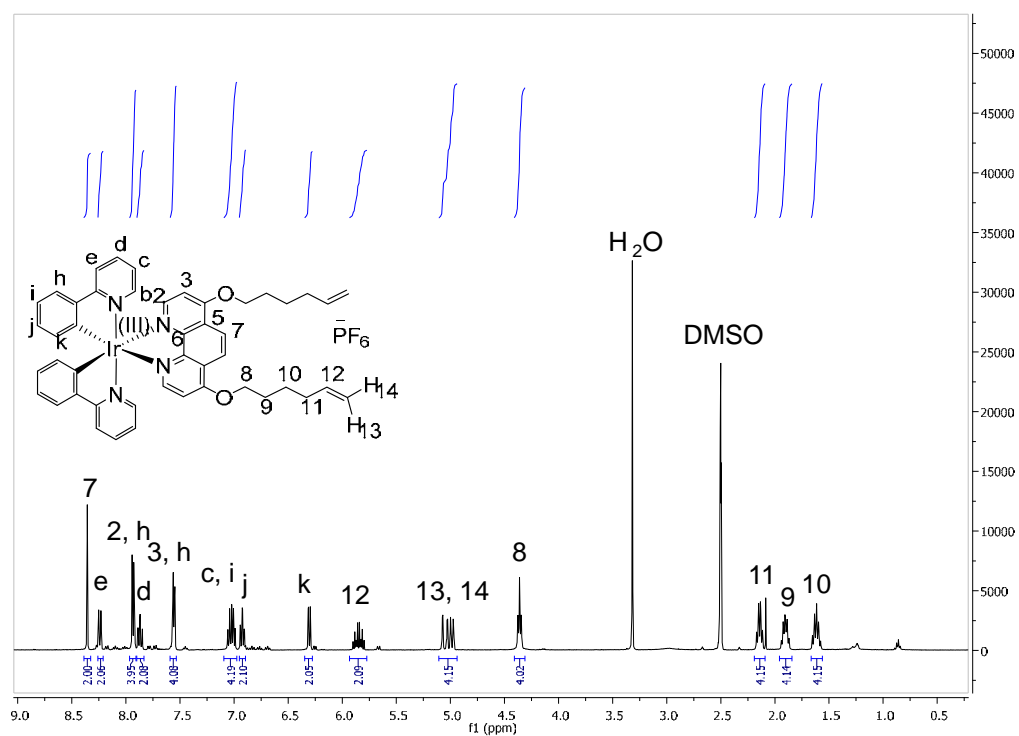
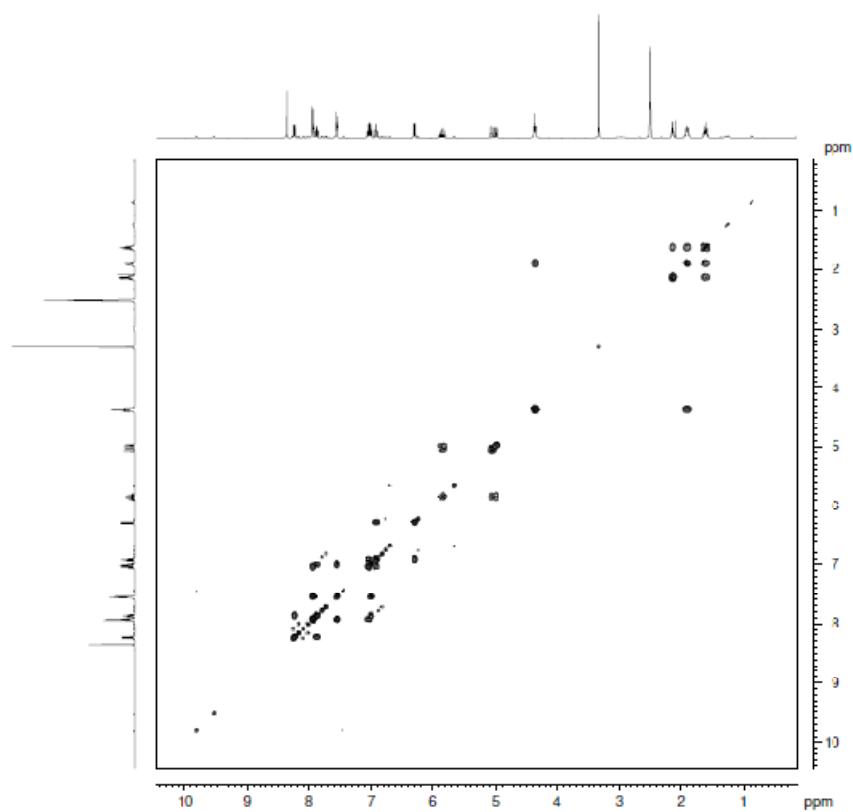
**Figure A37**  $^1\text{H}$ ,  $^{13}\text{C}$ -HSQC NMR spectrum of *IrBpySac*, in  $d_6$ -DMSO.

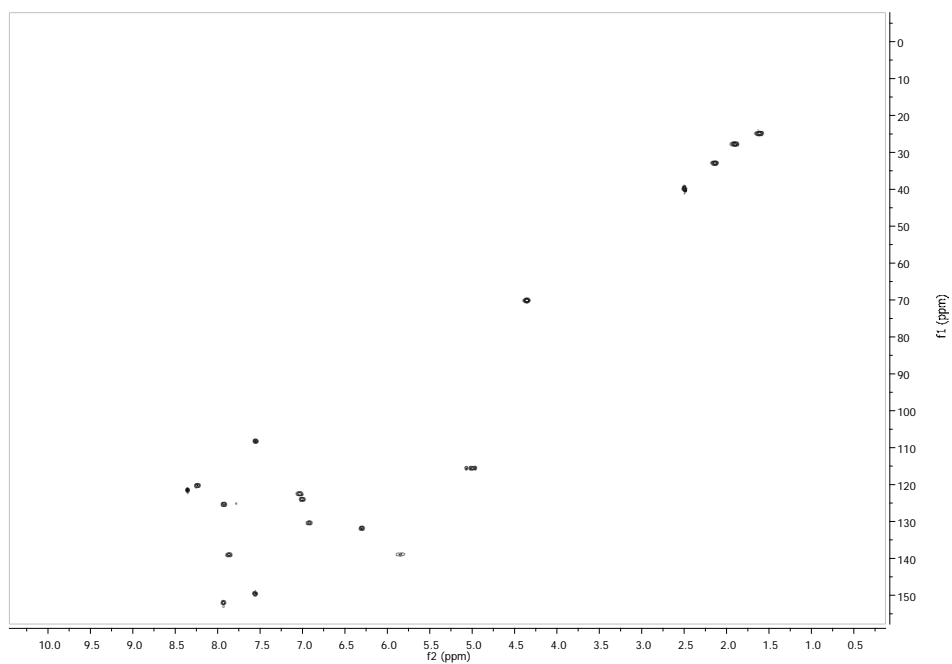


**Figure A38** High resolution ES-TOF+ mass spectrum of *IrBpySac* parent peak (bottom), calculated spectrum (top).

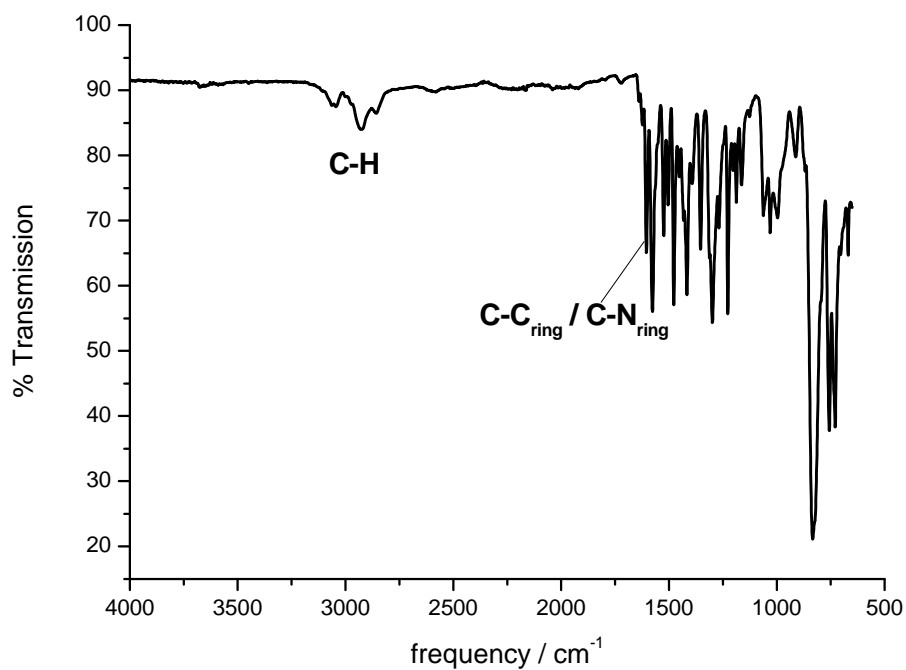


**Figure A39** FT-IR spectrum of *IrBpySac* solid powder.

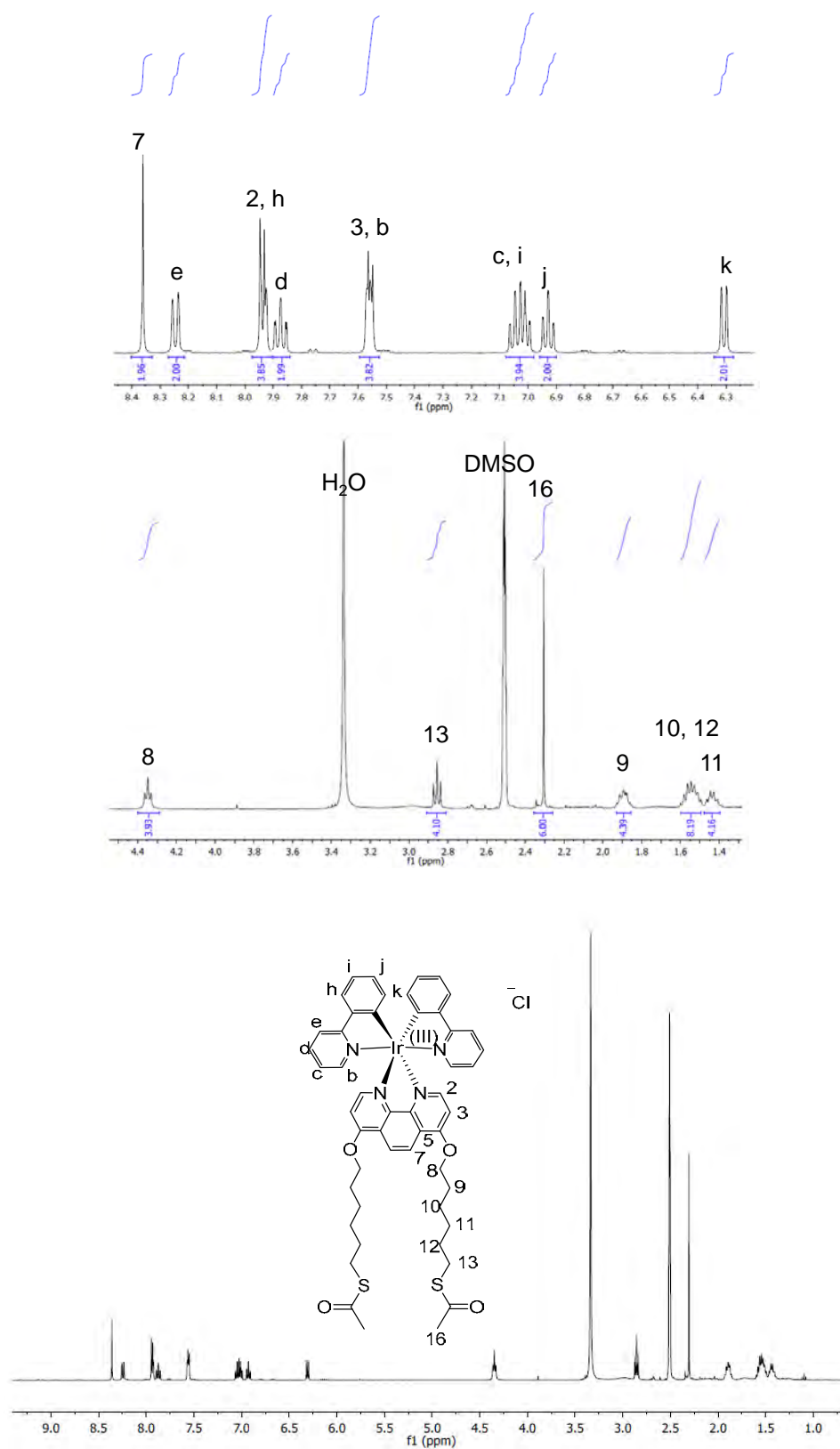
**-9.6 NMR and FT-IT Spectra of IrPhenHex****Figure A40**  $^1\text{H}$  NMR spectrum of *IrPhenHex* in  $d_6$ -DMSO**Figure A41**  $^1\text{H}$ - $^1\text{H}$  COSY NMR spectrum of *IrPhenHex*, in  $d_6$ -DMSO.



**Figure A42**  $^1\text{H}$ ,  $^{13}\text{C}$ -HSQC NMR spectrum of *IrPhenHex*, in  $d_6$ -DMSO.



**Figure A43** FT-IR spectrum of *IrPhenHex* solid powder.

**-9.7 NMR, HRMS and FT-IR Spectra of IrPhenSac**

**Figure A44**  $^1\text{H}$  NMR spectrum of  $[\text{IrPhenSac}]\text{Cl}$  in  $d_6\text{-DMSO}$ , zoom of aliphatic region (top), zoom of aromatic region (middle) and full spectrum (bottom).

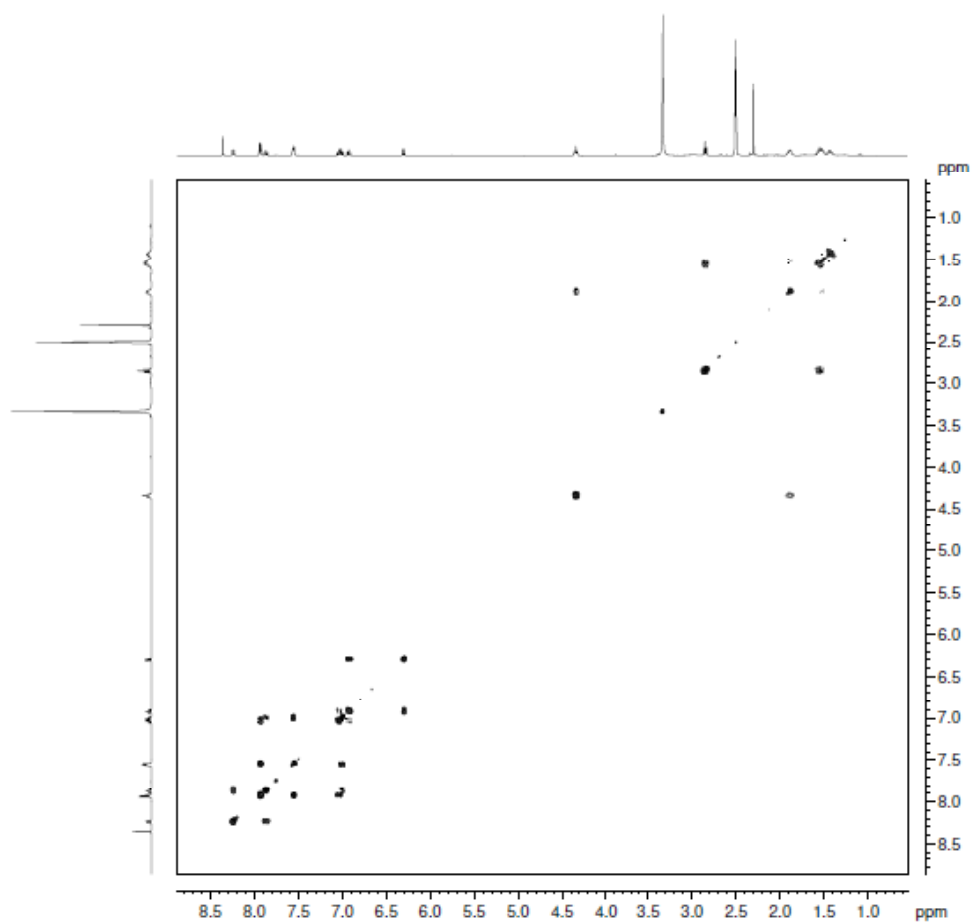


**Figure A45**  $^1\text{H}$ - $^1\text{H}$  COSY NMR spectrum of  $[\text{IrPhenSAc}]\text{PF}_6$  in  $d_6$ -DMSO.

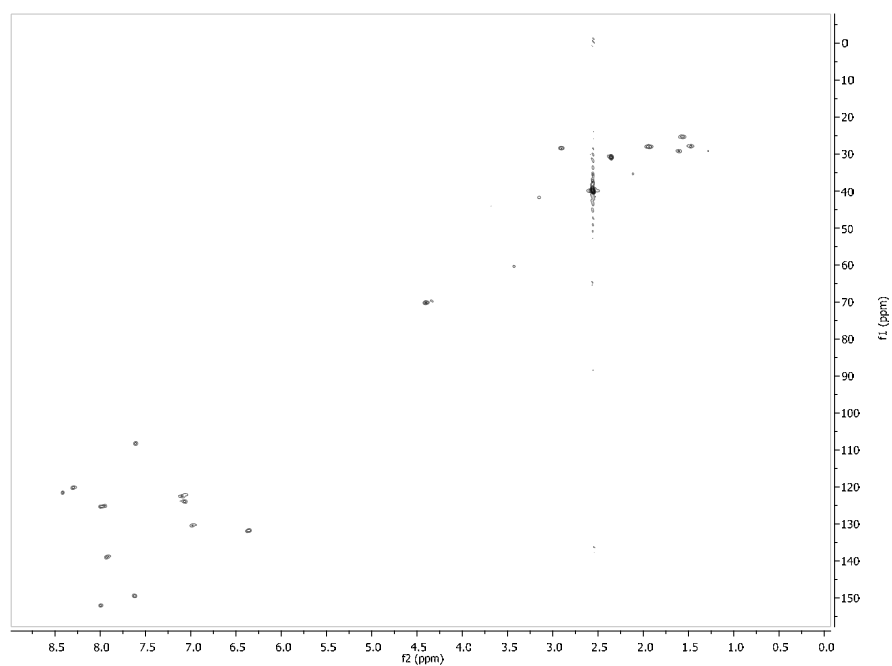


**Figure A46**  $^1\text{H}$ ,  $^{13}\text{C}$ -HSQC NMR spectrum of  $[\text{IrPhenSAc}]\text{PF}_6$ , in  $d_6$ -DMSO.

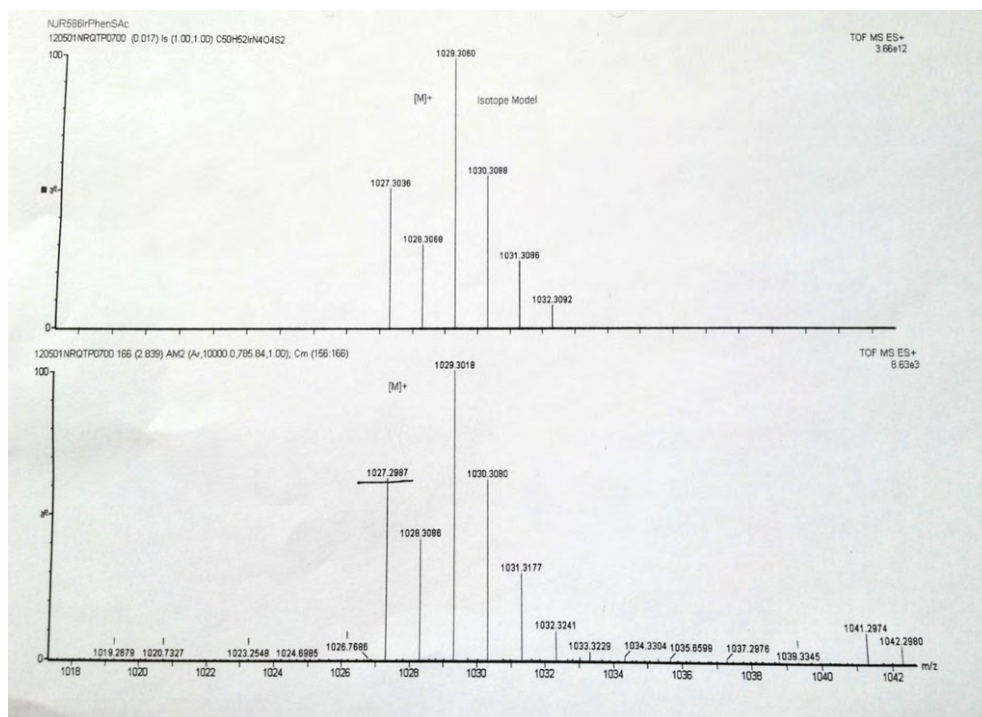


**Figure A47** High resolution ES-TOF+ mass spectrum of  $[IrPhenSAC]PF_6$  parent peak (bottom), calculated spectrum (top).

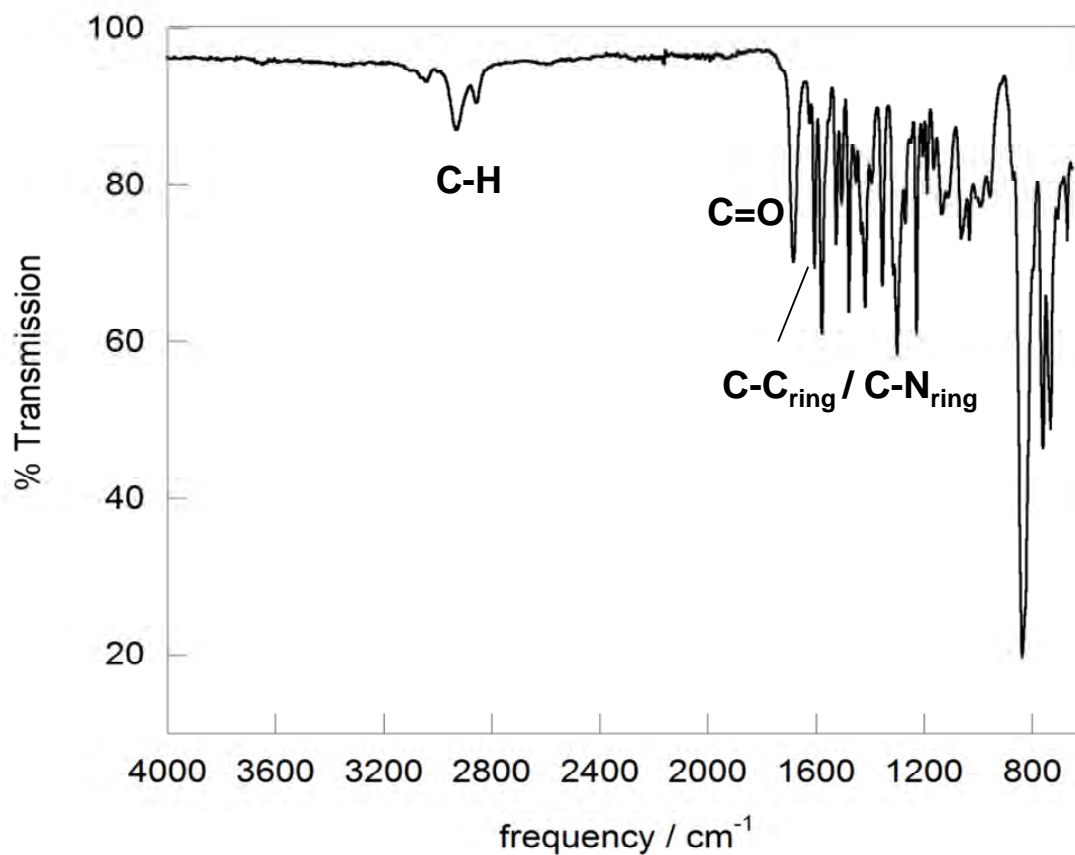


**Figure A48** FT-IR spectrum of  $[IrPhenSAC]PF_6$  solid powder

[A34]

## Appendix 10: Luminescence Excitation Spectra of IrBpySAc and IrPhenSAc

### -10.1 Luminescence Excitation Spectra of IrBpySAc in CH<sub>3</sub>CN and 1% CH<sub>3</sub>CN, H<sub>2</sub>O.

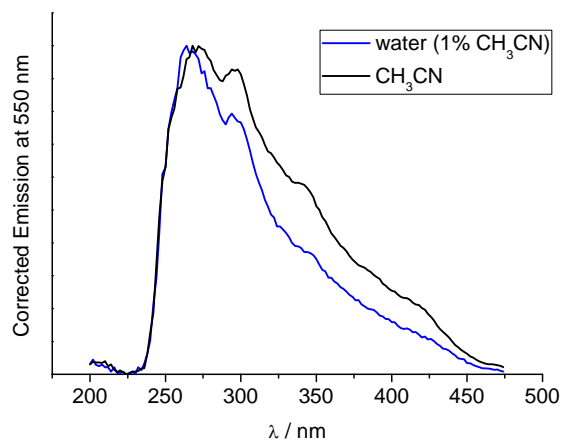


**Figure A49** Luminescence excitation spectra of 9 μM IrPhenSAc in CH<sub>3</sub>CN and in 1% CH<sub>3</sub>CN, H<sub>2</sub>O, λ<sub>em</sub> = 550 nm. Spectra corrected for instrument response.

### -10.2 Luminescence Excitation Spectra of IrPhenSAc in CH<sub>3</sub>CN and 1% CH<sub>3</sub>CN, H<sub>2</sub>O.

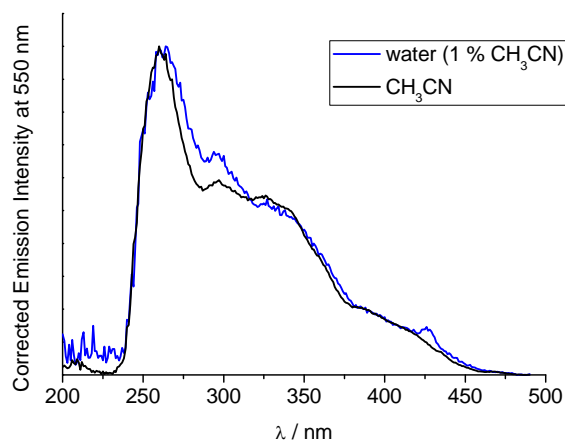


**Figure A50** Luminescence excitation spectra of 9 μM IrPhenSAc in CH<sub>3</sub>CN and in 1% CH<sub>3</sub>CN, H<sub>2</sub>O λ<sub>em</sub> = 550 nm. Spectra corrected for instrument response.

## Appendix 11: Control Steady-state Luminescence Spectra of IrBpySAC and IrPhenSAC

### -11.1 Aqueous Emission of IrBpySAC, in the presence of Zonyl® 7950 Surfactant

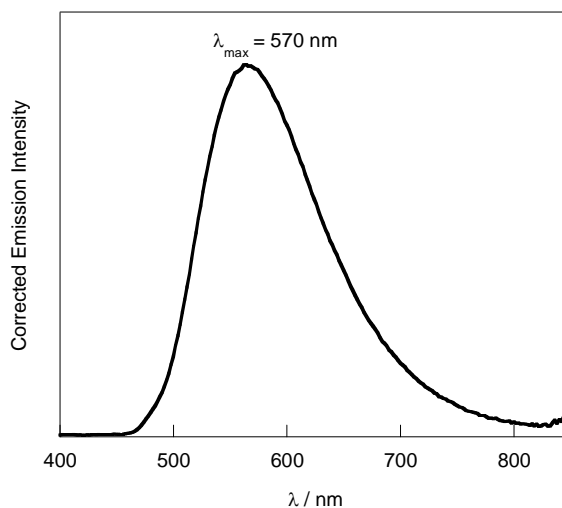


**Figure A51** Steady-state luminescence spectrum of 20 μM IrBpySAC, with 1 mM Zonyl® 7950 in 1% CH<sub>3</sub>CN/H<sub>2</sub>O. Spectrum corrected for instrument response.

### -11.2 Aqueous Emission of IrPhenSAC in the presence of Zonyl® 7950 Surfactant

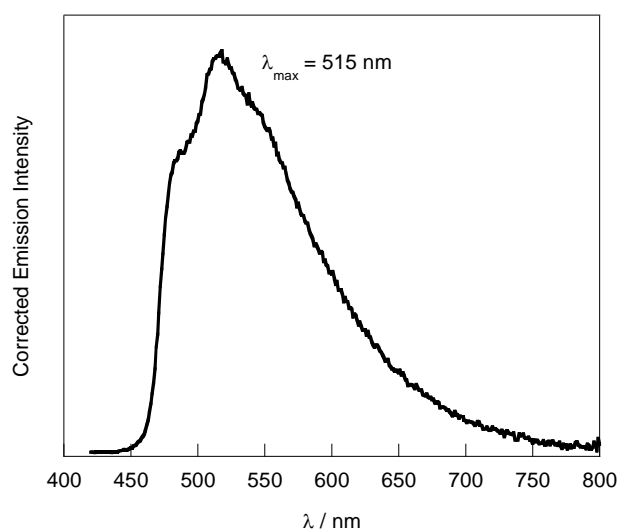


**Figure A52** Steady-state luminescence spectrum of 20 μM IrPhenSAC, with 1 mM Zonyl® 7950 in 1% CH<sub>3</sub>CN/H<sub>2</sub>O. Spectrum corrected for instrument response.

## Appendix 12: Control Steady-state Luminescence Spectra of Similar Ir(III) Cyclometallated Complexes<sup>1</sup>

### -12. 1 Emission of [Ir(ppy)<sub>2</sub>(phen)]Cl in CH<sub>3</sub>CN and in 1% CH<sub>3</sub>CN, H<sub>2</sub>O.

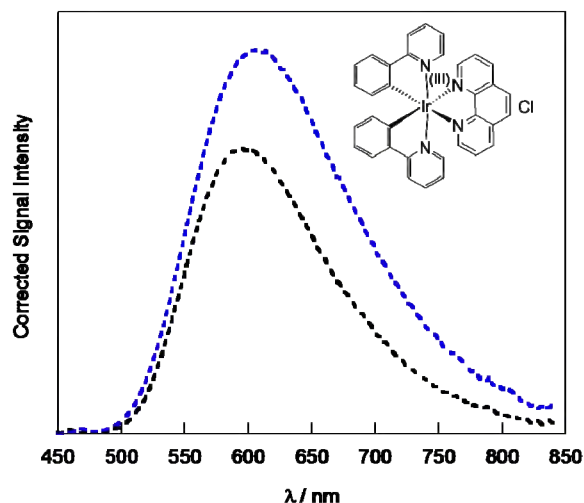


**Figure A53** Steady-state luminescence spectrum of 20 μM [Ir(ppy)<sub>2</sub>(phen)]Cl (structure shown in Figure inset) in CH<sub>3</sub>CN (black) and in 1% CH<sub>3</sub>CN/H<sub>2</sub>O (blue). Spectrum corrected for instrument response.

### -12. 2 Emission of [Ir(ppy)<sub>2</sub>(bpy-et-NH<sub>2</sub>)]Cl in CH<sub>3</sub>CN and in 1% CH<sub>3</sub>CN, H<sub>2</sub>O.

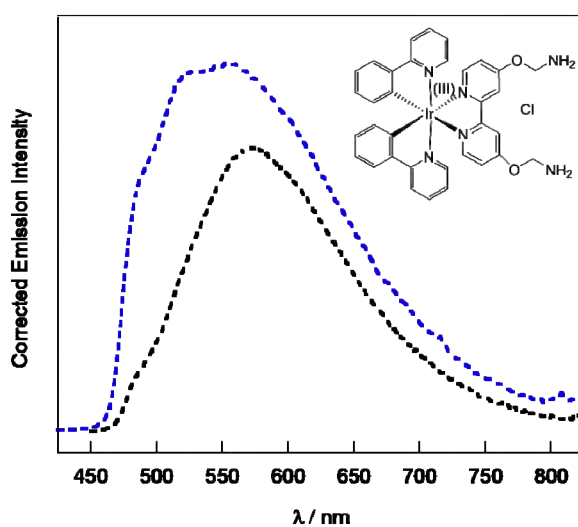


**Figure A54** Steady-state luminescence spectrum of 20 μM [Ir(ppy)<sub>2</sub>(bpy-et-NH<sub>2</sub>)]Cl (structure shown in Figure inset) in CH<sub>3</sub>CN (black) and in 1% CH<sub>3</sub>CN/H<sub>2</sub>O (blue). Spectrum corrected for instrument response.

<sup>1</sup> Lewis, D. J.; Dore, V.; Rogers, N. J.; Mole, T. K.; Nash, G. B.; Angeli, P.; Pikramenou, Z. *Langmuir* **2013**, *29*, 14701.

## Appendix 13: Luminescence Lifetimes of the IrBpySAc and IrPhenSAc Complexes, and Ir(III)-functionalised Nanoparticles

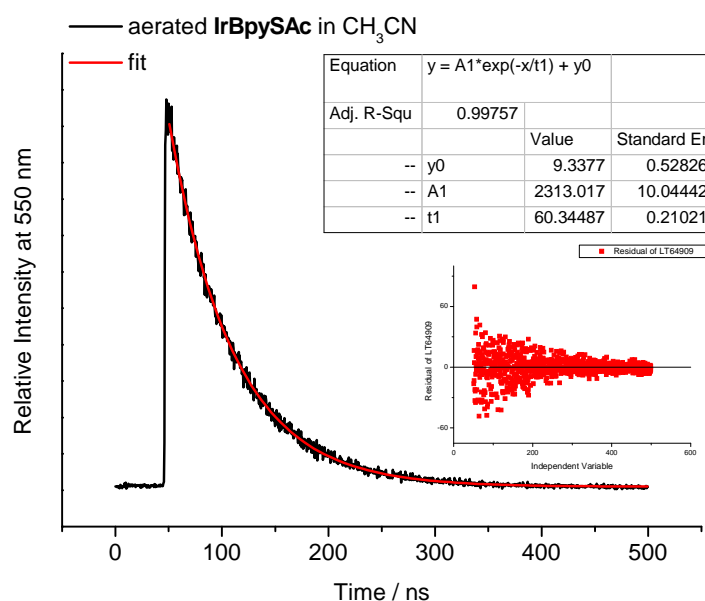


**Figure A55** Luminescence lifetime data of aerated IrBpySAc measured in CH<sub>3</sub>CN solution,  $\lambda_{exc} = 375$  nm,  $\lambda_{em} = 550$  nm Monoexponential fit shown in red. Residual shown in inset.

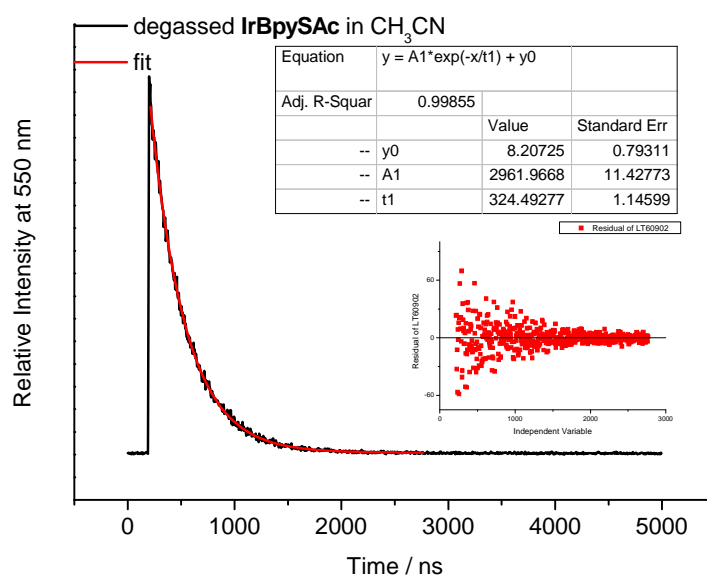


**Figure A56** Luminescence lifetime data of deaerated IrBpySAc measured in CH<sub>3</sub>CN solution,  $\lambda_{exc} = 375$  nm,  $\lambda_{em} = 550$  nm Monoexponential fit shown in red. Residual shown in inset.

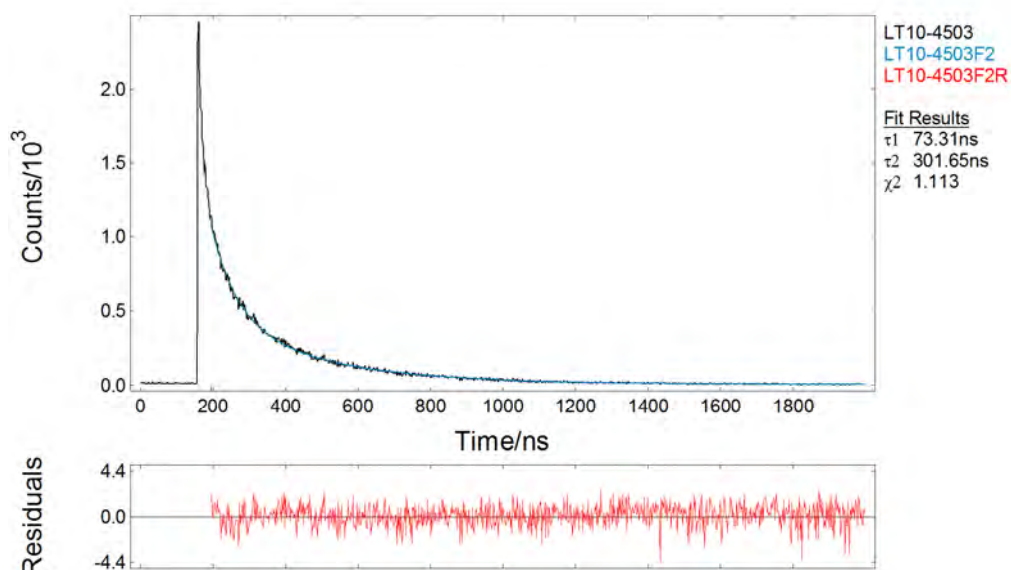


**Figure A57** Luminescence lifetime data of aerated **IrBpySAC** measured in 1%  $\text{CH}_3\text{CN}$ ,  $\text{H}_2\text{O}$  solution,  $\lambda_{\text{exc}} = 375 \text{ nm}$ ,  $\lambda_{\text{em}} = 550 \text{ nm}$ . Biexponential fit shown in blue, residual shown in red.

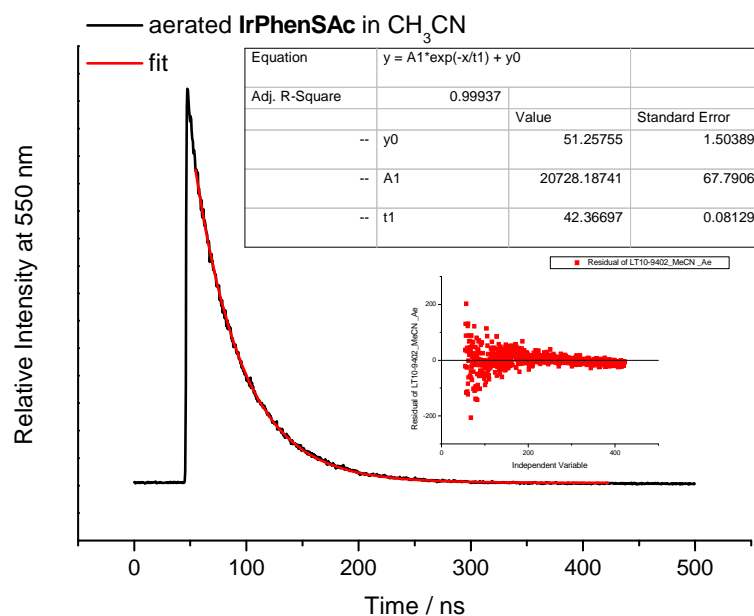


**Figure A58** Luminescence lifetime data of aerated **IrPhenSAC** measured in  $\text{CH}_3\text{CN}$  solution,  $\lambda_{\text{exc}} = 375 \text{ nm}$ ,  $\lambda_{\text{em}} = 550 \text{ nm}$ . Monoexponential fit shown in red, residual shown in inset.

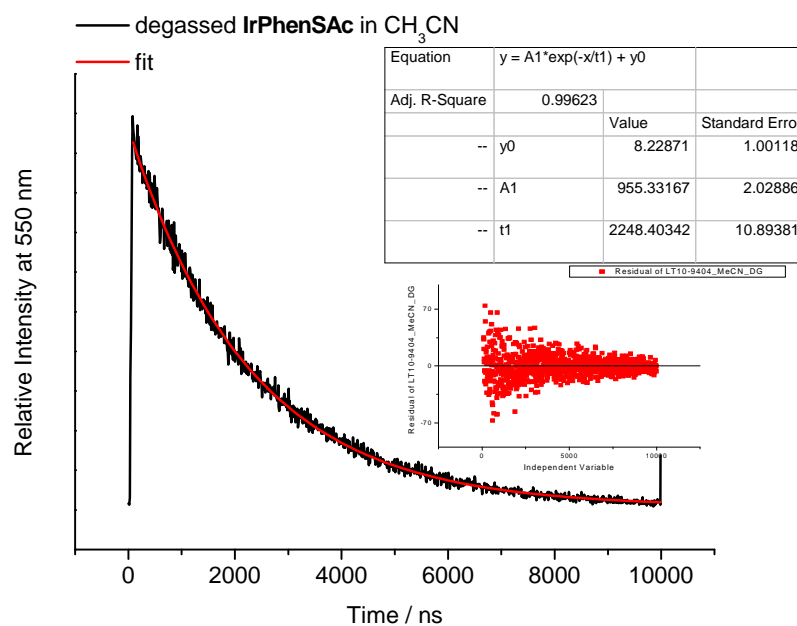


**Figure A59** Luminescence lifetime data of deaerated **IrPhenSAC** measured in CH<sub>3</sub>CN solution,  $\lambda_{exc} = 375$  nm,  $\lambda_{em} = 550$  nm. Monoexponential fit shown in red, residual shown in inset

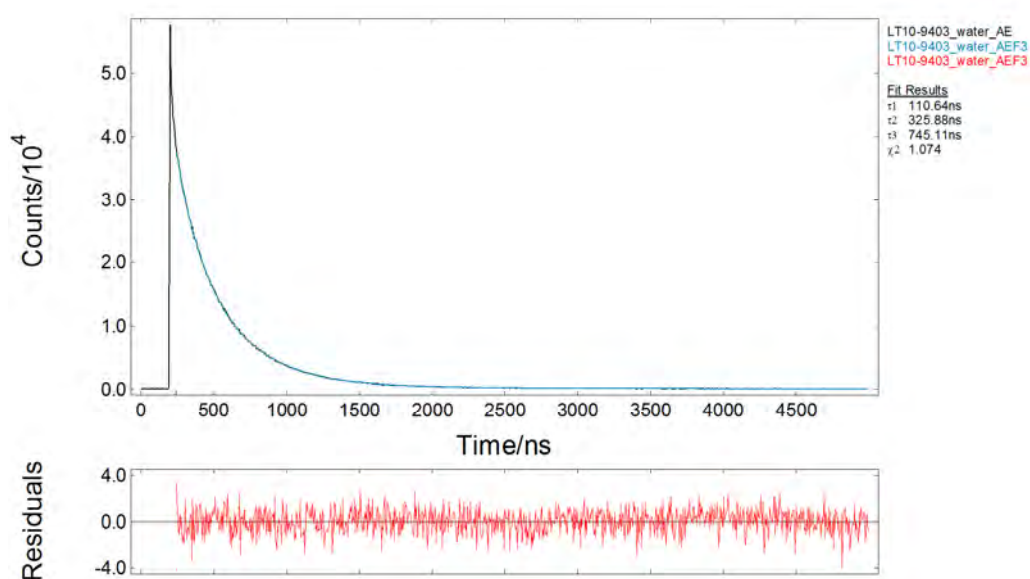


**Figure A60** Luminescence lifetime data of aerated **IrPhenSAC** measured in 1% CH<sub>3</sub>CN, H<sub>2</sub>O solution,  $\lambda_{exc} = 375$  nm,  $\lambda_{em} = 550$  nm. Triexponential fit shown in blue, residual shown in red.

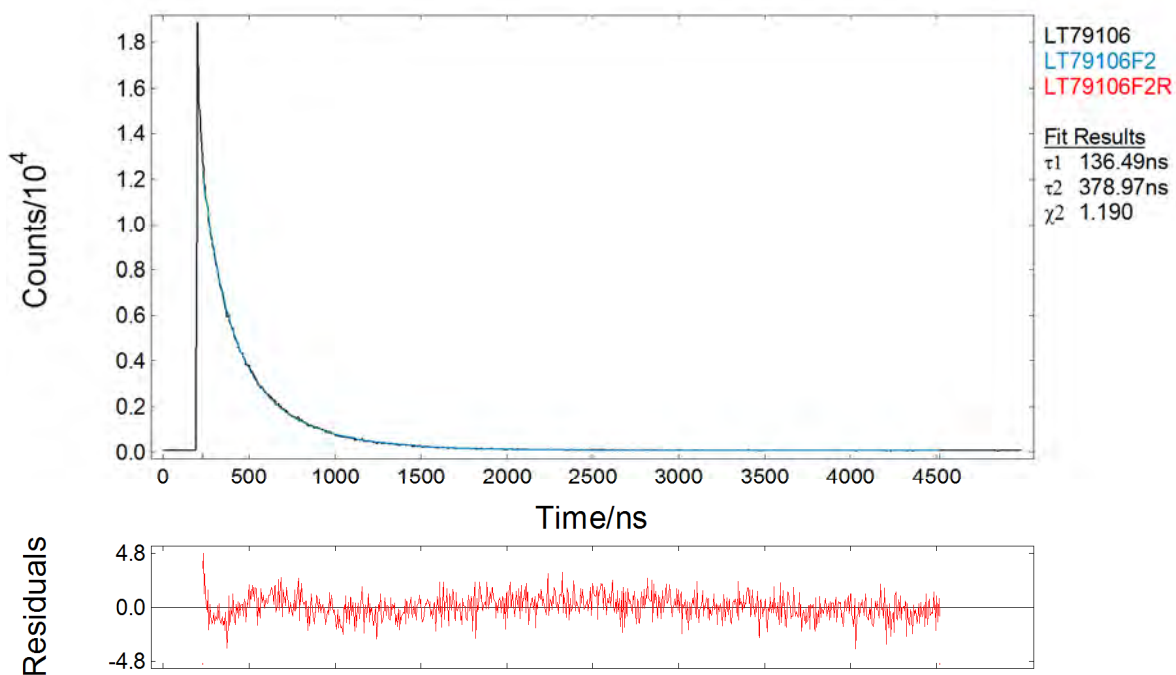


**Figure A61** Luminescence lifetime data of aerated 20  $\mu\text{M}$  IrBpySAc, with 1 mM Zonyl® 7950 in 1%  $\text{CH}_3\text{CN}/\text{H}_2\text{O}$ .  $\lambda_{\text{exc}} = 375 \text{ nm}$ ,  $\lambda_{\text{em}} = 550 \text{ nm}$ . Biexponential fit shown in blue, residual shown in red.

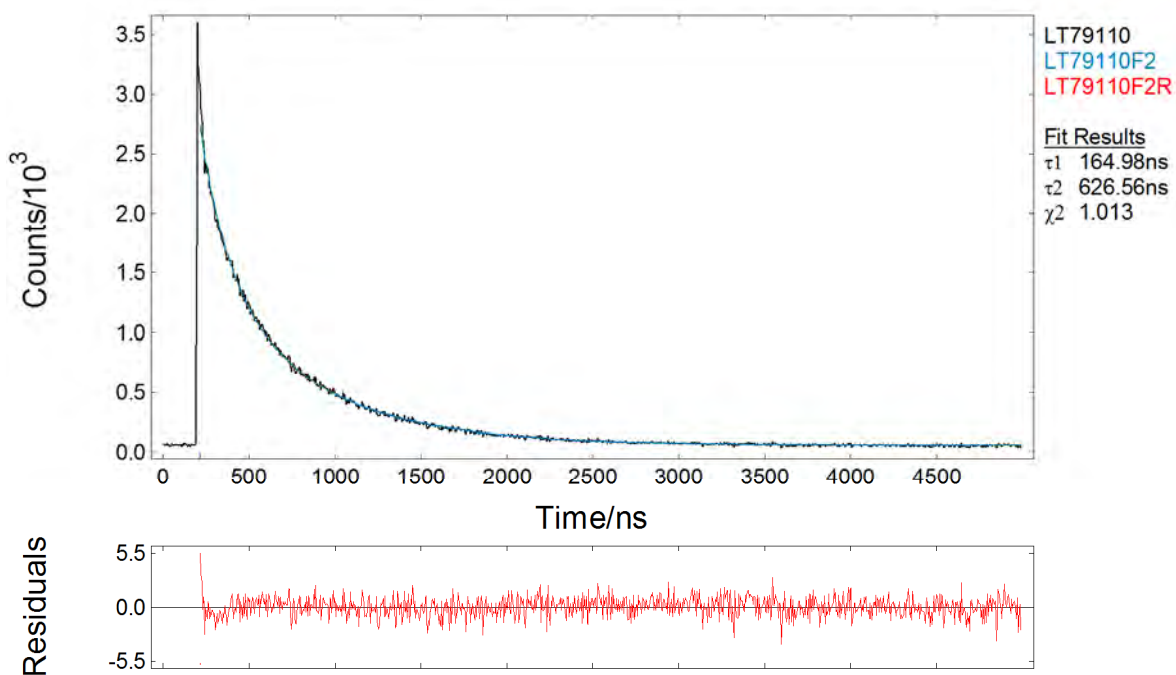


**Figure A62** Luminescence lifetime data of deaerated 20  $\mu\text{M}$  IrBpySAc, with 1 mM Zonyl® 7950 in 1%  $\text{CH}_3\text{CN}/\text{H}_2\text{O}$ .  $\lambda_{\text{exc}} = 375 \text{ nm}$ ,  $\lambda_{\text{em}} = 550 \text{ nm}$ . Biexponential fit shown in blue, residual shown in red.

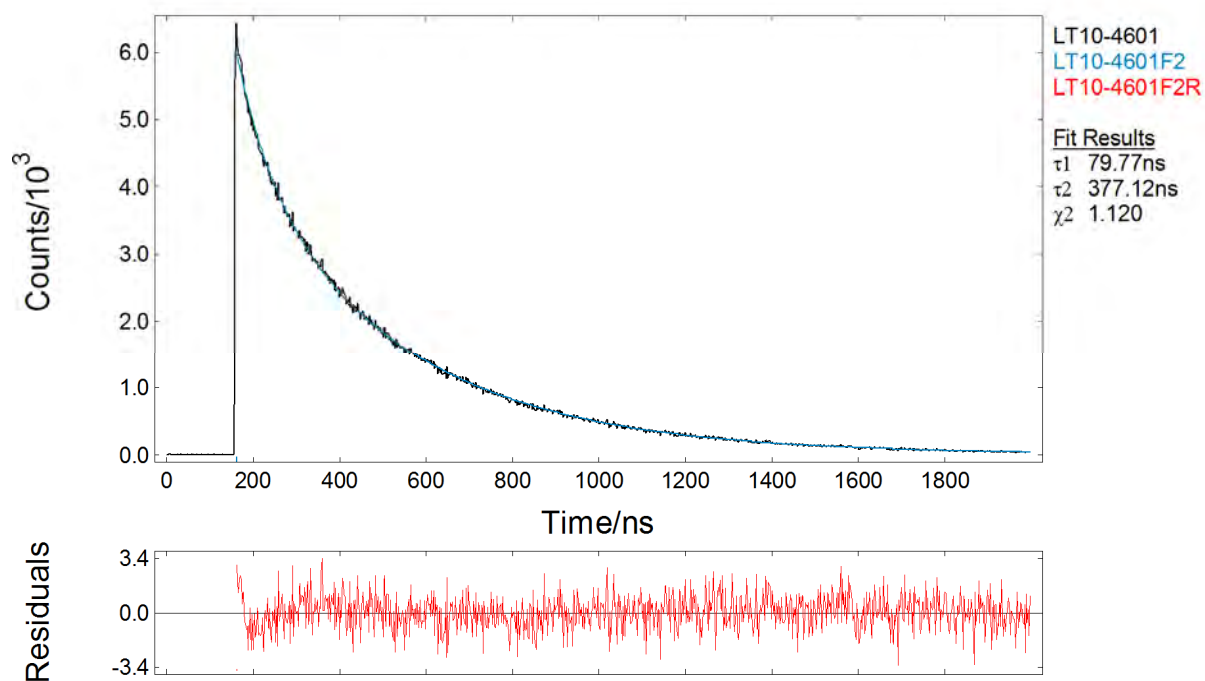


**Figure A63** Luminescence lifetime data of aerated 1 nM IrBpy-Z•AuNP13 in deionised water,  $\lambda_{exc} = 375$  nm,  $\lambda_{em} = 550$  nm. Biexponential fit shown in blue, residual shown in red.

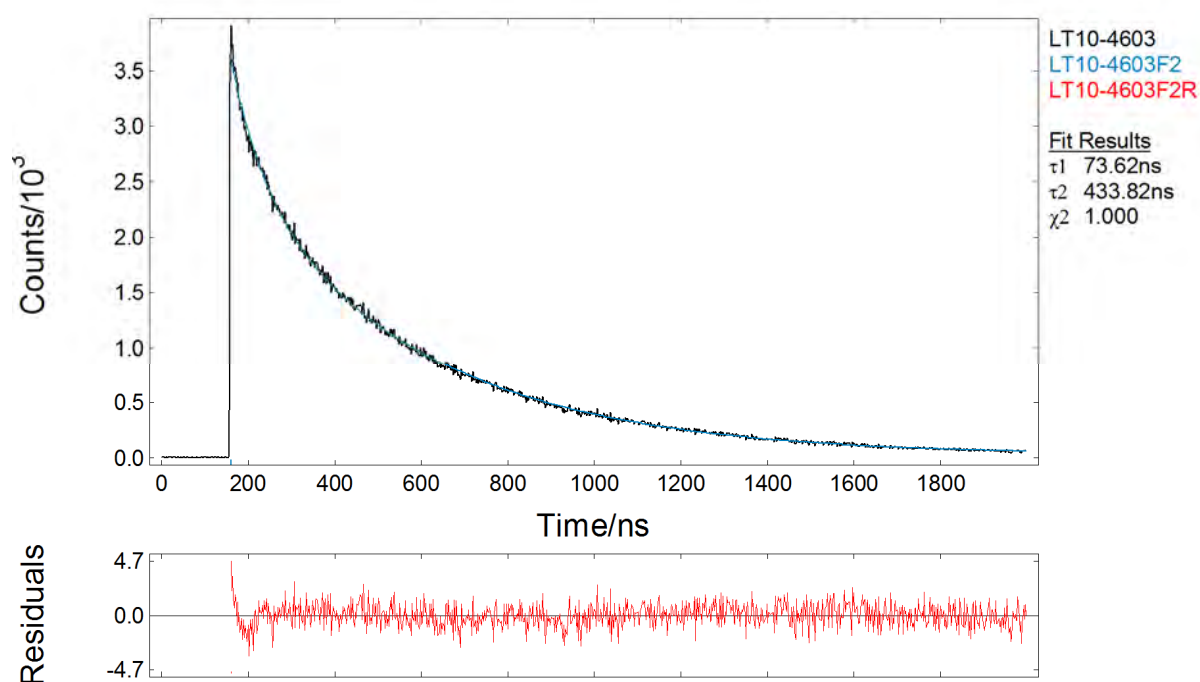


**Figure A64** Luminescence lifetime data of deaerated 1 nM IrBpy-Z•AuNP13 in deionised water,  $\lambda_{exc} = 375$  nm,  $\lambda_{em} = 550$  nm. Biexponential fit shown in blue, residual shown in red.

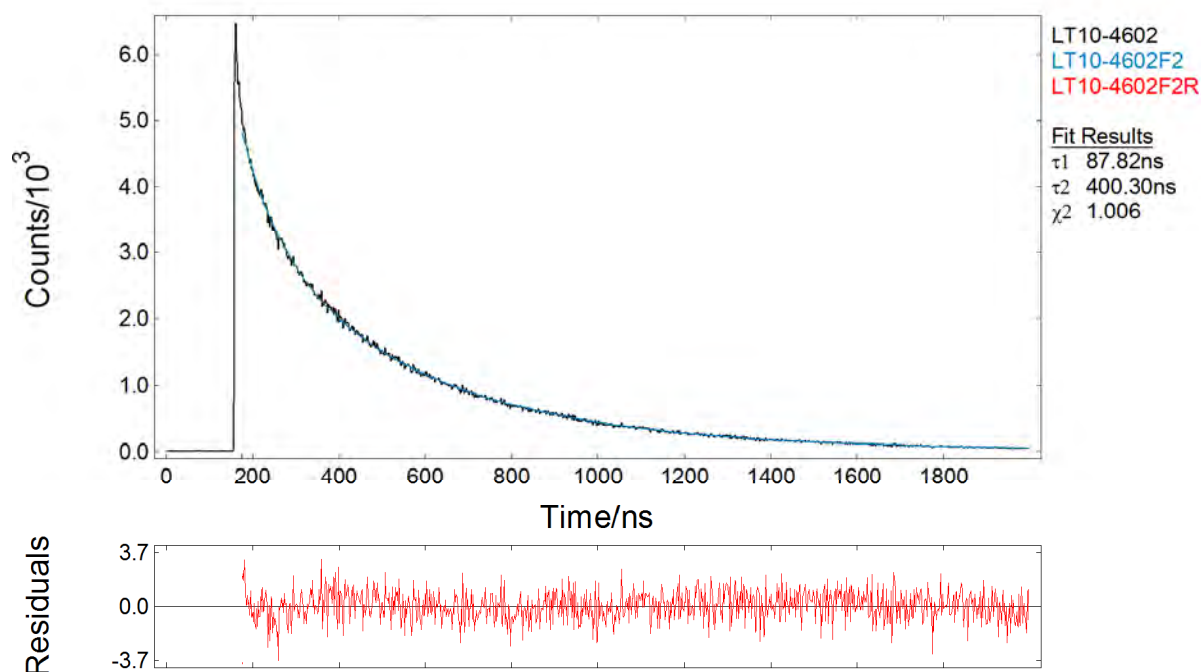


**Figure A65** Luminescence lifetime data of aerated 10 pM IrBpy-Z•AuNP100 in deionised water,  $\lambda_{exc} = 375$  nm,  $\lambda_{em} = 550$  nm. Biexponential fit shown in blue, residual shown in red.

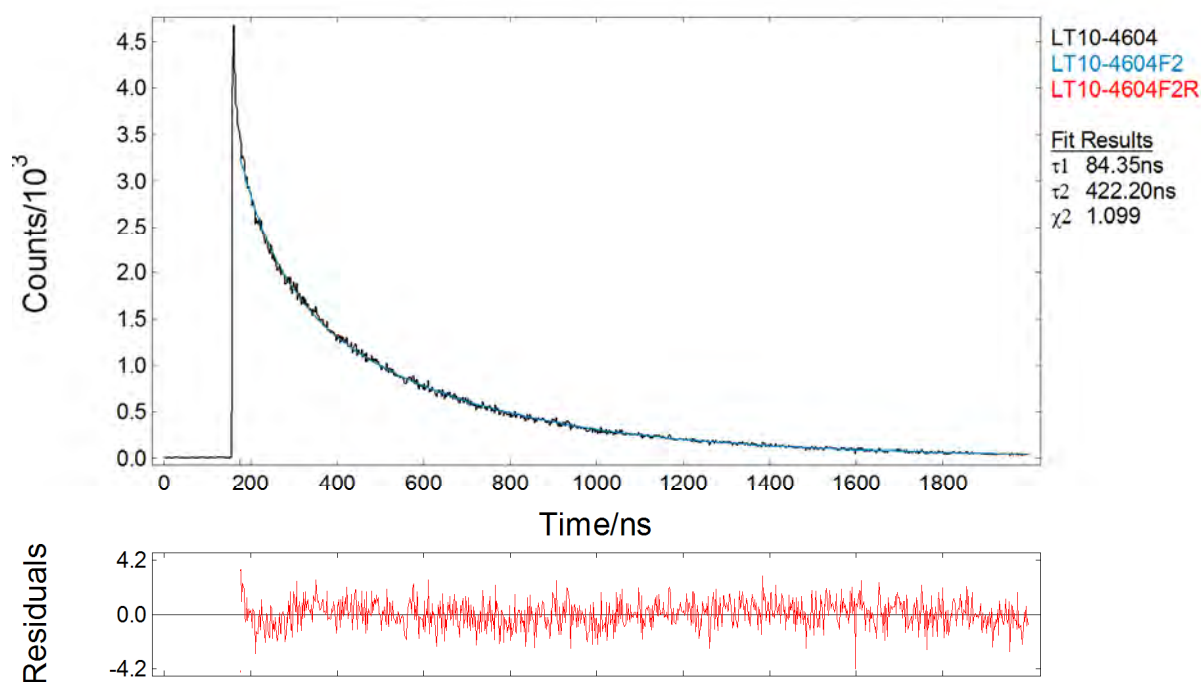


**Figure A66** Luminescence lifetime data of deaerated 10 pM IrBpy-Z•AuNP100 in deionised water,  $\lambda_{exc} = 375$  nm,  $\lambda_{em} = 550$  nm. Biexponential fit shown in blue, residual shown in red.

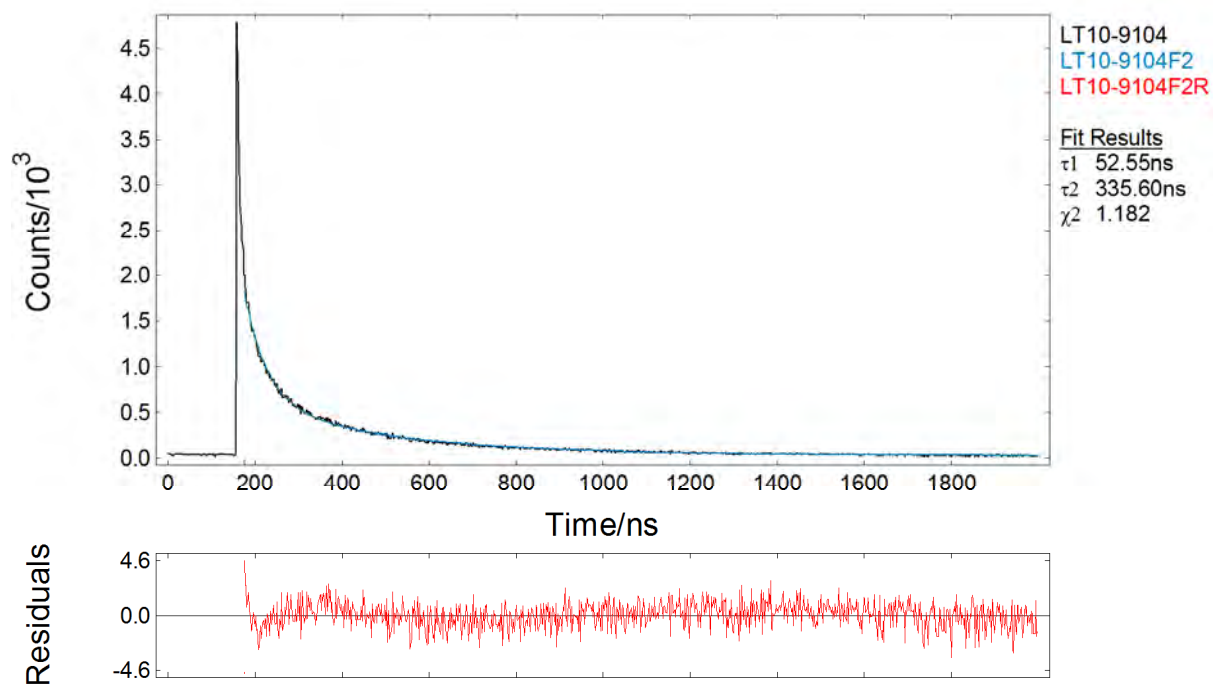


**Figure A67** Luminescence lifetime data of aerated 10 pM IrPhen-Z•AuNP100 in deionised water,  $\lambda_{exc} = 375$  nm,  $\lambda_{em} = 550$  nm. Biexponential fit shown in blue, residual shown in red.

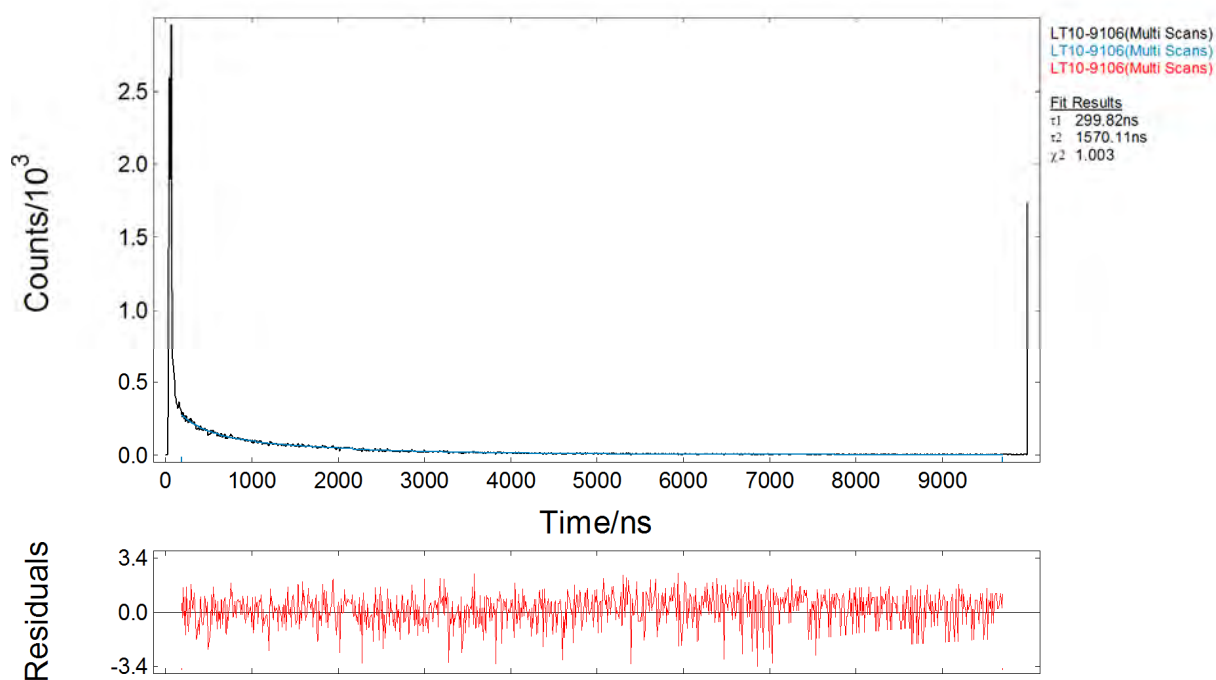


**Figure A68** Luminescence lifetime data of deaerated 10 pM IrPhen-Z•AuNP100 in deionised water,  $\lambda_{exc} = 375$  nm,  $\lambda_{em} = 550$  nm. Biexponential fit shown in blue, residual shown in red.

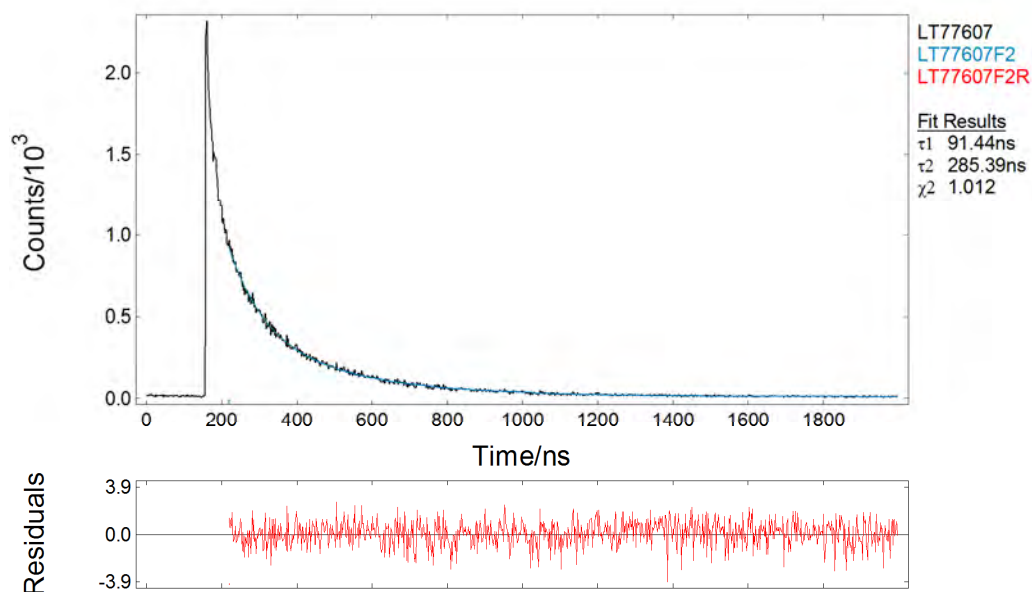
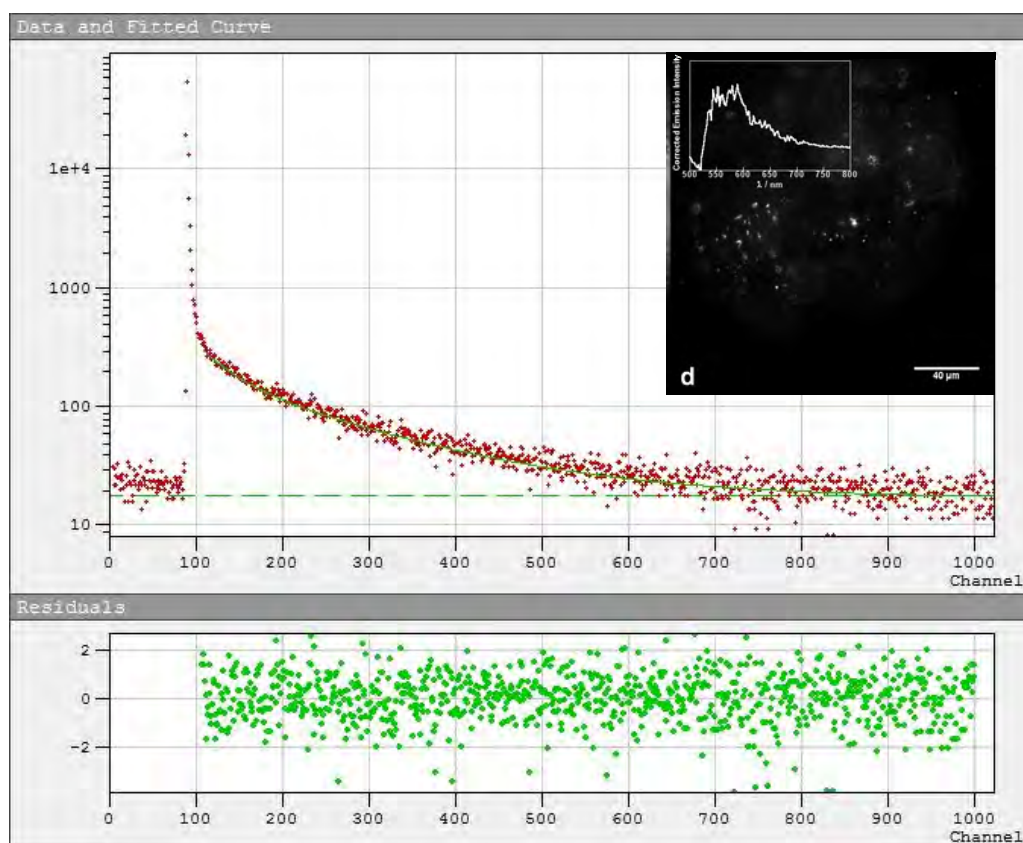


**Figure A69** Luminescence lifetime data of aerated 1 nM IrBpy-GdQ•AuNP13 in deionised water,  $\lambda_{exc} = 375$  nm,  $\lambda_{em} = 550$  nm. Biexponential fit shown in blue, residual shown in red.



Fitting: lifetime = 65 ns (15%), 320 ns (85%), reduced chi-square = 1.028.

**Figure A70** Luminescence lifetime data taken from field of view in epiluminescence image shown in Figure 5.25d (Chapter Five, Section 5.6.3) and in inset, of IrBpy-Z•AuNP100 in the skeletal leg muscle of murine tissue.

**Appendix 14: Fluid Calculation for Flow in a Rectangular Capillary****Tube**

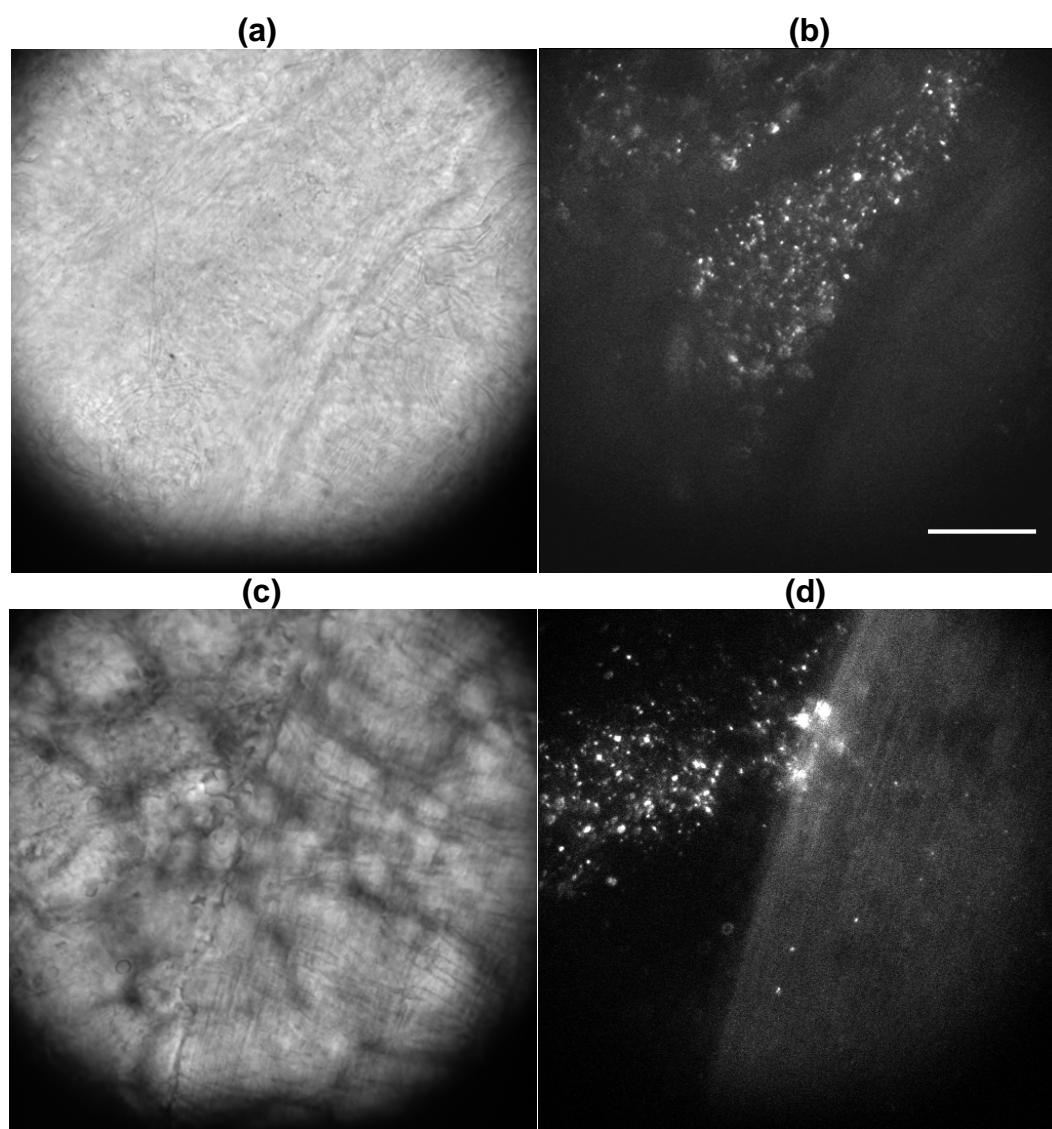
An adaptation of Poiseuille flow for vessels of rectangular cross section can be used to predict the flow velocities, assuming that the width of the channel is much greater than the height, and thus the flow is considered as between infinitely wide, parallel plates:

$$V = \frac{6Q}{wh^3} \left( \frac{h^2}{4} - x^2 \right)$$

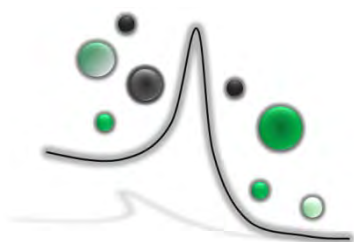
Q = volumetric flow rate, = 5  $\mu\text{L min}^{-1}$ , w = channel width, = 1 mm, h = channel height, = 0.1 mm, x = displacement from the centre of the channel.

$$V = \frac{6 \times 5 \times 10^{-9} / 60}{1 \times 10^{-3} \times (1 \times 10^{-4})^3} \left( \frac{(1 \times 10^{-4})^2}{4} - 0^2 \right) = 1.25 \times 10^{-3} \text{ m s}^{-1}$$

$$= \underline{\underline{1250 \mu\text{m s}^{-1}}}$$

**Appendix 15: Additional Epiluminescence Images of IrBpy-Z•AuNP100****Particles in *Ex-vivo* Murine Tissue**

**Figure A71** Bright field (a and c) image and epiluminescence images ( $\lambda_{exc} = 405 \text{ nm}$ ,  $\lambda_{em} > 510$  (b and d) of blood capillaries in lung tissue (a and b), and in the mesentery tissue (c and d) of a mouse injected with **IrBpyS•AuNP100**. White scale bar represents 40  $\mu\text{m}$ .



---

# Publications

---

**N. J. Rogers** (50 %) and Z. Pikramenou (50 %), University of Birmingham, '*Coated Nanoparticles*', Patent WO2013004989-A1, 2013.

**N. J. Rogers**, S. Claire, G. Zikeli, S. Farabi, R. Harris, N. J. Hodges, Iain Styles, Z. Pikramenou, '*High coating of Ru(II) complexes on gold nanoparticles for single particle luminescence imaging in cells*', Chem. Commun, **50**, p617 (2014).

D. J. Lewis, V. Dore, **N. J. Rogers**, T. K. Mole, G. B. Nash, P. Angeli, Z. Pikramenou, '*Silica Nanoparticles for Micro-Particle Imaging Velocimetry: Fluorosurfactant Improves Nanoparticle Stability and Brightness of Immobilized Iridium(III) Complexes*' Langmuir, **29**, 14701 (2013).



- (51) International Patent Classification:  
*B01J 2/00* (2006.01) *G01N 33/50* (2006.01)
- (21) International Application Number:  
PCT/GB2012/000555
- (22) International Filing Date:  
28 June 2012 (28.06.2012)
- (25) Filing Language: English
- (26) Publication Language: English
- (30) Priority Data:  
1111516.9 1 July 2011 (01.07.2011) GB
- (71) Applicant (for all designated States except US): **THE UNIVERSITY OF BIRMINGHAM** [GB/GB]; Edgbaston, Birmingham, West Midlands B15 2TT (GB).
- (72) Inventors; and
- (75) Inventors/Applicants (for US only): **PIKRAMENOU, Zoe** [GR/GB]; c/o School of Chemistry, University of Birmingham, Edgbaston, Birmingham, West Midlands B15 2TT (GB). **ROGERS, Nicola** [GB/GB]; 63 Ashbrook Road, Stirchley, Birmingham, West Midlands B30 2XE (GB).
- (74) Agent: **WARD, David**; Marks & Clerk LLP, Alpha Tower, Suffolk Street Queensway, Birmingham B1 1TT (GB).

- (81) Designated States (unless otherwise indicated, for every kind of national protection available): AE, AG, AL, AM, AO, AT, AU, AZ, BA, BB, BG, BH, BR, BW, BY, BZ, CA, CH, CL, CN, CO, CR, CU, CZ, DE, DK, DM, DO, DZ, EC, EE, EG, ES, FI, GB, GD, GE, GH, GM, GT, HN, HR, HU, ID, IL, IN, IS, JP, KE, KG, KM, KN, KP, KR, KZ, LA, LC, LK, LR, LS, LT, LU, LY, MA, MD, ME, MG, MK, MN, MW, MX, MY, MZ, NA, NG, NI, NO, NZ, OM, PE, PG, PH, PL, PT, QA, RO, RS, RU, RW, SC, SD, SE, SG, SK, SL, SM, ST, SV, SY, TH, TJ, TM, TN, TR, TT, TZ, UA, UG, US, UZ, VC, VN, ZA, ZM, ZW.
- (84) Designated States (unless otherwise indicated, for every kind of regional protection available): ARIPO (BW, GH, GM, KE, LR, LS, MW, MZ, NA, RW, SD, SL, SZ, TZ, UG, ZM, ZW), Eurasian (AM, AZ, BY, KG, KZ, RU, TJ, TM), European (AL, AT, BE, BG, CH, CY, CZ, DE, DK, EE, ES, FI, FR, GB, GR, HR, HU, IE, IS, IT, LT, LU, LV, MC, MK, MT, NL, NO, PL, PT, RO, RS, SE, SI, SK, SM, TR), OAPI (BF, BJ, CF, CG, CI, CM, GA, GN, GQ, GW, ML, MR, NE, SN, TD, TG).

Published:

— with international search report (Art. 21(3))

(54) Title: COATED NANOPARTICLES

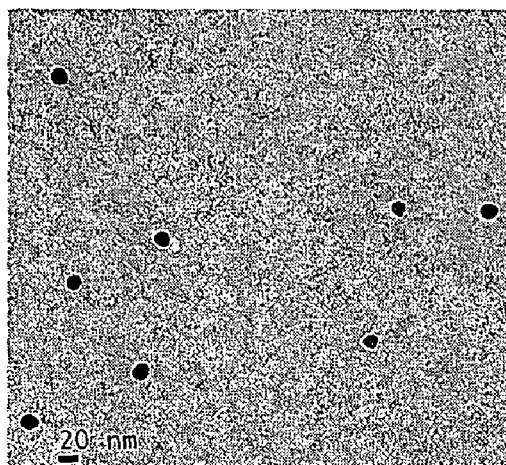


Figure 2

(57) Abstract: The present invention relates to a method for preparing a composition comprising nanoparticles of a noble metal functionalised with at least one type of metal complex and surfactant. The method comprises providing a first solution comprising nanoparticles and surfactant, and a second solution comprising a first type of metal complex, and adding the second solution to the first solution. Each nanoparticle has a loading of at least 500 and the method permits independent control of particle size and loading and enables large particles with high loading to be reproduced without agglomeration.

# High coating of Ru(II) complexes on gold nanoparticles for single particle luminescence imaging in cells†

Cite this: *Chem. Commun.*, 2014, 50, 617

Received 4th October 2013,  
Accepted 5th November 2013

DOI: 10.1039/c3cc47606e

www.rsc.org/chemcomm

Nicola J. Rogers,<sup>‡a</sup> Sunil Claire,<sup>‡b</sup> Robert M. Harris,<sup>c</sup> Shiva Farabi,<sup>a</sup> Gerald Zikeli,<sup>a</sup> Iain B. Styles,<sup>d</sup> Nikolaus J. Hodges<sup>\*c</sup> and Zoe Pikramenou<sup>\*a</sup>

**Gold nanoparticles are efficiently labelled with a luminescent ruthenium complex, producing 13 and 100 nm diameter, monodisperse red-emissive imaging probes with luminescence lifetimes prolonged over the molecular unit. Single, 100 nm particles are observed in whole cell luminescence imaging which reveals their biomolecular association with chromatin in the nucleus of cancer cells.**

The design of coordination metal complexes as cellular probes has attracted much research interest based on their distinctive/unique photophysical and electrochemical properties.<sup>1–3</sup> However, nanoscale probes are more ideal for detecting spatially localised cellular probes in luminescence imaging. Indeed, gold nanoparticles and quantum dots have been used for a plethora of biochemical and therapeutic applications.<sup>4–7</sup> We have combined these approaches, and demonstrated labelling gold nanoparticles (AuNPs) with luminescent metal complexes, so that the nanoprobe bears the distinct optical signature of the luminescent agent, independent of the particle properties.<sup>8,9</sup> Such designed probes offer multimodal detection taking advantage of gold's high electron density, and also lack the blinking effect observed in quantum dots. We demonstrated 13 nm AuNP coated with neutral (uncharged) lanthanide lumophores and different modalities to image them in cells.<sup>10</sup> When co-coated with a pH sensitive peptide, selective cell uptake could be achieved.<sup>11</sup>

To explore metal lumophores with still more efficient light excitation in the visible region, we have now chosen highly photo-stable ruthenium(II) polypyridyl complexes. However, a new strategy is required for the coating of AuNPs since the positive charge of the ruthenium complex leads to flocculation of the AuNPs in aqueous solutions; this challenge is addressed herein. Association of ruthenium complexes with AuNPs has previously been studied using electrostatic interactions,<sup>12</sup> thiol exchange methods using Brust-type<sup>13</sup> nanoparticles,<sup>14–17</sup> or by direct reduction of Au<sup>3+</sup> by NaBH<sub>4</sub>.<sup>18–20</sup> All of these methods lead to nanoparticles with sizes smaller than 10 nm that are relatively polydisperse, with limited control over the coating of the ruthenium probe. To increase sensitivity and spatial resolution in imaging,<sup>21</sup> nanoparticles with large Au cores and high number of labels are desirable.

In this communication, we now report an efficient coating method for water soluble gold nanoparticles, 13 (AuNP13) and 100 (AuNP100) nm in diameter, with a ruthenium complex that allows luminescence imaging of non-aggregated, single nanoparticles in cells, revealing interesting biomolecular interactions. The preparation of **RuS-AuNP13** and **RuS-AuNP100** was achieved by controlling the coating of the nanoparticle surface with a non-ionic fluorinated surfactant, Zonyl 7950 (Scheme 1) prior to the addition of the surface-active ruthenium complex, **RuSH** (ESI†). **RuSH** has two thiol groups for attachment to gold nanoparticles and a hexyl spacer group to distance the ruthenium centre from the surface.<sup>22</sup>

<sup>a</sup> School of Chemistry, The University of Birmingham, Edgbaston, B15 2TT, UK.  
E-mail: z.pikramenou@bham.ac.uk

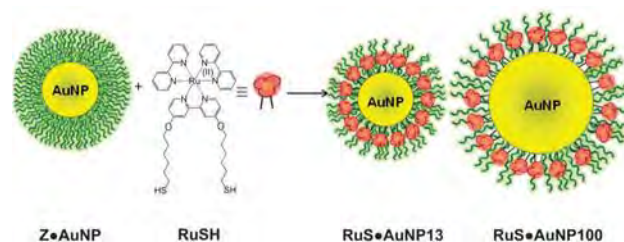
<sup>b</sup> PSIBS Doctoral Training Centre, The University of Birmingham, Edgbaston, B15 2TT, UK

<sup>c</sup> School of Biosciences, The University of Birmingham, Edgbaston, B15 2TT, UK.  
E-mail: hodgesn@adf.bham.ac.uk

<sup>d</sup> School of Computer Sciences, The University of Birmingham, Edgbaston, B15 2TT, UK

† Electronic supplementary information (ESI) available: Details of methods used in compound and nanoparticle synthesis and characterisation are provided together with cell imaging information and cytotoxicity results. See DOI: 10.1039/c3cc47606e

‡ Share equal contribution.



**Scheme 1** Controlling nanoparticle labelling with metal complexes to avoid flocculation. Method for preparation of **RuS-AuNP13** and **RuS-AuNP100**.

Zonyl<sup>®</sup> 7950 was chosen to stabilize nanoparticles and inhibit flocculation induced from the positively charged ruthenium complex. It bears a hydrophilic polar head group and a hydrophobic chain and its interaction with gold surfaces has been demonstrated.<sup>23–25</sup> We isolated and characterised the **Z-AuNP13** and **Z-AuNP100** and then added the **RuSH** complex to yield **RuS-AuNP13** and **RuS-AuNP100** (ESI<sup>†</sup>). The surface environment of the nanoparticle changes with the addition of the cationic complex and partial displacement of the surfactant as confirmed using zeta potential studies and X-ray photoelectron spectroscopy analysis of the Au 4f region. Analysis of the inductively-coupled plasma optical emission spectroscopy (ICP-OES) results, based on the Au:Ru ratio, gives  $10^3$  ruthenium complexes per **AuNP13** (ESI<sup>†</sup>). For the case of **RuS-AuNP100**, the number of RuS complexes per AuNP, was estimated to be  $10^5$  based on calculations from the <sup>1</sup>MLCT UV-Vis absorption of the supernatant from centrifugation due to their insufficient digestion for ICP-OES. The Zonyl enables a very high loading on the nanoparticles and the extent of loading per surface area is similar in both sizes, allowing for an estimated surface area of  $\sim 0.5 \times 0.5$  nm per ruthenium complex. The TEM images and dynamic light scattering studies confirm the uniformity of the nanoparticles. The **RuS-AuNP100** can also be tracked as single particles by NanoSight analysis (ESI<sup>†</sup>).

It is striking that isolated **RuS-AuNP13** and **RuS-AuNP100** display luminescence lifetimes of 340 ns and 360 ns ( $\pm 10\%$ ), indicating not only no quenching from the gold surface but indeed an enhancement compared to the free molecular **RuSH** complex  $260 \pm 6\%$  ns in water with 1% CH<sub>3</sub>CN. The larger particles can also be imaged as a *single RuS-AuNP100* in flow in a microchannel using luminescence microscopy (Fig. 1a). A luminescence spectrum, collected from the image, confirms the characteristic <sup>3</sup>MLCT profile centred at 640 nm with a blue shift from the free **RuSH** complex emission (650 nm), attributed to the influence of the Zonyl hydrophobic environment. To further examine the effect of the addition of **Z-AuNP** to **RuSH**, the luminescence lifetime of **RuSH** was monitored during addition of a solution of **Z-AuNP** to **RuSH** (Fig. 1b). A 50%

increase of the luminescence lifetime is observed upon binding of **RuSH** to **Z-AuNP100** or **Z-AuNP13** (Fig. 1b and ESI<sup>†</sup>). These titration results are consistent with the isolated **RuS-AuNP13** and **RuS-AuNP100** lifetimes. The saturation point in Fig. 1b is consistent with the  $10^5$  loading estimated above from UV-Vis absorption. The luminescence lifetime of **RuSH** mixed with Zonyl 7950 is 400 ns ( $\pm 3\%$ ), indicating that the effect of the Zonyl is the dominant cause of the extended lifetime of the nanoparticles.

To study the potential of **RuS-AuNP13** and **RuS-AuNP100** in cellular imaging, they were incubated with A549 human lung cancer cells. Cytotoxicity assays using both MTT (mitochondrial function) and adenylate kinase release (cell membrane integrity) showed that there was no statistically significant toxicity of the nanoparticles when compared to a water matched control, at concentrations of up to 5 times the concentration used for imaging studies (ESI<sup>†</sup>). To monitor the uptake and accumulation of particles in cells over time we performed a pulse-chase experiment (ESI<sup>†</sup>) using confocal fluorescence microscopy for detection. Interestingly, even after 3 days of the chase experiment, which we estimate as representing approximately three cell divisions based on the number of nuclei per field of view, many cells still contained labelled **RuS-AuNP13** particles, demonstrating the stability, long half-life and poor clearance of **RuS-AuNP13** particles. Although nuclear localisation could not be excluded, there was little or no evidence of **RuS-AuNP13** within the nucleus at any of the time points investigated. However, when the larger nanoparticles were used, more detailed information could be extracted. Cells incubated with **RuS-AuNP100** displayed clear visualisation of individual **RuS-AuNP100** nanoparticles as evidenced by both confocal luminescence and confocal reflection microscopy (Fig. 2).

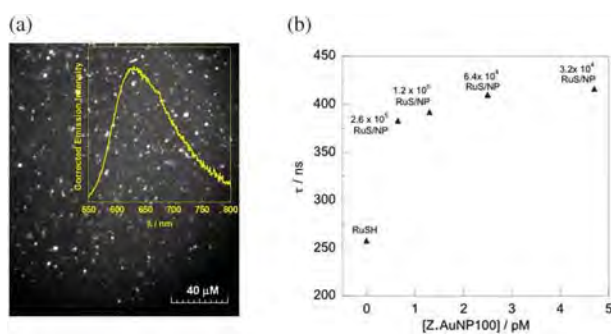


**Fig. 1** (a) Luminescence image and spectrum (inset) of a solution of **RuS-AuNP100** in flow within a 100  $\mu\text{m}$  deep, 1 mm wide ibidi microchannel, using epiluminescence microscopy.  $\lambda_{\text{exc}} = 450$  nm,  $\lambda_{\text{em}} > 510$  nm. The emission spectrum (inset) is taken from the field of view in the image. (b) Effect of nanoparticle addition to the lifetime of **RuSH** (0.17  $\mu\text{M}$ , 1% CH<sub>3</sub>CN in H<sub>2</sub>O) by monitoring the luminescence at 630 nm upon titration of **Z-AuNP100** 0–400  $\mu\text{M}$  (40 pM),  $\lambda_{\text{exc}} = 450$  nm.

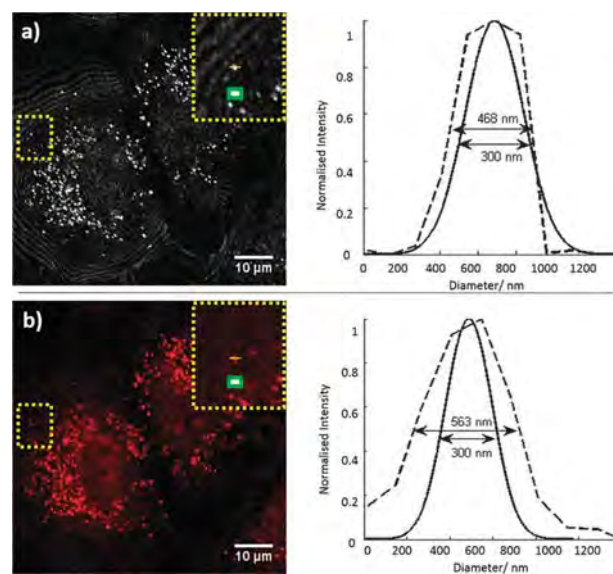


**Fig. 2** Confocal images of single **RuS-AuNP100** nanoparticles in A549 cells. (a) Reflection microscopy image  $\lambda_{\text{exc}} = 488$  nm,  $\lambda_{\text{em}} = 478$ –498 nm and (b) ruthenium luminescence image  $\lambda_{\text{exc}} = 453$  nm,  $\lambda_{\text{em}} = 555$ –800 nm. Respective comparisons of the measured point-spread function of the microscope convolved with a model of the nanoparticle sphere (solid-line), and the experimental intensity profile of a nanoparticle from the inset (dashed-line) are shown on the right. Scale bar 10  $\mu\text{m}$ , inset scale-bar 1  $\mu\text{m}$ , acquisition time 70 s.

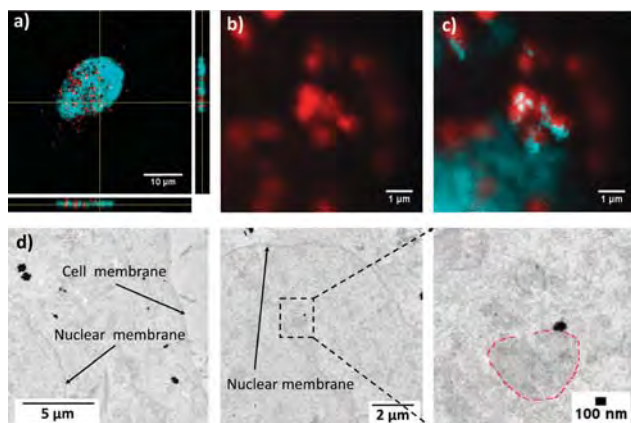


**Fig. 3** Imaging nuclear localisation of **RuS-AuNP100** in A549 cells. (a) Orthogonal view of the central z-stack slice (xz plane below, yz plane-right) from a single cell, illustrating ruthenium luminescence from within the central z-planes containing the Hoechst luminescence. (Scale bar 10  $\mu\text{m}$ ; acquisition time 75 s). (b) Ruthenium luminescence image and (c) corresponding overlay with Hoechst nuclear stain; acquisition time = 60 s, showing association of chromatin with **RuS-AuNP100** particles inside the nucleus (Scale bar 1  $\mu\text{m}$ ; acquisition time = 60 s). (d) Transmission electron micrographs (70–90 nm slice width) of A549 cell dosed with **RuS-AuNP100**; magnified inset shows interaction of nanoparticles with condensed chromatin (red dashed-line). Scale bars 5  $\mu\text{m}$ , 2  $\mu\text{m}$  and 100 nm.

Gold nanoparticles appear as bright spots in the confocal reflection images based on the strong scattering signal of the gold. The confocal luminescence signal confirms the ruthenium red luminescence of the particles (Fig. 2). Co-localisation of signals in the red and the reflection images confirm the stability of the nanoprobe after 24 h incubation. To further analyse the results, we used a convolution of the measured point-spread function from the confocal luminescence measurements using a simple model of the nanoparticle sphere (Fig. 2). The model predicts the estimated observable particle width in the luminescence images to be 250–300 nm (due to light diffraction effects) and is consistent with actual measurements performed. In complementary cell studies, the **RuS-AuNP13** are observed only as accumulations of nanoparticles, due to their smaller diameter and limited resolution (ESI<sup>†</sup>).

Analysis of the confocal luminescence images of the cells treated with **RuS-AuNP100** reveal co-localisation of red particles and Hoechst 33258 emission in some cells, confirming that few of these nanoparticles can localise in the nucleus (Fig. 3). This is in contrast to **RuS-AuNP13** which were absent from the nucleus, although this could be attributed to low spatial resolution as accumulations of the 13 nm AuNPs are required for their visualisation. Still more revealing is that some of the single nanoparticles appear to be localized to a condensed area of Hoechst staining, indicative of nuclear chromatin material containing genomic DNA (Fig. 3). The confocal luminescence images are further supported by TEM studies (Fig. 3). In the TEM images of the A549 cells treated with **RuS-AuNP100**, particles can be seen in close proximity to optically dense regions of the nucleus, which are attributed to condensed chromatin. These results indicate an interaction of the nanoparticles with chromatin that is visualised using the aforementioned microscopy techniques.

In conclusion, by employing the Zonyl 7950 surfactant we have achieved a very high loading of a luminescent transition metal complex on AuNPs of different sizes. This has enabled the design of nanoprobe that can be imaged at single nanoparticle resolution in cells by conventional and widely available optical microscopy methods. These nanoparticles do not present any significant cytotoxicity in cells and are stable in cells without losing their coating. Their strong luminescence allows imaging of particle association with DNA condensed material in the nucleus. These nanoprobe therefore present great potential in the detection and monitoring of biomolecular interactions at the level of a single nanoprobe. Applications may also be envisaged in the development of new nanomaterials with properties encoded by the grafted transition metal complex.

We wish to thank EPSRC, the Leverhulme Trust and the University of Birmingham for funding and support. Some instruments used in this study were supplied through Birmingham Science City: Innovative Uses for Advanced Materials in the Modern World (West Midlands Centre for Advanced Materials Project 2) with support from Advantage West Midlands (AWM) and partial funding from the European Regional Development Fund (ERDF).

## Notes and references

- 1 N. P. E. Barry and P. J. Sadler, *ACS Nano*, 2013, **7**, 5654–5659.
- 2 D.-L. Ma, H.-Z. He, K.-H. Leung, D. S.-H. Chan and C.-H. Leung, *Angew. Chem., Int. Ed.*, 2013, **52**, 7666–7682.
- 3 E. J. New, A. Congreve and D. Parker, *Chem. Sci.*, 2010, **1**, 111–118.
- 4 E. C. Dreaden, A. M. Alkilany, X. Huang, C. J. Murphy and M. A. El-Sayed, *Chem. Soc. Rev.*, 2012, **41**, 2740–2779.
- 5 D. A. Giljohann, D. S. Seferos, W. L. Daniel, M. D. Massich, P. C. Patel and C. A. Mirkin, *Angew. Chem., Int. Ed.*, 2010, **49**, 3280–3294.
- 6 K. Saha, A. Bajaj, B. Duncan and V. M. Rotello, *Small*, 2011, **7**, 1903–1918.
- 7 P. Nativo, I. A. Prior and M. Brust, *ACS Nano*, 2008, **2**, 1639–1644.
- 8 D. J. Lewis, T. M. Day, J. V. MacPherson and Z. Pikramenou, *Chem. Commun.*, 2006, 1433–1435.
- 9 A. C. Savage and Z. Pikramenou, *Chem. Commun.*, 2011, **47**, 6431–6433.
- 10 D. J. Lewis, C. Bruce, S. Bohic, P. Cloetens, S. P. Hammond, D. Arbon, S. Blair-Reid, Z. Pikramenou and B. Kysela, *Nanomedicine*, 2010, **5**, 1547–1557.
- 11 A. Davies, D. J. Lewis, S. P. Watson, S. G. Thomas and Z. Pikramenou, *Proc. Natl. Acad. Sci. U. S. A.*, 2012, **109**, 1852–1867.
- 12 T. Huang and R. W. Murray, *Langmuir*, 2002, **18**, 7077–7081.
- 13 M. Brust, M. Walker, D. Bethell, D. J. Schiffrin and R. Whyman, *Chem. Commun.*, 1994, 801–802.
- 14 M. Jebb, P. K. Sudeep, P. Pramod, K. G. Thomas and P. V. Kamat, *J. Phys. Chem. B*, 2007, **111**, 6839–6844.
- 15 P. Pramod, P. K. Sudeep, K. G. Thomas and P. V. Kamat, *J. Phys. Chem. B*, 2006, **110**, 20737–20741.
- 16 R. B. P. Elmes, K. N. Orange, S. M. Cloonan, D. C. Williams and T. Gunnlaugsson, *J. Am. Chem. Soc.*, 2011, **133**, 15862–15865.
- 17 L. Zedler, F. Theil, A. Csaki, W. Fritzsche, S. Rau, M. Schmitt, J. Popp and B. Dietzek, *RSC Adv.*, 2012, **2**, 4463–4471.
- 18 M. S. Vickers, J. Cookson, P. D. Beer, P. T. Bishop and B. Thiebaud, *J. Mater. Chem.*, 2006, **16**, 209–215.
- 19 Y. Yu, M. Zhou and H. Cui, *J. Mater. Chem.*, 2011, **21**, 12622–12625.
- 20 C. R. Mayer, E. Dumas, A. Michel and F. Sécheresse, *Chem. Commun.*, 2006, 4183–4185.
- 21 W. S. Chang, B. Willingham, L. S. Slaughter, S. Dominguez-Medina, P. Swanglap and S. Link, *Acc. Chem. Res.*, 2012, **45**, 1936–1945.
- 22 P. Bertonecello, E. T. Kefalas, Z. Pikramenou, P. R. Unwin and R. J. Forster, *J. Phys. Chem. B*, 2006, **110**, 10063–10069.
- 23 C. Lu, Y. Zu and V. W.-W. Yam, *Anal. Chem.*, 2007, **79**, 666–672.
- 24 Y. Tang, J. Yan, X. Zhou, Y. Fu and B. Mao, *Langmuir*, 2008, **24**, 13245–13249.
- 25 F. Li and Y. B. Zu, *Anal. Chem.*, 2004, **76**, 1768–1772.

# Silica Nanoparticles for Micro-Particle Imaging Velocimetry: Fluorosurfactant Improves Nanoparticle Stability and Brightness of Immobilized Iridium(III) Complexes

David J. Lewis,<sup>†,||</sup> Valentina Dore,<sup>‡,||</sup> Nicola J. Rogers,<sup>†,||</sup> Thomas K. Mole,<sup>†</sup> Gerard B. Nash,<sup>§</sup> Panagiota Angeli,<sup>\*,‡</sup> and Zoe Pikramenou<sup>\*,†</sup>

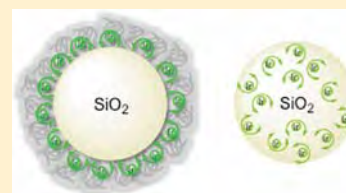
<sup>†</sup>School of Chemistry, University of Birmingham, Edgbaston, Birmingham B15 2TT, United Kingdom

<sup>‡</sup>Chemical Engineering Department, University College London, Torrington Place, London, WC1E 7JE, United Kingdom

<sup>§</sup>School of Clinical and Experimental Medicine, Medical School, University of Birmingham, Birmingham B15 2TT, United Kingdom

## Supporting Information

**ABSTRACT:** To establish highly luminescent nanoparticles for monitoring fluid flows, we examined the preparation of silica nanoparticles based on immobilization of a cyclometalated iridium(III) complex and an examination of the photophysical studies provided a good insight into the Ir(III) microenvironment in order to reveal the most suitable silica nanoparticles for micro particle imaging velocimetry ( $\mu$ -PIV) studies. Iridium complexes covalently incorporated at the surface of preformed silica nanoparticles, [Ir-4]@Si500-Z, using a fluorinated polymer during their preparation, demonstrated better stability than those without the polymer, [Ir-4]@Si500, as well as an increase in steady state photoluminescence intensity (and therefore particle brightness) and lifetimes which are increased by 7-fold compared with nanoparticles with the same metal complex attached covalently throughout their core, [Ir-4]@Si500. Screening of the nanoparticles in fluid flows using *epi*-luminescence microscopy also confirm that the brightest, and therefore most suitable particles for microparticle imaging velocimetry ( $\mu$ -PIV) measurements are those with the Ir(III) complex immobilized at the surface with fluorosurfactant, that is [Ir-4]@Si500-Z.  $\mu$ -PIV studies demonstrate the suitability of these nanoparticles as nanotracers in microchannels.



## INTRODUCTION

The miniaturization of chemical systems offers many advantages including continuous processing, improved yields or purity, and reduction of side-products and of waste.<sup>1–3</sup> Microfluidic devices incorporating novel channel architectures encourage mixing in a passive manner.<sup>4,5</sup> The increased surface to volume ratio means that interfacial phenomena such as Marangoni and Taylor flows become significant.<sup>6</sup> Such microchannels can also be used as high-throughput analytical platforms for a range of interesting targets<sup>7–9</sup> or as devices to extract certain molecules from solution.<sup>10</sup> Particle imaging velocimetry (PIV) is a popular image analysis technique used to extract Eulerian velocity fields by dividing a flow domain into windows of interrogation and using pairs of images to produce a displacement vector from a cross-correlation routine.<sup>11,12</sup> With the advent of micro-PIV ( $\mu$ -PIV),<sup>13</sup> smaller particles are required to investigate microchannels. Nanoparticles present a unique opportunity to exploit a bottom-up approach to materials fabrication to produce tracers for  $\mu$ -PIV. We have been interested in strategies for attaching luminescent probes in nanoparticles, using 13 nm gold nanoparticles as a scaffold on which to assemble metal complexes,<sup>14</sup> for their delivery and imaging into cells both selectively<sup>15</sup> and nonselectively.<sup>16</sup> We recently employed luminescent silica nanoparticles<sup>17</sup> based on their wider availability in sizes that can be tracked with high accuracy. Metal complexes incorporated into silica nano-

particles display far superior stability to that of organic dyes as fluorophores in  $\mu$ -PIV experiments,<sup>18</sup> thus conferring the benefit of an increased shelf life and solution recycling.

Iridium(III) polypyridyl complexes, especially cyclometalated complexes, have excellent photophysical properties within the set of  $d^6$  metals and often display high quantum yields.<sup>19</sup> The bright luminescence from iridium(III) complexes has been exploited for in vitro imaging applications<sup>20</sup> as well as incorporation into materials for organic light-emitting diodes (OLEDs).<sup>21,22</sup> While the incorporation of ruthenium(II) complexes into silica is fairly well explored,<sup>23–29</sup> reports of the incorporation of cyclometalated iridium(III) species, which in general are more hydrophobic, into silica are relatively few, by either covalent<sup>18,30</sup> or noncovalent means,<sup>31–33</sup> although supramolecular switches have been used to both entrap and release an iridium(III) complex in mesoporous silica using redox, light, pH changes, or electrochemical stimuli.<sup>34–37</sup>

To develop brightly luminescent nanoparticles with metal complexes for  $\mu$ -PIV applications an evaluation of the photophysical properties with the mode of metal complex attachment is highly desirable, to avoid issues with leakage of the lumophore that are unavoidable in simple adsorption-based

**Received:** August 16, 2013

**Revised:** September 30, 2013

**Published:** October 28, 2013